



ПЯТНАДЦАТЫЙ
МОСКОВСКИЙ
МЕЖДУНАРОДНЫЙ
СИМПОЗИУМ
ПО ИССЛЕДОВАНИЯМ
СОЛНЕЧНОЙ СИСТЕМЫ

21–25 ОКТЯБРЯ 2024

ИНСТИТУТ
КОСМИЧЕСКИХ
ИССЛЕДОВАНИЙ
МОСКВА

3

THE FIFTEENTH
MOSCOW
SOLAR SYSTEM
SYMPOSIUM

21–25 OCTOBER 2024

SPACE RESEARCH
INSTITUTE
MOSCOW

21 OCTOBER:

SESSION MARS

22 OCTOBER:

SESSION VENUS

SESSION GIANT PLANETS

23 OCTOBER:

SESSION MOON AND MERCURY

24 OCTOBER:

SESSION SMALL BODIES
(INCLUDING COSMIC DUST)

25 OCTOBER:

SESSION EXTRASOLAR PLANETS
SESSION ASTROBIOLOGY

ПЯТНАДЦАТЫЙ МОСКОВСКИЙ СИМПОЗИУМ ПО ИССЛЕДОВАНИЯМ СОЛНЕЧНОЙ СИСТЕМЫ 15M-S³

**октябрь 21-25, 2024
ИНСТИТУТ КОСМИЧЕСКИХ ИССЛЕДОВАНИЙ
РОССИЙСКОЙ АКАДЕМИИ НАУК
МОСКВА, РОССИЯ**

THE FIFTEENTH MOSCOW SOLAR SYSTEM SYMPOSIUM 15M-S³

**october 21-25, 2024
SPACE RESEARCH INSTITUTE
OF RUSSIAN ACADEMY OF SCIENCES
MOSCOW, RUSSIA**

спонсоры:

- Институт космических исследований РАН
- Институт геохимии и аналитической химии им. Вернадского РАН
- Брауновский университет (США)

sponsored by:

- Space Research Institute RAS
- Vernadsky Institute of Geochemistry and Analytical Chemistry RAS
- Brown University, USA

ISBN 978-5-00015-068-9

DOI: 10.21046/15MS3-2024

© Федеральное Государственное Бюджетное Учреждение Науки
ИНСТИТУТ КОСМИЧЕСКИХ ИССЛЕДОВАНИЙ РОССИЙСКОЙ АКАДЕМИИ НАУК (ИКИ РАН)
2024

TABLE OF CONTENT

INTRODUCTION

PROGRAM COMMITTEE

PROGRAM

overview PROGRAM

scientific PROGRAM

ABSTRACTS

INFORMATION

ADDRESS

METRO MAP

REGISTRATION AND INFORMATION DESK

ORAL SESSIONS, location

POSTER SESSIONS, location

INTERNET ACCESS AND WiFi

SOCIAL PROGRAM

LUNCH POINTS

THE FIFTEENTH MOSCOW SOLAR SYSTEM SYMPOSIUM 15M-S³

**SPACE RESEARCH INSTITUTE
MOSCOW, RUSSIA
october 21–25, 2024**

Starting from 2010, the Space Research Institute holds annual international symposia on Solar system exploration. Main topics of these symposia include wide range of problems related to formation and evolution of Solar system, planetary systems of other stars; exploration of Solar system planets, their moons, small bodies; interplanetary environment, astrobiology problems. Experimental planetary studies, science instruments and preparation for space missions are also considered at these symposia.

The Fifteenth Moscow international Solar System Symposium (15M-S3) will be held from October 21 till 25, 2024

THE FOLLOWING SESSIONS WILL BE HELD DURING THE SYMPOSIUM:

OPENING SESSION

- Session. MARS
- Session. VENUS
- Session. GIANT PLANETS
- Session. MOON AND MERCURY
- Session. SMALL BODIES (INCLUDING COSMIC DUST)
- Session. EXTRASOLAR PLANETS
- Session. ASTROBIOLOGY

Space Research Institute holds this symposium with participation of the following organizations:

- Vernadsky Institute of Geochemistry and Analytical Chemistry RAS, Russia
- Brown University, USA
- Schmidt Institute of Physics of the Earth RAS, Russia
- Keldysh Institute of Applied Mathematics RAS, Russia
- Kotelnikov Institute of Radio-engineering and Electronics RAS, Russia
- Sternberg Astronomical institute, Moscow State University, Russia

Symposium website: <https://ms2024.cosmos.ru>

Contact email address: ms2024@cosmos.ru

PROGRAM COMMITTEE

chair:

acad. **ZELNYI L.M.** IKI RAS

members:

BAZILEVSKIY A.T. GEOHI RAS

BIBRING J.-P. IAS,CNRS, France

BOROVIN G.K. Keldysh AMI RAS

HEAD III J. Brown University, USA

KORABLEV O.I. IKI RAS

KOSTITSYN Y.A. GEOHI RAS

MITROFANOV I.G. IKI RAS

RODIN A.V. IKI RAS

SHEVCHENKO V.V. GAISH MSU

SMIRNOV V.M. IRE RAS

TAVROV A.V. IKI RAS

VAISBERG O.L. IKI RAS

VOROBYOVA E.A. MSU

ZAKHAROV A.V. IKI RAS

ZASOVA L.V. IKI RAS

secretary:

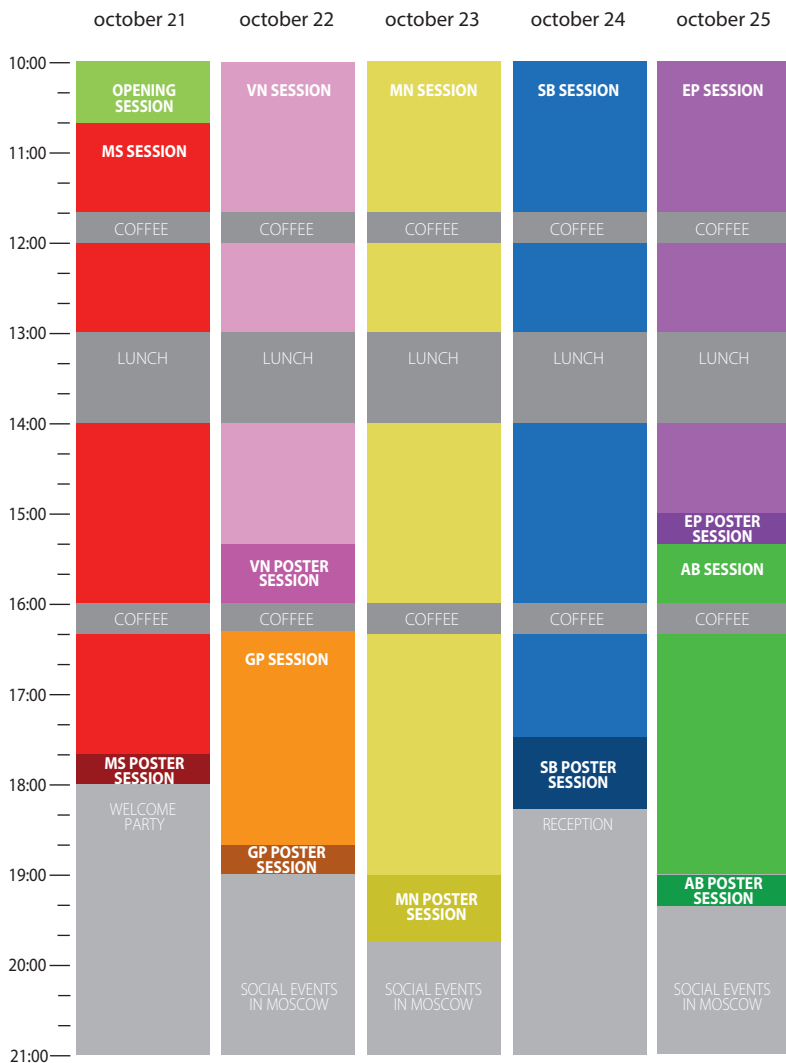
ROSTE O.Z. IKI RAS

PROGRAM

overview 15M-S³ program

THE FIFTEENTH MOSCOW SOLAR SYSTEM SYMPOSIUM

Space Research Institute, 21–25 October 2024



- **MS SESSION:** MARS SESSION
- **VN SESSION:** VENUS SESSION
- **GP SESSION:** GIANT PLANETS SESSION
- **MN SESSION:** MOON AND MERCURY SESSION
- **SB SESSION:** SMALL BODIES (INCLUDING COSMIC DUST) SESSION
- **EP SESSION:** EXTRASOLAR PLANETS SESSION
- **AB SESSION:** ASTROBIOLOGY SESSION

15M-S³ SCIENTIFIC PROGRAM

MONDAY, 21 OCTOBER 2024

10.00–10.40

OPENING SESSION

Convener: **Lev ZELENYI**
conference hall, second floor

10.40–18.05



MARS SESSION

Convener: **Oleg KORABLEV**
conference hall, second floor

10.40–11.00	Anna FEDOROVA et al	Mars-Express: 20 years of atmospheric and surface measurements in Mars orbit	15MS3-MS-01
11.00–11.15	Alexander LOMAKIN et al	Aerosol scattering correction of SPICAM-IR surface spectra	15MS3-MS-02
11.15–11.30	Mikhail LUGININ et al	HCl uptake on water ice aerosols in the atmosphere of Mars from the ACS MIR data	15MS3-MS-03
11.30–11.50	Alexander TROKHIMOVSKIY et al	Measurements of hydrogen chloride in Martian atmosphere during the aphelion season	15MS3-MS-04
11.50–12.10	COFFEE-BREAK		
12.10–12.30	Denis BELYAEV et al	Seasonal water vapor abundance and saturation in the Martian mesosphere and thermosphere	15MS3-MS-05
12.30–12.45	Dariia KOSSOVA et al	Study of diffusion regimes in the vertical structure of Martian atmosphere	15MS3-MS-06
12.45–13.00	Ekaterina STARICHENKO et al	2.5 years of observation of gravity wave activity in the Martian atmosphere from the ACS/TGO experiment	15MS3-MS-07
13.00–14.00	LUNCH		
14.00–14.20	Ekaterina CHOLOVSKAIA and Mikhail IVANOV	Clay minerals in the upper part of Nirgal Vallis, Mars	15MS3-MS-08
14.20–14.40	Mikhail IVANOV and James HEAD	Time constraints on the formation of valley networks on Alba Patera, Mars (preliminary results)	15MS3-MS-09
14.40–15.00	Jun CHU et al	Morphological features along the fixed contour lines indicating water level changes in the Holden crater on Mars	15MS3-MS-10
15.00–15.20	Egor KULIK and Tamara GUDKOVA	Constraints on the viscoelastic properties of the Martian mantle by the Chandler wobble period	15MS3-MS-11
15.20–15.40	Anton SALNIKOV et al	Challenges and Approaches in Constructing Mars' Magnetic Field Models from Satellite Data	15MS3-MS-12

15.40–16.00	Hui LI et al	Statistical Properties of Plateau-like Turbulence Spectra in the Martian Magnetosheath: Maven Observation	15MS3-MS-13
-------------	---------------------	---	-------------

16.00–16.20	COFFEE-BREAK
-------------	--------------

16.20–16.40	Jordanka SEMKOVA et al	Radiation environment on TGO Mars orbit during solar particle events in 2024	15MS3-MS-14
-------------	-------------------------------	--	-------------

16.40–17.00	Boris IVANOV	New craters on Mars – expanding catalog in 2023-2024	15MS3-MS-15
-------------	---------------------	--	-------------

17.00–17.20	Elena PODOBNAYA et al	An expanded catalog of recent meteoroid impact sites on Mars	15MS3-MS-16
-------------	------------------------------	--	-------------

17.20–17.40	Elena KARPOVICH et al	Unmanned aircraft for Mars exploration: preparing a scale model for flight tests	15MS3-MS-17
-------------	------------------------------	--	-------------

17.40–18.05	POSTER SESSION, SESSION MARS
-------------	------------------------------

5 posters * 5 min

Nadezhda CHUJKOVA et al	The evolution of Mars and the possible dynamics of its interior	15MS3-MS-PS-01
--------------------------------	---	----------------

Ekaterina CHOLOVSKAIA and Mikhail IVANOV	Geological structure of the upper part of Nirgal Vallis, Mars	15MS3-MS-PS-02
---	---	----------------

Tatiana MOROZOVA and Sergey POPEL	Instabilities in dusty plasma in the atmosphere of Mars associated with the passage of meteoroids	15MS3-MS-PS-03
--	---	----------------

Daria MOROZOVA and Oleg VAISBERG	Variation in Plasma Composition During the Rotation of Mars' Magnetopause	15MS3-MS-PS-04
---	---	----------------

Sergei KULIKOV and Alexander SKALSKY	Proxies to interplanetary conditions at Mars by an artificial neural network	15MS3-MS-PS-05
---	--	----------------

18.05–19.30	WELCOME PARTY
-------------	---------------

10.00–16.00

2 VENUS SESSION

Convener: **Ludmila ZASOVA**
conference hall, second floor

10.00–10.20	Masahiro TAKAGI et al	Planetary-scale waves and quasi-periodic variation of the equatorial jet in the Venus atmosphere	15MS3-VN-01
10.20–10.40	Jose SILVA et al	Stationary mesoscale features on Venus' dayside clouds	15MS3-VN-02
10.40–11.00	Liudmila ZASOVA et al	Peculiarities of the Venus Upper Cloud Layer Circulation During the 24 th Solar Activity Cycle	15MS3-VN-03
11.00–11.20	Dmitrij TITOV	Venus atmospheric dynamics: digging into the Venus Express observations	15MS3-VN-04
11.20–11.40	Yutian CAO et al	Modeling studies of Venusian ionosphere and upper atmosphere	15MS3-VN-05
11.40–12.00	COFFEE-BREAK		
12.00–12.15	Elizaveta FEDOROVA et al	Distributions of CO ₂ , HDO and H ₂ O concentration and temperature in the mesosphere of Venus based on SOIR/VEx observations for 2006–2014	15MS3-VN-06
12.15–12.30	Daria EVDOKIMOVA et al	Venus lower atmosphere properties from SPICAV-IR/VEX measurements in NIR transparency windows	15MS3-VN-07
12.30–12.45	Arina SHIMOLINA et al	Geological history of Theia Mons and graben system (mostly dyke swarm) mapping in the northern area of Beta Regio	15MS3-VN-08
12.45–13.00	Dmitry DOBRITSA et al	Meteoroid impacts analysis for a spacecraft en route to Venus	15MS3-VN-09
13.00–14.00	LUNCH		
14.00–14.20	Lev ZELENYI et al	Venera-D mission for comprehensive study of Venus	15MS3-VN-10
14.20–14.40	Vladislav ZUBKO et al	Analysis of the prospective mission scenario with determination of attainable landing sites on Venus under technical restrictions to lander-orbiter functioning	15MS3-VN-11
14.40–15.00	Piero D'INCECCO et al	The active volcanoes of Kamchatka as suitable terrestrial analogs within the AVENGERS initiative: an opportunity for in-situ operational tests for future landing Venus missions.	15MS3-VN-12
15.00–15.20	Joshita SHARMA	Payload Module for Long Duration Venus Exploration	15MS3-VN-13

Marina PATSAEVA et al	Wind speed variations at the Venus cloud top level from UVI/Akatsuki images (283 and 365 nm)	15MS3-VN-PS-01
Dmitry GORINOV et al	Horizontal winds in the lower clouds of Venus from VIRTIS/VEx and IR2/Akatsuki 1.74 μm observations	15MS3-VN-PS-02
Vladimir OGIBALOV et al	Emissions in the 4.3–1.05 μm bands of carbon dioxide molecules, outgoing from a planetary atmosphere on existence of a layer with wind velocity gradient	15MS3-VN-PS-03
Evgeniya GUSEVA and Mikhail IVANOV	The spatial-genetic relationship of the coronae sourcing lava flows and large volcanoes of Venus	15MS3-VN-PS-04
Danil MALYSHEV and Mikhail IVANOV	Preliminary insights into the evolution of central type volcanism on Venus	15MS3-VN-PS-05
Vladislav ZUBKO and A.A. BELYAEV	A simple geometrical approach for solving the eclipse problem	15MS3-VN-PS-06
Tamara GUDKOVA and Alexey BATOV	On load numbers for Venus	15MS3-VN-PS-07
Oliveira AMORIM and Tamara GUDKOVA	The effect of the dense atmosphere of Venus on the Love numbers	15MS3-VN-PS-08
Oliveira AMORIM and Tamara GUDKOVA	On the Chandler Wobble of Venus	15MS3-VN-PS-09
Oliveira AMORIM and Tamara GUDKOVA	The validation of the method for calculating the Chandler Wobble of Venus	15MS3-VN-PS-10



GIANT PLANETS SESSION

Convener: **Valery SHEMATOVICH**
conference hall, second floor

16.20–16.40	Igor ALEXEEV et al	Alfven wings in the sub-Alfvenic flow of magnetized plasma formed outside the magnetosphere of a celestial body, and the possible generation of auroras in the atmosphere of the central body and in the atmosphere of the satellite	15MS3-GP-01
16.40–17.00	Andrey KIRILLOV	The study of the role of metastable nitrogen in collisional molecular processes of the upper and middle atmosphere of Titan	15MS3-GP-02

17.00–17.20	Nikolai KISELEV et al	Changes in the longitude polarization dependence of Jupiter's moon Io as evidence of the long-term variability of its volcanic activity	15MS3-GP-03
17.20–17.40	Nikita SIMBIREV et al	The flight to Neptune and its moons Triton and Nereid as a demonstration of the possibility of using low-thrust engines in missions to giant planets	15MS3-GP-04
17.40–18.00	Anatoly GOLOVKOV and I.Yu. ILYINA	Calculation of the position of the beginning point of the galactic year in the orbit of the Solar system in the Galaxy	15MS3-GP-05
18.00–18.20	Philipp VYSIKAYLO	Non-stationary 3D perturbation theory for describing nonlinear interaction of electric field with matter in plasma with current. Vysikaylo's electric field shock waves and plasma nozzles	15MS3-GP-06
18.20–18.40	Zhonghua YAO	The Frontiers of Jovian Sciences and Perspective	15MS3-GP-07

18.40–19.00

POSTER SESSION, SESSION GIANT PLANETS

3 posters * 6 min

Vladimir VDOVICHENKO et al	Absorption variations in the ammonia bands of 645 and 790 nm along the central meridian of Jupiter in 2023	15MS3-GP-PS-01
Vladimir VDOVICHENKO et al	Investigation of variations in methane absorption bands along the central meridian of Jupiter in 2023	15MS3-GP-PS-02
Vladimir VDOVICHENKO	Methodological aspects of the study of ammonia-methane absorption variations in the atmosphere of Jupiter	15MS3-GP-PS-03

10.00–19.45

4 MOON AND MERCURY SESSION

Conveners: **Igor MITROFANOV, Maxim LITVAK**
conference hall, second floor

10.00–10.20	Alexander KOZYREV et al	MGNS experiment science investigation during cruise to Mercury onboard ESA MPO/BepiColombo mission	15MS3-MN-01
10.20–10.40	Zhiyong XIAO et al	Recent geological activity on Mercury	15MS3-MN-02
10.40–11.00	Olga CHERNENKO	Design and optimizing an interplanetary trajectory of a spacecraft to Mercury	15MS3-MN-03
11.00–11.20	Anton SANIN	Mapping of polar lunar water	15MS3-MN-04
11.20–11.40	Alexander BASILEVSKY et al	Lobate rimmed craters in PSR parts of the lunar south-polar craters Faustini and Shoemaker	15MS3-MN-05

11.40–12.00

COFFEE-BREAK

12.00–12.20	Ilia KUZNETSOV et al	Lunar dusty plasma and its investigation proposal	15MS3-MN-06
12.20–12.40	Michael SHPEKIN and R. T. FERREYRA	Lunar craters without signs of the matter melting and the matter emissions	15MS3-MN-07
12.40–13.00	Lianghai XIE and Lei LI	Global Hall MHD Simulations of the Solar Wind Implantation Flux on the Lunar Surface	15MS3-MN-08

13.00–14.00

LUNCH

14.00–14.20	Lev ZELENYI and Igor MITROFANOV	Lunar mission on the Northern and Southern Poles with two identical landers: goals and objectives	15MS3-MN-09
14.20–14.40	Mikhail MALENKOV et al	Development of a project of key objects of mobile robotics for the lunar station	15MS3-MN-10
14.40–15.00	Ivan AGAPKIN and Egor SOROKIN	Application of Selective Laser Melting for lunar soil analogue	15MS3-MN-11
15.00–15.20	Artem LYSENKO	3D printing of lunar regolith: testing physical conditions for implementation of SLM technology	15MS3-MN-12
15.20–15.40	Andrey SHUGAROV et al	A concept of a simple small-sized (5-10 kg) lunar astronomical UV telescope using high TRL components	15MS3-MN-13
15.40–16.00	Habibullo ABDUSSAMATOV	Moon-based continuous coordinate- photometric monitoring of the asteroid-comet hazard throughout the celestial sphere	15MS3-MN-14

16.00–16.20 COFFEE-BREAK

16.20–16.40	Huijuan WANG et al	Recent progress on the lunar-based UV-Optical-IR telescope for ILRS	15MS3-MN-15
16.40–17.00	Maya DJACHKOVA et al	Optical imaging of the Moon landing site, as the data for hazard avoidance	15MS3-MN-16

17.00–19.00 **LUNAR REGOLITH**
 Convener: Mikhail GERASIMOV
 conference hall, second floor

17.00–17.20	Svetlana DEMIDOVA et al	Unexpected components in Chang'E-5 soil sample	15MS3-MN-17
17.20–17.40	Egor SOROKIN et al	Experimental data on the occurrence and chemical composition of metallic iron nanospherules and comparison with data from the Chang'E-5 lunar soil	15MS3-MN-18
17.20–18.00	Mikhail GERASIMOV et al	Morphology of impact induced condensates: lunar findings and experiment	15MS3-MN-19
18.00–18.20	Maxim ZAITSEV et al	Volatiles in the lunar regolith delivered by Chang'E-5 mission: preliminary results	15MS3-MN-20
18.20–18.40	Sergei VOROPAEV et al	Olivine studies under lunar surface conditions	15MS3-MN-21
18.40–19.00	Lidiia LAKHMANOVA and Svetlana DEMIDOVA	Spinel-bearing lithologies in the lunar highland meteorites	15MS3-MN-22

19.00–19.45 **POSTER SESSION, SESSION MOON AND MERCURY**
 15 posters * 3 min

Jinsong PING et al	Preliminary ground optical polarization observation of the Moon	15MS3-MN-PS-01
Alexander BASILEVSKY et al	Photogeological analysis of ShadowCam images on the permanently shadowed floor of lunar crater Shoemaker	15MS3-MN-PS-02
Ekaterina FEOKTISTOVA and Zhanna RODIONOVA	Analysis of the crater depths in the polar regions of the Moon and Mercury	15MS3-MN-PS-03
Yury NEFEDYEV et al	Creation of a comprehensive fundamental selenographic catalog of impact craters based on data from modern lunar missions and satellite remote monitoring	15MS3-MN-PS-04
Yuri BONDARENKO et al	Radar mapping of the South Polar region of the Moon at 4.2 cm wavelength	15MS3-MN-PS-05

Alexander KOSOV et al	Moon's gravity field investigation by PKD instrument deployed on Luna-26 Orbiter	15MS3-MN-PS-06
Polina SAVVATIMOVA et al	Application of cryocooling systems for the mission of Lunar polar sample return	15MS3-MN-PS-07
Alexandra UVAROVA and M.Yu. MAKOVCHUK	Creation of soils-analogues for scientific equipment testing	15MS3-MN-PS-08
Alexander GUSEV et al	Infrastructure development of the Moon IX: 3D printing on lunar regolith	15MS3-MN-PS-09
Ekaterina FABER and R. R. KASPRANSKY	Challenges and innovations in lunar environment simulation for analog missions	15MS3-MN-PS-10
Olga TURCHINSKAYA and Evgeny SLYUTA	Landing site choice for Luna-27 mission in the Moon South Polar Region	15MS3-MN-PS-11
Alexander KRASILNIKOV et al	The three-dimensional geological model of the VIPER mission landing area	15MS3-MN-PS-12
Alexander SAFRONOV	Theory of the origin of terrestrial and lunar ores	15MS3-MN-PS-13
Vladimir NAZAROV et al	Joint Luna Data Center (JLDC) Project	15MS3-MN-PS-14
Azariy BARENBAUM	Influence of Sun, Moon and planets on Earth's gravitational field:discovery of gravitons and estimation their energy	15MS3-MN-PS-15

10.00–18.15

5 SMALL BODIES SESSION

including cosmic dust

Conveners: **Alexander BASILEVSKY**, **Alexander ZAKHAROV**
conference hall, second floor

10.00–10.20	Sergey POPEL et al	Dusty plasma processes in the vicinity of comets	15MS3-SB-01
10.20–10.40	Nikolay BORISOV	Influence of the dielectric permittivity of the surface layer on charging of dust grains on airless cosmic bodies	15MS3-SB-02
10.40–11.00	Alexander KROT and Irina SAVINYKH	Development of radiotomography algorithms for the study of electron clouds in the ionosphere and structures in the dusty plasma using low-orbital satellite systems	15MS3-SB-03
11.00–11.20	Vladimir BUSAREV et al	Sublimation-driven dust activity of primitive asteroids suggests that they contain water ice	15MS3-SB-04
11.20–11.40	Jian-Yang LI and DART Investigation Team	Long-Term Evolution of the Dimorphos Tail	15MS3-SB-05
11.40–12.00	COFFEE-BREAK		
12.00–12.10	Sergei IPATOV	Migration of bodies ejected from Mars	15MS3-SB-06
12.10–12.20	Evgeniya PETROVA and V. I. GROKHOVSKY	Experimental transformation of the Chelyabinsk LL5 meteorite matter of light-colored lithology into dark-colored lithology	15MS3-SB-07
12.20–12.30	Anna KARTASHOVA et al	Analysis of the meteor showers characteristics	15MS3-SB-08
12.30–12.40	Sergey PAVLOV et al	Association of sporadic meteors with NEAs of the rubble pile type	15MS3-SB-09
12.40–12.50	Akos KERESZTURI et al	Mineral changes by laboratory based proton irradiation on meteorites to understand space weathering and asteroid properties	15MS3-SB-10
12.50–13.00	Yulia IZVEKOVA et al	Atmospheric Dunes as Possible Manifestation of Meteoric Dusty Plasma	15MS3-SB-11
13.00–14.00	LUNCH		
14.00–14.10	Marina SHCHERBINA et al	Preliminary Results of the Polarimetric Observation Program of NEAs at the 2.6-m Telescope of CrAO and the 2-m Telescope of the Peak Terskol Observatory	15MS3-SB-12

14.10–14.20	Iliia KUZNETSOV et al	Ultraviolet irradiation influence on the Lunar dust dynamics	15MS3-SB-13
14.20–14.30	Mohamad ABDELAAL et al	Electromagnetic Phenomena in Dust Particle Dynamics under Simulated Martian Atmosphere: An Experimental Study	15MS3-SB-14
14.30–14.40	Alina MERKULOVA et al	The Effect of Cometary Outbursts on the Orbits of Comets in the Oort Cloud	15MS3-SB-15
14.40–14.50	Kristina LOBANOVA and Alexander MELNIKOV	Influence of size and shape of an asteroid on perturbations in its rotational dynamics during close approach to the Earth	15MS3-SB-16
14.50–15.00	Aleksandr TOLSTOY et al	3D shape reconstruction of an asteroid from its light curves as a convex polyhedron	15MS3-SB-17
15.00–15.10	Eduard KUZNETSOV et al	Analysis of scenarios for the formation of the young Emilkowalski asteroid family	15MS3-SB-18
15.10–15.20	Galina O. RYABOVA	The PSP/WISPR dust trail and the Geminid stream	15MS3-SB-19
15.20–15.30	Vladislav SIDORENKO	Some remarks about the Earth's quasi-satellites population	15MS3-SB-20
15.30–15.40	Gleb KUCHEROV et al	Accumulation and recombination of radicals as an energy source for active processes in icybodies of the Solar System	15MS3-SB-21
15.40–15.50	Andrey SHUGAROV and Boris SHUSTOV	A system to detect day-time asteroids (SODA) of the "Milky Way" project	15MS3-SB-22
15.50–16.00	Boris KONDRATYEV and V. S. KORNOUKHOV	Secular evolution and stability of rings around rotationally asymmetrical bodies. Revisiting the problem	15MS3-SB-23
16.00–16.20	COFFEE-BREAK		
16.20–16.30	Boris KONDRATYEV	The new formula for the angular velocity of rotating equilibrium figures	15MS3-SB-24
16.30–16.40	Maxim PUPKOV et al	Construction of transfer trajectories of the spacecraft to asteroids passing near Sun-Earth libration points	15MS3-SB-25
16.40–16.50	Yuri MEDVEDEV et al	On the outbursts of the Centaur 174P/Echeclus	15MS3-SB-26
16.50–17.00	Maxim NYRTSOV et al	Analysis of the surfaces of celestial bodies applying equal-area projections of the triaxial ellipsoid	15MS3-SB-27

17.00–17.10	Tatiana SALNIKOVA and E.I. KUGUSHEV	Long-term presence of cosmic masses near libration points	15MS3-SB-28
17.10–17.20	Roman ZOLOTAREV and Boris SHUSTOV	On the parameters of NEOs encounters with the Earth	15MS3-SB-29
17.20–17.30	Vladimir TCHERNYI and S.V. KAPRANOV	Unsolved problems of gravitational models of the origin of Saturn's visible dense rings and how J. K. Maxwell's discovery in 1865 that dense rings are not solid, but consist of separate pieces of matter, can help in this	15MS3-SB-30

17.30–18.15

**POSTER SESSION,
SESSION SMALL BODIES (INCLUDING COSMIC DUST)**

15 posters * 3 min

Maria SERGIENKO et al	Connection of the April chi-Librids meteor shower with Near-Earth asteroids	15MS3-SB-PS-01
Dmitry SHOKHRIN et al	Low-frequency nonlinear dust-acoustic perturbations in the dustymagnetosphere of Saturn: Zakharov-Kuznetsov equation description	15MS3-SB-PS-02
Stanislav KUZNETSOV and Vladimir BUSAREV	Dust injection into the plasma sheath near the surface of active asteroids	15MS3-SB-PS-03
Tatiana MOROZOVA and Sergey POPEL	The influence of the magnetic field on the processes occurring in the dusty plasma of meteoroid tails	15MS3-SB-PS-04
Yulia IZVEKOVA et al	Mercurian dusty exosphere: effects of anomalous dissipation	15MS3-SB-PS-05
Andrey DUBINSKY et al	Water formation on asteroids and dusty plasma system above the asteroid's surface	15MS3-SB-PS-06
Marina SHCHERBINA and D.A. KOVALEVA	Spectral analysis and classification of near-Earth and Mars-crossing asteroids using Gaia DR3 Data	15MS3-SB-PS-07
Valeria KHLESTUNOVA et al	New map of Europa: Update from Juno mission data	15MS3-SB-PS-08
Maksim KHOVRICHEV et al	Astrometric remeasurement of Pulkovo photographic observations of the 433 Eros taken from 1900 to 1940	15MS3-SB-PS-09
Maksim KHOVRICHEV et al	Verification of the association between the 2002GJ8, 2016 NO16 asteroids and the August Draconids (AUD)	15MS3-SB-PS-10

Vladimir EFREMOV et al	Determination of the small meteor particles properties from observational data	15MS3-SB-PS-11
Mirhusen NARZIEV and H.F. KHUJANAZAROV	Streams and associations of meteoroids according to the results of radar observations in HisAO for January 1970	15MS3-SB-PS-12
Vladimir VDOVICHENKO et al	Asteroid (4) Vesta: spectrophotometric presuppositions of the presence of a large crater 20 years before its discovery by the Dawn spacecraft.	15MS3-SB-PS-13
Nickolay PEROV and A.I. SMIRNOV	A model of giant planets satellites mass distributions over the semimajor axes of the orbits	15MS3-SB-PS-14
Nickolay PEROV and A. S. NIKOLAEVA	On the evolution of initial circular orbits of comets with variable mass	15MS3-SB-PS-15

18.15–20.00

RECEPTION

10.00–15.20

6 EXTRASOLAR PLANETS SESSION

Convener: **Alexander TAVROV**
conference hall, second floor

10.00–10.20	Sergei IPATOV	Migration of planetesimals in the TRAPPIST-1 and GLISSE 581 exoplanetary systems	15MS3-EP-01
10.20–10.40	Alexander KROT	Development of the analytical models of protoplanetary formation in extrasolar systems within the framework of the statistical theory	15MS3-EP-02
10.40–11.00	Eduard KUZNETSOV and Alexander PERMINOV	Study of stability of the compact planetary system K2-72	15MS3-EP-03
11.00–11.20	Anastasiia IVANOVA et al	The mass-period distribution of low-mass exoplanets discovered by the radial velocity method. Improvement of the observational selection correction method	15MS3-EP-04
11.20–11.40	Vladislava ANANYEVA and Alexander TAVROV	Website on exoplanets Planetary Systems (allplanets.ru)	15MS3-EP-05
11.40–12.00	COFFEE-BREAK		
12.00–12.20	Ildar SHAIKHISLAMOV et al	Kinetic modelling of the Super-Hot Jupiter Kelt9b	15MS3-EP-06
12.20–12.40	Anton KROTOV et al	Magnetosphere of Osiris in the stellar wind stream	15MS3-EP-07
12.40–13.00	Marina RUMENSKIKH et al	Chemical diversity of exoplanetary atmospheres and its observational evidence	15MS3-EP-08
13.00–14.00	LUNCH		
14.00–14.20	Anastasiia AVTAEVA et al	A self-consistent model of the influence of the host star on the atmosphere of sub-neptune GJ3470b	15MS3-EP-09
14.20–14.40	Roman EVDOKIMOV and Valery SHEMATOVICH	Comparative analysis of the photoevaporation and core-powered mass-loss efficiency for the atmosphere of the young mini-neptune HD207496b	15MS3-EP-10
14.40–15.00	Maksim GOLUBOVSKY et al	Measurement of reaction rates of metastable helium atom for astrophysical applications	15MS3-EP-11
15.00–15.20	POSTER SESSION, SESSION EXTRASOLAR PLANETS		
	2 posters * 10 min		
	Valery KOTOV	Superfast exoplanets and motion of the Sun and Earth	15MS3-EP-PS-01
	Elena BELENKAYA	Magnetic exoplanets in the sub-Alfvénic stellar wind may act as a kind of interplanetary magnetic field collimator	15MS3-EP-PS-02

15.20–19.20

7 ASTROBIOLOGY SESSION

Convener: **Oleg KOTSYURBENKO**
conference hall, second floor

15.20–15.40	Vladimir KOMPANICHENKO	Thermodynamic transformation of organic microsystems as an impetus for the emergence of life forms on Earth and other planets	15MS3-AB-01
15.40–16.00	Sergey BULAT et al	Thermophiles: the extraordinary extraterrestrials next door	15MS3-AB-02
16.00–16.20	Oleg KOTSYURBENKO	Systems approach to astrobiology	15MS3-AB-03
16.20–16.40	COFFEE-BREAK		
16.40–17.00	Yuming FU et al	Surface Bacterial Dynamics and Biosafety Assessment during the Lunar Palace 365 Bioregenerative Experiment	15MS3-AB-04
17.00–17.20	Valery SHEMATOVICH et al	Astrobiological issues of the auroral nitric oxide formation in the N ₂ -O ₂ atmospheres of the terrestrial-type planets	15MS3-AB-05
17.20–17.40	Sohan JHEETA	Reactive Oxygen Species: Possible Implications for the Emergence of Life	15MS3-AB-06
17.20–18.00	Frank TRIXLER	No problem with the water problem: using ubiquitous nanogeochemical conditions to achieve abiotic RNA synthesis in water	15MS3-AB-07
18.00–18.20	Anatoliy K. PAVLOV	Nearby Supernovas and Gamma Ray Bursts as possible sources the sharply increase of mutations rate and lethal effects for Earth's biosphere	15MS3-AB-08
18.20–18.40	Mikhail ZARUBIN et al	Biological researches in the deep underground facilities of Baksan Neutrino Observatory and it's relevance to astrobiology analogue studies	15MS3-AB-09
18.40–19.00	Ximena ABREVAYA et al	The EXO-UV program: latest advances of experimental studies to investigate the biological impact of UV radiation on exoplanets	15MS3-AB-10

19.00–19.20

POSTER SESSION, SESSION ASTROBIOLOGY

2 posters * 10 min

Alexander TERTYSHNIKOV	Variations of F10,7 on new dates of meteor shower maxima	15MS3-AB-PS-01
Alexander GURIDOV et al	Bacteria of the coolant fluid Triol from the active thermal control system of the International Space Station	15MS3-AB-PS-02

ABSTRACTS

SESSION 1. MARS (MS)
ORAL SESSION

MARS-EXPRESS: 20 YEARS OF ATMOSPHERIC AND SURFACE MEASUREMENTS IN MARS ORBIT

A. A. Fedorova¹, O. Korablev¹, L. Zasova¹, N. Ignatiev¹,
A. Trokhimovskiy¹, A. Lomakin¹, F. Montmessin², M. Giuranno³,
J.-P. Bibring⁴ and all CoIs and scientists of PFS, OMEGA and SPICAM
teams

¹ Space Research Institute RAS, Moscow, Russia, fedorova@cosmos.ru

² LATMOS-UVSQ, Guyancourt, France

³ IAPS Istituto di Astrofisica e Planetologia Spaziali, INAF Istituto Nazionale di Astrofisica, Rome, Italy

⁴ Institut d'Astrophysique Spatiale, Orsay, France

KEYWORDS:

Mars-Express, Mars, atmosphere, surface, spectroscopy

ABSTRACT:

In 2024, it was 20 years since the Mars Express orbiter began its scientific program in orbit around Mars. The spacecraft has several spectrometers on board, from the UV to the thermal IR spectral range, and Russian scientists made a major contribution to its development and data processing. These are the PFS (Planetary Fourier Spectrometer), OMEGA (Observatoire pour la Mineralogie, l'Eau, les Glaces et l'Activite), and SPICAM (Spectroscopy for the Investigation of the Characteristics of the Atmosphere of Mars) spectrometers. Over the years of the mission's operation, a large amount of information on the composition, structure, and dynamics of the Martian atmosphere has been obtained. Long-term observations made it possible to conduct research on climate stability on the planet for the first time on Mars. The absorption bands of ice and minerals in the IR range allows to study the composition and seasonal changes in the polar caps, mapping the distribution of minerals on the surface of Mars, and construct the geological history of Mars. To 2024 some spectrometers stopped working, but the SPICAM IR channel and the OMEGA visible channel are still operating onboard the spacecraft. The results of the twenty-year operation of Mars-Express were published in the special issue of Space Science Reviews [1–6]. This work will present the most striking results in the field of studying the atmosphere and surface of Mars, obtained with the participation of Russian scientists.

REFERENCES:

- [1] Montmessin F., Fedorova A., Alday J. et al. Mars' Water Cycle and Escape: A View from Mars Express and Beyond // Space Sci Rev 220, 77 (2024). <https://doi.org/10.1007/s11214-024-01099-6>.
- [2] Vandaele A. C., Aoki S., Bauduin S. et al. Composition and Chemistry of the Martian Atmosphere as Observed by Mars Express and ExoMars Trace Gas Orbiter // Space Sci Rev 220, 75 (2024). <https://doi.org/10.1007/s11214-024-01109-7>.
- [3] Määttänen A., Fedorova A., Giuranna M. et al. Dust and Clouds on Mars: The View from Mars Express // Space Sci Rev 220, 63 (2024). <https://doi.org/10.1007/s11214-024-01092-z>.
- [4] González-Galindo F., Gérard J.C., Soret L. et al. Airglow and Aurora in the Martian Atmosphere: Contributions by the Mars Express and ExoMars TGO Missions // Space Sci Rev 220, 42 (2024). <https://doi.org/10.1007/s11214-024-01077-y>.
- [5] Sánchez-Lavega A., del Río-Gaztelurrutia T., Spiga A. et al. Dynamical Phenomena in the Martian Atmosphere Through Mars Express Imaging // Space Sci Rev 220, 16 (2024). <https://doi.org/10.1007/s11214-024-01047-4>.
- [6] Cardesin-Moinelo A., Godfrey J., Grotheer E. et al. Mars Express: 20 Years of Mission, Science Operations and Data Archiving // Space Sci Rev 220, 25 (2024). <https://doi.org/10.1007/s11214-024-01059-0>.

AEROSOL SCATTERING CORRECTION OF SPICAM-IR SURFACE SPECTRA

A. Lomakin^{1,2}, A. Fedorova², F. Montmessin³, O. Korablev²

¹ HSE University, Moscow, Russia, aleksander.lomakin96@gmail.com

² Space Research Institute RAS, Moscow, Russia

³ LATMOS, UVSQ Université Paris-Saclay, Sorbonne Université, CNRS Paris, France

KEYWORDS:

aerosols, IR spectroscopy, surface of planets, planetary ices, CO₂ ice

INTRODUCTION:

Atmosphere of Mars is rather dusty, which leads to light being scattered significantly while traveling through the atmosphere. Failure to account for this scattering results in systematic errors of retrievals of surface albedos or parameters of various gases in the Mars atmosphere [1, 2].

Earlier, we used SPICAM-IR [3], a near infrared (1–1.7 μm) spectrometer to map CO₂ ice and H₂O ice on the surface of Mars. Both ices have absorption bands in the SPICAM-IR spectral range. We used depth of absorption bands in spectral reflectance to map the prevalence of both ices on the surface of Mars. Scattering on the dust is known to modify surface albedo, which leads to significantly less deep absorption bands.

We used a 16-stream multiple scattering algorithm (DISORT [4]) with MCD 6.1 (PCM) [5] as a forward model of radiative transfer, and then used it to retrieve surface albedo from SPICAM-IR spectra. We show a clear spectra of CO₂ and H₂O in the spectral range 1–1.7 μm and present the effect of the dust correction on mapping of polar ice on Mars. We also show maps of CO₂ and H₂O ice cleared from dust scattering.

REFERENCES:

- [1] Langevin Y., Doute S., Vincendon M. et al. No signature of clear CO₂ ice from the “cryptic regions” in Mars’ south seasonal polar cap // *Nature*. 2006. V. 442. P. 790–792. <https://doi.org/10.1038/nature05012>
- [2] Wolff M.J., Smith M.D., Clancy R. T. et al. Wavelength dependence of dust aerosol single scattering albedo as observed by the Compact Reconnaissance Imaging Spectrometer // *J. Geophys. Res.* 2009. V. 114. Article 2009JE003350. <https://doi.org/10.1029/2009JE003350>
- [3] Korablev O., Bertaux J.-L., Fedorova A. et al. SPICAM IR acousto-optic spectrometer experiment on Mars Express // *J. Geophysical Research: Planets*. 2006. V. 111.
- [4] Stamnes K., Tsay S.-C., Wiscombe W., Jayaweera K. Numerically stable algorithm for discrete-ordinate-method radiative transfer in multiple scattering and emitting layered media // *Applied Optics*. 1988. V. 27. Iss. 12. P. 2502–2509. <https://doi.org/10.1364/AO.27.002502>.
- [5] Forget F. et al. Improved general circulation models of the martian atmosphere from the surface to above 80 km // *J. Geophysical Research: Planets*. 1999. V. 104(E10). P. 24155–24175. DOI: 10.1029/1999je001025.

HCL UPTAKE ON WATER ICE AEROSOLS IN THE ATMOSPHERE OF MARS FROM THE ACS MIR DATA

M. Luginin¹, A. Trokhimovskiy¹, B. Taysum², A. Fedorova¹,
O. Korablev¹, K. Olsen³, F. Montmessin⁴, F. Lefevre⁴

¹ Space Research Institute RAS, Moscow, Russia
mikhail.luginin@phystech.edu

² German Aerospace Center, Institute of Planetary Research, Berlin, Germany

³ Department of Physics, University of Oxford, Oxford, UK

⁴ LATMOS/CNRS, Universite Paris-Saclay, Sorbonne Universite, Guyancourt, France

KEYWORDS:

infrared observations, atmosphere of Mars, solar occultation, atmospheric chemistry

INTRODUCTION:

In 2020, hydrogen chloride (HCl) in the gas phase was discovered in the atmosphere of Mars with the Atmospheric Chemistry Suite (ACS) onboard the Trace Gas Orbiter (TGO) mission [1]. Observations reveal a seasonal increase in the volume mixing ratio (VMR) up to 5 ppbv during the perihelion season, followed by a sudden drop down to undetectable values (<0.1 ppbv) [2, 3]. The fast disappearance of HCl from the atmosphere is at variance with previous estimations of a few months HCl lifetime based on gas-phase chemistry [3, 4].

Based on the laboratory measurements [5], the uptake of HCl onto water ice cloud particles could play an significant role [1, 3]. In this work, we show observational evidence of a pronounced HCl and water ice anticorrelation above 20 km, manifested as particularly HCl-rich layers at altitudes where water ice was absent. This result supports the rapid HCl removal mechanism competing with atmospheric mixing at a diurnal rate.

OBSERVATIONS:

We have analysed data collected by ACS during the second half of the Martian year (MY) 34 and covering two complete MY 35 and MY 36. In all, we analysed 784 occultations providing profiles of temperature, HCl (if any), water vapor, and aerosol extinction and mass loading.

METHOD OF ANALYSIS:

The retrieval of HCl profile abundances is based on the iterative Levenberg-Marquardt algorithm with Tikhonov regularisation. We retrieve volume mixing ratios of HCl from the ACS MIR data covering wavenumber range 2922.5–2927.4 cm⁻¹; the uncertainty on the retrieved quantities is given by the covariance matrix of the solution. The temperature and water vapor profiles used as a priori information are taken from available ACS NIR products.

Simultaneous measurements of continuum absorption by ACS NIR in the 0.76–1.6 μm spectral range and ACS MIR in the 3.09–3.46 μm is used to determine microphysical properties of dust and water ice particles. The “onion peeling” technique is applied to obtain vertical profiles of the spectral dependence of aerosol extinction coefficient, which are then fitted to produce the effective radius, number density, and mass loading of water ice and dust.

RESULTS:

An example of a local anticorrelation between HCl and water ice is shown in Figure 1. At 40–50 km, a gap in aerosol extinction at ~3 μm (water ice band) indicates an absence of water ice, while mineral dust particles can still be detected (Panels A and B). HCl is found to be maximum at altitudes where water ice is missing (Panel C), suggesting rapid hydrogen chloride uptake on water ice.

Out of the 137 occultations with prominent HCl abundances and 93 observations with water ice gap observed during the perihelion season, 11 were found to intersect and feature clear “HCl in ice-holes” cases with measurable water ice load above and below the hydrogen chloride maximum. Panel D of the Figure shows profiles of HCl VMR and aerosol extinction at 3.1 μm from those observations. In order to compare the various cases, all profiles have been normalized to [0,1] and vertically shifted to align all HCl maxima at 45 km. The averages of normalized profiles (bold lines) clearly demonstrate an anticorrelation between HCl and water ice.

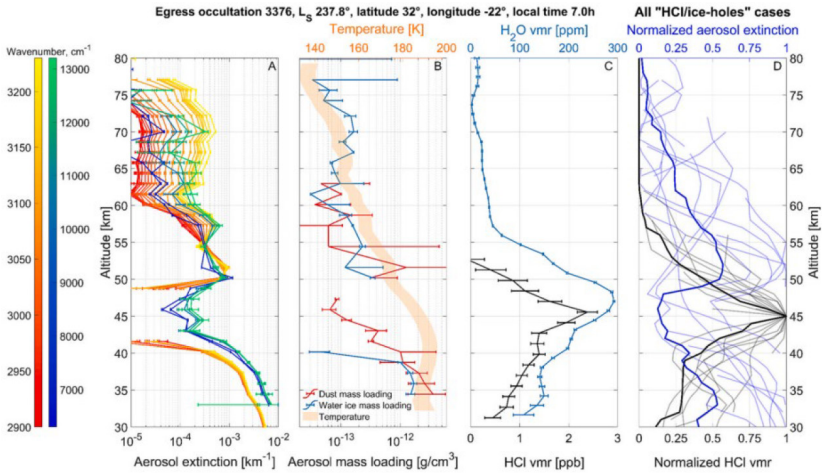


Fig. 1. An illustration of the anticorrelation between the HCl abundance and water ice from a single observation (Panels A, B, and C) and from all “HCl in ice-holes” cases (Panel D). Panel A: The aerosol extinction profiles at 3.09–3.46 μm and 0.76–1.6 μm measured by MIR and NIR, respectively. Panel B: Retrieved aerosol mass loading profiles of dust (red) and water ice (blue), bottom axes; temperature profile retrieved from NIR data. Panel C: volume mixing ratio of HCl and H_2O . Panel D: profiles of HCl VMR (black lines) and aerosol extinction at 3.1 μm (blue lines) normalized to [0, 1] and shifted to align all HCl maxima at 45 km; mean profiles are shown in bold.

REFERENCES:

- [1] Korabev O., Olsen K. S., Trokhimovskiy A. et al. Transient HCl in the atmosphere of Mars // *Science Advances*. 2021. V. 7. Iss. 7. 9 p. <https://doi.org/10.1126/sciadv.abe4386>.
- [2] Olsen K. S., Trokhimovskiy A., Montabone L. et al. 2021. Seasonal reappearance of HCl in the atmosphere of Mars during the Mars year 35 dusty season // *Astronomy and Astrophysics*. 2021. V. 647. Article A161. 14 p. <https://doi.org/10.1051/0004-6361/202140329>.
- [3] Aoki S., Daerden F., Viscardy S. et al. Annual appearance of hydrogen chloride on Mars and a striking similarity with the water vapor vertical distribution observed by TGO/NOMAD // *Geophysical Research Letters*. 2021. V. 48. Iss. 11. Article e2021GL092506. 11 p. <https://doi.org/10.1029/2021GL092506>.
- [4] Krasnopolsky V. A. Photochemistry of HCl in the martian atmosphere // *Icarus*. 2022. V. 374. <https://doi.org/10.1016/j.icarus.2021.114807>.
- [5] Kippenberger M., Schuster G., Lelieveld J., Crowley J. N. et al. Trapping of HCl and oxidised organic trace gases in growing ice at temperatures relevant to cirrus clouds // *Atmospheric Chemistry and Physics*. 2019. V. 19, Iss. 18. P. 11939–11951. <https://doi.org/10.5194/acp-19-11939-2019>.

MEASUREMENTS OF HYDROGEN CHLORIDE IN MARTIAN ATMOSPHERE DURING THE APHELION SEASON

A. Trokhimovskiy, O. I. Korablev, A. A. Fedorova

Space Research Institute RAS, Moscow, Russia, trokh@cosmos.ru

KEYWORDS:

Mars atmosphere, minor species, solar occultation, infrared spectroscopy

ABSTRACT:

Mars is reputed to lack ongoing volcanic activity. However, its dynamic interior was revealed by Insight, and clues to volcanism younger than 1 million years have accumulated, possibly associated with seismic activity at Cerberus Fossae and the Alba Mons volcano. Volcanic gases were identified as one of the primary targets of the ExoMars Trace Gas Orbiter (TGO) mission. While SO_2 would testify to ongoing eruptive activity, evidence of active magma chambers in pre- and post-eruptive periods may be better identified by seepage of other gases, such as hydrogen chloride (HCl). TGO spectrometers reported HCl at ppb levels in the atmosphere of Mars in the perihelion period (southern spring and summer), but seasonality and spread were used to infer an atmospheric source. Here, we report HCl detections by the Atmospheric Chemistry Suite (ACS) of TGO in the aphelion season north and east of the Alba Mons volcano. Existing atmospheric models cannot explain these observations. Using CaSSIS and HiRISE cameras of TGO and Mars Reconnaissance Orbiter, we identify narrow (<1 m), fresh fissures not reported before, which we interpret to be HCl channels rooted into active igneous bodies at depth, interacting with the permafrost closer to the surface, and seeping to the atmosphere. Our results are interpreted as the first evidence of ongoing igneous processes in the Martian interior.

SEASONAL WATER VAPOR ABUNDANCE AND SATURATION IN THE MARTIAN MESOSPHERE AND THERMOSPHERE

D. A. Belyaev¹, A. A. Fedorova¹, J. Alday², A. Trokhimovskiy¹,
F. Montmessin³, O. I. Korablev¹

¹ Space Research Institute RAS, Moscow, Russia, dbelyaev@cosmos.ru

² School of Physical Sciences, The Open University, Milton Keynes, UK

³ LATMOS/CNRS, Université Paris-Saclay, Sorbonne Université
Guyancourt, France

KEYWORDS:

Martian atmosphere, water vapor, mesosphere, thermosphere, IR spectroscopy, water escape, water saturation

INTRODUCTION:

We present water vapour distribution encompassing the mesosphere and thermosphere of Mars, from 50 to 125 km, exceeding the maximum altitudes where remote sensing has been able to observe water to date. The altitude profiles emphasize Martian Years (MY) from 34th to 37th including the last Global Dust Storm (GDS) in MY34. Our results are based on solar occultation measurements in the 2.66–2.70 μm wavelength range by Atmospheric Chemistry Suite (ACS) on board the ExoMars Trace Gas Orbiter (TGO) [1]. This spectral range possesses strong CO_2 and H_2O absorption lines allowing sensitive temperature and density retrievals in the mesosphere and thermosphere [2].

RESULTS:

We report that the maximum water mixing ratio varies from 10 to 50 ppmv at 100–125 km during dust seasons (GDS and regional storms), as well as at the southern summer of MY34–MY37. During other seasons water remains below 2 ppmv, especially at aphelion. We have also estimated the condition of water saturation using simultaneously retrieved temperature and pressure profiles [3]. A supersaturation of water is observed during perihelion above 80 km, where the saturation ratio exceeds 10. Those values confirm recent results by Fedorova et al. [4] derived from the near-IR channel of ACS below 100 km. The observed seasonal high water abundance and saturation in the transit zone of mesosphere/thermosphere increases density of the atomic hydrogen fed by photolysis of H_2O molecule that subsequently rises its escape from the planet.

REFERENCES:

- [1] Korablev O.I. et al. The Atmospheric Chemistry Suite (ACS) of three spectrometers for the ExoMars 2016 trace gas orbiter // Space Science Reviews. 2018. V. 214. No. 1. <https://doi.org/10.1007/s11214-017-0437-6>.
- [2] Belyaev D.A. et al. Revealing a high water abundance in the upper mesosphere of Mars with ACS onboard TGO // Geophysical Research Letters. 2021. Article e2021GL093411. <https://doi.org/10.1029/2021GL093411>.
- [3] Belyaev D.A. et al. Thermal structure of the middle and upper atmosphere of Mars from ACS/TGO CO_2 spectroscopy // J. Geophysical Research: Planets. 2022. V. 127. Article e2022JE007286. <https://doi.org/10.1029/2022JE007286>.
- [4] Fedorova A. A. et al. A two-Martian years survey of the water vapor saturation state on Mars based on ACS NIR/TGO occultations // J. Geophysical Research: Planets. 2022. V. 128. Article e2022JE007348. <https://doi.org/10.1029/2022JE007348>.

STUDY OF DIFFUSION REGIMES IN THE VERTICAL STRUCTURE OF MARTIAN ATMOSPHERE

D. A. Kossova¹, D. A. Belyaev^{2,1}, E. S. Starichenko², A. S. Medvedev³

¹ HSE University, Faculty of Physics, Moscow, Russia, dakossova@edu.hse.ru

² Space Research Institute RAS, Moscow, Russia

³ Max Planck Institute for Solar System Research, Göttingen, Germany

KEYWORDS:

Martian atmosphere, turbulent diffusion, solar occultation, homopause, temperature

ABSTRACT:

In the vertical structure of the Martian atmosphere turbulent and molecular diffusion regimes can be distinguished. Turbulent diffusion dominates in the lower atmosphere, the homosphere, where molecules are uniformly mixed with each other. In the upper, less dense, atmosphere (namely the heterosphere) molecular mixing with diffusive separation of individual gas components prevails. A boundary layer, where turbulent diffusion changes to the molecular one that is individual for each component, is called homopause (located in a range of heights from 100 to 130 km) [1]. When modeling the vertical transport of atmospheric particles a consideration of the mentioned diffusion coefficients plays a significant role. Currently, there is no universal method for determining the coefficient of turbulent diffusion due to its complex nature, which combines various dynamic processes including internal gravity waves. Generally, due to the lack of experimental data on the distribution of wind speed and temperature, the literature provides empirical formulas for calculating this coefficient, as well as the corresponding correction parameters [2, 3]. For the most accurate estimation of the diffusion coefficients the vertical distribution of atmospheric density and temperature is necessary, especially in the homopause region, where both turbulent and molecular components need to be considered.

This paper presents an analysis of the vertical temperature and density profiles derived from measurements by the Russian spectrometric complex ACS (Atmospheric Chemistry Suite) onboard TGO (Trace Gas Orbiter) of the ExoMars mission [4]. Since April 2018, the middle infrared channel of ACS (ACS-MIR) has been sounding the Martian atmosphere in the solar occultation mode. The instrument, being an echelle spectrometer, measures atmospheric transmission spectra with high sensitivity and resolving power (~30 000) in the carbon dioxide absorption bands around 2.7 μm . It allows retrieving the density and temperature of the atmosphere over a wide range of altitudes (from 10 to 180 km), covering the troposphere, mesosphere and thermosphere of Mars [5]. Based on the ACS data, various approaches to determine diffusion coefficients are considered, namely parametric models [2, 6] and a method that takes into account the contribution of wave effects in the atmosphere [7]. According to the results of the processed observations over 2.5 Martian years, seasonal and latitudinal variations of the homopause altitude have been revealed, as well as its dependence on atmospheric density and diffusion coefficients in this transition region.

REFERENCES:

- [1] *Bougher S.W. et al.* Chapter 14: Upper Atmosphere and Ionosphere // *The Atmosphere and Climate of Mars*. Cambridge Univ. Press, 2017. DOI: 10.1017/9781107016187.
- [2] *Krasnopolsky V. A.* Spectroscopy and photochemistry of planetary atmospheres and ionospheres: Mars, Venus, Titan, and Pluto. Cambridge Univ. Press, 2019. <https://doi.org/10.1017/9781316535561>.
- [3] *Slipski M. et al.* Variability of Martian turbopause altitudes // *J. Geophysical Research: Planets*. 2918. V. 123(11). P. 2939–2957. <https://doi.org/10.1029/2018JE005704>.

- [4] *Korablev O.I. et al.* The Atmospheric Chemistry Suite (ACS) of three spectrometers for the ExoMars 2016 trace gas orbiter // *Space Science Reviews*. 2018. V. 214(1). <https://doi.org/10.1007/s11214-017-0437-6>.
- [5] *Belyaev D.A. et al.* Thermal structure of the middle and upper atmosphere of Mars from ACS/TGO CO₂ spectroscopy // *J. Geophysical Research: Planets*. 2022. V. 127(10). Article e2022JE007286. <https://doi.org/10.1029/2022JE007286>.
- [6] *Yoshida N. et al.* Variations in vertical CO/CO₂ profiles in the Martian mesosphere and lower thermosphere measured by the ExoMars 35 TGO/NOMAD: Implications of variations in eddy diffusion coefficient // *Geophysical Research Letters*. 2022. V. 49. Iss. 10. Article e2022GL098485. <https://doi.org/10.1029/2022GL098485>.
- [7] *Lindzen R. S.* Turbulence and stress owing to gravity wave and tidal breakdown // *J. Geophys. Res.: Oceans*. 1981. V. 86. Iss. C10. P. 9707–9714. DOI: 10.1029/JC086iC10p09707.

2.5 YEARS OF OBSERVATION OF GRAVITY WAVE ACTIVITY IN THE MARTIAN ATMOSPHERE FROM THE ACS/TGO EXPERIMENT

E. D. Starichenko¹, D. A. Belyaev¹, A. S. Medvedev², A. A. Fedorova¹, O. I. Korablev¹, F. Montmessin³, A. Trokhimovskiy¹

¹ Space Research Institute RAS, Moscow, Russia starichenko.ed@phystech.edu

² Max Planck Institute for Solar System Research, Göttingen, Germany

³ LATMOS/IPSL, UVSQ Université Paris-Saclay, UPMC Univ. Paris, CNRS, Guyancourt, France

KEYWORDS:

gravity waves, Martian atmosphere, Trace Gas Orbiter, Atmospheric Chemistry Suite, solar occultation

INTRODUCTION:

Gravity waves (GWs) are omnipresent in planetary atmospheres and originate from displacements of air parcels. Since they re-distribute energy and momentum between atmospheric layers, GWs greatly affect atmospheric dynamics. In this work, we study the activity of GWs in the Martian atmosphere from solar occultation experiments conducted by the infrared spectrometers of Atmospheric Chemistry Suite (ACS) [1] on board the Trace Gas Orbiter (TGO).

OBSERVATIONS:

ACS is a part of the TGO, which represents the ESA-Roscosmos ExoMars 2016 collaborative mission. The instrument consists of three infrared channels [1]: near-IR (NIR, 0.73–1.6 μm), middle-IR (MIR, 2.3–4.2 μm) and thermal-IR (TIRVIM, 1.7–17 μm). In this work, we use the data obtained from the MIR and NIR instruments, operating in solar occultation mode since April 2018. ACS-MIR is a cross-dispersion echelle spectrometer that allows for retrieving temperature and density vertical profiles in the strong 2.7 μm CO₂ absorption band covering the broad altitude range of 20–180 km [2, 3]. ACS-NIR, an echelle spectrometer combined with an acousto-optic tunable filter, measures the atmospheric structure in the 1.57 μm CO₂ band at altitudes from 10 to 100 km [4, 5]. Both ACS channels possess a high resolving power, exceeding $\sim 25\,000$, signal to noise ratio more than 1000, and sound the atmosphere with the vertical resolution of 0.5–2.5 km. During simultaneous occultations, the instruments lines of sight target identical tangent points that provide confidential cross validation between the retrieved atmospheric profiles. Presently, we report the observations for 2.5 Martian years (MY), from the middle of MY 34 (April 2018) to the end of MY 36 (December 2022), counting ~ 960 occultations of MIR and $\sim 12\,300$ occultations of NIR.

RESULTS:

In order to derive the parameters of GWs, we use the method described in [6]. We determine and analyze such characteristics of GWs as the acceleration (wave drag), vertical flux of horizontal momentum, potential energy and Brunt-Väisälä frequency, which characterizes the stability of GWs propagation.

Our recent work [7] presents the results of the 2 Martian years of observation of gravity waves in the Martian atmosphere. One of the results of the study is presented on Figure 1, which describes the latitude-altitude distributions of potential energy of gravity waves in different seasons. It is seen that wave activity is distributed symmetrically with respect to the equator during the equinoctial seasons, while the maximum is shifted to the winter hemisphere during solstices.

In this work we present the increased statistics of gravity waves including 2.5 Martian years.

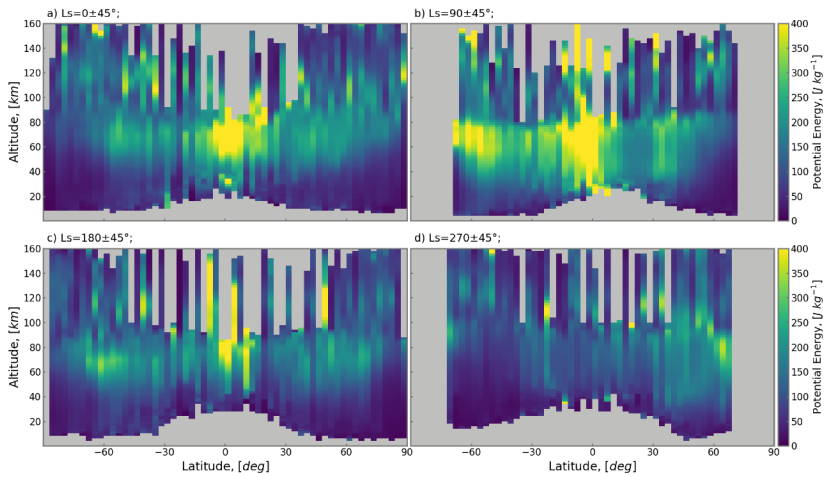


Fig. 1. Latitude-altitude distributions of the retrieved wave potential energy (per unit mass) E_p for four representative seasons centered around a) $L_s = 0^\circ$, b) 90° , c) 180° and d) 270° . The period of MY34 GDS is excluded

REFERENCES:

- [1] Korabev O., Montmessin F., and ACS Team. The Atmospheric Chemistry Suite (ACS) of three spectrometers for the ExoMars 2016 Trace Gas Orbiter // Space Sci. Rev. 2018. V. 214. P. 7. DOI: 10.1007/s11214-017-0437-6.
- [2] Belyaev D. et al. Revealing a high water abundance in the upper mesosphere of Mars with ACS onboard TGO // Geophysical Research Letters. 2021. V. 48. Article e2021GL093411. DOI: 10.1029/2021GL093411.
- [3] Belyaev D. et al. Thermal Structure of the Middle and Upper Atmosphere of Mars from ACS/TGO CO_2 Spectroscopy // J. Geophysical Research: Planets. Under Review. 2022.
- [4] Fedorova A. et al. Stormy water on Mars: The distribution and saturation of atmospheric water during the dusty season // Science. 2020. Article eaay9522. DOI: 10.1126/science.aay9522.
- [5] Fedorova A. et al. A two-Martian year survey of the water vapor saturation state on Mars based on ACS NIR/TGO occultations // J. Geophysical Research: Planets. 2022.
- [6] Starichenko E. et al. Gravity wave activity in the Martian atmosphere at altitudes 20–160 km from ACS/TGO occultation measurements // J. Geophysical Research: Planets. 2021. V. 126. Article e2021JE006899. DOI: 10.1029/2021JE006899.
- [7] Starichenko E. D., Medvedev A. S., Belyaev D. A. et al. Climatology of gravity wave activity based on two Martian years from ACS/TGO observations // Astronomy Astrophysics. 2024. V. 683. <https://doi.org/10.1051/0004-6361/202348685>.

CLAY MINERALS IN THE UPPER PART OF NIRGAL VALLIS, MARS

E. S. Cholovskaia¹, M. A. Ivanov²

¹ *Lomonosov Moscow State University, Faculty of Geology
Moscow, Russia, cattcholovskaya@yandex.ru;*

² *Vernadsky Institute of Geochemistry and Analytical Chemistry RAS
Moscow, Russia, Mikhail_Ivanov@brown.edu*

KEYWORDS:

Mars, Nirgal, Her Desher, valley, channel, clay

INTRODUCTION:

The discovery of clay minerals within the ancient southern highlands of Mars has closed the long-existing controversy between the obvious geomorphological features of liquid water activity and the apparent absence of its geochemical and mineralogical work [1]. Various hypotheses have been put forward to explain the formation of phyllosilicates either as the result of the surface weathering in warm and wet conditions [2–4] or and in the subsurface due to various processes in cold and dry climate [5]. Important constrains on these models can be obtained by studying the regional geological context of the clay mineral accumulations and reconstructing the sequence of events that caused their formation, deposition and redistribution. The introduction of such constrains is the main purpose of our study.

STUDY AREA AND METHODS:

The territory of the upper part of the Nirgal Vallis between 20–29°S and 42–52°W was chosen as the study area. Clay-rich rocks in this area are exposed in the walls of HerDesher and Nirgal Vallis, as well as in some impact craters.

To analyze the distribution, morphological and topographic features of clay-rich deposits and their host rock we used: the THEMIS (resolution 100 m/px), CTX (resolution 6 m/px), HiRISE (resolution up to 0.25 m/px) images and the MOLA topographic data (resolution ~460 m/px).

As the data for studying the spectral characteristics of the surface, the MTRDR images from the CRISM spectrometer were used, which contain the full spectral range (IR+VNIR) and have primary adjustments [6]. We analyzed 13 images obtained in the study area using the analysis tool “CRISM Analysis Toolkit” (CAT), developed for the ENVI software [7]. Summary of the spectral parameters [6, 8] and the spectral ratio method were used for identification and spatial mapping of the spectrally different units.

RESULTS AND DISCUSSION:

In our research we studied clay minerals exposed in the walls of the Her Desher Vallis and in small impact craters in this region using all available CRISM data (Figure 1).

Her Desher Vallis extends in the studying area for 116 km from NW to SE. It is an isolated fluvial system with no tributaries. In the cross-section, the valley has a U-shaped shape, its width increases from 1 km in the north to 7.5 km in the south, possibly forming an elongated basin. The depth of Her Desher increases from 60 m at the northern edge to 1.2 km at the southern edge. The valley has sharp bends along its entire length, some of which are close to 90°.

The main feature of Her Desher is the presence of clearly defined layered strata exposed in its walls. The stratum with clay minerals lies on the ancient lava flows and, in turn, is overlain by the younger lava flows (Figure 2). A mixture of saponite and nontronite in this layer was identified using spectral data analysis. At the northern end of the valley the content of clay minerals in these layer decreases, however, the presence of an absorption band of about 1.9 μm in the same layer indicates the presence of hydrated material that is not identified by other bands.

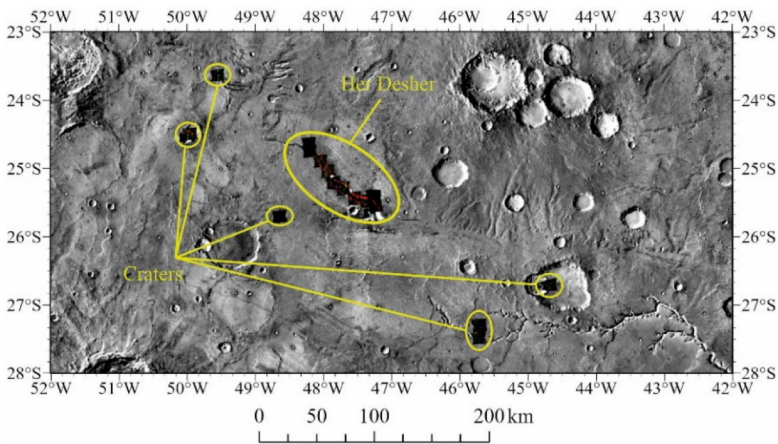


Fig. 1. Daytime images of THEMIS and draped over them CRISM images studied in our research

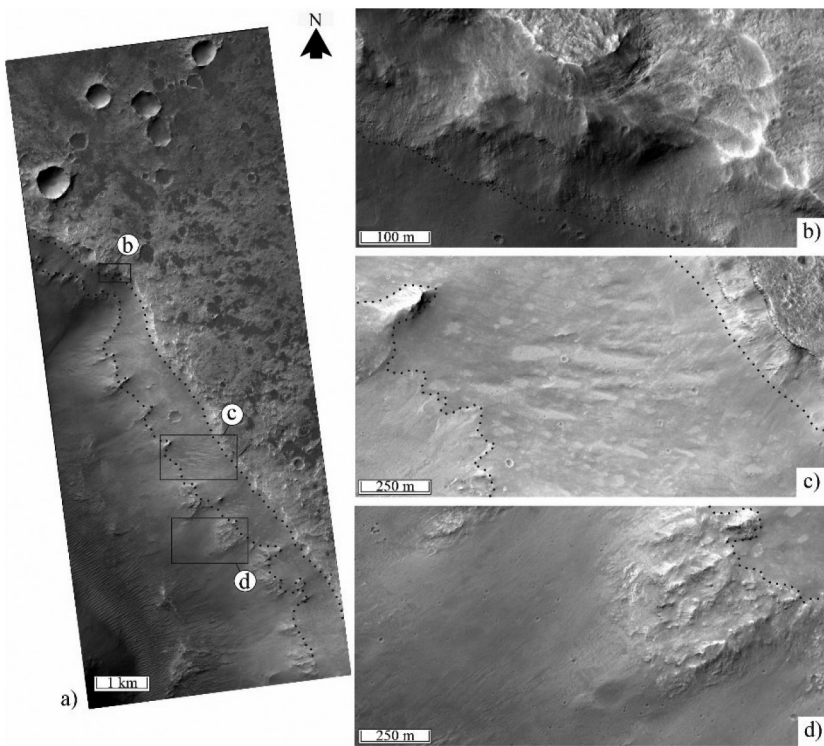


Fig. 2. The left wall of Her Desher at its southern end (a) and different layers exposed on the walls (b–d); pieces of the HiRISE image PSP_007086_1545

In craters within the Early Hesperian lava plains, the Fe-Mg smectites were also identified; they are represented by a mixture of saponite and nontronite [9]. There are no Al-rich clay minerals in the studied objects. Nirgal Vallis cuts through the ejecta of at least one crater containing clay minerals. This suggests that the formation of phyllosilicates predated the formation of the valley (Amazonian [9]). Thus, the fluvial activity that has cut Nirgal Vallis acted as the re-distributor of clays that have been formed earlier (Noachian and maybe Hesperian times).

CONCLUSION:

The outcrops of the Fe-Mg smectite layer in the walls of Her Desher Vallis are underlain and overlain by volcanic rocks, probably basalt flows.

The absolute model age of the upper volcanic formation was estimated to be ~3.6 Ga, that is, as Early Hesperian. It is obvious that the underlying volcanic formation is older and could have been formed in the Noachian period, for example, as a result of the activity of a large shield volcano in the northeastern part of the studying area [9]. In the Late Noachian period, the flux of impactors was still high and large impact events could have caused temporary and local warming, leading to melting of surface/sub-surface ice. The resulting liquid water could accumulate in the topographic depressions of large craters or form temporary hydrothermal systems there [10, 11], which could lead to the formation of local accumulations of Fe-Mg phyllosilicates.

REFERENCES:

- [1] Carr M. H. *The Surface of Mars*. Cambridge University Press, 2006. 307 p.
- [2] Bish D. L., Carey J. W., Vaniman D. T., Chipera S. J. Stability of hydrous mineral on the Martian surface // *Icarus*. 2003. V. 164. Iss. 1. P. 96–103. [https://doi.org/10.1016/S0019-1035\(03\)00140-4](https://doi.org/10.1016/S0019-1035(03)00140-4).
- [3] Bibring J. P., Langevin Y., Gendrin A. et al. Mars surface diversity as revealed by the OMEGA/Mars express observations // *Science*. 2005. V. 307. Iss. 5715. P. 1576–1581. DOI: 10.1126/science.110880.
- [4] Poulet F., Bibring J. P., Mustard J. F., Gendrin A., Mangold N., Langevin Y., Arvidson R. E., Gondet B., Gomez C. OMEGA team. Phyllosilicates on Mars and implications for early Martian climate // *Nature*. 2005. V. 438. No. 7068. P. 623–627.
- [5] Ehlmann B. L., Mustard J. F., Murchie S. L., Bibring J. P., Meunier A., Fraeman A. A., Langevin Y. Subsurface water and clay mineral formation during the early history of Mars // *Nature*. 2011. V. 479. No. 7371. P. 53–60.
- [6] Viviano-Beck C. E., Seelos F. P., Murchie S. L., Kahn E. G., Seelos K. D., Taylor H. W., Taylor K., Ehlmann B. L., Wisemann S. M., Mustard J. F., Morgan M. F. Revised CRISM spectral parameters and summary products based on the currently detected mineral diversity on Mars // *J. Geophysical Research: Planets*. 2014. V. 119. No. 6. P. 1403–1431.
- [7] Morgan F., Seelos F. P., Murchie S. L. CAT Tutorial // CRISM Workshop held in conjunction with the 40th Lunar and Planetary Science Conf. 2009.
- [8] Pelkey S. M., Mustard J. F., Murchie S. L., Clancy R. T., Wolff M., Smith M., Milliken R., Bibring J. P., Gendrin A., Poulet F., Langevin Y., Gondet B. CRISM multispectral summary products: Parameterizing mineral diversity on Mars from reflectance // *J. Geophysical Research: Planets*. 2007. V. 112. No. 8.
- [9] Cholovskaia E. S., Ivanov M. A. Geological structure of the upper part of Nirgal Vallis, Mars // 15th Moscow Solar System Symp. 2024.
- [10] Newsom H. E. Hydrothermal alteration of impact melt sheets with implications for Mars // *Icarus*. 1980. V. 44. No. 1. P. 207–216.
- [11] Newsom H. E., Hagerty J. J., Goff F. Mixed hydrothermal fluids and the origin of the Martian soil // *J. Geophysical Research: Planets*. 1999. V. 104. No. 4. P. 8717–8728.

TIME CONSTRAINTS ON THE FORMATION OF VALLEY NETWORKS ON ALBA PATERA, MARS (PRELIMINARY RESULTS)

M. A. Ivanov¹, J. W. Head²

¹ Vernadsky Institute of Geochemistry and Analytical Chemistry RAS
Moscow, Russia, mikhail_ivanov@brown.edu

² Brown University, Providence RI, USA, James_Head@brown.edu

KEYWORDS:

Mars, Alba Patera, valley networks, volcanism, fluvial processes

INTRODUCTION:

The volcano of Alba Patera [1–4] represents a site with numerous valley networks (VN) of a fluvial nature [5, 6]. In contrast to the Noachian-Hesperian VN elsewhere on Mars, these on Alba Patera formed much later, during the Amazonian period [7, 8]. Thus, the Alba valley networks (AVN) possibly indicate environments of an effective, although local, atmosphere transportation of water, perhaps indicating a transient excursion of warm and wet climate conditions in the Amazonian, or perhaps an example of volcano-ice interactions (e.g., [9]). The main goal of our work was to introduce the timing constraints on the formation of the AVN using their stratigraphic relationships with the surroundings, the topographic configuration of the AVN, and crater size-frequency distribution (CSFD) measurements of the Alba lava flows to calibrate the relative ages.

GENERAL SHAPE OF THE ALBA PATERA VOLCANO:

The MOLA data (1/128 degrees resolution [10]) shows that the volcano consists of the following major parts (Figure 1): (1) the main body with broad summit plateau, (2) the western and eastern lobes, and (3) the summit dome [11]. These parts play an important role in the spatial distribution of the fluvial features. Slopes of the main body of Alba and the lobes are covered by numerous lava flows (e.g., [12]).

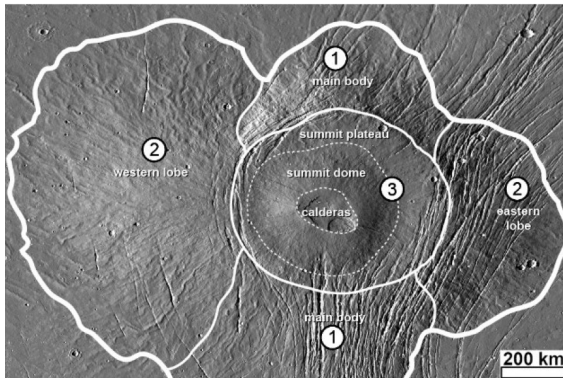


Fig. 1. Major parts of Alba Patera

MAIN FLUVIAL FEATURES ON ALBA PATERA:

Although a global map of the spatial distribution of the VN exist [6], close inspection of Alba Patera reveals that a large number of the AVN are not represented in the global map. Thus, we have updated the global map by our mapping of the AVN with the help of the seamless mosaics of the CTX images [<https://murray-lab.caltech.edu/CTX/beta01.html>]. As the result of our mapping, we can conclude that the fluvial features of Alba Patera are strongly concentrated on its northern flanks [13] and mostly represented by (1) narrower shorter and longer sinuous channels and (2) broader steep-sided canyons (Figure 2). These features characterize the uppermost edge of the Alba main body; both the summit plateau and the summit dome lack the well-developed channels.

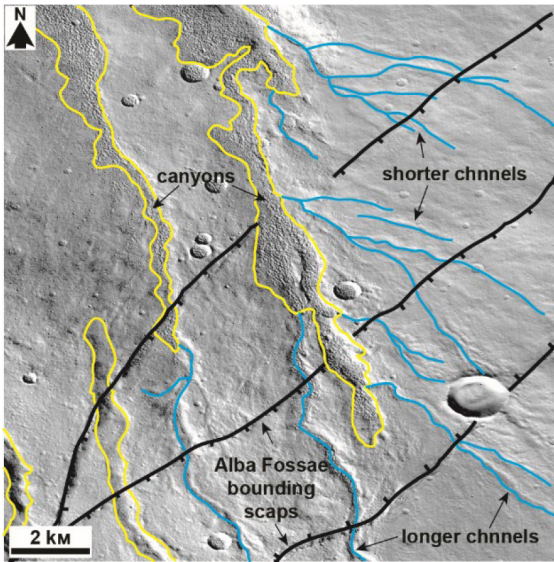


Fig. 2. Main fluvial features on Alba Patera

The channels have a U-shaped transverse profile and vary in length from a few kilometers to many tens of kilometers. The width of the channels is usually several hundred meters and remains about the same along the entire length of a channel. Usually, the channels appear as morphologically distinct features. The absolute majority of the channels (~67 % of the population) are shorter than 2.5 km; only a few channels (~1 %) are longer than 20 km. These channels extend from the northern edges of the summit plateau down to the base of the volcano; the shorter channels in many cases represent tributaries of the longer ones.

The canyons have a box-shaped transverse profile; they always are spatially associated with the channels and may occur at their different stretches. The canyons are wider than the channels (~factor of 2) and typically are bounded by steep walls. The floors of the canyons are flat, without discernible traces of the channels.

TOPOGRAPHIC CONFIGURATION OF THE CHANNELS AND CANYONS:

We investigated the longitudinal profiles of the two longest channels. The first channel (~108 km long) has no canyons but shows a radical change of its course from NW (upper 2/3 of the channel) to NE (lower 1/3 of the channel). The mean gradient along the channel also changes from ~2.2 o/km within the upper segment to ~0.9 o/km within the lower segment. The slopes of both segments are similar to the regional slope of the volcano flanks, and lava flows near the channel also mirror the change of their trend from NW to NE.

The second channel (~60 km long) is straighter and has three canyons near its origin (~5 km long), along the middle portion (~7.5 km long), and at the end (~30 km long). The profile of the second channel is more uniform with the mean slope of ~2.5 grad/km within the upper half of the channel and ~1.1 grad/km within the lower half. Although the upper and lower halves of the channel are characterized by different gradients, the channel-basin systems in either the upper or lower segments show no difference in the gradient. In the upper portion, the gradient varies from 2.2 (channel segments) to 2.8 o/km (basin segments); and in the lower portion the gradient varies from 1.0 (channel segment) to 1.2 grad/km (basin segment).

ABSOLUTE MODEL AGES (AMA) OF LAVA FLOWS ON ALBA PATERA:

In order to put constraints on the timing of the fluvial activity, we conducted CSFD measurements on six lava flows; three are at the caldera complex and the other three are on the northern flank of the main body. We have estimated the AMAs for the summit flows as: 1.51, 1.49, and 1.40 Ga and

for the flank flows as: 1.82, 1.22, and 1.10 Ga (Amazonian). The topographically upper portions of the flank flows and the upper stretches of the channels are cut by the graben of Alba Fossae (Figure 2), which, thus, represent the youngest features of Alba Patera.

DISCUSSION/CONCLUSIONS:

Both the distribution and topographic configuration of the fluvial features on the northern side of Alba Patera are controlled by the variations of the regional slope on the volcano flanks. Thus, the observable fluvial features characterize the late phases of the volcano development. The large range of the AMAs of the lava flows suggests that the process of the volcano formation was extended. Does the formation of the fluvial features correspond to different episodes of volcanic activity or does it completely postdate volcanism on Alba? The relationships of the channels with the lava flows suggests that the flows control the course of the channels and, thus, are older. The topographic configuration of the canyons provides additional evidence for this interpretation. If the canyons have been formed by the enhanced fluvial side erosion their floors systematically must have lower topographic gradient compared with that of the channels where the down-cut erosion dominated. Our measurements show, however, that the gradients within the channels and canyons are the same. Thus, we interpret the canyons as the gaps between neighboring lava flows that existed earlier and controlled flows of water.

In our study, we found no evidence of either embayment/superposition of the longer channels by lava flows or for the multistage fluvial activity on Alba Patera. Because of this, we consider all such channels as the ones formed during a single episode that largely postdated effusive volcanism. The fluvial activities during this episode may have been related to the enhanced geothermal heating as it was proposed for some other Martian volcanoes [9]. In this case, the absolute model age of the lower stratigraphic limit of the fluvial systems is presented by the AMA of the youngest volcanic flows(s), which in our study is ~ 1.1 Ga. The upper limit is introduced by the Alba Fossae graben.

REFERENCES:

- [1] *Cattermole P.* Linear volcanic features at Alba Patera, Mars — Probable spatter ridges // *J. Geophysical Research*. 1986. V. 91. Iss. B13. P. E159–E165. <https://doi.org/10.1029/JB091iB13p0E159>.
- [2] *Cattermole P.* Sequence, rheological properties, and effusion rates of volcanic flows at Alba Patera, Mars // *J. Geophysical Research*. 1987. V. 92. Iss. B4. P. E553–E560. <https://doi.org/10.1029/JB092iB04p0E553>.
- [3] *Cattermole P.* Volcanic flow development at Alba Patera, Mars // *Icarus*. 1990. V.83. Iss. 2. P. 453–493. [https://doi.org/10.1016/0019-1035\(90\)90079-O](https://doi.org/10.1016/0019-1035(90)90079-O).
- [4] *Schneeberger D. M., Pieri D. C.* Geomorphology and stratigraphy of Alba Patera, Mars // *J. Geophysical Research*. 1991. V. 96. Iss. B2. P. 1907–1930. <https://doi.org/10.1029/90JB01662>.
- [5] *Gulick V. C., Tyler D., McKay C.P., Haberle R. M.* Episodic ocean-induced CO₂ greenhouse on Mars: Implications for fluvial valley formation // *Icarus*. 1997. V. 130. Iss. 1. P. 68–86. doi: 10.1006/icar.1997.5802.
- [6] *Hynek M., Beach M., Hoke M. R. T.* Updated global map of Martian valley networks and implications for climate and hydrologic processes // *J. Geophysical Research*. 2010. V. 115. Iss. E9. Article E09008. <https://doi.org/10.1029/2009JE003548>.
- [7] *Hoke M. R. T., Hynek B. M.* Valley network age determinations: Multiple periods of formation // *Proc. Lunar and Planetary Science Conference 38*. Houston, USA. 2007. Article 1209.
- [8] *Fassett C. I., Head J. W.* The timing of Martian valley network activity: Constraints from buffered crater counting // *Icarus*. 2008. V. 195. Iss. 1. P. 61–89. <https://doi.org/10.1016/j.icarus.2007.12.009>.
- [9] *Fassett C. I., Head J. W.* Valley formation on Martian volcanoes in the Hesperian: Evidence for melting of summit snowpack, caldera lake formation, drainage and erosion on Ceranius Tholus // *Icarus*. 2007. V. 189. Iss. 1. P. 118–135. <https://doi.org/10.1016/j.icarus.2006.12.021>.
- [10] *Smith D. E., Zuber M. T., Solomon S. C. et al.* The global topography of Mars and implications for surface evolution // *Science*. 1999. V. 284. Iss. 5419. P. 1495–1503. DOI: 10.1126/science.284.5419.1.

- [11] *Ivanov M.A., Head J.W.* Alba Patera, Mars: Topography, structure, and evolution of a unique late Hesperian-early Amazonian shield volcano. // *Journal of Geophysical Research*. 2006. V. 111. Iss. E9. Article E09003. <https://doi.org/10.1029/2005JE002469>.
- [12] *Mouginis-Mark P.J., Wilson L., Zimbelman J.R.* Polygenic eruptions on Alba Patera, Mars // *Bull. Volcanology*. 1988. V. 50. P. 361–379. doi:10.1007/BF01050636.
- [13] *Gulick V.C., Baker V.R.* Origin and evolution of valleys on Martian volcanoes. // *J. Geophysical Research*. 1990. V. 95. Iss. B9. P. 14325–14344. <https://doi.org/10.1029/JB095iB09p14325>.

MORPHOLOGICAL FEATURES ALONG THE FIXED CONTOUR LINES INDICATING WATER LEVEL CHANGES IN THE HOLDEN CRATER ON MARS

J. Chu¹, M. A. Ivanov², A. M. Nikishin¹

¹ Lomonosov Moscow State University, Faculty of Geology
Moscow, Russia, vladimirchujun@yandex.ru

² Vernadsky Institute of Geochemistry and Analytical Chemistry RAS
Moscow, Russia, Mikhail_Ivanov@brown.edu

KEYWORDS:

Holden crater, Uzboi, knickpoint, contour line, water level

INTRODUCTION:

The Holden crater is located in the Uzboi-Ladon-Morava (ULM) outflow channel system in Margaritifer Terra and likely formed in the Noachain. Existing studies of outcrops [1–4] suggest that there was a lake in Holden crater, and the high-energy water deposition from the Uzboi Vallis reworked the layered sediments formed in the original low-energy water environment [4]. To study the geological processes that possibly occurred in the putative Holden Lake as it gradually dried up, we use CTX and HiRISE images and MOLA DEM to reveal the geomorphological features of water level changes in the crater.

THE LONGITUDINAL PROFILE OF UZBOI VALLIS:

After the formation of Holden crater, Uzboi Vallis was blocked and a lake was formed, with the lake surface reaching -350 m [2, 5]. At this time, some water may also have entered Holden crater by seepage [5]. Subsequently, the Holden crater rim breached, and a large amount of water entered Holden crater [2, 4, 6]. There is no obvious outflow from Holden crater [6], so the input from Uzboi Vallis plays an important role in the water level in Holden. We selected three elevations along the lower portion of Uzboi Vallis, -1200 , -1840 , and -2160 m (Figure 1). The -1200 m elevation corresponds to the inner terrace in Uzboi Vallis, and the -1840 and -2160 m levels are two knickpoints of the channel inside Holden. The contour lines at these elevations outline interiors of both the Holden crater and Uzboi Vallis. (Figure 2)

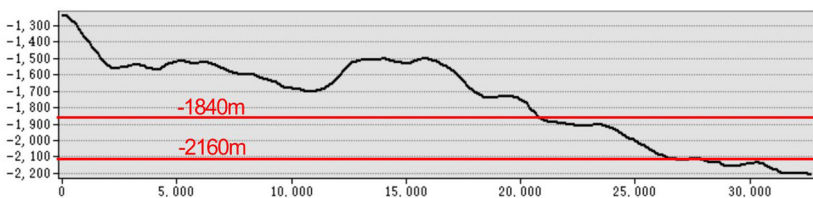


Fig. 1. Longitudinal profile along Uzboi Vallis (location see Figure 2, black line), two knickpoints at -1840 and -2160 m are seen

MORPHOLOGICAL FEATURES NEAR EACH FIXED CONTOUR LINES:

1. -1200 m contour line: It is connected to the Uzboi Vallis inner terrace, indicating the water level formed by the water input from Uzboi just after the dam was breached. In Holden crater, it possibly indicates the highest water level reached in the crater depression.
2. -1840 m contour line: One knickpoint appears in the Uzboi Vallis channel at -1840 m, which may suggest a drop in water levels in Holden crater (e.g. [7]). Along the western wall of the crater, the ridges of the alluvial fans diverged above this elevation, indicating the formation of the lower fans (Figure 2, red points). The cliff in the northwest of Holden crater floor is near this contour line, which may be suggestive of the drop of water level. (Figure 2, arrow 1).

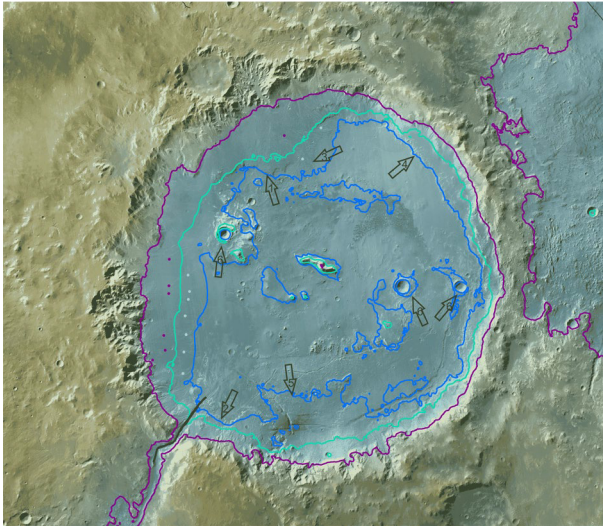


Fig. 2. Holden crater, MOLA DEM covered on CTX images. Contour lines: -1200 m (violet), -1840 m (sky blue), -2160 m (dark blue). Black line represents the location of profile in Figure 1, arrows with numbers and points represent morphological features described in text

3. -2160 m contour line: Another knickpoint appears in the Uzboi Vallis channel at -2160 m suggesting transient water level (e.g. [7]). On the eastern side of the Uzboi breach, the -2160 m contour line almost coincides with the outcrop of layered sediments (Figure 2, arrow 2), suggesting that the Uzboi fluvial regime had changed from accumulation to erosion perhaps due to the water level drop. On the alluvial fans in the west of crater, there are also divergent points of ridges above this level (Figure 2, yellow points). In the northeast of Holden, -2160 m marks the lowest crater floor (Figure 2, arrow 4). In the south of Holden crater floor, part of the rough plain is above the -2160 m contour line (Figure 2, arrow 5). The large, bowl-shaped impact craters in the western and eastern portions of the Holden crater floor (Figure 2, arrow 6) have rims above -2160 m, indicating that there is no sediment infilling and these impact craters were formed after the water level dropped lower than -2160 m.

CHRONOLOGY:

We have performed the crater size-frequency distribution (CSFD) measurements to reveal the general sequence of events in the southern portion of the Holden floor. The morphology of this area allows its division into the eastern dark plains and the western rough plains. The absolute model age (AMA) of these plains' areas are as follows: the eastern dark plains, one AMA estimates of 3.6 ± 0.03 Ga; the western rough plains show two AMAs of $3.1 (+0.2, -0.6)$ and $2.2 (\pm 0.1)$ Ga.

DISCUSSION AND CONCLUSIONS:

1. After the Uzboi breach, the water level in the Holden crater has reached the -1200 m level and then gradually lowered, with transient stable water bodies existing at -1840 and -2160 m levels.
2. Alluvial fans on the west side of Holden floor were formed after the Uzboi breach, and the water level controls extent of the alluvial fans.
3. After the Holden water level dropped to -2160 m, the water flow from Uzboi Vallis eroded and exposed the layered materials in the southern portion of the crater floor. The large trough at the Uzboi breach fan may have been formed later because it is lower than -2160 m.
4. The entire southern plain was formed in the period to 3.6 Ga, and the subsequent erosion formed the western rough plain, which occurred between 3.1 and 2.2 Ga.

5. The large, bowl-shaped impact craters on the Holden Crater floor were formed when the water level dropped below -2160 m, which is younger than 2.2 Ga.

ACKNOWLEDGMENTS:

This work is supported by China Scholarship Council and represents a part of the state order of GEOKHI for MAI.

REFERENCES:

- [1] *Grant J. A., Parker T. J.* Drainage evolution in the Margaritifer Sinus region, Mars // *J. Geophysical Research*. 2002. V. 107.
- [2] *Pondrelli M. et al.* Complex evolution of paleolacustrine system on Mars: An example from the Holden crater // *J. Geophys. Res.* 2005. V. 110.
- [3] *Grant J. A., Irwin P. R. III, Grotzinger J. P.* HiRISE imaging of impact megabreccia and sub-meter aqueous strata in Holden Crater, Mars // *Geology*. 2008. V. 36. P. 195–198.
- [4] *Grant J. A., Irwin P. R. III, Wilson S. A.* Aqueous depositional settings in Holden crater, Mars // *Lakes on Mars*. Elsevier, 2010. P. 323–346.
- [5] *Grant J. A. et al.* A lake in Uzboi Vallis and implications for Late-Noachian-Early Hesperian climate on Mars // *Icarus*. 2011. V. 212.
- [6] *Ivanov M. A., Hiesinger H.* Topographic characteristics and chronology of the Uzboi-Ladon fluvial system on Mars // 11th Moscow Solar System Symp. 2020.
- [7] *Duran S. et al.* Knickpoints in Martian channels indicate past ocean levels // *Scientific Reports*. 2019. V. 9(1). Article 15153.

CONSTRAINTS ON THE VISCOELASTIC PROPERTIES OF THE MARTIAN MANTLE BY THE CHANDLER WOBBLE PERIOD

E. A. Kulik, T. V. Gudkova

Schmidt Institute of Physics of the Earth RAS
Moscow, Russia, kulik.ea@ifz.ru, gudkova@ifz.ru

KEYWORDS:

Mars, Chandler wobble period, Martian mantle, viscoelasticity, Andrade rheology, tidal Love numbers, internal structure models

INTRODUCTION:

The main reason the Chandler wobble (CW) arises is that the axis of the planet's rotation is not collinear with the greatest moment of inertia axis. The CW was not observed on Mars during a long time. The value of the Chandler period on Mars was predicted theoretically in works [1–6]. Work [2] considered the influence of a liquid core, the non-elasticity of the planetary interior and the weak triaxiality of the figure of Mars on CW period. An attempt to determine experimentally the value of the Chandler wobble period was made in [7] and [8], but the authors of these works failed to identify the CW period because of the overlapping period of the mass redistribution over 1/3 of the Martian year. The wobble period was measured on Mars for the first time with good accuracy (206.9±0.5 days) from radio-tracking observations from Mars Odyssey, Mars Reconnaissance Orbiter, and Mars Global Surveyor [9]. The value of Martian Chandler wobble period is a new constraint in modeling construction of the planetary interior and provides us with great knowledge about the mantle rheological properties at long periods.

ELASTIC INTERNAL STRUCTURE MODELS:

Internal structure models are calculated using measured geodetic parameters (planet's average radius, mass, moment of inertia and Love number k_2) and data obtained from a Martian seismic experiment (density and thickness of the crust, radius of the core). The normalized moment of inertia value is 0.3640 ± 0.0006 , the tidal Love number $k_2 = 0.174 \pm 0.008$, the average crust thickness is 32–70 km and an average density is no more than 3100 kg/m^3 [10], the core radius is $1830 \pm 40 \text{ km}$ in [11] and $1650 \pm 20 \text{ km}$ in [12]. Data used for calculation of models are presented in Table 1.

Table 1. Data obtained from observations

Parameter of planet	Value	Source
Mass of Mars, M , $\times 10^{23} \text{ kg}$	6.4185	[9]
Average radius of Mars, R , km	3389.5	
Average moment of inertia, I/MR^2	0.3640 ± 0.0006	
Love number, k_2	0.174 ± 0.008	
Main moments of inertia A/MR^2 B/MR^2 C/MR^2	0.362976 0.363229 0.365067	
Angular rotation speed of Mars ω , $\times 10^{-5} \text{ s}^{-1}$ $T = 2\pi/\omega$, $\times 10^4 \text{ s}$	7.088191 8.8643	[13, 14]
Crust thickness, l_{crust} , km	32–70	[10, 15]
Average crust density, ρ_{crust} , kg/m^3	2700–3100	
Core radius, r_{core} , km	1830 ± 40 1650 ± 20	[11] [12]
CW period, T_{CW} , days	206.9 ± 0.5	[9]

ANDRADE RHEOLOGY:

To take into account viscoelastic properties of the Martian mantle, Andrade rheology is used. In the Andrade viscoelastic model, the complex shear modulus $\tilde{\mu}$ is equal to $1/\tilde{J}$, where \tilde{J} is so called complex compliance of material calculated by the formula [16]

$$\tilde{J}(\chi) = J \left[1 + (i\tau_M \chi)^{-\alpha} \Gamma(1 + \alpha) \right] - \frac{i}{\eta \chi},$$

where $J = 1/\mu$, $\tau_M = \eta/\mu$ is the Maxwell time, Γ is the gamma function, χ is the tidal frequency, and α is the Andrade parameter.

Unfortunately, the parameter α is not determined by now. Its value is usually taken within range 0.2–0.5 [16].

In modeling the piecewise constant viscosity distribution is used. Viscosity of the crust η_0 is assumed to be the parameter of the distribution, viscosity of the upper layer of the mantle is taken $10^{-2}\eta_0$, middle mantle — $10^{-1}\eta_0$, lower mantle — η_0 . Viscosity in the molten layer at the basement of the mantle, recently discovered in [12], is set to 10^9 Pa·s, which corresponds to the inelastic state.

CHANDLER WOBBLE PERIOD:

The value of CW period for a triaxial elastic body with a liquid core is derived from the formula [5]

$$T_W = T_E \left(1 - \frac{(A_c B_c)^{1/2} / (AB)^{1/2}}{1 - k_2/k_0} \right),$$

where T_E is the Euler period, and k_2 is the tidal Love number with taking into account dependence on frequency (i.e., Love number for an inelastic model).

RESULTS:

Models are constructed at different values of Andrade parameter and viscosity parameter. Values of CW period with regard to the Andrade parameter for different models are shown on Figure 1. Lines on the graph represent the range of acceptable values of CW period, and numbers designate the exponent of the viscosity parameter. According to Figure 1, models with viscosity parameter in range 10^{21} – 10^{27} Pa·s meet the constraint of the observed value of Chandler period. Since it is unlikely viscosity of the crust to be more than 10^{24} Pa·s, Andrade parameter takes the value about 0.3–0.5.

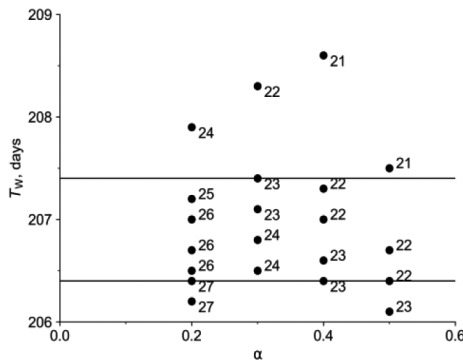


Fig. 1. Dependence of model values of CW period on parameters of Andrade rheology. Numbers on the graph indicate the exponent of the viscosity parameter. The range of acceptable values of Chandler period are shown by horizontal lines

ACKNOWLEDGMENTS:

This work was carried out under a State Assignment of the Schmidt Institute of Physics of the Earth RAS.

REFERENCES:

[1] Zharkov V.N., Molodensky S.M. On determination of physical parameters of the Martian core by data of its rotation // Solar System Research. 1994. V. 28. P. 86–97.

- [2] *Zharkov V.N., Molodensky S.M.* Chandler's period of weakly triaxial models of Mars // *Solar System Research*. 1995. V. 29. No. 4. P. 341–344.
- [3] *Zharkov V.N., Molodensky S.M.* On the Chandler wobble of Mars // *Planetary and Space Science*. 1996. V. 44. P. 1457–1462.
- [4] *Zharkov V.N., Gudkova T.V.* Construction of Martian interior model // *Solar System Research*. 2005. V. 39 (5). P. 343–373.
- [5] *Zharkov V.N., Gudkova T.V.* The period and Q of the Chandler wobble of Mars // *Planetary and Space Science*. 2009. V. 57. P. 288–295.
- [6] *Harada Y.* Reconsideration of the anelasticity parameters of the Martian mantle: Preliminary estimates based on the latest geodetic parameters and seismic models // *Icarus*. 2022. V. 383. Article 114917.
- [7] *Konopliv A.S., Yoder C.F. et al.* A global solution for the Mars static and seasonal gravity, Mars orientation, Phobos and Deimos masses, and Mars ephemeris // *Icarus*. 2006. V. 182. P. 23–50.
- [8] *Konopliv A.S., Asmar S.W. et al.* Mars high resolution gravity fields from MRO, Mars seasonal gravity, and other dynamical parameters // *Icarus*. 2011. V. 211. P. 401–428.
- [9] *Konopliv A.S., Park R.S. et al.* Detection of the Chandler wobble of Mars from orbiting spacecraft // *Geophysical Research Letters*. 2020. V. 47. Article e2020GL090568.
- [10] *Wieczorek M.A., Broquet A. et al.* InSight constraints on the global character of the Martian crust // *J. Geophysical Research: Planets*. 2022. V. 127. Article e2022JE007298.
- [11] *Stähler S.C., Khan A. et al.* Seismic detection of the Martian core // *Science*. 2021. V. 373. P. 443–448.
- [12] *Samuel H., Drilleau M. et al.* Geophysical evidence for an enriched molten silicate layer above Mars's core // *Nature*. 2023. V. 622. P. 712–717.
- [13] *Lemoine F.G., Smith D.E. et al.* An improved solution of the gravity field of Mars (GMM-2b) from Mars Global Surveyor // *J. Geophysical Research*. 2001. V. 106. Iss. E10. Article 23359–23376.
- [14] *Yuan D.-N., Sjogren W.L. et al.* Gravity field of Mars: A 75th degree and order model // *J. Geophysical Research*. 2001. V. 106. Iss. E10. Article 23359–23376.
- [15] *Knapmeyer-Endrun B., Panning M.P. et al.* Thickness and structure of the Martian crust from InSight seismic data // *Science*. 2021. V. 373. P. 438–443.
- [16] *Castillo-Rogez J.C., Efroimsky M., Lainey V.* The tidal history of Iapetus: Spin dynamics in the light of a refined dissipation model // *J. Geophysical Research: Planets*. 2011. V. 116. Iss. E9.

CHALLENGES AND APPROACHES IN CONSTRUCTING MARS' MAGNETIC FIELD MODELS FROM SATELLITE DATA

A. M. Salnikov^{1,2}, A. V. Batov^{1,2}, I. E. Stepanova¹, T. V. Gudkova¹

¹ *Schmidt Institute of Physics of the Earth RAS, Moscow, Russia*
salnikov@ifz.ru

² *Trapeznikov Institute of Control Sciences RAS, Moscow, Russia, batov@ifz.ru*

KEYWORDS:

Mars, magnetic field, analytical continuation, regularization, satellite data modeling

INTRODUCTION:

We discuss the process of forming satellite data samples by considering various selection strategies, including sampling measurements using different grid systems [1], selecting data obtained at specific altitudes above the Martian surface, and choosing data collected in the absence of direct sunlight (nighttime data). These criteria are essential for creating an optimal data sample necessary for constructing an accurate and reliable model of the Martian crust's magnetic field using the S-approximation method.

METHOD AND RESULTS:

The study utilizes data from nearly a decade of measurements (October 10, 2014, to February 14, 2024) from the Mars Atmosphere and Volatile Evolution (MAVEN) spacecraft. By combining MAVEN and Mars Global Surveyor (MGS) data, the accuracy of magnetic field models can be significantly improved [1]. Modern approaches to modeling Mars' magnetic field include the Equivalent Source Dipoles (ESD) method [2], spherical harmonics [3], and Physics-Informed Neural Networks (PINN) [4].

We employ the S-approximation method [5], which is based on the summation of simple and double layers, for approximating the magnetic field and constructing analytical continuations of the model field. We compare results with models from [2] and [3]. Sampling strategies are designed using MAVEN's calibrated data, supplemented with MGS data where needed, and include filtering for nighttime data to reduce distortions caused by external magnetic influences. The study area encompasses the combined landing zone of the InSight lander and Zhurong rover missions.

ACKNOWLEDGMENTS:

The study was supported by a grant from the Russian Science Foundation No. 23-27-00392, <https://rscf.ru/project/23-27-00392/>.

REFERENCES:

- [1] *Malkin Z.* A New Equal-area isolatitudinal grid on a spherical surface // *Astronomical J.* 2019. V. 158, No. 4. P. 158.
- [2] *Langlais B. et al.* A New model of the crustal magnetic field of Mars using MGS and MAVEN // *JGR: Planets.* 2019. V. 124, No. 6. P. 1542–1569.
- [3] *Morschhauser A., Lesur V., Grott M.* A spherical harmonic model of the lithospheric magnetic field of Mars // *J. Geophysical Research: Planets.* 2014. V. 119, No. 6. P. 1162–1188.
- [4] *Delcourt T., Mittelholz A.* A new model of the lithospheric magnetic field of Mars using a physics-informed neural network // 10th Intern. Conf. Mars. 2024.
- [5] *Stepanova I. E. et al.* On finding the analytical continuation of the magnetic field of Mars from satellite data using a combined approach // *Geophysical Research.* 2023. V. 24, No. 2. P. 58–83.

STATISTICAL PROPERTIES OF PLATEAU-LIKE TURBULENCE SPECTRA IN THE MARTIAN MAGNETOSHEATH: MAVEN OBSERVATIONS

H. Li¹, W. Jiang², X. Liu², D. Verscharen³, C. Wang²

¹ *National Space Science Center, Chinese Academy of Sciences
Beijing, China hli@nssc.ac.cn*

² *Chinese Academy of Sciences, China*

³ *University College London, United Kingdom*

KEYWORDS:

ABSTRACT:

The Martian magnetosheath provides us with a natural laboratory to study plasma turbulence in the presence of pickup ions and locally generated instabilities. Unlike the typical magnetic-field spectra with a single spectral scaling at magnetohydrodynamics (MHD) scales in Earth's magnetosheath, the magnetic-field spectra in the Martian magnetosheath during 4 years of Mars Atmosphere and Volatile Evolution observations frequently present an additional spectral break-point with a shallow slope at MHD scales which we define as a plateau-like spectral feature. The average occurrence rate of plateau-like magnetic-field spectra is 56.6 % of our measurement intervals. At moderate pick-up angles, the occurrence rate increases to a maximum of ~70.0 %. Furthermore, we present a positive correlation with the local ion density and anti-correlations with the local β , and the solar Extreme Ultra Violet irradiance. A similar occurrence rate in the quasi-perpendicular and the quasi-parallel magnetosheath (60.1% vs. 52.9 %) indicates that the plateau-like spectra are more likely formed locally than in the upstream solar wind. Our results suggest that energy injection from pickup ion driven micro-instabilities, for example, in the form of proton cyclotron waves, has insufficient time to evolve into a fully developed cascade in such a confined space like the Martian magnetosheath.

RADIATION ENVIRONMENT ON TGO MARS ORBIT DURING SOLAR PARTICLE EVENTS IN 2024

J. Semkova¹, V. Benghin³, R. Koleva¹, K. Krastev¹, Yu. Matviichuk¹, B. Tomov¹, N. Bankov¹, St. Maltchev¹, Ts. Dachev¹, I. Mitrofanov², D. Golovin², M. Mokrousov², M. Litvak², A. Kozyrev², V. Shurshakov³, S. Drobyshev³

¹ Space Research and Technology Institute, Bulgarian Academy of Sciences Sofia, Bulgaria, jsemkova@stil.bas.bg

² Space Research Institute RAS, Moscow, Russia

³ Institute of Biomedical Problems RAS, Moscow, Russia

KEYWORDS:

Mars, ExoMars TGO, radiation measurements, galactic cosmic rays (GCR), solar energetic particle (SEP) event, comparison

ABSTRACT:

The dosimetric telescope Liulin-MO for measuring the ionizing radiation environment onboard the ExoMars Trace Gas Orbiter (TGO) is a module of the Fine Resolution Epithelial Neutron Detector (FREND) [1, 2].

Presented are the main results from Liulin-MO measurements in TGO Mars science orbit (400 km altitude, 74° inclination) of the radiation doses and particle fluxes of GCR and of SEP events occurred in the first half of 2024. The results show that the dose rate and particle flux of GCR in April 2024 during the increasing phase of the 25th solar cycle are about 40 % of the corresponding values measured during the 24th solar cycle minimum in March – August 2020.

During the increasing phase of the 25th solar cycle a number of SEP events were observed in TGO Mars orbit [3–5]. In this paper we discuss the SEP events registered by Liulin-MO from January to June 2024. The SEP event that started on 20 May 2024 is the most powerful measured up to the moment on TGO. During this event the SEPs dose is 24.7 mGy in silicon-equal to the dose for about 200 days from GCR in undisturbed conditions. Measurements by Liulin-MO during SEP events are compared to measurements by other satellites and instruments around the Earth and in the heliosphere.

The results of the radiation measurements on TGO are of importance for assessment of the radiation risk and planning of the future manned and robotic missions to Mars. The Liulin-MO observations during SEP events in Mars orbit may contribute to the investigation of the distribution of the solar cosmic rays in the heliosphere.

REFERENCES:

- [1] Mitrofanov I., Malakhov A., Bakhtin B. et al. Fine Resolution Epithelial Neutron Detector (FREND) onboard the ExoMars Trace Gas Orbiter // *Space Science Reviews*. 2018. V. 214. Iss. 5. Article 86. <https://doi.org/10.1007/s11214-018-0522-5>.
- [2] Semkova J., Koleva R., Benghin V. et al. Charged particles radiation measurements with Liulin-MO dosimeter of FREND instrument aboard ExoMars Trace Gas Orbiter during the transit and in high elliptic Mars orbit // *Icarus*. 2018. V. 303. P. 53–66. <https://doi.org/10.1016/j.icarus.2017.12.034>.
- [3] Semkova J., Koleva R., Benghin V. et al. Observation of the radiation environment and solar energetic particle events in Mars orbit in May 2018 – June 2022 // *Life Sciences in Space Research*. 2023. V. 39. P. 106–118. <https://doi.org/10.1016/j.lssr.2023.03.006>.
- [4] Guo J., Li X., Zhang J., Dobynde M.I. et al. The first ground level enhancement seen on three planetary surfaces: Earth, Moon, and Mars // *Geophysical Research Letters*. 2023. V. 50. Article e2023GL103069. <https://doi.org/10.1029/2023GL103069>.
- [5] Semkova J., Benghin V., Koleva R. et al. New Results of Radiation Study on Board TGO ExoMars in 2018–2023 // *Solar System Research*. 2024. V. 58. No. 4. P. 367–376.

NEW CRATERS ON MARS — EXPANDING CATALOG IN 2023–2024

B. A. Ivanov

Institute of Geosphere Dynamics RAS, baivanov@idg.chph.ras.ru

KEYWORDS:

Mars, impact craters, atmospheric shock waves, dust, HiRIse

INTRODUCTION:

The HiRISE camera onboard of MRO spacecraft continue to make images of small “new” impact craters despite technical problems appeared last year. Together with many groups we continue to update the catalog of new craters to improve the general impact statistics and to find new examples of a complex interaction patterns of Martian atmospheric shock waves with the surface. The operation of the first Martian seismometer at the InSight landing point open the opportunity to count “new” impacts with seismic data.

SMALL IMPACT CRATERS WITH KNOWN (APPROXIMATELY) DATES OF ORIGIN:

Starting with the first impact craters formed in the limited time period (“dated” craters) found by Malin et al. [1], the perfect operation of the HiRISE camera onboard the Mars Reconnaissance Orbiter (MRO) has allowed us documented about 1200 impact sites covered with “before” and “after” images [2].

Currently (July 2024) the list of “new” dated impact craters is expanded from ~1200 [2] to ~1700 cases despite the partial failure of the HiRISE imaging system in July 2023. One unit (RED4) of the detector failed in the middle of the swath. The RED4 image gap is filled by a near-infrared CCD (IR10) for black and white images.

The failure results in an “blind” (empty) right half of COLOR images. which is filled by a near-infrared CCD (IR10) with lower resolution and a poorer contrast [3]. However, in many cases it is possible to find and to measure “new” craters in the empty part of images.

ATMOSPHERIC SHOCK WAVE INTERACTION WITH MARTIAN SURFACE:

With some inconvenience we continue to select “new” impact craters enlarging our collection. Figure 1 show the “scimitar” image ESP_080120_1895 (30 August 2023) formed due to oblique impact from North. We can see the combination of the red channel (left strip), RGB combination (central color strip) and the failed part of the sensor filling with IR channel data (right strip). These combinate images allow the HiRISE team to keep the experiment working.

Another type of atmospheric shock wave interaction is the collision of a pair of hemispherical shock wave, generated at the impact at the dusty surface. Figure 2 shows a hyperbolic surface trace formed by air shock wave collision (ESP_080164_1905, captured 2 September 2023; the impact occurs between July 2020 and April 2023). A projectile was split into a few fragments, created a cluster with largest craters of 9 m in diameter. The atmospheric shock waves from this impact of from a neighbor 5 m crater collided and formed a hyperbolic trace at a dusty surface (Figure 2).

SEISMIC SIGNALS FROM SMALL IMPACTS WITH VISIBLE CRATERS:

The technique to trace “new” impacts is now available due to seismic registration onboard of the InSight lander [4]. Within the continuing accumulation of data, a few strong seismic events have been observed, and several events are now interpreted as seismic waves from meteoroid impacts. This gives us the unique opportunity to know the exact date and time of impacts [5]. For example, the large new crater formation S1000a occurred September 18, 2021 17:48:00 UTC [6] and was imaged in low resolution with MARCI and in high resolution 27 February 2022 (ESP_073077_2155) [7].

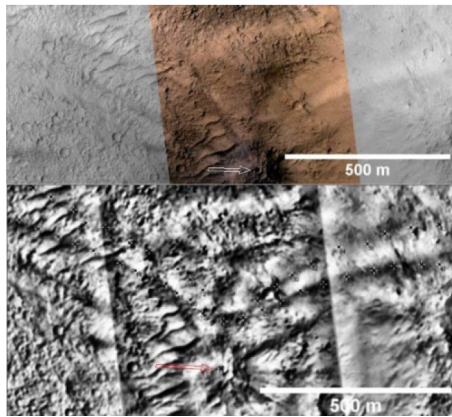


Fig. 1. The ESP_080120_1895 image comminated various channels to recover the HRSC data. The crater (pointed with an arrow) is about 7 m in diameter. The upper original image is processed to reveal contrast features as a “scimitar” outlined with small crosses (visible with the proper image expansion). We believe the “scimitar” is formed due to ballistic and explosion atmospheric shock wave interaction. The impact occurs between July 2019 and November 2021. Image processing with Image J software (<https://imagej.net/ij/>)

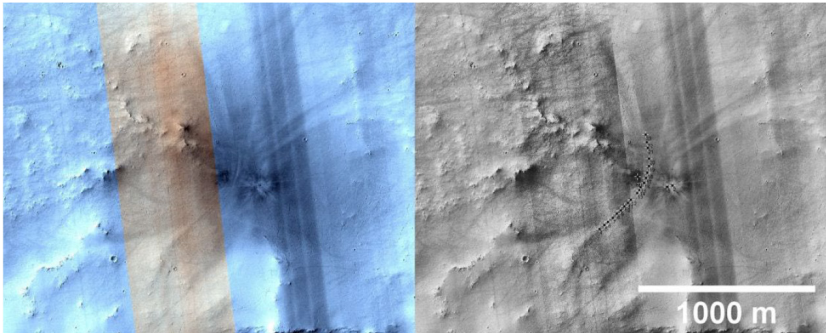


Fig. 2. The impact of a body shattered during the atmospheric passage (image ESP_080164_1905 captured 2 September 2023 not later than 3 years after formation. Left panel — the combined image of B/W, COLOR systems, with the substitute of IR lower resolution channel right of the colored strip). Right panel — B/W processing of the original image with the measured hyperbolic collision footprint of atmospheric shock waves depicted (small black crosses). The footprint geometry fits the delay of 0.35 seconds between two impacts. Totally about 20 small craters belong to this cluster with a total effective diameter of 11.5 m. Image processing with Image J software (<https://imagej.net/ij/>)

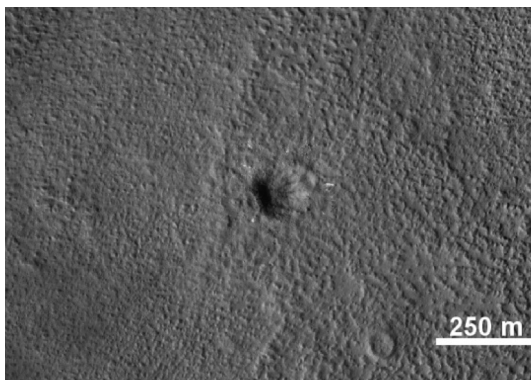


Fig. 3. The impact crater formed 18.09.2022, 17:48:00 UTC, imaged with HiRISE. The crater diameter is about 140 m. The surrounding surface has been changed with ejecta in area of $\sim 10 \times 10$ km [7]

The comparison of HiRISE/CTX technique to detect “new” impacts with InSight seismic records demonstrates that within uncertainties the impact rate of small bodies on Mars could be estimated (after correction to the global coverage) as 280–360 craters with diameters $D_{eff} > 8$ m per year [8].

CONCLUSIONS:

The combination of imaging and seismic monitoring gives a new technique to estimate the impact flux on Mars.

ACKNOWLEDGMENTS:

The project is supported with the state order of Ministry of science and higher education, Russian Federation (project № 122032900178-7).

REFERENCES:

- [1] *Malin M. C., Edgett K. S., Posiolova L. V. et al.* Present-day impact cratering rate and contemporary gully activity on Mars // *Science*. 2006. V. 314. Iss. 5805. P. 1573–1577. DOI: 10.1126/science.11351.
- [2] *Daubar I. J., Dundas C. M., McEwen A. S. et al.* New Craters on Mars: An Updated Catalog // *J. Geophys. Research: Planets*. 2022. V. 127. Iss. 7. Article e2021JE007145. <https://doi.org/10.1029/2021JE007145>.
- [3] *McEwen A. S., Byrne S. and HiRISE Team.* The Future of High-Resolution Orbital Imaging of Mars // *LPSC 55*. 2024. Woodlands, Texas. Article 1176.
- [4] *Banerdt W. B., Smrekar S. E., Don Banfield et al.* Initial results from the InSight mission on Mars // *Nature Geoscience*. 2020. V. 13. Iss. B2. P. 183–189. DOI:10.1038/s41561-020-0544-y.
- [5] *Rajšić A., Miljković K., Wójcicka N. et al.* Seismic Efficiency and Seismic Moment for Small Craters on Mars Formed in the Layered Uppermost Crust // *J. Geophysical Research: Planets*. 2023. V. 128. Iss. 4. Article e2022JE007698. <https://doi.org/10.1029/2022JE007698>.
- [6] *Ceylan S., Clinton J. F., Giardini D. et al.* The marsquake catalogue from InSight, sols 0–1011 // *Phys. Earth and Planet, Inter*. 2022. V. 333. Article 106943. <https://doi.org/10.1016/j.pepi.2022.106943>.
- [7] *Posiolova L. V., Lognonné P., Banerdt W. B. et al.* Largest recent impact craters on Mars: Orbital imaging and surface seismic co-investigation // *Science*. 2022. V. 378. Iss. 6618. P. 412–417.
- [8] *Zenhäusern G., Wójcicka N., Stähler S. C. et al.* An estimate of the impact rate on Mars from statistics of very-high-frequency marsquakes // *Nature Astronomy*. 2024. 14 p. <https://doi.org/10.1038/s41550-024-02301-z>.

AN EXPANDED CATALOG OF RECENT METEOROID IMPACT SITES ON MARS

E. D. Podobnaya, O. P. Popova, B. A. Ivanov, D. O. Glazachev
Sadovsky Institute of Geosphere Dynamics RAS
Moscow, Russia, epodobnaya@idg.ras.ru

KEYWORDS:

Mars, impact site, cluster, crater, size-frequency distribution, catalog

INTRODUCTION:

Repeated imaging of the Martian surface was conducted during the last decades to find new dated impact sites of meter-sized meteoroids. Impact sites are considered “new” if there is at least one image taken before impact [1]. There are over 1400 freshly formed impact sites detected by the summer of 2023 [2], which consists of a previously published catalog [1, 3] and approximately 245 additional impact sites that we have added [4]. More than half (57 %) of the impacting cosmic bodies disintegrate in the atmosphere and form crater clusters due to rarified martian atmosphere [5].

The study of clusters on Mars allows us to study the details of the interaction between meteoroids and the atmosphere that are poorly detailed on Earth. The study of Martian clusters provides a unique opportunity to estimate meteoroid parameters independently, to investigate different types of fragmentation for objects of different composition and origin.

IMPACT SITES ON MARS:

The size frequency distribution (SFD) of small bodies in the Solar System, as well as the distribution of formed craters, provides information about the origin and evolution of these bodies. Our catalog data provided an estimate of the exponent in the differential and cumulative SFD of craters, which was lower than assumed in most works, but close to the estimates obtained from the unexpanded catalog. Destroyed and undestroyed meteoroids are described by a same distribution.

A classification of meteoroid impact sites on Mars was proposed [6]. Suggested groups were generalized into 3 types of impact sites: a dominant main crater, 2 comparable largest craters, and 3 or more comparable largest craters, all supplemented (or not) by significantly smaller craters. We suggest that the highlighted groups may correspond to different types of impactors and/or different types of meteoroid disintegration in the atmosphere. The group with the two largest craters looks heterogeneous at the moment, and perhaps requires splitting into two subgroups.

The estimates of the exponent in the diameter distribution for meteoroids that formed the selected groups of impact sites are in good agreement with the estimates obtained for clusters, and slightly lower than the known estimates for the size distribution of terrestrial bolides.

ACKNOWLEDGMENTS:

The research was supported by RSF (project No. 23-27-00432, <https://rscf.ru/project/23-27-00432/>).

REFERENCES:

- [1] *Daubar I.J., Dundas C.M., McEwen A.S. et al.* New Craters on Mars: An Updated Catalog // *J. Geophysical Research: Planets*. 2022. V. 127. Iss. 7. eArticle 2021JE007145. <https://doi.org/10.1029/2021JE007145>.
- [2] *McEwen A.S. and 30 co-authors.* The high-resolution imaging science experiment (HiRISE) in the MRO extended science phases (2009–2023) // *Icarus*. 2023. V. 419. Article 115795. <https://doi.org/10.1016/j.icarus.2023.115795>.
- [3] *Neidhart T., Sansom E.K., Miljković K. et al.* Diversity of new Martian crater clusters informs meteoroid atmospheric interactions // *J. Geophysical Research: Planets*. 2023. V. 128. Iss. 4. Article e2022JE007611. <https://doi.org/10.1029/2022JE007611>.
- [4] *Podobnaya E., Popova O., Ivanov B., Glazachev D.* Classification of the updated catalog of recent impact sites on Mars // *Dynamic Processes in Geospheres*. 2023. V. 15. No 4. P. 72–82 (in Russian). DOI: 10.26006/29490995_2023_15_4_72.

- [5] *Hartmann W.K., Daubar I.J., Popova O.P., Joseph Emily C.S.* Martian cratering 12. Utilizing primary crater clusters to study crater populations and meteoroid properties // *Meteoritics and Planetary Science*. 2018. V. 53. Iss. 4. P. 672–686. <https://doi.org/10.1111/maps.13042>.
- [6] *Ivanov B.A., Melosh H.J., McEwen A.S., HIRISE Team.* Small impact crater clusters in high resolution HiRISE images // *Proc. 39th Annual Lunar and Planetary Science Conference*. Texas. USA. 2008. Abstr. 1221.

UNMANNED AIRCRAFT FOR MARS EXPLORATION: PREPARING A SCALE MODEL FOR FLIGHT TESTS

E. A. Karpovich, T. S. Kombaev, D. Gueraiche

*Moscow Aviation Institute (National Research University)
Moscow, Russia, karpovichea@mai.ru, kombaew@ya.ru*

KEYWORDS:

Mars exploration aircraft, flight testing, scaling, boxwing

ABSTRACT:

The 2021–2024 Ingenuity helicopter's flights on Mars demonstrated the feasibility of an aircraft flying in conditions significantly different from those on Earth, and inspired scientists and engineers in many countries to design various types of flying robots for exploring celestial bodies.

The report highlights the results of the conceptual design of an unmanned aircraft for Mars exploration, as well as the design features of its scaled model for flight testing on Earth.

The current version of the aircraft layout is a vertical takeoff and landing box wing, without a fuselage and empennage, without control surfaces, with a solar electric propulsion system providing thrust, control, and balance. In case of using the aircraft as a secondary payload, the mass of the vehicle is about 6 kg with a wingspan of 1 m, the mass of the payload of the aircraft is 500 g. The flight range of such an aircraft may be up to 47 km with an endurance of 14 min at a speed of 55 m/s and an altitude of 10 m.

A vertical takeoff and landing aircraft on Mars will be able to either carry out measurements in the planetary boundary layer on the required time scales, or deliver instruments to specified locations and carry out measurements on the surface.

The following flight profiles of the aircraft have been considered to date:

- 1) maximum-range flight, transfer of a scientific station, measurements on the surface;
- 2) measurements in the planetary boundary layer:
 - mapping in the horizontal plane;
 - measurement of atmospheric parameters in the vertical plane;
- 3) measurements inside the crater.

Sets of scientific instruments have been selected for these flight profiles.

In addition, an assessment of the radiation load on the components of the aircraft throughout the mission has been carried out.

In preparation for testing the flying model of the aircraft on Earth, the following goals and objectives have been formulated:

- 1) evaluation and verification of the aerodynamic characteristics of the model;
- 2) testing the operability of the distributed power plant to ensure trim and control in vertical and horizontal flight modes;
- 3) testing the methods used to optimize the propeller and airfoils of the blades and wings;
- 4) enhancing the methods of selecting and optimizing the propeller-engine group;
- 5) studying the features of boundary layer development on the wing of an aircraft with a distributed propulsion under high turbulence and low Reynolds numbers conditions;
- 6) tailoring the methods for recalculating the characteristics measured on the model to the basic version of the Martian aircraft;
- 7) verifying and optimizing design, technological and layout solutions;
- 8) collecting data to set the control system and autopilot;

- 9) determining the possibility and practicing the methods of working with sensors (hot wire anemometers and piezoelectric sensors) on the surface of the model;
- 10) development of landing procedure and landing gear design;
- 11) development and optimization of typical flight profiles for the Martian aircraft.

To ensure the possibility of solving the above-mentioned problems, especially in terms of aerodynamics and flight dynamics, the flying model of the aircraft must be correctly scaled for terrestrial conditions; in addition, efficient methods for recalculating the aerodynamic characteristics of the aircraft must be determined.

The differences between the flying model and the basic version of the Martian aircraft as a secondary payload include, in particular:

- absence of solar panels;
- flight conditions;
- probably, materials and components.

SESSION 1. MARS (MS-PS)
POSTER SESSION

THE EVOLUTION OF MARS AND THE POSSIBLE DYNAMICS OF ITS INTERIOR

N. A. Chujkova, L. P. Nasonova, T. G. Maksimova

*Lomonosov Moscow State University, Sternberg Astronomical Institute
Moscow, Russia, Chujkova@sai.msu.ru, Nason@sai.msu.ru*

KEYWORDS:

Mars, evolution, internal structure, internal gravitational field, convective movements

ABSTRACT:

Our conclusions about the evolution of Mars and the possible dynamics of its internal structure were made based on an analysis of the maps we constructed of potential and gravity anomalies in various layers of Mars [1]. Maps of density anomalies in these layers were obtained by a new solution to the inverse problem of gravimetry [2] based on the latest data on the external gravitational field and topography of Mars. The internal gravitational anomalies we identified in various layers could lead to convective movements in the mantle and core of Mars. However, the resulting flows of electrically conductive matter on the meridian planes, although they can create a toroidal magnetic field, are in the opposite direction in the northern and southern hemispheres, and due to their practical symmetry, the total field is reduced to zero. Similar flows in planes parallel to the equatorial plane cannot create a global magnetic poloidal field.

As for the early stage of the evolution of Mars (≈ 3 billion years ago), based on photographs of the surface of Mars taken by space probes, conclusions were drawn about the structure of the relief of Mars (the presence of canyons (the largest Valles Marineris), traces of ancient rivers and ancient lava eruptions volcanoes in the Tharsis region [3]). In addition, an analysis of the evolution of Mars is in some modern articles, as well as in reports at the Moscow symposia on the study of the Solar System. However, neither the reports nor the articles considered the dynamics of the interior of Mars due to the lack of geophysical, seismic and other observations inside Mars.

REFERENCES:

- [1] Chujkova N. A., Nasonova L. P., Maksimova T. G. Anomalies of density, stresses and the gravitational field inside Mars // Bull. Moscow University. 2012. V. 67, No. 2. P. 218–225. DOI: 10.3103/S0027134912020075.
- [2] Chujkova N. A., Nasonova L. P., Maksimova T. G. A new solution to the inverse problem of gravimetry for terrestrial planets and its verification for the Earth // Astronomy, Geodesy and Geophysics. Scientific and technical collection. M.: Publ. House "Center for Geodesy, Cartography and IPD". 2018. P. 90–113 (in Russian).
- [3] Ksanfomality L. V. Mars // Solar System. M.: Fizmatlit. 2017. P. 175–221.

GEOLOGICAL STRUCTURE OF THE UPPER PART OF NIRGAL VALLIS, MARS

E. S. Cholovskaia¹, M. A. Ivanov²

¹ Lomonosov Moscow State University, Faculty of Geology
Moscow, Russia, cattcholovskaya@yandex.ru;

² Vernadsky Institute of Geochemistry and Analytical Chemistry RAS
Moscow, Russia, Mikhail_Ivanov@brown.edu

KEYWORDS:

Mars, Nirgal, Her Desher, valley, channel, clay

INTRODUCTION:

Discovered on Mars clay minerals can be diagnostic of past climatic conditions [1, 2]. In order to constrain possible formation models of phyllosilicates, it is necessary to put them into the geological context of the territory where they are located.

For this research, the area that includes the upper part of Nirgal Vallis was selected (Figure 1). In this region, the clay-rich layers are exposed in the walls of Her Desher and Nirgal Vallis as well as in the walls, ejecta and on the floors of some impact craters. Previously conducted research of this territory [3–5] considered different features but little was done to link the phyllosilicates with the regional geological context, which is crucially important for the understanding of the interrelation between various processes and their time frames. In our research, we focused on the reconstruction of the general geological history of study area, which allows identification of the relationships between genetically different deposits, in particular phyllosilicates, and their formation processes.

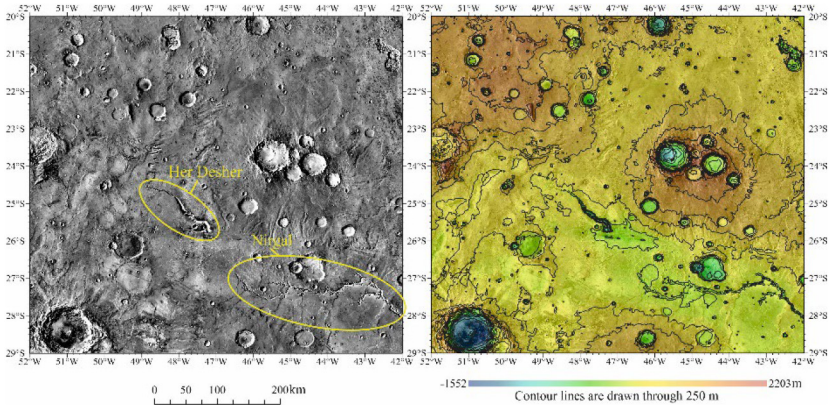


Fig. 1. Day-time images of THEMIS (left) and MOLA topography draped over them (right)

STUDY AREA AND METHODS:

The study area is located between 20–29°S and 45–52°W and overlaps the northwest part of the highlands of Noachis Terra. The total area is ~316 000 km². Most of the territory is located between 500–2000 m and consists of three elevated features separated by a low-lying plains.

The photobase of our research were the THEMIS images (100 m/px resolution). A digital elevation model (DEM) based on the MOLA data (~460 m/px resolution) was used to estimate the topographic configuration of the study area. More detailed study of the surface was conducted using data from the context camera CTX and high-resolution images from the HiRISE camera.

The absolute model ages (AMA) of surface deposits were determined by statistical analysis of size-frequency distribution (CSFD) of impact craters

within morphologically homogeneous units using the ArcGIS toolbar CraterTools and the CraterStats2 software.

RESULTS AND DISCUSSION:

Morphological homogeneous units were determined by their characteristic morphological and topographical features, and their relative (stratigraphic) age was established by the principle of superposition at the contacts with the other units. Based on the identification of stratigraphic units, a geological map of the studying area was compiled (Figure 2). The two most widespread units characterize the main features of the geological history of the studying area.

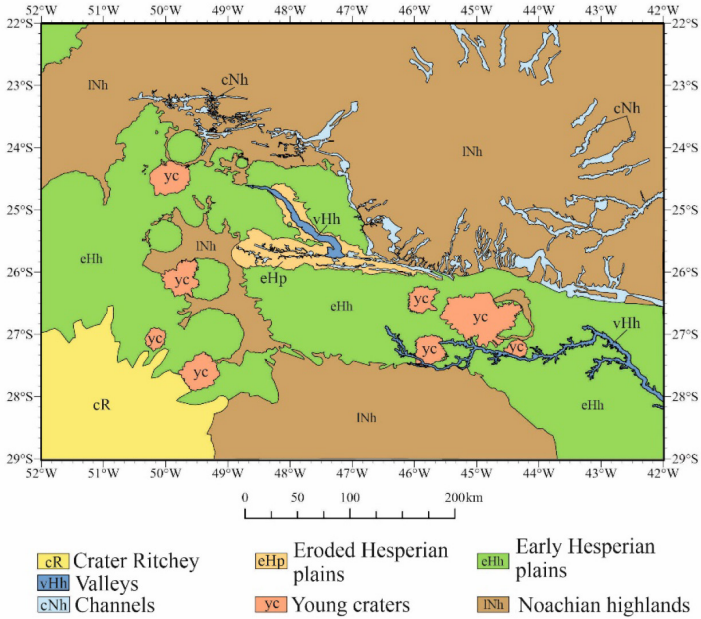


Fig. 2. Geological map of studying area

More ancient of these are the highlands (INh unit) the AMA of which is estimate to be ~ 3.8 Ga (Figure 2). This unit has very uneven, bumpy/hummocky surface with many impact craters. Some of them reach ~ 55 km in diameter and ~ 2 km in depth. In the north-eastern part of the studying area, the INh unit forms a conical hill with a diameter of 250 km and a height of 2 km, which we interpret as an ancient shield volcano. A characteristic feature of the uplift is the radial pattern of small channels on its flanks (Figure 1); they likely mark the first, Noachian, episode of fluvial erosion in the region (unit cNh, Figure 2). Signs of fluvial activity are also noted in ancient impact craters, although the timing of this activity, early Noachian or late Hesperian, remains to be open.

The younger major unit is unit eHh, which represents extensive lava plains with the AMA of ~ 3.6 Ga (Early Hesperian time). The gently undulating surface of the plains is less cratered and deformed in places by narrow and low wrinkle ridges. The material of the plains flooded craters of the Noachian age and small channels at the base of the possible volcano (Figure 2).

The surface of the Hesperian plains is cut by the canyons of Her Desher and Nirgal Vallis; these features mark the second episode of fluvial erosion in the study area. CSFD measurements on the floor of Her Desher Vallis is consistent with the AMA, 2.4–2.8 Ga.

CONCLUSION:

Our photogeological analysis of the northwestern part of Noachis Terra showed the presence of at least two episodes of fluvial activity: the earlier (Noachian) and the later (early Amazonian). Since water is necessary for the formation of phyllosilicates, the main question of our study is the fol-

lowing: which of the noted fluvial episodes could be responsible for the formation of clay minerals, and which for their redistribution. Both of them? Not one? We address this problem in our other abstract [6].

REFERENCES:

- [1] *Bibring J.P., Langevin Y., Gendrin A. et al.* Mars surface diversity as revealed by the OMEGA/Mars express observations // *Science*. 2005. V. 307. Iss. 5715. P. 1576–1581. DOI: 10.1126/science.110880.
- [2] *Poulet F., Bibring J.P., Mustard J.F. et al.* Phyllosilicates on Mars and implications for early martian climate // *Nature*. 2005. V. 438. No. 7068. P. 623–627. DOI: 10.1038/nature04274.
- [3] *Sun V.Z., Milliken R.E.* The geology and mineralogy of Ritchey crater, Mars: Evidence for post-Noachian clay formation // *J. Geophysical Research: Planets*. 2014. V. 119. Iss. 4. P. 810–836. <https://doi.org/10.1002/2013JE004602>.
- [4] *Buczowski D.L., Wyrick D.Y., Seelos K.D. et al.* Her Desher and Nirgal Valles: An integrated geomorphic, structural and mineralogic evaluation of ground-water flow in NW Noachis Terra // 52nd Lunar and Planetary Science Conference. Held virtually. 2021. No. 2548. P. 1748.
- [5] *Harish V.S., Mangold N.* Evidence for fluvial and glacial activities within impact craters that excavated into a Noachian volcanic dome on Mars // *Icarus*. 2021. V. 361. Article 114397. <https://doi.org/10.1016/j.icarus.2021.114397>.
- [6] *Cholovskaja E.S., Ivanov M.A.* Clay minerals in the upper part of Nirgal Vallis, Mars // 15th Moscow Solar System Symp. 2024.

INSTABILITIES IN DUSTY PLASMA IN THE ATMOSPHERE OF MARS ASSOCIATED WITH THE PASSAGE OF METEORIODS

T. I. Morozova, S. I. Popel

Space Research Institute RAS, Moscow, Russia, timoroz@yandex.ru

KEYWORDS:

meteoroids, dusty plasmas, meteoroid tail, modulatory interaction, low-frequency noises, Mars, dust acoustic waves.

INTRODUCTION:

Data on recording the low-frequency noise in the Martian atmosphere by ground-based vehicles were obtained in a frequency range similar to terrestrial electroacoustic noise from the passage of meteoric bodies [1]. It is assumed that in the case of the Martian atmosphere, these electromagnetic noises can also be observed from passages of meteoroids or from dusty plasma regions at 60 and 100 km.

DISCUSSION:

It is assumed that the low-frequency noise recorded on the surface of Mars may be associated with a charged dust component in its atmosphere and the occurrence of sound perturbations in such a dust system that modulate the electromagnetic wave from the Sun. It is also shown that it can be associated with plasma-dust processes in meteoroid tails. The mechanism for the excitation of modulatory instability of an electromagnetic wave associated with a dust acoustic mode in the Martian atmosphere, namely in dust clouds at an altitude of 60 and 100 km, where the dusty plasma with particles of frozen carbon dioxide is detected, is described. It is shown that the development of modulatory instability is due to the influence of high-frequency electromagnetic waves on the dusty plasma in the Martian atmosphere from both natural sources (solar radiation, lightning discharges) and anthropogenic nature (from equipment from space satellites and from stations on the surface of the planet). The parameters of electromagnetic pump waves, at which the active development of modulatory instability of electromagnetic waves associated with the dust acoustic mode is expected, and the modulatory instability growth rates are found. The development of the modulatory instability in the dusty plasma of Martian clouds, in turn, can explain the occurrence of low-frequency noise recorded by equipment on the surface of Mars. The relation between observed radio noise in the range of 3 Hz – 3 kHz and plasma-dust processes in the Martian atmosphere, in particular, in dust clouds at 60 and 100 km, as well as in dusty plasma meteoroid tails, where the dust concentration is high, is discussed. It is also assumed that modulatory instability of electromagnetic waves associated with ion acoustic mode also takes in meteoroid tails in martian atmosphere that can explain the whole range of observed low-frequency noises together with modulatory instability of electromagnetic waves associated with the dust acoustic mode.

ACKNOWLEDGMENTS:

The work was supported by the Foundation for the Advancement of Theoretical Physics and Mathematics "BASIS".

REFERENCES:

- [1] *Kozakiewicz J., Kulak A., Kubisz J., Zietara K.* Extremely low frequency electromagnetic investigation on Mars // *Earth, Moon and Planets*. 2016. V. 118. V. 103. <https://doi.org/10.1007/s11038-016-9493-2>.

VARIATION IN PLASMA COMPOSITION DURING THE ROTATION OF MARS' MAGNETOPAUSE

D. N. Morozova, O. L. Vaisberg

Space Research Institute RAS, Moscow, Russia, timoroz@yandex.ru

KEYWORDS:

Mars, magnetosheath, magnetopause, magnetosphere, attractor

ABSTRACT

Utilizing high temporal resolution data from the Mars Atmosphere and Volatile Evolution [1] satellite, this study analyzes the thin layers within Mars' plasma envelope. The focus is on the magnetic structure of Mars' daytime magnetopause. Findings indicate that the solar wind, after encountering the shock wave on Mars' dayside, does not directly engage with the Martian ionosphere. Instead, a 200–300 km thick plasma and magnetic field layer forms the daytime magnetosphere, positioned between the magnetosheath and the ionosphere [2]. There are two identified types of daytime magnetospheres:

- 1) the more common type features heated and accelerated O^+ ions located between the ionosphere and Mars' hot stream;
- 2) the other type includes accelerated O^+ ions within the magnetosheath, forming a continuous accelerated beam and creating a plume.

A magnetic structure exists between the magnetosheath and the magnetosphere, rotating almost without size alteration. This structure is observed in the latter part of the $n_p/(n_p + n_h)$ transition from approximately 1 to 10^{-2} . The transition from the magnetosheath to the magnetosphere is smooth in terms of energy density and ion composition, marked by a decrease in proton flux and an increase in heavy ion flux.

REFERENCES:

- [1] *Jakosky B.M., Grebowsky J.M., Luhmann J.G., Brain D.A.* Initial results from the MAVEN mission to Mars // *Geophysical Research Letters*. 2015. V. 42. Iss. 21. <https://doi.org/10.1002/2015GL065271>.
- [2] *Vaisberg O.L., Shuvalov S.D.* Properties and sources of the dayside Martian magnetosphere // *Icarus*. 2020. V. 354. Article 114085. <https://doi.org/10.1016/j.icarus.2020.114085>.

PROXIES TO INTERPLANETARY CONDITIONS AT MARS BY AN ARTIFICIAL NEURAL NETWORK

S. V. Kulikov, A. A. Skalsky

Space Research Institute RAS, Moscow, Russia, sv.kulikov93@yandex.com

KEYWORDS:

Mars, solar wind proxies, artificial neural network, magnetosheath, crust magnetization

ABSTRACT:

The solar wind (SW) plasma parameters and interplanetary magnetic field (IMF) affect the states of the Martian ionosphere and atmosphere and, consequently, variations of the magnetic field at the planetary surface.

The actual constellation of spacecraft at Mars does not allow to have a permanent *in situ* monitor of solar wind and IMF parameters. For a number of interesting events observed at the Martian surface, simultaneous measurements of plasma and magnetic field are available only in the magnetosheath region of the Mars plasma environment.

Following ideas described in [1], an artificial neural network is developed that provides proxies to SW and IMF parameters based on measurements in the magnetosheath region. To train the neural network, the magnetization of the Martian crust was used as an extra input parameter in addition to the density, temperature, and velocity of the magnetosheath plasma. It is shown that magnetization of the Martian crust is essential for better prediction of IMF.

REFERENCES:

- 1 *Ruhunusiri S., Halekas J. S., Espley J. R. et al.* An artificial neural network for inferring solar wind proxies at Mars // *Geophysical Research Letters*. 2018. V. 45. Iss. 20. P. 10,855–10,865. <https://doi.org/10.1029/2018GL079282>.

SESSION 2. VENUS (VN)
ORAL SESSION

PLANETARY-SCALE WAVES AND QUASI-PERIODIC VARIATION OF THE EQUATORIAL JET IN THE VENUS ATMOSPHERE

M. Takagi¹, H. Ando¹, M. Imai², N. Sugimoto³, Y. Matsuda⁴

¹ Kyoto Sangyo University,
takagi.masahiro@cc.kyoto-su.ac.jp

² The University of Tokyo

⁴ Keio University

⁵ Tokyo Gakugei University

KEYWORDS:

4-day wave, 5-day wave, Rossby-Kelvin instability, equatorial jet

INTRODUCTION:

It has been known that planetary-scale waves such as the 4-day and 5-day waves exist in the cloud layer (about 45–70 km altitudes) on Venus [1]. These waves are expected to play important roles in the formation of atmospheric general circulation and the maintenance of the superrotation (SR) by their transport of angular momentum and heat. However, they are poorly understood yet. In order to interpret observations and understand the Venus atmospheric dynamics, it is necessary to elucidate what these waves are and what they do. In this study, we reproduced these waves in a Venus general circulation model (GCM) and investigated their structure, generation mechanism, and dynamical effects on the general circulation [2, 3].

MODEL:

We use a simple Venus GCM named AFES-Venus [4, 5]. The resolution is T42 with 120 layers covering 0–120 km altitudes. The solar heating is based on a recent radiative transfer model [6]. The infrared radiative process is approximated by a Newtonian cooling scheme. The reference temperature is based on observations and assumed to be horizontally uniform. The initial condition is an idealized superrotating state. The model is integrated for 53 Earth years. We analyze data obtained in a quasi-equilibrium state in the last 3 Earth years.

RESULTS:

Zonal-mean zonal wind:

The fast SR is maintained in the GCM. At ~70 km near the cloud top, the zonal-mean zonal wind velocity is almost constant in low latitudes, and weak jets are formed in mid-latitudes. This distribution is consistent with recent observations [7]. Note that the SR rotates slower in lower latitudes and faster in higher latitudes in terms of angular velocity. The rotation period of SR at 70 km is about 4 days in low latitudes and 2 days in high latitudes. The Fourier analysis of horizontal wind shows that several waves exist around the cloud layer. We focus on waves with a zonal wavenumber of 1 and periods of 3.3 days, 5.8 days, and 7 days.

3.3-day wave:

The 3.3-day wave exists in 65–80 km, consisting of a Kelvin mode in low latitudes and Rossby modes in mid-latitudes symmetric about the equator. The zonal phase velocity is faster than the SR in the equatorial region. This structure is consistent with observations of the 4-day wave at the cloud top [8]. The coupling of the Kelvin and Rossby modes induces equatorward angular momentum (AM) transport, accelerating the SR in the equatorial region. The result suggests that the 3.3-day wave could correspond to the 4-day wave and it is excited by the Rossby-Kelvin instability [9].

5.8-day wave:

The 5.8-day wave exists in 25–80 km. Its horizontal structure is symmetric about the equator, but it changes significantly with altitudes. Below 56 km, a Kelvin mode is predominant in low latitudes. In 40–65 km, a pair of Ross-

by modes appears in high latitudes. In 50–80 km, another pair of Rossby modes appear in mid-latitudes and predominates above 65 km. The structure at 70 km is quite similar to the 5-day wave [10, 11]. The Kelvin mode exists below the critical surface, where the phase velocity of the wave equals to the zonal-mean zonal wind velocity. On the other hand, the high-latitude and mid-latitude Rossby modes exist above the critical surface. These structures indicate that the 5.8-day wave is also excited by the Rossby – Kelvin instability; the Kelvin mode is connected with high-latitude and mid-latitude Rossby modes on different isentropic surfaces. The 5.8-day wave induces the equatorward AM transport below the critical surface, producing the equatorial jet at 45–53 km altitudes. Note that the 5.8-day wave also produces significant poleward heat transport in the cloud layer although the Rossby-Kelvin instability is not baroclinic instability.

7-day wave:

The 7-day wave is antisymmetric about the equator, dominated by vortices in mid- and high latitudes. The horizontal structure is divided by 4 critical latitudes; the phase velocity relative to the SR is westward in the equatorial region and high latitudes and eastward in mid-latitudes. The equatorial region is also dominated by vortices similar to the equatorial Rossby wave [12]. The result suggests that the 7-day wave consists of the three Rossby modes: the westward equatorial Rossby mode, the eastward mid-latitude Rossby mode, and the westward high-latitude Rossby mode. In the lower cloud layer (45–52 km), the 7-day wave produces the poleward and equatorward AM transport across the critical altitudes, decelerating the equatorial jet and accelerating the SR in mid-latitudes. As a result, the SR becomes close to a solid body rotation in low and mid-latitudes. These results suggest that the equatorial jet, which is produced by the 5.8-day wave, is destroyed by the 7-day wave.

Quasi-periodic variation of the equatorial jet:

The SR in the lower cloud layer varies quasi-periodically with a period about 280 Earth days. As the 5.8-day wave grows, the equatorial jet becomes faster. As the equatorial jet matures, the 7-day wave begins to grow. As the 7-day wave grows, the equatorial jet becomes slower and the SR in mid-latitudes becomes faster. After the growth of 7-day wave, the zonal-mean zonal wind velocity becomes almost constant in low latitudes equatorward of 45°. As the 7-day wave decays, the 5.8-day wave grows again, and the equatorial jet becomes faster. In this way, the quasi-periodic variation of the equatorial jet is caused by the alternating development of the 5.8-day and 7-day waves. This result could provide a possible explanation of the equatorial jet inferred from the Akatsuki observation [13].

SUMMARY:

The 4-day (3.3-day) and 5-day (5.8-day) waves observed at the cloud top were reproduced in the GCM. These waves are excited by the Rossby – Kelvin instability. The 7-day wave, which has not been observed yet, is excited by the shear instability due to the equatorial jet. The equatorial jet in the lower cloud layer is produced by the 5.8-day wave and destroyed by the 7-day wave. Its quasi-periodic variation with a timescale of about 280 Earth days is caused by the alternating development of these waves. Recently, a similar result has been obtained in an independent GCM [14]. Other unknown waves may be hidden in the cloud layer. To understand the Venus atmospheric dynamics, we need further observations for waves, SR, and meridional circulation.

REFERENCES:

- [1] *Del Genio A. D., Rossow W.* Planetary-scale waves and the cyclic nature of cloud top dynamics on Venus // *J. Atmos. Sci.* 1990. P. 293–318.
- [2] *Takagi M. et al.* A GCM study of the 4-day and 5-day waves in the Venus atmosphere // *JGR Planets.* 2021. V. 127. Article e2021JE007164.
- [3] *Takagi M. et al.* Formation and quasi-periodic variation of equatorial jet caused by planetary-scale waves in the Venusian lower cloud layer // *JGR Planets.* 2022. V. 128. Article e2023JE007922.
- [4] *Sugimoto N. et al.* Baroclinic instability in the Venus atmosphere simulated by GCM // *JGR Planets.* 2014. V. 119. P. 1950–1968.

- [5] *Suzuki A. et al.* A sensitivity study of the thermal tides in the Venusian atmosphere: structures and dynamical effects on the superrotation // JGR. Planets. 2022. V. 127. Article e2022JE007243.
- [6] *Haus R., Kappel D., Arnold G.* Radiative heating and cooling in the middle and lower atmosphere of Venus and responses to atmospheric and spectroscopic parameter variations // Planetary and Space Sci. 2015. V. 117. P. 262–294.
- [7] *Machado P. et al.* Venus atmospheric dynamics at two altitudes: Akatsuki and Venus Express cloud tracking, ground-based doppler observations and comparison with modeling // Atmosphere. 2021. V. 12. P. 1–28.
- [8] *Kouyama T. et al.* Vertical propagation of planetary-scale waves in variable background winds in the upper cloud region of Venus // Icarus. 2015. V. 248. P. 560–568.
- [9] *Iga S., Matsuda Y.* Shear-instability in a shallow water model with implications for the Venus atmosphere // J. Atmos. Sci. 2005. V. 62. P. 2514–2527.
- [10] *Kouyama T. et al.* Long-term variation in the cloud-tracked zonal velocities at the cloud top of Venus deduced from Venus Express VMC images // JGR Planets. 2013. V. 118. P. 37–46.
- [11] *Imai M. et al.* Planetary-scale variations in winds and UV brightness at the Venusian cloud top: periodicity and temporal evolution // JGR Planets. 2019. V. 124. P. 1–25.
- [12] *Matsuno T.* Quasi-geostrophic motions in the equatorial area // J. Meteor. Soc. Japan. 1966. V. 44. P. 25–43.
- [13] *Horinouchi T. et al.* Equatorial jet in the lower to middle cloud layer of Venus revealed by Akatsuki // Nature Geosci. 2017. V. 10. P. 646–651.
- [14] *Lai D., Lebonnois S., Li T.* Planetary-scale wave activity in Venus cloud layer simulated by the Venus PCM // JGR. Planets. 2024. V. 129. Article e2023JE008253.

STATIONARY MESOSCALE FEATURES ON VENUS' DAYSIDE CLOUDS

J. E. Silva¹, T. Imamura², A. Cardesin-Moinelo^{3,4,5}, Y. J. Lee¹, P. Machado⁵, D. Espadinha⁵

¹ Planetary Atmospheres Group, Institute for Basic Science Daejeon, South Korea, josesilva@ibs.re.kr

² Graduate School of Frontier Sciences, The University of Tokyo Kashiwa, Japan

³ European Space Astronomy Centre, Madrid, Spain

⁴ Institute of Astrophysics of Andalusia, Glorieta de la Astronomia Granada, Spain

⁵ Institute of Astrophysics and Space Sciences, University of Lisbon, Astronomical Observatory of Lisbon, Lisbon, Portugal

KEYWORDS:

Venus, atmosphere, waves, imaging, dynamics

ABSTRACT:

Venus' atmosphere remains a dynamic and mysterious system which not only completely covers the surface of the planet but is believed to have had a dramatic impact on how the planet evolved. The current mechanisms that drive its behaviour and how it plays with both intrinsic aspects of the planet and outside influence, have continuously been pieced together for decades, from remote observations to climate modelling, in an attempt to coalesce into a uniform picture of atmospheric circulation. Thus, it falls unto us to understand each of these drivers and how large a role they play in the grand picture. Atmospheric waves seem to be one of the key players at various scales.

Atmospheric gravity waves on Venus have garnered increasing attention in the past decade, sparked by the first observation of a planetary scale bow-shape by the Japanese space mission Akatsuki in December 2015 [1]. The still ongoing mission has thus far provided a continuous cover of the planet's cloud layer, including further detection and characterization of stationary waves on the top of the clouds with the Ultraviolet Imager (UVI) which is sensitive to ultraviolet reflected solar radiation, and at slightly lower levels thanks to the capabilities of the Longwave Infrared Camera (LIR) which uses thermal imaging in the mid-infrared.

For the past decade, most efforts to study gravity waves on Venus have been directed towards understanding both their forcing mechanisms and their influence on atmospheric circulation. Because these waves are driven by such a fundamental force as gravity and also since they can transport energy and momentum across several atmospheric layers, finding these structures on the atmospheres of other planets becomes another tool in understanding their contribution to their planets' energy budget in the atmosphere.

These waves can be generated by a multitude of sources, including flow over topography like mountains and valleys or through convection cells, which can produce different characteristics on the generated waves. Gravity waves with orographic origins have been widely studied on Earth and a similar mechanism has been proposed for Venus, supported by the presence of the aforementioned stationary waves, which are fixed relative to topography and are commonly associated with prominent mountains on Venus. However, these waves are detected near 60–70 km above the surface and require a positive statically stable environment to be able to propagate, a condition which seems to not always be in place between the surface and the cloud layer. Modelling efforts have been able to reproduce the largest of these structures and how they may propagate from the surface to the top of the clouds where we observe them [2], but such efforts for smaller-scale features are still ongoing.

Since gravity waves feature a wide range of scales and characteristics, other generating sources like convection or shear instability have been proposed. Knowledge of the origin of these waves would also aid in the understanding of their role in the larger picture of Venus' atmosphere dynamics and quantify their influence at various scales.

Ongoing work for the detection of these waves has already provided some headway with a broadening coverage of past and emerging data sets at 0.283, 3.8, 5 and 10 μm wavelengths [3–6], focusing on waves propagating at seemingly different altitudes. The higher spatial resolution of images gathered from several spacecraft allows the identification and characterization of progressively smaller and more varied wave shapes. Such data sets include instruments from Venus Express (Vex), namely the Visible and Infrared Thermal Imaging Spectrometer (VIRTIS) and from Akatsuki including UVI and the 2 μm Camera (IR2), targeting the upper clouds on the dayside with ~ 20 km/pixel resolution, covering the equator and mid-latitudes with Akatsuki and high southern latitudes with VEx.

In this work we propose to combine data from LIR (8–12 μm), IR2 (2.02 μm), UVI (283, 365 nm) and VIRTIS-M (0.25–1 μm), at several wavelength targeting the dayside clouds of Venus, in an effort to describe and analyse mesoscale stationary structures. The selected wavelength ranges covered by these instruments can provide a view of the top and middle cloud layer where stationary waves are observable. Our goal is to characterize these smaller scale unmoving structures relative to the topography of Venus, in terms of their retrievable morphological and dynamical parameters, as well as their global distribution. Through these efforts, we hope to expand current knowledge of stationary features detected on Venus and also combine observations at several wavelengths to infer on possible three-dimensional properties of these features and their influence on the atmospheric flow. Additionally, with a larger coverage from several instruments, we will broaden the possible distribution of stationary features to a wider latitudinal coverage and time period, which enables a comparison of the behaviour of these mesoscale structures at different latitudes and possible influence of both the underlying topography and local wind flow regime on the morphology and dynamics of these waves.

REFERENCES:

- [1] *Fukuhara T. et al.* Large stationary gravity wave in the atmosphere of Venus // *Nature: Geoscience*. 2017. <https://www.nature.com/articles/ngeo2873>.
- [2] *Lefevre M. et al.* Mesoscale modeling of Venus' bow-shape waves // *Icarus*. 2005. V. 335. Article 113376. <https://doi.org/10.1016/j.icarus.2019.07.010>.
- [3] *Fukuya K. et al.* Horizontal structures of bow-shaped mountain wave trains seen in thermal infrared images of Venusian clouds taken by Akatsuki LIR // *Icarus*. 2022. V. 378, Article 114936. <https://doi.org/10.1016/j.icarus.2022.114936>.
- [4] *Kitahara T. et al.* Stationary features at the cloud top of Venus Observed by Ultraviolet Imager onboard Akatsuki // *J. Geophysical Research: Planets*. 2019. V. 124. P 1266–1281.
- [5] *Kouyama T. et al.* Topographical and Local Time Dependence of large Stationary Gravity Waves Observed at the Cloud top of Venus // *Geophysical Research Letters*. 2017. V. 44. P. 12098–12105.
- [6] *Peralta J. et al.* Stationary waves and slowly moving features in the night upper clouds of Venus // *Nature: Astronomy*. 2017. V. 1. Article 0187. <https://www.nature.com/articles/s41550-017-0187>.

PECULIARITIES OF THE VENUS UPPER CLOUD LAYER CIRCULATION DURING THE 24th SOLAR ACTIVITY CYCLE

L. V. Zasova, I. V. Khatuntsev, M. V. Patsaeva, N. I. Ignatiev,
D. A. Gorinov

Space Research Institute RAS, Moscow, Russia,
zasova@cosmos.ru

KEYWORDS:

Venus, atmosphere, dynamic, meridional circulation

INTRODUCTION:

Monitoring of the movement of the cloud features by cameras installed on the orbiters is the effective method to study a dynamics of Venus atmosphere. Two very successful experiments were carried out are VMC/VEX (Venus Monitoring Camera on board of Venus Express) [1, 2], functioned from 2006 to 2013, and the Akatsuki /JAXA [3] camera, functioned in 2015–2024 years. The VMC /VEX camera acquired images of the day side of Venus in three spectral ranges — UV (365 nm), VIS (513 nm) and NIR (965 nm). The 24th solar cycle was covered by the measurements in the UV spectral range except the maximum around 2014 year: the VMC UV (365 nm) channel worked during the arise of the solar activity and the UVI (365 nm) Akatsuki camera worked during its decline (Figure 1).

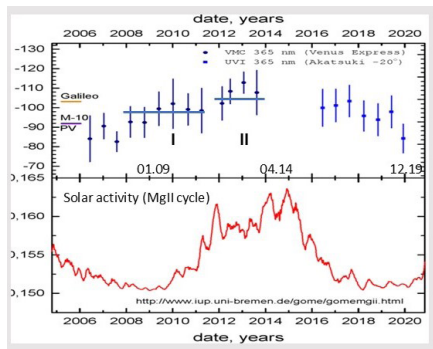


Fig. 1. Zonal velocity at the cloud top, measured by VMC and UVI (top). For comparison, the curve of the MgII index variation during the 24th solar cycle is given (bottom). Numbers along x-axis are the dates of two minima and a maximum of the cycle

Mapping of the displacement of the cloud features simultaneously in the VMC spectral ranges gives possibility to estimate the wind velocity fields in the cloud top region, at height 70 ± 2 km in UV, inside or around low boundary of the upper clouds, 60 ± 2 km in VIS, and at the upper boundary of the middle clouds 55 ± 2 km in NIR. The boundaries of the cloud layers are taken from [4].

DISCUSSION:

The zonal velocity at the cloud top measured by VMC is shown in Figure 1. To characterize the solar activity cycle, the curve of the MgII index is given also. With increasing solar activity, the wind speed increases. There are no measurements at the maximum of the cycle. At the decline of solar activity, the Akatsuki measurements continue the series, the speed decreases when the Sun approaches the minimum of activity.

Further, we will consider only the VMC results obtained for a half of the 24th solar cycle, but in three filters, which correspond to different levels in the atmosphere. From the VMC results, two sets of data were separated with different zonal speeds, I — so-called “slow” period, close to minimum of the solar cycle and II — “fast” near its maximum.

The calculated averaged zonal and meridional wind speed profiles for “slow” and “fast” periods are shown in Figure 2.

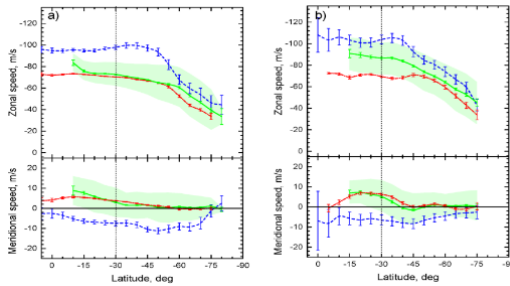


Fig. 2. Mean latitudinal profiles of the zonal (top) and meridional (bottom) winds derived for the (a) “slow” and (b) “fast” subsets, obtained in the VMC channels: UV (blue), VIS (green) and NIR (red). In the southern hemisphere, negative meridional velocities mean the direction of the horizontal flow towards the South pole, and the positive ones — towards the equator [5]

In the “slow” period, related to the minimum of the cycle (2006–2011) at mid-latitudes, the averaged zonal and meridional velocities in the NIR (red) and VIS (green) channels coincide (at $\varphi \leq 60^\circ$ S), and in the “fast” period (2012–2014) — zonal velocities in the UV and VIS increase approximately by of 10 and 20 m/s respectively, but they practically do not change in the NIR band.

The purpose of this paper is to try to find the explanation of the velocity changes occurring in the cloud layer of Venus during the first half of the 24th solar cycle.

During the observation period of VMC VEX, 2006–2014, from the minimum of the 24th solar cycle to near maximum, the albedo of the full disk of Venus in the UV channel decreased by up to 2 times, that is Venus is darkened [6]. The “unknown” UV absorber (320–500 nm) is located in the upper cloud layer. Being concentrated in a narrow layer about 10 km thick in the upper clouds $(58-70) \pm 2$ km, it absorbs nearly half of the solar energy consumed by Venus, providing energy to thermal tides, which in turn maintain a superrotation.

With the increasing of the solar activity, when it approaches to the maximum of the cycle, the UV albedo decreases, i.e. the absorption of solar energy increases (we don’t know what is causing it — far UV, X-rays, galactic cosmic rays, changes in the clouds, it’s not that important). What really important is that the absorption in the UV increases, and hence the additional energy can strengthen the thermal tide, causing acceleration of superrotation — most probably, at those levels, where the absorber is located, that is in the upper clouds. It is not known to what extent the UV absorption spectral feature changes, it can’t be excluded that it becomes so wide that the absorption at 513 nm also increases. Indeed, zonal wind velocity at 30° S, measured in UV increases by about of 10%, but also it increases by 20 % in VIS. If to admit that the vertical wind shear is about 2 m/s/km, then the upper cloud layer observed in “fast” period has to increase its altitude at 10–15 km at maximum of solar cycle, which doesn’t look realistic. Most probably, the acceleration in the upper clouds around maximum of the cycle is not tied directly to the change of altitude.

In the NIR channel, the zonal velocity weakly depends on the solar cycle. The levels, observed in NIR refer to the upper boundary of the middle cloud layer, and the acceleration of superrotation does not have a noticeable effect there.

Thus, in the second half of the mission we see the growth of the velocity observed at two levels (UV and VIS) both of them refer to the upper cloud layer, where the UV absorber is located.

It was offered [7] to describe the meridional circulation in Venus atmosphere by alternating direct and indirect Hadley cells. VMC found the position of the direct Hadley cell in the upper clouds in three spectral channels: in UV — the direct branch (direction toward the pole) and in VIS and NIR — the return one (toward equator). However, the required indirect cell at “slow” period was not identified. During the “slow” period, VIS and IR observations look as if they are related to the same level — possibly to the return branch of the direct Hadley cell (we see the equality of zonal and meridional velocities there). Note that in the “fast” period close to the maximum of the 24th solar cycle the ambiguity in determining position of these levels is removed.

RESULTS:

- It was found that the acceleration connected to the Solar cycle is observed in the upper clouds, where the “unknown” absorber resides. Decrease of the UV-albedo leads to increase of absorption of the energy, strengthening a thermal tide and accelerating the superrotation.
- The direct Hadley cell covers the upper cloud layer. The ambiguity in determining its lower boundary is removed due to the observations in the high-velocity “fast” region, when the zonal velocity measured in UV and VIS (but not in IR) increases by about 10–15 % near the cycle maximum.
- Position of levels, observed in NIR correspond to the upper boundary of the middle clouds (55±2 km). They may be considered as the upper branch (directed to equator) of indirect Hadley cell, which probably covers the middle cloud layer.
- Using the VIRTIS/VEX measurements in the 1.74 μm channel, which allows to probe the lower cloud layer on the night side of Venus, a direct Hadley cell fragmentary was discovered in the lower cloud layer [8].

In general, it may be concluded that our study indicates the existence of three Hadley cells, identified in the clouds of Venus, which belong to three cloud layers: direct branches in the upper and low clouds, and the indirect one in the middle clouds

REFERENCES:

- [1] Titov D.V., Svedhem H., Koschny D. et al. Venus Express science planning // *Planet. Space Sci.* 2006. V. 54. P. 1279–1297. <https://doi.org/10.1016/j.pss.2006.04.017>.
- [2] Svedhem H., Titov D.V., Taylor F.W., Witasse O. The Venus Express mission // *J. Geophys. Res.* 2009. V. 114. Article E00B33. <https://doi.org/10.1029/2008JE003290>.
- [3] Nakamura M., Imamura T., Ishii N. et al. AKATSUKI returns to Venus // *Earth Planet Sp.* 2016. V. 68. P. 75. <https://doi.org/10.1186/s40623-016-0457-6>.
- [4] Knollenberg R. G., Hunten D. M. The Microphysics of the Clouds of Venus: Results of the Pioneer Venus Particle Size Spectrometer Experiment // *J. Geophys. Res.* V. 85. Iss. A13. P. 8039–8058.
- [5] Khatuntsev I.V., Patsaeva M.V., Zasova L.V. et al. Winds from the visible (513 nm) images obtained by the Venus monitoring camera onboard Venus Express // *J. Geophys. Res.: Planets.* 2022. V. 127. Article e2021JE007032. <https://doi.org/10.1029/2021JE007032>.
- [6] Lee Y.J., Jessup K.L., Perez-Hoyos S. et al. Long-term variations of Venus' 365-nm albedo observed by Venus Express, Akatsuki, MESSENGER, and Hubble Space Telescope // *Astron. J.* 2019. V. 158. No. 3. Article 126. <https://doi.org/10.3847/1538-3881/ab312>.
- [7] Schubert G. General circulation and dynamical state of the Venus atmosphere // *Venus / Eds: Hunten D., Colin L., Donahue T., Moroz V.I.* Tucson, AZ: Univ. Arizona Press, 1983. P. 681–765.
- [8] Gorinov D. A., Zasova L. V., Khatuntsev I. V. et al. Winds in the lower cloud level on the nightside of Venus from VIRTIS-M (Venus Express) 1.74 μm images // *Atmosphere.* 2021. V. 12. P. 186. <https://doi.org/10.3390/atmos12020186>.

VENUS ATMOSPHERIC DYNAMICS: DIGGING INTO THE VENUS EXPRESS OBSERVATIONS

D. V. Titov

*Sun Yat-sen University, School of Atmospheric Sciences
Zhuhai Campus, China*

KEYWORDS:

Venus, dynamics, clouds, winds, stability

ABSTRACT:

Dynamics of the Venus atmosphere is still one of unsolved fundamental problems in the planetary physics. ESA's Venus Express collected long imaging time series of the planet in several wavelengths from UV to near-IR. It was later amended by JAXA's Akatsuki observations thus providing the longest almost uninterrupted monitoring over about 26 Venus years. The imaging allowed determination of wind speeds at different levels within the cloud deck thus enabling significant progress in characterization of the mean atmospheric circulation. The analysis revealed wind variability including changes with altitude, latitude, local solar time as well as influence of the surface topography and long term 12.5 years periodicity [1].

The images also provided morphological evidences of dynamical processes at the cloud level. UV dark low latitudes were found to be dominated by convective mixing that brings UV absorbers from depth, while bright uniform clouds at middle-to-high latitudes are typical for the regions with suppresses vertical mixing. The latter feature correlates with drastic increase of the total cloud opacity poleward from $\sim 60^\circ$ latitude that likely indicates presence of a dynamical mixing barrier here. Similarity of the global UV cloud morphology at the cloud top (~ 70 km) and that in the deep cloud (50-55 km) observed in the near-IR on the night side suggested similar morphology shaping processes throughout the cloud deck. Venus Express observed gravity waves poleward of 65° N concentrated at the edges of Ishtar Terra likely indicating their generation by wind interaction with the surface [2].

Venus Express performed about 800 radio occultations providing precise measurements of the atmospheric temperature structure and static stability parameter in the altitude range 40–90 km [3]. The Richardson number latitude-altitude field derived from the wind and temperature measurements suggests presence of convection in the cloud deck and stable mesosphere above it with the convective layer extending to greater depth at high latitudes [4]. The talk will summarize the Venus Express observations related to the atmospheric dynamics and propose an outlook for further analysis of these data.

REFERENCES:

- [1] *Khatuntsev I. V. et al.* Twelve-year cycle in the cloud top winds derived from VMC/Venus Express and UVI/Akatsuki imaging // *Atmosphere*. 2022. V. 13. Article 2023. <https://doi.org/10.3390/atmos13122023>.
- [2] *Titov D. V. et al.* Morphology of the cloud tops as observed by the Venus Express Monitoring Camera. DOI: 10.1016/j.icarus.2011.06.020.
- [3] *Tellmann et al.* Small-scale temperature fluctuations seen by the VeRa Radio Science Experiment on Venus Express // *Icarus*. 2012. V. 221. P. 471–480.
- [4] *Piccialli A. et al.* Dynamical properties of the Venus mesosphere from the radio-occultation experiment VeRa onboard Venus Express // *Icarus*. 2011. DOI: 10.1016/j.icarus.2011.07.016.

MODELING STUDIES OF VENUSIAN IONOSPHERE AND UPPER ATMOSPHERE

Y. Cao, J. Cui, H. Gu, X. Wu

*Planetary Environmental and Astrobiological Research Laboratory,
School of Atmospheric Sciences, Sun Yat-sen University, China*

KEYWORDS:

Venus, Ionosphere, upper atmosphere, photochemical model, Monte Carlo model, kinetic model

ABSTRACT:

A series of models has been developed by our group to investigate the variability of the Venusian ionosphere and upper atmosphere, including a photochemical model, a Monte Carlo model, and a kinetic model. We incorporated a detailed photochemical model with a comprehensive chemical network and evaluated how these processes influence ion distribution. We concluded that both protonation and Coulomb interactions significantly affect the ionospheric structure, particularly at higher altitudes, leading to notable differences in ion density profiles compared to earlier models [1]. Utilizing a Monte Carlo model, we also examined the variations in escape fluxes under different solar activities and highlighted the significant role of thermal O concentration near the exobase in moderating escape. Our results suggested that knock-on by hot O likely plays the dominant role in driving total atmospheric hydrogen and helium escape on Venus at the present epoch, with a significant portion contributed from regions below the exobase [2]. In addition, we used a multi-stream kinetic model to compute the electron energy spectrum, focusing on identifying spectral features associated with the ionization of neutral species like CO₂ and O. The findings emphasized the role of transport in influencing suprathermal electron intensities and revealed that these electrons are primarily produced in deeper atmospheric regions and transported upwards [3].

REFERENCES:

- [1] Wu X., Cui J. *et al.* Modeling the structure of the dayside Venusian ionosphere: Impacts of protonation and Coulomb interaction // *Astronomy and Astrophysics*. 2024. V. 685. Article A160.
- [2] Gu H., Cui J. *et al.* Hydrogen and helium escape on Venus via energy transfer from hot oxygen atoms // *Monthly Notices of the Royal Astronomical Society*. 2021. V. 501. P. 2394–2402.
- [3] Cui J., Galand M. *et al.* Suprathermal electron spectra in the Venus ionosphere // *J. Geophysical Research*. 2011. V. 116. Article A04321.

DISTRIBUTIONS OF CO₂, HDO AND H₂O CONCENTRATION AND TEMPERATURE IN THE MESOSPHERE OF VENUS BASED ON SOIR/VEX OBSERVATIONS FOR 2006–2014

E. S. Fedorova, D. A. Belyaev, A. A. Fedorova, O. I. Korablev

Space Research Institute RAS, Moscow, Russia,

lisaoneechan@gmail.com

KEYWORDS:

water vapor, Venus atmosphere, solar occultation, isotopic ratio, vertical profiles

ABSTRACT:

Water vapor, as one of the minor gas constituents of the atmosphere of Venus, plays an essential role in the chemical and physical processes on the planet and in the evolution of its climate. The D/H ratio, which is ~100–300 times higher than Earth's SMOW (Standard Mean Ocean Water), most likely indicates that Venus has rapidly lost a large amount of its water, or that the isotopic ratio has changed gradually due to the processes of hydrogen escape and outgassing. For the first time, the HDO/H₂O ratio in the Venusian mesosphere was obtained by [1] based on SOIR/VEx data from year 2006 to 2007, and was found to be 240 ± 25 times greater than on Earth. At the same time, according to [2] measurements in the lower layers of the atmosphere, this ratio exceeds the terrestrial one by 157 ± 30 times.

In this work, we present the mesospheric distributions of H₂O, HDO, and CO₂ concentration and temperature retrieved from the SOIR/VEx (Solar Occultation in the InfraRed) experiment in the solar occultation mode. Our dataset covers the entire duration of the experiment, from 2006 to 2014. SOIR is an acousto-optic echelle spectrometer and a part of the Venus Express mission [3]. It carried out measurements of the atmospheric transition in the spectral range of 2.3–4.3 μm with the resolving power of about 25000, which made it possible to detect thin molecular absorption lines of H₂O and, HDO together with abundant CO₂ bands. The range of accessible altitudes when operating in the solar occultation mode starts from 65–70 km (directly above the cloud layer), which makes SOIR ideally suited for the studies of mesosphere. At this stage, the altitude profiles of CO₂, H₂O, HDO concentrations and temperature were retrieved from the measured transmission spectra. Our retrieval algorithm, being different from the analysis of [4], was developed at IKI and previously applied for analogous solar occultation experiment ACS in the martian atmosphere [5, 6]. As a result, the obtained altitude profiles allowed estimating the HDO/H₂O isotopic ratio vertically distributed in the mesosphere in quantity of 200–250 times respectively to SMOW. The presented dataset would also allow searching for events of the mesospheric water saturation that might be linked with possible ice clouds around the mesopause.

ACKNOWLEDGMENTS:

This work is funded by grant of the Russian Science Foundation No. 23-12-00207, <https://rscf.ru/project/23-12-00207/>.

REFERENCES:

- [1] *Fedorova A., Korablev O., Vandaele A. C. et al.* HDO and H₂O vertical distributions and isotopic ratio in the Venus mesosphere by SOIR spectrometer on board Venus Express // *J. Geophys. Res.* 2008. V. 113.
- [2] *Donahue T.M., Grinspoon D.H., Hartle R.E., Hodges R.R. Jr.* Ion/neutral Escape of Hydrogen and Deuterium: Evolution of Water, Venus II: Geology, Geophysics, Atmosphere, and Solar Wind Environment. University of Arizona Press, 1997. 385 p.
- [3] *Nevejans D., Neefs E., Van Ransbeeck E. et al.* Compact high-resolution spaceborne echelle grating spectrometer with AOTF based order sorting for the infrared domain from 2.2 to 4.3 micrometer // *Applied Optics.* 2006. V. 45(21). P. 5191–5206.

- [4] *Mahieux A., Robert S., Piccialli A. et al.* The SOIR/Venus Express species concentration and temperature database: CO₂, CO, H₂O, HDO, H³⁵Cl, H³⁷Cl, HF individual and mean profiles // *Icarus*. 2023. V. 405.
- [5] *Fedorova A., Montmessin F., Korablev O. et al.* Stormy water on Mars: The distribution and saturation of atmospheric water during the dusty season // *Science*. 2020. V. 367.
- [6] *Belyaev D., Fedorova A., Trokhimovskiy A. et al.* Revealing a High Water Abundance in the Upper Mesosphere of Mars With ACS Onboard TGO // *Geophysical Research Letters*. 2021. V. 48.

VENUS LOWER ATMOSPHERE PROPERTIES FROM SPICAV-IR/VEX MEASUREMENTS IN NIR TRANSPARENCY WINDOWS

D. G. Evdokimova¹, A. A. Fedorova¹, N. I. Ignatiev¹, M. S. Zharikova¹, O. I. Korablev¹, F. Montmessin², J.-L. Bertaux²

¹ Space Research Institute RAS, Moscow, Russia, daria.evdokimova@cosmos.ru

² Laboratoire Atmosphères, Milieux, Observations Spatiales, Sorbonne Université, Université de Versailles — Saint-Quentin-en-Yvelines, Guyancourt, France

KEYWORDS:

Venus, cloud optical depth, water vapor, transparency windows

INTRODUCTION:

The chemical processes and composition of Venus atmosphere are mainly controlled by its densest part, located in and below the cloud layer (47–70 km). However, the composition of the lower atmosphere remains insufficiently studied due to the opacity of the cloud layer over a wide spectral range and the strong absorption of carbon dioxide at high pressure and temperature near the surface. Carbon dioxide (CO₂) and water vapor (H₂O), the most effective greenhouse gases, are responsible for the heating of the planet surface. A small fraction of the thermal infrared radiation emitted by the lower atmosphere and surface can be observed remotely in narrow intervals, i.e., atmospheric transparency windows, on the Venus night side [1].

The present study examines the spectral interval of 1.0–1.3 μm, covering transparency windows at 1.0, 1.1, 1.18, 1.28, and 1.31 μm. In this spectral range, the thermal emission originates from the hot surface and the first scale height of the atmosphere (0–20 km). The radiation intensity is primarily influenced by the scattering in the sulfuric acid clouds. Additionally, it is dependent on the surface emissivity and the absorption of H₂O at 0.9–1.0 and 1.10–1.20 μm. It should be noted that the 1.28-μm window is contaminated by an O₂ (α¹Δ_g) airglow at 1.27 μm produced at 96 km [1].

OBSERVATIONS BY SPICAV-IR/VEX:

The infrared (IR) channel of the SPICAV spectrometer on board the Venus Express spacecraft performed observations of the planet night side in 2006–2014. The instrument measured spectra of five considered windows with a high resolving power of ~1400 [2]. The SPICAV IR observations encompassed the majority of the Venus globe.

RADIATIVE TRANSFER MODEL:

The measured spectra are analyzed using a multiple scattering radiative transfer model. The model is based on the DISORT program package, which implements the discrete ordinate method for pseudo-spherical geometry [3]. Vertical profiles of atmospheric temperature, pressure, and density were obtained from the VIRA database. The absorption of CO₂, H₂O, and HDO is calculated from the “High-T”, BT2, and VTT spectroscopic databases [4]. It is assumed that H₂O is uniformly mixed beneath clouds. The HDO/H₂O ratio is fixed at a value that is 127 times lower than the terrestrial one [4]. Aerosol particles are assumed to be spherical and consist of 75 %-H₂SO₄ solution. The optical depth, single scattering albedo and asymmetry parameter are calculated using Mie theory based on the cloud model of Haus et al., 2016 [5]. The variable parameters of the model are the H₂O volume mixing ratio (VMR), cloud opacity and surface emissivity. The model is capable of reproducing the O₂ (α¹Δ_g) airglow contribution based on the HITRAN database [6].

RESULT:

The retrieved cloud optical depth exhibits considerable variability. Its mean value with a standard deviation is 40±6. The optical depth is calculated at 1 μm. The preliminary analysis of H₂O VMR in the lower atmosphere yields a value of 26.8±1.5 ppm.

REFERENCES:

- [1] *Pollack J. B., Dalton J. B., Grinspoon D. et al.* Near-infrared light from Venus' night-side: a spectroscopic analysis // *Icarus*. 1993. V. 103. No. 1. P. 1–42. DOI: 10.1006/icar.1993.1055.
- [2] *Korablev O., Fedorova A., Bertaux J.-L. et al.* SPICAV IR acousto-optic spectrometer experiment on Venus Express // *Planetary and Space Science*. 2012. V. 65. No. 1. P. 38–57. DOI: 10.1016/j.pss.2012.01.002.
- [3] *Lin Z., Stamnes S., Jin Z. et al.* Improved discrete ordinate solutions in the presence of an anisotropically reflecting lower boundary: Upgrades of the DISORT computational tool // *J. Quantitative Spectroscopy and Radiative Transfer*. 2015. V. 157. P. 119–134. DOI: 10.1016/j.jqsrt.2015.02.014.
- [4] *Fedorova A., Bézard B., Bertaux J.-L. et al.* The CO₂ continuum absorption in the 1.10- and 1.18- μ m windows on Venus from Maxwell Montes transits by SPICAV IR onboard Venus express // *Planetary and Space Science*. 2015. V. 113. No. P. 66–77. DOI: 10.1016/j.pss.2014.08.010.
- [5] *Haus R., Kappel D., Tellmann S. et al.* Radiative energy balance of Venus based on improved models of the middle and lower atmosphere // *Icarus*. 2016. V. 272. P. 178–205. DOI: 10.1016/j.icarus.2016.02.048.
- [6] *Bertaux J.-L., Hauchecorne A., Lefèvre F. et al.* The use of the 1.27 μ m O₂ absorption band for greenhouse gas monitoring from space and application to Micro-Carb // *Atmospheric Measurement Techniques*. 2020. V. 13. No. 6. P. 3329–3374. DOI: 10.5194/amt-13-3329-2020.

GEOLOGICAL HISTORY OF THEIA MONS AND GRABEN SYSTEM (MOSTLY DYKE SWARM) MAPPING IN THE NORTHERN AREA OF BETA REGIO

A. S. Shimolina¹, R. E. Ernst², H.El. Bilali²

¹ Tomsk State University, Faculty of Geology and Geography, Tomsk, Russia, arina051299@gmail.com

² Department of Earth Sciences, Carleton University, Ottawa, Canada

KEYWORDS:

Theia Mons, Rhea Mons, Beta Regio, volcanoes, Venus, planetary geology

INTRODUCTION:

The focus of this research is detailed mapping of lava flows and graben-fissure-fracture ("graben" for short) systems of Theia Mons and nearby areas at a scale of 1:500,000 [3]. Lava flow units (96 mapped) belonging to Theia Mons volcano were combined into 22 groups and then into 6 flow packages. About 10,000 extensional lineaments (graben-fissure-fracture systems) were mapped and grouped into 19 systems, of which 15 are interpreted to overlie dyke swarms: 2 radiating systems are associated with Centers 1 and 2, and 13 other systems belong to other (older and unrelated) magmatic centers in the region. A partial circumferential set may also be present, associated with Center 2. Four other extensional lineaments sets are inferred to represent sets of normal faults associated with rift zones (Devana and Zverine, and additional rift zones). These rift zones exhibit two sets of 'triple junction' geometry, which are approximately focused on Centers 1 and 2.

GEOLOGICAL HISTORY OF THEIA MONS:

Recognition of 2 centers:

Two separate Centers 200 km apart for Theia Mons were recognized based on radiating graben sets (interpreted to overlie dyke swarms), converging flows and triple junction rift systems. Center 2 is younger and associated with the main caldera of Theia Mons. Center 1 is older and has no surface expression, presumably because it is covered by the younger **flows of Center 2**.

Center 1 (24°51' N, 78°10' W) consists of sheet flows with low radar brightness and which extend to a maximum to 770 km from the center. Center 2 (22.7° N, 81.0° W) coincides with the currently preserved central caldera and consists of lava flows of low radar brightness with a maximum length of 680 km, followed by a second pulse of radar-bright lobate flows that can be traced back to the center.

Geological history:

The geological history (Figure 1) begins at Center 1 with a large radiating dyke swarm followed by radiating flows and triple junction rifting at Center 1. Then presumably occurred a shift to Center 2 with the same sequence: radiating dyke swarm, followed by flows (in two Stages, 2a and 2b): Stage 2a flows have great length and low radar brightness, and Stage 2b features lobate flows with high radar brightness. The final event at Center 2 was triple junction rifting represented by the main rift systems of Devana Chasma (north and south) and Zverine Chasma. A possible shift to a third future magmatic center (400 km further to the southeast) is suggested by the locus of the negative Bouguer gravity anomaly (Figure 2) [2].

MAPPING OF THE GRABEN SYSTEMS OF NORTHERN BETA REGIO:

Over an area of 2 million square kilometers, 13,000 individual grabens (graben-fissure-fractures) were mapped and separated into more than 100 systems (Figure 3). Previous detailed mapping of the grabens in the area included 3,000 units [1]. About 70 of these systems do not belong to known structures such as chasms or lineae. 5 of them appear to be circumferential.

15 other systems were found in tessera and transitional terrain areas.

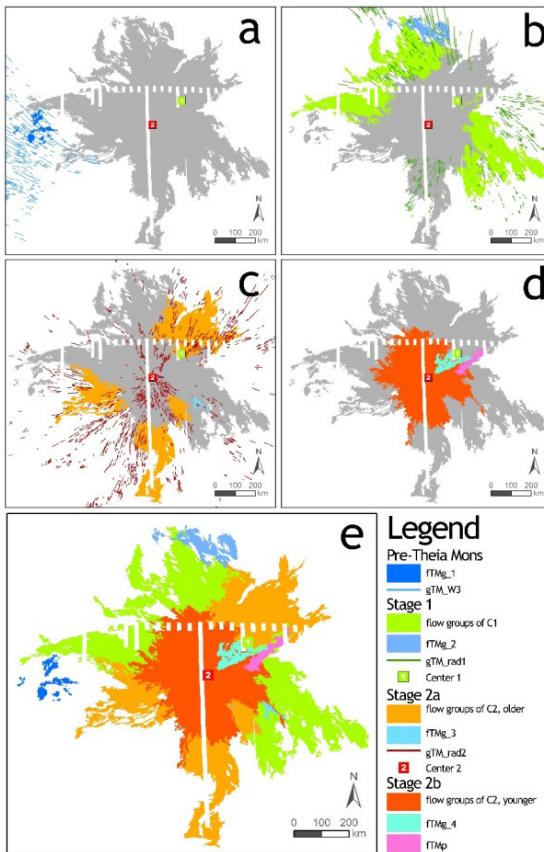


Fig. 1. Scheme of Theia Mons' volcanic evolution by stages

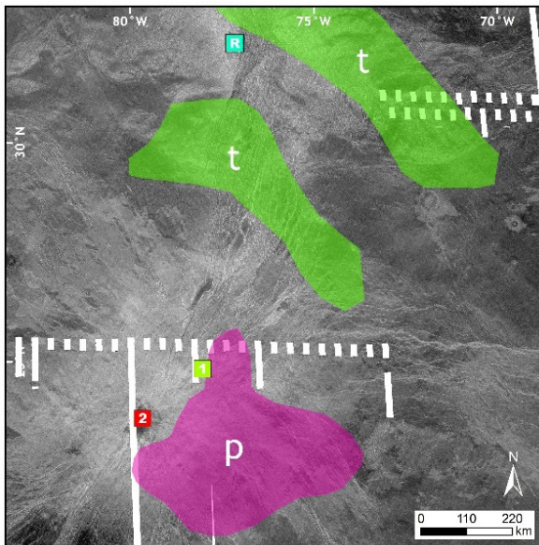


Fig. 2. SAR image of Theia Mons with fields limiting the threshold of -250 mgal Bouguer anomaly. Green fields with label "t" connected with tessera and transitional-to-tessera terrains. Pink field with label "p" does not have tessera terrain inside of it, and instead marks the buoyant underlying plume. Labels "1" and "2" mark two magmatic centers of Theia Mons. Label "R" marks Rhea Mons

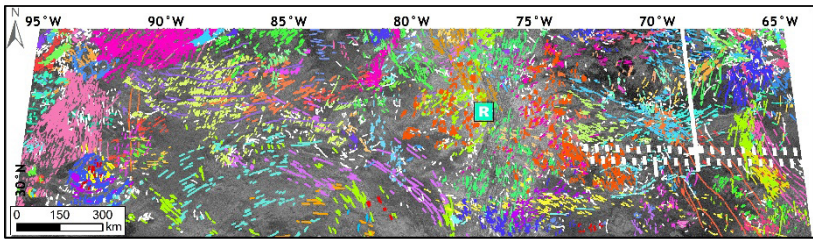


Fig. 3. Mapped graben systems of northern part of Beta Regio. Label "R" marks Rhea Mons

ACKNOWLEDGMENTS:

Magellan SAR images obtained from <https://astrogeology.usgs.gov/search/?pmi-target=venus> based on the data from <https://pdsimaging.jpl.nasa.gov/volumes/magellan.html#mgnFMAP>.

REFERENCES:

- [1] Ernst R.E., Desnoyers D.W., Head J.W., Grosfils E.B. Graben–fissure systems in Guinevere Planitia and Beta Regio (264–312° E, 24–60° N), Venus, and implications for regional stratigraphy and mantle plumes/diapirs // *Icarus*. 2003. V. 164. P. 282–316.
- [2] Senske D.A., Schaber G.G., Stofan E.R. Regional topographic rises on Venus: Geology of Western Eistla Regio and comparison to Beta Regio and Atla Regio // *J. Geophysical Research*. 1992. V. 97. Iss. E8. P. 13,395–13,420.
- [3] Shimolina A.S., Ernst R.E., El Bilali H. Lava flows of Theia Mons volcano, Beta Regio plume center, Venus // *LPSC LIV*. 2023. Abstr. 1159.

METEOROID IMPACTS ANALYSIS FOR A SPACECRAFT ON ROUTE TO VENUS

D. B. Dobritsa¹, E. S. Gordienko¹, A. V. Simonov¹, G. O. Ryabova²

¹ *Lavochkin Association, Khimki, Moscow Region, Russia,
dbord@yandex.ru*

² *Tomsk State University, Tomsk, Russia*

KEYWORDS:

meteoroids, impact risk assessment, spacecraft, space mission, Venus.

INTRODUCTION:

The work assessed the level of meteoroid impacts during the flight of a spacecraft to Venus in the form of the meteoroid flux density on the face of a conventional cube, oriented relative to the moving coordinate system associated with the spacecraft. We estimate the probability of non-perforation of the cube faces as a structures with a single and double wall.

The trajectory of the interplanetary segment was calculated based on maximizing the mass of the spacecraft in orbit around Venus [1] and corresponds to the optimal Earth-Venus flight with duration of less than 200 days. The dates of arrival to Venus are determined by the criterion of minimizing the characteristic speed of transfer the vehicle to operational orbit as a satellite of Venus [2]. The meteoroid flux density was calculated using the state standard model of the spatial distribution of meteoroid matter [3].

To calculate structures with one wall, the Cour-Palais ballistic equation [4], used for plates made of metallic materials, was used. For a two-wall structure representing a Whipple protection, the Christiansen-Cour-Palais equation was used [5].

The probability of non-penetration of the walls of an oriented cube with a side of 1 m was calculated. A plate made of aluminum alloy AMg6 with a thickness of 1.5 mm was considered as a single-wall structure. To calculate the structure with a double wall, an external (shielding) wall made of AMg6 with a thickness of 0.5 mm was added, at a distance of 50 mm from the first.

An assessment of meteoroid hazard based on the GOST [3] can be taken as a basis when designing interplanetary expeditions. However, to clarify the level of impacts, recent studies carried out by various space missions should be taken into account. In particular, the Helios [6] and STEREO [7] missions confirm the existence of a dust ring in the orbit of Venus. We provide a brief review of instrumental studies of the dust environment within heliocentric distances between 0.7 and 1.0 a.u., performed in the last 10–15 years.

ACKNOWLEDGMENTS:

In this work G. O. Ryabova was supported by the state assignment of Ministry of Science and Higher Education of the Russian Federation (theme No. FSWM-2024-0005).

REFERENCES:

- [1] *Simonov A. V., Kovaleva S. D., Gordienko E. S. et al. Specifics of designing trajectories of perspective spacecraft for Venus exploration // Engineering J.: Science and Innovation. 2021. No. 10(118). DOI: 10.18698/2308-6033-2021-10-2122 (in Russian).*
- [2] *Gorinov D., Eismont N. A., Zasova L. V. et al. Venera-D mission scenario and trajectory // Solar System Research. 2019. V. 53. No. 7. P. 92–99. DOI:10.1134/S0038094619070062.*
- [3] GOST 25645.128–85 [The State Standard of the USSR]. Meteoric matter. Spatial distribution model. M.: USSR State Committee for Standards, 1985. 24 p.
- [4] *Cour-Palais B. G. Hypervelocity impact in metals, glass and composites // Intern. J. Impact Engineering. 1987. V. 5. P. 221-237. [https://doi.org/10.1016/0734-743X\(87\)90040-6](https://doi.org/10.1016/0734-743X(87)90040-6).*

- [5] *Ryan S., Christiansen E.L.* A ballistic limit analysis programme for shielding against micrometeoroids and orbital debris // *Acta Astronautica*. 2011. V. 69. P. 245–257. DOI: 10.1016/j.actaastro.2011.04.012.
- [6] *Leinert C., Moster B.* Evidence for dust accumulation just outside the orbit of Venus // *Astronomy and Astrophysics*. 2007. V. 472. P. 335–340. DOI: 10.1051/0004-6361:20077682
- [7] *Jones M.H., Bewsher D., Brown D.S.* Imaging of a circumsolar dust ring near the orbit of Venus // *Science*. 2013. V. 342. P. 960–963. DOI: 10.1126/science.1243194.

VENERA-D MISSION FOR COMPREHENSIVE STUDY OF VENUS

L. M. Zelenyi¹, O. I. Korablev¹, L. V. Zasova¹, M. V. Gerasimov¹,
N. I. Ignatiev¹, D. S. Rodionov¹, D. V. Strelnikov¹, M. A. Ivanov²,
N. A. Eismont¹, D. A. Gorinov¹

¹ Space Research Institute RAS, Moscow, Russia,
dmitry_gorinov@cosmos.ru

² Vernadsky Institute of Geochemistry and Analytical Chemistry RAS
Moscow, Russia

KEYWORDS:

Venus, mission, orbiter, lander, balloon

ABSTRACT:

Venera-D is a planned mission to study atmosphere, surface and surrounding plasma of Venus to resolve the fundamental questions of difference between climates of Venus and Earth. It can also help understand environments of the terrestrial planets of the Solar and extrasolar systems, as well as the shed light on the question of their potential habitability. The Venera-D mission architecture combines the orbiter, the lander and two airborne balloons to use different approaches to obtain knowledge about Venus.

The Orbiter on the polar orbit is focused on studying thermal structure, dynamics and the composition of the atmosphere (both above and below clouds) and magnetosphere.

The Lander is the primary element of the Venera-D mission, which distinguishes it from the other currently planned Venus missions [1]. It contains the scientific payload to study the elemental and mineralogical composition of the surface and near subsurface materials after drilling to a few cm depth and taking samples, as well as the structure and chemical composition of the atmosphere down to the surface, including the abundances and isotopic ratios of the trace and noble gases, direct chemical analysis of cloud aerosols, and the geomorphology of the landing site.

The mission will also include aerial platforms — paired balloons to operate for up to one month at the 53–55 km altitudes. Such modules can provide unique in situ information on the meteorological parameters, composition of the atmosphere, cloud structure, composition and microphysics, nature and distribution of the UV absorber. They will also investigate the potential cloud habitability.

The Venera-D project, which is planned to be launched in 2031, will be an important complementation to the other future Venus missions (VERITAS, DAVINCI, EnVision, and possibly Shukrayaan-1 and VOICE). Venera-D has unique capabilities such as surface sampling and long-term in situ cloud measurements, and instrumentation that can work in synergy with the parallel missions. A coordination of efforts between missions and their scientific instruments is crucial to answer the most important fundamental questions about our mysterious neighbor planet.

REFERENCES:

- [1] *Widemann T., Smrekar S.E., Garvin J.B. et al. Venus Evolution Through Time: Key Science Questions, Selected Mission Concepts and Future Investigations // Space Science Reviews. 2023. V. 219. No. 56.*

ANALYSIS OF THE PROSPECTIVE MISSION SCENARIO WITH DETERMINATION OF ATTAINABLE LANDING SITES ON VENUS UNDER TECHNICAL RESTRICTIONS TO LANDER-ORBITER FUNCTIONING

V. A. Zubko, N. A. Eismont, K. S. Fedyaev, R. R. Nazirov, L. V. Zasova, D. A. Gorinov, A. A. Belyaev

*Space Research Institute RAS, Moscow, Russia,
v.zubko@iki.rssi.ru*

KEYWORDS:

Venus, trajectory design, landing sites, flyby mission

INTRODUCTION

Venus, since the beginning of the space exploration era, has been a subject of great interest [1–5]. Many missions have been sent to study this planet either directly or through flyby trajectories. In recent years, interest in exploring Venus has increased significantly, as new theories about the possibility of life have emerged after announce about the detection of traces of phosphine in the upper atmosphere of the planet in 2020 [6]. Despite being speculative, these theories open up the possibility of finding life beyond Earth.

To this time, several missions are being developed to explore the planet [7–12]. Two of these missions are DAVINCI+ (NASA) [8-9] and Venera-D (Roscosmos) [3, 7, 13], both planned to be launched after 2029 and to study Venus using a decent vehicle.

One of the challenges associated with exploring the planet is a selection of the most suitable location on the surface to collect highly accurate scientific data. However, this choice is limited to a few sites available for landing a lander, mainly due to both purely ballistic constraints such as the entry angle of the lander and launch opportunities as well as natural restrictions such as slow rotation of the planet. These factors can be addressed by using approaches such as those proposed in [13, 14, 15], which may increase the number of attainable sites. However, if a complex configuration such as a lander-orbiter is used, the solution complexity increases significantly. Therefore, it is necessary to continue extending the proposed techniques in order to account for this case.

METHODS IN USE

The primary focus of the current investigation is to explore the ballistic trajectory of a spacecraft's journey to Venus, utilizing the gravity assist maneuver concept, which was initially proposed in previous works [15–16]. The primary objective of utilizing gravity assist in these studies is to employ it as a tool for altering the potential landing sites towards the desired destination. Within this framework, the spacecraft transits to a resonant orbit using solely the gravitational pull of the planet, and after completing one revolution around the orbit, it returns to the vicinity of the desired location on the planet. The key challenge here lies in developing a method that enables the calculation of a resonant orbit tailored to the specific landing location. This aspect has been explored in previous studies, where a methodology for designing spacecraft orbits has been proposed. However, this approach is limited to determining unrestricted landing locations, without considering more intricate mission scenarios where lander/orbiter constraints may be involved. The primary goal of this study is to delve into this possibility and to develop and analyze a flight scheme that incorporates both a lander and an orbiter.

RESULTS

In the paper, the main focus is on finding attainable landing areas for the Venera-D lander, taking into account various constraints. All possible

constraints applicable to Venera-D, as stated in [13], were considered. These constraints result from the technical requirements for the orbiter and its mission objectives, and they limit the attainable landing sites. Additionally, calculations were carried out to determine these sites for the lander, considering constraints of functioning the lander/orbiter configuration. As a result, maps were created to visually represent the attainable areas that can be used to select an appropriate landing site for the mission.

Additionally, an algorithm based on B-plane targeting and differential corrections for numerical modeling of spacecraft trajectories is applied. This algorithm considers the n-body model of motion, relativity corrections, and non-gravitational perturbations. The algorithm is used to improve the accuracy of the found solution after using the developed approach.

REFERENCES

- [1] *Limaye S.S., Garvin J.B.* Exploring Venus: next generation missions beyond those currently planned // *Frontiers in Astronomy and Space Sciences*. 2023. V. 10. Article 1188096. <https://doi.org/10.3389/fspas.2023.1188096>
- [2] *Glaze L.S., Wilson C.F., Zasova L.V. et al.* Future of Venus Research and Exploration // *Space Science Reviews*. 2018. <https://doi.org/10.1007/s11214-018-0528-z>.
- [3] *Senske D., Zasova L., Economou T et al.* The Venera-D concept, scientific exploration of Venus in the post-2025 time // *Planetary Science Vision 2050 Workshop*. 2017.
- [4] *Basilevsky A.T., Ivanov M.A., Head J.-W. et al.* Landing on Venus: Past and Future // *Planetary and Space Science*. 2007. V. 55(14). <https://doi.org/10.1016/j.pss.2007.09.005>.
- [5] *Ivanov M.A., Zasova L., Gregg T.K.P.* Venera-D Landing Site Constraints // 10th Moscow Solar System Symposium 9M-S3. 2018. P. 58–59.
- [6] *Greaves J.S., Richards A.M.S., Bains W. et al.* Phosphine gas in the cloud decks of Venus // *Nature Astronomy*. 2021. V. 5. P. 655–665. <https://doi.org/10.1038/s41550-020-1174-4>.
- [7] *Eismont N.A., Zasova L.V., Simonov A.V. et al.* Venera-D Mission scenario and trajectory // *Solar System Research*, 2019. V. 53. No. 7. P. 578–585. DOI: 10.1134/S0038094619070062.
- [8] *Garvin J.B., Getty S.A., Arney G.N. et al.* Revealing the Mysteries of Venus: The DAVINCI Mission // *The Planetary Science J*. 2022. V. 3. No. 5. Article 117.
- [9] *Garvin J., Getty S., Arney G. et al.* DAVINCI+: Deep atmosphere of Venus investigation of noble gases, chemistry, and imaging plus // 51st Lunar and Planetary Science Conf. 2020. Article 2599.
- [10] *Smrekar S., Dyar M., Hensley S. et al.* VERITAS (Venus Emissivity, Radio Science, InSAR, Topography And Spectroscopy): A Proposed Discovery Mission // AAS/Division for Planetary Sciences Meeting. 2016. V. 48. P. 207–216.
- [11] *Widemann T., Ghail R., Wilson C. et al.* EnVision: Europe's proposed mission to Venus // American Geophysical Union, Fall Meeting. 2020. Article P022-02.
- [12] *Beauchamp P., Gilmore M.S., Lynch R.J. et al.* Venus Flagship Mission Concept: A Decadal Survey Study // IEEE Aerospace Conf. (50100). 2021. V. 48. Article 2326. P. 1–18. DOI: 10.1109/AERO50100.2021.9438335.
- [13] *Simonov A.V., Kovaleva S.D., Gordienko E.S. et al.* Features of trajectory design of prospective spacecrafts for Venus exploration // *Engineering J.: Science and Innovations*. 2021. Iss. 10. (in Russian). <http://doi.org/10.18698/2308-6033-2021-10-2122>.
- [14] *Kosenkova A.V.* Investigation of reachable landing sites in the 'VENERA-D' mission for various types of a lander // *AIP Conf. Proc.* 2021. V. 2318. Iss. 1. DOI: 10.1063/5.0035839.
- [15] *Eismont N.A., Nazirov R.R., Fedyayev K.S. et al.* Resonant orbits in the problem of expanding the reachable landing areas on the surface of Venus // *Astronomy Letters*. 2021. V. 47. No. 5. P. 316–330. DOI: 10.1134/S1063773721050042.
- [16] *Zubko V.A., Eismont N.A., Fedyayev K.S. et al.* A method for constructing an interplanetary trajectory of a spacecraft to Venus using resonant orbits to ensure landing in the desired region // *Advances in Space Research*. 2023. V. 72. Iss. 2. P. 161–179.

THE ACTIVE VOLCANOES OF KAMCHATKA AS SUITABLE TERRESTRIAL ANALOGS WITHIN THE AVENGERS INITIATIVE: AN OPPORTUNITY FOR IN-SITU OPERATIONAL TESTS FOR FUTURE LANDING VENUS MISSIONS

P. D'Incecco¹, J. Filiberto², J. B. Garvin³, G. N. Arney³, S. A. Getty³, E. Kohler³, L. M. Zelenyi⁴, L. V. Zasova⁴, O. Korablev⁴, M. A. Ivanov⁵, J. W. Head⁶, D. A. Gorinov⁷, S. Bhattacharya⁷, S. S. Bhiravarasu⁷, D. Putrevu⁷, I. López⁸, R. Ghail⁹, P. Mason¹⁰, J. Brossier¹¹, C. Monaco^{12, 13}, S. Branca¹³, R. A. Corsaro¹³, D. Trang¹⁴, J. R. Crandall¹⁵, N. Mari¹⁶, M. Blackett¹⁷, G. Komatsu¹⁸, A. Kosenkova¹⁹, I. Flynn²⁰, S. Aveni²¹, N. Lang²², B. Thomson²³, I. Pagano²⁴, S. Cassisi¹, G. Eggers²⁵, R. E. Ernst²⁶, H. El Bilali²⁶, T. Kremic²⁷, J. Lustig-Yaeger²⁸, N. Izenberg²⁸, L. Bruzzone²⁹, M. El Yazidi³⁰, E. Ferroni¹, D. Coero Borga³¹, C. Badia¹, S. Parisini³², G. Fiasconaro³³, S. Cussini³⁴, M. Dolci¹, N. Cantiello¹, E. Brocato^{1, 35}, G. Di Achille¹

¹ National Institute for Astrophysics, Astronomical Observatory of Abruzzo, Teramo, Italy,

piero.dincecco@inaf.it

² Astromaterials Research and Exploration Science Division, NASA Johnson Space Center, USA

³ NASA Goddard Space Flight Center, Greenbelt, USA

⁴ Space Research Institute RAS, Moscow, Russia

⁵ Vernadsky Institute of Geochemistry and Analytical Chemistry RAS, Moscow, Russia

⁶ Department of Geological Sciences, Brown University, Providence, USA

⁷ Space Applications Centre, Indian Space Research Organization, Ahmedabad, India

⁸ Tecvolrisk Research Group. Departamento de Biología, Geología, Física y Química Inorgánica. Universidad Rey Juan Carlos, Madrid, Spain

⁹ Earth Sciences, Royal Holloway, University of London, UK

¹⁰ Department of Earth Science and Engineering, Imperial College London, London

¹¹ National Institute for Astrophysics — Institute for Space Astrophysics and Planetology, Rome, Italy

¹² Dipartimento di Scienze Biologiche Geologiche e Ambientali, Università di Catania, Italy

¹³ Istituto Nazionale di Geofisica e Vulcanologia, Osservatorio Etneo— Sezione di Catania, Italy

¹⁴ Hawai'i Institute of Geophysics and Planetology, University of Hawai'i at Mānoa, Honolulu, USA, Space Science Institute, Boulder, USA

¹⁵ Eastern Illinois University, Department of Geology and Geography, Charleston, USA

¹⁶ Department of Earth and Environmental Sciences, University of Pavia, Pavia, Italy

¹⁷ Centre for Agroecology, Water and Resilience, Coventry University, UK

¹⁸ IRSPS, Università G. d'Annunzio, Pescara, Italy

¹⁹ Bauman Moscow State Technical University, Moscow, Russia

²⁰ University of Pittsburgh, USA

²¹ Sapienza University of Rome, Italy

²² NASA Headquarters, USA

²³ University of Tennessee, Knoxville, USA

²⁴ National Institute for Astrophysics — Osservatorio Astrofisico di Catania, Italy

²⁵ Wesleyan University, USA

²⁶ Department of Earth Sciences, Carleton University, Ottawa, ON, Canada

²⁷ NASA Glenn Research Center, Cleveland, USA

- ²⁸ *Space Exploration Sector, Johns Hopkins University Applied Physics Laboratory, Laurel, MD, USA*
- ²⁹ *Department of Information Engineering and Computer Science, University of Trento, Italy*
- ³⁰ *Università Cattolica, Roma, Italy*
- ³¹ *National Institute for Astrophysics — Headquarters, Roma, Italy*
- ³² *National Institute for Astrophysics — Istituto di Radioastronomia, Bologna, Italy*
- ³³ *National Institute for Astrophysics — Institute of Space Astrophysics and Cosmic Physics, Palermo, Italy*
- ³⁴ *National Institute for Astrophysics — Osservatorio di astrofisica e scienza dello spazio, Bologna, Italy*
- ³⁵ *INAF — Osservatorio Astronomico di Roma*

KEYWORDS:

planetary geology, Venus, volcanism terrestrial analogs

ABSTRACT:

The next decade will see the return to Venus thanks to a number of missions which have been recently selected and proposed for launch. The Roscosmos Venera-D mission, along with the NASA DAVINCI, NASA VERITAS, ESA EnVision, the ISRO Shukrayaan-1, and the CNSA VOICE missions will open a new era for the exploration of the Earth's hellish twin planet.

The next missions to Venus should be able to shed new light on the science questions such as: a) whether the volcanic activity on this planet is locally constrained, or volcanism acts on a global scale, b) the rate of the present-day volcanic activity, and c) the style of volcanism on Venus, whether it is predominantly effusive, or the occurrence of local episodes of pyroclastic volcanism is also possible. In preparation for the future missions to Venus, the Analogs for VENUS' Geologically Recent Surfaces (AVENGERS) initiative will select and analyze a number of active terrestrial volcanoes as suitable analogs for the identification and analysis of active volcanism on Venus.

Among the future missions to Venus, the Roscosmos Venera-D is the only one to be equipped with a lander which will analyze the elemental and mineralogical composition of the surface. As the young topographic rises (areas characterized by recent volcano-tectonic activity) on Venus are being proposed as one of the possible terrain types for the Venera-D landing, it is crucial to look for volcanic areas on Earth where to perform operational tests such as surface drilling and in-situ elemental composition analysis. To this regard, we propose here the analysis of the active volcanoes of the Kamchatka Peninsula in Russia as a very suitable analog for the Venera-D mission, as well as for the analysis of surface change detection due to ongoing eruptions. The Kamchatka Peninsula is located on the eastern margin of the Eurasia plate, in proximity of the Kuril-Kamchatka subduction zone. The volcanoes of the Kamchatka Peninsula are among the most active volcanoes of the world, making them a suitable terrestrial analog in the search for active volcanism on Venus. Moreover, the volcanoes of Kamchatka are characterized by pyroclastic activity. Since the previous Soviet Venera and Vega missions landed over areas which elemental composition was most likely consistent with that of tholeiitic basalts, performing operational tests over areas characterized by pyroclastic activity also offers the unique opportunity to provide us the tools to potentially interpret the diverse output given by landing over portions of the surface of Venus possibly characterized by explosive volcanic products.

Finally, the frequent eruptions characterizing the volcanoes of the Kamchatka Peninsula make them also a suitable terrestrial analog for the possible detection of ongoing eruptions on Venus by future missions, which can be achieved by comparing two (or more) radar images of the same volcano (and its surroundings) in two (or more) different moments of time.

PAYLOAD MODULE FOR LONG DURATION VENUS EXPLORATION

J. Sharma

*Moscow Aviation Institute, Moscow, Russia,
sharma.joshita14@gmail.com*

KEYWORDS:

multi-layer insulation, heat flux, phase-changing material, methyl fumarate, krypton

INTRODUCTION:

Study of Venus has remained to be of great interest for a long while, ranging from Planetary Science to Astrobiology, however the lack of long-term study of the planet has proved as a hinderance to the purpose. Previous missions to Venus which include the Venera and Vega programs have been capable to successfully land on the surface of Venus and provide essential data that have been of great importance within the scientific community as well as that could help with the further engineering of Landers for the planetary surface, including surface as well as atmospheric data.

Venus being the Planet with great similarity to Earth, can allow its study to be necessary for the further study of the evolution of Earth like planets, as well act as a model to the climatic scenarios on Earth. Each of these scenarios is dependent on the long-term study of the planet conditions that have yet remained to be fulfilled.

By the means of this works it is intended to create a design for a robust payload module that would be capable to endure and function in the High Temperature and Pressure as well as the corrosive conditions of the Venutian environment.

THERMAL PROTECTION:

Upon landing on the surface of Venus, a module is expected to face temperatures around $475\text{ }^{\circ}\text{C}$ ($\sim 748\text{ K}$) with atmospheric pressure of around 9.2 MPa . The most imperative is to maintain the temperature within the Payload Bay so as to allow the proper functioning of the electronic devices, which are generally expected to function until the temperature of $125\text{ }^{\circ}\text{C}$ ($\sim 398\text{ K}$). Considering the fact that Sphere has the highest volume-to-surface area ratios, it would allow the least area for the interaction of the environment with the Payload Bay, however that would still allow a large flux to penetrate into the instrument compartment, to prevent which layers of Multi-layer Insulation composed of silver/gold foil can be placed inside the primary exterior component of the Sphere. Within the work, 40-layers of silver/gold and foil showed a massive reduction in the radiative heat flux to a value of 8.83 W/m^2 . Secondly, considering the effect of the conductive heat flux will also be greatly increased in the high-pressure environment as it is on Venus, a layer of insulating material is also of need on the module. The considered material on the module is Krypton, due to its extremely low conductivity as well its potential low increase in the overall mass of the module. The conductive heat flux thus could be reduced to a value of 44.18 W/m^2 .

A layer of Phase-Changing Material would allow to maintain the temperature to a lower value than the outside temperature for a great duration of time, for this purpose the considered material is the Organic PCM, Methyl Fumarate, that when calculated for the atmospheric conditions of Venus would Melt at a temperature of $124.46\text{ }^{\circ}\text{C}$ ($\sim 400\text{ K}$), allowing the equipment to function in a moderate temperature.

Considering the overall calculated Heat Flux, the value received is 53.01 W/m^2 through the outermost layer of Methyl Fumarate ($d \sim 1\text{ m}$), thus giving total power to be 166.45 W , additionally the equipment are expected to dissipate power, which can be approximated to 100 W . The total power thus would be 266.45 W/m^2 .

Through the calculation of a layer of Methyl Fumarate of thickness 0.2 m, the total time for Methyl Fumarate to reach a temperature of 125 °C will be 10 days, thus allowing the equipment in the module to function for a time period of 10 days.

MASS AND SIZE:

The design of the module is separated into different layers, with the outermost layer made of Ti-6Al-4V weighing ~180 kg, while beneath it would lie layers of gold/silver foil weighing ~62 kg. The mass of the 10 cm thick layer of Krypton, would be ~1.5 kg, while the mass of the layer of Methyl Fumarate, that would lie beneath the Krypton would be ~480 kg. This would allow the overall mass of the module, without the scientific apparatus to be 723.5 kg. The size of such module would be of radius 0.805 m, allowing a volume of 0.113 m³ for equipment.

REFERENCES:

- [1] *Svedhem H., Titov D.V., Taylor F.W., Witasse O.* Venus as a more Earth-like planet // *Nature*. 2007. V. 450(7170). P. 629–632. DOI: 10.1038/nature06432.
- [2] *Pradhan D., Moore D., Francis A. et al.* Materials for high temperature digital electronics // <https://arxiv.org>. 2024. DOI: 10.48550/arXiv.2404.03510.
- [3] *Hamja A., Rahman M.* Paper on phase change materials // Intern. Conf. Mechanical Engineering and Renewable Energy. 2013.

SESSION 2. VENUS (VN-PS)
POSTER SESSION

WIND SPEED VARIATIONS AT THE VENUS CLOUD TOP LEVEL FROM UVI/AKATSUKI IMAGES (283 AND 365 NM)

M.V. Patsaeva, I.V. Khatuntsev, N.I. Ignatiev

Space Research Institute RAS, Moscow, Russia, marina.pats@cosmos.ru

KEYWORDS:

Venus, mesosphere, atmospheric dynamics

INTRODUCTION:

UV (283 and 365 nm) images obtained by Ultraviolet Imager (UVI/Akatsuki) from December 2015 to August 2021 were used to study the mesosphere dynamics. Wind vectors were derived by the digital tracking technique [1–3]. We have studied the difference in the latitude dependence of the zonal and meridional speed and in local time dependence of zonal speed between 283 and 365 nm channels. Research was carried out for two Venusian years: 07 (October 2019 – April 2020) and 11 (April 2022 – September 2022). Images obtained in 365 nm channel are referred to the cloud top level (70±2 km), while in 283 nm channel — to a bit higher level of the upper cloud haze containing sulfur dioxide (SO₂).

RESULTS:

The dependence of the zonal speed on the local time and latitude for both channels in two Venusian years is shown in Figure 1. Analysis of the mean zonal speed in the equatorial band (20°N–20°S) shows an increase in the zonal speed in the 283 nm channel compared to 365 nm. The mean zonal speed in one hour region around minimum for 07 year is -82.64 ± 0.03 (SD = 0.42) m/s in 283 nm channel and -80.81 ± 0.02 (SD = 0.34) m/s in 365 nm. The ones for 11 year is -88.52 ± 0.03 (SD = 0.4) m/s in 283 nm channel and -83.61 ± 0.02 (SD = 0.3) in 365 nm. At the same time there is a shift of the zonal speed minimum associated with the heat tide towards the morning in 365 nm channel compared to 283 nm. Position of the zonal speed minimum for 07 year corresponds to 11.27 ± 0.04 (SD = 0.58) h in 283 nm channel and 10.97 ± 0.04 (SD = 0.58) h in 365 nm. The ones for 11 year corresponds to 11.73 ± 0.04 (SD = 0.58) h in 283 nm channel and 11.34 ± 0.04 (SD = 0.58) h in 365 nm.

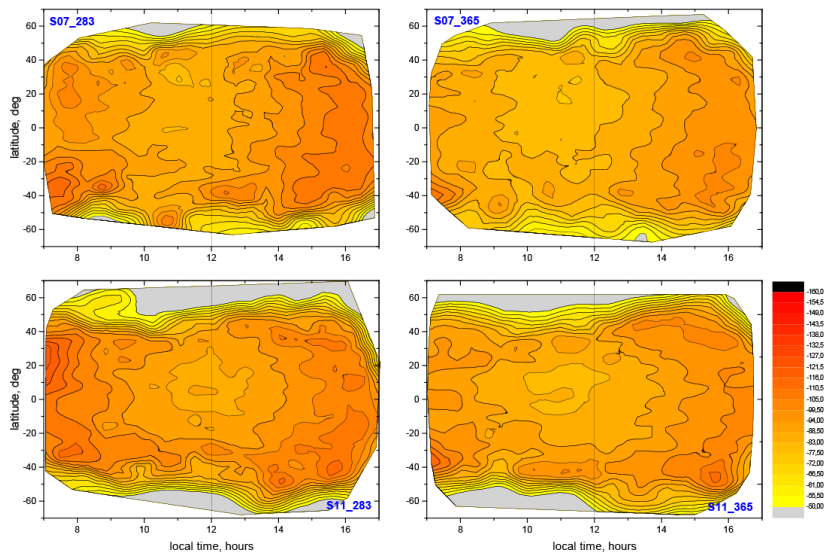


Fig. 1. Variations in the zonal component of the mean horizontal flow depending on local time and latitude for 07 (top line) and 11 (bottom line) Venusian years in 283 (left column) and 365 (right column) nm channels

Averaged latitudinal zonal speed profiles show an increase in the zonal speed in 283 nm channel compared to 365 nm from $\sim 50^\circ$ N to 50° S for both years. Averaged latitudinal meridional speed profiles don't show difference in meridional speed behavior in 283 and 365 nm channels.

CONCLUSION:

The higher zonal speed in the 283 nm channel compared to 365 nm obtained for two Venusian years suggests that, at least in some cases, the maximum speed is achieved above the cloud top. The absence of a similar difference in meridional velocities in the 283 and 365 nm channels indicates that the direction of the horizontal flow is stably maintained in the altitude range under consideration.

REFERENCES:

- [1] *Khatuntsev I. V., Patsaeva M. V., Titov D. V. et al.* Cloud level winds from the Venus Express Monitoring Camera imaging // *Icarus*. 2013. V. 226. Iss. 1. P. 140–158. <https://doi.org/10.1016/j.icarus.2013.05.018>.
- [2] *Patsaeva M. V., Khatuntsev I. V., Patsaev D. V. et al.* The relationship between mesoscale circulation and cloud morphology at the upper cloud level of Venus from VMC/Venus Express // *Planetary and Space Science*. 2015. V. 113–114. No. 08. P. 100–108. <https://doi.org/10.1016/j.pss.2015.01.013>.
- [3] *Patsaeva M. V., Khatuntsev I. V., Titov D. V. et al.* Wind Speed Variations at the Venus Cloud Top above Aphrodite Terra According to Long-term UV Observations by VMC/VENUS Express and UVI/AKATSUKI // *Solar System Research*. 2024. V. 58. No. 2. P. 148–162. DOI:10.1134/S0038094623700053.

HORIZONTAL WINDS IN THE LOWER CLOUDS OF VENUS FROM VIRTIS/VEX AND IR2/AKATSUKI 1.74 μm OBSERVATIONS

D. A. Gorinov, L. V. Zasova, I. V. Khatuntsev, M. V. Patsaeva, N. I. Ignatiev, A. V. Turin

Space Research Institute RAS, Moscow, Russia, dmitry_gorinov@cosmos.ru

KEYWORDS:

Venus, circulation, infrared imagery, lower clouds

ABSTRACT:

The atmosphere of Venus is in constant motion. Its dynamics are dominated by the so-called “retrograde zonal superrotation”, a global zonal wind that reaches peak velocity of about 100 m/s at the altitude of around 70 km. This altitude corresponds to the upper boundary of the thick cloud layer that enshrouds the entire planet [1]. Measuring winds deeper within the clouds, at the lower cloud level (45–50 km) is a challenge, as the cloud morphology cannot be seen in visible or UV light [2]. Aside from in situ probing, it can be done remotely by imaging Venus in several “infrared spectral windows” — narrow wavelength ranges where thermal emission from the hot surface and near-surface atmosphere is not fully absorbed by the massive CO₂ atmosphere. When passing through the lower cloud, this emission is only partially absorbed and thus can show the cloud morphology due to variations in optical thickness [3].

Long-term monitoring of the lower cloud dynamics was performed from the Venusian orbit by the VIRTIS (Venus InfraRed Thermal Imaging Spectrometer) instrument onboard Venus Express [4, 5] and the IR2 camera onboard Akatsuki [6, 7].

VIRTIS had monitored the clouds from 2006 to 2008 in the Southern Hemisphere. Analyses of the partial datasets [3, 8] and the full dataset [9] in 1.74 μm showed a consistent latitudinal profile of zonal speed of ~60 m/s between 0 and 70 °S. The mean meridional wind speed was mostly equatorward (magnitude of a few m/s) with a potential finding of a return branch of a Hadley cell in the near-equatorial latitudes.

The IR2 camera observed the clouds of Venus during 2016. First results from the joint analysis of 1.74, 2.26 and 2.32 μm images showed a radically different pattern of circulation, with overall faster wind velocities (up to 15 m/s) and the presence of an “equatorial jet” [10]. Such dramatic long-term changes were suggestively attributed to the change of cloud opacity due to SO₂ variations [11].

This work compares full datasets of VIRTIS and IR2 cloud tracking data in 1.74 μm to study long-term variations of the atmospheric circulation.

REFERENCES:

- [1] Schubert G. General circulation and dynamical state of the Venus atmosphere // Venus. 1983. P. 681–765.
- [2] Peralta J., Lee Y.J., McGouldrick K. et al. Overview of useful spectral regions for Venus: An update to encourage observations complementary to the Akatsuki mission // Icarus. 2017. V. 288. P. 235–239.
- [3] Sánchez-Lavega A., Hueso R., Piccioni G. et al. Variable winds on Venus mapped in three dimensions // Geophys. Res. Lett. 2008. V. 35. Article L13204.
- [4] Svedhem H., Titov D. V., Taylor F. W. et al. The Venus Express mission // J. Geophys. Res. 2009. V. 114. Article E00B33.
- [5] Piccioni G., Drossart P., Suetta E. et al. VIRTIS: The Visible and Infrared Thermal Imaging Spectrometer // ESA Special Publication. 2007. V. 1295. P. 1–27.
- [6] Nakamura M., Imamura T., Ishii N. et al. Akatsuki returns to Venus // Earth, Planets and Space. 2016. V. 68. No. 75.
- [7] Satoh T., Sato T.M., Nakamura M. et al. Performance of Akatsuki/IR2 in Venus orbit: the first year // Earth, Planets and Space. 2017. V. 69. Article 154.
- [8] Hueso R., Peralta J., Sánchez-Lavega A. Assessing the long-term variability of Venus winds at cloud level from VIRTIS–Venus Express // Icarus. 2012. V. 217. P. 575–598.

- [9] *Gorinov D. A., Zasova L. V., Khatuntsev I. V. et al.* Winds in the Lower Cloud Level on the Nightside of Venus from VIRTIS-M (Venus Express) 1.74 μm images // *Atmosphere*. 2021. V. 12. No. 2. Article 186.
- [10] *Horinouchi T., Murakami S., Satoh T. et al.* Equatorial jet in the lower to middle cloud layer of Venus revealed by Akatsuki // *Nat. Geosci.* 2017. V. 10. P. 646–651.
- [11] *Peralta J., Muto K., Hueso R. et al.* Nightside Winds at the Lower Clouds of Venus with Akatsuki/IR2: Longitudinal, Local Time, and Decadal Variations from Comparison with Previous Measurements // *ApJS*. 2018. V. 239. P. 29–45.

EMISSIONS IN THE 4.3–1.05 μm BANDS OF CARBON DIOXIDE MOLECULES, OUTGOING FROM A PLANETARY ATMOSPHERE ON EXISTENCE OF A LAYER WITH WIND VELOCITY GRADIENT

V. P. Ogibalov^{1,2}, L. V. Belyakova¹, I. V. Voytko¹, E. M. Pastushok¹, E. I. Rasputina¹, S. A. Starostina¹

¹ *Admiral Makarov State University of Maritime and Inland Shipping Saint Petersburg, Russia*

² *Department of Atmospheric Physics, Saint Petersburg State University Saint Petersburg, Petrodvorets, Russia, vpo563@mail.ru*

KEYWORDS:

Radiative transfer, planetary atmospheres, wind field gradient, Venus, molecular bands, carbon dioxide

INTRODUCTION:

The establishment of the existence of large-scale wind currents in the atmospheres of planets with velocities of the order of the speed of sound and with significant velocity gradients (for example, the phenomenon of super-rotation above the cloud layer of the atmosphere of Venus [1], as well as the strongest winds in the Solar System in the atmosphere of Neptune [2]) makes it relevant to take this factor into account in problems of modeling radiation in the IR-bands of atmospheric gas molecules.

At angles of view that differ from the direction of viewing in the nadir, there is a non-zero projection of wind speed on the beam of view, and as a result of the Doppler effect, there is a shift in the volume absorption coefficient of radiation in frequency. There are two things to consider: 1) the spectral dependence of the volume coefficient of radiation absorption in the core of the spectral line of atmospheric gases is very strong and 2) its values themselves at frequencies near the central frequency of the line are the largest. Therefore, even small frequency shifts can lead to a significant change in the volume absorption coefficient of radiation and, consequently, to a change in the radiation transfer pattern. Thus, the study of the possible influence of large-scale vertical gradients of horizontal wind speed is an urgent task for the optics of planetary atmospheres.

In the paper [3], within the framework of a simplified model, the problem of radiative transfer in the spectral lines of the 4.3 μm band of the CO_2 molecules in the planetary atmosphere was considered with taking into account the frequency shift of the volume radiation absorption coefficient due to the Doppler Effect. In this paper, we study the variability of the values of the outgoing radiation intensity depending on the optical thickness in the NIR bands of the CO_2 molecules (i.e. bands about 4.3, 2.7, 2.0, 1.6, 1.4 and 1.05 μm).

MODEL:

In general, the model adopted in this work follows the models outlined in [3]. We consider a planet whose atmosphere is stationary relative to the surface, with the exception of a certain layer that moves parallel to the equator at a speed comparable to the speed of sound. The atmosphere is considered to be plane-parallel with pressure distributed according to the barometric law with values characteristic of the above-cloud layer in the atmosphere of Venus, with a temperature having a linear vertical gradient (see [3], Figure 1, left panel), and consisting entirely of molecules of the principal isotopologue $^{12}\text{C}^{16}\text{O}_2$. It is obvious that the maximum changes in the shape of the spectrum of the outgoing radiation will be in the case when the azimuthal angle of viewing is equal to 0° .

In order for the formulated model of the wind profile to approximately correspond to the observed velocity field above the cloud layer in the atmo-

sphere of Venus, the following values were chosen: the center of the moving layer was at an altitude of $z_m = 30$ km, the half-width of the layer was $\Delta z_m = 10$ km and the magnitude of the velocity in the center $u_0 = 1$ Mach. For the sake of simplicity, it is assumed that at all altitudes in the planetary atmosphere, local thermodynamic equilibrium is performed and the Doppler contour of the spectral line is adopted. Cosine of the solar zenith angle of viewing is equal to $\mu = 0.1$.

Since this work is of a demonstration nature, the radiation field is considered at frequencies only for the most intense band line with values of the central frequency ν_0 and the Einstein coefficient of spontaneous emission A_0 , characteristic of the BIC bands of about 4.3, 2.7, 2.0, 1.6, 1.4 and 1.05 μm of molecules of the principal isotopologue $^{12}\text{C}^{16}\text{O}_2$.

RESULTS:

The values of the radiation intensity outgoing at the upper boundary of the planetary atmosphere were modeled for the cases of a stationary atmosphere and a moving atmosphere (i.e., in the presence of a moving layer). The presentation of the results is given in Figure 1 in the terms of a ratio of the intensities of outgoing radiation for a moving and stationary atmosphere depending on the dimensionless frequency

$$X = \frac{\nu - \nu_0}{\Delta\nu_D},$$

which is convenient for studying the manifestations of macroscopic wind velocity gradients on the spectrum of outgoing radiation.

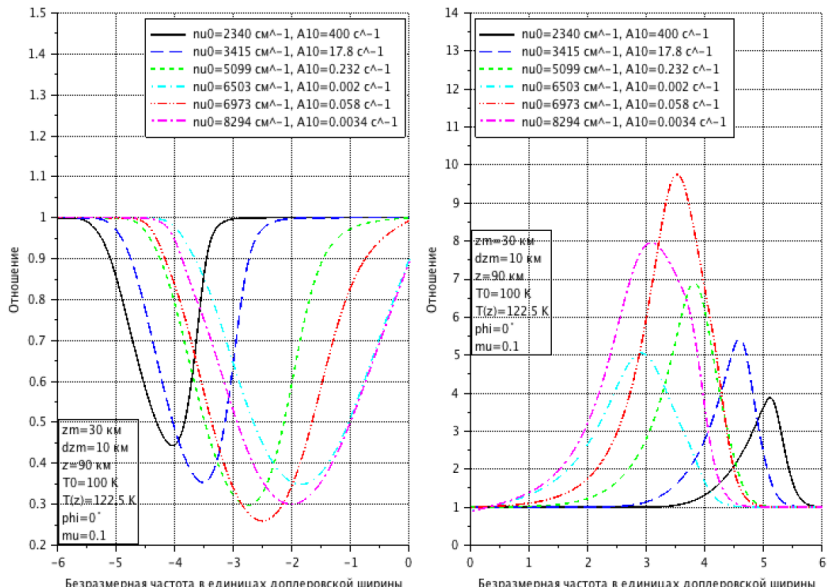


Fig. 1. The ratio of the spectrum of outgoing radiation for a moving atmosphere (velocity in the center of the layer is equal to 1 Mach) to the spectrum of outgoing radiation for a stationary medium for various NIR bands of CO_2 (versus to the dimensionless frequency)

The following characteristic values were taken as the main optical parameters on which the optical thickness of the planetary atmosphere in the BIC bands of the $^{12}\text{C}^{16}\text{O}_2$ molecule depends: $\nu_0 = 2340$ cm^{-1} and $A_0 = 400$ s^{-1} for the 4.3 μm band; $\nu_0 = 3415$ cm^{-1} and $A_0 = 17.8$ s^{-1} for the band 2.7 μm ; $\nu_0 = 5099$ cm^{-1} and $A_0 = 0.232$ s^{-1} for the 2.0 μm band; $\nu_0 = 6503$ cm^{-1} and $A_0 = 0.002$ s^{-1} for the 1.6 μm band; $\nu_0 = 6973$ cm^{-1} and $A_0 = 0.058$ s^{-1} for the 1.4 μm band; $\nu_0 = 8294$ cm^{-1} and $A_0 = 0.0034$ s^{-1} for the 1.05 μm band. It can be concluded from the Figure 1 that the Doppler effect is most noticeably taken into account for a spectral line with a central frequency $\nu_0 = 6973$ cm^{-1} and a coefficient of spontaneous emission $A_0 = 0.058$ s^{-1} ,

and least noticeably for a line with $\nu_0 = 2340 \text{ cm}^{-1}$ and $A_0 = 400 \text{ s}^{-1}$. It can be assumed that the magnitude of the effect of this type of variation (i. e., how great the influence of the moving layer is for lines of different bands) depends on the combination of the values of the central frequency and the Einstein coefficient of spontaneous emission.

It can also be seen that the frequencies at which the maxima and minima for different lines are located differ from each other.

CONCLUSIONS:

It is shown that the presence of a layer moving in the atmosphere for a certain frequency range in the near and middle parts of the wings of spectral lines can significantly affect the intensity of radiation leaving the planetary atmosphere at the upper boundary. These changes can reach hundreds of percent, both upward and downward. Moreover, these changes do not compensate for each other, because they are significantly nonlinear in nature.

The main conclusions are as follows. 1) The distribution over the spectrum of radiation leaving the atmosphere at the upper boundary, in the presence of a large-scale vertical gradient of the wind horizontal velocity, strongly depends on the parameters of the spectral line of the band (the central frequency ν_0 and the Einstein coefficient of spontaneous emission A_0). 2) When the spectral parameters of the line vary, the intensity of outgoing radiation changes in different ways for frequencies located at different distances from the central frequency. 3) In this case, the change in radiation intensity in the presence of a moving layer in the atmosphere has a very different character from the given line (band) to the another line (band).

The latter circumstances can be used to diagnose the characteristics of large-scale wind movements in planetary atmospheres. The analysis of the results of this work allows us to hope that further studies of this problem for more realistic models of both spectral bands and models of large-scale vertical wind velocity gradients may be appropriate.

REFERENCES:

- [1] *Mendonç J. M., Read P. L.* Exploring the Venus global super-rotation using a comprehensive general circulation model // *Planetary and Space Science*. 2016. V. 134. P. 1–18. DOI: 10.1016/j.pss.2016.09.001.
- [2] *Mousis O., Atkinson D. H., Cavalié T.* Scientific rationale for Uranus and Neptune in situ explorations // *Planetary and Space Science*. 2018. V. 155. P. 12–40. DOI: 10.1016/j.pss.2017.10.005.
- [3] *Ogibalov V. P., Bordovskaya Yu. I.* Influence of wind fields with macroscopic velocity gradients on the IR CO_2 band emissions outgoing from a planetary atmosphere // *Proc. SPIE. 28th Intern. Symp. Atmospheric and Ocean Optics: Atmospheric Physics*. 2022. V. 12341. Article 123411O. DOI: 10.1117/1.2.2645401.

THE SPATIAL-GENETIC RELATIONSHIP OF THE CORONAE SOURCING LAVA FLOWS AND LARGE VOLCANOES OF VENUS

E. N. Guseva, M. A. Ivanov

Vernadsky Institute of Geochemistry and Analytical Chemistry RAS
Moscow, Russia, guseva@geokhi.ru, ivanov.m@geokhi.ru

KEYWORDS:

Venus, topography, late volcanism, coronae, volcanoes, lobate plains, rifts, volcanic activity

INTRODUCTION:

Our study is based on the analyses of topography and spatial distribution of coronae sourcing younger lava flows and large volcanoes on Venus. These structures are widespread (hundred features) on the planet [1, 2].

The coronae are large (up to 2500 km in diameter), circular features [1, 2], which probably represent the surface manifestations of mantle diapirs [3–5]. Three topographic classes characterize coronae: D, W, U (domes, depressions with a central peak, simple depressions, Figure 1) [6]. These classes probably correspond to the different stages of evolution of the parent diapirs [7]. The volcanic activity of most coronae died out in the pre-Atlian times. Only a small proportion of coronae (17 %) exhibits volcanic activity in the form of flows of lobate plains [6].

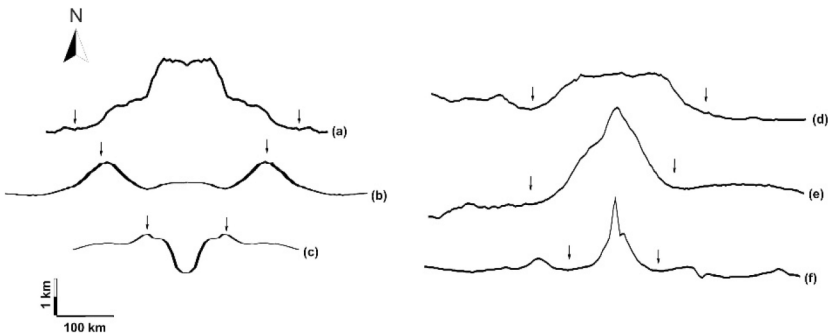


Fig. 1. Topographic profiles, left: coronae, the sources of lobate plains: (a) Nahastan Mons, class D; (b) Ereshkigal, class W; (c) Rind, class U; right: large volcanoes: (d) Kokyanwuti Mons, group 1; (e) Idunn Mons, group 2; (f) Xochiquetzal Mons, group 3. Arrows indicate the topographic boundaries of coronae and large volcanoes

The volcanoes are large topographical constructions, more than 100 km in diameter [8, 9], that are comparable in size to the coronae sourcing lobate plains. Three size groups characterize topography of volcanoes: (1) the largest flat-topped (up to 740 km in diameter), (2) medium conical (up to 425 km) and (3) small conical (up to 240 km) (Figure 1). All of them are relatively young volcanic edifices formed during the Atlian period [8–10]. Multiple lava flows extend along the slopes of volcanoes for hundreds of kilometers and, when merging, form complexes of lobate plains [8, 11–14].

The purpose of this study was to determine how are the coronae — sources of lobate plains related to large volcanoes in terms of the spatial distribution and to determine if there is a genetic link between coronae and volcanoes.

METHODS:

In our work, we compared the published catalogs of volcanic structures [1, 2] with the global geological map of Venus, which shows fields of lobate plains [10]. We studied the morphology of the coronae and volcanoes using the traditional photogeological analysis based on the C1-MIDR images (resolution 225 m/px). Using this method, we assessed the stratigraphic

position of coronaes and volcanoes. The topographic configuration of these structures was studied by topographic profiles through these structures constructed from the Magellan topographic map (resolution 5 km/px).

RESULTS:

We have identified the main areas of mutual distribution of the corona-sources of lobate plains (90 structures) and volcanoes (89 structures). The corona-sources of all topographic classes and volcanoes, mainly the large flat-topped (group 1) and medium conical (group 2) (total 53 % of the entire population), are concentrated in the Beta-Atla-Themis (BAT), Eistla and Metis Regiones (Figure 2). Small conical volcanoes (group 3, 47 % of the total population) have a broader distribution over the surface (Figure 2).

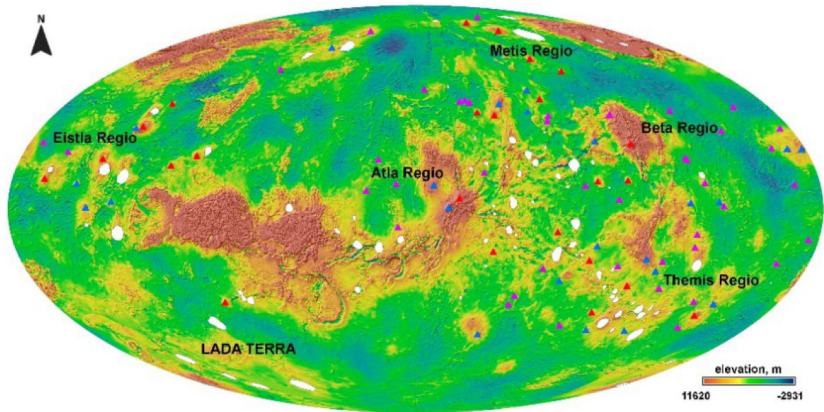


Fig. 2. Distribution of the corona-sources of three topo-classes (white) and volcanoes of three groups: the largest flat-topped (group 1, red), the medium conical (group 2, blue) and the small conical (group 3, purple). The base topographic map in equal-area Mollweide projection, central meridian is 180°

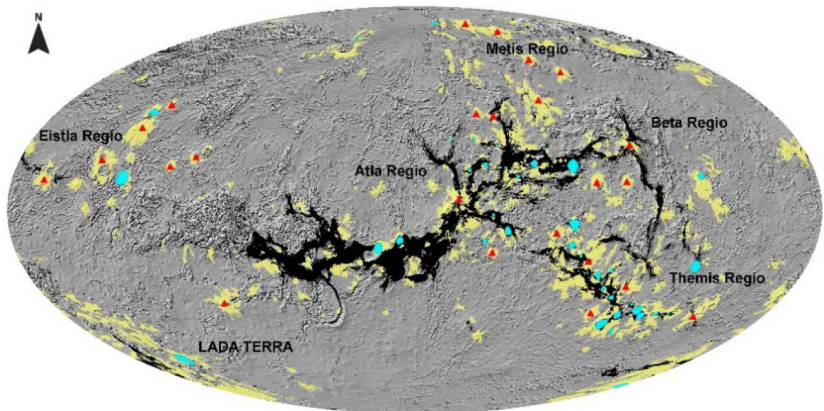


Fig. 3. Distribution of the corona-sources D-class (blue) and the largest flat-topped volcanoes (red); lobate plains — yellow, rift zones — black; geological boundaries according to [10]; Mollweide projection, central meridian 180°

The dome-shaped corona-sources (class D, 44 %) and the large flat-topped volcanoes (group 1, 27 %) are most often spatially associated with each other and are also associated with rift zones in the BAT region (Figure 3). It is conceivable that such volcanoes may represent the results of an extended evolution of coronaes when large edifices formed over the sites of prolonged magmatic activity.

CONCLUSION:

Based on the results of our work, we can conclude the following: (1) corona-sources of lobate plains, the largest flat-topped and medium-conical

volcanoes occur mainly in three areas, the BAT, Eistla, and Metis Regiones; (2) the dome-shaped corona-sources and the largest flat-topped volcanoes are often spatially associated with each other and such volcanoes might represent the results of advanced evolution of coronae; (3) the studied features mark the main areas of late volcanism on Venus.

REFERENCES:

- [1] *Stofan E.R., Sharpton V.L., Schubert G. et al.* Global distribution and characteristics of coronae and related features on Venus: Implications for origin and relation to mantle processes // *J. Geophysical Research*. 1992. V. 97. Iss. E8. P. 13.347–13.378. <https://doi.org/10.1029/92JE01314>.
- [2] *Crumpler L.S., Aubele J.C.* Volcanism on Venus // *Encyclopedia of Volcanoes* / Eds. Houghton B., Rymer H., Stix J., McNutt S., Sigurdson H. San Diego: Acad. Press. 2000. P. 727–770.
- [3] *Nikishin A.M.* Tectonics of Venus: A review // *Earth, Moon, and Planets*. 1990. V. 50. P. 101–125.
- [4] *Pronin A.A., Stofan E.R.* Coronae on Venus: Morphology, classification, and distribution // *Icarus*. 1990. V. 87. P. 452–474. DOI: 10.1016/0019-1035(90)90148-3.
- [5] *Stofan E.R., Smrekar S.E.* Large topographic rises, coronae, large flow field, and large volcanoes on Venus: Evidence for mantle plumes? // *Geological Society of America Special Paper*. 2004. V. 388. P. 841–861. <https://doi.org/10.1130/0-8137-2388-4.841>.
- [6] *Guseva E.N., Ivanov M.A.* Spatial and genetic relationships of coronae, lobate plains and rift zones of Venus // *Solar System Research*. 2023. V. 57(2). P. 112–121. DOI: 10.1134/S003809462302003X.
- [7] *Smrekar S.E., Stofan E.R.* Corona formation and heat loss on Venus by coupled upwelling and delamination // *Science*. 1997. V. 277. Iss. 5330. P. 1289–1294.
- [8] *Head J.W., Crumpler L.S., Aubele J.C. et al.* Venus volcanism: Classification of volcanic features and structures, associations, and global distribution from Magellan data // *J. Geophysical Research*. 1992. V. 97. P. 13.153–13.197. <https://doi.org/10.1029/92JE01273>.
- [9] *Crumpler L.S., Aubele J.C., Senske D.A., Keddie S.T., Magee K.P., Head J.W.* Volcanoes and centers of volcanism on Venus // *Venus II: Geology, geophysics, atmosphere, and solar wind environment* / eds. Bougher S.W., Hunten D.M., Philips R.J. The University of Arizona Press, 1997. 697–756.
- [10] *Ivanov M.A., Head J.W.* Global geological map of Venus // *Planetary and Space Science*. 2011. V. 59. P. 1559–1600. DOI: 10.1016/j.pss.2011.07.008.
- [11] *Senske D.A., Head J.W., Stofan E.R., Campbell D.B.* Geology and structure of Beta Regio, Venus: Results from Arecibo radar imaging // *Geophysical Research Letters*. 1991. V. 18. Iss. 6. P. 1159–1162. <https://doi.org/10.1029/91GL01001>.
- [12] *Basilevsky A.T., Head J.W.* Beta Regio, Venus: Evidence for uplift, rifting, and volcanism due to a mantle plume // *Icarus*. 2007. V. 192(1). P. 167–186. DOI: 10.1016/j.icarus.2007.07.007.
- [13] *Ivanov M.A., Head J.W.* The history of volcanism on Venus // *Planetary and Space Science*. 2013. V. 84. No. 12. P. 66–92. DOI: 10.1016/j.pss.2013.04.018.
- [14] *Hahn R.M., Byrne P.K.* A Morphological and Spatial Analysis of Volcanoes on Venus // *J. Geophysical Research*. 2023. V. 128. Iss. 4. Article e2023JE007753. <https://doi.org/10.1029/2023JE007753>.

PRELIMINARY INSIGHTS INTO THE EVOLUTION OF CENTRAL TYPE VOLCANISM ON VENUS

D. G. Malyshev, M. A. Ivanov

*Vernadsky Institute of Geochemistry and Analytical Chemistry RAS
Moscow, Russia, malyshev.danil13@gmail.com, mikhail_ivanov@brown.edu*

KEYWORDS:

Venus, volcanism, shield volcanoes, coronae, planetary geology

INTRODUCTION:

Numerous volcanic centers on Venus include among others shield volcanoes and coronae [1]. The volcanoes are characterized by their dome/cone-shaped topography and a radial pattern of lava flows while the coronae manifest itself by tectonized annular rim and many of them lack distinct volcanic features [2]. While the models of the formation of volcanoes and coronae are abundant [e.g., 3, 4], only a few papers [e.g., 5–7] consider the relative ages of the volcanoes and coronae. However, their stratigraphic relationships likely represent a crucial component of our understanding of the thermal evolution of Venus. In this work we present preliminary results suggesting the change of the style of central volcanism on Venus through time.

CHARACTERISTICS OF THE VOLCANOES AND CORONAE:

Large volcanoes are volcanic centers (100 km in diameter) characterized by radially dispersed lava flows, often associated with concentric or radial fractures. They are concentrated in areas with positive relief.

Coronae are circular or elongated structures consisting of a ring of fractures (sometimes ridges) that surrounds topographically positive or negative areas with numerous volcanic and tectonic landforms. Some of the coronae have a peripheral moat, and many of them show numerous lava flows radially diverging; the characteristic diameters of the coronae range from 200 to 250 km. Topographically, the coronae have a variety of shapes, including domed elevations, plateaus, plateaus with central depressions and fringed depressions.

DOCUMENTED RELATIVE AGES OF THE VOLCANOES AND CORONAE:

Previously, analysis of impact crater densities indicated that shield volcanoes, on the average, have surface ages younger than those of coronae [8, 9]. Geological mapping of other areas on Venus demonstrated that shield volcanoes are stratigraphically younger than nearby coronae [e.g., 5, 7]. In [6] the examples where coronae evolution overlap with adjacent volcanic edifices were reported. Recently, the evidence that only 17 % of all coronae on Venus are sources of young lava flows was presented [10].

SUMMARY:

It can be seen that there is no systematic research on the analysis of volcanoes and coronae relative ages on the global scale. We emphasize the significance of that since, based on the previous works, it will imply that during the earlier stages of Venus' evolution its loss of the internal heat was dominated by the formation of coronae, whereas at the later stages, the primary role in this process was played by the large volcanoes. The main goal of our study is to link the different styles of the heat loss with the existing stratigraphic model of Venus [11]. To achieve that, the further analysis of the neighboring volcanoes and coronae local stratigraphy on a planetary scale is needed.

REFERENCES:

- [1] *Crumpler L. S., Aubele J.C.* Volcanism on Venus // Encyclopedia of Volcanoes / eds. Sigurdsson H. et al. Academic Press, 2000. P. 727–770.
- [2] *Ivanov M.A., Head J.W.* The history of volcanism on Venus // Planetary and Space Science. 2013. V. 84. No. 12. P. 66–92. DOI: 10.1016/j.pss.2013.04.018.

- [3] *McGovern P.J., Solomon S.C.* Growth of large volcanoes on Venus' Mechanical models and implications for structural evolution // *J. Geophysical Research*. 1998. V. 103. Iss. E5. P. 11071–11101. <https://doi.org/10.1029/98JE01046>.
- [4] *Smrekar S.E., Stofan E.R.* Corona Formation and Heat Loss on Venus by Coupled Upwelling and Delamination // *Science*. 1997. V. 277. No. 5330. P. 1289–1294. DOI: 10.1126/science.277.5330.1289.
- [5] *McGill G.E.* Hotspot evolution and Venusian tectonic style // *J. Geophysical Research*. 1994. V. 99. No. E11. P. 23149–23161. <https://doi.org/10.1029/94JE02319>.
- [6] *Stofan E.R., Guest J.E., Brian A.W.* Geologic Map of the Hecate Chasma Quadrangle (V–28), Venus // U.S. Geological Survey. 2012. Scientific Investigations Map 3163.
- [7] *Dohm J.M., Tanaka K.L., Skinner J.A.* Geologic Map of the Metis Mons Quadrangle (V–6), Venus // U.S. Geological Survey. 2011. Scientific Investigations Map 3158.
- [8] *Namiki N., Solomon S.C.* Impact Crater Densities on Volcanoes and Coronae on Venus: Implications for Volcanic Resurfacing // *Science*. 1994. V. 265. No. 5174. P. 929–933. DOI: 10.1126/science.265.5174.929.
- [9] *Price M., Suppe J.* Mean age of rifting on Venus deduced from impact crater densities // *Nature*. 1994. V. 372. P. 756–759.
- [10] *Guseva E.N., Ivanov M.A.* Coronae—Sources of Young Volcanism on Venus: Topographic Features and Estimates of Productivity // *Solar System Research*. 2024. V. 58(1). P. 78–87. DOI: 10.1134/S0038094624010039.
- [11] *Ivanov M.A., Head J.W.* Global geological map of Venus // *Planetary and Space Science*. 2011. V. 59(13). P. 1559–1600. DOI: 10.1016/j.pss.2011.07.008.

A SIMPLE GEOMETRICAL APPROACH FOR SOLVING THE ECLIPSE PROBLEM

V. A. Zubko, A. A. Belyaev

Space Research Institute RAS, Moscow, Russia, v.zubko@iki.rssi.ru

KEYWORDS:

occultation events, shadow function, eclipse duration

INTRODUCTION:

The problem of predicting the eclipses of satellites by the central body has been a long-standing problem in astrodynamics. This is important mainly for determining the evolution of orbital parameters affected by non-gravitational perturbations from sunlight pressure. It has also been found to be useful in studying the dynamics of satellite trajectories using electric propulsion. Two main approaches have been identified to solve this problem: the first one involves finding time intervals using numerical methods based on solving the shadow equation directly [1–3], while the second one involves obtaining analytical solutions using geometric representations or algebraic transformations of the problem [4–11].

THEORY:

This research focuses on the problem of determining the entry and exit points of the penumbra and umbra of a satellite occulted by a central body in orbit by deriving an analytical, closed-form equation. The approach used in this research is based on a geometrical representation similar to [4–11], with the distinguishable difference that in the current work, it is supposed that the conical surface formed by the intersection of light rays and the central body can be cut by the orbital plane of the satellite. The result of this intersection, the figure formed in the orbital plane, can be represented as a second-order curve in the plane (further referred to as the shadow curve). The position of the satellite's penumbra/umbra can be determined by the intersection between the shadow curve and the satellite's orbit.

RESULTS:

Building on this foundation, an analytical model has been constructed and contrasted with existing analytical [4–8, 11, 14] and numerical ones [3, 9, 10, 12, 13]. This comparison was conducted for the cases of the Earth, Mars, and Venus. Subsequently, the framework was applied to the problem of determining the duration of atmospheric occultation of a satellite. It has been demonstrated that the model constructed is well-suited for addressing practical problems.

REFERENCES:

- [1] Montenbruck O. Gill E. *Satellite Orbits: Models, Methods, Applications*. Berlin: Springer, 2005. 369 p.
- [2] Vallado D. A. *Methods of Astrodynamics, a Computer Approach*, 1991.
- [3] Montenbruck O., Gill E., Lutze F. *Satellite orbits: models, methods, and applications // Applied Mechanics Reviews*. 2002. V. 55(2). P. B27–B28. <https://doi.org/10.1115/1.1451162>.
- [4] Neta B., Vallado D. On satellite umbra/penumbra entry and exit positions // *J. Astronautical Sciences*. 1998. V. 46. No. 1. P. 91–103.
- [5] Stoddard L.G. Eclipse of an Artificial Earth Satellite, *Astronaut // Sciences Review*. 1961. V. 3. P. 9–16.
- [6] Patterson G.B. Graphical method for prediction of time in sunlight for a circular orbit // *American Rocket Society J*. 1961. V. 31. P. 441–442. <https://doi.org/10.2514/8.5501>.
- [7] Peckham G.W. *The orbital shadow time of an Earth satellite*. Air Force Institute of Technology, 1960. 126 p.
- [8] Geyling F. T., Westerman H. R. *Introduction to orbital mechanics*. Addison-Wesley Educational Publishers Inc, 1971. 349 p.
- [9] Escobar P. *Methods of orbit determination*. N.Y.; L.: John Wiley and Sons, 1965. 363 p.
- [10] Mullins L. D. Calculating satellite umbra/penumbra entry and exit positions and times // *J. Astronautical Sciences*. 1991. V. 39. P. 411–422.

- [11] *Dobroslavskiy A. V.* On Estimating the Average Stay of an Artificial Satellite in the Area of the Earth's Shadow while Moving in the Ecliptic Plane // *Cosmic Research*. 2020. V. 58(6). P. 501–507. DOI:10.1134/S0010952520060027.
- [12] *Zhang J., Wang K., Yan B., Wang L.* Eclipse analysis for small-eccentricity orbits using analytical model // *Advances in Space Research*. 2022. V. 70. Iss. 8. P. 2323–2333. DOI: 10.1016/j.asr.2022.06.071.
- [13] *Adhya S., Sibthorpe A., Ziebart M., Cross P.* Oblate earth eclipse state algorithm for low-earth-orbiting satellites // *J. Spacecraft Rockets*. 2004. V. 41. No. 1. P. 157–159. <https://doi.org/10.2514/1.1485>.
- [14] *Nugnes M., Colombo C., others,* A New Analytical Method for Eclipse Entry/Exit Positions Determination Considering a Conical Shadow and an Oblate Earth Surface // *2022 AAS/AIAA Astrodynamics Specialist. Conf.* 2022. P. 1–19.

ON LOAD NUMBERS FOR VENUS

T. V. Gudkova, A. V. Batov

Schmidt Institute of Physics of the Earth RAS, Moscow, Russia

gudkova@ifz.ru, batovalex@yandex.ru

KEYWORDS:

Venus, planetary interiors, load Love numbers

INTRODUCTION:

Venus is similar to Earth in mass and average radius, but the dynamic processes in the interior of these planets are very different. Mantle convection is the main mechanism responsible for heat loss and the evolution of Venus, and is driven by several mantle plumes. There is now established evidence of modern volcanism on Venus [1, 2]. The surface of Venus is dominated by a number of high topographic structures (see, for example, [3]). Questions of interpretation (geoid anomalies and gravitational anomalies) of the non-equilibrium part of the gravitational field of Venus raise a lot of controversy, and the discussion about what part of the anomalous gravitational field can be supported elastically, and what part of the anomalies can arise in the mantle and be supported by dynamic processes is not completed (see, for example, [4]). The load coefficient method [5] takes into account that when an anomalous mass (an anomalous density wave) is added, deformation of the interfaces occur. In this work, we present load Love numbers calculated for a number of Venus models using topography and gravitational field data up to the 70th degree and order.

METHOD:

When interpreting gravitational anomalies, it is possible to use two polar approaches: static (equations of the theory of elasticity) and dynamic (equations for a viscous fluid). Purely elastic approach — the model is a limiting case. The elastic and viscoelastic approaches are equivalent from a mathematical point of view, with the solution of the elastic problem being the key to solving the viscoelastic case. The static approach (Green's function method) in the technique of load coefficients for a load arbitrarily distributed in the interior of the planet, for an elastic spherical model of the planet is present in [5]. The planet is modeled as an elastic self-gravitating body with radius-dependent density, compression modulus, and shear modulus. To calculate load coefficients, a system of equations is solved, which includes: elastic equilibrium equation; Poisson's equation relating the anomalous gravitational potential to the density distribution [5].

The sources of density inhomogeneities in the planet's interior are inhomogeneities associated with changes in temperature and chemical composition, as well as deformation of interfaces, such as the crust-mantle boundary and phase transition boundaries at which there are density jumps. The expression for the total anomalous potential, which takes into account the global deformation of the planet under the influence of the anomalous layer, acting on the planet as a load and leading to additional disturbance of the potential, has the form:

$$\Delta V = 4\pi GR \sum_{i,n,m} \left(\frac{r}{R}\right)^{n+2} \frac{R_{i,n,m}(r)(1+k_n(r))}{(2n+1)} Y_{i,n,m}(\phi, \lambda),$$

where G is the gravitational constant; R is the average radius of the planet; $k_n(r)$ are load numbers of order n for a density anomaly buried at depth r . Load numbers $k_n(r)$ and $K_n(r) = 1 + k_n(r)$ are the Green's function — were introduced in [5].

To determine the load coefficients from surface and buried density anomalies, a system of elastic equilibrium equations for a gravitating planet is solved, which is reduced to a system of six first-order ordinary differential equations [5]. The equations are integrated from the boundary of the outer liquid core. To solve the equations, the Runge–Kutta method is used, the boundary conditions are set on the surface or at the depth of the anom-

alous density wave. Calculations are carried out for each harmonic up to degree and order n , based on the accuracy of determining the gravitational field at the moment.

OBSERVATIONAL DATA:

We use topography data (model SHTJV360u, [6]) and gravity field data (model SHGJ180u, [7]). These models are a series of fully normalized coefficients that are available on the Planetary Data System website (<http://pds-geosciences.wustl.edu>). The simulation is carried out for harmonics only up to the 70th degree and order, since the poor correlation between the gravitational field and topography for harmonics above 70 means the inaccuracy of the short-period components in the gravitational field model [8]. Venus is the most disequilibrium planet in the solar system. The gravitational field of Venus can be divided into an equilibrium component (the field of hydrostatically equilibrium Venus) and a nonequilibrium one, using the hypothesis that Venus is earth-like and the figure of the equilibrium planet is "fixed" as it was in a distant era [9]. Let us take the surface of effectively equilibrium Venus as the reference surface.

RESULTS:

The normalized coefficients of the nonequilibrium gravitational field of Venus are related to the amplitudes of anomalous density waves R_{nm} located at depth r_j and load numbers k_n :

$$C_{ginm} = \sum_{j=0}^N \frac{R_{inm}^j}{R\rho_0} \frac{3(1+k_n(r_j))}{(2n+1)} (r_j)^{n+2},$$

(where ρ_0 is the average density of the planet, r_j are the levels of the occurrence of anomalous masses).

Load numbers $kn(r)$ were calculated for a number of models of the internal structure of Venus from [10]. The depth distributions of the load numbers $k_n(r)$ were obtained for various models of the inhomogeneous elasticity of Venus (elastic model and model with lithosphere). Load coefficients $k_n(r)$ and $h_n(r)$ (with the opposite sign) for the test model of the internal structure are shown in Figure 1 for $n = 2 \dots 70$ and depths: on the surface, at the crust-mantle boundary and at some depths in the mantle.

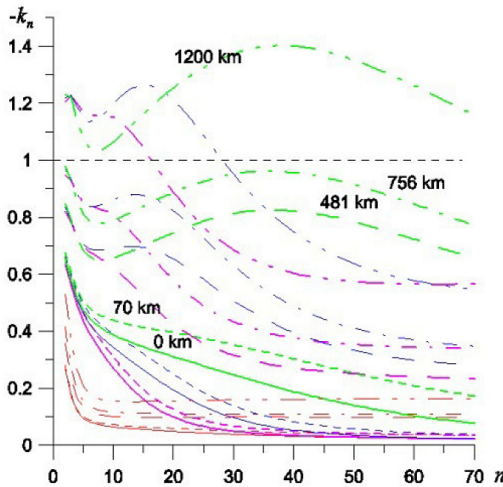


Fig. 1. Load numbers $kn(r)$ (with the opposite sign) for the elastic model of Venus (red lines); models with a lithosphere thickness of 100 km (green lines), 300 km (blue lines) and 500 km (pink lines) as a function of the spherical harmonic number n for different depths of anomalous density waves: on the surface 0 km, at a crust-mantle depth of 70 km, at depths of 481, 756 and 1200 km. The horizontal dotted line corresponds to the value $k_n(r) = -1$ (isostasy)

The choice of the load depth in the mantle (setting the anomalous mass in the mantle, which drives the convective flow) is a slight simplification

of the physical mechanism and is an approximation of the rather complex real distribution of anomalous masses in the mantle. The value $(-k_n(r_j)) = 1$ is complete isostatic compensation, the physical reason is the effect of deformation of the elastic shells of the mantle located above the weakened layer. For $0 < (-k_n(r_j)) < 1$ we have partial compensation of the anomalous density wave under consideration. The choice of compensation level is necessary to calculate the stressed state of the interior of Venus.

CONCLUSION:

Numerical modeling of loading Love numbers was carried out for various models of Venus, using a static approach for loading on the surface (planet topography) and for buried anomalous density waves, according to topography and gravitational field data. The choice of the load depth in the mantle is a slight simplification of the physical mechanism and is an approximation of the rather complex distribution of anomalous masses in the mantle.

ACKNOWLEDGMENTS:

The study was performed based on funding of Russian Scientific Foundation No. 23-22-00074, <https://rscf.ru/project/23-22-00074/>.

REFERENCES:

- [1] *Smrekar S. E., Stofan E. R., Mueller N., Treiman A., Elkins-Tanton L., Helbert J., Piccioni G., Drossart P.* Recent hotspot volcanism on Venus from VIRTIS emissivity data // *Science*. 2010. V. 328(5978). P. 605–608.
- [2] *Shalygin E. V., Markiewicz W. J., Basilevsky A. T., Titov D. V., Ignatiev N. I., Head J.-W.* Active volcanism on Venus in the Ganiki Chasma rift zone // *Geophysical Research Letters*. 2015. V. 42. P. 4762–4769.
- [3] *Ivanov M. A., Head J.-W.* Global geological map of Venus // *Planetary and Space Science*. 2011. V. 59(13). P. 1559–1600.
- [4] *Huang J., Yang A., Zhong S.* Constraints of the topography, gravity and volcanism on Venusian mantle dynamics and generation of plate tectonics // *Earth and Planetary Science Letters*. 2013. V. 362. P. 207–214.
- [5] *Marchenkov K. I., Lyubimov V. M., Zharkov V. N.* Calculation of loading coefficients for deep density anomalies // *Doklady Akademii nauk SSSR*. 1984. V. 15. No. 2. P. 583–586 (in Russian).
- [6] *Rappaport N. J., Konopliv A. S., Kucinskas A. B.* An improved 360 degree and order model of Venus topography // *Icarus*. 1999. V. 139. P. 19–31.
- [7] *Konopliv A. S., Banerdt W. B., Sjogren W. L.* Venus gravity: 180th degree and order model // *Icarus*. 1999. V. 139. P. 3–18.
- [8] *Menshchikova T. I., Gudkova T. V., Zharkov V. N.* Analysis of the topography and gravity data for the Earthlike Venus // *Solar System Research*. 2021. V. 55. No. 1. P. 11–19.
- [9] *Zharkov V. N., Gudkova T. V.* On parameters of the Earth-like model of Venus // *Solar System Research*. 2019. V. 53. No. 1. P. 1–4.
- [10] *Gudkova T. V., Zharkov V. N.* Models of the internal structure of the Earth-like Venus // *Solar System Research*. 2020. V. 54. No. 1. P. 20–27.

THE EFFECT OF THE DENSE ATMOSPHERE OF VENUS ON THE LOVE NUMBERS

D. O. Amorim¹, T. V. Gudkova²

¹ *Moscow Institute of Physics and Technology, Moscow, Russia*
amorim.dargilan@gmail.com

² *Schmidt Institute of Physics of the Earth RAS, Moscow, Russia*
gudkova@ifz.ru

KEYWORDS:

Venus, planetary interiors, atmosphere, tidal Love numbers

INTRODUCTION:

The VERITAS [1] and EnVision [2] missions plan to obtain more accurate values of Love number k_2 and moment of inertia and measure two still uncertain parameters — tidal phase shift and Love number h_2 . Comparing the results of these missions with the available interior structure models of Venus will make it possible to clarify the internal structure of Venus. Venus has a dense atmosphere. The influence of the dense atmosphere of Venus on the Love numbers should be taken into account.

OBSERVATIONAL DATA AND VENUS' MODELS:

Observational data used in constructing models of the internal structure of Venus are given in Table 1: mass of the planet M_0 (without atmosphere), average radius R , dimensionless moment of inertia I/M_0R^2 , tidal Love number k_2 , pressure P_s and atmospheric density ρ_s on the surface. The test interior structure model is taken from [7].

Table 1. Observational data for Venus

Parameters	Parameter values	Links
Mass M_0 , kg	$4.8673 \pm 0.00011 \cdot 10^{24}$	[3]
Mean radius R , km	6051.8	
Moment of inertia I/M_0R^2	0.337 ± 0.024	[4]
Love number k_2	0.295 ± 0.033	[5]
Atmospheric pressure at the surface P_s , MPa	9.3	[6]
Density of the atmosphere at the surface ρ_s , kg/m ³	65	

METHOD:

The method for calculating Love numbers is described in detail in [8]. Models of Venus have no internal core and the integration of tidal deformation begins from the boundary of the liquid core with the initial conditions from [9].

We will use the same notation as in [8]. Tidal deformation is expressed through 6 quantities: y_1 and y_3 have the meaning of radial and tangential displacements that arise due to tidal deformation; y_2 and y_4 are the radial and tangential stress components, y_5 is the change in gravitational potential, and y_6 depends on y_s , y_1 and the density of the medium.

When calculating the Love numbers of a planet without an atmosphere (or with a weak atmosphere that has little effect on tidal deformation), the following surface boundary conditions are often used:

$$y_2^S = 0, \quad y_4^S = 0, \quad y_6^S = (2n+1)g_0^S - (n+1)y_5^S/R, \quad (1)$$

where R is the radius of the planet, and g_0^S denotes gravitational acceleration on an underformed surface. Here and below, the superscript S denotes the value of a quantity on the surface.

The first two equalities mean that there is no stress on the surface. If there is an atmosphere above the surface, the condition on y_4 will not change in any way, since this quantity is proportional to the shear modulus of the material (see [8]), and in gases it is equal to zero.

The new condition on y_2 is obtained from the same considerations as the condition during the transition from the inner core of the Earth to the outer core [8]. In liquid and gaseous media the following relationship holds [9]:

$$y_2 = \rho_0 (g_0 y_1 - y_5). \quad (2)$$

Therefore, from the condition of continuity of y_1 , y_2 and y_5 we obtain a new condition on y_2 :

$$y_2^S = \rho_A (g_0^S y_1^S - y_5^S) \quad (3)$$

where ρ_A denotes the density of the atmosphere directly above the planet's surface.

The third condition in (1) is obtained from the properties of the potentials and the discontinuity in the derivative of the potential y_5 due to the density contrast at the transition from the crust to vacuum. If we do not neglect the fact that there is a medium with non-zero density above the surface, an additional term should appear in the third condition (1):

$$y_6^S = (2n + 1)g_0^S - (n + 1)y_5^S / R - 4\pi G \rho_A y_1^S. \quad (4)$$

The new term, in the case of Venus, is approximately 0.3–0.5 % of the rest. There should be one more term in (4), which depends on the change in atmospheric potential due to tidal deformation. Its value, however, is unknown and can only be calculated by integrating the differential equations from [9] over the atmosphere.

Even on Venus, the mass of the entire atmosphere is only 0.01 % of the mass of the planet. Since the change in atmospheric potential is proportional to the mass of the atmosphere itself, we believe that its contribution to (4) is small and can be neglected. Thus, the system is closed at the surface without the need to integrate atmospheric deformation.

The new boundary conditions on the surface then take the form:

$$y_2^S = \rho_A (g_0^S y_1^S - y_5^S), \quad y_4^S = 0, \quad y_6^S = (2n + 1)g_0^S - (n + 1)y_5^S / R - 4\pi G \rho_A y_1^S. \quad (5)$$

RESULTS:

Our calculations show that the "atmosphere" correction reduces the Love numbers by approximately 3 %, which is comparable to the ratio of the atmospheric density ρ_A to the density of the planet's crust. In [10] the atmosphere is taken into account by integrating its deformation without the approximation that we made; as a result, in [10] the atmosphere reduces the Love numbers by 3–4 %, which is very close to our results.

In the work [3], the atmosphere is also taken into account when calculating Love numbers, but it is stated that its influence is 7–8 %, which is twice as much as in the work [10] and in this work. The explanation for this is most likely the following: in [3] the atmosphere is replaced by a layer with a constant density of 36.5 kg/m^3 and a thickness of 100 km, the mass of such an atmosphere is approximately 3.5 times greater than the real mass of the atmosphere of Venus.

Thus, we believe that our approximation allows us to take into account the influence of the atmosphere when calculating Love numbers with good accuracy and in a very simple way — by changing the boundary conditions on the surface without additional integration.

CONCLUSION:

The method of Love numbers calculation was proposed that allows us to take into account the influence of the dense atmosphere of Venus in a very simple way. Our results show that the atmosphere reduces k_2 by about 3 %. This value is quite significant and the influence of the atmosphere should not be neglected.

ACKNOWLEDGMENTS:

The study was performed based on funding of Russian Scientific Foundation No. 23-22-00074, <https://rscf.ru/project/23-22-00074/>.

REFERENCES:

- [1] *Cascioli G., Hensley S., De Marchi F., Breuer D., Durante D., Racioppa P., Iess L. Mazarico E., Smrekar S.E.* The determination of the rotational state and interior structure of Venus with VERITAS // *Planetary Science J.* 2021. V. 2. P. 220–231.
- [2] *Rosenblatt P., Dumoulin C., Marty J.-C., Genova A.* Determination of Venus' interior structure with EnVision // *Remote Sensing.* 2021. V. 13. Article 1624.
- [3] *Saliby C., Fienga A., Briaud A., Mémín A., Herrera C.* Viscosity contrasts in the Venus mantle from tidal deformations // *Planetary and Space Science.* 2023. V. 231. Article 105677.
- [4] *Margot J.-L., Campbell D.B., Giorgini J.D., Jao J.S., Snedeker L.G., Ghigo F.D., Bon-sall A.* Spin state and moment of inertia of Venus // *Nature Astronomy.* 2021. V. 5(7). P. 676–683.
- [5] *Konopliv A.S., Yoder C.F.* Venusian k_2 tidal Love number from Magellan and PRO tracking data // *Geophysical Research Letters.* 1996. V. 23(14). P. 1857–1860.
- [6] *Steinberger B., Werner S., Torsvik T.* Deep versus shallow origin of gravity anomalies, topography and volcanism on Earth, Venus and Mars // *Icarus.* 2010. V. 207. P. 564–577.
- [7] *Amorim D.O., Gudkova T.V.* Internal structure of Venus based on the PREM model // *Solar System Research.* 2023. V. 57. No. 5. P. 414–425.
- [8] *Amorim D.O., Gudkova T.* Constraining Earth's mantle rheology with Love and Shida numbers at the M2 tidal frequency // *Physics of the Earth and Planetary Interiors.* 2024. V. 347. Article 107144.
- [9] *Saito M.* Some problems of static deformation of the Earth // *J. Physics of the Earth.* 1974. V. 22(1). P. 123–140.
- [10] *Dumoulin C., Tobie G., Verhoeven O., Rambaux N.* Tidal constraints on the interior of Venus // *J. Geophysical Research: Planets.* 2017. V. 122(6). P. 1338–1352.

ON THE CHANDLER WOBBLE OF VENUS

D. O. Amorim¹, T. V. Gudkova²

¹ *Moscow Institute of Physics and Technology, Moscow, Russia*
amorim.dargilan@gmail.com

² *Schmidt Institute of Physics of the Earth RAS, Moscow, Russia*
gudkova@ifz.ru

KEYWORDS:

Venus, planetary interiors, Love numbers, Chandler Wobble period

INTRODUCTION:

A study of the Chandler Wobble of Venus was carried out based on Earth-like models of the planet. Predictive estimates of the period of the Chandler Wobble of Venus have been obtained. For the most plausible models of the internal structure of Venus with a core radius in the range of 3288 ± 167 km, the period of the Chandler wobble is 30–48 thousand years. The large error in the results is mainly due to the large scatter of possible values of the precession constant of Venus.

OBSERVATIONAL DATA AND INTERIOR STRUCTURE MODELS:

The internal structure models of Venus are based on the observed values of the moment of inertia and tidal Love number k_2 [1, 2]. In [3] it was found that the core radius of Venus R_c is more likely to be in interval 3288 ± 167 km. Here we calculate the period of the Chandler oscillation TCW of Venus for models with a core radius $R_c = 3100$ – 3500 km. The models also differ in parameter B , which expresses the deviation of the density in the Venusian core from the density of the Earth's core. As in [4], the parameter B varies in the range 0.98–1.02. For each combination of values of R_c and B , the model value of the mean moment of inertia I is calculated. To calculate the Chandler period TCW it is also necessary to know the precession constant.

The figure of Venus is much closer to a sphere compared to the figure of the Earth. The equatorial and polar radii of Venus differ by less than 100 m [5], while on Earth they differ by more than 20 km. This means that the difference $C - \bar{A}$, and, accordingly, the precession constant of Venus will be much less than for the Earth.

Venus's precession constant has not yet been measured. Nevertheless, there are estimated values obtained from various considerations [5–7]. All estimates lie in the range from $1.3 \cdot 10^{-5}$ to $1.9 \cdot 10^{-5}$, which is approximately 200 times less than the constant precession of the Earth. From equation (3) in [8] it is clear that this should lead to a noticeable increase in the period of the Chandler Wobble. In addition, Venus's rotation period is 243 days, which also leads to an increase in TCW.

Note that the available estimates of the precession constant of Venus differ by more than 30 %, while for the Earth H_{\min} and H_{\max} differ by only 1 %. It will be shown below that the uncertainty in the precession constant of Venus is the main source of error in estimates of the period of its Chandler oscillation TCW.

RESULTS:

The secular Love number K_0 is proportional to the square of the planet's rotation period and the difference (see equation (4) in [8]). The value $C - \bar{A}$, in turn, is proportional to the precession constant. As a result we get

$$K_0 \sim t^2 H. \quad (1)$$

The mass, radius and moment of inertia of Venus and Earth differ by only a few percent, but the rotation period of Venus is 243 times greater than the rotation period of the Earth, and the precession constant is about 200 times less. Consequently, the secular Love number of Venus is more than 200 times higher than the secular Love number of Earth.

The quantity L_2 (see equation (6) in [8]) depends on the ratio of the Love number k_2 to the secular Love number K_0 . The Love number k_2 of the Earth at the period of the Chandler wobble is approximately 0.35 [8, 9]. The sec-

ular K_0 number of the Earth is in the range from 0.945 to 0.955 (depending on the value of the constant precession H). Consequently, the Earth's k_2/K_0 ratio is slightly less than 0.4, and the L_2 value provides a correction to TCW of the order of 60 %.

As will be shown below, the tidal Love number k_2 of Venus during the Chandler Oscillation period is approximately 0.9. The secular Love number K_0 of Venus, in turn, exceeds 200 (due to the very long rotation period of the planet). This means that the difference between the Chandler Wobble period TCW, determined by formula (5) in [8], and the T_1 value is less than 0.5 %. For this reason, any variation in viscosity and rheological model ultimately leads to minor changes in the TCW value. Therefore, the calculation of the period of the Chandler wobble of Venus is carried out with a fixed viscosity profile and one rheological parameter α . For all models of Venus, the calculation of k_2 uses the low viscosity profile from [4] and the Andrade rheology with $\alpha = 0.1$ and $\zeta = 1$.

The obtained results of determining the TCW of Venus are shown in Figure 1. For each value of the core radius, the values of the precession constant and the parameter B are varied, we have an interval of possible TCW values. The forecast period of the Chandler wobble TCW of Venus is approximately 30–48 thousand years.

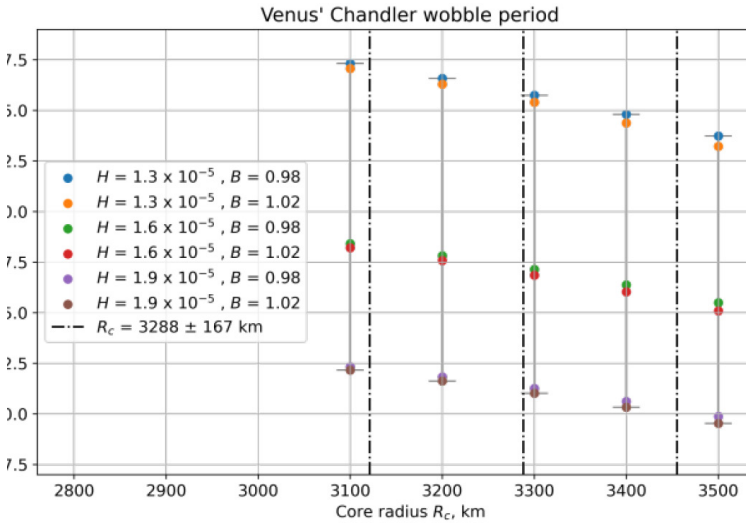


Fig. 1. Model values of the period of the Chandler wobble of Venus TCW for different combinations of the core radius R_c , constant precession H and parameter B . The dashed lines highlight the interval of the most probable models of the internal structure of Venus according to [4]

Varying the constant precession H leads to a change in TCW by tens of percent, and varying the core radius R_c and parameter B by several percent. Variation of viscosity and rheology leads to a negligible change in the TCW value, and with the given accuracy of determining the constant precession constant H , it makes no sense to take this into account.

The model values of k_2 for Venus at the period of the Chandler Wobble TCW are in the range from 0.82 to 0.95. The calculation of k_2 was performed using the algorithm proposed in [4]. A change in viscosity could lead to a noticeable change in k_2 , but due to the large value of K_0 of Venus, this would have no effect on the period of the Chandler Wobble TCW.

CONCLUSION:

To calculate the TCW of Venus, models of the internal structure from [3] were used. The prognostic value of the period of the Chandler Wobble of Venus is in the range from 30 to 48 thousand years. The huge error is primarily due to the large scatter in theoretical estimates of the precession constant of Venus.

The period of the Chandler wobble was recently measured for Mars [10]. If the VERITAS and EnVision missions [11, 12] can measure the period of the Chandler Wobble of Venus, then the TCW value will provide an additional constraint on models of the internal structure

ACKNOWLEDGMENTS:

The study was performed based on funding of Russian Scientific Foundation No. 23-22-00074, <https://rscf.ru/project/23-22-00074/>.

REFERENCES:

- [1] *Konopliv A. S., Yoder C. F.* Venusian k_2 tidal Love number from Magellan and PRO tracking data // *Geophysical Research Letters*. 1996. V. 23(14). P. 1857–1860.
- [2] *Margot J.-L., Campbell D. B., Giorgini J. D., Jao J. S., Snedeker L. G., Ghigo F. D., Bonsor A.* Spin state and moment of inertia of Venus // *Nature Astronomy*. 2021. V. 5(7). P. 676–683.
- [3] *Amorim D. O., Gudkova T. V.* Internal structure of Venus based on the PREM model // *Solar System Research*. 2023. V. 57. No. 5. P. 414–425.
- [4] *Amorim D. O., Gudkova T.* Constraining Earth's mantle rheology with Love and Shida numbers at the M2 tidal frequency // *Physics of the Earth and Planetary Interiors*. 2024. V. 347. Article 107144.
- [5] *Zharkov V. N., Gudkova T. V.* Onparameters of the Earth-like model of Venus // *Sol. Syst. Res.* 2019. V.53. № 1. P. 1–4.
- [6] *Shen M., Zhang C. Z.* The dynamical flattenings of Mercury and Venus // *Earth, Moon, and Planets*. 1988. V. 41. P. 289–294.
- [7] *Cottereau L., Souchay J.* Rotation of rigid Venus: a complete precession-nutation model // *Astronomy and Astrophysics*. 2009. V. 507. P. 1635–1648.
- [8] *Amorim D. O., Gudkova T. V.* The validation of the method for calculating the Chandler Wobble of Venus: Abstr. // 15th Solar System Research symp. 2024.
- [9] *Chen W., Chen Y., Ray J., Luo J., Cheng L. J.* Free decay and excitation of the Chandler wobble: Self-consistent estimates of the period and quality factor // *J. Geodesy*. 2023. V. 97. Article 36.
- [10] *Konopliv A. S., Park R. S., Rivoldini A., Baland R. M., Le Maistre S., Van Hoolst T., Yseboodt M., Dehant V.* Detection of the Chandler wobble of Mars from orbiting spacecraft // *Geophysical Research Letters*. 2020. V. 47. Article e2020GL090568.
- [11] *Cascioli G., Hensley S., De Marchi F., Breuer D., Durante D., Racioppa P., Iess L., Mazarico E., Smrekar S. E.* The determination of the rotational state and interior structure of Venus with VERITAS // *Planetary Science J.* 2021. V. 2. P. 220–231.
- [12] *Rosenblatt P., Dumoulin C., Marty J.-C. Genova A.* Determination of Venus' interior structure with EnVision // *Remote Sensing*. 2021. V. 13. Article 1624.

THE VALIDATION OF THE METHOD FOR CALCULATING THE CHANDLER WOBBLE OF VENUS

D. O. Amorim¹, T. V. Gudkova²

¹ *Moscow Institute of Physics and Technology, Moscow, Russia*
amorim.dargilan@gmail.com

² *Schmidt Institute of Physics of the Earth RAS, Moscow, Russia*
gudkova@ifz.ru

KEYWORDS:

Earth, Venus, planetary interiors, Love numbers, Chandler Wobble period

INTRODUCTION:

The method for calculating the period of the Chandler Wobble for Venus has been developed and tested on Earth. To take into account the inelasticity of the planet's interior, Andrade rheology is used, and the parameters of the rheological model are determined, which can explain the observed period of the Chandler Wobble of the Earth.

METHOD:

The calculation of the Chandler Wobble period TCW is based on the approach from [1]. Let us denote by A, B and C the dimensionless principal moments of inertia of a planet. Then we can introduce a value equal to half the sum of the main equatorial moments of inertia A and B,

$$\bar{A} = (A + B)/2. \quad (1)$$

From the theory of free rotation of a rigid body it is known [2] that an axisymmetric body with a rotation period t has its own free nutation period T_0 , determined by the formula

$$T_0 = t \left(\frac{C - \bar{A}}{\bar{A}} \right)^{-1}, \quad (2)$$

The first correction can be introduced into formula (2), related to the presence of a liquid core, then the period of free nutation of a planet with a liquid core is equal to

$$T_1 = t \left(\frac{C - \bar{A}}{\bar{A} - \bar{A}_l} \right)^{-1}, \quad (3)$$

where \bar{A}_l is an analogue of the quantity \bar{A} , but related to the liquid core.

Let us introduce the secular Love number K_0 , which corresponds to the model of an entirely liquid planet with the same distributions of density and bulk moduli as for a real planet [3]:

$$K_0 = \frac{3GM}{R^3} \left(\frac{t}{2\pi} \right)^2 (C - \bar{A}). \quad (4)$$

For a real planet with an elastic shell and a liquid core, the period of the Chandler Wobble TCW can be written with sufficient accuracy as [1, 3]

$$T_{CW} = T_1 \left(1 - \frac{k_2}{K_0} \right)^{-1}. \quad (5)$$

Let us introduce the notations

$$L_1 = \left(\frac{C - \bar{A}}{\bar{A} - \bar{A}_l} \right)^{-1}, \quad L_2 = \left(1 - \frac{k_2}{K_0} \right)^{-1}. \quad (6)$$

Then the period of the Chandler Wobble TCW can be written as

$$T_{CW} = tL_1L_2. \quad (7)$$

When calculating Love numbers, spherically symmetrical planetary models are usually used. The method for calculating Love numbers is described in detail in [4, 5]. The moment of inertia of a spherical model of the planet is defined as $I = (A + B + C)/3$, and it is calculated for interior structure models

of the Earth and Venus. To calculate the Chandler period TCW, we need to know the moments C and \bar{A} . They can be expressed in terms of the quantity I using the precession constant $H = (C - A)/C$:

$$C = I \frac{3}{3 - 2H}, \quad \bar{A} = C(1 - H). \quad (8)$$

Thus, from the spherical models of the planet and knowing the precession constant, we can calculate L_1 and K_0 . To find TCW, all that remains is to determine the tidal Love number k_2 .

Algorithms for calculating k_2 for Earth and Venus are described in detail in [5]. The main problem is that the Love number k_2 is a complex function that depends on the tidal frequency. Thus, equation (7) is actually an implicit equation with an unknown TCW:

$$T_{CW} - tL_1L_2(T_{CW}) = 0. \quad (9)$$

It is necessary to find the TCW value at which equation (9) is satisfied. We use the Newton method from the Scipy library [6], and use the value of T_1 as an initial approximation.

THE VALIDATION OF NUMERICAL METHOD:

As a model of the Earth, we use an adaptation of the PREM model from [5], for which the moment of inertia I is 0.330705. Estimates of the constant precession of the Earth are in the range from $H_{\min} = 0.00326073$ to $H_{\max} = 0.00329587$ [7].

The zero approximation of the Chandler period according to formula (2) (Eulerian period) for Earth models is $T_0 = 302.4 - 305.7$ days, and the period taking into account the liquid core according to formula (3) $T_1 = 268.2 - 271.1$ days. Accounting for the elasticity of the interior according to equation (9) depends on the tidal Love number k_2 , which, in turn, depends on the distribution of viscosity in the Earth's interior and on the values of the Andrade rheology parameters α and ζ (see, for example, [5]).

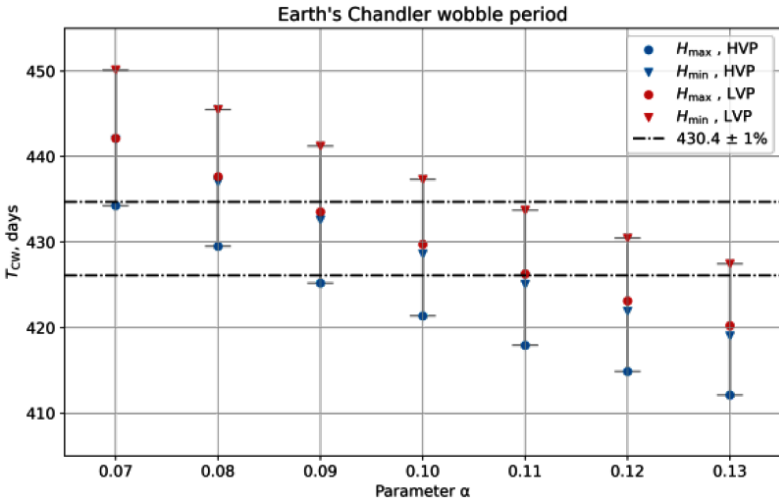


Fig. 1. Comparison of model values of the Earth's TCW Chandler Wobble period with the observed value from [8]

In this work, when calculating the Love number k_2 , we use the same viscosity profiles as in [5]. HVP denotes the high viscosity profile (crust -10^{24} , upper mantle -10^{21} , transition zone -10^{22} , lower mantle -10^{23} , inner core -10^{22} Pa-s), and LVP denotes the low viscosity profile (crust -10^{21} , upper mantle -10^{19} , transition zone -10^{21} , lower mantle -10^{22} , inner core -10^{14} Pa-s). For simplicity, the value of the parameter ζ is taken equal to one, and the parameter α is varied.

The observed period of the Earth's Chandler wobble is 430.4 days [8]. Here we will use period values in the range of $430.4 \pm 1\%$. The results of calcu-

lating the period of the Chandler Wobble TCW according to equation (9) for two values of precession constant (H_{\min} and H_{\max}), two viscosity profiles (LVP and HVP) and a set of values of the parameter α are shown in Figure 1. For each value of α from the interval 0.07–0.13, a certain range of model TCW values is obtained due to the uncertainty of the precession constant and viscosity profile. The spread of model TCW values is greater than the width of the used permissible interval $430.4 \pm 1\%$. Note that models with $\alpha = 0.09$ – 0.11 give Chandler period TCW values closest to the observed value from [8]. The calculation method outlined above makes it possible to estimate the Earth's TCW with good accuracy (2–3%), which is sufficient for preliminary models of Venus.

The tidal Love number k_2 of the Earth were calculated on the period of the Chandler Wobble TCW for each of the considered combinations of the viscosity profile and the value of H . In [8] the Love number k_2 was obtained based on observations of the Chandler Wobble of the Earth: $k_2 = 0.35011 - 0.00226i$. Comparison of our model values with this estimate (within $\pm 1\%$) allows us to conclude that models with $\alpha = 0.1$ – 0.12 can explain the observed value of k_2 .

CONCLUSION:

This study proposes a scheme for calculating the period of the Chandler Wobble based on [1]. Comparison of the obtained model values with the observed value of TCW from [8] allowed us to confirm that the method is correct (with an accuracy of 2–3%).

ACKNOWLEDGMENTS:

The work was carried out with budget funding from the Schmidt Institute of Physics of the Earth of the Russian Academy of Sciences.

REFERENCES:

- [1] Zharkov V.N., Molodensky S.M. On the Chandler wobble of Mars // Planet and Space Sci. 1996. V. 44. P. 1457–1462.
- [2] Landau L.D., Lifshitz E.M. Mechanics. Elsevier, 1982. 224 c.
- [3] Molodensky M.S. The theory of nutation and diurnal Earth tides // Comm. Obs. Roy. Belgique. 1961. V. 188. S. Geophys. No. 58. P. 25–56.
- [4] Amorim D.O., Gudkova T.V. Internal structure of Venus based on the PREM model // Sol. Syst. Res. 2023. V. 57. No. 5. P. 414–425.
- [5] Amorim D.O., Gudkova T. Constraining Earth's mantle rheology with Love and Shida numbers at the M2 tidal frequency // Phys. Earth and Planet. Interiors. 2024. V. 347. Article 107144.
- [6] Virtanen P., Gommers R., Oliphant T.E. et al. SciPy 1.0: Fundamental algorithms for scientific computing in Python // Nature Methods. 2020. V. 17. P. 261–272.
- [7] Liu C., Huang C., Zhang M. The principal moments of inertia calculated with the hydrostatic equilibrium figure of the Earth // Geodesy and Geodyn. 2017. V. 8. P. 201–205.
- [8] Chen W., Chen Y., Ray J. et al. Free decay and excitation of the Chandler wobble: Self-consistent estimates of the period and quality factor // J. Geodesy. 2023. V. 97. Article 36.

**SESSION 3. GIANT PLANETS (GP)
ORAL SESSION**

ALFVEN WINGS IN THE SUB-ALFVENIC FLOW OF MAGNETIZED PLASMA FORMED OUTSIDE THE MAGNETOSPHERE OF A CELESTIAL BODY, AND THE POSSIBLE GENERATION OF AURORAS IN THE ATMOSPHERE OF THE CENTRAL BODY AND IN THE ATMOSPHERE OF THE SATELLITE

I. I. Alexeev¹, A. S. Lavrukhin¹, D. V. Nevsky^{1,2}

¹ Skobeltsyn Institute of Nuclear Physics Lomonosov Moscow State University Moscow, Russia, lavrukhin@physics.msu.ru

² Lomonosov Moscow State University, Faculty of Physics, Moscow, Russia iialexeev@mail.ru

KEYWORDS:

Jupiter, Alfven wings, Ganymede, Exoplanet

ABSTRACT:

An interaction of tidal locked (Galilean) moons of Jupiter with the Jovian magnetospheric plasma flowing past them is considered. The magnetospheric plasma driven by Jupiter magnetic field into solid corotation with the planet till the Ganymede's orbit distance. In this case, there are a violation of frozen-in condition at "slipping contacts", which are formed in the region where the open field line bundle touched the planet atmosphere of the central body and the moon's atmosphere (or the moon exosphere). Outside these regions due to the high conductivity of collisionless magnetospheric plasma the field aligned electric field is small, and plasma corotate with the Jupiter. However, perturbations moving along the Jupiter disk are tied on the ionospheric "spot" of the moon. Each moon orbit around the planet at its own Keplerian velocity. A moon spot is a cross section of the open field line bundle which connecting the Jupiter's conductive ionosphere with the moon's body. The disturbance occurring in the magnetosphere is formed by field aligned currents forming the so-called Alfven wings between the moon and the planet. For Ganymede, which has its own magnetic field and apparently a conducting core that "captures" the penetrating magnetospheric field, a second slipping contact occurs already when charged ions collide with neutrals of the Ganymede exosphere. We discuss the mechanisms of generation of accelerated electron beams by the field aligned electric potential drop and, as a result, the atmosphere UV emission have been observed. The corresponding "auroras" are directly fixed by both the Hubble images and in the images obtained by the UV cameras of the Juno spacecraft operating in the Jupiter system and flying by the Ganymede at a relatively short distance.

THE STUDY OF THE ROLE OF METASTABLE NITROGEN IN COLLISIONAL MOLECULAR PROCESSES OF THE UPPER AND MIDDLE ATMOSPHERE OF TITAN

A. S. Kirillov

Polar Geophysical Institute, Apatity, Murmansk region, Russia, kirillov@pgia.ru

KEYWORDS:

Titan, upper and middle atmosphere, metastable nitrogen, cosmic rays, solar UV photons, radicals

ABSTRACT:

Molecular nitrogen N_2 is the main molecular gas in the atmospheres of Titan (a moon of Saturn), Triton (a moon of Neptune) and Pluto. The second gas in total concentration in the atmospheres of the planets is methane CH_4 . We study the kinetics of the triplet $A^3\Sigma_u^+$, $B^3\Pi_g$, $W^3\Delta_u$, $B^3\Sigma_u^-$, $C^3\Pi_u$ states of molecular nitrogen at altitudes of the upper (700–1200 km) and middle (50–250 km) atmosphere of Titan during the precipitation of solar UV photons and galactic cosmic rays into the atmosphere. The calculations take into account intramolecular and intermolecular electron energy transfer during inelastic collisions of electronically excited molecular nitrogen with N_2 , CH_4 and CO molecules. The interaction constants of electronically excited molecular $N_2(A^3\Sigma_u^+)$ with N_2 and CO molecules are calculated according to quantum chemical approximations and show good agreement with the available experimental data. It is shown that there is a significant contribution of electronically excited N_2 in the excitation of CO($a^3\Pi$) at the altitudes of 700–1200 km of the Titan's upper atmosphere. The interaction of electronically excited N_2 molecules with molecules of methane CH_4 , acetylene C_2H_2 , ethylene C_2H_4 , ethane C_2H_6 in the Titan's middle atmosphere at altitudes of 50–250 km was studied. The dominance of reactions with metastable molecular nitrogen $N_2(A^3\Sigma_u^+)$ in the formation of C_xH_y radicals at these altitudes was shown for the first time.

CHANGES IN THE LONGITUDE POLARIZATION DEPENDENCE OF JUPITER'S MOON IO AS EVIDENCE OF THE LONG-TERM VARIABILITY OF ITS VOLCANIC ACTIVITY

N. N. Kiselev^{1,2}, H. G. Dyachenko³, N. V. Karpov², K. A. Antoniuk¹

¹ *Crimean Astrophysical Observatory, Nauchnij, Russia, kiselevnn42@gmail.com*

² *Institute of Astronomy RAS, Moscow, Russia*

³ *Junior Academy of Sciences "Explorer", Simferopol, Russia*

KEYWORDS:

polarimetry, longitude and phase polarization dependences, variations in activity volcanism on Io

ABSTRACT:

New polarization measurements of Jupiter's moon Io in the *UBVRI* bands were obtained at phase angles between 10 and 12° with the polarimeters, mounted on the 2.6 m Shajn reflector of the Crimean Astrophysical Observatory and the 2 m Ritchey – Chrétien – Coudé telescope of the Peak Terskol Observatory in August 2023 – February 2024. Using new data and published data [1] in the same range of phase angles, the longitude (orbital) polarization dependences $P(L)$ of the satellite, independent on the polarization phase curves, were constructed. The amplitude of $P(L)$ in the V-band does not exceed 0.1 %, it is deepest ≈ -0.17 % at $L \approx 270^\circ$ (the trailing side), and shallowest ≈ -0.12 % near $L \approx 130^\circ$. This reflects minor local changes in Io's surface properties with longitude. This differs markedly from the parameters of the longitude dependence for Io obtained by [2], which find that orbital polarization variations of 0.4 to 0.5 % for $\alpha > 10^\circ$ and negative branch is deepest near $L = 160^\circ$, and shallowest near $L = 300^\circ$. This may be a consequence of changes in the reflective properties of local areas of Io's surface as a result of long-term changes in Io's local or global volcanic activity.

REFERENCES:

- [1] *Kiselev N. N., Rosenbush V. K., Leppälä A. et al. New Polarimetric Data for the Galilean Satellites: Io and Ganymede Observations and Modeling // The Planetary Science J. 2024. V. 5(10). 16 p.*
- [2] *Zellner B., Gradie J. // Veverka J. Planetary Satellites / ed. Burns J. A. Tucson, Arizona: Univer. Arizona Press, 1977. Ch. 10.*

THE FLIGHT TO NEPTUNE AND ITS MOONS TRITON AND NEREID AS A DEMONSTRATION OF THE POSSIBILITY OF USING LOW-THRUST ENGINES IN MISSIONS TO GIANT PLANETS

N. A. Simbirev¹, A. A. Sukhanov¹, O. L. Starinova²

¹ *Space Research Institute RAS, Moscow, Russia*
nikita.simbiryov@yandex.ru, sasha.su2@hotmail.com

² *Samara National Research University, Samara, Russia, solleo@mail.ru*

KEYWORDS:

Triton, Nereid, Neptune, low-thrust engines, gravitational maneuvers

ABSTRACT:

The paper suggests a possible scenario of a flight to Neptune's moons Triton and Nereid. At the moment, Triton and Nereid remain among the least studied moons in Solar system. A detailed study of Triton can confirm a number of theories about its origin. As it is assumed that Triton is a captured object that originally formed as an independent ice dwarf in the outer Solar system. The study of Nereid, the third largest satellite of Neptune with the greatest eccentricity among all known moons, will help to better understand the evolution of the Neptune moon system and confirm or refute the hypothesis that Triton was captured by Neptune's gravity and seriously destroyed the original system of its moons. A significant problem in the study of giant planets and their satellites is the lack of effective space transport systems that allow delivering a large payload over such long distances. One of the most promising solutions to this problem is the use of propulsion systems with low thrust, ensuring the implementation of the flight with minimal expenditure of the working fluid. However, the necessity to use a powerful power plant as part of a spacecraft (compared to a high-thrust propulsion system), as well as the long flight duration, limit the scope of use of electric propulsion systems. The rare convergence of Neptune and Jupiter, which will occur in the early 2030 s, will make possible a gravitational maneuver around Jupiter on the way to Neptune, thereby significantly reducing the flight time and the necessary amount of propellant. The scenario allows a spacecraft with low-thrust engines to reach Neptune by performing two gravitational maneuvers near Earth and one gravitational maneuver near Jupiter. The flyby of Triton and Nereid is carried out within the framework of one mission and make possible to explore the surface of both moons from a distance of 10 thousand km. The achievement of this task is carried out by using a modern ion propulsion system with a specific impulse of 3500 s and a thrust of 0.15°N. It is shown that with an initial mass of 850 kg and a mission duration of 29 years, the total cost of the propellant will not exceed 350 kg.

REFERENCES:

- [1] *Sukhanov A. A. Astrodynamics. M.: IKI RAS, 2010. 202 p.*
- [2] *Ivashkin V. V., Petukhov V. G. Trajectories of a low-thrust flight between the orbits of the Earth and the Moon during the Collecting of the capture orbit by the Moon // Preprints of IPM named after M. V. Keldysh. 2008. 32 p.*
- [3] *Leb H. V., Mogulkin A. I., Obukhov V. A. et al. Analysis of a reusable lunar transport vehicle using a nuclear power plant. M.: Nauka, 2021. 25 p.*
- [4] *Ellis D. Miner T. Encyclopædia Britannica: electronic version. 2016. <https://www.britannica.com/place/Triton-astronomy>.*

CALCULATION OF THE POSITION OF THE BEGINNING POINT OF THE GALACTIC YEAR IN THE ORBIT OF THE SOLAR SYSTEM IN THE GALAXY

A.V. Golovkov¹, I.Yu. Ilyina²

¹ The Center for World-System Research, Irkutsk, Russia, sibia@yandex.ru

² Research and Production Corporation 'Space Monitoring Systems, Information and Control and Electromechanical Complexes' named after A. G. Iosifian, Moscow, Russia

KEYWORDS:

Galactic year, galactic orbit, solar system, tectonic magmatic cycle

INTRODUCTION:

In the works of O. G. Sorokhtin [3] and A. S. Monin [2], 20 tectonic magmatic cycles were identified reflecting the natural periodization of the Earth's development from the Eoarchean to the present. The currently incomplete Alpine tectonomagmatic cycle began 93 million years ago. In the work of the classic of geological science V. E. Khain [4], a hypothesis was presented with the assumption that tectonomagmatic cycles reflect the time periods of the Solar System's revolution around the center of the Galaxy. If this is indeed the case, then we have the opportunity to calculate the position of the starting point of the current galactic year in the orbit of the Solar system in the Galaxy.

RESULTS:

To calculate, we use the duration of the galactic year of 230 million years (<https://bigenc.ru/c/galakticheskii-god-4bca85>), the location of the Solar System in orbit around the center of the Galaxy indicated on the map at the link (https://commons.wikimedia.org/wiki/File:Milky_Way_Arms_ssc2008-10.svg) and the time of 93 million years spent on the passage of the Solar System part of the orbit from the beginning of the galactic year to the present position. Further, 360° of the full conditionally closed orbit of the Sun are divided into 230 parts of the full galactic year (the duration of each part is 1 million years). As a result, for every million years of the galactic year, there are 1.5652° of the galactic orbit of the Sun. We multiply this result by 93 parts of the galactic year traveled by the Sun from the beginning of the galactic year to its present position in galactic orbit in 93 million years. We get 145.6 degrees, which we postpone from the present position of the Sun to reverse its movement. As a result, we find the starting point of the current galactic year of the Alpine tectonomagmatic cycle in the galactic orbit of the Sun. We connect this point with the center of the Galaxy, we get a ray coming from the center of the Galaxy. Its direction coincides with the direction of the long axis of the ellipse formed by the projection of the Galaxy's bridge on the plane of the galactic disk.

DISCUSSION AND CONCLUSIONS:

Along this direction [5], a large-scale collimated energy flow spreads from the center of the Galaxy (from the supermassive black hole Sagittarius A*) into its outer space. Every new galactic year in the Earth's past began when this ray crossed the galactic orbit of the Solar System. At the same time, there was an increase in endogenous activity on Earth — a new tectonomagmatic cycle was beginning. Variations in the duration of tectonomagmatic cycles in the history of the Earth from 100 to 490 million years. years indicate that in the history of the Solar System there have been changes in the duration of galactic years associated with changes in the distance from the center of the Galaxy to the orbit of the Solar System [1].

REFERENCES:

[1] Golovkov A. V., Smirnov F. A. Tectonomagmatic cycles in the natural resource turnover of the Earth, the Solar system and the Galaxy. Nature-like technolo-

- gies on the way to a space technological order. Book I. Moscow: Akademika, 2022. 400 p.
- [2] *Monin A. S.* The History of the Earth. Leningrad: Nauka, 1977. 228 p.
 - [3] *Sorokhtin O. G.* Differentiation of the Earth's matter and the development of tectonic processes // *Izv. USSR Academy of Sciences. Physics of the Earth.* 1972. No. 7. P. 55–67.
 - [4] *Khain V. E.* General geotectonics. 2nd ed., reprint. and add. Moscow: Nedra, 1973. 511 p.
 - [5] *Yousef-Zade F., Wardle M., Kunneriath D. et al.* ALMA Detektion of Bipolar Outflows: Evidence for Low-mass Star Formation within 1 pc of Sgr A* // *Astrophysical J. Letters.* 2017. V. 850(2). Iss. L30. <https://doi.org/10.3847/2041-8213/aa96a2>.

NON-STATIONARY 3D PERTURBATION THEORY FOR DESCRIBING NONLINEAR INTERACTION OF ELECTRIC FIELD WITH MATTER IN PLASMA WITH CURRENT. VYSIKAYLO'S ELECTRIC FIELD SHOCK WAVES AND PLASMA NOZZLES

P. I. Vysikaylo

Independent researcher, Moscow, Russia, filvys@yandex.ru

KEYWORDS:

ambipolar diffusion; ambipolar drift; perturbation theory; violation of electrical neutrality; electric field shock waves; Vysikaylo's plasma nozzles

INTRODUCTION:

Electrical phenomena occur on all planets of the Solar System (Figure 1), in the heliosphere (since the Sun has a positive charge of 1400 C [1]), in the Earth's atmosphere (Figure 1b, it is charged up to 500,000 C) and even between galaxies (Figure 1c). In [1] the reasons for the occurrence of weak solar wind are explained and all its parameters from the charge of the Sun are determined. These phenomena are studied in laboratories around the world. I have theoretically predicted shock waves of the electric field and self-forming plasma nozzles (Figure 2) and discovered L_1 points (Figure 1b), lines and planes of cumulation of plasma ambipolar flows in non-uniform plasma with current.

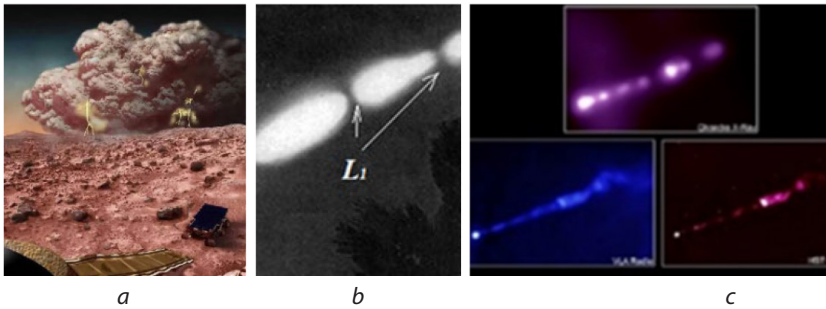


Fig. 1. Electrical phenomena: *a* — electrical dust storms on Mars; *b* — bead lightning in the Earth's atmosphere, L_1 Vysikaylo-Euler's cumulation points; *c* — the central region of the M 87 galaxy with an active nucleus. Jet size ~ 1.5 kpc. We observe jet stratification and formation of cumulation regions. Hubble Telescope (NASA)

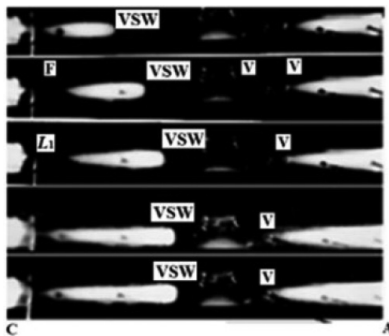


Fig. 2. This is photographic evidence of the formation of Vysikaylo's shock waves — VSW and Vysikaylo's plasma nozzles — V (in plasma with current). $U = 40$ m/s (from A to C), $J_0 = 3 \mu\text{A}/\text{cm}^2$, Density/varies from 0.33 to 1.52 mA/cm². F — Faraday dark space. L_1 is Vysikaylo's cumulation point between positively charged luminous plasma structures (cathode spot and positive column)

PERTURBATION THEORY:

The model of the processes of transport of charged plasma particles without a magnetic field includes the equations for the balance of the number of ions:

$$\frac{\partial n_\alpha}{\partial t} + \text{div}(n_\alpha \mathbf{V}_\alpha) = I_\alpha - R_\alpha, \quad (1)$$

where n_α is the concentration of positive or negative ions; $\mathbf{V}_\alpha = \mu_\alpha \mathbf{E}$ is the ion drift velocity, which is a function of the control parameter E/N , I_α ; R_α — sources and sinks of ions. To equation (1) it is necessary to add electrodynamic equations:

$$\text{rot} \mathbf{E} = 0; \quad (2)$$

$$\text{div} \mathbf{E} = 4\pi\rho, \quad (3)$$

where $\rho = e \left(\sum_{\alpha=1}^m z_\alpha n_\alpha - n_e \right)$; z_α is the ion charge, m is the number of different

types of ions. Instead of the electron balance equation (as in the case of ions), we will take into account the total current density. To do this, we add the balance equations for electrons and all kinds of ions (multiplying them by the corresponding charge) and take into account that charged particles of different signs in the volume are born and die simultaneously, using (3), we get:

$$\nabla \mathbf{j} = 0, \quad (4)$$

where $\mathbf{j}/e = (\partial \mathbf{E}/\partial t)/(4\pi e) - n_e \mathbf{V}_e + \sum_{\alpha=1}^m z_\alpha n_\alpha \cdot \mathbf{V}_\alpha + \nabla(D_e n_e) \dots D_e$ is the electron diffusion coefficient (... this is an allowance for ion diffusion).

From (3) — $n_i = n_e + \nabla \mathbf{E}/(4\pi e) - \sum_{\alpha=1}^{m-1} z_\alpha n_\alpha$, we will substitute it in (4). In this case, (4) will take the form [1–4]:

$$\begin{aligned} \mathbf{j}/e = & 1/(4\pi e) \cdot (\partial \mathbf{E}/\partial t) - n_e \mathbf{V}_e + \sum_{\alpha=1}^{m-1} z_\alpha n_\alpha \cdot \mathbf{V}_\alpha + z_i \mathbf{V}_i \left(n_e - \sum_{\alpha=1}^{m-1} z_\alpha n_\alpha \right) + \\ & + \nabla \mathbf{E}/(4\pi e) + \nabla(D_e n_e) \dots, \end{aligned} \quad (5)$$

PERTURBATION THEORY PARAMETERS:

The order of magnitude of terms in (5) with respect to the term with a drift structure is determined by the following values: τ_M/τ , 1 , $(\mu_i/\mu_j)l_E/L$, $l_u/L \dots$ Usually, one can neglect the diffusion of ions, which we will do. Here τ characteristic charge change time, $\tau_M = 1/(4\pi e \mu_j n_e)$ Maxwellian space charge neutralization time, μ_j — effective plasma mobility taking into account the mobility of ions and electrons, $l_{E0} = \mathbf{E}_0/(4\pi n_e)$ vectorized characteristic size of electric field strength change. If the parameters $\Omega \tau_M$, $(\mu_i/\mu_j)l_E/L$ and l_u/L are small, then the system of hydrodynamic equations and the Poisson's equation can be solved using perturbation theory [2–4]. The smallness of the parameter $(\mu_i/\mu_j)l_E/L \ll 1$ can also be observed at $l_{E0}/L \gg 10$, since $\mu_i/\mu_j \approx \mu_i/\mu_e$.

The 4D equation of the balance of positive ions (1) is modified taking into account the violation of electro-neutrality [2–4]:

$$\begin{aligned} \frac{\partial n_e}{\partial t} - \frac{\partial [(I_{E0}/\mu_{e0}) \nabla] (\mu_{e0} n_e)}{\partial t} + (\mathbf{j}/e) \nabla (\mu_{+0}/\mu_{e0}) + \mathbf{U} \nabla n_e - \\ - \nabla (\mathbf{U} (I_{E0}/\mu_{e0}) \nabla (\mu_{e0} n_e)) - \nabla \{ I_{E0} (\mu_{+0} \mathbf{E}_0/\mu_{e0} \nabla) \cdot (\mu_{e0} n_e) \} - \\ - \beta n_e (I_{E0}/\mu_{e0}) \nabla (\mu_{e0} n_e) = I_i - R_{i0}; \quad I_{E0} = E_0/(4\pi n_e). \end{aligned} \quad (6)$$

Here the terms with the **vector** — I_{E0} appeared from the Poisson equation for the electric field strength (\mathbf{E}) $n_e = \nabla \mathbf{E}/(4\pi e) + n_e$ and the conditions for the current density $\nabla \mathbf{j} \nabla (e \mu_e n_e) = 0$; $\beta n_e I_{E0}$ is the speed of the ambipolar recombination flow caused by the violation of electrical neutrality in the plasma with current [4], \mathbf{U} is the gas pumping speed, β is the effective coefficient of ion-electron recombination. I_{E0} — vectorized characteristic

size of the electric field strength inhomogeneity [4] determines the dimensions (**including in orthogonal directions due to space charge**) of the transition regions of stationary and non-stationary inhomogeneous plasma 3D structures. The **second term** with mixed derivatives with respect to time and spatial coordinates has no analogues in hydrodynamics (this term describes the Pekarik's effect [2]) and the sixth term (in the 1D approximation) is similar to diffusion. However, due to the vectorization of the Vysikaylo-Poisson's ambipolar diffusion coefficient, charged 3D plasmoids have a number of geometric features, different from Mach's shock waves. For example, longitudinal and transverse diffusion processes and the corresponding characteristic transition profiles (3D dimensions) are significantly determined by the local component of the electric field and the concentration of electrons (and not ions!) [2–4]. For limited three-dimensional plasma structures, 3D features also appear in this fourth term, leading, in particular, to additional ambipolar diffusion removal of gas-discharge plasma to the walls of the gas-discharge tube (see [3]) in the direction orthogonal to the discharge current. This leads to a local increase in plasma loss on the tube walls, a local increase in the E/N parameter, and a local increase in the glow intensity in the shock wave of the electric field. The third term in (6) describes the ambipolar drift of the plasma, caused by different dependences of the electron and ion mobilities on the parameter E/N . In nitrogen of a special frequency it can reach up to $V_a \approx 70$ m/s and is directed from small to large values of E/N . In nitrogen, it is directed from the Faraday dark space to the anode [2–4].

CONCLUSION:

In our works we theoretically prove that the cumulation (self-focusing) of charged particles in an inhomogeneous plasma (with current) is a universal property of cumulative-dissipative structures with characteristic sizes from 10^{-15} to 10^{26} m [1–5]. Everywhere at these dimensions we observe similar phenomena of the formation of flows of charged particles and pulsation of the electric field, as an additional special component of the plasma.

In gas-discharge plasma, I was the first to prove the presence of a 3D-vector I_{E0} in the **vectorized coefficients of ambipolar diffusion transfer**, and their features were studied in detail theoretically (6) and experimentally (Figure 2). Their presence indicates the possibility of forming processes of ambipolar 3D transfer of plasma profiles and generating both processes of sputtering and cumulation and dynamic surface tension of inhomogeneous plasma 3D structures. The control parameters of these processes are two parameters: E/N и E/n_e [1–4].

In 1985 we were the first to predict and experimentally in 1986–1987 to study photographically and using double probes: 1) plasma glow profiles, 2) expansion of the plasma cross-section in Vysikaylo's shock waves stopped by gas pumping ($U = 50$ m/s, Figure 2) and 3) narrowing of the discharge cross-section in the region of the self-forming Vysikaylo's plasma nozzle, see Figure 2 (an analogue of the Lovel's nozzle).

REFERENCES:

- [1] Vysikaylo P.I. Quantitative investigation nonequilibrium inhomogeneous plasma of the heliosphere with runaway electrons // IEEE Trans. Plasma Science. 2022. V. 50. No. 4. P. 810–816. DOI: 10.1109/TPS.2022.3160189.
- [2] Vysikaylo P.I. Model of ambipolar processes in cumulative-dissipative self-focusing structures in plasma. Part 1. Perturbation theory for Vysikaylo's Structures in plasma with current // IEEE Trans. Plasma Science. 2023. V. 51. No. 8. P. 2160–2164. DOI: 10.1109/TPS.2023.3296771.
- [3] Vysikaylo P.I. Model of ambipolar processes in cumulative-dissipative self-focusing structures in plasma. Part 2: Classification of ambipolar drifts with current in the zeroth approximation according to the Vysikaylo' perturbation theory // IEEE Trans. Plasma Science. 2024. V. 52. No. 1. P. 30–35. DOI: 10.1109/TPS.2023.3342269.
- [4] Vysikaylo P.I. Model of ambipolar processes in cumulative-dissipative self-focusing structures in plasma. Part 3: Classification of ambipolar diffusions in plasma with current in the first approximation according to the Vysikaylo's perturbation theory // IEEE Trans. Plasma Science. 2024. V. 52. No. 8. P. 1–6. DOI: 10.1109/TPS.2024.3350370.

- [5] *Vysikaylo P.I.* Cumulative quantum mechanics — quantum-size effects for: nano-, angstrom- and femto-technologies // *Nano Carbons*. 2024. V. 2(1). Article 1297. DOI: <https://doi.org/10.59400/n-c.v2i1.1297>.

THE FRONTIERS OF JOVIAN SCIENCES AND PERSPECTIVE ON FUTURE EXPLORATIONS

Z. Yao

*Department of Earth Sciences, University of Hong Kong, Hong Kong, China
yaozh@hku.hk*

KEYWORDS:

Jupiter, space science, planetary exploration, Moon

ABSTRACT:

Jupiter is the largest planet in the solar system, and its complex system of satellites forms a planet system highly coupled with space and geology. Jupiter has the strongest magnetic field in the solar system, creating a vast and powerful space environment that produces auroral radiation hundreds of times stronger than that of Earth. Studying Jupiter's magnetic field helps understand the origin, evolution, and characteristics of planetary magnetic fields in the solar system. Since entering Jupiter's orbit in 2016, the Juno spacecraft has been exploring the Jupiter environment including the moons. In 2023, the European Space Agency's Jupiter Icy Moons Explorer (JUICE) and the upcoming NASA's Europa Clipper will provide important opportunities for exploring the habitability of Jupiter's satellites. China's future deep space exploration plans will also include exploration of the Jupiter system. This presentation will review important discoveries in Jupiter exploration and discuss relevant cutting-edge exploration targets and opportunities.

**SESSION 3. GIANT PLANETS (GP-PS)
POSTER SESSION**

ABSORPTION VARIATIONS IN THE AMMONIA BANDS OF 645 AND 790 NM ALONG THE CENTRAL MERIDIAN OF JUPITER IN 2023

V. D. Vdovichenko, P. G. Lysenko, V. A. Filippov, A. M. Karimov
Fesenkov Astrophysical Institute, Almaty, Kazakhstan, vdv1942@mail.ru

KEYWORDS:

Jupiter, troposphere, clouds, methane, ammonia

INTRODUCTION:

The formation of absorption bands of methane and ammonia does not occur in the same way precisely because ammonia condenses, forming clouds at atmospheric level below the tropopause, and at high altitudes its content drops sharply.

In addition, it participates in the formation of a deeper layer of ammonium hydrosulfide NH_4SH , and can also enter the aqueous ammonia cloud layer located even lower. Consequently, the formation of ammonia absorption bands observed in the visible and near-infrared spectral regions occurs inside a multi-tiered cloud layer during multiple scattering and in purely gaseous gaps between cloud layers. Therefore, visible variations in the intensity of NH_3 absorption bands can be interpreted as a consequence of changes in the structural characteristics of clouds, as well as the size and concentration of cloud particles. All this should affect the relative amount of gaseous ammonia in different regions of Jupiter.

In 2004, we found a pronounced decrease in the intensity of the NH_3 absorption band with a wavelength of 787 nm [1]. The decrease in absorption in this band begins almost from the equator, and its maximum falls at the planetographic latitude of 10°N , then the absorption increases again, approaching the latitude of 20°N .

The NH_3 absorption band with a wavelength of 645 nm also shows a decrease in the low latitudes of the Northern Hemisphere. In the temperate latitudes of the Northern Hemisphere, the absorption in this band is systematically lower than in the Southern Hemisphere.

In subsequent years, the existence of this decrease was annually confirmed by our spectral observations, although the effect is variable [2–5].

In this article, we continue our research in this direction, especially since the significant depletion of gaseous NH_3 in the low latitudes of the Northern Hemisphere in the NEB (Northern Equatorial Belt) region is confirmed by the results of a study in the microwave range using high-resolution VLA [6].

VARIATIONS OF MERIDIONAL ABSORPTION IN THE AMMONIA BANDS OF 645 AND 790 NM:

The studied ammonia absorption bands of 645 and 790 nm differ in their intensity (Figure 1, left). The band of 645 nm is shallower, consequently, it penetrates deeper, reaching, apparently, the second and third layers of clouds. The 790 nm band is slightly deeper and, unlike the 645 nm band, may not capture the lower cloud layers, but is formed in the uppermost cloud cover and in the purely gaseous gap located under it. Figure 1 on the right shows a comparison of the effective optical paths for the formation of absorption bands of ammonia C_a^* and methane C_m^* in the form of spectral coefficients for ammonia for two ammonia bands of 645 and 790 nm. For clarity, here is an image of the Jupiter on the same date 04.11.2023, taken from the Japanese website ALPO Japan [7].

$C^* = (C_m^* + C_a^*)$ is an equivalent absorption path proportional to the average number of molecules of absorbing gases in the visual beam for methane (C_m^*) and for ammonia (C_a^*) [8].

Comparing the variations of C_a^* in the central core for the studied ammonia absorption bands, it can be noted that in 2023 these variations are most pronounced in the NH_3 645 nm band and slightly weaker in the NH_3 790 nm

band. However, in the 790 nm band, ammonia deficiency is more pronounced in the northern hemisphere near the border of the light equatorial zone (EZ) and the dark Northern Equatorial Belt (NEB).

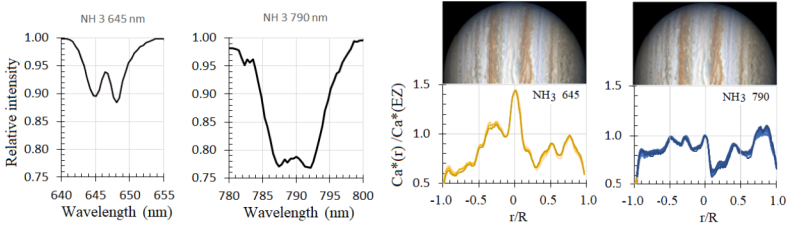


Fig. 1. On the left are the profiles of the ammonia absorption bands 645 and 790 nm. On the right are the variations of C_a^* normalized to the center of the disk for the absorption of ammonia of 645 and 790 nm along the central meridian of Jupiter on 11.03.2023

NH_3/CH_4 ratio

More interesting results are observed from a comparison of absorptions ammonia and methane uptake along the central meridian of Jupiter. For this purpose, the absorption bands of CH_4 and NH_3 , which are similar in position and intensity, were used.

The short-wavelength minimum of the ammonia band of 645 nm, free from the superposition of the methane band, can be compared with the methane band of 705 nm.

The ammonia band of 790 nm can be compared with the short-wave spectrum of the methane band of 790 nm, free from the ammonia band influence.

At the same time, comparing the absorption variations of ammonia and methane across the Jupiter disk, it is necessary to take into account five points:

- methane in the Jupiter's atmosphere does not condense and, consequently, must be evenly mixed;
- we selected pairs of absorption bands of ammonia and methane that are similar in wavelength and intensity;
- the intensities of the absorption bands are quite small, and the influence from a cloudless pure gas atmosphere for both methane and, moreover, for ammonia can be neglected;
- in this regard, the conditions for the formation of these absorption bands in both gases in the scattering-absorbing atmosphere of Jupiter should be identical or close to it.
- therefore, all variations in the course of ammonia uptake to methane should be attributed to ammonia.

Figure 2 on the left shows such a comparison of C_a^* in the center of the shortwave minimum of the ammonia absorption band of 645 nm and C_m^* in the center of the methane absorption band of 705 nm. A similar comparison was made for the ammonia absorption band of 790 nm and the shortwave minimum of the methane band of 790 nm (Figure 2, right).

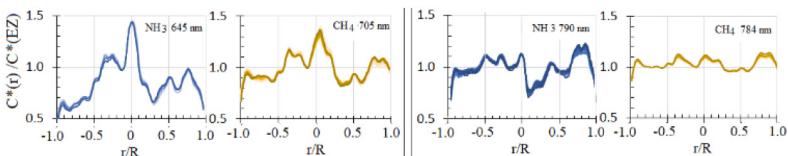


Fig. 2. On the left is a comparison of the meridional course of C_a^* in the shortwave minimum of the ammonia absorption band of 645 nm and C_m^* in the core of the methane absorption band of 705 nm. On the right is a comparison of the meridional course of C_a^* in the core of the ammonia absorption band of 790 nm and C_m^* in the shortwave minimum of the methane absorption band at 784 nm

Figure 3 shows variations in the meridional course ammonia absorption in two wavelengths with respect to methane and among themselves.

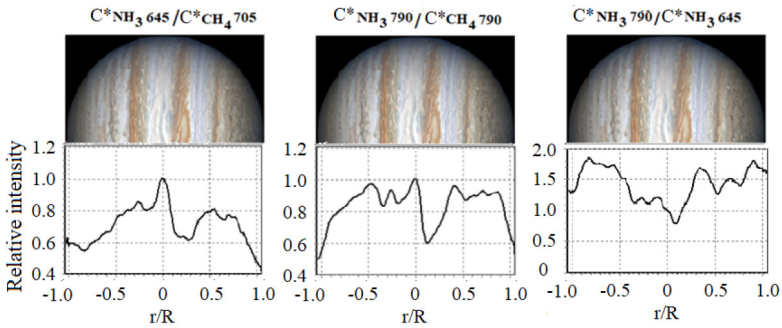


Fig. 3. Latitudinal (meridional) variations of the ratios $\text{NH}_3 645/\text{CH}_4 705$ (left), $\text{NH}_3 790/\text{CH}_4 790$ (middle) and $\text{NH}_3 790/\text{NH}_3 645$ (right)

It can be seen from the figures that the maximum ammonia deficiency occurs in the dark Northern Equatorial belt NEB, capturing the transition regions with neighboring light zones EZ and Northern Tropical Zone (NTrZ). Here, the ammonia deficiency reaches 40–60 % relative to EZ. At the same time, in the absorption band of 790 nm, the ammonia deficiency in the transition zone of EZ and NEB is more clearly expressed. For it, the correlation with the zonal structure of the cloud layers of the planet is quite clearly shown. The light zones correspond to an increased content of ammonia, and dark belts correspond to a reduced content. For both absorption bands, there is also a noticeable decline in the region of high latitudes and polar zones.

The ratio of the two ammonia absorption bands to each other (Figure 3, right) shows for a stronger NH_3 absorption band of 790 nm against the background of a weakly pronounced zonal structure a tendency to increase ammonia absorption in the high latitude region, which can be considered as evidence of the manifestation of the cosine effect due to the presence of an extended cloudless pure gas layer in the atmosphere under the upper visible cloud cover of Jupiter.

ACKNOWLEDGMENT:

The work is carried out within the framework of the Project No. BR20280974 "Program of fundamental astrophysical research in Kazakhstan: observations and theory", financed by the Ministry of Education and Science of the Republic of Kazakhstan)

REFERENCES:

- [1] *Tejfel V. et al.* // Bull. AAS. 2005. V. 37. P. 682.
- [2] *Tejfel V.G., Vdovichenko V.D., Karimov A.M. et al.* On the NH_3 absorption depression observable at Northern low latitudes of Jupiter // American Astronomical Society. 2016.
- [3] *Tejfel V.G., Karimov A.M., Vdovichenko V.D.* Strange latitudinal variations of the ammonia absorption on Jupiter // Bull. American Astronomical Society. 2005. V. 37. No. 3. P. 682.
- [4] *Tejfel V.G., Vdovichenko V.D., Lysenko P.G. et al.* Ammonium in Jupiter's Atmosphere: Spatial and Temporal Variations of the NH_3 Absorption Bands at 645 and 787 nm // Solar System Research. 2018. V. 52. No. 6. P. 480–494.
- [5] *Tejfel V.G., Vdovichenko V.D., Lysenko P.G. et al.* The weak ammonia absorption bands study from zonal spectrophotometry of Jupiter // EPSC Abstr. 2019. V. 13. 2 p.
- [6] *de Pater I. et al.* // Science. 2016. V. 352. Iss. 6290. P. 1290–1294.
- [7] <https://alpo-j.sakura.ne.jp/indexE>.
- [8] *Vdovichenko V.D., Lysenko P.G., Filippov V.A.* Investigation of variations in methane absorption bands along the central meridian of Jupiter in 2023 // 15th Moscow Solar System Symp. 2024.

INVESTIGATION OF VARIATIONS IN METHANE ABSORPTION BANDS ALONG THE CENTRAL MERIDIAN OF JUPITER IN 2023

V. D. Vdovichenko, P. G. Lysenko, V. A. Filippov

Fesenkov Astrophysical Institute, Almaty, Kazakhstan, vdv1942@mail.ru

KEYWORDS:

Jupiter, troposphere, clouds, methane, ammonia

INTRODUCTION:

The behavior of methane absorption bands of varying intensity along the central meridian of Jupiter depends on the vertical structure, optical density and position of the upper boundary of the cloud cover at different latitudes of the planet.

The improved technique for processing Jupiter spectrograms, described by us in the previous article [1], allows us to present absorption variations along the studied zone or the central meridian of Jupiter, as well as variations in absorption band profiles, residual intensities, central depths and equivalent absorption band widths in absolute form, and also in relation to the center of the Jupiter disk or any other area [2].

VARIATIONS OF THE EQUIVALENT C^* PATH IN THE CENTERS OF THE METHANE ABSORPTION BANDS:

Since the methane absorption bands we studied at 705, 619, 727, 790, 861 and 886 nm vary greatly in their intensity, depths and equivalent widths, it is very inconvenient to compare the variations of these values in absolute form.

A certain parameter is needed that reflects a single physical process of the formation of absorption bands in a scattering-absorbing medium. For example, the residual Bost intensity in each wavelength can be represented as:

$$\text{Bost}_\nu = I_\nu / I_c \approx \exp(-C^*),$$

where I_ν is the intensity of the absorption band at a given wavelength; I_c — intensity in a continuous spectrum at the same wavelength; $C^* = (C_m^* + C_a^*)$ is an equivalent absorption path proportional to the average number of molecules of the absorbing gases methane (C_m^*) and ammonia (C_a^*) (on the beam of vision).

In a sense, C_m^* and C_a^* for a given wavelength reflect the depth of radiation penetration for the studied part of the planet in a complex layered scattering-absorbing model of the atmosphere.

Therefore, in our opinion, for absorption bands that differ greatly in their intensity, as well as for a correct comparison of absorption variations in the center of each band and in its wings, it is optimal to represent the variations in the form of a comparison of equivalent absorption paths with $C^* \approx \text{Ln}(\text{Bost}_\nu)$.

A positive point in this case is also the fact that in the graphical representation, the behavior of the curves in this case is identical to the course of the absorption variation curves, represented in the traditional form of changes in the depths of the absorption bands, i.e., the rise of the curve on the graph in both cases means an increase in absorption, and a decline, respectively, a decrease in absorption.

The result of this representation of absorption variations for two absorption bands of CH_4 705 and 886 nm, which differ in intensity as much as possible, is shown in Figure 1 on the left.

The result was a bit unexpected. The shallowest methane band of 705 nm with a central depth of $R = 0.15$ and the deepest methane band of 886 nm with $R = 0.9$ give an almost mirror-like course of absorption variation along the central meridian of Jupiter.

It is clearly seen that the extreme values (minimum for 886 nm and maximum for 705 nm) coincide and for this date fall on the border of the Equatorial zone (EZ) and the Northern Equatorial Belt (NEB) at a relative distance of radius $r/R = 0.07$. The remaining bands, as their intensity changes, occupy an intermediate position (Figure 1, right). Looking at Figure 1, one can draw attention to another very important feature in the meridional course of absorption. Despite the fact that for both hemispheres, the general trend of absorption with latitude changes almost to the opposite with increasing absorption depth, nevertheless, the zonal structure is quite confidently traced, but with one very important feature. For the southern hemisphere, the position and sign of the extremes on the curves corresponding to dark and light cloud formations are preserved. While for the northern hemisphere, the sign of extremes changes to the opposite with increasing intensity of absorption bands.

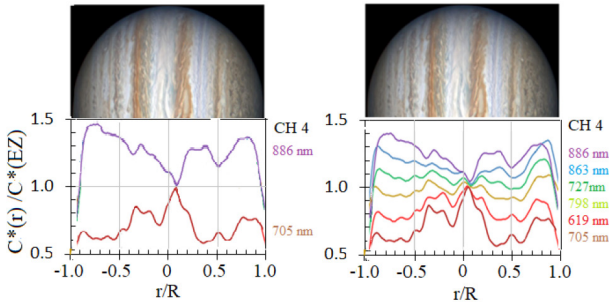


Fig. 1. Comparison of variations of C^* , normalized to its value in the center of the planet's disk, for 6 bands of methane absorption. For clarity, images of Jupiter (RGB) on the same date and longitude of the central meridian are shown above (<https://alpo-j.sakura.ne.jp/indexE>)

VARIATIONS OF C^* IN THE WINGS OF THE METHANE ABSORPTION BANDS:

In the previous section, we examined the features of absorption variation in the centers of 6 methane absorption bands along the central meridian of Jupiter. However, we must not forget that the absorption bands we are studying cover a fairly large range of wavelengths (about 3000 Å). Therefore, it is interesting to trace whether there are any variations along the profiles of each absorption band, and especially for the deep CH_4 band of 886 nm.

Despite the pronounced variations in intensity, the band profiles, at first glance, retain similarity ratios and we have not received any additional information about variations in the absorption band profiles. It was also not possible to detect them when examining each absorption band in detail separately. To check this and identify some possible features, you can take the ratio of the contours of the absorption bands of various sections of the disk to their profile in any reference area. The light Equatorial zone EZ is most often used for this purpose.

Figure 2 on the left shows the maximum range in variations of this ratio of absorption band profiles in the range of 600–930 nm from the south pole to the north pole. As we can see, the amplitude of the change in residual intensities is very impressive. For example, for the deepest band of methane at 886 nm, it changes more than twice near the polar regions.

Figure 2 on the right shows the same data, but without polar regions in the range of relative radius from -0.9 to $+0.9$ ($\pm 65^\circ$).

From such a comparison, one can see an interesting feature in the behavior of absorption bands along the central meridian of Jupiter. In the entire latitude range $\pm 65^\circ$, the absorption bands of methane 619 and 705 nm, as well as ammonia 645 nm, show an increased value of residual intensities, which corresponds to a decrease in absorption relative to the center of the disk. These effects can be traced in more detail by a detailed examination of the behavior of each absorption band.

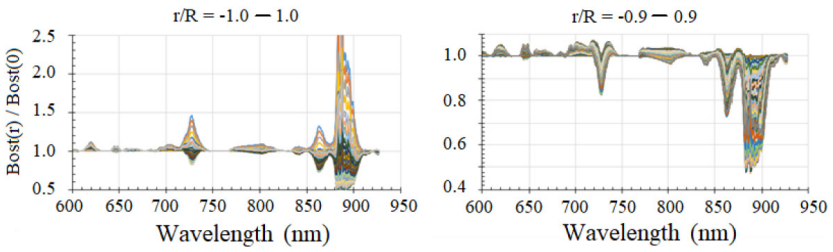


Fig. 2. On the left shows the maximum range in the ratio of absorption band profiles normalized to that in the center of the disk in the range of 600–930 nm from the south pole to the north pole. On the right is the maximum span in variations of absorption band profiles normalized to that in the center of the disk in the range of 600–930 nm without polar regions in the range of relative radius from -0.9 to $+0.9$ ($\pm 65^\circ$)

For example, Figures 3–6 show variations in the absorption band profiles of 727.790 and 886 nm with respect to the profile in EZ.

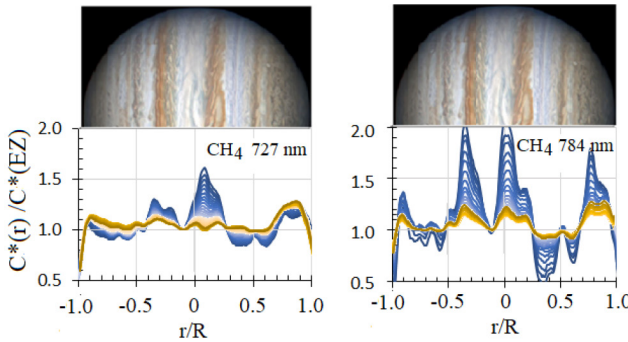


Fig. 3. Comparison of the appearance of Jupiter [3] with variations of C^* for the wings (blue color) and for the core (brown color) of methane bands. normalized to their value in the center of the planet's disk. On the left is CH_4 727 nm. On the right is CH_4 784 nm

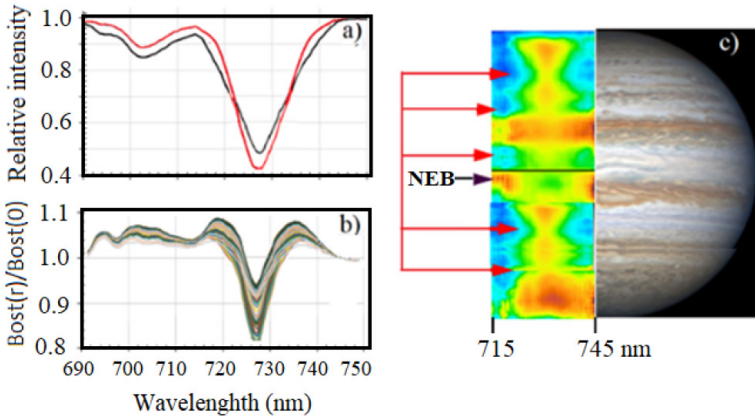


Fig. 4. Maximum differences in the profiles of the methane absorption band of 727 nm (a); variations in the absorption band profiles of CH_4 727 nm with respect to its value in the center of the disk when moving along the central meridian (b). A fragment of the color map is shown on the right (see [1]), which indicates the problem areas of Jupiter, in which the wings of the absorption band of 727 nm are narrowed. The 886 nm band is characterized by the largest variations in the central depth — from 0.6 to 0.9. Accordingly, its residual intensity varies from 0.1 at low and middle latitudes of the Northern and Southern hemispheres ($r/R = -0.9 \dots +0.9$) to 0.3 near the North Pole and to 0.4 near the South Pole, i.e. more than by 4 times (Figure 5)

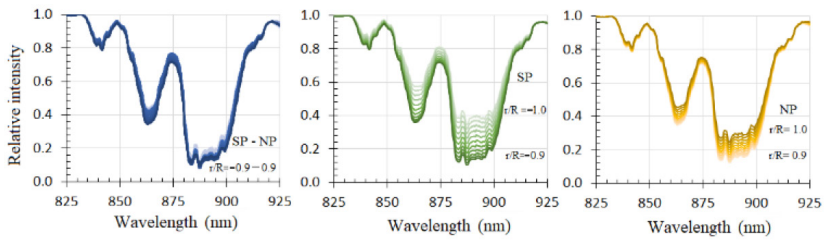


Fig. 5. Maximum variations in the intensity of the CH_4 band of 889 nm Interesting metamorphoses are taking place in the core of this band. Despite the external similarity (or similarity) in the profile, near the polar regions $r/R = 0.85\text{--}0.95$, an inversion is observed in the details of the core of the CH_4 absorption band of 889 nm with respect to the profile for the equatorial region (Figure 6)

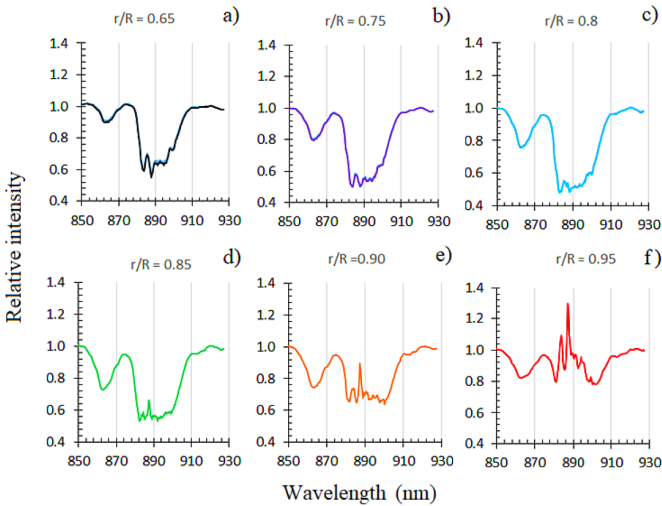


Fig. 6. Maximum differences in the core profile of the 886 nm absorption band in the polar regions with respect to the profile of the equatorial region. Near the polar regions $r/R = 0.85\text{--}0.95$, an inversion is observed in the details of the core of the absorption band with respect to the profile of the equatorial region

In the center of the shortwave minimum of the 784 nm band, C_m^* variations are approximately the same, but more pronounced, as in the core of the 727 nm methane band. In the wings of the absorption bands, free from the influence of the ammonia band, C_m^* variations reach a span of 100%. The maximum variations occur in the boundary regions between StrZ-SEB and EZ-NTrZ (Figure 3, right).

But the most interesting result is observed in the methane bands 727 and 861 nm — attenuated absorption in the wings of the bands and increased absorption in their central core. This fact indicates the deformation of the profile of this absorption band relative to the reference region when moving along the central meridian.

ACKNOWLEDGMENT:

The work is carried out within the framework of the Project No. BR20280974 “Program of fundamental astrophysical research in Kazakhstan: observations and theory”, financed by the Ministry of Education and Science of the Republic of Kazakhstan.

REFERENCES:

- [1] *Vdovichenko V.D.* Methodological aspects of the study of variations of ammonia-methane absorption in the atmosphere of Jupiter // 15th Moscow Solar System Symp. 2024.
- [2] *Vdovichenko V.D., Karimov A.M., Kiriyeenko G.A. et al.* Molecular absorption bands in the study of the Jupiter troposphere // *Izvestia of the National Acad. Sciences Republic Kazakhstan. Ser. Physics and Mathematics.* 2020. V. 3. P. 26–33.

METHODOLOGICAL ASPECTS OF THE STUDY OF AMMONIA-METHANE ABSORPTION VARIATIONS IN THE ATMOSPHERE OF JUPITER

V. D. Vdovichenko

Fesenkov Astrophysical Institute, Almaty, Kazakhstan, vdv1942@mail.ru

KEYWORDS:

Jupiter, troposphere, clouds, methane, ammonia

INTRODUCTION:

Methane and ammonia create absorption bands in both the visible and near-infrared regions of the Jupiter spectrum. The intensity of the bands depends not only on the absorption coefficients that determine the profile of the absorption band, but also on the scattering-absorbing medium in which they are formed. According to variations in the characteristics of absorption bands of different intensities, it is possible to study the structural features of various cloud belts characteristic of the cloudy atmosphere of Jupiter [1–3]. And since in the following articles we will talk about small variations of methane and ammonia absorption across the Jupiter disk, it is reasonable to ask about the reliability of the presented results. Unfortunately, little attention is paid in the literature to the details of the methodology of observation and processing of observational material. We decided to fill this gap.

METHODS OF OBSERVATION, SELECTION AND SORTING OF OBSERVATIONAL MATERIAL:

Our spectral observations were performed using a diffraction spectrograph, SGS with a CCD camera ST-7XE, mounted in a 7.5-meter Cassegrain focus of a 0.6-meter Zeiss-600 telescope.

Over the past 20 years (from 2004 to 2023), we have accumulated a huge amount of material in the form of tens of thousands of CCD spectrograms, which is needed in operational processing and comprehensive analysis.

For Jupiter, for example, these are spectrograms of the central meridian, spectrograms of the main cloud belts of Jupiter: EZ, NEB, SEB, NTrZ, STrZ, as well as spectrograms of STrZ and central Meridian during the passage of the Great Red Spot (GRS) through them (Figure 1, left), as well as numerous scans of the disk planets with the orientation of the spectrograph slit parallel to the equator of the planet.

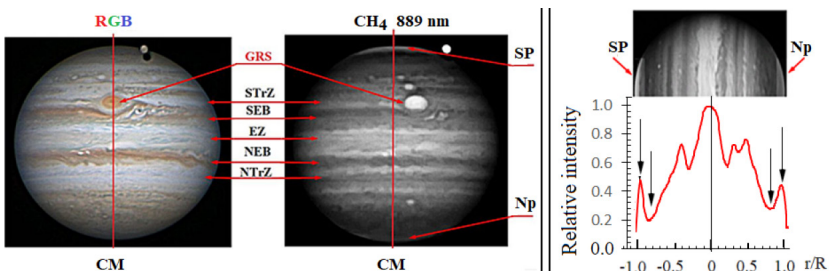


Fig. 1. On the left is the appearance of Jupiter in the RGB system and in the center of the methane absorption band of 886 nm (<https://alpo-j.sakura.ne.jp/indexE>). The studied cloud structures of Jupiter are indicated. At the top right is a fragment of the image of Jupiter in the core of the 889 nm methane absorption band, at the bottom is a section across the dispersion of the spectrogram of the central meridian of Jupiter at the same wavelength

Unfortunately, for various reasons, not all spectrograms are suitable for further processing and analysis. Therefore, the primary task is to select spectrograms by quality. The most reliable method is the analysis of spectro-

grams of the central meridian, namely its sections in the core of the deep absorption band of methane 889 nm.

The fact is that for many years, images of Jupiter in the center of the deep methane absorption band of 886 nm (Figure 1, right, above) show the presence of brightenings in the polar regions caused by the presence of a highly located aerosol haze. These anomalous brightenings are clearly visible on good-quality Jupiter spectrograms (Figure 1, bottom right). Weakly pronounced brightenings or their absence indicate a low quality of the spectrograms.

Since the variations observed in the intensities of the absorption bands are usually insignificant, obtaining the observational material and its processing require a special methodological approach and special computer programs for processing the obtained material.

To do this, in the Delphi environment, we have developed an author's program that allows us to process two-dimensional numeric arrays 765×510 px almost instantly using this algorithm. The arrays are pre-prepared by the standard CCDOP55 program from Jupiter spectrograms in digitized (*.txt) form.

A PROGRAM FOR VIEWING AND PROCESSING JUPITER SPECTROGRAMS:

The programs are displayed on the main screen (Figure 2):

- a regular CHETROGRAM in black and white and a color chart with an adjustable color gradient;
- spectrum of the center of the Jupiter disk;
- the current spectrum of the spectrogram area under the cursor is;
- the ratio of the current spectrum to the spectrum of the center of the disk;
- sections of the central meridian in the continuous spectrum, in the methane absorption band of 889 nm and the current section under the mouse cursor, as well as the ratio of the current section to the section in the continuous spectrum;
- 15 program controls.

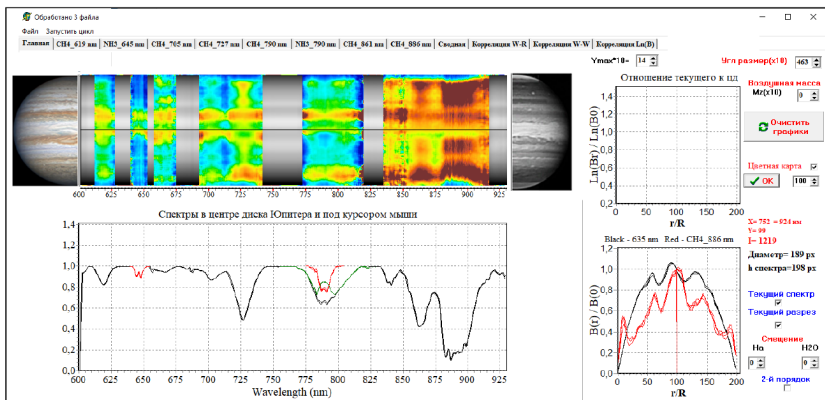


Fig. 2. The main page of the program (explanations in the text)

At the top of the main page there are labels of 12 additional pages of the program with graphical output for each absorption band of 5 main parameters and their correlation links. All values are normalized to the center of the disk. The absolute values are given in the corresponding output text files.

DESCRIPTION OF THE PROGRAM OPERATION:

- at the beginning of the work, the program downloads auxiliary files, reads the source array (765×510 pixel matrix), including the brightness distribution along the central meridian or other studied area of the planet;
- line by line divides it into a function of the unevenness of the sensitivity of the CCD matrix;

- according to a certain algorithm (by the method of sequential approximation), it determines the position of the working field and positions it strictly unambiguously;
- takes into account the angular dimensions of the planet;
- subtracts the spectral background by interpolating it across the dispersion across the entire spectrogram;
- takes into account the spectral transmission function of the entire optical path and the sensitivity of the matrix;
- according to laboratory spectra of methane, sections of the continuous spectrum are defined where there is obviously no absorption of this gas. An interpolation curve of a continuous spectrum in the entire spectral range is carried out using them;
- takes into account the spectral sensitivity of the matrix, adjusts all spectra to the reference spectrum, line-by-line calculates the levels of the continuous spectrum;
- the residual intensities of the absorption bands of methane and ammonia along the studied zone or the central meridian are calculated line by line;
- the program has a flexible and intuitive interface for configuring the display parameters of the main program window (15 controls);
- accounting for the angular size of the planet, telluric bands of water vapor absorption and accounting for changes in air mass;
- preview of the spectrum of the center of the planet's disk and the spectra of individual parts and their relationship;
- interactive (using the mouse) viewing of the ratio of the spectra of any part of the disk in relation to the spectrum of the disk center;
- displays a color map of small variations in the intensity of the absorption bands along the selected zone;
- confident identification of extremely small (from 2 %) variations in profiles and intensities of absorption bands across the planet's disk;
- calculates the profiles of the absorption bands of methane and ammonia, their residual intensities, central depths and equivalent widths, as well as brightness distributions along the studied zone in sections of the continuous spectrum and in the centers of 6 absorption bands (Figure 3a — an example for the CH₄ band of 886 nm)
- Graphically displays correlations between the 18 determined values (Figure 3b);
- displays the results in graphical and tabular form (75 graphs and 24 tables);
- can batch process a group of files;
- processing time of one file is 5 seconds, processing a package of 10 files of 765×510 numeric matrices takes 40–50 seconds.

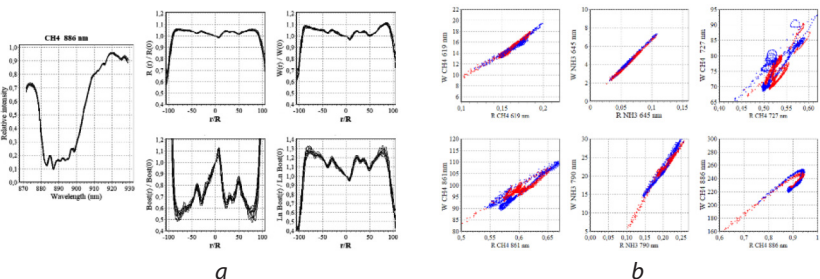


Fig. 3. An example of the output of the main parameters for the methane band of 886 nm (10 spectrograms (a)); an example of correlation links (b)

After processing the files in the loop, the program automatically creates a folder in the source folder in which it saves all the processing results in the form of 75 graphic and 24 text tabular files.

Depending on the purpose of the study, the results of text files can be easily transferred to Excel. Then plot partial and complete information both along the spectrum for individual zones and across, i.e., for example, along

the entire central meridian in different wavelengths, including the wings of the absorption bands. You can build an isometric 3D map of any of the parameters.

ACKNOWLEDGMENT

The work is carried out within the framework of the Project No. BR20280974 “Program of fundamental astrophysical research in Kazakhstan: observations and theory”, financed by the Ministry of Education and Science of the Republic of Kazakhstan)

REFERENCES:

- [1] *Vdovichenko V. D., Karimov A. M., Kiriyyenko G. A. et al.* Zonal features of the behavior of weak molecular absorption bands on Jupiter // *Astronomical Bull.* 2021. V. 55. No. 1. P. 38–49.
- [2] *Vdovichenko V. D., Karimov A. M., Kiriyyenko G. A. et al.* Molecular absorption bands in the study of the Jupiter troposphere // *Proc. National Acad. Sciences Republic Kazakhstan. Ser. Physics and Mathematics.* 2020. V. 3. P. 26–33.
- [3] *Vdovichenko V. D., Kiriyyenko G. A.* Study of the Jupiter, Mars, Titan and Vesta. LAP LAMBERT Academic Publ. 2013.

**SESSION 4. MOON AND MERCURY (MN)
ORAL SESSION**

MGNS EXPERIMENT SCIENCE INVESTIGATIONS DURING CRUISE TO MERCURY ONBOARD ESA MPO/BEPICOLOMBO MISSION

A. S. Kozyrev¹, J. Benkhoff², M. L. Litvak¹, I. G. Mitrofanov¹, A. B. Sanin¹

¹ Space Research Institute RAS, Moscow, Russia, kozyrev@cosmos.ru

² European Space Agency, ESTEC, Noordwijk, The Netherlands

KEYWORDS:

BepiColombo, MPO, Mercury, MGNS, nuclear planetology

ABSTRACT:

BepiColombo is a joint mission of the European Space Agency (ESA) and the Japan Aerospace Exploration Agency (JAXA), which is a comprehensive study of Mercury through two orbiters will be inserted into special polar orbits around the planet: MPO (ESA) and Mio (JAXA). The BepiColombo spacecraft was launched on October 20, 2018 and is currently on a cruise to Mercury, which is a long journey into the interior heliosphere [1]. The trajectory of the performed part of the cruise includes one flyby of Earth (in April 2020), two flybys of Venus (in October 2020 and August 2021) and four flybys of Mercury (in October 2021, June 2022, June 2023 and September 2024). To achieve its final orbit around the planet, the BepiColombo spacecraft will have to perform two more Mercury flybys (December 2024 and January 2025) [2].

The MGNS instrument developed at the Space Research Institute of the Russian Academy of Sciences is designed to detect neutron and gamma ray fluxes. It is located inside the MPO spacecraft structure. The main scientific task of the MGNS instrument is to study the elemental composition of Mercury's subsurface [3, 4].

During the cruise, the MGNS instrument monitors the radiation background of the prompt spacecraft emission due to bombardment by energetic particles of Galactic Cosmic Rays. In addition, the MGNS instrument also performed measurements during flybys of the Earth, Venus and Mercury to measure the neutron and gamma ray albedo of the upper atmosphere of the Earth and Venus and the surface of Mercury. As additional scientific tasks, the instrument detects cosmic gamma-ray bursts for their subsequent localization by the Inter Planetary Network (IPN) [5]. During the cruise, localization and publication of circulars for about 33 gamma-ray bursts were completed by use MGNS gamma-ray data.

This presentation will provide a brief overview of the cruise of the BepiColombo mission and the results that have been obtained from the MGNS experiment data.

REFERENCES:

- [1] Benkhoff J., Murakami G., Baumjohann W., et al. BepiColombo — Mission Overview and Science Goals // Space Science Reviews. 2021. V. 217.
- [2] Mangano V., Dósa M., Fränz M. et al. BepiColombo science investigations during cruise and flybys at the Earth, Venus and Mercury // Space Sci Rev. 2021. V. 217. Article 23.
- [3] Mitrofanov I. G. et al. The Mercury Gamma and Neutron Spectrometer (MGNS) onboard the Planetary Orbiter of the BepiColombo mission // Planetary and Space Science. 2010. V. 58. P. 116–124.
- [4] Mitrofanov I. G., Kozyrev A. S., Lisov D. I. et al. The Mercury Gamma-Ray and Neutron Spectrometer (MGNS) onboard the Mercury Planetary Orbiter of the BepiColombo Mission: Design updates and first measurements in space // Space Science Reviews. 2021. V. 217. Iss. 5. Article 67.
- [5] Kozyrev A. S., Benkhoff J., Litvak M. L. et al. Localization of cosmic gamma-ray bursts in interplanetary space with MGNS/BepiColombo and HEND/Mars Odyssey experiments // Planetary and Space Science. 2022. V. 224. Article 05594.

RECENT GEOLOGICAL ACTIVITY ON MERCURY

Z. Xiao, Y. Wang, R. Xu

School of Atmospheric Sciences, Sun Yat-sen University, Guangzhou, China

KEYWORDS:

Mercury, volatiles, hollows, smooth plains, impact craters

ABSTRACT:

The inner-most planet in the Solar System, Mercury features unique geophysical and geochemical characteristics. The formation and evolution of Mercury are the key information to understand the distribution of planet-forming materials and the migration of celestial bodies in the Solar System's early history. The differentiation of the magma ocean formed the core, mantle, and crust. The exchange of materials and energy among different geospheres directly influences the evolution of Mercury. The crustal compositions provide insights into mantle substances, and the mantle dynamic processes are the key driving force of geological activities.

A recent puzzling discovery about Mercury is the unexpected high content of volatile compared to the general trend of inner Solar System bodies. Landforms formed with the involvement of volatiles are widely distributed on the surface of Mercury. Nonetheless, the composition, sources, and their association with internal activities of Mercury's surface volatiles remain unknown.

In this conference, we report recent advances on the study of recent geological activity on the surface of Mercury, with a focus on volatile activities. We utilized impact craters as probes to investigate deep materials and potential connections between crustal volatiles and mantle heterogeneity of Mercury, as well as their spatiotemporal correlations. The main results are summarized as the following:

- (i) Hollows are small irregular-shaped depressions with steep walls and flat floor formed by the loss of shallow volatiles. We carefully extracted the spatially correlated reflectance spectra for different facies of hollows, proposing that volatiles are mainly lost from steep hollow walls. The growth of hollows is controlled by the destabilization and collapse of the hollow walls. We constrained a maximum model age of $\sim 10^3$ thousand years for the global population of hollow for the first time. We predict that an active rejuvenation of volatiles has occurred in the shallow crust of Mercury.
- (ii) Dark spots on Mercury are recently-formed thin and low-reflectance materials that are related with volatile activity and supposed to be much shorter-lived than their central hollows. We investigated reflectance spectra, sub-resolution roughness, and temporal changes of dark spots using the full-mission dataset of MESSENGER. We find that dark spots have the highest concentration of graphite and an intense outgassing origin. Temporal imaging for dark spots reveals no detectable reflectance changes in 30 Earth months, and possibly over 40 Earth years, providing a reference for modeling the spectral behavior of graphite caused by space weathering on Mercury.
- (iii) We study the stratigraphic ages and reflectance spectral features of low-reflectance materials (LRM) on Mercury. We find that LRM with similar stratigraphic ages and geologic context have varying graphite contents, indicating a potential volcanic origin. Using impact craters as probes, we find widespread lateral and/or stratified compositional heterogeneities within the crust of high-magnesium terranes (HMR) on Mercury. The results indicate that HMR was derived from multiple mantle sources and/or had undergone different degrees of partial melting. We confirm compositional zoning in the mantle and the existence of prolonged local thermal anomalies. LRM are the main units on Mercury hosting volatile-involved landforms, indicating that early-stage man-

tle-source magma might be richer in volatiles, and/or that volatiles tend to form or migrate within LRM.

- (iv) We updated the global inventory of 315 smooth plains on Mercury, classifying their absolute model ages and possible origins. We reveal that both large and small smooth plains on Mercury were dominantly emplaced within ~200 million years around 3.7 Ga. Small smooth plains formed by effusive volcanism are preferentially located around the large impact basins (e.g., Caloris, Rembrandt). Together with the distribution of similarly aged large smooth plains, our results reveal that peaked formation of large impact basins may be a major trigger for this short-term and global-wide volcanism. The mantle sources of smooth plains were significantly different with those forming HMR and intercrater plains, indicating changes in depth and/or degree of partial melting over time. Widespread graphite absorption features across smooth plains, yet no hollows and dark spots formed, indicating that graphite may not be the primary volatile in the subsurface of Mercury.
- (v) We conduct a comprehensive analysis of volatile activity on the surface of Mercury and its implications to mantle heterogeneities. We suggest that the compositional and structural heterogeneities of the mantle have existed throughout its geological history. The upward migration of volatile-rich magma may be the key factor driving crustal volatile activities. Ancient geological units (e.g., LRM) on Mercury are the primary regions of volatile activities, while similar-aged high-reflectance plains typically lack hollows and dark spots. We suggest a weak correlation between volatiles and the main dark phases (e.g., microcrystalline graphite and metallic iron) on the surface of Mercury, and sulfides may be the main volatile substances.

REFERENCES:

- [1] *Blewett D.T., Chabot N.L. et al.* Hollows on Mercury: MESSENGER Evidence for Geologically Recent Volatile-Related Activity // *Science*. 2011. V. 333. P. 1856–1859.
- [2] *Head J.W., Chapman C.R., Strom R.G. et al.* Flood Volcanism in the Northern High Latitudes of Mercury Revealed by MESSENGER // *Science*. 2011. V. 333. P. 1853–1856.
- [3] *Blewett D.T., Vaughan W.M., Xiao Z. et al.* Mercury's hollows: Constraints on formation and composition from analysis of geological setting and spectral reflectance // *J. Geophysics Research*. 2013. V. 118. P. 1–20. DOI: 10.1029/2012JE004174.
- [4] *Banks M.E., Xiao Z., Watters T.R. et al.* Duration of activity on lobate-scarp thrust faults on Mercury // *J. Geophysics Research*. 2015. V. 120(11). P. 1751–1762. DOI: 10.1002/2015JE004828.
- [5] *Blewett D.T., Stadermann A.C., Susorney H.C. et al.* Analysis of MESSENGER high-resolution images of Mercury's hollows and implications for hollow formation // *J. Geophys. Res. Planets*. 2016. V. 121. P. 1798–1813. DOI: 10.1002/2016JE005070.
- [6] *Xiao Z., Strom R.G., Blewett D.T. et al.* Dark spots on Mercury: A distinctive low-reflectance material and its relation to hollows // *J. Geophysics Research*. 2013. V. 118. P. 1752–1765. DOI: 10.1002/jgre.20115.
- [7] *Wang Y., Xiao Z., Chang Y., Cui J.* Lost volatiles during the formation of hollows on Mercury // *J. Geophysical Research: Planets*. 2020. V. 125(9). Article e2020JE006559. DOI: 10.1029/2020JE006559.
- [8] *Xiao Z., Xu R., Wang Y. et al.* Recent dark pyroclastic deposits on Mercury // *Geophysical Research Letters*. 2021. V. 48. Article e2021GL092532. <https://doi.org/10.1029/2021GL092532>.
- [9] *Wang Y., Xiao Z., Chang Y. et al.* Short-term and global-wide effusive volcanism on Mercury around 3.7 Ga // *Geophysical Research Letters*. 2021. Article e2021GL094503. DOI: 10.1029/2021GL094503.
- [10] *Wang Y., Xiao Z., Xu R.* Multiple mantle sources of high-magnesium terranes on Mercury // *J. Geophysical Research: Planets*. 2022. V. 127. Article e2022JE007218. DOI: 10.1029/2022JE007218.
- [11] *Xu R., Xiao Z., Wang Y., Xu R.* Pitted-ground volcanoes on Mercury // *Remote Sensing*. 2022. V. 14(17). Article 4164. <https://doi.org/10.3390/rs14174164>.
- [12] *Wang Y., Xiao Z., Xu R. et al.* Dark spots on Mercury show no signs of weathering during 30 Earth months // *Communications Earth and Environment*. 2022. V. 3. Article 299. DOI: 10.1038/s43247-022-00634-z.

- [13] *Xu R., Xiao Z., Wang Y., Cui J.* Less than one weight percent of graphite on the surface of Mercury // *Nature Astronomy*. 2024. V. 8. P. 280–289. DOI: 10.1038/s41550-023-02169-5.

DESIGN AND OPTIMIZING AN INTERPLANETARY TRAJECTORY OF A SPACECRAFT TO MERCURY

O. S. Chernenko

Space Research Institute RAS, Moscow, Russia, sol4.ch@mail.ru

KEYWORDS:

Mercury, trajectory design, gravity assists, deep space maneuvers

INTRODUCTION:

During the period of spacecraft exploration of the planets of the Solar System, there has been less interest in Mercury than in Venus and Mars, in part because of the difficulty in constructing a time- and energy-optimal trajectory from an orbit around the Earth to a target orbit around Mercury. Nevertheless, Mercury remains relevant for study. It falls into the category of Earth-group planets, the study of which will provide a better understanding of the formation of the Earth, as well as for understanding the formation of exoplanets, since many such planets are located quite close to their stars. Determining the most optimal trajectory in terms of energy and time characteristics is still a significant challenge, and the construction, analysis, and selection of such a route is the focus of this paper. The main idea begins with the fact that one of the difficulties of the flight is the repayment of a significant part of the Earth's orbital velocity (about 30 km/s). Currently, no spacecraft is capable of flying directly to Mercury, and a complex strategy of multiple gravity assists is commonly used. The main requirements for the mission are improvements on the characteristics of existing missions to Mercury [1, 2]. Several trajectories are presented that include the use of gravity assists around the inner planets of the solar system, such as Earth, Venus and Mercury, as well as deep space maneuvers between gravity assists to improve the phasing and energy efficiency of the route. All of this, with optimal performance, allows the spacecraft to reach its target orbit in a relatively shorter time compared to NASA's MESSENGER spacecraft, which took 6.6 years to reach Mercury, as well as the BepiColombo spacecraft, a joint project of ESA and JAXA, whose journey will take 7.2 years. The total characteristic velocity expended for all maneuvers described in this paper remains around the 1959.45 m/s value of the MESSENGER spacecraft.

TRAJECTORY DESIGN:

The objective functional of the problem is the total characteristic velocity of the mission and represents the sum of impulses: departure, intermediate ones during trajectory maneuvers, and approach. It is computed according to the criteria for the final conditions of spacecraft movement. The vector of optimized parameters includes the moments of time characterizing the passages of intermediate planets, the initial moment and the final approach moment to the destination planet. Additionally, points related to the execution of the deep space maneuvers included. However, the phase state of the planet (coordinates and velocity) can only be determined based on time, not the specific locations of the deep space maneuvers. Consequently, the position of the deep space maneuver is not predetermined and also needs to be optimized. Gravity assists are assumed to be passive.

RESULTS:

When conducting numerical calculations, three solutions were obtained within the scope of this study that most effectively satisfy all the criteria for designing an alternative trajectory. The reference start date (UTC) for all trajectories is May 29, 2040 at 00:00:00. Actual launch dates are January 31, 2047, February 26, 2046, and May 11, 2044. The flights last 5.66, 6.87 and 4.55 years, respectively. There are five gravity assists on two trajectories and three gravity maneuvers on the third, with deep space maneuvers in between, including one after the impulse given by the upper stage to start the heliocentric portion of the trajectory and before the orbital approach impulse around Mercury. Velocity impulses given by the upper stage for

the first, second and third trajectories: 4971, 5075 and 6144 m/s respectively. Spacecraft characteristic velocity: 2037, 2054 and 2022 m/s. Examples of launch vehicle and upper stage systems capable of placing a spacecraft into a given orbit are also given, and the required mass of the spacecraft and the mass of its propellant are also estimated.

REFERENCES:

- [1] *Wilson M. N., Engelbrecht C. S., Trela M. D.* Flight Performance of the MESSENGER propulsion system from launch to orbit insertion // Proc. 48th Joint Propulsion Conf. 2012. P. 6491–6514.
- [2] *Benkhoff J., Murakami G., Baumjohann W., Besse S., Bunce E.* BepiColombo — Mission Overview and Science Goals // Space Science Reviews. 2021. V. 217. No. 8. P. 647–702.

MAPPING OF POLAR LUNAR WATER

A. B. Sanin, I. G. Mitrofanov, M. L. Litvak

Space Research Institute RAS, Moscow, Russia, djachkova@np.cosmos.ru

KEYWORDS:

Moon, polar regions, water, LEND

ABSTRACT:

Lunar Exploration Neutron Detector (LEND) is working onboard NASA Lunar Reconnaissance Orbiter since 2009 [1]. The main goal of LEND measurements is mapping of lunar neutron emission produced in nuclear reactions in the shallow subsurface due to bombardment by charged particles of Galactic Cosmic Rays. The flux of this emission in the epithermal energy range is known to depend on the content of hydrogen in the lunar regolith, which is thought to be directly linked with the mass fraction of subsurface water.

In the very beginning of the LRO mission, the number of lunar polar regions were found by LEND with rather high fraction of water, highly likely in the form of water ice [2]. They are not necessarily associated with the Permanently Shadowed Regions, PSRs, as it has been supposed before LEND investigation, but might be also regions with daily solar illumination.

This report will review the most recent data from LEND based on the rich statistics of 15 years long observations. The most accurate map of water will be presented for the Southern polar area of the Moon.

REFERENCES:

- [1] *Mitrofanov I. G. et al.* Lunar Exploration Neutron Detector for NASA Lunar Reconnaissance Orbiter // *Space Science Reviews*. 2010. V. 150. Iss. 1–4. Article 183.
- [2] *Mitrofanov I. G. et al.* Hydrogen mapping of the lunar south pole using the LRO Neutron Detector Experiment LEND // *Science*. 2010. V. 330. Iss. 6003. Article 483.

LOBATE RIMMED CRATERS IN PSR PARTS OF THE LUNAR SOUTH-POLAR CRATERS FAUSTINI AND SHOEMAKER

A. T. Basilevsky¹, B. A. Ivanov², S. S. Krasilnikov³

¹ Vernadsky Institute of Geochemistry and Analytical Chemistry RAS
Moscow, Russia, atbas@geokhi.ru

² Institute of Geosphere Dynamics RAS, Moscow, Russia

³ Hong Kong Polytechnic University, Hong Kong, China

KEYWORDS:

Moon, permanently shadowed areas, ShadowCam images, lobate-rimmed craters, relative depth, water ice in regolith, process of formation

INTRODUCTION:

This study is based on the analysis of images taken by the ShadowCam camera hosted onboard the Korea Pathfinder Lunar Orbiter [1]. This camera provides a possibility to obtain images in the permanently shadowed parts of lunar polar craters using the very faint light reflected from the Sun-illuminated tops of the crater rims. Resolution of these images is ~ 1.7 m/px. Images are now available at several sites, including <https://data.ser.asu.edu/>, which was used by us. The first results of studies of the ShadowCam images were presented at the 55th Lunar and Planetary Science Conference, see e. g., [2]. The mentioned abstract shortly describes craters having specific lobate-rimmed morphology, which was suggested by [2] to be due to presence of water ice in the target material. Here we shortly describe three of such craters and consider possible mechanism of their formation.

DESCRIPTION:

Figures 1 and 2 show the ShowCam images of three lobate-rimmed craters and crossing them topographic profiles based on LOLA measurements.

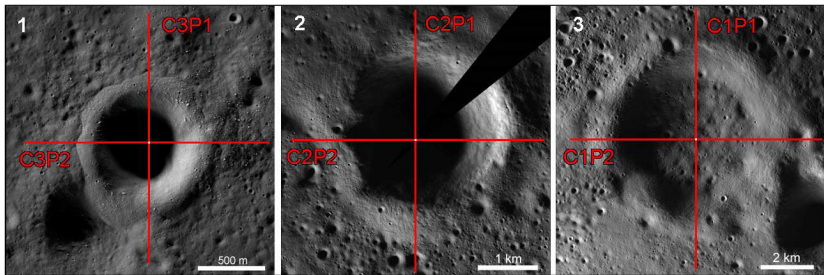


Fig. 1. The lobate-rimmed craters on the floor of crater Shoemaker: C3 — crater with $D = 1.12$ km, C2 — crater with $D = 3$ km, and crater Tooley (C1) with $D = 7$ km

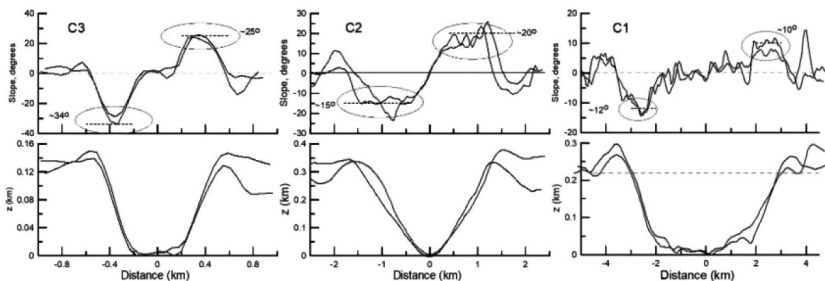


Fig. 2. The LOLA based [3] topographic profiles crossing the considered craters are shown in Figure 1. Upper plots show slope angles along altimetric profiles at lower plots. Crater Tooley (C1) has the most shallow slopes from 10 to 12°

It is seen in Figures 1 and 2 that craters of this morphology have prominent rims whose outer ends are rather clear. It is especially obvious in the case

of the C2 crater. Steepness of the outer slopes of the crater rims reach 10° . Steepness of the inner crater slopes reach 30 to 35° for the smallest crater with $D = 1.12$ km, being much smaller (10 to 15°) for craters 3 and 7 km in diameter. The depth to diameter ratio (d/D) ratio decreases from 0.12 to 0.04 with crater diameter growth. Below we consider how these parameters of the crater morphology could be explained.

SLOW CRATER COLLAPSE IN ICE-CONTAINING TARGETS:

We do not have enough experience to interpret available crater images regarding the ice content at extremely low temperatures. Spectral imaging of shadowed polar lunar craters reveals H_2O coating the regolith particles (see data and discussion of earlier results in [4]).

Basing on available results, we can assume a possibility of a quasi-viscous flow under a crater. For example, [5] got a crater in a viscous-plastic gel dropping a steel ball (Figure 3). Here, the non-linear rheology results in a partial impact cavity relaxation

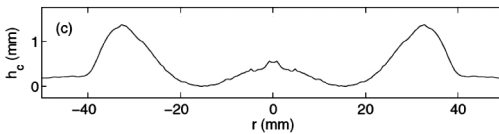


Fig. 3. Partially relaxed crater [5] after a steel ball falling into a viscous-plastic target

An interesting rheological effect visible in Figures 3 and 4 is the elevated rim with steeper outer slopes ($\sim 12^\circ$) than inner slopes (max $\sim 7^\circ$)

One more possible approach to explain visible crater specific in potential ice bearing targets could be borrowed from [6] where the idea of repeated seismic shaking was investigated with a model of slow viscose crater collapse.

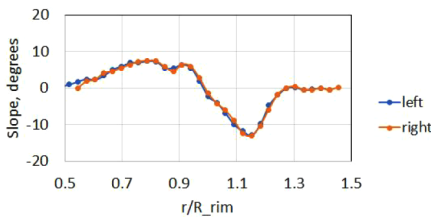


Fig. 4. Slopes in a central part of a crater shown in Figure 3. Left and right profiles are barely identical

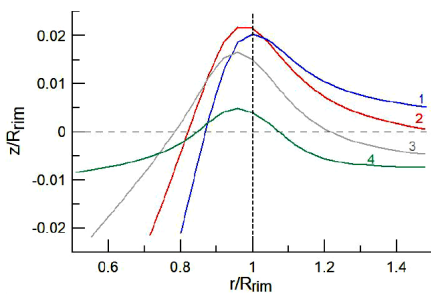


Fig. 5. Crater rim profile evolution assuming a viscose flow of the target material around a simple crater: 1 — the assumed initial crater profile; 2–4 — the evolution of the crater rim due to viscose relaxation of the crater depression [6] (note the large vertical exaggeration of the plot)

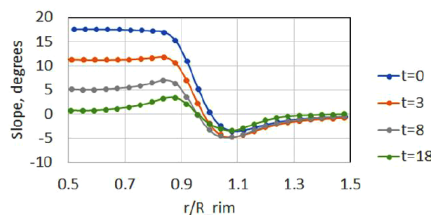


Fig. 6. The evolution of the local slope inclination for the crater relaxation shown in Figure 5. Scaled times, t , are listed in the legend

The model, shown in Figure 5, demonstrates a wide shallow subsidence zone beyond the crater rim, what is partially an artificial effect of a finite target size. For scaled times $t > 3$ maximal inner slope (positive) decreases

from 17 to 3.3° , while the outer (negative) slope tend to be in the range -5 to -3.5° making the crater profile more symmetrical relative to the visible rim crest. This is in contrast with the assumed “fresh” crater ($t = 0$), where the inner slope of $\sim 18^\circ$ is much steeper than the outer slope of 4 to 5° .

In the viscous subsidence model presented in Figures 3 and 4 the length of slope between points of minimal inner and maximum outer rim slopes is approximately constant and is equal $\sim 0.25R_0$.

More sophisticated models with “viscosity” varied with distance should be tested.

DISCUSSION:

Despite a large database for strength and cratering in permafrost soils we find relatively low number of papers about mechanical properties for ice-bearing lunar regolith. Typical recent research [7] predicts a Coulomb-Mohr model behavior for lunar soil simulants with 4 to 10 % water content at 110 K. In [7] various strength parameters are normalized to 1-D compressive strength, f_c , which vary from ~ 1.5 to ~ 5 MPa for this water (ice) content. Static friction varies from ~ 1.2 to ~ 0.9 while pressure increases to $\sim 6f_c$. This approach allows researchers to plan future penetration experiments. The dynamic behavior of water-bearing regolith (including the anticipated ice friction melting) is still under investigation.

The modeling data shown in Figures 3 to 6 illustrate some expected crater profile specifics for quasi-viscous target material mechanics. The problem here is the non-linear behavior of real target materials, reflected in visible lobate-rimmed morphology. The problem deserves more attention in the future.

CONCLUSIONS:

We continue to analyze impact craters morphology with specific lobate-rimmed morphology in lunar polar areas. This study includes better description of images together with a search of relevant experimental and numerical modeling of impact cratering in ice-bearing targets.

ACKNOWLEDGEMENTS:

The authors are grateful to the ShadowCam team, Strate University of Arizona, NASA USA and the Korea Aerospace Administration for possibility to work with the ShadowCam images as well as to the LOLA LRO team for opportunity to work with their products.

REFERENCES:

- [1] *Robinson M. S. et al.* ShadowCam — Seeing in the dark // EPSC Abstr. 2017. V. 11. Article EPSC2017-506.
- [2] *Robinson M. S. et al.* Seeing in shadows // 55th LPSC: 2024. Article 1669.
- [3] http://pds-geosciences.wustl.edu/lro/lro-l-lola-3-rdr-v1/lrolol_1xxx/browse/lola_gdr/.
- [4] *Wilk K. A. et al.* Variations in surface adsorbed H₂O on lunar soils and relevant minerals // *Icarus*. 2024. V. 411. Article 115945.
- [5] *Tabuteau H. et al.* Impact of spherical projectiles into a viscoplastic fluid // *Phys. Rev. E*. 2011. V. 84. No. 3. Article 031403.
- [6] *Ivanov B. A.* The end-member model of quasi-viscous relaxation of impact craters in lunar regolith // *Dynamic Processes in Geospheres: Proc. IDG RAN*. 2018. V. 10. P. 54–61 (in Russian). http://idg.chph.ras.ru/data_files/%23СБОРНИК_2018_8.11_CORR.pdf.
- [7] *Xiao J., Jiang S., Tang J. et al.* A study of high-velocity penetration on icy lunar regolith simulants, *International // J. Mechanical Sciences*. 2024. VI. 271. Article 109147. <https://doi.org/10.1016/j.ijmecsci.2024.109147>.

LUNAR DUSTY PLASMA AND ITS INVESTIGATION PROPOSAL

I. Kuznetsov¹, A. Zakharov¹, G. Dolnikov¹, I. Dokuchaev¹, A. Lyash¹,
A. Dubov¹, M. Abdelaal¹, V. Grushin¹, A. Kartasheva¹, E. Kronrod^{3,4},
T. Morozova¹, S. Popel¹, A. Poroykov², I. Shashkova¹, O. Voshchan¹

¹ Space Research Institute RAS, Moscow, Russia, kia@cosmos.ru

² National Research University "Moscow Power Engineering Institute"
Moscow, Russia

³ Vernadsky Institute of Geochemistry and Analytical Chemistry RAS
Moscow, Russia

⁴ Kazan Federal University, Kazan, Russia

KEYWORDS:

dust, lunar dust, dusty plasma, lunar lander, Luna-25, Luna-27, Moon, asteroids

INTRODUCTION:

Atmosphereless bodies are covered by a dust particles layer. Under the sun irradiation conditions, solar wind interaction, micrometeorites bombardment these dust particles start moving and levitating. Under the anthropogenic influence the amount of the lofted off particles could become danger for the mechanical parts of the spacecraft, solar arrays and cosmonauts in the case of manned missions.

It is important to investigate the dynamics of the dusts in order to study how to prevent the influence of dust during the lunar exploration.

DUST MONITORING INSTRUMENT:

Based on the ideas of the PmL instrument for Luna-25 mission a number of improvements for the next generation dusty plasma monitoring instrument is suggested. The possible orbit or in-situ configuration for the instrument is proposed.

ACKNOWLEDGEMENTS:

The study was carried out with the financial support of Russian Science Foundaton, grant No. 24-12-00064, <https://rscf.ru/project/24-12-00064/>.

LUNAR CRATERS WITHOUT SIGNS OF THE MATTER MELTING AND THE MATTER EMISSIONS

M. I. Shpekin¹, R. T. Ferreyra²

¹ Kazan Federal University, Russia, MichaelS1@yandex.ru

² Universidad Nacional de Córdoba, Argentina
ricardo.tomas.ferreyra@unc.edu.ar

KEYWORDS:

impact crater, impact crater structure, Aitken crater floor, bulbous fields, crater topography, Lunar quickmap, crater diameter, crater deep, crater formation process, lunar soil melt, impactor, domes formation

INTRODUCTION:

The classic idea of impact craters is that all craters are divided into two groups: simple and complex. If the crater has a central peak, then the crater is complex. If there is no peak, then the crater is simple. However, the achievements of orbital observations in recent years have made it possible to detect craters that do not belong to these two groups.

One of the first publications in this direction was a report presented at the 14th Moscow Symposium on the Solar System. The authors examined the “bulbous fields” area at the floor of young impact Aitken crater. The task was to understand the unusual topography of a group of 5 small craters included in the named area. The surface of the floor of three of the five craters is covered with domes, which led to the naming of such surfaces as “bulbous fields”. During the analysis, the authors found that one of the five craters differs markedly from the others in its topography. In particular, this crater attracted attention by the topography of the floor. There was no melt of matter in the form of solidified magma at its floor, as happens in simple craters. But the central peak in this crater is also missing. Instead, a smooth convex surface covered with small impact craters is confidently visible. It is also characteristic that in the vicinity of this crater there is no material of the substance ejected as a result of the impact that led to the formation of the crater. As a working hypothesis, the authors suggested that the described crater contains the body of the impactor, which deepened when falling into the molten lake of the Aitken crater floor.

At the same time, the impactor did not undergo destruction. This could be due to the fact that at the time of the shock of the impactor, the surface of the Aitken bottom had not yet completely cooled down, and the melt substance was in a viscous state. As a result of the introduction of the impactor's body into the bottom of the Aitken, a shock wave arose, which could lead to the formation of domes of “bulbous fields”. The energy of this shock wave was apparently enough not only to form domes, but also to break through the cover of the bottom of the Aitken in two places near the rim of craters with domes. As a result, and this is clearly visible in the ultra-high resolution images, the melt of the substance in the two named places came to the surface of the Aitken bottom, headed south towards the Aitken rim and formed lava tubes.

This report attempts to find similar craters in other regions of the Moon. The presence of such craters on the Moon is not only of theoretical interest, since it expands and complements the generally accepted idea of simple and complex craters. The practical significance of such craters lies in the fact that small asteroids, meteorites or fragments of them may turn out to be preserved impactors.

Then such craters appear to be objects of increased interest for upcoming lunar expeditions.

Table 1 shows the list of 6 craters whose bottom shape is noticeably different from most other lunar craters.

Table 1. List of the lunar craters with unusual floor shape

Nº	Name	Lat, deg	Long, deg	D1, km	D2, km	Comments
1	Nameless	-16.66	174.16	4.3	1.5	Near the Aitken G crater
2	Chebyshev V	-33.51	226.01	21.8	7.5	In the center of Chebyshev crater
3	Sanford C	33.85	222.62	18.5	4.5	Sanford C, 175 km northwest of the large crater Kovalevskaya
4	Nameless	-14.49	269.56	3.3	0.6	On the bottom of the Mare Orientale, 80 km east of the Maunder crater
5	Nameless	-17.78	267.15	1.6	0.4	In the center of the Mare Orientale, 30 km east of the Hohmann crater
6	Nameless	-19.43	263.07	4.3	1.0	On the Mare Orientale, approx-ly in the middle between the craters Hohmann and Hohmann Q

ACKNOWLEDGMENT:

We acknowledge the use of imagery from Lunar quickmap (<https://quickmap.lroc.asu.edu>), a collaboration between NASA, Arizona State University and Applied Coherent Technology Corp.

REFERENCES:

- [1] *Shpekin M.I., Shishkina V.S.* The structure features of young impact craters in the area of "bulbous fields" on the aitken crater floor // 14th Moscow Solar System symposium 14M-S3: Book of Abstr. 2023. P. 143–145.
- [2] *Ferreira R. T., Shpekin M. I.* A fluid dynamical model to shape complex craters // 34th Intern. Conf. Interaction of Intense Energy Fluxes with Matter (EOS-2019): Book of Abstr. 2019. 397 p.
- [3] *Shpekin M., Ferreira R.* Estimation of the state of matter in young impact craters on the Moon based on the orbital observations // WCCM-APCOM2022, 10 p. DOI: [dx.doi.org/10.23967/wccm-apcom.2022.047](https://doi.org/10.23967/wccm-apcom.2022.047).
- [4] *Shpekin M. I.* Relief of the marginal zone of the Moon in the area of the Orientale Mare. Kazan, Dep. VINITI, No. 2652. 1973. 52 p.
- [5] *Watts C. B.* The Marginal Zone of the Moon // Astronomical papers. V. 17. Washington: U.S. Nautical Almanac Office, 1963. 951 p.
- [6] *Nefedev A. A.* Karty rel'efa kraevoi zony Lunny na obshchem nulevom urovne // Kazan': Izd-vo Kazan. un-ta. 1958. 149 p. (in Russian).
- [7] *Shpekin M. I., Salimov R. R., Semenov A. A.* Orbital photogrammetry of selected relief elements with evidences of geological activity in Aitken crater on the far side of the Moon // IOP Conf. Ser.: Earth and Environmental Science. Vladivostok, 2021. Article 062020. DOI: 10.1088/1755-1315/666/6/062020.
- [8] *Shpekin M. I.* Relief of the Orientale Mare // 16 Microsymposium Vernadsky-Brown on comparative planetology. Moscow, 1993.
- [9] *Famutdinov B. M.* Topographic characteristics of the Orientale Mare and the Mirny Sea according to the Zond-8 image processing data: Diploma thesis. Kazan state university, 1986. 78 p.
- [10] *Shpekin M. I., Sitdikova R. A., Khairullina A. I.* Photogrammetry of the volcano and its surroundings on the far side of the Moon // Collection of papers of the 9th Intern. Scientific and Practical Conf. "Research, Development and Application of High Technologies in Industry". 2010. V. 2. P. 283–288.
- [11] *Shpekin M. I.* The Last Apollo Orbit Pass over the Tsiolkovsky crater // Intern. Conf. Astronomy and World Heritage: Across Time and Continents. 2009. P. 219–221.

GLOBAL HALL MHD SIMULATIONS OF THE SOLAR WIND IMPLANTATION FLUX ON THE LUNAR SURFACE

L. Xie, L. Li

State Key Laboratory of Space Weather, National Space Science Center, Chinese Academy of Sciences, Beijing, China, xielianghai@nssc.ac.cn

KEYWORDS:

solar wind-Moon interaction, lunar mini-magnetosphere, Hall MHD simulation

INTRODUCTION:

The Moon represents an airless body with no global magnetic field nor significant atmosphere, where solar wind can directly interact with the lunar surface. With a small part of solar wind protons are reflected from the surface, most solar wind particles are implanted into the surface, leaving a plasma cavity downstream from the Moon. These implanted solar wind particles can alter the physical and compositional properties of the lunar surface, and result in a space weathering process of the surface [1]. Meanwhile, the implanted protons are believed to be an important source for the lunar water group species ($\text{H}_2\text{O}/\text{OH}$), which results in a diurnal variation in the water concentration (Sunshine et al. 2009). In addition, some lunar surface components can be released from the surface by solar wind sputtering, providing an important source for the lunar exosphere [2].

It is important to know the solar wind implantation flux on the lunar surface for both the surface weathering and water production processes. Here we try to study the solar wind implantation flux on the lunar surface with global Hall MHD simulations. The shielding effects of both the Earth's magnetosphere and the lunar magnetic anomalies are considered. The model uses a 450-degree spherical harmonic model to represent the lunar crustal fields and includes the Hall term to study the lunar mini-magnetosphere (LMM). Previously, the model could successfully capture both the sheath of LMM in orbit [3] and the reduced flux of LMM on the surface [4].

We consider that the Moon moves in the GSE XY plane with $1a$ distance of about $60R_E$ to the Earth (Figure 1). We use phase angles in the GSE coordinate system to indicate the different locations of the Moon around the Earth. We choose 8 typical phase angles with an increment of 45° . As shown in Figure 2, the normalized number flux basically show a circular shape with the maximum flux at the subsolar point, consistent with a cosine function of the solar wind incidence angle. However, the circular shape can be interrupted by the magnetic anomalies due to the magnetic shielding effect. Apart from the shielding of lunar magnetic anomalies, there is also a shielding of the Earth's magnetosphere, which leads to a very low implanted flux when the Moon in the magnetotail (phase angle equals to 180°).

To investigate the long-term effect of solar wind implantation and relate it to the space weathering of lunar surface, we calculate the integrated implantation flux over one lunation. We divide the lunar orbit into 72 intervals and calculate the normalized implantation flux (number flux or energy flux) for each interval with the global Hall MHD model. We add all of the normalized fluxes together and divide the sum by 72 to obtain the average flux per lunation. Such an average flux can be used to evaluate the long-term effect of solar wind implantation. As shown in Figure 3, the average energy flux are decreasing with an increasing latitude, associated with the dependence on solar wind incidence angles. Additionally, these fluxes show a longitudinal variation with a minimum flux at 0° longitude, caused by the shielding of Earth's magnetosphere. In addition, there are many local flux cavities associated with the magnetic anomalies. These cavities are co-located with most lunar swirls found by [5] and [6].

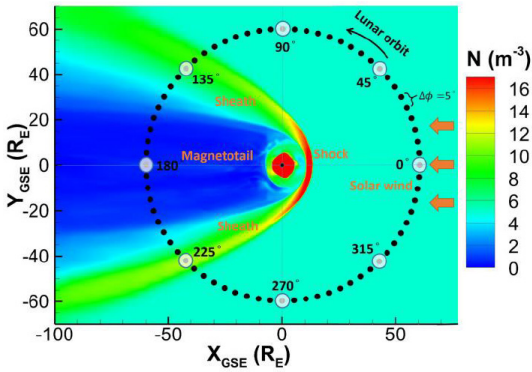


Fig. 1. Different locations of the Moon during its orbit around the Earth. The color contours show the number densities of the Earth’s magnetosphere. The black dots show the different lunar locations in the GSE XY plane, in which the circled dots indicate the locations with an interval of 45°, whose implantation flux maps are shown in Figure 2

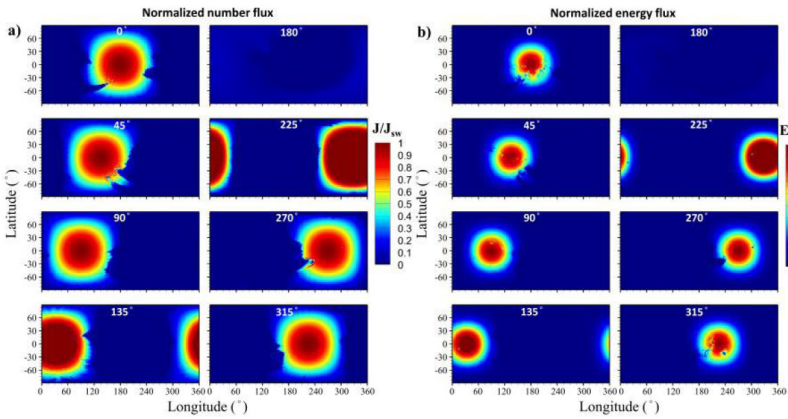


Fig. 2. The maps of implanted number flux at different phase angles, in which the number fluxes are normalized by the solar wind number flux (a). The maps of implanted energy flux at different phase angles, in which the energy fluxes are normalized by the solar wind energy flux (b)

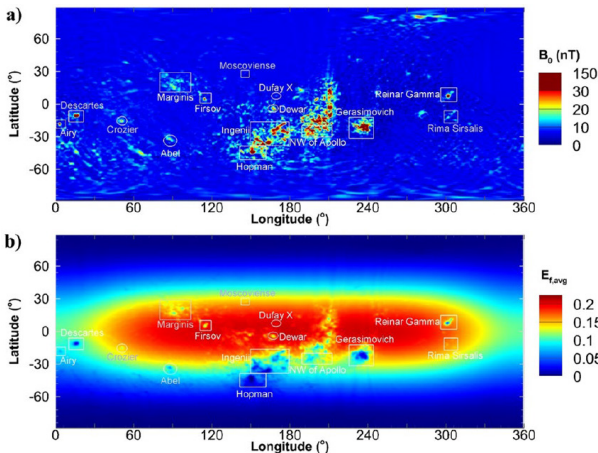


Fig. 3. The map of magnetic field strength on the lunar surface, obtained from the 450-degree spherical harmonic model (a). The map of the average energy flux over one lunation, in which the rectangles indicate the locations of lunar swirls found so far (b)

In general, our results provide a global map of the solar wind implantation flux on the lunar surface and are useful for evaluating the large-scale effect of solar wind implantation and sputtering on the space weathering and the water or gas generation of the surface. Next, a Monte Carlo model is needed to study the shielding effect of magnetic anomalies on the generation and immigration of water molecules and other exospheric species.

REFERENCES:

- [1] Pieters C.M., Noble S.K. Space weathering on airless bodies // *Geophysical Research: Planets*. 2016. V. 121. Iss. 10. P. 1865–1884. <https://doi.org/10.1002/2016JE005128>.
- [2] Sarantos M., Killen R.M., Glenar D.A. et al. Metallic species, oxygen and silicon in the lunar exosphere: Upper limits and prospects for LADEE measurements // *J. Geophysical Research*. 2012. V. 117. Article A03103. DOI: 10.1029/2011JA017044
- [3] Xie L., Li L., Zhang Y., et al. Three-dimensional Hall MHD simulation of lunar minimagnetosphere: General characteristics and comparison with Chang'E-2 observations // *J. Geophysical Research*. 2015. V. 120. Iss. 8. P. 6559–6568. <https://doi.org/10.1002/2015JA021647>.
- [4] Xie L., Li L., Zhang A. et al. Inside a Lunar Mini-Magnetosphere: First Energetic Neutral Atom Measurements on the Lunar Surface // *Geophysical Research: Letters*. 2021. V. 48. Iss. 13. Article e2021GL093943. <https://doi.org/10.1029/2021GL093943>.
- [5] Blewett D.T., Coman E.J., Hawke B.R. et al. Lunar swirls: examining crustal magnetic anomalies and space weathering trends // *Geophysical Research: Planets*. 2011. V. 116. Article E02002.
- [6] Denevi B.W., Robinson M.S., Boyd A.K. et al. The distribution and extent of lunar swirls // *Icarus*. 2016. V. 273. P. 53–67. <https://doi.org/10.1016/j.icarus.2016.01.017>.

LUNAR MISSION ON THE NORTHERN AND SOUTHERN POLES WITH TWO IDENTICAL LANDERS: GOALS AND OBJECTIVES

L. M. Zelenyi, I. G. Mitrofanov

Space Research Institute RAS, Moscow, Russia, roste@cosmos.ru

KEYWORDS:

Moon exploration, polar lunar science, twin landers to both poles

ABSTRACT:

Landing missions to the lunar south pole are now the major elements of the strategical plans of Moon exploration of leading space agencies. On the other hand, Moon has two poles, and the Northern one is thought to be as attractive place for investigation, as the Southern one. Moreover, the parallel studies of the Moon from both poles provides unique opportunities for understanding the internal structure of its body as well as the global exospheric processes around it.

Main goals of lunar polar landing missions will be considered.

Scientific, technical and economic arguments will be presented to perform the project Luna-27, as the twin of polar landers, one to North and another one to South poles, as the integrated scientific mission for the Moon investigation.

DEVELOPMENT OF A PROJECT OF KEY OBJECTS OF MOBILE ROBOTICS FOR THE LUNAR STATION

M. I. Malenkov, V. A. Volov, A. N. Bogachev, N. K. Guseva, E. A. Lazarev
 Scientific and Technical Center "ROCAD", Saint Petersburg, Russia
 m.i.malenkov@gmail.com

KEYWORDS:

Self-propelled chassis (SPC), Intelligent Mobile Platform (IMP)

INTRODUCTION

In the report on 13MS3, the authors analyzed domestic engineering solutions for the creation of a lunar station and proposed their concept for establishing a mobile robotics park to support various stages of the station's construction and development [1]. To ensure precise design and layout developments and computational-theoretical justifications, the Malapert massif was selected as the construction site for the station [2]. Cylindrical modules with approximate characteristics of the ISS modules were selected as characteristic cargoes that will need to be transported from the landing area to the installation site. Cylindrical modules with characteristics similar those of the ISS modules were chosen as representative cargoes to be transported from the landing area to the installation site. The far side of the moon was identified as a primary objective for expeditions, where scientific equipment could be delivered, and an automatic observatory branch established. Along the planned route (approximately 400–600 km) and in its most interesting surroundings, activities such as soil drilling, scientific research, and the installation of a high-speed communication line between the observatory and the station, along with mobile communication, are envisioned.

DESIGN OF THE SELF-PROPELLED CHASSIS FOR INTELLIGENT MOBILE PLATFORM:

The authors propose creating a complete mobile robotics suite for the lunar station, ranging from rovers for surveying the construction site to mobile robotic complexes (MRC) for long-distance expeditions, based on 2–3 modifications of the IMP. The design of the self-propelled chassis (SPC) for the IMP is illustrated in Figure 1. Built-in and mounted sensors of the SPC are not shown in Figure 1; their purpose and design will be determined at later stages of development.

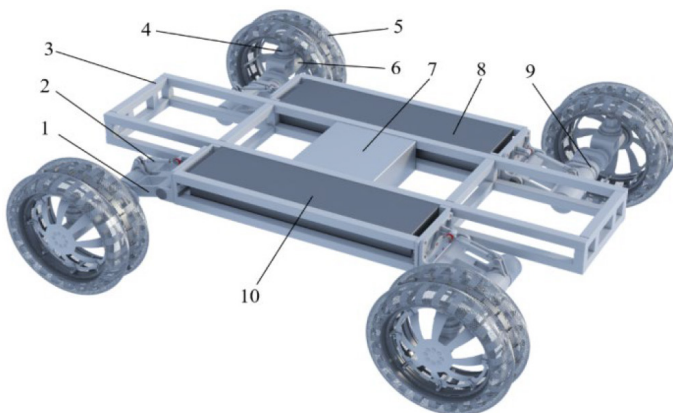


Fig. 1. Self-propelled chassis for the intelligent mobile platform: 1, 2 — Balancer and reactive traction bar of the passive (torsion) suspension [2]; 3 — Self-propelled chassis frame; 4 — Steering drive of the motor-wheel; 5 — Metal-elastic wheel with profile mesh tire [3]; 6 — Traction drive of the motor-wheel; 7 — Chassis automation unit; 8, 10 — Traction battery and the control battery; 9 — Drive of the active double-lever suspension [4]

As seen in Figure 1, the SPC IMP, unlike the SPC Lunokhod-1, includes rechargeable battery packs since all autonomous tests of the automatic docking-coupling unit (ADCU) of the IMP can only be performed in motion. Regarding the design of the SPC, there are significant changes. To support the functions of the IMP and the placement of mounted equipment, the SPC is assembled on a rigid frame, and its chassis consists of 4 identical support-drive modules (SDM) [5]. The SDM includes a metal-elastic wheel with built-in traction and steering drives, as well as a drive for the active double-lever suspension, which is connected to the frame using the torsion lever-balance passive suspension developed on Lunokhod-1. The passive suspension operates at speeds from 1 to 5 km/h. The active suspension is engaged during IMP maneuvering at a speed of 1 km/h. The IMP also includes an onboard local navigation system and an automatic docking-coupling unit (ADCU).

HEAD LINK OF THE MRC BASED ON STANDARDIZED IMPs:

By the present time, the authors have developed projects for the head link of the MRC, which can be called the "lunar train" (Figure 2), and a two-link coupling for the transportation and installation of lunar station modules.



Fig. 2. Conceptual Design of the Head (Piloted) Link of the Lunar Train: 1, 9 — Active and passive parts of the ADCU; 2 — Cabin windshield; 3 — Airlock chamber for surface access; 4 — Pin antenna; 5 — Highly directional antenna; 6 — Panoramic camera (in deployment); 7 — Solar panel (in deployment); 8 — Airlock chamber for docking with the second link of the lunar train; 10 — Self-propelled chassis of the IMP

The mass of the IMP is up to 500 kg, the total mass of the link is 3000 kg, the power of the traction motors of the motor-wheels is 400 W, and the maximum slope angle on the regolith is 20°. Details are provided in the report. All technical solutions are protected by A. S. patents or are in the process of being patented. The new developments build upon the creative foundation of A. L. Kemurdzian's school.

ACKNOWLEDGEMENTS:

We thank prof. M. A. Ivanov and prof. A. T. Basilevsky of the V. I. Vernadsky Institute of Geochemistry and Analytical Chemistry of the Russian Academy of Sciences (GEOKHI RAS) for their support of the project concerning the movement conditions of the MRC in the Malapert massif area. We also thank D. V. Sidorov for his contribution to the development of 3D-models and animations.

REFERENCES:

- [1] *Basilevsky A. T. et al.* Potential lunar base on mons malapert: topographic, geologic and trafficability considerations // *olar System Research*. 2019. V. 53. No. 5. P. 383–398.
- [2] *Bechvay N. E. et al.* Independent balancing suspension of wheels transport. Vehicles with built-in motors. A. S. 272076 dated 13.09.1968. MPK B60g 11/20.

- [3] *Mitin B. V. et al.* Vehicle Wheel. A. S. 839740 of 30.11.1979. M.KI.V60V 1/100.
- [4] *Volov V.A. et al.* Wheel-walking propulsion with the function of active suspension. Patent RF No. 2671661 for application No. 2017122305 dated 06/23/2017. MPK I62V 57/02/
- [5] *Malenkov M. I. et al.* New design and layout solutions for manipulation system, Movement and navigation system for improving the mobility of planetary rovers // Technical Sciences. 2017. No. 3. P. 42–54.

APPLICATION OF SELECTIVE LASER MELTING FOR LUNAR SOIL ANALOGUE

I. A. Agapkin, E. M. Sorokin

*Vernadsky Institute of Geochemistry and Analytical Chemistry RAS
Moscow, Russia, agapkin@geokhi.ru*

KEYWORDS:

Moon, additive manufacturing, selective laser melting, lunar soil analogue, in situ resource utilization

INTRODUCTION:

In the context of In-Situ Resource Utilization (ISRU), applying additive manufacturing technologies with lunar regolith as the primary building material for lunar infrastructure development appears to be the most promising approach [1]. Selective Laser Melting (SLM) presents a promising approach for additive manufacturing of lunar construction materials, offering a distinct advantage in its ability to produce durable components of diverse geometries with relatively high speed [2, 3]. This technique eliminates the need for additional binding agents, relying solely on the energy input of the laser to consolidate the powdered material. This inherent characteristic renders SLM particularly suitable for utilizing lunar regolith as a primary construction material. This paper presents the results of the initial phase of research on applying SLM to lunar soil simulant samples. Volcanic ash from the Kamchatka Peninsula, with chemical, mineralogical, and granulometric properties similar to lunar regolith, was used as a simulant.

SAMPLE PREPARATION:

The particle size of lunar regolith is comparable to that of terrestrial volcanic ash [4]. Furthermore, some volcanic ashes share similar chemical and mineralogical compositions with lunar regolith [5]. From the perspective of implementing additive manufacturing technologies, mimicking the chemical and mineralogical composition of lunar regolith is a crucial requirement for the simulant. For this study, volcanic ash samples from Tolbachik volcano (Kamchatka Peninsula) were chosen as a lunar regolith simulant. X-ray fluorescence analysis was employed to determine the chemical composition of the Tolbachik samples and compare it with the Apollo-12 mission sample, known for its low titanium content [6]. Table 1 shows that Tolbachik and Apollo 12 possess a similar chemical composition.

Table 1

Sample, %	Tolbachik	Lunar regolith (Apollo 12) [6]
L. O.I.*	0.32	0.004
Na ₂ O	2.51	0.48
MgO	7.09	9.91
Al ₂ O ₃	13.58	13.71
SiO ₂	51.45	46.17
P ₂ O ₅	0.17	0.31
K ₂ O	0.92	0.27
CaO	11.53	10.55
TiO ₂	1.06	3.07
MnO	0.12	0.22
FeO	9.96	15.41

The mineral composition of the sample was also determined using X-ray diffraction analysis: plagioclase (45 %), potassium feldspar (4.8 %), pyroxene (39.7 %), and olivine (10.5 %). The amorphous phase content in the sample can reach up to 30 %. Lunar regolith exhibits magnetic properties, which influence sintering processes. Therefore, volcanic sand from Khalaktyrsky beach (ranging from 10 to 30 %) was added to the sample,

with the assumption of minor changes in the chemical, mineralogical, and granulometric compositions.

EXPERIMENT:

The study utilized a BetaMark 2000 setup equipped with a Nd-YAG laser. During the experiments, the primary objective was to achieve the sintering of the most durable sample with minimal energy and time expenditure. A critical task was to determine the optimal configurations of the laser system that satisfy the experimental criteria. Numerous experiments were conducted with various laser settings. It was observed that samples with lower volcanic sand content sintered less effectively. A component measuring 14×4×2 mm was fabricated in two cycles under the following processing parameters: laser pulse frequency of 50 kHz, printing speed of 6 mm/s, and current of 13 A. The sample comprised 70 % volcanic ash and 30 % volcanic sand. (Figure 1, left). A series of experiments were performed within these setting ranges. Microhardness measurements were conducted on the sintered samples using a Shimadzu DUH-211s instrument (Figure 1, right). The average microhardness value was 630 HV.

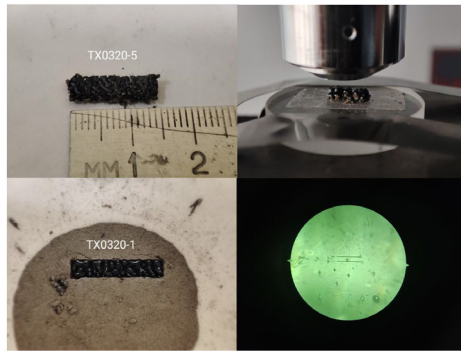


Fig. 1. Result of SLM experiment (left); Microhardness determination (right)

RESULTS:

The research demonstrated that the presence of volcanic magnetic sand enhances the sintering process. Optimal laser system configurations were identified, allowing the creation of 14×4×2 mm components with a microhardness value of 630 HV. Further research plans involve developing a methodology for creating larger components and investigating the influence of the chemical, mineralogical, and physical properties of the samples on sintering processes.

REFERENCES:

- [1] *Isachenkov M. et al.* Regolith-based additive manufacturing for sustainable development of lunar infrastructure: An overview // *Acta Astronautica*. 2021. V. 180. P. 650–678.
- [2] *Goulas A., Friel R.J.* 3D printing with moon dust // *Rapid Prototyping J.* 2016. V. 22. No. 6. P. 864–870.
- [3] *Ginés-Palomares J.C. et al.* Laser melting manufacturing of large elements of lunar regolith simulant for paving on the Moon // *Scientific Reports*. 2023. V. 13. No. 1. Article 15593.
- [4] *Agapkin I.A.* The Kamchatka Volcanic Ashes as a Lunar Soil Analogue (Physical Properties) // *13th Moscow Solar System Symp.* 2022. P. 170–172.
- [5] *Slyuta E.N. et al.* Natural Lunar Test Site on Earth // *13th Moscow Solar System Symp.* 2022. P. 164–166.
- [6] *Just G. H. et al.* Geotechnical characterisation of two new low-fidelity lunar regolith analogues (UoM-B and UoM-W) for use in large-scale engineering experiments // *Acta Astronautica*. 2020. V. 173. P. 414–424.

3D PRINTING OF LUNAR REGOLITH: TESTING PHYSICAL CONDITIONS FOR IMPLEMENTATION OF SLM TECHNOLOGY

A. M. Lysenko^{1,2}, T. M. Tomilina^{1,2}, D. I. Lisov¹, P. R. Savvatimova^{1,2},
A. A. Anikin¹, I. G. Mitrofanov¹

¹ Space Research Institute RAS, Moscow, Russia, lysenko@imash.ac.ru

² Mechanical Engineering Research Institute RAS, Moscow, Russia

KEYWORDS:

Moon exploration, lunar regolith, 3D printing, SLM

ABSTRACT:

Currently, there is an active process of “returning humans to the Moon,” where significant attention is focused on the utilization of lunar regolith, as a material for *in-situ* fabrication of lunar infrastructure elements. The feasibility of using regolith in this context has been demonstrated in several studies (see, as example, [1–3]), including ones by the authors of this paper. Testing samples were produced from the regolith simulants using additive manufacturing techniques, specifically selective laser melting (SLM). After proving the feasibility of fusing samples from the lunar regolith simulants, the authors focused on more detailed investigations to identify the best physical conditions of SLM for creating bulk products in the form of a three-dimensional structure from individual melted tracks of lunar regolith.

The paper presents the results of detailed studies of single tracks produced by SLM to determine the optimal conditions of melting, such as particle size distribution of the used powder, power for melting and layer thickness. The paper also presents the initial results of theoretical modeling of the laser fusion process of the lunar regolith layer.

About 1,000 single tracks have been produced and analyzed. The best conditions of the SLM process are identified for further experiments of 3-D printing with the laboratory prototype of the Lunar Printer instrumentation.

REFERENCES:

- [1] Goulas A., Binner J. G. P., Harris R. A. et al. Assessing extraterrestrial regolith material simulants for in-situ resource utilization based 3D printing // *Applied Materials Today*. 2017. V. 6. P. 54–61.
- [2] Tomilina T., Kim A., Lisov D., Lyzenko A. Porosity and compressive strength of test samples produced by SLM using rock gabbro-dabase based powder as a lunar regolith simulant // *Acta Astronautica*. 2024. T. 215. P. 493–495.
- [3] Tomilina T. M., Kim A. A., Lisov D. I., Lyzenko A. M. A Lunar Printer Experiment on Laser Fusion of the Lunar Regolith in the Luna-Grunt Space Project // *Cosmic Research*. 2023. V. 61. No. 4. P. 314–323.

A CONCEPT OF A SIMPLE SMALL-SIZED (5–10 KG) LUNAR ASTRONOMICAL UV TELESCOPE USING HIGH TRL COMPONENTS

A. Shugarov¹, M. Sachkov¹, H. Wang^{2,3}, X. Jiang^{2,3}, V. Shmagin¹,
A. Buslaeva¹, I. Savanov¹, X. Zhang^{2,3}, J. Wang^{2,3}

¹ Institute of Astronomy RAS, Moscow, Russia, shugarov@inasan.ru

² National Astronomical Observatory China CAS, Beijing, China
wanghj@nao.cas.cn

³ University CAS, Beijing, China, xjjiang@nao.cas.cn

KEYWORDS:

UV astronomy, Moon-based telescope, ILRS, UV detector

ABSTRACT:

The project of a relatively simple and small-sized (5–10 kg) Lunar astronomical telescope for the UV and optical spectral ranges using already-proven space technical solutions can be proposed for upcoming missions to the Moon, for example, for the Russian LUNA missions. Such a telescope can be considered as a pathfinder for the future larger aperture lunar-based UV-Optical-IR telescope for ILRS [1, 2] in both scientific and technological aspects.

We consider two main options to quickly build a small astronomical telescope using already proven high Technology Readiness Levels (TRL) components. The first option is to use a space laser communication telescope with a 2-axis mount with a flight heritage by replacing the laser with a scientific UV-optimized detector and modifying the telescope to operate in the UV-range. The second option is to use a modified advanced star tracker by replacing its optics and detector with UV-optimized enlarged ones.

The technological aspects that can be evaluated and verified by a small Moon-based telescope are: the effect of the Moon's dust on astronomical optics and the efficiency of different protection methods (if implemented on a small telescope), stability of the Moon lander on the lunar regolith at the sub-arcsecond level, experience in conducting astronomical observations in difficult scattering light conditions and thermal conditions on the Moon during the Moon's day and night. The real experimental data from this small Moon telescope will be of high importance to design future ILRS missions [3].

The location of the telescope on the Moon will allow to probe new unique methods of astronomical observations from the Moon, that can't be done from other orbits close to the Earth:

- synchronous observation in triangulation mode with Moon and ground base telescopes (Moon-Earth base) of dangerous asteroids in the near-Earth space for faster and more accurate determination of their orbits,
- observation of asteroids and comets close to the Sun from the Moon,
- evaluation of the efficiency of occultation observation by the Moon surface or Moon crater hill.

Among other common scientific tasks for a small Moon telescope, we can mention: gravitational wave counterparts, TDE, shock waves and explosions of young supernovae, the Universe in the ultraviolet range using deep co-adds, observation of the Earth's exosphere and its composition, extent and interaction with solar wind and solar flares, three-dimensional view of the Earth's exosphere from lunar orbit, etc.

The lack of sensitivity of a small aperture telescope can be partially compensated by the huge amount of time it would spend observing each object of interest. A modern CMOS detector with sub-electron readout noise allows for digital co-adding of a large number of images taken using a dithering technique to obtain sufficiently detailed images with diffraction-limited angular resolution and high dynamic range. Also, such a CMOS

allows for a digital TDI mode of observation for the Moon telescope without a mount. To provide multiband UV photometry several multilayer filters can be deposited on the CMOS detector, such an approach allows for avoiding of movable parts.

The parameters of the laser communication telescope mount are suitable for astronomical purposes since it provides tracking with an accuracy of 1 arcsec while the space platform may rotate with an angular speed of ≥ 0.5 deg/s, the resulting area of the telescope repointing is about $180 \times 90^\circ$. The weight of the optical assembly without electric controller units is about 5 kg and the expected total weight of the telescope with harnesses and control units is less than 10 kg. The required installation space on the Moon lander including clearance for telescope repointing is 400×400 mm.

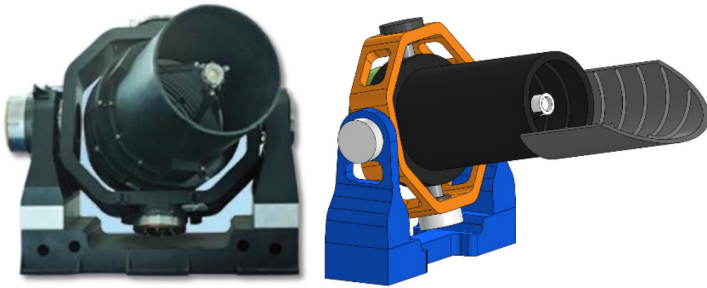


Fig. 1. Left: space laser communication telescope with an aperture of 70 mm from a Chinese company; right: the concept of a compact 70 mm UV-optical lunar astronomical telescope based on a similar design

The laser communication telescope will be modified to achieve diffraction-limited quality at 115 nm (resolution of 2 arcsec) and to provide better scattering light supersession (Figure 1). The estimated delivery time of a flight sample of the telescope based on a laser communication terminal, with modification to be used for astronomy, is about 2 years. The main telescope parameters are:

Aperture	70 mm
Focal length	2000 mm
Field of view	0.38 \times 0.38 deg (on the detector 13.3 \times 13.3 mm)
Spectral range	125–900 nm
D_{80}	0.30 μ m at 125 nm (\sim 2 arcsec)
Pixel scale	0.43 arcsec/pixel (4.25 μ m)
Detector format	3120 \times 3120 pixels (GSENSE4225BSI CMOS)



Fig. 2. An off-the-shelf star tracker from a Chinese company with an aperture of 80 mm (left) and its baffle tube (right)

Another approach to build the Lunar UV telescope for upcoming missions to the Moon using available components with a flight heritage is to use an advanced star tracker but replace its lens with an UV-optimized one of

a larger aperture, use an UV-enhanced sCMOS, and have an ultra-wide field of view of $\sim 5.5 \times 5.5$ deg. Such a telescope will be fixed on the Moon lander and observation will be performed in a passive scan mode. Alternatively, an active scan mode with a compact mount can be realized. The expected mass budget is less than 10 kg.

The implementation of a simple small-sized (5–10 kg) lunar astronomical telescope will provide valuable experience in conducting astronomical observations from the Moon and allow us to design future more ambitious missions, such as the ILRS astronomical UV-Optical-IR telescope.

REFERENCES:

- [1] Wang H., Chen X., Sachkov M. et al. A brief introduction to the astronomical research for ILRS // Intern. Workshop on Overall Science Objectives of ILRS. 2023.
- [2] Wang H., Sachkov M., Dong S. et al. Optimizing scientific objectives for the lunar-based UV-optical-IR telescope for ILRS // 14th Moscow Solar System Symp.: Abstr. Book. 2023. P. 119–120.
- [3] Shugarov A. S., Wang H., Dong S. et al. The concept of Lunar-based astrophysical telescope for international lunar research station // Vestnik NPO Lavochkina. 2022. No. 1(55). P. 3–9.
- [4] Shugarov A. S., Sachkov M., Wang H. et al. Astrophysical UV-optical-IR telescope for the international lunar research station // 14th Moscow Solar System Symp.: Abstr. Book. 2023. P. 154–156.
- [5] Sachkov M., Shugarov A., Shmagin V. Ana Inés Gómez de Castro: The concept of lunar-based astrophysical telescope for international lunar research station (ILRS) // Proc. SPIE. V. 12181: Space Telescopes and Instrumentation. 2022. Ultra-violet to Gamma Ray. Article 121812V.

MOON-BASED CONTINUOUS COORDINATE-PHOTOMETRIC MONITORING OF THE ASTEROID-COMET HAZARD THROUGHOUT THE CELESTIAL SPHERE

H. I. Abdussamatov

Pulkovo Observatory RAS, Saint Petersburg, Russia, abduss@gaoran.ru

KEYWORDS:

asteroid-comet hazard, lunar platforms, single system two twin telescopes, protect lens telescope

INTRODUCTION:

Potentially dangerous near-Earth asteroids and comets, especially those approaching the Earth from the side of the Sun, constitute the largest threat, since they are more numerous than massive bodies and appear unexpectedly. Therefore, they are still the least studied celestial bodies, and those which present the greatest danger. Continuous coordinate-photometric monitoring and research of the asteroid-comet hazard throughout the celestial sphere requires the creation of long-term stationary space platforms precisely on the surface of the Moon facing the Earth.

CONTINUOUS COORDINATE-PHOTOMETRIC MONITORING OF THE ASTEROID-COMET HAZARD:

The lunar platforms that we develop consist of a system of two twin telescopes working sequentially as a single telescope only in the daytime continuously during 100 % of the lunar day in the automatic mode as a single telescope, according to the joint science program of observations of the stellar field (patents No. 2591263 and 155044 of Russia). Twin telescopes will be placed along the equator on the opposite edges apparent surface of the Moon at the longitude $\pm(81\pm 0.1^\circ)$ and at the latitude $\pm(0\pm 1^\circ)$. The lunar platforms present a single system of two modernized special optical robotic twin telescopes with the primary mirror of the diameter 300 mm and with a sliding visor (SOTR-300VM). The alt-azimuthal mounting of SOTR-300VM robotic telescopes along two axes provides any necessary tilts and azimuthal directions of the telescope tube at a needed angle, which makes it possible to observe astronomical objects over the entire celestial sphere above the lunar horizon up to the altitude 90° and for all azimuths. To protect the lens of the telescope from the solar and Earth's radiation at the angular separation of more than 15° , the hood will be used, consisting of two halves of a cylinder, fold back to horizontal sides along the tube in the course of transportation. The telescopes will use (single or mosaic) CCD matrix $\sim 32\times 32$ mm ($\sim 8000\times 8000$ pixels) as the radiation detector. By shielding the entrance pupil from solar and terrestrial radiation with a hood the twin telescopes can also detect asteroids and comets approaching the Earth from the side of the Sun (at an angular separation exceeding 15°), thereby contributing very substantially into planetary defense. Continuously during 100% of the lunar day the system of twin telescopes sequentially, taking turns only throughout the daytime will survey the stellar field of the entire sky over the total broad working field of view $2.2\times 2.2^\circ$ (over the entire spectral range 0.2–2 micron and in its three individual broad bands) with a resolution of $\sim 1''/\text{pixel}$. And this system will be carrying out coordinate-photometric monitoring and study of potentially dangerous near-Earth asteroids and comets, especially those approaching the Earth from the side of the Sun and also supernovae and novae. The very slow axial rotation of the Moon will significantly increase the accuracy of positioning with the optical telescope, which will make it possible to significantly lengthen the time of exposure and, consequently, significantly increase the number of used stars and identified asteroids and comets. The system of SOTR-300VM sequentially will be able to provide a complete survey of the stellar field of the entire sky with the exposure of 30–60 s for

the time of the 360 hours taking into account the semidiurnal axial rotation of the Moon. An individual survey of an area of the sky around the Sun at an angular separation exceeding 15° will be carried out for every 36 hours. Thereby, the system of SOTR-300VM telescopes will be able to detect bodies with the diameter above 10 m, the most interesting from the point of the asteroid and comet hazard. The system of SOTR-300VM telescopes will become a professional "Space Patrol" carrying out the early detection of near-Earth asteroids and comets, especially those approaching the Earth from the side of the Sun. There is no other alternative "non-lunar" methods or ways for continuously monitoring throughout the celestial sphere of this most important problem of the asteroid-comet hazard.

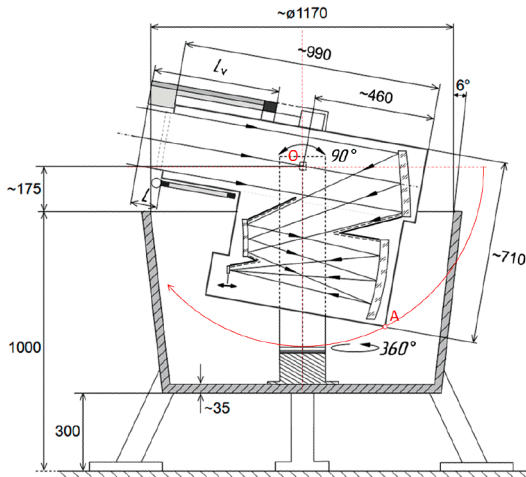


Fig. 1. Longitudinal section of SOTR-300VM with a folded-out frosted glass in a dustproof bowl and its overall dimensions (the sun lens hood not indicated)

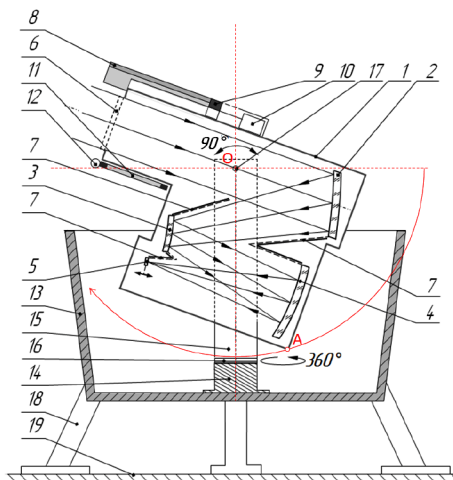


Fig. 2. The general view of SOTR-300VM with a reclined diffusing glass in the dust-protecting cup in the longitudinal section. The optical system is placed within a reliable hermetic enclosure

In order to protect the mirror from the surface-borne particles of charged lunar dust, SOTR-300VM is mounted in the central zone of a special cup, which displays the shape of upturned truncated cone. In the horizontal position of the tube, the lower edge of the entrance pupil of the telescope is higher than the upper level of the cup, and the edges of the tube without the visor in the vertical projection do not reach the upper inner surface of the cone of the cup. The cup features supporting legs with the vertical

height of about 300 mm; they are calculated taking into account the total mass of the set and all possible overweight, including those occurring in the course of landing of the set onto the Moon's surface. The cup is made so that it may be placed above a relatively smooth flat area with an incline up to 7° on the lunar surface with its upper level at the height exceeding 1000 mm above the surface. To protect the telescope mirror from the surface-borne charged particles of the lunar dust, the outer surfaces of the cup and the entrance pupil, as well as the surface of the mirror, are covered with electrically isolated conducting envelopes, connected with the electrical power unit placed in the cup. The electrical power unit displays electric charge with the specified frequency of the polarity inversion — in particular, depending on the alternation of day and night (patents No. 164303 and 2613048 of the Russia). A sliding visor and a charge drain protect the optical elements from lunar dust and its electric charge. A specialized dust-protecting cup of SOTR-300VM will be adapted as a landing module with soft landing engines to install the telescope on a required area of the lunar surface. To this end, a successful experience of mounting in 2013 of the China Lunar-based Ultraviolet Telescope (LUT), analogous in all technical parameters, without a landing unit and without the assistance of cosmonauts may be used. SOTR-300VM with lightweight mirrors in the protecting cup, without the solar panels and soft-landing engines will have mass of one set less than 100 kg, and the dimensions — less than $1500 \times 1500 \times 1500$ mm, and the required electric power — about 200 W.

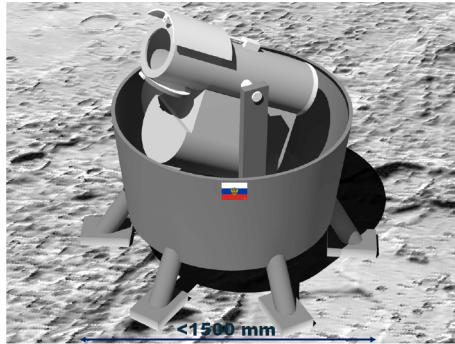


Fig. 3. General view of the SOTR-300VM complex on the lunar surface (solar panels, soft landing engines and a sun lens hood not indicated)



Fig. 4. Functioning of the system of two SOTR-300VM carrying out the all-sky survey by monitoring near-Earth asteroids and comets, particularly moving from the side of the Sun, supernovae and novae in daytime, as a single telescope

CONCLUSIONS:

1. The system of twin telescopes will be continuously carrying out coordinate-photometric monitoring and study of potentially dangerous near-Earth asteroids and comets, especially those approaching the Earth from the side of the Sun, and also supernovae and novae. SOTR-300VM

telescopes of the Lunar Observatory (LO) will be able to detect bodies with the diameter above 10 m, the most interesting from the point of the asteroid and comet hazard.

2. Obviously, the complex of tasks solved by the LO will remain extremely important in solving fundamental scientific and applied problems throughout this century and beyond. Therefore, this system of twin telescopes of the LO should be updated every 15–20 years with a new modernized system with an extended science program to carry out continuous research.

REFERENCES:

- [1] *Abdussamatov H.I.* Moon-based monitoring of the Earth's energy imbalance and climate, near-Earth asteroids and comets, potentially habitable exoplanets, supernovae and novae // *J. Indian Society of Remote Sensing*. 2024. V. 52(10). <https://doi.org/10.1007/s12524-024-01971-6>.

RECENT PROGRESS ON THE LUNAR-BASED UV-OPTICAL-IR TELESCOPE FOR ILRS

H. J. Wang^{1,2}, M. Sachkov³, S. Dong⁴, X. Bai^{1,2}, A. Shugarov³,
X. Jiang^{1,2}, H. Tian⁵, N. Jiang⁶, Y. Deng^{1,2}, G. Zhao^{1,2}, X. Zhang^{1,2},
V. Shmagin³, B. Shustov³, S. Sichevskij³, A. Buslaeva³, I. Savanov³,
J. Wang^{1,2}, J. Wang¹, H. Zhi¹, L. Wang^{1,2}, B. Yan^{7,8}, Y. Tang^{7,8}, X. Zeng¹,
T. Li^{1,2}

¹ National Astronomical Observatories, Chinese Academy of Sciences (NAOC)
Beijing, China, wanghj@nao.cas.cn

² University of Chinese Academy of Sciences, Beijing, China
xybai@nao.cas.cn

³ Institute of Astronomy RAS, Moscow, Russia, msachkov@inasan.ru

⁴ Department of Astronomy, School of Physics, Peking University
Beijing, China, dongsubo@pku.edu.cn

⁵ School of Earth and Space Sciences, Peking University, Beijing, China
huitian@pku.edu.cn

⁶ Department of Astronomy, University of Science and Technology of China
Hefei, China, jnac@ustc.edu.cn

⁷ School of Physics, Zhejiang University of Technology, Hangzhou, China,
boyan@zjut.edu.cn

⁸ Collaborative Innovation Center for Bio-Med Physics Information
Technology of ZJUT, Zhejiang University of Technology, Hangzhou, China

KEYWORDS:

UV-Optical-IR telescope, lunar-based, ILRS, evolution of galaxies, transients, habitability

ABSTRACT:

Thanks to the unique advantages of the lunar-based environment, we have the opportunity to conduct multi-wavelength, high-precision observations with an unprecedentedly wide wavelength coverage, extending from extreme ultraviolet (EUV) to infrared (IR). With a lunar-based UV-Optical-IR telescope/array, we can study the evolution of galaxies, explore high-energy transients and variable events in the local universe, investigate the habitability of exoplanets based on space weather phenomena and the influence of small bodies in planetary systems, and discover new terrestrial exoplanets in the habitable zones [1–9]. We will provide some new considerations and recent progress on the scientific and technic aspects of the lunar-based UV-Optical-IR telescope/array for the International Lunar Research Station (ILRS) in this talk.

REFERENCES:

- [1] Wang H., Sachkov M., Dong S. et al. Optimizing scientific objectives for the lunar-based UV-optical-IR telescope for ILRS // 14th Moscow Solar System Symp. 14M-S3: Abstr. book. 2023. P. 119–120. DOI: 10.21046/14MS3-2023.
- [2] Shugarov A. S., Sachkov M., Wang H., Dong S. et al. Astrophysical UV-optical-IR telescope for the international lunar research station // 14th Moscow Solar System Symp. 14M-S3: Abstr. book. 2023. P. 154–156. DOI: 10.21046/14MS3-2023.
- [3] Wang H., Sachkov M., Dong S. et al. A brief introduction about the science of the Lunar-based UV-Optical-IR telescope for ILRS // 2023 Asia-Pacific Regional IAU Meeting (APRIM 2023). 2023.
- [4] Wang H., Chen X., Sachkov M. et al. A brief introduction to the astronomical research for ILRS // Intern. Workshop on Overall Science Objectives of ILRS. 2023.
- [5] Shugarov A. S., Wang H., Dong S. et al. The concept of Lunar-based astrophysical telescope for international lunar research station // Vestnik NPO Lavochkina. 2022. Vyp. 1(55). P. 3–9 (in Russian). DOI: 10.26162/LS.2022.71.64.001.
- [6] Shugarov A., Dong S., Wang H. et al. The concept of moon-based UV survey to study transients and variables // 13th Moscow Solar System Symp. 13M-S3: Abstr. book. P. 106–107. DOI: 10.21046/13MS3-2022.
- [7] Wang H., Sachkov M., Dong S. et al. Science of the lunar-based UV-optical-IR telescope for ILRS // 13th Moscow Solar System Symp. 13M-S3: Abstr. book. 2022. P. 108. DOI: 10.21046/13MS3-2022.

- [8] *Shugarov A., Sachkov M., Wang H. et al.* The concept of Lunar-based UV-Optical-IR Telescope for ILRS //12th Moscow Solar System Symp. 12M-S3: Abstr. book. 2021. P. 441–443. DOI: 10.21046/12M-S3.
- [9] *Sachkov M., Shugarov A. Shmagin V., de Castro A. I. G.* The concept of lunar-based astrophysical telescope for international lunar research station (ILRS) // Proc. SPIE. V. 12181: Space Telescopes and Instrumentation. 2022: Ultraviolet to Gamma Ray. Article 121812V. DOI: 10.1117/12.2629619.

OPTICAL IMAGING OF THE MOON LANDING SITE AS THE DATA FOR HAZARD AVOIDANCE

M. V. Djachkova, I. G. Mitrofanov, D. I. Lisov, M. L. Litvak, B. S. Zhukov
Space Research Institute RAS, Moscow, Russia, djachkova@np.cosmos.ru

KEYWORDS:

Moon, landing, LRO, LROC, roughness

ABSTRACT:

Safe landing as the top priority of the lander missions can be reached by the hazard avoidance systems installed onboard the spacecraft. Optical cameras are usually used as a component of the hazard avoidance system. In this work, we investigate the representation of the relief hazards, i.e. dangerous slopes and surface roughness, in the optical images, and thus a usability of optical camera for the purposes of safe landing in terms of relief.

The distribution of brightness in the optical image should be determined by the distribution of surface slope and aspect (azimuth of the slope). Thus, the surface roughness, expressed by the variability of two angles — slope and azimuth, will be expressed in the variability of the brightness of the surface area. The images taken by Narrow Angle Camera onboard Lunar Reconnaissance Orbiter [1] were used in this analysis. The Vector Ruggedness Measure (VRM, [2]) was used as a characteristic of the variability of slope and azimuth. VRM quantitatively determines the roughness of the terrain by measuring the dispersion of vectors orthogonal to the surface of the terrain. The comparison between the image brightness for different Sun altitudes and the terrain characteristics was performed. The results showed no strong correlation between the values of brightness and VRM especially for the low-Sun images.

However, the variety of brightness can be used as a parameter for surface suitability for landing. We suggest several procedures for image processing that would help to select an optimal landing site and increase the level of the landing safety.

REFERENCES:

- [1] *Robinson M. S. et al. Lunar Reconnaissance Orbiter Camera (LROC) Instrument Overview // Space Science Reviews. 2010. V. 150. P. 81–124.*
- [2] *Sappington J. M. et al. Quantifying Landscape Ruggedness for Animal Habitat Analysis: A case Study Using Bighorn Sheep in the Mojave Desert // J. Wildlife Management. 2007. V. 71. P. 1419–1426.*

UNEXPECTED COMPONENTS IN CHANG'E-5 SOIL SAMPLE

S. I. Demidova, C. A. Lorenz, D. D. Badyukov, L. A. Lakhmanova,
N. N. Kononkova

*Vernadsky Institute of Geochemistry and Analytical Chemistry RAS
Moscow, Russia, demidova.si@yandex.ru*

KEYWORDS:

Chang'E-5, regolith, High-Mg Suite rocks, Fe oxide, metal-sulfide aggregates

INTRODUCTION:

Chang'e-5 delivered 1.731 kg of soil sample from the mare basalt region of the northern Oceanus Procellarum in 2020. Recent years the soil sample was carefully studied by all available methods. To understand the source materials that have contributed to the landing site region we focused on search for unusual components in the Chang'E-5 soil sample. Here we report preliminary results of study of some exotic components found.

SAMPLE AND METHODS:

1.5g of Chang'E-5 soil sample was exchanged and stored in the Lunar Sample Collection of Russian Academy of Sciences. Less than 0.01 mg of the sub-sample represented by the drilled material was placed on the carbon tape and carbon coated for preliminary EDS analysis (energy dispersive spectroscopy) and imaging with a Tescan Mira 3 FEG SEM at the Vernadsky Institute (Moscow, Russia). The secondary electron (SE) imaging of the surface was carried out with an electron beam accelerating voltage of 10 kV at a working distance of 5 mm. Acquisition of additional BSE and qualitative elemental maps was conducted with an electron beam accelerating voltage of 20 kV at a working distance of 15 mm. After that the fragments were mounted in the polished thin sections. Unfortunately the Fe-oxide grain was lost during preparation. Major element compositions of other fragments were determined using the Electron Probe MicroAnalysis (EPMA) facility with wavelength-dispersive spectrometers (WDS) CAMECA SX-100 at the Vernadsky Institute (Moscow, Russia).

RESULTS:

A fragment of an impact melt monomict breccia #1 (150×200 μm in size) contains fragments of anorthositic-troctolitic rocks and minerals embedded into a glassy matrix. Mg-rich olivine (Fo₈₄₋₈₆) is associated with Ca-rich plagioclase (An₉₅₋₉₇) with single pyroxene fragment (En₄₂Wo₃₇). Matrix glass has low alkalis and TiO₂ (0.5 and 0.6 wt% respectively), high Al₂O₃ content (16 wt%) and MG# number (58 at %). Olivine has 0.5-0.6 wt% of Al₂O₃, 0.7–0.8 wt% of CaO and 0.2 wt% of Cr₂O₃.

The small Fe oxide particle #2 (35×40 μm in size) represents a fragment of a once spherical particle with a strong metallic shine. An amazing feature of the fragment is a texture similar to framboidal. The spherule consists of aggregate of crystals with smoothed octahedral habitus (2–4 μm in size). The spherical part of the fragment is covered with evenly distributed small (0.2–3 μm in size) debris of lunar mineral fragments and glass spherules. The mineral phases are mostly represented by plagioclase, pyroxene and ilmenite with rare silica, K-glass, Cr-ulvöspinel, and single phosphate and Zr-phases and are constituent to the mineral phases observed in Chang'E-5 basalts. The chip side of the fragment is fragmentally covered with thin nm-sized glass films and glass splashes on its surface.

Unusual metal grains #3 are 1-5 μm "haired" crystals represented by densely packed aggregates of elongated filamentous crystals of 50–150 nm in width. They are present as individual grains in the regolith or in association with fine troilite aggregates. These aggregates are common on the surfaces and interiors of some glassy particles [1]. Metal «haired» crystals are characterized by Ni-free composition.

DISCUSSION:

The regolith is dominated by fragments of local rocks and their derivatives but always contains material brought from far located areas as well as exogenic material. Chang'E-5 sample is dominated by intermediate-Ti mare basalts of (~2.0 Ga) [2] with only rare fragments of introduced rocks, such as: high-Ti vitrophyre, a low-Ti basalt, an olivine-pyroxenite, a magnesian anorthosite, an evolved lithology and a Mg-rich olivine fragment [3], iron meteorite fragment [4] as well as space weathering products represented by rare Ti phases [5] and Cu-sulfide, native copper and FeCo alloy assemblage [6].

High-Mg Suite rock #1

The mineral chemistry as well as matrix glass composition clearly distinguishes this impact melt breccia from the Chang'E-5 basaltic unit characterized by more Fe- and Ti- and alkali-rich composition as well as different mineral association. High MG# and Cr content in olivine is more constituent to the High-Mg Suite highland rocks [7] not previously described in Chang'E-5 soil sample.

Fe-oxide #2

EDS analyses and crystal form of the Fe-oxide suggest that this fragment could be magnetite framboid similar to observed in terrestrial and chondritic material [8]. We do not believe that this fragment was produced by terrestrial contamination as there are clear evidences of staying in the regolith. However the origin of the fragment is debatable. Previously magnetite has been found in Apollo 16 lunar breccia 60016 as magnetite-troilite silicate assemblage [9]. Besides that magnetite was mentioned as sub-microscopic magnetite in the isolated spherical iron-sulfide grains (<2 µm in diameter) in the Chang'E-5 lunar fines [10] but framboid texture is not mentioned for this finds and sulfides have not been observed in the studied fragment. Framboidal texture results probably from rapid nucleation in environments where magnetite is strongly supersaturated which can be achieved by changing pH and/or temperature [8] but oxidized environment is required for its formation that is unexpected for the lunar highly reduced conditions. Small magnetite framboid-like crystals 5–15 µm in size were noted in carbonaceous chondrites of CI, CR, CM groups where they often replace Fe sulfides as pseudomorphs, frequently being formed by aqueous alteration processes [11–13]. But the absence of sulfides as well as rather big size of the studied framboid distinguishes it from chondritic ones too.

Metal "haired" crystals #3

Systematic occurrence of the metal-sulfide association clearly indicates it as source of the individual "haired" metal grains. The aggregates consist of Ni-poor native iron and troilite and possibly are not concerned with processing of meteorite material due to the impacts but connected to the troilite precipitation. The latter occurs on the surface of vesicular glasses and can be interpreted as condensates from gaseous or fluid phase initially present in the closed vesicle due to pressure and temperature drop when the vesicle became opened. We suggest that this type of native iron could be formed due to a thermal decomposition of troilite.

So, new finds give us some additional information about lithological diversity and surficial regolith processes in the region of Chang'E-5 landing site.

REFERENCES:

- [1] Yan P., Xiao Z., Wu Y., Pan Q., Wu Y. Iron-rich grain-decorated depressions on surfaces of lunar impact glasses // *J. Geophys. Res.: Planets*. 2024. V. 129. e2024JE008284
- [2] Che X., Nemchin A. A., Liu D., Long T., Wang C., Norman M. D., Joy K. H. et al. Age and composition of the youngest basalts on the Moon returned by the Chang'e-5 // *Science*. 2021. V. 374. P. 887–890.
- [3] Zeng X., Li X., Liu J. Exotic clasts in Chang'e-5 regolith indicative of unexplored terrane on the Moon // *Nat. Astron.* 2023. V. 7. P. 152–159.
- [4] Liu X., Gu L., Tian H., Li J., Tang X., Hua S., Lin Y. First classification of iron meteorite fragment preserved in Chang'e-5 lunar soils // *Sci. Bull.* 2024. V. 69. P. 554–561.
- [5] Zeng X., Wu Y., Yu W. Unusual Ti minerals on the Moon produced by space weathering // *Nat. Astron.* 2024. V. 8. P. 732–738.

- [6] *Li J., Gu L., Tang X., Liu X., Hu S., Lin Y.* First discovery of impact-induced vapor deposition of native copper, FeCo alloy and digenite from Chang'e-5 lunar soil // *Icarus*. 2024. V. 415. Article 116082.
- [7] *Shearer C. K., Elardo S. M., Petro N. E., Borg L. E., McCubbin F. M.* Origin of the lunar highlands Mg-suite: An integrated petrology, geochemistry, chronology, and remote sensing perspective // *Am. Mineral*. 2015. V. 100. P. 294–325.
- [8] *Sawlowicz Z.* Framboids: from their origin to application // *Mineralogical Transactions*. 2000. V. 88. 80 p.
- [9] *Joy K. H., Visscher C., Zolensky M. E., Mikouchi T., Hagiya K., Ohsumi K., Kring D. A.* Identification of magnetite in lunar regolith breccias 60016: Evidence for oxidized conditions at the lunar surface // *Meteorit. Planet. Sci.* 2015. V. 50. P. 1157–1172.
- [10] *Guo Z., Li C., Li Y., Wen Y., Wu Y., Jia B., Tai K., Zeng X., Li X., Liu J., Ouyang Z.* Sub-microscopic magnetite and metallic iron particles formed by eutectic reaction in Chang'e-5 lunar soil // *Nat. Commun.* 2022. V. 13. Article 7177.
- [11] *Zolensky M. E., Ivanov A. V., Yang S. V., Mittlefehldt D. W., Ohsumi K.* The Kaidun meteorite: Mineralogy of an unusual CM1 lithology // *Meteorit. and Planet. Sci.* 1996. V. 31. P. 484–493.
- [12] *Lipschutz M. E., Zolensky M. E., Bell M. S.* New petrographic and trace element data on thermally metamorphosed carbonaceous chondrites // *Antarct. Met. Res.* 1999. V. 12. P. 57.
- [13] *Chan Q. H. S., Zolensky M. E., Martinez J. E., Tsuchiyama A., Miyake A.* Magnetite plaquettes are naturally asymmetric materials in meteorites // *Am. Mineral*. 2016. V. 101. P. 2041–2050.

EXPERIMENTAL DATA ON THE OCCURRENCE AND CHEMICAL COMPOSITION OF METALLIC IRON NANOSPHERULES AND COMPARISON WITH DATA FROM THE CHANG'E-5 LUNAR SOIL

E. M. Sorokin¹, O. I. Yakovlev¹, E. N. Slyuta¹, M. V. Gerasimov²,
M. A. Zaitsev², K. M. Ryazantsev¹

¹ Vernadsky Institute of Geochemistry and Analytical Chemistry RAS
Moscow, Russia, egorgeohim@ya.ru

² Space Research Institute RAS, Moscow, Russia

KEYWORDS:

lunar soil, space weathering, np-Fe⁰, laser experiment, micrometeorite bombardment, Chang'e-5

INTRODUCTION:

As a result of micrometeorite bombardment, nano- and submicroscopic spherules of metallic iron (npFe⁰) form in regolith grains of airless bodies. The presence of nanophase iron (npFe⁰) significantly alters the reflection spectrum of such bodies — it weakens the characteristic absorption bands in the visible and near-infrared ranges, shifts the intensity of reflected light toward longer wavelengths, and reduces the overall albedo [1–3]. npFe⁰ is formed through the condensation of vapor generated by the shock evaporation of lunar rocks during micrometeorite bombardment. Nanophase iron is particularly often found as a thin amorphous film on the surface of mineral particles [4, 5].

EXPERIMENTAL METHODS, TECHNIQUE AND STUDY

OF THE SAMPLES:

For the experiment a pulsed neodymium glass laser was used. The laser radiation wavelength was 1.06 μm, the pulse duration was 10⁻³ s, and the pulse energy was ~600–700 J. The energy flux density was ~10⁶–10⁷ W/cm². The temperature at the “impact” point was of the order of 4000–5000 K, which corresponded to the evaporation temperature during high-speed impact processes with collision velocities of the order of 10–15 km/s [6, 7]. In the experiment, we used several types of targets — tholeiite recrystallized basalt, basalt glass, several types of olivines. Craters were analyzed for basaltic glass and olivine, both in plan and profile. Spherules npFe⁰ up to 5 μm in size were analyzed by the EDS method. To determine the chemical composition of submicron iron spherules, we analyzed craters in targets made of ferruginous olivine and basalt glass.

The analysis was performed on a TESCAN MIRA 3 scanning electron microscope with an X-MAX 80 EDS analyzer (Vernadsky institute).

RESULTS:

In our experiments, we obtained relatively large spherules ranging in size from a few microns to 5 μm: 29 spherules in basalt glass and 36 in Fe-olivine. These spherules can be analyzed using a scanning electron microscope (Figure 1). Although the determination of oxygen using the EDS method is semi-quantitative and is influenced by the oxidation of the metal phase in air, as well as within the scanning electron microscope chamber. For instance, up to 1.5 % oxygen is detected in the cobalt standard due to the formation of an oxide film. We can indirectly demonstrate that high concentrations of elements in their reduced state are present, even considering possible contamination from condensate material that may have deposited from the vapor cloud above the crater.

Trace elements detected in these micron-sized spherules include Ni (<1 %), Si (up to 5 %), P (up to 14 %), S (up to 0.2 %), along with other elements (Table 1). The content of elements such as Al, Mg, and Ca correlates directly

with the oxygen content, while P, Si, and Ni do not show this correlation (Figure 2).

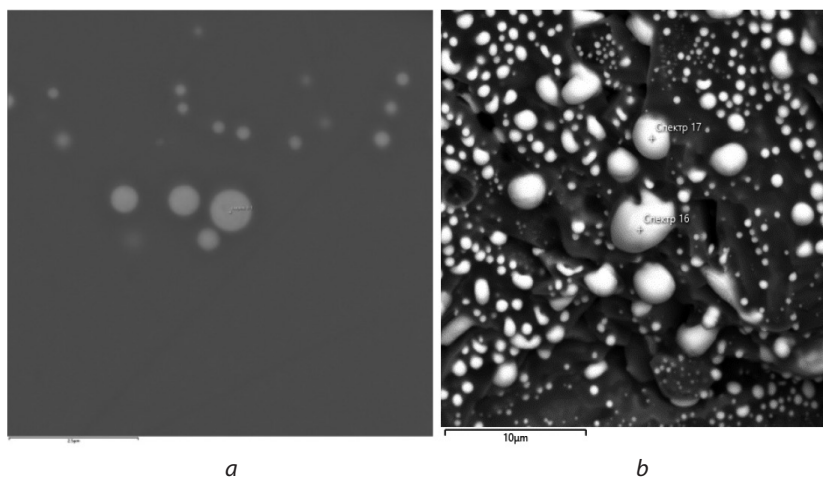


Fig. 1. Sub-microspheres which were analyzed by SEM EDS method: *a* — in basalt glass (2,5 μm); *b* — in olivine

CONCLUSION:

Metallic iron spherules were produced in a laser experiment, with the largest ones measured using the EDS method on a scanning electron microscope. The analyses indirectly indicated that within the brief duration of the experiment, approximately a millisecond, both the thermal reduction of iron oxide and silica occurred, with silicon subsequently dissolving in the iron melt. Additionally, the melt became enriched with siderophilic elements such as phosphorus (P) and sulfur (S).

REFERENCES:

- [1] Hapke B. // *J. Geophys. Res.* 2001. V. 106. P. 10039–10073.
- [2] Pieters C. M. et al. // *Meteorit. Planet. Sci.* 2000. V. 35(5). P. 1101–1107.
- [3] Pieters C. M., Noble S. K. // *J. Geophys. Res. Planets.* 2016. V. 10. Article 121.
- [4] Keller L. P., McKay D. S. // *Science.* 1993. V. 261. P. 1305–1307.
- [5] Keller L. P., McKay D. S. // *Geochim. Cosm. Acta.* 1997. V. 61. P. 1–11.
- [6] Gerasimov M. V. et al. // *Lab. Astrophys. Space Res.* 1999. V. 236. P. 279–330.
- [7] Sorokin E. M. et al. // *Proc. 52nd Lunar and Planetary Sci. Conf.* 2021. Article 1975.

MORPHOLOGY OF IMPACT INDUCED CONDENSATES: LUNAR FINDINGS AND EXPERIMENT

M. V. Gerasimov¹, O. I. Yakovlev², S. I. Demidova²

¹ Space Research Institute RAS, Moscow; Russia, mgerasim@cosmos.ru

² Vernadsky Institute of Geochemistry and Analytical Chemistry RAS
Moscow, Russia

KEYWORDS:

vaporization, condensation, Chang'E-5 lunar regolith, morphology of condensates, nano-globules

INTRODUCTION:

Processing of silicates during hypervelocity collisions is a fundamental process which affects the evolution of solid material in the Solar system and in the Universe as well. Impacts on planetary surfaces proceed at velocities in excess of 10 km/s and provide partial or complete vaporization of colliding material. Subsequent expansion and cooling of impact-generated vapor plumes produce condensed particles with nanometer sizes. Investigation of trends of differentiation of silicate material during impact-induced vaporization is important for understanding of early evolution of planetary bodies. Laboratory simulation of impact-induced vaporization — condensation processes is limited to a few millimeter scales. It is important to know the relevance of laboratory produced condensates to that produced in nature during real impacts.

The Moon has preserved impact-produced condensates which can be found on surfaces of lunar rocks and glasses. These condensates was found to have composition noticeably different from melts (e. g. [1, 2]) that shows deep differentiation of silicate material during high-temperature pulse processing.

Experiment:

The goal of our work was to produce experimentally impact-simulated condensates with different elemental composition and compare their morphology with that on lunar condensates. Simulation of impact-generated condensates was done using laser pulse technology [3]. We used diverse samples representing terrestrial rocks and minerals, meteorites, and volatile-rich mixtures to simulate cometary impacts. We tried to compare laboratory produced condensates with that found on Chang'E-5 Luna regolith samples based on their morphology.

We have discovered several types of condensates which have twins among lunar condensates (e.g. Figure 1, 2). Histograms of condensed nano-globules indicate that both lunar condensed particles and that from experiments have the main mode about 30–50 nm.

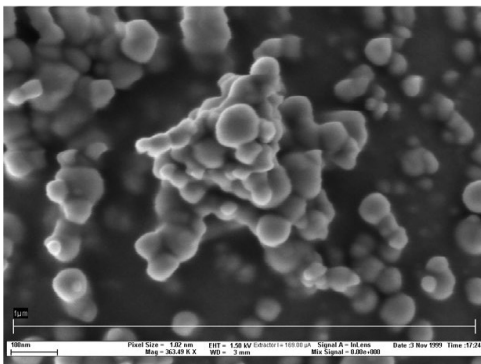


Fig. 1. Condensed nano-globules on a surface of glass droplet from laser-pulse experiment with carbonaceous chondrite Murchison (CM2)

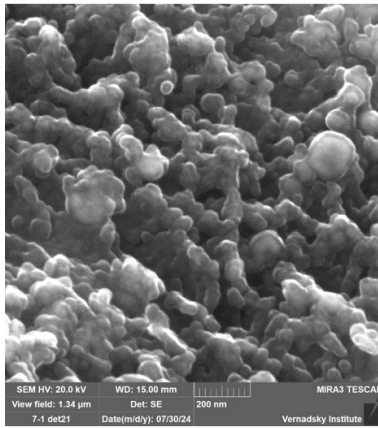


Fig. 2. Condensed nano-globules on a surface of Chang'E-5 regolith particle

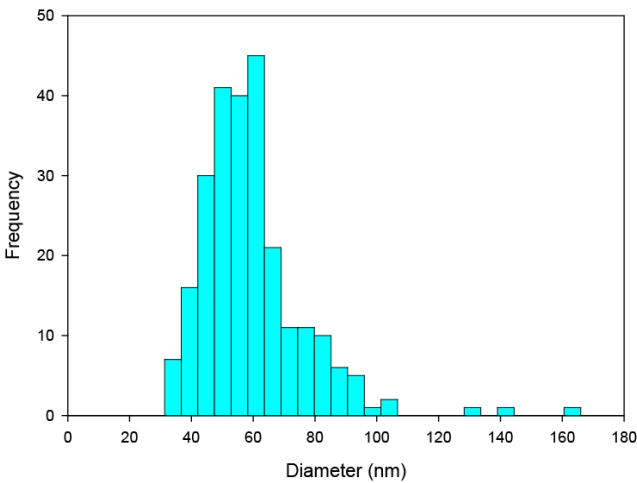


Fig. 3. Histogram of Figure 2 nano-globules dimensions

REFERENCES:

- [1] Keller L. P., McKay D. S. The nature and origin of rims on lunar soil grains // *Geochim. et Cosmochim. Acta.* 1997. V. 61. No. 11. P. 2331–2341.
- [2] Warren P. H. Lunar rock-rain: Diverse silicate impact-vapor condensates in an Apollo-14 regolith breccias // *Geochim. et Cosmochim. Acta.* 2008. V. 72. P. 3562–3585.
- [3] Gerasimov M. V. et al. Physics and chemistry of impacts // *Earth, Moon, and Planets.* 1998. V. 80. No. 1–3. P. 209–259.

VOLATILES IN THE LUNAR REGOLITH DELIVERED BY CHANG'E-5 MISSION: PRELIMINARY RESULTS

M. A. Zaitsev, M. V. Gerasimov, A. S. Kuzovchikova

Space Research Institute RAS, Moscow, Russia, mzaitsev@cosmos.ru

KEYWORDS:

lunar matter, volatile components, Chang'E-5, pyrolysis mass spectrometric analysis

INTRODUCTION:

During the previous missions, lunar matter samples from over a dozen areas were delivered to the Earth. The elemental (including isotopic) and mineral composition of the samples was determined, that gave a general idea of the lunar matter and its age. The composition of volatile components was also studied. Generally, the lunar matter is depleted in volatile components and the early impression was that the Moon is totally degassed planetary body. Detailed investigation of lunar regolith samples and basalts provided valuable information on chemical composition and concentration of volatiles. Volatile components can come into the interior of the Moon with its building blocks (planetesimals) and then transported to lunar surface due to magmatic/volcanic activity. The sources of volatiles can be asteroids, comets and interplanetary dust, emitting a variety of volatile components during their impact-initiated processing. The source of hydrogen and water can also be solar wind interaction with the lunar soil. Each source has its distinctive properties which can be used for interpretation of the volatiles source. Investigation of the lunar volatiles is important since it provides valuable information on current evolutionary activity of the Moon.

The abundances of some volatile components in the lunar regolith according to the literature sources [1–16] are shown in Table 1:

Table 1. Abundances of some volatiles in the lunar regolith [1–16]

Substance	CO ₂ /CO	H ₂ O	H ₂	H ₂ S	CH ₄ /C ₂ H ₆	HCN	N ₂	He	Ne	Ar	Kr	Xe
Abundances in the lunar regolith, ppm of mass (µg/g)	≤200/≤500	0,06–5	2–55	10–100	(0,4–3,2)/(0,1–9)	1–2,6	12–130	14–84	1,2–26	0,47–12,3	6,5·10 ⁻⁵ –0,06	9,0·10 ⁻⁵ –3,8·10 ⁻³

EXPERIMENTS:

We studied parts of two samples of lunar regolith from Chang'E-5 mission provided by the China National Space Administration (CNSA) to the Russian Federation: the scooped sample CE5C0100 GYFM007 and the drilled sample CE5Z0900 GYFM001.

As terrestrial contamination dramatically affects extraterrestrial samples, especially volatiles-poor ones, the special infrastructure was made to work with the regolith samples, to prevent and control possible contamination. A glove chamber was built, which was equipped with the system giving extra pure nitrogen (≥99,9999 %) from the special generator or/and gas cylinders. The chamber was also equipped with a vacuum system, which was used for outgassing the content of the chamber prior starting any manipulations with the regolith. The gas atmosphere in the chamber was constantly monitored with DSQ II mass-spectrometer for gas and light volatile impurities during all of preparation stages and manipulations with the regolith. Heavier impurities were trapped with complex 0.25×3.5" adsorption tubes

and analyzed periodically with GS/MS analytical complex (Chromatec-Crystal 5000.2 GC/MSD) equipped with a dual stage thermal desorption system. For the pyrolysis — mass-spectrometric analysis a lunar matter sample (accurately weighed) was placed inside a 5.0 mm O.D.×2.0 mm I.D.×100 mm length quartz test tube inside the glove chamber. The open side of the tube was then connected with a Vespel ferrule to a special gas-vacuum gasket. The gasket had been connected previously to the GC-column inlet of the DSQ II mass-spectrometer through a special valve that could be opened by heating of its heating coil. MS-analysis was started and the valve was then opened. As the tube was vacuumed and tested for leaks, the gas/vacuum system prior the MS-detector was removed from the chamber by opening a dedicated plug. Then the system was placed inside a GC-thermostat (in order to heat gas pipes to prevent the adsorption of volatiles) and the end of the tube (~20 mm) was put inside the furnace equipped with a silicon carbide tube heater. The thermostat was heated up to 250 °C with 50 °C/min rate. After that the furnace with the tube was heated up to 1500 °C with the same rate. The same procedures were conducted for the empty test tubes, calibration and test samples.

The work is in progress. Some preliminary results will be reported.

ACKNOWLEDGMENTS:

The authors are cordially grateful to the CNSA for providing of the two samples of lunar regolith delivered by Chang'E-5 mission and the Committee on Extraterrestrial Matter of the Russian Academy of Sciences for its permission for using some parts of these samples in our experiments.

REFERENCES:

- [1] *Becker R. H.* // Proc. 11th Lunar Planet. Sci. Conf. Geochim. Cosmochim. Acta. 1980. Article 1743.
- [2] *Carr R. H., Bustin R., Gibson E. K.* A pyrolysis/gas chromatographic method for the determination of hydrogen in solid samples // *Analytica Chimica Acta*. 1987. V. 202. P. 251–256.
- [3] *Epstein S., Taylor H. P., Jr.* // Proc. Apollo 11 Lunar Sci. Conf. Geochim. Cosmochim. Acta. 1970. Article 1085.
- [4] *Epstein S., Taylor H. P., Jr.* The concentration and isotopic composition of hydrogen, carbon and silicon in Apollo 11 lunar rocks and minerals // *Science*. 1970. V. 167. Article 533.
- [5] *Epstein S., Taylor H. P., Jr.* // Proc. 2nd Lunar Sci. Conf. Geochim. Cosmochim. Acta. 1971. Article 1421.
- [6] *Epstein S., Taylor H. P., Jr.* // Proc. 6th Lunar Sci. Conf. Geochim. Cosmochim. Acta. 1975. Article 1771.
- [7] *Haskin L., Warren P.* Lunar chemistry // *Lunar Sourcebook. A User's Guide to the Moon* / eds. Heiken G. H., Vaniman D. T., French B. M. N.Y.: Cambridge Univ. Press. 1991. P. 357–474.
- [8] *Hintenberger H., Weber H. W., Voshage H. et al.* Concentration and isotopic abundances of the rare gases, hydrogen and nitrogen in Apollo 11 lunar matter // *Proc. of the Apollo 11 Lunar Conference*. 1970. V. 2. P. 1269–1282.
- [9] *Ivanov A. V.* Volatiles in lunar regolith samples: A survey // *Solar System Research*. 2014. V. 48. P. 113–129. DOI: 10.1134/S0038094614020038.
- [10] *McCubbin F. M., Vander Kaaden K. E., Tartèse R. et al.* Magmatic volatiles (H, C, N, F, S, Cl) in the lunar mantle, crust, and regolith: Abundances distributions, processes, and reservoirs // *American Mineralogist*. 2015. V. 100. P. 1668–1707. <http://dx.doi.org/10.2138/am-2015-4934CCBYNCND>.
- [11] *Paul R. Merlivat L., Nief G., Roth E.* // Proc. 3rd Lunar Sci. Conf. 1972. Geochim. Cosmochim. Acta. Article 1473.
- [12] *Petrowski C., Kerridge J. F., Kaplan I. R.* // Proc. 5th Lunar Sci. Conf. Geochim. Cosmochim. Acta. 1974. Article 1939.
- [13] *Simoneit B. R., Christiansen P. C., Burlingame A. L.* Volatile element chemistry of selected lunar, meteoritic, and terrestrial samples // *Geochim. Cosmochim. Acta*. 1974. V. 2. P. 1635–1650.
- [14] *Stoennner R. W., Davis R., Jr., Norton K., Bauer M.* // Proc. 5th Lunar Sci. Conf. 1974. Geochim. Cosmochim. Acta. Article 2211.
- [15] *Wszolek P. C., Simoneit B. R., Burlingame A. L.* Studies of magnetic fines and volatile-rich soils: Possible meteoritic and volcanic contributions to lunar carbon and light element chemistry // *Geochim. Cosmochim. Acta*. 1973. V. 2. P. 1693–1706.

- [16] *Zadorozhniy I. K., Ivanov A. V.* Content and isotopic composition of noble gases in the basic regolith probes of Luna-24 // Lunar soil from Mare Crisium. Moscow: Nauka, 1980. P. 287–299 (in Russian).

OLIVINE STUDIES UNDER LUNAR SURFACE CONDITIONS

S. A. Voropaev, N. V. Dushenko, V. S. Fedulov, A. P. Krivenko, E. V. Jarkova, S. A. Kulikova

*Vernadsky Institute of Geochemistry and Analytical Chemistry RAS
Moscow, Russia, voropaev@geokhi.ru*

KEYWORDS:

olivine, Moon, heating, degassing, water, Raman spectra, crystal structure

INTRODUCTION:

As was shown by the field research of the SPA area of Chinese ChangE-4 mission, olivine is one of the main minerals of the lunar mantle along with pyroxenes [1]. The structural features of this mineral are well studied, which makes it possible to use it as an indicator of the lunar surface' processes [2]. Also, olivines, pyroxenes, Fe-Ti oxides and plagioclases are indicators of the content of Si, Fe, Mg, Ti, Al in the environment as they crystallize at high temperatures. In particular, estimation of the abundance, possible forms and evolution of the lunar rocks' water in the past is actual task, now.

As a rule, minerals transform when external conditions change and are exposed to gases (chemical and physical weathering). Because of this, their identification and characterization of properties are of significant interest to a wide range of researchers — planetary scientists and astronomers. For these purposes, spectroscopy is widely used in remote sensing and astronomical observations of extraterrestrial objects. Spectroscopic methods for studying silicates usually use wavelengths in the visible and infrared spectrum, at which rocks have diagnostic characteristics. In particular, olivines were discovered and studied on the surfaces of Mercury, the Moon, Mars, and a number of asteroids based on analysis of thermal IR spectra [3].

METHODS:

Using gas chromatography, a quantitative assessment of the release of water during stepwise heating in helium from 200 to 1000 °C of olivines and other silicates from igneous rocks (avachite) most similar to the assumed rocks of the lunar mantle was made [4].

Table 1. Gas total content during step heating of the main silicates

Gas/T, °C	Abundance, µg/g 200–1000 °C		
	Olivine	Diopside (Cpx)	Matrix
H ₂	5,5	–	–
N ₂	746	1568	1117
CO ₂	151	515	435
H ₂ O	18,4	0,653	1,78

Table 1 shows the specific content (µg/g) of the main gases released during isothermal exposure after 15 min from olivines and other silicates. In the temperature range 600–800°C, a noticeable increase in the release of water begins, which is apparently associated with a restructuring of the crystal lattice of the mineral. The matrix is significantly dehydrated compared to olivines, but contains more nitrogen (N₂) and carbon dioxide (CO₂). Diopside grains contain even less water than the matrix, but more gases.

The process of restructuring the crystal structure of minerals during thermal metamorphism without oxygen access, accompanied by the release of hematite, Fe₂O₃, is considered by the methods of Raman and IR spectroscopy. The absence of magnetite was shown by X-ray diffraction analysis (see Figure 1).

The structural role of hydroxyl groups –OH and iron of variable valence Fe²⁺/Fe³⁺ will be shown by the example of olivines crystallizing from magma with different oxygen abundance (fO₂ fugitivity).

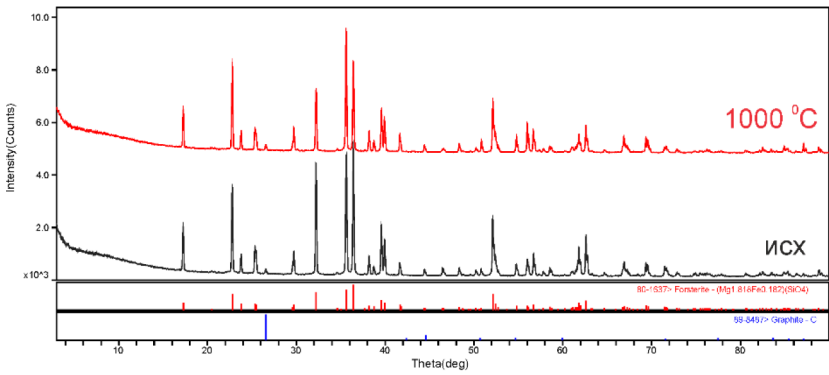


Fig. 1. X-ray diffractograms of olivine: before (black) and after heating (red)

RESULTS AND DISCUSSION:

An assessment of the amount of dissolved gases in a silicate melt from a fluid can be carried out using the so-called activity coefficients γ_i [5]

$$X_i \gamma_i = a_i,$$

where X_i is the mole fraction of dissolved in melt component i (H_2O , CO_2 etc.), a_i is the activity of the i -component in the fluid (approximately partial pressure of i -gas). Activity coefficients (γ_i) make it possible to quickly estimate the relative solubility of gases in silicate melts. An analysis of these values shows that the composition of gases in the silicate melt is shifted relative to the fluid and the magnitude of the shift is determined by the different degrees of solubility of the components.

The distribution of water in the Moon' interior is important for elucidating the origin of the Moon, the features of the crystallization of the lunar magmatic ocean and the assessment of the duration of lunar volcanism. Although the used olivines of basalts from Kamchatka, unlike lunar ones, were formed under moderately reducing conditions, measurement methods can also be successfully applied to silicates delivered by Chang'E-5 [6]. The gases preserved in their crystal lattice seem to contain more CH_4 , CO and H_2 , which will need to be taken into account when choosing methods for subsequent analysis. The spatial distribution of OH/H_2O on the lunar surface was analyzed according to the data of the M3 Chandrayan-1 instrument (India) and a connection was made to the outcrops of igneous rocks [7].

ACKNOWLEDGMENTS:

The work was carried out with the support of the Ministry of Education and Science of the Russian Federation within the framework of the state assignment of the Institute of Geochemistry and Analytical Chemistry, Russian Academy of Sciences.

REFERENCES:

- [1] Gou S. et al. Forsteritic olivine and magnesium-rich orthopyroxene materials measured by Chang'E-4 rover // *Icarus*. 2020. V. 345. P. 113776–113788.
- [2] Hamilton V.E. Thermal infrared (vibrational) spectroscopy of Mg–Fe olivines: A review and applications to determining the composition of planetary surfaces // *Chem. Erde*. 2010. V. 70. P. 7–33.
- [3] Bowey J. E., Lee C., Tucker C. et al. Temperature effects on the 15–85 μm spectra of olivines and pyroxenes // *Mon. Not. R. Astron. Soc.* 2001. V. 325. P. 886–896.
- [4] Voropaev S. A. et al. Degassing features of the main silicate minerals at the temperature range 200–1000 $^{\circ}C$ // *Solar System Research*. 2024. V. 58(6). P. 682–695.
- [5] Holloway J. R., Jakobsson S. Volatile solubilities in magma: Transport of volatiles from mantles to planet surfaces // *J. Geophys. Res.: Solid Earth*. 1986. V. 91. No. B4. P. D505–D508.
- [6] Li C. et al. Characteristics of the lunar samples returned by the Chang'E-5 mission // *Nat. Sci. Rev.* 2022. V. 9. Id. nwab188.
- [7] Bandfield J. L. et al. Widespread distribution of OH/H_2O on the lunar surface inferred from spectral data // *Nature Geoscience*. 2018. V. 11. P. 173–177.

SPINEL-BEARING LITHOLOGIES IN THE LUNAR HIGHLAND METEORITES

L. A. Lakhmanova^{1,2}, S. I. Demidova¹

¹ Vernadsky Institute of Geochemistry and Analytical Chemistry RAS
Moscow, lakhmanova.lida@list.ru

² Lomonosov Moscow State University, Department of Geology
Moscow, Russia

KEYWORDS:

spinel, lunar highland meteorites, spinel troctolite, pink spinel anorthosite

INTRODUCTION:

Pink spinel is a rare mineral phase in lunar rocks commonly occurring in spinel troctolites and rare spinel cataclases of deep-seated origin. Based on remote sensing data spinel-rich rocks are present on the rims and central peaks of large impact craters on the Moon. They are expected to be enriched in plagioclase and poor in mafic minerals (olivine±pyroxene <5 %) and are referred as pink spinel anorthosite (PSA) previously not mentioned in lunar material [1]. In an attempt to find the source rocks of the spinel-rich occurrences on the lunar surface systematic study of spinel-bearing association in lunar highland meteorites is performed. Here we report preliminary study of pink spinel fragments and discuss corresponding mineral associations found in two lunar highland meteorites Dhofar 025 and 311.

SAMPLE AND METHODS:

Two polished thin section of lunar meteorites Dhofar 025 and 311 were studied using standard methods of optical and electron microscopy using Tescan Mira 3 FEG SEM equipped with EDS detector at the Vernadsky Institute (Moscow, Russia). Analyses of the mineral phases were conducted with an electron beam accelerating voltage of 20 kV at a working distance of 15 mm and 1 µm beam size.

RESULTS:

Dhofar 025 is an impact melt breccia containing numerous diverse lithic and mineral fragments of typical highland rocks mainly of anorthositic composition [2]. Pink spinel is present mainly as monomineral fragments in the matrix (10–20 µm in size, rarely up to 70 µm) (Figure 1). Most of them are crystals with resorbed edges surrounded by corona-like reaction rim consisting of presumably olivine microlites (1–2 µm) situated in a feldspathic glass (Figure 1a–d) similar to described in NWA 10401 lunar meteorite [3]. Rounded and clastic fragments are also present in the meteorite (Figure 1e, g, h). Spinel has high-Al and -Mg composition (Mg# = Mg/(Mg + Fe), at %, 78–90). Besides that there is a population of high-Mg olivine grains (Fo_{86–93}) among mineral fragments.

A unique spinel-bearing object (30×50 µm) was found in a large anorthite fragment (300×700 µm) in the meteorite. Spinel grain makes up the core of the object and is present in its outer part in fine symplectite intergrowths with presumably plagioclase.

Dhofar 311 is a highland breccia with different rocks and mineral fragments embedded in a glassy impact melt matrix. Spinel is present as mineral fragments, olivine-spinel intergrowth (Figure 2) and a single fragment of spinel troctolite. The latter (300×600 µm in size) has igneous texture and consists of plagioclase (An_{95–97}) and olivine (Fo_{80–88}) with minor Mg-Al spinel (Mg# is 81–82). Spinel of intergrowth and mineral fragments has similar composition.

DISCUSSION:

Both studied meteorites contain abundant fragments of Mg-Al spinel however no spinel-bearing rocks has been observed in the Dhofar 025 meteorite suggesting that their source lithology was disintegrated during impact processes. Reaction rim around most of the spinel crystals suggest that spinel has been dissolved in the matrix impact melt when the temperature

decreases forming olivine and plagioclase. This is predicted by olivine-anorthite phase diagram on which spinel is stable only at high temperature [4]. The presence of both high-Mg spinel and olivine fragments population in the Dhofar 025 suggests that spinel troctolites could be the source rock in the meteorite. However the spinel-bearing object with symplectite texture differs from most spinel fragments and may be derived from another source. As it was previously shown spinel-bearing symplectite texture could be produced by solid state reactions in the deep-seated crustal rocks but spinel should associate with aluminosilicate, extremely rare mineral in the lunar material [5] which was not noted in the Dhofar 025 meteorite.

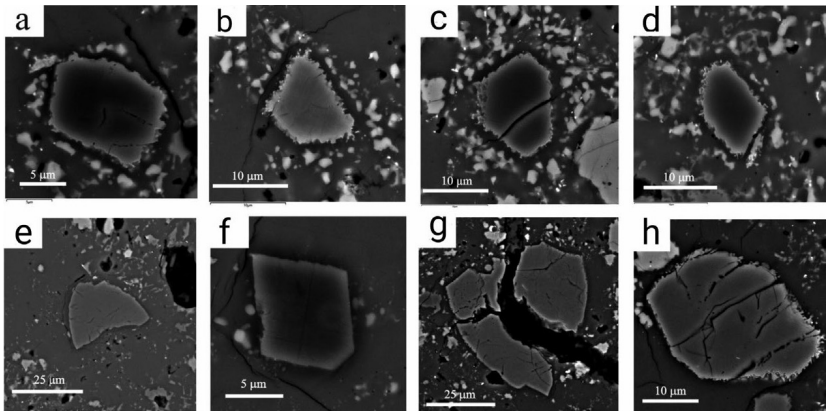


Fig. 1. BSE images of spinel fragments in the Dhofar 025 lunar meteorite

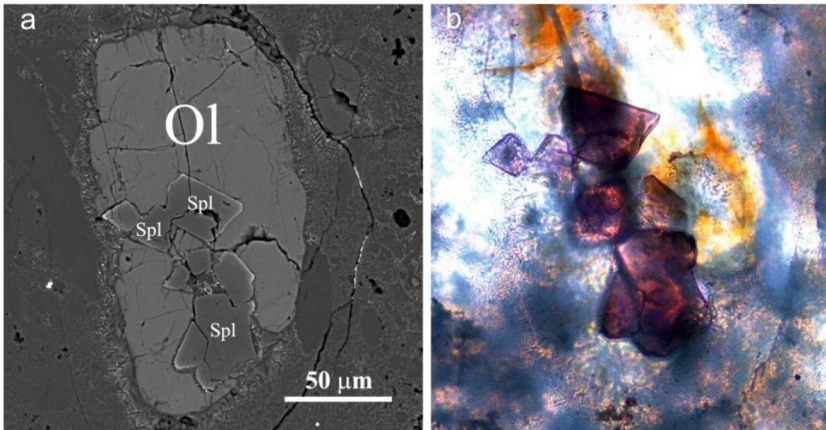


Fig. 2. BSE image (a) and an image in transmitted light (b) of spinel-olivine intergrowth in the Dhofar 311 lunar meteorite

Similarity of the composition of spinel fragments, intergrowth and spinel troctolites in the Dhofar 311 meteorite is a strong evidence of belonging them to the same source. So, spinel troctolites are thought to be highly probable source rocks for the spinel fragments in both studied meteorites. None of the spinel fragments correspond to the spinel anorthosites characteristics established by the spectral data M^3 [1]. Meanwhile recent studies have shown the presence of possible PSA source in the lunar meteorite NWA 13191 [6].

REFERENCES:

- [1] Pieters C. M., Besse S., Boardman J. et al. Mg-spinel lithology: A new rock-type on the lunar farside // *J. Geophys. Res.* 2011. V. 116. Article E00G08.
- [2] Demidova S. I., Nazarov M. A., Ryazantsev K. M., Anosova M. O., Ntaflou T., Brandstätter F. Enigmatic cathodoluminescent objects in the Dhofar 025 lunar meteorite: origin and sources // *Petrology*. 2017. V. 25. P. 139–149.

- [3] *Gross J., Prissel T.C., Korotev R.L., Parman S.W.* Unique pink spinel symplectite assemblage in Northwest Africa (NWA) 10401: Breakdown reaction through solid-state diffusion and potential relation to Apollo-17 samples // 48th Lunar Planet. Sci. Conf. 2017. Article 2589.
- [4] *Osborn E.F., Tait D.B.* The system diopside-forsterite-anorthite // *Amer. J. Sci.* 1952. P. 413–433.
- [5] *Nazarov M., Aranovich L.Y., Demidova S., Ntaflos T., Brandstätter F.* Aluminous enstatites of lunar meteorites and deep-seated lunar rocks // *Petrology.* 2011. V. 19. P. 13–25.
- [6] *Xie L.F., Chen H.Y., Miao B.K., Song W.L., Xia Z.P., Zhang C.T., Chen G.Z., Zhang J.Y., Zhao S.Z., Gao X.K.* A possible origin of the lunar spinel-bearing lithologies as told by the meteorite NWA 13191 // *Am. Mineral.* 2024. V. 109. P. 457–470.

**SESSION 4. MOON AND MERCURY (MN-PS)
POSTER SESSION**

PRELIMINARY GROUND OPTICAL POLARIZATION OBSERVATION OF THE MOON

J. Ping^{1,2}, W. Wang^{1,4}, M.-Y. Wang², F. Kou³, X.-W. Han⁴

¹ *University of Chinese Academy of Sciences, Beijing, China, jsping@bao.ac.cn*

² *National Astronomical Observatories, Chinese Academy of Sciences Beijing, China*

³ *Nanjing Institute of Astronomical Optics and Technology, Chinese Academy of Sciences, Nanjing, China*

⁴ *Changchun Observatory, National Astronomical Observatories, Chinese Academy of Sciences, Changchun, China*

KEYWORDS:

Optical polarization, ground observation, Moon

INTRODUCTION:

Optical polarization methods play a crucial role in the Earth and planetary remote sensing. Lunar scientific observation helps reveal the Moon's surface features and physical properties, aiding our understanding of its origin and evolution. Optical techniques are essential in this study, with polarization imaging used to estimate lunar regolith grain size [1–4] and the refractive index [5]. Historically, the Umov effect considered only geometric grain size, ignoring material heterogeneity. This method, focusing on the Umov effect, has been adopted by a Korean lunar remote sensing orbiter for grain size detection [6].

Polarization of scattered sunlight from the Moon offers new insights into its surface. Polarimetric remote sensing has detected heterogeneous ground materials, suggesting it could reveal the Moon's uneven composition. The polarization state effectively distinguishes material states on Earth. To test this idea, we conducted lunar polarimetric observations to detect lunar surface compositions.

OBSERVATION:

We performed the first visible white light polarimetric observations of the Moon using a 0.2m Schmidt-Cassegrain telescope in Xinjiang, China. The imaging instrument, a division of the focal plane polarization camera, uses a Sony IMX250 MZR polarization chip. Linearly polarized light is represented by Stokes parameters, and its linear degree of polarization (DOP) P . Each micropolarizer array corresponds to each pixel of the image sensor. Focal-plane polarimetric imaging doesn't acquire circular polarization, which is negligible for the Moon [8]. Stokes parameters are estimated using micropolarizer measurements, with bicubic interpolation improving resolution and reducing errors [9, 10].

The instrument is calibrated using standard astronomical methods. Stokes parameters image data subtract bias, dark, and flat-field images through a data reduction pipeline. The non-polarized standard stars correct measured Stokes parameters before lunar observations. DOP images of the observed lunar surface are calculated using Stokes parameters.

We observed the near-Earth side of the Moon from August to October 2022, obtaining frames for several minutes each night. Calibrated and mosaiced frames were used to create a DOP map in Figure 1. Higher white light polarization was noted in lunar maria than in highlands, with Oceanus Procellarum showing a maximum polarization of almost 20%. This indicates that the DOP map contains information about lunar composition, consistent with ground mineral soil features.

SIMPLE DISCUSSION:

To investigate the correlation between DOP parameters and lunar soil composition, we compared DOP of lunar sampling sites with FeO abundances from Apollo, Luna, and Chang'E-5 missions [8, 11]. FeO abundance results from DOP map inversion were compared with Kaguya Lunar Multiband Imager data [12]. A remarkable linear correlation between

DOP parameters and average FeO contents at each site was found in Figure 2.

Furthermore, the fitted correlation equation in Figure 2 here can be used to invert the FeO map, and a result is presented in Figure 3.

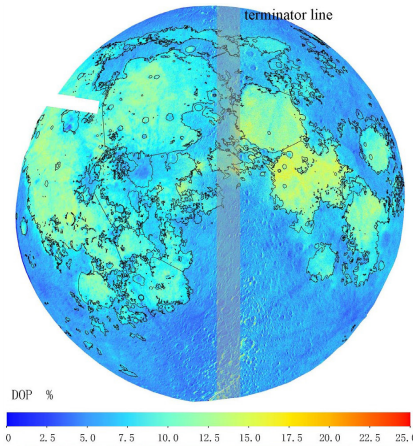


Fig. 1. The lunar nearside DOP map of white light by our observation data

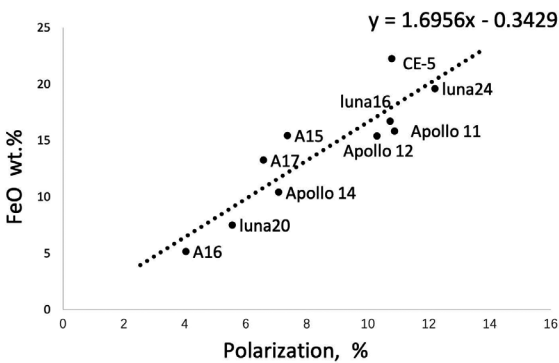


Fig. 2. Graph of the average FeO contents of soils from each site or station plotted against the average polarization parameters computed from our observation data. The Pearson correlation coefficient is 0.8905. The equation of the best linear fit is shown in the figure

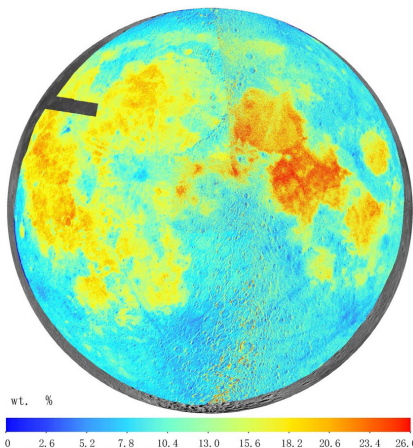


Fig. 3. Mapping of the FeO abundances with our polarization data using the linear fit in Figure 2

Future work will provide reference and calibration samples for in-orbit probes and conduct ground-based polarimetric observations of the Moon and other planetary objects in different spectral bands using narrow-band filters.

REFERENCES:

- [1] *Dollfus A., Titulaer C.* Polarimetric Properties of the Lunar Surface and its Interpretation. Part III // *Astronomy and Astrophysics*. 1971. V. 12. Article 199.
- [2] *Shkuratov Y. G.* // *Planetary and Space Science*. 1981. V. 25. 490.
- [3] *Shkuratov Y., Opanasenko N.* Polarimetric and photometric properties of the Moon: telescope observation and laboratory simulation. 2. The positive polarization // *Icarus*. 1992. V. 99. Iss. 2. P. 468–484. [https://doi.org/10.1016/0019-1035\(92\)90161-Y](https://doi.org/10.1016/0019-1035(92)90161-Y).
- [4] *Jeong M., Kim S. S., Garrick-Bethell I. et al.* Multi-band polarimetry of the lunar surface. I. Global properties // *Astrophysical J. Supplement Series*. 2015. V. 221. No. 1. Article 16. DOI: 10.1088/0067-0049/221/1/16.
- [5] *Fearnside A., Masding P., Hooker C.* Polarimetry of moonlight: A new method for determining the refractive index of the lunar regolith // *Icarus*. 2016. V. 268. P. 156–171. <https://doi.org/10.1016/j.icarus.2015.11.038>.
- [6] *Sim C. K., Kim S. S., Jeong M. et al.* Observational strategy for KPLO/PolCam measurements of the lunar surface from orbit // *Astronomical Society of the Pacific*. 2019. V. 132. No. 1007. Article 015004.
- [7] *Shkuratov Y., Kaydash V., Korokhin V. et al.* Optical measurements of the Moon as a tool to study its surface // *Planetary and Space Science*. 2011. V. 59. Iss. 13. P. 1326–1371. <https://doi.org/10.1016/j.pss.2011.06.011>.
- [8] *Blewett D. T., Lucey P. G., Hawke B. R., Jolliff B. L.* Clementine images of the lunar sample-return stations: Refinement of FeO and TiO₂ mapping techniques // *J. Geophysical Research*. 1997. V. 102. Iss. E7. P. 16319–16325. <https://doi.org/10.1029/97JE01505>.
- [9] *Ratliff B. M., LaCasse C. F., Tyo J. S.* Interpolation strategies for reducing IFOV artifacts in microgrid polarimeter imagery // *Optics Express*. 2009. V. 17. P. 9112–9125. <https://doi.org/10.1364/OE.17.009112>.
- [10] *Gao S., Gruet V.* Bilinear and bicubic interpolation methods for division of focal plane polarimeters // *Optics Express*. 2011. V. 19. Iss. 27. P. 26161–26173.
- [11] *Li C., Hu H., Yang M.-F. et al.* Characteristics of the lunar samples returned by the Chang'E-5 mission // *National Science Review*. 2021. V. 9(2). nwab188. DOI:10.1093/nsr/nwab188.
- [12] *Lemelin M., Lucey P. G., Miljkovi K. et al.* The compositions of the lunar crust and upper mantle: Spectral analysis of the inner rings of lunar impact basins // *Planetary and Space Science*. 2019. V. 165. P. 230–243. <https://doi.org/10.1016/j.pss.2018.10.003>.
- [13] *Dong T., Yulong F., Wei H. et al.* // *J. Tsinghua Univ. (Sci. Technol.)*. 2023. V. 63. 433.
- [14] *Gillis J. J., Jolliff B. L., Elphic R. C.* A revised algorithm for calculating TiO₂ from Clementine UVVIS data: A synthesis of rock, soil, and remotely sensed TiO₂ concentrations // *J. Geophysical Research*. 2003. V. 108. Article 5009. doi:10.1029/2001JE001515/
- [15] *Heiles C.* 9286 Stars: An Agglomeration of Stellar Polarization Catalogs // *Astronomical J.* 2000. V. 119. No. 2. Article 923.
- [16] *Lemelin M., Lucey P. G., Gaddis L. R., Hare T., Ohtake M.* Global map products from the Kaguya multiband imager at 512 ppd: Minerals, FeO, and OMAT // 47th Lunar and Planetary Science Conf. 2016. Article 2994.
- [17] *Lucey P. G., Blewett D. T., Hawke B. R.* Model near-infrared optical constants of olivine and pyroxene as a function of iron content // *Geophysical Research*. 1998. V. 103. Iss. E1. P. 1703–1713.
- [18] *Nelson D., Koeber S., Daud K. et al.* Mapping lunar maria extents and lobate scarps using LROC image products // 45th Lunar and Planetary Science Conf. 2014. Article 2861.
- [19] *Powell S. B., Gruet V.* Calibration methods for division-of-focal-plane polarimeters // *Optics Express*. 2013. V. 21. P. 21039–21055.
- [20] *Ramaprakash A. N., Rajarshi C. V., Das H. K. et al.* RoboPol: a four-channel optical imaging polarimeter // *Monthly Notices of the Royal Astronomical Society*. 2019. V. 485. Iss. 2. P. 2355–2366. <https://doi.org/10.1093/mnras/stz557>.
- [21] *Słowikowska A., Krzeszowski K., Żejmo M. et al.* Calibration of the liverpool telescope RINGO3 polarimeter // *Monthly Notices of the Royal Astronomical Society*. 2016. V. 458. Iss. 1. P. 759–771.
- [22] *Turnshek D. A., Bohlin R. C., Williamson R. L. I. et al.* An Atlas of Hubble Space Telescope Photometric, Spectrophotometric, and Polarimetric Calibration Objects // *Astronomical J.* 1990. V. 99. Article 1243. DOI: 10.1086/115413.

- [23] *Tyo J.S., Goldstein D.L., Chenault D.B., Shaw J.A.* "Review of passive imaging polarimetry for remote sensing applications // Applied Optics. 2006. V. 45. Iss. 22. P. 5453–5469. <https://doi.org/10.1364/AO.45.005453>.

PHOTOGEOLOGICAL ANALYSIS OF SHADOWCAM IMAGES ON THE PERMANENTLY SHADOWED FLOOR OF LUNAR CRATER SHOEMAKER

A. T. Basilevsky¹, S. S. Krasilnikov², Y. Li³

¹ Vernadsky Institute of Geochemistry and Analytical Chemistry RAS
Moscow, Russia, atbas@geokhi.ru

² Hong Kong Polytechnic University, Hong Kong, China

³ Suzhou Vocational University, Suzhou, China

KEYWORDS:

Moon, permanently shadowed areas, ShadowCam, hill-shade images, elephant hide texture, lobate-rimmed craters, relative depth, water ice

INTRODUCTION:

This work is a continuation of analysis of the surface morphology of the permanently shadowed floor of lunar crater Shoemaker [1], which used the hill-shade images and crater depth/diameter (d/D) measurements based on the LOLA DTMs [2]. It was shown in [1] that the surface morphology of the permanently shadowed floor of crater Shoemaker is nearly identical to that of the regularly illuminated mare surface at the Lunokhod-2 working area and the surface of the highland plain of the Apollo-16 landing site, being dominated by populations of craters smaller than 1 km in diameters. Craters on Shoemaker floor have approximately the same d/D as those within the Lunokhod-2 and Apollo-16 areas. The observed surface morphology of the Shoemaker floor is the result of meteorite bombardment like in other areas of the Moon. Used in the present study the ShadowCam images [3] with a resolution of ~ 1.6 m/px show much more details of the surface morphology of the permanently shadowed floor of crater Shoemaker [4].

DESCRIPTION:

Figure 1 is a hill-shade image of Shoemaker crater with shown 4.5×6 km large Study areas.

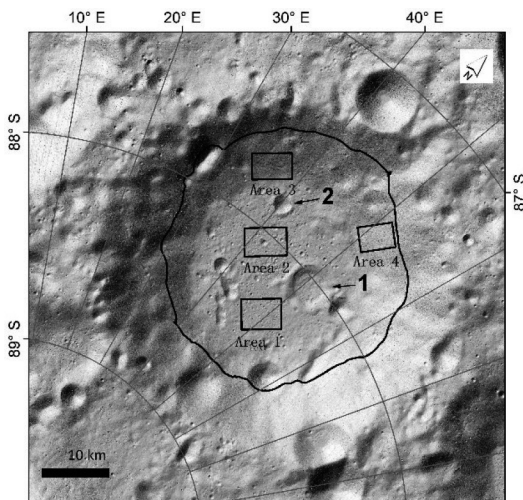


Fig. 1. The hill-shade image of Shoemaker crater with four Study areas. Study areas 1 and 2 are on the Shoemaker floor's sub-horizontal surface (0.5 to 2° on 200 – 1000 m baseline). Study areas 3 and 4 are in the lower parts of Shoemaker inner slopes, which steepness on 200 – 1000 m baseline is 12 to 16°

Figure 2 provides a possibility to compare the morphology seen in the hill-shade and ShadowCam images of Shoemaker study areas 1 and 2.

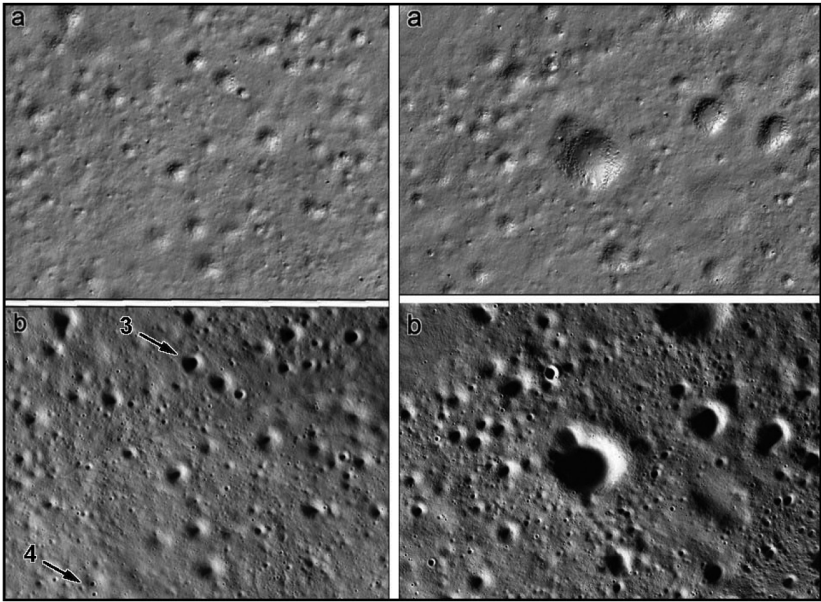


Fig. 2. It shows hill-shade (upper parts) and ShadowCam (lower parts) images of Shoemaker study areas 1 (left) and 2 (right)

It is seen in Figure 2 that while used in [1] the hill-shade images showed most of craters larger than 50–100 m in diameter, the ShadowCam images provide a possibility to see craters by order of magnitude smaller. Using the ShadowCam images confirmed the general conclusion of [1] that surface morphology of the permanently shadowed floor of crater Shoemaker is dominated by population of craters smaller than 1 km.

Figure 3 provides a possibility to compare the morphology seen in the hill-shade and ShadowCam images of Shoemaker study areas 3 and 4.

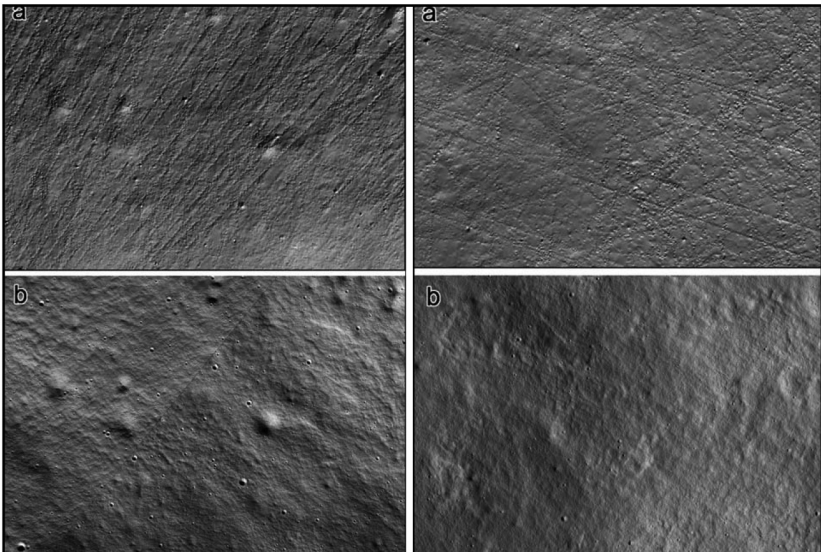


Fig. 3. It shows hill-shade (upper parts) and ShadowCam (lower parts) images of Shoemaker study areas 3 (left) and 4 (right)

It is seen in Figure 3 that the used in [1] hill-shade images are spoiled by numerous linear artefacts. In area 3, a few craters with diameters of about 100 to 300 m are seen, while in area 4, only linear artefacts. The ShadowCam im-

ages in Figure 3 represent the decameter-scale wavy surface texture, called the “elephant hide” texture [5–7]. It is typical for slopes in the areas with normal solar illumination and now we see that it is also present on the permanently shadowed slopes. It is seen that small craters in areas 3 and 4 are very rare, which is obviously due to their fast destruction by the downslope material movement [8].

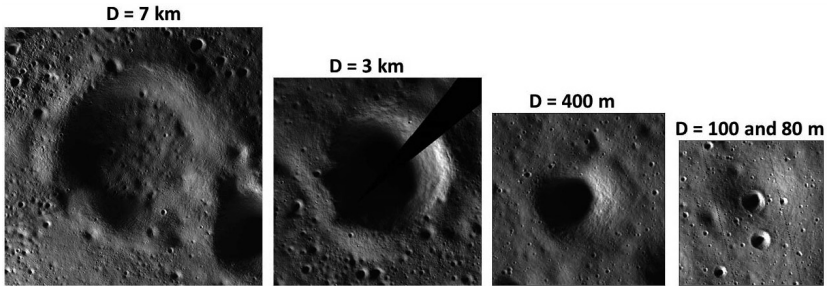


Fig. 4. Some lobate-rimmed craters on the Shoemaker floor: 1) crater Tooley (arrow 1 in Figure 1); 2) unnamed 3-km crater (arrow 2 in Figure 1); 3) 400-m crater (arrow 3 in Figure 2 lower left); 4) 100- and 80-m craters (arrow 4 in Figure 2 lower left)

In the ShadowCam images are seen craters of specific lobate-rimmed morphology, that is probably due to presence of water ice in the target material that provides to, at least, some part of crater ejecta a possibility of viscous flow [4, 9].

CONCLUSIONS:

The above considerations confirmed the conclusion of [1] that the morphology of the permanently shadowed floor of Shoemaker crater is dominated by small craters. Future studies hopefully will allow to describe the morphometry (especially d/D) of the decameter-scale craters. The surface of the lower parts of permanently shadowed inner slopes of crater Shoemaker has the “elephant hide” texture, which is also typical for normally illuminated areas. The ShadowCam images showed the presence of lobate-rimmed craters, whose morphology is probably indicative of water ice in the target material.

ACKNOWLEDGEMENTS:

Authors are grateful to ShadowCam team, State University of Arizona, NASA USA and Korea Aerospace Administration for possibility to work with the ShadowCam images.

REFERENCES:

- [1] *Basilevsky A. T., Li Y.* Surface morphology inside the PSR area of lunar polar crater Shoemaker in comparison with that of the sunlit areas // *Planet. and Space Sci.* 2024. V. 241. Article 105839.
- [2] https://pds-geosciences.wustl.edu/lro/lro-l-lola-3-rdr-v1/lrolol_1xxx/DATA/LOLA_GDR/POLAR/J_P2/LDEC_875S_5M.JP2.
- [3] *Robinson M.S et al.* ShadowCam — Seeing in the dark // *EPSC Abstr.* 2017. V. 11. Article EPSC2017-506.
- [4] *Robinson M. S. et al.* Seeing in shadows // *55th Lunar and Planet. Sci. Conf.* 2024. Article 1669.
- [5] *Kreslavsky M. A., Bondarenko N. V., Head J. W.* Ubiquity of “elephant hide” texture on the Moon // *52nd Lunar and Planet. Sci. Conf.* 2021. Article 1826.
- [6] *Bondarenko N. V., Kreslavsky M. A., Zubarev A., Nadezhdina I.* “Elephant hide” texture on the moon: preliminary results on topographic properties // *53rd Lunar and Planet. Sci. Conf.* 2022. Article 2469.
- [7] *Kreslavsky M. A., Zubarev A., Nadezhdina I., Bondarenko N. V.* Non-diffusive regolith transport on the Moon // *54th Lunar and Planet. Sci. Conf.* 2023. Article 1834.
- [8] *Basilevsky A. T.* On the evolution rate of small lunar craters // *Proc. 7th Lunar Sci. Conf.* 1976. P. 1005–1020.
- [9] *Basilevsky A. T., Ivanov B. A., Krasilnikov S. S.* Lobate rimmed craters in PSR parts of the lunar south-polar craters Faustini and Shoemaker // *15th Moscow Solar System Symp.* 2024.

ANALYSIS OF THE CRATER DEPTHS IN THE POLAR REGIONS OF THE MOON AND MERCURY

E. A. Feoktistova, Zh. F. Rodionova

*Lomonosov Moscow State University, Sternberg Astronomical Institute
Moscow, Russia hrulis@yandex.ru*

KEYWORDS:

Moon, craters, morphometry, measurements, coordinates, diameters, statistical analysis, DEM

INTRODUCTION:

Morphometric catalogues of craters with diameters of 10 km and more have been used for lunar northern and southern polar regions limited by latitudes $\pm 60^\circ$ [1, 2] and a part of the new Mercurian morphological catalogue [3] for its polar regions. To create a relief DEM, data from the LOLA altimeter of the LRO probe and the MLA altimeter of the Messenger probe were used. [4]. The catalogues define: coordinates of craters, diameters, angles of inclinations of inner and outer slopes, maximum and minimum heights of the bottom and crests of ramparts, depths and depth-to-diameter ratios. Using the ArcGIS Desktop and the CraterTools add-on module, 1320 craters for the South Polar region and 2302 craters for the North Polar region were digitized and measured for the Moon.

A new morphological catalog of Mercury craters was created at SAI MSU together with MIIGAIK based on data obtained during the flights of the MESSENGER spacecraft and the Mariner 10 spacecraft. The new catalog includes information on the coordinates, diameters and morphology of 12365 craters with diameters ≥ 10 km [3]. Morphological description of 12365 craters was carried out at the SAI MSU. Determination of the depth of craters was carried out in MIIGAIK using the CraterTools module of the ArcGIS package. In order to more accurately localize craters and outline their edges, as well as to better examine their internal structure, an additional layer is used — relief hillshading, built on the basis of a DEM. Digitization of craters was carried out using map sheets at a scale of 1:5 000 000. There are 830 craters with a diameter > 10 km in the North polar region of Mercury, and 1072 craters in the South polar region.

ANALYSIS OF THE CATALOGUES:

We have published in [4] that the average craters depths in the southern polar region of the Moon are greater than in the northern one about 1.5 km. This should probably be explained by the presence of lava at the bottom of many craters in the northern polar. But the average depths of the craters on the near and far sides of the polar regions of the Moon are practically the same [4]. Figure 1 show the distribution of craters for the polar regions of the Moon by maximum depths depending on diameters The craters of the northern polar region are shown in blue, and the southern one in red.

Table 1. Maximum and average depths of craters in the northern and southern polar regions of the Moon

Diameter, km	North		South	
	Maximum depth, km	Average depth, km	Maximum depth, km	Average depth, km
10–20	4.7	1.5	4.6	1.8
20–40	4.7	2.1	5.5	2.7
40–80	6.2	3.2	7.4	3.9
80–160	7.9	4.6	9.2	5.8
>160	10.8	6.1	9.6	7.4

Table 1 show that the maximum depths of lunar craters are increased with diameters: from 4.7 to 10.8 km (North region), from 4.6 to 9.6 km (South

region). The average values of crater depths also increased with increasing diameters: from 1.5 to 6.1 km (North region), and from 1.8 to 7.4 km (South region).

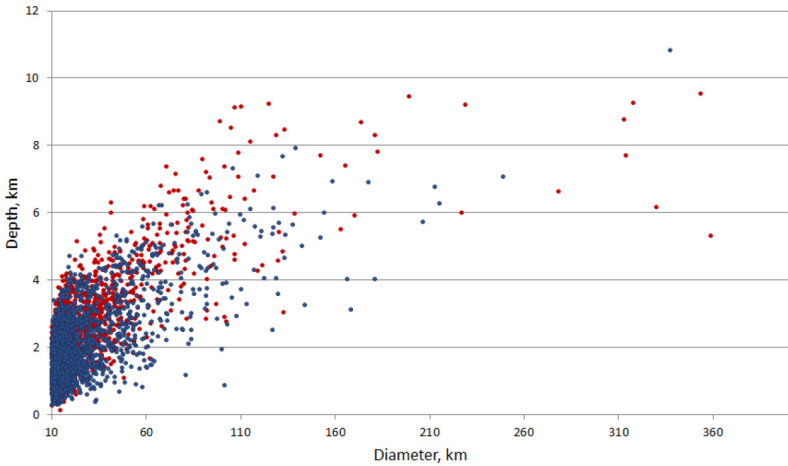


Fig. 1. Distribution of craters by maximum depths depending on diameters for the polar regions of the Moon. The craters of the northern polar region are shown in blue, and the southern one in red

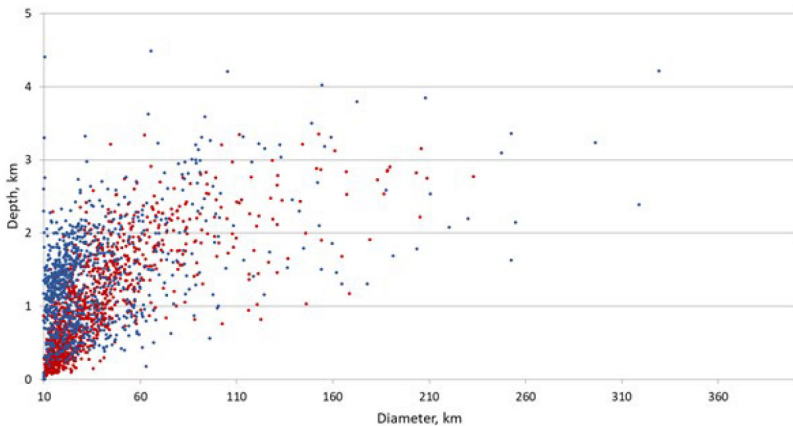


Fig. 2. Distribution of craters by maximum depths depending on diameters for the polar regions of the Mercury. The craters of the northern polar region are shown in blue, and the southern one in red

Maximum crater depth in the northern region of Mercury is in Borealis Planitia diameter 785 km, depth 5.6 km, but in southern one is in unnamed basin with coordinates: -59.4° S, 1.8° W, diameter 614.4 km, depth 4.4 km (Table 2). These maximum values are not shown in Figure 2 due to the large size.

Table 2. Values of the maximum and average depths of craters in the northern and southern polar regions of Mercury

Diameter, km	North		South	
	Maximum depth, km	Average depth, km	Maximum depth, km	Average depth, km
10–20	2.3	1.1	2.3	0.4
20–40	3.3	1.3	2.6	0.8
40–80	4.5	1.5	3.3	1.5
80–160	4.2	2.3	3.3	2
>160	5.6	2.6	4.4	2.7

The maximum crater depths in the northern polar region of Mercury are slightly greater than in the southern one. The average depths values in the southern polar region are lower than in the northern one. Note that the crater depths on Mercury are significantly less than those on the Moon. Pike noted this in his paper [5] and explained it by the different accelerations when bodies fall on the surface of the Moon and Mercury.

CONCLUSION:

The maximum and average depths of lunar craters in the diameter ranges: 10–20, 20–40, 40–80, 80–160 km and more than 160 km systematically increase with increasing size in the North and South regions. Lunar craters of the south polar region are deeper than those of the north.

The maximum crater depths in the northern polar region of Mercury are slightly greater than in the southern one. The craters of the northern polar region of Mercury in the diameter range from 10 to 40 km are on average deeper than the craters of the southern polar region.

REFERENCES:

- [1] *Slodarz N.A., Rodionova Zh.F.* Morphological catalogue of the craters of the Moon / Department of Lunar and Planetary Research Lomonosov State University. 2021. 78 p. <http://selena.sai.msu.ru/>.
- [2] *Slodarz N.A., Rodionova Zh. F., Levitskaya T.I.* Morphometric catalog of craters of the south polar region of the Moon. / Department of Lunar and Planetary Research Lomonosov State University. 2020. 46 p. // <http://selena.sai.msu.ru/Rod/Publications/morph-catalog-craters-moon/morph-catalog-craters-moon.htm>.
- [3] <http://selena.sai.msu.ru/Rod/Publications/Mercury/Catalog.xlsx>.
- [4] *Slodarz N.A., Rodionova Zh.F.* Comparison of the cratering of the north and south polar regions of the Moon // 12th Moscow Solar System Symp. 2021.
- [5] *Pike R.J.* Geomorphology of impact craters on Mercury // Mercury / Eds. F. Vilas, C. R. Chapman, M. S. Matthews. Tucson: Univ. of Arizona Press, 1988. P. 165–273.

CREATION OF A COMPREHENSIVE FUNDAMENTAL SELENOGRAPHIC CATALOG OF IMPACT CRATERS BASED ON DATA FROM MODERN LUNAR MISSIONS AND SATELLITE REMOTE MONITORING

Y. A. Nefedyev¹, A. O. Andreev², Y. A. Kolosov¹

¹ Kazan Federal University, Kazan, Russia, star1955@mail.ru

² Kazan State Power Engineering University, Kazan, Russia
andreev.alexey93@gmail.com

KEYWORDS:

impact craters, neural networks, artificial intelligence

ABSTRACT:

The main goal of the research is to solve fundamental problems in the field of selenography and planetophysics. The relevance of the work is that currently there is no fundamental reference network on the surface of the Moon, including the distribution of lunar objects formed under the influence of space impactors, containing their selenodetic characteristics and related to the selenocentric dynamic coordinate system. In this work, for the first time in world practice, a method has been developed for constructing a complex digital selenographic model based on data from modern lunar missions and selenodetic monitoring of lunar impact craters. This will make it possible to construct a system of craters distribution on the lunar surface that were formed by slow asteroids. The model is created based on the analysis of optical data from satellite observations of lunar objects using criteria such as the ratio of stratigraphic characteristics, morphological features and optical structure of the objects. In order to ensure the reliability of the analysis of a huge array of observational data, methods of transfer deep machine learning and construction of neural networks will be used. It should be noted that the subjectivity of manual detection and the limitations of automatic detection with different types of data lead to significant discrepancies in the planetophysical characteristics of craters [1]. Typical crater characteristics include large extents, order-of-magnitude differences in diameter, large shape changes due to overburdening or filling, and variable and complex morphology. The existing automatic detection algorithms [2] based on pattern recognition and machine learning (ML) can identify crater characteristics largely from the general characteristics of the craters. The modern studies on manual processing methods and the ones based on artificial intelligence have allowed us to study only a number of simple craters and, thus, have not taken into account irregularly shaped and seriously destroyed craters that could have formed in early periods and include important information about the content of useful resources of asteroid origin [3–5]. This paper is dedicated to one of the tasks of studying such objects. Another important aspect is the coordinate support of lunar objects. Despite the outstanding results in this direction obtained from observations taken by the Apollo, Zond, LRO, and Kaguya space missions, the task of creating a selenodetic model has not yet been fully solved. Modern navigation selenographic networks have different accuracies for the coordinate axes, and may even have an ellipsoidal distribution of errors. It is widely believed that, for instance, the orbits of the LRO and GRAIL space missions were reconstructed and tied to the Earth's coordinate system with an accuracy of about a meter over the entire observation interval [6].

Within our research the following works were carried out:

1. A method was created and a system for its practical use was developed to bring diverse satellite optical observations into a single system. For this purpose, an analysis of the comparative efficiency of the method for affine transformation, optimal polynomial approximation, orthogonal transformation without and taking into account systematic er-

rors and solving a system of simultaneous equations was performed. The created method was verified using satellite observations, and as a result, a single digital database of optical observations from the Apollo, Clementine, Kaguya and LRO satellite missions was built.

2. Software for impact crater sampling was developed. For this purpose, an algorithm for selecting impact craters was constructed based on the relationship between stratigraphic characteristics, morphological features and their optical structure using methods of transfer deep machine learning and construction of neural networks, verification of the created algorithm was performed using satellite observations and an assessment of the accuracy of the created software algorithm in selecting impact craters corresponding to the specified parameters was carried out.
3. A software package was created to bring diverse satellite optical observations into a single system and a model of the macrofigure of the physical surface of the Moon was created based on observations from the Apollo, Zond, Clementine, Kaguya, LRO, and GRAIL space missions.

The implementation of the works based on modern satellite data and methods of planetary geodesy will increase a spacecraft's accuracy of coordinate and time support and the efficiency of landing on the Moon. The results of the work will find application in international space programs for lunar exploration. To determine the positions of craters, methods of modern information and mathematical, space observation technologies and precise coordinate and time support, multiparameter analysis, data from modern selenocentric reference systems, as well as the data obtained by the Apollo, Clementine, Kaguya and LRO space missions are used. Particular attention is paid to the lunar polar regions. The modeling proposed in this paper will help to establish optimal conditions for the placement of measuring equipment on the lunar surface and to develop an effective schedule for upcoming observations.

ACKNOWLEDGEMENTS:

This work was supported by Russian Science Foundation, grant No. 24-22-00260, <https://rscf.ru/project/24-22-00260/>.

REFERENCES:

- [1] *Robbins S.J., Antonenko I., Kirchoff M.R.* The variability of crater identification among expert and community crater analysts // *Icarus*. 2014. V. 234. P. 109–131.
- [2] *Vijayan S., Vani K., Sanjeevi S.* Crater detection, classification and contextual information extraction in lunar images using a novel algorithm // *Icarus*. 2013. V. 226. No. 1. P. 798–815.
- [3] *Esteva A., Kuprel B., Novoa R.A.* Dermatologist-level classification of skin cancer with deep neural networks // *Nature*. 2017. V. 542. No. 7639. P. 115–118.
- [4] *Silburt A., Ali-Dib M., Zhu C.* Lunar crater identification via deep learning // *Icarus*. 2019. V. 317. P. 27–38.
- [5] *Fassett C.I., Head J.W., Kadish S.J.* Lunar impact basins: Stratigraphy, sequence and ages from superposed impact crater populations measured from Lunar Orbiter Laser Altimeter (LOLA) data // *J. Geophysical Research: Planets*. 2012. V. 117. No. E12.
- [6] *Mazarico E., Rowlands D.D., Neumann G.A.* Orbit determination of the lunar reconnaissance orbiter // *J. Geodesy*. 2012. V. 86. P. 193–207.

RADAR MAPPING OF THE SOUTH POLAR REGION OF THE MOON AT 4.2 cm WAVELENGTH

Yu. S. Bondarenko, D. A. Marshalov, S. R. Pavlov, A. L. Tolstoy
Institute of Applied Astronomy RAS, Sain. Petersburg, Russia
bondarenko@iaaras.ru

KEYWORDS:

Moon, radar Mapping, radar backscatter, circular polarization ratio

INTRODUCTION:

We present new detailed radar maps covering the southern polar region of the near side of the Moon up to the 50th parallel of south latitude with a spatial resolution of about 75 m per pixel. The maps are based on the mosaic of radar images at 4.2 cm wavelength referenced to the selenographic coordinate system. We prepared the maps for diffuse and specular polarization components of the radar echo as well as for their ratio or Circular Polarization Ratio (CPR) which is a measure of roughness, number of rocks, and material composition on the lunar surface and in the regolith at the radar signal penetration depth. A configurable Lunaserv Web Map Service [1] supporting projection and layers changing has been adopted to provide access to our lunar radar data at <http://luna.iaaras.ru/> (Figure 1).

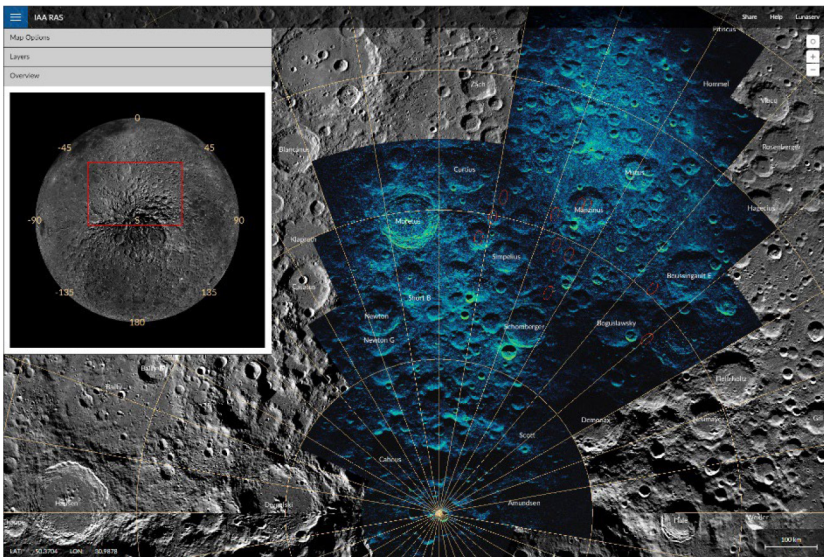


Fig. 1. Lunar Radar Maps web-interface with the IAA RAS CPR mosaic at 4.2 cm wavelength shown on top of the LROC WAC global mosaic [2] rendered in an orthographic projection centered at south pole

RADAR OBSERVATIONS AND DATA PROCESSING:

The radar images were obtained from a series of 2023 observations [3, 4] carried out with the 64-m TNA-1500 antenna at the Bear Lakes Satellite Communications Center of the SDB MPEI and the 13.2-m RT-13 radio telescopes at the Svetloe and Zelenchukskaya Observatories of the IAA RAS in a bistatic configuration at a wavelength of 4.2 cm. At this wavelength the radar signals can penetrate the lunar regolith to a depth up to 1 m and are sensitive to surface and suspended rocks larger than 1 cm. The high spatial resolution was achieved through the focused processing algorithm that avoids the radar image smearing at a long integration time. The receiving-system noise temperature measurements during the entire observation sessions provided a reliable estimate of the echo CPR values. We also applied a new numerical method for converting time delay and frequen-

cy of the echo to selenographic coordinates, considering the variation of these parameters over the entire integration interval [5].

CONCLUSIONS:

The resulting lunar radar maps show about 40 % of the permanently shadowed regions area, not observable by optical Earth-based instruments, which may hide water ice deposits. Obtained CPR values allow the physical characteristics of the southern polar region to be estimated. Thus, the new radar maps can be used to study the hidden from visible imaging features of the lunar surface and near-surface regolith layer, including the search for ice deposits, as well as for planning future lunar missions.

ACKNOWLEDGEMENTS:

We want to thank the technical staff at the Bear Lakes Satellite Communications Center of the SDB MPEI and the Svetloe and Zelenchukskaya Observatories of the IAA RAS for their assistance in organizing and conducting radar observations of the Moon. This work was supported by the Russian Science Foundation (project No. 23-22-00254).

REFERENCES:

- [1] *Estes N. M., Hanger C. D., Licht A. A., Bowman-Cisneros E.* Lunaserv web map service: history, implementation details, development, and uses // 44th Lunar and Planetary Science Conf. 2013. No. 1719. Article 2609.
- [2] *Robinson M. S., Brylow S. M., Tschimmel M. et al.* Lunar Reconnaissance Orbiter Camera (LROC) instrument overview // *Space Science Reviews*. 2010. V. 150. Iss. 1–4. P. 81–124. <https://doi.org/10.1007/s11214-010-9634-2>.
- [3] *Bondarenko Yu. S., Marshalov D. A., Zinkovsky B. M., Mikhailov A. G.* Radar Images of the Candidate Spacecraft Landing Sites on the Moon // *Astronomy Letters*. 2024. V. 50. P. 92–97. <https://doi.org/10.1134/S1063773724600127>.
- [4] *Bondarenko Yu. S., Marshalov D. A., Zinkovsky B. M., Mikhailov A. G.* Radar Images of Permanently Shadowed Regions at the South Pole of the Moon // *Solar System Research*. 2024. V. 58. No. 4. P. 394–403. <https://doi.org/10.1134/S0038094624700217>.
- [5] *Pavlov S. R., Bondarenko Yu. S., Marshalov D. A.* Lunar Radar Mapping Technique // *Trans. IAA RAS*. 2023. Iss. 67. P. 3–7. DOI: 10.32876/ApplAstron.67.3-7.

MOON'S GRAVITY FIELD INVESTIGATION BY PKD INSTRUMENT DEPLOYED ON LUNA-26 ORBITER

A. S. Kosov, L. S. Roshkov, V. S. Roshkov

Space Research Institute RAS, Moscow, Russia, akosov@cosmos.ru

KEYWORDS:

microwaves, Moon, gravity anomaly

INTRODUCTION:

The Objectives of the PKD experiment are: investigation of the gravitation field anomaly and orbit parameters by precise one way Doppler shift measurement (PKD — Ground Station).

The Ka band receiver (PKD) has been included into scientific payload of the Luna-Resource-1 orbiter. The receiver is intended to obtain the signal from Earth's transmitter. It will allow precise measurements of Doppler shift and, therefore, of the relative velocity and acceleration.

Table 1. The main parameters of the Lunar Orbiter Ka band Receiver

Parameter	Value
Central frequency	32 GHz (Ka-band)
Bandwidth	0.5 MHz
Noise temperature	150 K
Antenna beam width	120°
Short term frequency stability (Allan variance)	$8 \cdot 10^{-14}$
Accuracy of the dV/dt measurements	$3 \cdot 10^{-3} \text{ cm/s}^2$

The layout of the PKD experiment has shown on Figure 1 below.

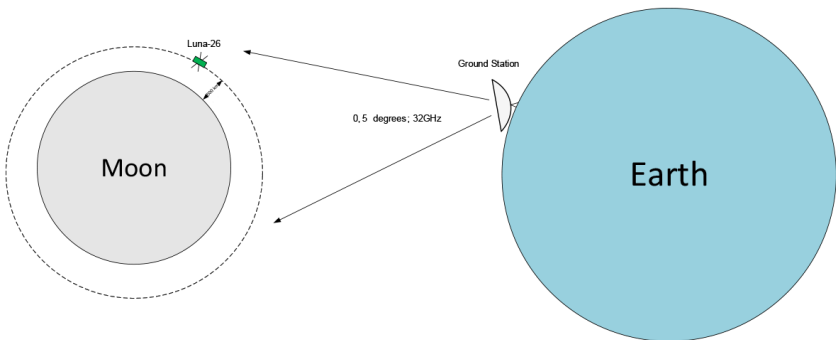


Fig. 1

The PKD experiment competes with most successful GRAIL experiment performed by NASA.

The comparison of PKD and GRAIL4 is in the Table 2.

Table 2. The main parameters of the PKD experiment and GRAIL NASA experiment.

Parameter	PKD experiment	GRAIL experiment
Allan Deviation:		
1 s	$\leq 1 \cdot 10^{-13}$	$\leq 3 \cdot 10^{-13}$
10 s	$\leq 8 \cdot 10^{-14}$	$\leq 3 \cdot 10^{-13}$
100 s	$\leq 1 \cdot 10^{-13}$	$\leq 3 \cdot 10^{-13}$
Accuracy, mGal	3–5	5–10
Resolution, km	5–10	10–20
Area of investigation	Visible side of the Moon	Full Moon
Ground network	Yes	Yes

REFERENCES:

- [1] *Gromov V.D., Kosov A.S.* The Objectives of the Radioscience Experiment in Luna-Resource and Luna-Glob Space Projects // 6th Moscow Solar System Symposium. 2015. 6MS3-MN-20. P. 43–44.
- [2] *Dehant V. et al.* Geodesy instrument package on the Moon for improving our knowledge of the Moon and the realization of reference frames // Planetary and Space Science. 2012. V. 68. P. 94–104.
- [3] *Kosov A.S. et al.* Radioscience experiments for Martian and Lunar missions // 8th Moscow Solar System Symp. 2017. 8MS3-IM-17.
- [4] *Turyshev S.G., Williams J.G.* Space-based tests of gravity with laser ranging // Intern. J. Modern Physics D. 2007. V. 16. No. 12a. P. 2165–2179. <https://doi.org/10.1142/S0218271807011838>.
- [5] *Williams J.G. et al.* Improving LLR tests of gravitational theory // Intern. J. Modern Physics D. 2004. V. 13, No. 03. P. 567–582.

APPLICATION OF CRYOCOOLING SYSTEMS FOR THE MISSION OF LUNAR POLAR SAMPLE RETURN

P. R. Savvatimova^{1,2}, T. M. Tomilina^{1,2}, I. G. Mitrofanov¹

¹ *Space Research Institute RAS, Moscow, Russia, Savvatimova_n.docx*

² *Mechanical Engineering Research Institute RAS, Moscow, Russia*

KEYWORDS:

Moon exploration, lunar regolith, samples return, cryocooling in space

ABSTRACT:

Currently, scientific interest in lunar sample return missions has increased significantly. Recent discoveries have provided evidence that the lunar polar regolith contains a large fraction of water ice in the shallow subsurface [1]. Such water, at least partially, is thought to be delivered to the poles of the Moon by comets, and is stored there in the form of permafrost due to very low temperature of the polar regolith about 100–150 K.

Biochemical analyses of lunar permafrost is of great scientific importance, since cometary water is known to contain many complex biochemical components, including some amino acids. To study such lunar substance, it is necessary to deliver its samples to the Earth in an initially frozen state.

Therefore, it is necessary to develop a special cryo-cooling system for the lunar pole samples return mission that will keep these samples frozen during the flight back to Earth. This report reviews the most appropriate ways for design such system based on the solutions already proposed [2–3] and on some new ideas that can be developed in the future. In addition, the requirements for integration of the system on spacecraft are considered depending on total mass of returning samples.

REFERENCES:

- [1] *Mitrofanov I. G. et al. Hydrogen mapping of the lunar south pole using the LRO Neutron Detector Experiment LEND // Science. 2010. V. 330. Iss. 6003. P. 483.*
- [2] *Kittel P., Feller J., Roach P. et al. Cryocoolers for space // Intern. Thermal Detectors Workshop. 2004. P. 1–3.*
- [3] *Collaudin B., Passvogel T. The FIRST and Planck 'Carrier' missions // Description of the cryogenic systems // Cryogenics. 1999. V. 39. P. 157–165.*

CREATION OF SOILS-ANALOGUES FOR SCIENTIFIC EQUIPMENT TESTING

A. V. Uvarova, M. Yu. Makovchuk

*Vernadsky Institute of Geochemistry and Analytical Chemistry RAS
Moscow, Russia, uvarova@geokhi.ru*

KEYWORDS:

soil-analogue, lunar testing site, lunar soil, lunar regolith

INTRODUCTION:

Testing scientific equipment designed for the study of lunar regolith requires the creation of soil conditions similar to the studied object, as they significantly influence the state and functioning of mechanisms and systems. When evaluating the performance of chassis and landing platforms, it is essential to consider the mechanical properties of the regolith, such as its bearing capacity, porosity, and compaction under different loads. However, the use of original lunar regolith is not feasible due to the limited quantity of samples brought back. Additionally, conducting tests in a vacuum environment is often difficult or impossible, while lunar soil changes its properties in Earth's atmosphere.

Therefore, there is a need to create soil analogs that can be produced in large volumes using relatively simple technology and readily available materials. The Laboratory of Geochemistry of the Moon and Planets at GEOKHI RAS is engaged in the development of soil analogs for large-scale tests and other experiments.

APPROACH TO DEVELOPING SOIL-ANALOGUES:

The development of soil-analogues depends primarily on the purpose of the experiments. Testing drilling tools, assessing wheel mobility, or evaluating landing capabilities require a significant volume of soil, typically several cubic meters. It is crucial to model the physical and mechanical properties of the soil, such as density, porosity, bearing capacity, and other parameters influenced by grain-size distribution and shape. Such soil-analogues can be crafted from readily available and inexpensive components, where the mineral composition is of secondary importance. Components should be selected in appropriate fractions and mixed in the necessary proportions.

For testing spectrometric analysis instruments and determining thermo-physical properties, it is essential to match the mineral and chemical composition. Creating such an analogue is a more complex task, as it requires grinding and crushing of a rock closely resembling lunar regolith in composition to achieve the necessary parameters. Crushing results in angular particles characteristic of lunar regolith, while grinding facilitates obtaining fine fractions less than 0.1 mm. Sieving the mixed blends through a sieve column and subsequent mixing in required proportions are necessary steps for modeling the grain-size distribution.

RESULTS AND DISCUSSION:

The laboratory has developed soil analogues for various experiments. One of the first was VI-75 [1], created for large-scale drop tests for the "Luna-25" mission. It was produced using the aforementioned method without considering mineral composition. The lunar soil analogue VI-75 matches the original lunar soil in all measurable control parameters of physical and mechanical properties and grain-size distribution. VI-75, like real lunar soil, is characterized by high cohesion, with particles capable of sticking together and forming clumps on the surface under mechanical impact (Table 1).

Our laboratory has also developed analogue that closely resemble the mineral composition of lunar regolith. VI-LH1 is one of the most accessible and affordable analogues of highland lunar soil. This analogue is highly similar in chemical and mineralogical composition to most other analogues, while also possessing certain advantages. Most parameters of VI-LH1 correspond to the highland regolith collected by the Apollo-16 mission and align well

with other highland simulants, confirming its high capability to mimic many properties of lunar soils.

Table 1. Comparison of properties of soil-analogues and lunar soil

Samples	$\rho_s, \text{g/cm}^3$	$\rho, \text{g/cm}^3$	φ, degree	c, kPa
VI-75 [1]	2.56	1.50–1.93	46–21	0–11
VI-HL1	2.86	1.29–1.81	42.4–40.4	2.5–15.8
Lunar soil [3][4]	2.3–3.2	1.12–1.92	46.5–25	0–1.8

REFERENCES:

- [1] *Slyuta E. N., Grishakina E. A., Makovchuk V. Yu., Agapkin I. A.* Lunar soil-analogue VI-75 for large-scale experiments // *Acta Astronautica*. 2021. No. 187. P. 447–457.
- [2] *Mironov D. D., Uvarova A. V., Slyuta E. N., Sorokin E. M., Agapkin I. A., Grishakina E. A.* VI-LH1 — lunar highlands simulant for large scale experiments // 14th Moscow Solar System Symp. 2023. P. 110–112.
- [3] *Carrier W. D. III, Olhoeft G. R., Mendell W.* Physical properties of the lunar surface // *Lunar Sourcebook* / Eds. Heiken G., Vaniman D., French B.M. Cambridge: Cambridge Univ. Press, 1991. P. 475–594.
- [4] *Slyuta E. N.* Physical and mechanical properties of the lunar soil (A review) // *Solar System Research*. 2014. V. 48(5). P. 330–353.

INFRASTRUCTURE DEVELOPMENT OF THE MOON IX: 3D PRINTING ON LUNAR REGOLITH

A. V. Gusev¹, Z. G. Meng², J. S. Ping³

¹ Kazan Federal University, Department of Mathematical Methods in Geology, Kazan, Tatarstan, Russia, agusev33@gmail.com

² College of Geoexploration Science and Technology, Jilin University Changchun, China

³ National Astronomical Observatory CAS, Beijing, China

KEYWORDS:

Moon, crust, geological exploration, 3D printing

INTRODUCTION:

Over the past decade, the China Lunar Exploration Program (CLEP), also known as the Chang'e Project (CE), has achieved novel, remarkable and important results. It has successfully developed and demonstrated the engineering capabilities needed to reach and return astronauts from the lunar surface [1]. Lunar exploration is essential to elucidating the origin of the Earth-Moon system and is a critical first step toward advancing humankind's exploration of deep space. In particular, the CE project achieved the first-ever landing and in-situ exploration of the far side of the Moon and collected the youngest volcanic cores from the Procellarum KREEP terrane. These achievements have greatly expanded our current understanding of the interior structure and spatiotemporal evolution of the Moon [2].

China and Russia's lunar exploration plans include 3D printing building bricks from lunar soil. China intends to test printing bricks from lunar soil in the coming years, which would be a major step toward establishing a base on the Moon. China is currently working on the next batch of lunar missions, including Chang'E-6, which was collected the first samples from the far side of the Moon in June 2024, and the multi-mission Chang'E-7, scheduled for launch in 2026, which will search for icy water in Moon's shadowed craters [3].

China's Chang'E-8 mission is planned for 2028 and, in addition to landing on the Moon, may include tests on using resources found on the lunar surface. This plan encompasses two primary phases: the first crewed lunar landing and exploration, followed by a thousand-kilometer scale scientific expedition to construct a geological cross-section across the lunar surface. Chinese scientists confirm that they are exploring the possibility of 3D printing building blocks from materials found on the lunar surface [4].

Ding Liyu, a scientist from Huazhong University of Science and Technology, China presented a prototype of a six-legged, insect-like robot that he called a "super mason". As a result, building habitations beyond Earth is vital not only to humanity's quest to explore the Moon, but also to China's strategic needs as a lunar space power. If these construction technologies prove effective, they will be used to build the International Lunar Research Station (ILRS), which China and Russia will begin building in the 2030 [5].

3D PRINTING:

On July 21, 1969, Neil Armstrong took his first steps on the Moon, on a surface covered in lunar dust. Now, 55 years later, scientists are developing technology that will make 3D printing possible using lunar dust. To be able to build a lunar station for further space travel without transporting heavy building materials from Earth.

A new global space race is in full swing with very enticing end goals such as the establishment of a multifunctional base on the Moon. As part of this lunar renaissance, NASA has awarded multi-million-dollar contracts to US firms for regolith 3D printing technologies to establish permanent lunar bases by 2040. What and who is fueling this worldwide boom in 3D printing

manufacturing on the Moon? How feasible is this construction technology in the harsh lunar environment?

3D printing for space lunar construction activities has been considered and tested for many years: China, Russia, the USA and the EU are working on producing lunar blocks from lunar regolith analogues. 3D printing for space activities has been considered and tested for many years: the European Space Agency (ESA) is working on producing building bricks from lunar soil simulant, and Airbus is preparing to send a metal 3D printer to the ISS. Such capabilities mean that building blocks can be produced on the Moon instead of delivered from Earth, which will significantly reduce their cost.

Building a lunar base is a strategic challenge for humanity on Earth. To avoid transporting heavy building materials from Earth to the Moon, scientists are developing the possibility of using lunar regolith in the work of powerful 3D printers. They will be able to print the building blocks directly on site — so-called additive manufacturing.

Prof. Ross Friel from Halmstad University leads a team of researchers working on autonomous additive manufacturing (also called 3D printing) that can and should be used on the Moon and for exploration of the planets of the solar system [6]. According to Ross Friel it is economically and technically advantageous to use the Moon as a launch site due to its weak gravity, extremely transparent atmosphere and clear astronomical observational sky, as well as the ability to use hydrogen and oxygen obtained from lunar ice for rocket fuel. The lunar building material must withstand and protect astronauts from harmful cosmic radiation and small meteoroids. By melting the initial building material on Earth that has the properties of the lunar regolith, it is possible to print various types of textures using a specially designed 3D printer: a) compact cubes, b) a potential filter structure, c) a screw and nut showing the printing accuracy, and d) a building block in the form of a puzzle piece and as a first step towards interconnected building components to create compact material structures directly on the Moon.

In the future, scientists will continue to develop construction technologies for an autonomous 3D printer that can function effectively on the Moon. They will tighten the parameters of ground tests to more accurately simulate the conditions on the Moon's surface: a) under ultra-high vacuum, b) exposing the terrestrial simulant of the lunar regolith to cosmic radiation, and c) high-speed collisions with objects simulating small meteorites [6].

LUNAR REGOLITH:

One of the most important components of NASA's Artemis program will be the Gateway lunar orbiter. It will orbit the Moon and provide essential support for lunar missions. From lunar orbit, astronauts will travel to the Moon's surface, landing where no human has gone before, at the Moon's South Pole. This is an ideal location for a future base camp, given its potential access to ice deposits and other geological resources. NASA's long-term goal is to create a permanent habitat at the base camp that could house up to four astronauts for a month. We cannot approach building a habitat on the Moon in the same wasteful way that we do on Earth. We must learn to live off the Earth and use the Moon's resources, because every kilogram we send there is worth a million dollars. The most promising material we can use is lunar soil or regolith. Regolith is a layer of loose, unconsolidated lunar rock and dust that lies at the surface of the bedrock.

Lunar regolith was formed approximately 4.6 billion years ago by large and small meteorites that loosened the surface rocks. We can dig up this powder to make a new building material. While regular concrete is made up of water, aggregate, and cement, lunar concrete would be made from regolith and sulfur. Sulfur acts as a thermoplastic binder. Sulfur can be mixed with regolith, heated to its melting point, and then cooled to create lunar concrete. This sintering process can be achieved using concentrated sunlight. The resulting solid lunar concrete does not need to be cured, and it does not require water. Using this mixture as a base material, construction com-

panies around the world have come up with some outlandish proposals for lunar colonies [6].

In 2022, US firm ICON received an additional \$57.2 million to develop a 3D printing system for the Moon. They teamed up with Bjarke Ingels Group and Search+ to develop these doughnut-like igloos with waffle-like outer surfaces. The team is also experimenting with imitation lunar substance or synthetic regolith. Instead of a nozzle that spews out soft concrete, a high-intensity laser beam melts powdered regolith, turning it into a hard, durable building material. ICON then sends its test prints to NASA, where they are fired with a plasma torch at 4,000F. This test will tell us whether the regolith can be used for landing pads.

The next test will involve a robotic arm and laser operating inside NASA's Thermal Vacuum Chamber, which simulates the extreme cold, heat and vacuum conditions of the Moon. The deep vacuum and cheap solar energy open up new horizons for electronics, foundries, metalworking and materials science on the Moon. The Moon, with its spectacular landscapes and exotic features, will also be an attractive destination for tourists. When it comes to large-scale colonization of the Moon and Mars, 3D printing will be used to build roads and structures using their soil and regolith [6].

REFERENCES:

- [1] *Tang T., Meng Z. G., Lian Y. et al.* Extracting Mare-like Cryptomare Deposits in Cryptomare Regions Based on CE-2 MRM Data Using SVM Method // *Remote Sensing*. 2023. V. 15. Article 2010.
- [2] *Meng Z. G., Sun H., Wei Zh. et al.* Thermophysical properties of surface deposits in Tsiolkovsky crater and its geologic significance revealed by CE-2 MRM data // *Icarus*. 2024. V. 408. Article 115808.
- [3] *Meng Z. G., Tang T. Q., Dong X. G., Gusev A. V.* Analyzing the microwave thermal emission features of lunar regolith in Chang'E landing sites and its geologic significance. // *Scientia Sinica Physica, Mechanica and Astronomica*. 2023. V. 53. Iss. 3. P. 1–14 (in Chinese).
- [4] *Gusev A. V., Meng Z. G., Ping J. S.* Geological exploration of the Moon IV: Water and the mystery of the thermal budget of the early Moon // *Proc. 57th Scientific Readings in memory of K. E. Tsiolkovsky. RAS — RASTs. Section Modern Problems of Rocket and Space Technology*. 2023. P. 233–248 (in Russian).
- [5] *Ding L.* Chinese six-legged robot for the Moon. 2023. P. 1–2. <https://shazoo.ru/2023/04/19/142439/plany-kitaia-po-osvoeniiu-luny-vkliuaiut-3d-pecat-kirpicei-iz-lunnogo-grunta>.
- [6] *Gusev A. V., Meng Z. G., Ping J. S.* Construction — breakthrough development of the Moon: 3D printing on lunar surface // *Proc. 59th Scientific Readings in Memory of K. E. Tsiolkovsky. RAS — RASTs*. 2024. P. 1–4 (in Russian).

CHALLENGES AND INNOVATIONS IN LUNAR ENVIRONMENT SIMULATION FOR ANALOG MISSIONS

E. D. Faber, R. R. Kaspransky

Federal Scientific and Clinical Center of Space Medicine Federal Medical-Biological Agency of Russia, Moscow, Russia, faber.cat.rina@gmail.com

KEYWORDS:

Moon, analogue facilities, lunar exploration, lunar geology

ABSTRACT:

Accurate modeling of lunar surface conditions is critical in preparing for future lunar missions. The construction of the International Scientific Lunar Station is expected to be completed between 2035–2040 as part of the Russian-Chinese agreement and will subsequently lead to the return of human presence on the lunar surface [1]. This research examines a variety of methodologies and technologies used to reproduce critical factors in the lunar environment, such as lunar terrain reconstruction, lighting conditions, analog regolith composition and low gravity effects, and analyzes existing analog objects in the application to scientific issues of planetary science.

Within the analogue facility, specific mission scenarios can be simulated for cosmonaut training, including testing of geological and seismic regolith characterization techniques, in situ resource utilization technologies, rock mapping and storage, chemical soil sample analysis techniques, robotics, and extravehicular activity preparation [2].

Innovations in simulation technologies are also discussed, with an emphasis on advances aimed at improving the accuracy and completeness of analog environments used for crew training and equipment testing for future lunar missions. By evaluating these modeling approaches, this study aims to improve our understanding of the effectiveness of such projects in solving scientific problems associated with lunar exploration. The resulting data will help optimize analog facilities conditions, thereby increasing the readiness and safety of cosmonauts and equipment for operations on the lunar surface.

REFERENCES:

- [1] International Lunar Research Station: ILRS, Guide for Partnership. v1.0 / CNSA and Roscosmos. 2022. <https://www.roscosmos.ru/media/files/mnls.pdf>
- [2] Casini A. E. M., Mittler P., Cowley A. et al. Lunar analogue facilities development at EAC: the LUNA project // J. Space Safety Engineering. 2020. V. 7. Iss. 4. P. 510–518. <https://doi.org/10.1016/j.jsse.2020.05.002>.

LANDING SITE CHOICE FOR LUNA-27 MISSION IN THE MOON SOUTH POLAR REGION

O. I. Turchinskaya, E. N. Slyuta

Vernadsky Institute of Geochemistry and Analytical Chemistry RAS
Moscow, Russia. turchinskaya@geokhi.ru

KEYWORDS:

Moon, Luna-27, landing sites, solar illumination, visibility of Earth, surface slopes, digital elevation model

INTRODUCTION:

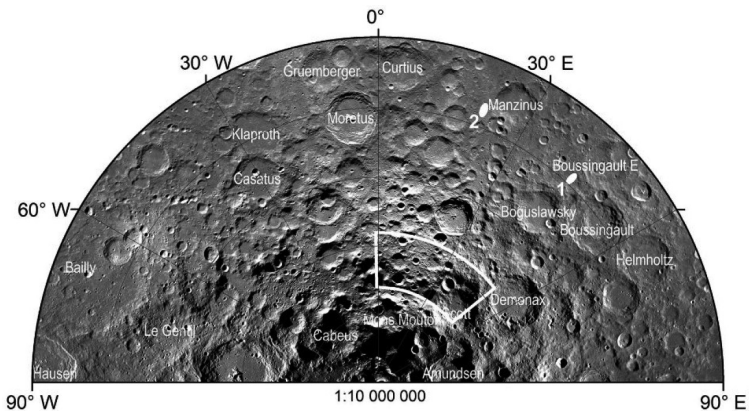


Fig. 1. Mosaic of images of the Southern Polar region up to 65°S in polar stereographic projection with a resolution of 100 m/pixel based on data from the WAC camera of the LRO spacecraft [28]. The boundaries of the Luna-27 mission's landing sector are shown in white. 1 — the main landing ellipse of the Luna-25 mission; 2 — the backup landing ellipse of the Luna-25 mission

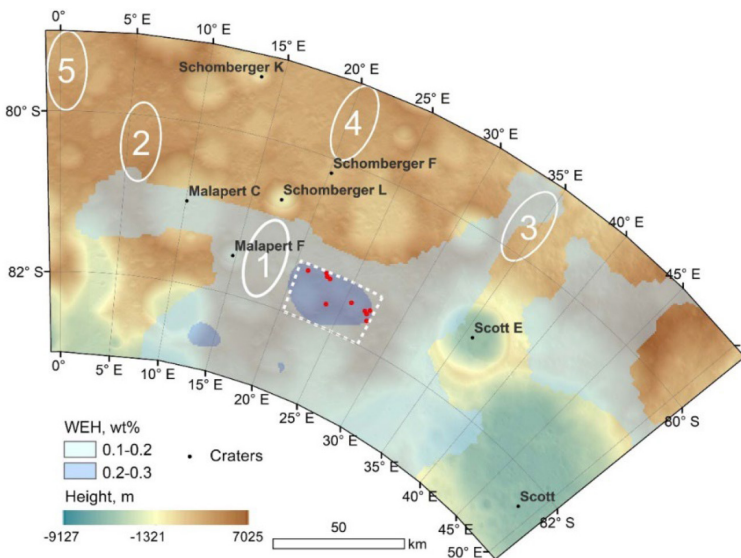


Fig. 2. Map of the landing sector in the South Polar region of the Moon based on data from NASA's LROC with an overlay map of WEH deposits [31]. The boundaries of the landing ellipses measuring 30×15 km are shown in white. The area suitable for landing with increased landing accuracy is shown with a white dashed line. The boundaries of the sites with increased landing accuracy measuring 0.5 km are shown in red

The Luna-27 mission is set to explore a sector in the Moon's South Polar region. Given the limitation on the duration of the landing spacecraft's orbit to 7 days due to the limited fuel supply for orientation and stabilization [1], the choice of the proposed landing area for ballistic reasons is confined to a sector by selenographic longitude in the range: from 51° E to 1°W (Figure 1).

This area features challenging terrain, necessitating a detailed analysis of slope distribution, solar illumination, and Earth visibility to identify viable landing sites. We developed a suitability map highlighting five potential sites, each measuring 30×15 km, that comply with critical scientific and technical criteria, such as slope gradients of less than 7–10°, solar illumination exceeding 35 %, and Earth visibility above 50 % [2]. The sites are prioritized based on the water equivalent hydrogen (WEH) content in the lunar soil [3, 4], with Site No. 1 being the most favorable, followed by Sites No. 2 and No. 3 as alternatives (Figure 2).

The study further shows that enhancing landing accuracy, reducing deviation to within 0.5 km from the target point, increases the number of scientifically valuable and technically feasible landing sites.

REFERENCES:

- [1] *Djachkova M. V., Mitrofanov I. G., Sanin A. B. et al.* Characterization of the luna-25 landing sites // *Sol. Syst. Res.* 55. 2021. P. 509–528. <https://doi.org/10.1134/S0038094621060034>.
- [2] *Djachkova M. V., Mitrofanov I. G., Sanin A. B., et al.* Selecting a landing site for the Luna 27 spacecraft // *Sol. Syst. Res.* 56. 2022. P. 145–154. <https://doi.org/10.1134/S0038094622030029>.
- [3] *Sanin A. B., Mitrofanov I. G., Litvak M. L. et al.* Hydrogen distribution in the lunar polar regions // *Icarus.* 2017. V. 283. P. 20–30. <https://doi.org/10.1016/j.icarus.2016.06.002>.
- [4] *Slyuta E. N., Turchinskaya O. I., Tretyukhina O. S. et al.* Forecast water ice reserves in the Moon Polar regions by the LEND data // *Lunar Planet. Sci. Conf.* 54. 2023. Article 1089. <https://www.hou.usra.edu/meetings/lpsc2023/pdf/1089.pdf>.

THE THREE-DIMENSIONAL GEOLOGICAL MODEL OF THE VIPER MISSION LANDING AREA

A. S. Krasilnikov¹, S. S. Krasilnikov², M. A. Ivanov¹, J. W. Head³

¹ Vernadsky Institute of Geochemistry and Analytical Chemistry RAS
Moscow, Russia, krasilnikov_as@geokhi.ru

² Planetary Remote Sensing Laboratory, Department of Land Surveying
and Geoinformatics, Hong Kong Polytechnic University
Hong Kong, PR China;

³ Brown University, Providence, RI, USA

KEYWORDS:

Moon, South Pole of the Moon, geological cross-section, crater ejecta, VIPER mission, South Pole-Aitken

INTRODUCTION:

The Volatiles Investigating Polar Exploration Rover (VIPER) mission — is a project developed through NASA's Science Mission Directorate (SMD), aimed at exploration of lunar polar volatiles [1]. As a sufficient part of the VIPER mission, it is planned to send a rover to carry out observations of the surface and subsurface. Modelling of the subsurface geological structure of the landing site and the traverse region will provide important information for successful accomplishment of the mission goals. Using data on the location of the primary and extended landing areas [2] and the new geological map of the south circumpolar region [3], we produced a three-dimensional stratigraphic reconstruction of the landing site and the exploration areas (Figure 1a, b). The reconstruction was done with the help of the models of the crater radial ejecta thickness decay proposed in [4–6].

ESTIMATIONS OF CRATER EJECTA THICKNESS:

To determine the ejecta thickness, the following models were used: (1) $T = 0.033R(r/R)^{-3}$ for craters in the 4–45 km diameter range [4]; (2) $T = 0.0078R(r/R)^{-2.61}$ (for craters in the 45–300 km diameter range [5]; and (3) $T = 2900(\pm 300) \cdot (r/R)^{-2.8(\pm 0.5)}$ for basins [6]. In all formulas, r is the distance from the center of the crater to the point of interest, R is crater radius; both are in meters.

CONSTRUCTING OF GEOLOGICAL THREE-DIMENSIONAL MODEL:

The three-dimensional stratigraphic reconstructions were produced using both the LOLA gridded topography (60 m/px resolution) [7, 8] as the surface topographic constraint (Figure 1a) and the recent geological map of the southern circumpolar region [3] as the stratigraphic constraint for the rock-stratigraphic units. When creating the model, a series of parallel geological cross-sections were constructed. They show the lower and upper limits of the stratigraphic units determined by the calculation of the ejecta thickness and refined by the local geological features. The absolute majority of the subsurface structure in the study is made up by the pre-Nectarian formations, the distinctive parts of which are the deposits of the earliest South Pole-Aitken and subsequent Amundsen-Ganswindt basins. The ejecta from the remaining pre-Nectarian craters were combined into a single composite layer because it is impossible to confidently determine the relative ages of these craters. In order to reconstruct the 3D-structure of the entire landing area (Figure 1a, b), we interpolated the thickness of the ejecta deposits of the same age between the neighboring parallel cross-sections. Such a reconstruction allows studying of the area geology in more detail and construct the geological cross-sections through any place of interest.

GEOLOGICAL STRUCTURE OF THE VIPER STUDY AREA:

The primary area is located on Mons Mouton, the flat-topped plateau that is ~100 km across and ~6 km high. Mons Mouton is likely to represent a rim massif of the SPA basin (Figure 1c, unit pN_{spa}) covered by younger ejecta deposits from nearby craters; the deposits have a maximum thickness of ~1800 m (Figure 1c, units pN_{agb} and pN).

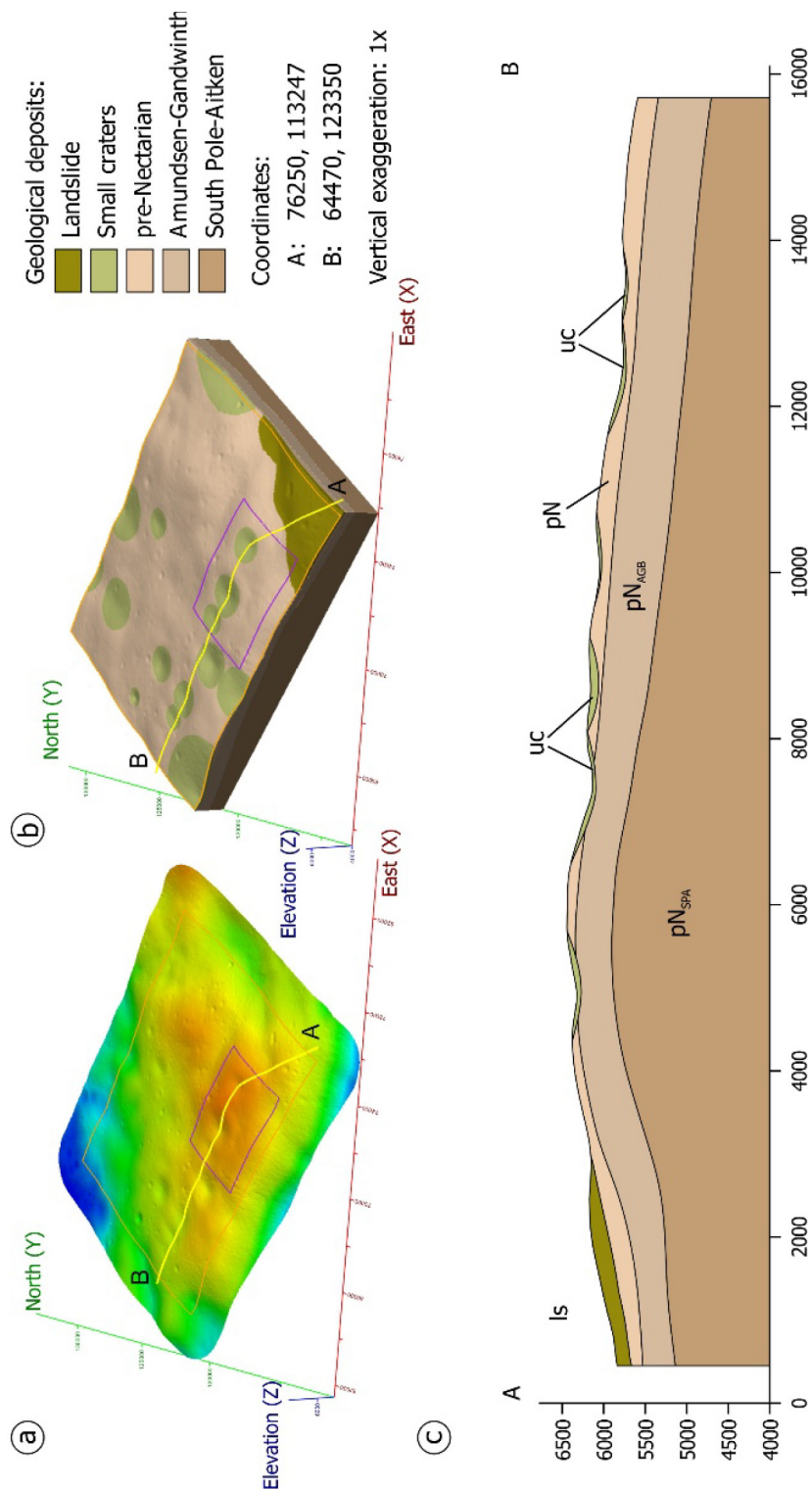


Fig. 1. Topographic (a) and geological three-dimensional model (b) with VIPER primary (violet) and extended (orange polygon) areas, and geological cross-section (c) through them (a, b — yellow line)

The Amundsen-Ganswindt basin (AGB) ejecta (Figure 1c, unit pN_{agb}) has a model thickness of ~800–1300 m in the study area. The composite layer of the pre-Nectarian craters (Figure 1c, unit pN) [3] consists of ejecta from craters Haworth, Shoemaker, Malapert, Scott, Nobile and two unnamed craters (~27 km and ~44.5 km, respectively) with a total model thickness of ~250–500 m. The southeastern part of the research area has a hill (Figure 1a) that may represent a block of material (in unit pN_{spa}) emplaced as a result of the SPA impact. We believe that the total thickness of the ejecta that overlaps the SPA deposits in the hill area should be less than the model calculations because the units were likely to have been affected by enhanced mass-wasting processes on the hill flanks, as typically seen on similar SPA basin mountain units such as Mons Malapert [9]. The southern part of the plateau has steeper slopes probably because it was affected by post-SPA impacts.

The study area has numerous smaller craters but even the largest of them likely were unable to penetrate through the pN layer if their excavation depth is estimated as 1/10 of the crater diameter (e.g., [10]). However, if the thickness of ejecta of the pre-Nectarian craters was significantly reduced on the top surface of the hill by the downslope mass wasting processes (say, by a factor of 2 to 3), then four craters with diameters 1–1.5 km in this area could have excavated materials of the pN_{agb} unit. Because this material was excavated by the Amundsen-Ganswindt impact from the deeper horizons of the lunar crust it has very high scientific potential.

SUMMARY:

The construction of a three-dimensional stratigraphic model of the area where the VIPER Mission Rover will work provides valuable information about the sites of the high scientific priority that likely have to be visited during the rover operations.

REFERENCES:

- [1] Colaprete A., Elphic R.C., Shirley M., Ennico-Smith K., Lim D.S.S., Zacny K., Caplain J., Seigler M., Balaban E., Beyer R., Falcone L., Mirmalek Z., Lees D. The Volatiles Investigating Polar Exploration Rover (VIPER) mission update // 53rd Lunar and Planetary Science Conf. 2022. Article 2675.
- [2] Beyer R.A., Alexandrov O., Balaban E., Colaprete A., Shirley M., Martinez-Camacho J., Siegler M. VIPER geospatial data for site selection and traverse planning // 54rd Lunar and Planetary Science Conf. 2023. Article 2377.
- [3] Krasilnikov S.S., Ivanov M.A., Head J.W., Krasilnikov A.S. Geologic history of the south circumpolar region (SCR) of the Moon // *Icarus*. 2023. V. 394. Article 115422.
- [4] Sharpton V.L. Outcrops on lunar crater rims: Implications for rim construction mechanisms, ejecta volumes and excavation depths // *J. Geophysical Research: Planets*. 2014. V. 119. P. 154–168.
- [5] Housen K.R., Schmidt R.M., Holsapple K.A. Crater ejecta scaling laws: fundamental forms based on dimensional analysis // *J. Geophysical Research: Solid Earth*. 1983. V. 88. P. 2485–2499.
- [6] Fassett C.I., Head J.-W., Smith D.E., Zuber M.T., Neumann G.A. Thickness of proximal ejecta from the Orientale Basin from Lunar Orbiter Laser Altimeter (LOLA) data: Implications for multi-ring basin formation // *Geophysical Research Letters*. 2011. V. 38. Iss. 17. Article L17201. 5 p. <https://doi.org/10.1029/2011GL048502>.
- [7] Smith D.E., Zuber M.T., Jackson G.B. et al. The Lunar Orbiter Laser Altimeter investigation on the Lunar Reconnaissance Orbiter Mission // *Space Science Reviews*. 2010. V. 150. P. 209–241. DOI: 10.1007/s11214-009-9512-y.
- [8] Barker M.K., Mazarico E., Neumann G.A., Smith D.E., Zuber M.T., Head J.W. Sun X. A new view of the lunar south pole from the Lunar Orbiter Laser Altimeter (LOLA) // *The Planetary Science J*. 2023. V. 4. No. 9. P. 1–36.
- [9] Basilevsky A.T., Krasilnikov S.S., Ivanov M.A., Malenkov M.I., Michael G.G., Liu T., Head J.W., Scott D.R., Lark L.L. Potential lunar base on Mons Malapert: topographic, geologic and trafficability considerations // *Solar System Research*. 2019. V. 53. P. 383–398.
- [10] Melosh H.J. *Impact Cratering: A Geologic Process*. N.Y.: Oxford Univ. Press, 1989. 253 p.

THEORY OF THE ORIGIN OF TERRESTRIAL AND LUNAR ORES

A. N. Safronov

*Obukhov Institute of Atmospheric Physics RAS
Moscow, Russia, safronov_2003@mail.ru*

KEYWORDS:

comet impact, galaxy storm, galaxy calm, elemental buoyancy theory, mantle-core layers, ores origin

INTRODUCTION:

The purpose of this work [1] is to study the origin of terrestrial and lunar ores. It is shown that ore deposits on the Earth and the Moon were mainly formed simultaneously with the separation of the Moon from the protoplanet and the formation of the oldest continents. This happened after the comet hit the surface of the protoplanet at a grazing angle [2]. The time of formation of terrestrial and lunar ores corresponds to the boundary between the Tonian and Cryogenian Periods (~720 Ma). Further in [2] it is shown that the theoretical basis for the stratification of the internal structure of planets and satellites is the Elemental Buoyancy Theory. In [2], this concept was generalized to the theory of isotope buoyancy. The violation of the stratification of isotopes and chemical elements with the depth of the molten magma of planets (satellites) forms the theoretical basis for the formation of ores on the surface of the Earth and Moon.

RESULTS:

The formation of terrestrial ores occurred as a result of the release of intermediate and heavy chemical elements from the deep layers of the protoplanet and the subsequent process of adhesion to old terrestrial geological faults. Please note that the terrestrial ore formation process is not a one-step process and include stage of comet impact, galaxy storm, and galaxy calm, see discussion in [1]. At different stages of the evolution of the planet and satellite, the process of ore formation differs greatly both in terms of the volume of ore formation and their localization. The results of this study are summarized in Table 1.

Table 1. The localization and qualitative comparison of the formation of ores, water, methane and diamonds at different stages of the evolution of the Moon-Earth system are presented

Period	Creation	Earth hemisphere		Moon	
		Southern	North	Nearside	Farside
Comet impact	Ores (intermediate and heavy elements)	Oldest faults		More, scattering	Less, in craters
	Diamonds	More, large size	Less, small size	None	Probably
	Water	None	Yes	Slightly	Slightly
	Methane and oil				
Galaxy storm	Ores (intermediate elements)	MORBs, LIPs		None	
Galaxy calm	Light elements, mainly sulphide	Volcanic lavas and ashes			

The processes of ore formation on the Moon differ on the near and far sides. The reverse side of the Moon is a single fragment of the protoplanetary lithosphere, so ores there could be formed mainly due to the overflow of igneous rocks over the edge of the lunar continent. On the nearside side, due to the rapid cooling, ores were formed in the navel area during the droplet-liquid separation of the Moon from the Earth. Due to the fact that the Moon separated at the first stage, the amount of water and methane on it is limited.

ed. In periods after the Cryogenian, volcanic, lava and sedimentary rocks on Earth could be enriched with intermediate elements due to the disruption of vertical stratification during galactic storms. The process of formation of the lunar ores is schematically shown in Figure 1.

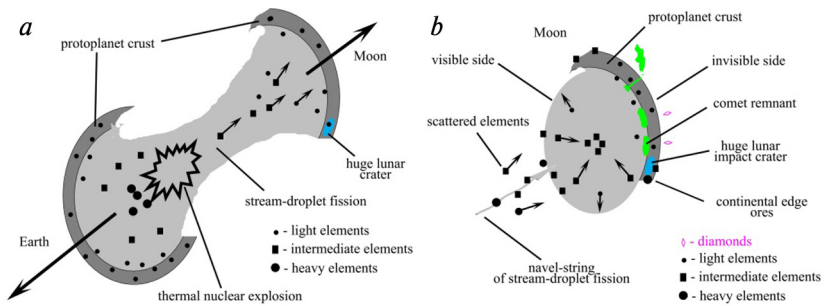


Fig. 1. The scheme illustrates the process of formation of lunar ores: (a) thermal nuclear explosion of a protoplanet after a collision with a comet. The Moon was created as a result of the viscous liquid-droplet separation from a piece of crust and the magmatic mass of a protoplanet; (b) the stage of cooling of the Moon and the formation of lunar ores. The huge lunar comet impact crater is filled by blue spots; the gaseous comet remnants under the crust are green; diamond deposits are shown by violet rhombuses, and the lunar volcano spews a gas plume which is also drawn in green as some comet remnants.

DISCUSSION:

Therefore, the theory of the spatial distribution of ores on the Earth and the Moon is based on the Elemental Buoyancy Theory (EBT). However, please do not confuse the theory of ore formation with the theory of the formation of chemical elements. Chemical elements can only be synthesized in nuclear reactors. Each star is a nuclear reactor, but the Sun has a weak reactor capable of mostly synthesizing only hydrogen and helium. According to most astrophysicists, all other chemical elements should have been brought into the Solar System from other stars. However, the author is surprised to find that the transfer equation is missing in the chemical models of galaxies (GCE). Note that in the 80 years of the existence of GCE models, none of the astrophysicists have asked a question about the transfer equation.

In addition to the theory of ore formation presented in [1], the author has developed a new theory of the synthesis of chemical elements. The results of this theory are presented in [3] and [4].

REFERENCES:

- [1] Safronov A. N. Theory of the Origin of Terrestrial and Lunar Ores // Intern. J. Geosciences. 2023. V. 14. P. 547–583. DOI: 10.4236/ijg.2023.146030.
- [2] Safronov A. N. The basic principles of creation of habitable planets around stars in the Milky Way Galaxy // Intern. J. Astronomy and Astrophysics. 2016. V. 6. P. 512–554. DOI: 10.4236/ijaa.2016.64039.
- [3] Safronov A. N. Life Origin in the Milky Way Galaxy: I. The stellar nucleogenesis of elements necessary for the life origin // J. High Energy Physics, Gravitation and Cosmology. 2024. V. 10. P. 647–680. DOI: 10.4236/jhepgc.2024.102040.
- [4] Safronov A. N. Life Origin in the Milky Way Galaxy: III. Spatial distribution of over-heated stars in the solar neighborhood // J. High Energy Physics, Gravitation and Cosmology. 2024. V. 10. P. 693–709. DOI: 10.4236/jhepgc.2024.102042.

JOINT LUNA DATA CENTER (JLDC) PROJECT

V. N. Nazarov¹, A. A. Abbakumov¹, V. V. Konoplev¹, W. Wang², X. Li²

¹ Space Research Institute, Moscow, Russia, Vladimir.Nazarov@cosmos.ru

² Deep Space Exploration Lab, Beijing, China, lixm@dseel.cc

KEYWORDS:

Moon, solar system, astronomy, cosmic ray, data bases, data processing

INTRODUCTION:

Planning and performing of science space experiments, both for projects under implementation and for future prospective projects, is impossible without taking into account previously obtained results. Moreover, for such areas as lunar exploration, which are in the field of interest of most foreign space agencies, it is especially important to rely on all available experience, i.e. obtained not only by respective domestic missions, but also on the results obtained by the whole world community.

As assistance for management of science space projects, as well as for principal investigators of particular experiments, to facilitate and improve the efficiency of their work, a joint Russian-Chinese initiative to create a Joint Luna Data Center (hereinafter — JLDC) was born. This initiative was supported by the Roscosmos State Corporation (hereinafter — Roscosmos) and the Chinese National Space Administration (hereinafter — CNSA) and the JLDC is currently being created.

The main Goals of JLDC include:

- To achieve the maximum possible scientific return on the background of the minimization of budget and technical risks.
- Deployment of multipurpose IT platform for joint science researches and operations.
- Preparation of a new generation of scientists and engineers for future projects.

ARCHITECTURE OF THE SYSTEM:

In accordance with the agreement between Roscosmos and CNSA, JLDC consists of two main nodes, Russian and Chinese. The corresponding designated entities can connect to the national main node, which consolidate the Russian and Chinese segments of JLDC.

At the same time, JLDC as a whole can be described using a hierarchical model that includes the following three levels:

- Technical level, which provides base technical facilities for data processing, storage and communications
- Functional level, which provides functional needed for science space operations.
- Expert level, which creates new knowledge based on research results and forms exploration plans

During designing of the JLDC, it was decided to expand the thematic sections of the Russian segment of the JLDC (the potential extension of the thematic coverage of the Chinese segment of JLDC is studied by the Chinese side). And now, in addition to the Moon exploration, it covers most other areas of space research.

CONCLUSION:

The article describes the general technical and technological aspects of the JLDC and various options for its use for different kinds of users.

ACKNOWLEDGMENTS:

A large number of researchers, programmers and engineers from various organizations are involved in the creation of JLDC. Therefore, the authors consider it their pleasant duty to express gratitude for the support of such organizations as:

- State Corporation for Space Activities Roscosmos.
- China National Space Administration (CNSA).

- Astro Space Center of P.N. Lebedev Physical Institute RAS (ASC LPI).
- Institute of Astronomy RAS (INASAN).
- Moscow State University of Geodesy and Cartography (MIIGAiK).
- Skobeltsyn Institute of Nuclear Physics, Lomonosov Moscow State University (SINP MSU).
- Vernadsky Institute of Geochemistry and Analytical Chemistry RAS (GEOKHI RAN).

INFLUENCE OF SUN, MOON AND PLANETS ON EARTH'S GRAVITATIONAL FIELD: DISCOVERY OF GRAVITONS AND ESTIMATION THEIR ENERGY

A. A. Barenbaum

Oil and Gas Research Institute RAS, Moscow, Russia, azary@mail.ru

KEYWORDS:

Schnol's experiments, near-Earth gravitational field, discovery of gravitons

ABSTRACT:

Based on analysis of macroscopic fluctuations of quantum processes studied by S.E. Schnoll and his colleagues, we established that these fluctuations caused by the cyclically changing influence of Sun, Moon and Solar System planets on gravitational field of rotating Earth. The carriers of this vector field are gravitons, which are virtual vector bosons. It is shown that these particles can be experimentally detected by modern quantum gravimeters, capable of "feeling" the gravitational attraction of solar mass stars at a distance of 4 kpc.

PROBLEM OF GRAVITONS:

According to modern concepts, all fundamental force interactions in nature (electromagnetic, strong, weak and gravitational) occur with transfer of energy quanta, which are carried by the corresponding elementary particles (real or virtual). For the first three interactions, these particles were predicted by the standard model of particle physics and have already been discovered, while gravitons, which are carriers of the gravitational interaction, are considered hypothetical particles and have not yet been discovered. It is expected that if gravitons exist, then they are neutral massless bosons moving at the speed of light, which in a weak gravitational field ensure the fulfillment of Newton's law of universal gravitation. Their spin is integer and their mass is $\sim 10^{-64}$ g (Wikipedia).

GOALS AND OBJECTIVES OF THE ARTICLE:

The article is based on an analysis of the results of experimental studies of macroscopic fluctuations (MFs) of various quantum processes, which Schnoll [1, 2] and his colleagues studied for 60 years. As a result, the researchers discovered that the histograms of the MF spectra depend on the latitude of the place, repeat with daily, monthly and annual periods, and also exhibit mirror symmetry after exactly half the corresponding period. For a long time, the phenomenon of MP and these facts remained inexplicable.

In [3], the author proposed an explanation of MF as a phenomenon caused by a change in near-Earth gravitational field under the influence of space objects surrounding Earth, which primarily include Sun, Moon and Solar System planets. During the Earth's axial rotation, they change their position on the celestial sphere relative to fixed points on earth's surface, which locally changes the force of gravity at these points and, as a result, causes macroscopic fluctuations in quantum processes.

This explanation presupposes the fulfillment of two conditions: 1) the near-Earth gravitational field is vector and, along with the attraction of Earth itself, is formed with the participation of other cosmic bodies; 2) the carriers of the force of attraction of bodies in Newton's law of gravity are gravitons. In this work, the author shows that both of these provisions are instrumentally confirmed by modern technical means that make it possible to register gravitons and estimate their energy.

JUSTIFICATION OF VECTOR STRUCTURE OF GRAVITATIONAL FIELD:

Table 1 shows estimates of the contributions to near-Earth gravitational field of Earth itself, as well as Sun, Moon and a number of planets in Solar

System. The magnitude of their contributions is expressed by acceleration α (cm/s^2) that they create on Earth's surface.

Calculations were carried out using the formula: $\alpha = GM/R^2$, where: G — gravitational constant; M — object mass; R — distance to the Earth's surface.

Table 1: Acceleration on Earth's surface created by space objects

Object	Mass M , kg	Distance R , km	Acceleration α , gal
Earth	$5.972 \cdot 10^{24}$	6378,1 6356,8	980.665
Sun	$1.989 \cdot 10^{30}$	$1.46 \cdot 10^8$ $1.52 \cdot 10^8$	59.6
Moon	$7.35 \cdot 10^{22}$	$3.62 \cdot 10^5$ $4.05 \cdot 10^5$	$3.74 \cdot 10^{-3}$ $2.99 \cdot 10^{-3}$
Venus	$5.974 \cdot 10^{24}$	$3.80 \cdot 10^7$ $2.61 \cdot 10^8$	$2.76 \cdot 10^{-5}$ $5.85 \cdot 10^{-7}$
Mars	$6.417 \cdot 10^{23}$	$5.46 \cdot 10^7$ $4.01 \cdot 10^8$	$1.43 \cdot 10^{-8}$ $2.67 \cdot 10^{-9}$
Jupiter	$1.9 \cdot 10^{27}$	$5.88 \cdot 10^8$ $9.67 \cdot 10^8$	$3.67 \cdot 10^{-5}$ $1.68 \cdot 10^{-5}$
Saturn	$5.9 \cdot 10^{26}$	$1.35 \cdot 10^9$ $1.69 \cdot 10^9$	$2.16 \cdot 10^{-8}$ $1.38 \cdot 10^{-8}$

Explanations: 1) for Earth, the equatorial and polar radii are indicated, the value of α is calculated for its average radius; 2) for Sun, the perihelion and aphelion distances of Earth are indicated, the value of α is calculated for the average distance; 3) calculations for Moon, Venus, Mars, Jupiter and Saturn were carried out at their minimum (upper number) and maximum (lower number) distance from Earth.

We see that the main contribution to the near-Earth gravitational field is made by Earth, followed by Sun, Moon and individual planets. However, the data in Table 1 indicate that although the force of Earth's gravitational attraction dominates, the contribution to the near-Earth gravitational field of other Solar System planets is not so small that it cannot be determined by modern gravimeters, which are designed to measure anomalies of Earth's gravitational field.

In this regard, we note that gravimeters have currently been developed with a sensitivity of more than $\alpha \approx 10^{-9} \text{ cm/s}^2$, which exceeds the threshold for detecting gravitational attraction of almost every planet in the Solar System. The sensitivity of cold-atomic quantum gravimeters is especially high [4]. These instruments measure the gravitational acceleration of an ensemble ($\sim 10^8$) of atoms (Cs or Rb) in a vacuum chamber cooled by a laser to a temperature ($\sim 10^{-5} \text{ K}$) at which they turn into a Bose-Einstein condensate. In this case, the acceleration of such a "quasiparticle" is determined by the readings of a laser interferometer that records quantum jumps in the energy of Bose-Einstein condensate. These devices operate in pulsed mode with a measurement cycle of the order of hundreds of milliseconds.

ESTIMATION OF GRAVITONS ENERGY:

We will perform this assessment for a quantum gravimeter [5]. We will find the energy of gravitons using the formula $W \approx aml$, where m_g is the mass of condensate particles falling as a single whole along a vacuum chamber of length $l = 15 \text{ cm}$. Let us assume that the ensemble of particles is a Bose-Einstein condensate consisting of $\sim 10^8$ atoms Cs (atomic weight of Cs = 132.9 g/mol) with a total mass $m = 2.2 \cdot 10^{-14} \text{ g}$.

We define the energy of gravitons at the sensitivity limit of the device $\alpha \approx 10^{-9} \text{ cm/s}^2$ as $W_{\min} \approx aml = (10^{-9} \text{ cm/s}^2) \cdot (2.2 \cdot 10^{-14} \text{ g}) \cdot 15 \text{ cm} = 2 \cdot 10^{-10} \text{ eV}$. At the same time, Sun's attraction force ($\alpha = 59.6 \text{ cm/s}^2$) will be $F_{\text{Sun}} = 1.31 \cdot 10^{-12} \text{ dynes}$, and the energy of its gravitons will be equal to $W_{\text{Sun}} = 1.25 \cdot 10^8 \text{ eV}$. We will consider the first value to be the energy threshold for registering gravitons with our gravimeter, and the second W_{Sun}

to be the energy of all “cosmic” gravitons that transferred their energy to the Bose-Einstein condensate Cs.

It was previously noted that the mass of 1 graviton is $m_g \sim 10^{-64}$ g. Let us assume that its energy is equal to $w_g = m_g c^2 = (10^{-64} \text{ g}) \cdot (3 \cdot 10^{10} \text{ cm/s})^2 = 5.6 \cdot 10^{-32}$ eV, is the same for gravitons of all objects in Table 1. Then the energy W_{Sun} can be represented as $W_{\text{Sun}} = n w_g$, where n is the number of gravitons (gravitational field quanta) that experienced interaction with the Cs condensate and completely transferred their energy to it. As a result, we obtain $n \approx (1.25 \cdot 10^8 \text{ eV}) / (2 \cdot 10^{-10} \text{ eV}) \approx 6 \cdot 10^{17}$.

This value is $\sim 6 \cdot 10^{17}$ times higher than the graviton detection threshold W_{min} . Therefore, a gravimeter with a sensitivity of $\sim 10^{-9} \text{ cm/s}^2$ will be able to detect the attraction of solar mass stars from distances $R \approx 8 \cdot 10^8 \text{ AU}$, i.e. $\sim 4 \text{ kpc}$.

Since gravitational energy is transferred by quanta, the relevant question is what wavelength and frequency they have. Let us express the energy of gravitons using Planck's formula: $w_g = hc/\lambda_g$, where $h = 6.626 \cdot 10^{-34} \text{ J}\cdot\text{s}$ is Planck's constant, c is the speed of light, λ_g is the graviton wavelength. From where we get $\lambda_g = hc/w_g = 4 \cdot 10^{15} \text{ cm}$. The value of λ_g turns out to be greater than the Solar System diameter.

Is it necessary to prove that at such a wavelength gravitons cannot interact in any way with the Bose-Einstein condensate? Of course, for this interaction to occur, gravitons must have $\lambda_g \sim 1 \text{ cm}$, which corresponds to the nano-second frequency range ($\sim 10^9 \text{ Hz}$), and their energy must be $\sim 10^{-5} - 10^{-4} \text{ eV}$. It is also obvious that gravitons do not “fly” to Earth from space, but are virtual vector bosons, which born in Bose-Einstein condensate and transferring the energy of gravitational field to it. In this case, the gravitational field itself is vector and is determined by the superposition of attraction forces of many space objects, but in our case, primarily those given in Table 1.

We substantiated this mechanism of interaction of photons with cosmic gravitational fields when explaining Hubble's law and cosmic microwave background [6].

CONCLUSIONS:

Using the example of the near-Earth gravitational field, it is shown:

- Gravity field is vector. Its dimension at each point in space is determined by the number of independent sources that create this field by their attraction in accordance with Newton's law.
- The gravitational field transfers its energy to material objects located in it by quanta. The carriers of gravitational energy quanta are virtual vector bosons. The questions of the virtual bosons masslessness and the magnitude of their spin require special study.
- It can be hoped that the use of modern quantum gravimeters for detecting gravitons will clarify their parameters and solve many other issues.

REFERENCES:

- [1] *Shnol S. E.* Cosmophysical factors in random processes. Stockholm: Svenska fysikarkivet, 2009. 388 p.
- [2] *Yudovich Ya. E., Ketris M. P.* Russian scientist Simon Shnoll and his heroes. Syktyvkar, Komi Republican Publ. House, 2023. 524 p.
- [3] *Barenbaum A. A.* Discussion of experiments of S. E. Shnoll: detection of corpuscular properties of gravity // Proc. VESEMPG-2024. Moscow: GEOKHI RAS, 2024 (in print).
- [4] *Vinogradov V. A., Karpov K. A., Turlapov A. V.* Quantum gravimeters on ultra-cold atoms // Al'manac of Modern Metrology. 2020. No. 4(24). P. 364–376.
- [5] *Pereira dos Santos F., Bonvalot S.* Cold-atom absolute gravimetry // Encyclopedia of Geodesy. 2016. P. 1–6.
- [6] *Barenbaum A. A.* Hubble's law and the cosmic microwave background in the absence of the big bang // Research Trends and Challenges in Physical Science. 2021. V. 4. P. 119–130. DOI: 10.9734/bpi/rtcps/v4/13528D.

SESSION 5. SMALL BODIES (SB) ORAL SESSION

DUSTY PLASMA PROCESSES IN THE VICINITY OF COMETS

S. I. Popel, A. P. Golub', L. M. Zelenyi

Space Research Institute RAS, Moscow, Russia, popel@cosmos.ru

KEYWORDS:

dusty plasmas, comet coma, dust ion-acoustic shock wave, dusty plasma formation, dynamics of dust particles.

ABSTRACT:

We present a description of dusty plasma processes in the vicinity of comets. We show that they can substantially impact, in particular, formation of the bow shock as a result of interaction of the comet coma with the solar wind. They can also reveal themselves in the situations when the comet is far from the Sun.

- (1) The bow shock can sometimes be interpreted as a variety of the dust ion-acoustic shock wave. The presence of charged dust leads to another important type of interaction, namely, interaction of protons of the solar wind with dust particles in the comet coma. For a typical comet nucleus with a radius of the order of 1 km and relatively dense coma (dust number densities exceeding 10^6 cm^{-3}), anomalous dissipation caused by charging of dust particles plays an important role in bow shock formation. Apparently, the nature of such a bow shock is similar to that of the ion-acoustic shock waves.
- (2) For a comet exhibiting parameters of the nucleus close to those of the nucleus of the Halley's comet, the dusty plasma in the vicinity of the nucleus forms due to electrostatic interactions, i.e., analogous to dusty plasma formation near other bodies without atmosphere (e.g., Mercury [1], the Moon [2], Mars satellites [3, 4]), provided that the distance from the comet to the Sun is at least ~ 3.5 AU. On the contrary, if the comet is closer to the Sun, the dynamics of dust particles is determined by the gas flow from the comet nucleus.

Although the history of studying comet dusty plasmas is relatively long, there are still unresolved problems, and successful solution of some of them requires accumulating new knowledge about the studied space objects. This goal can be achieved only in the course of future space missions.

ACKNOWLEDGEMENTS:

The study was supported by the Russian Science Foundation grant No. 24-12-00064, <https://rscf.ru/project/24-12-00064/>.

REFERENCES:

- [1] *Popel S. I., Golub' A. P., Zelenyi L. M.* Dusty plasmas above the sunlit surface of Mercury // *Phys. Plasmas*. 2023. V. 30. Article 043701. 9 p.
- [2] *Popel S. I., Zelenyi L. M., Golub' A. P., Dubinskii A. Yu.* Lunar dust and dusty plasmas: recent developments, advances, and unsolved problems // *Planet. Space Sci.* 2018. V. 156. P. 71–84.
- [3] *Golub' A. P., Popel S. I.* Nonstationary Processes in the Formation of a Dusty Plasma near the Surface of Phobos // *JETP Lett.* 2021. V. 113. P. 428–432.
- [4] *Golub' A. P., Popel S. I.* Non-Stationary Processes during the Formation of Dusty Plasma at the Surface of Deimos, the Satellite of Mars // *Plasma Phys. Rep.* 2021. V. 47. P. 826–831.

INFLUENCE OF THE DIELECTRIC PERMITTIVITY OF THE SURFACE LAYER ON CHARGING OF DUST GRAINS ON AIRLESS COSMIC BODIES

N. D. Borisov

Space Research Institute RAS, Moscow, Russia, borisov@izmiran.ru

KEYWORDS:

electric fields, solar wind plasma, dust grains, electric charges

ABSTRACT:

Electric charging of dust grains lying on the surfaces of airless cosmic bodies is caused by the action of the solar UV-radiation and the solar wind plasma. As a result of such charging the electric field is formed above the surface. This field acts on dust grains and tends to take off the grains from the surface. Such electrostatic mechanism is often attracted to explain the lofting of dust grains above the surfaces of airless cosmic bodies (the Moon, asteroids). Unfortunately, theoretical estimates show that in the general case the electric force is not strong enough to overcome the gravity and the adhesion forces. That is why different ideas are introduced to obtain stronger electric fields above the surface. For example, on uneven surface (craters or hills) in the terminator zone according to estimates local electric fields are much stronger than the electric field in the vicinity of a flat surface [1].

It is known that the surface layer of the airless cosmic bodies (the Moon, asteroids) consists of different chemical components (e.g., SiO_2 , Al_2O_3 , CaO , Fe). Due to this the dielectric permittivity of this layer is not constant and has various local values depending on the chemical composition. Investigations of samples taken from the Moon during Apollo missions confirm that the dielectric constant ϵ of the surface layer varies from approximately $\epsilon \approx 1.6$ to 15 and even more [2]. We argue that such variation of the dielectric constant should be taken into account while calculating electric charges (and hence electric forces) acting on dust grains. The dependence of dust grains charges on the dielectric constant of the surface layer was not discussed before. We show that in the case of high dielectric constant the electric force acting on dust grain lying on the surface can be one order of magnitude stronger than it was estimated before (without taken into account the magnitude of ϵ).

The obtained results can be applied to airless cosmic bodies with various dielectric constants of the surface layer. We argue that some amount of frozen water in the surface layer influences (depending on its concentration) the magnitude of the effective dielectric constant and hence the charging of dust grains.

ACKNOWLEDGMENTS:

This work is supported by the Russian Science Foundation, grant No. 24-12-00064, <https://rscf.ru/project/24-12-00064/>.

REFERENCES:

- [1] *Borisov N. D., Mall U.* Charging and motion of dust grains near the terminator of the moon // *Planetary and Space Science*. 2006. V. 54. P. 572–580.
- [2] *Olhoef G. R., Strangeway D. W.* Dielectric properties of the first 100 meters of the Moon // *Earth and Planet. Sci. Lett.* 1975. V. 24. P. 394–404.

DEVELOPMENT OF RADIOTOMOGRAPHY ALGORITHMS FOR THE STUDY OF ELECTRON CLOUDS IN THE IONOSPHERE AND STRUCTURES IN THE DUSTY PLASMA USING LOW-ORBITAL SATELLITE SYSTEMS

A. M. Krot, I. E. Savinykh

United Institute of Informatics Problems of the National Academy of Sciences of Belarus, Minsk, Belarus, alxkrot@newman.bas-net.by

KEYWORDS:

radiotomography, GPS, ionospheric plasma, TEC, dusty plasma, low-orbital satellites, mathematical modeling

INTRODUCTION:

The investigations of electron clouds in the ionospheric plasma and structures in the dusty plasma is based on different physical principles. In the case of ionospheric plasma, the determination of electron concentration is based on the phenomenon of dispersion of electromagnetic waves [1], and in the case of dusty plasma [2], the determination of mass density is based on the physical phenomena of absorption (damping) of electromagnetic waves. Nevertheless, the radiotomography methods turn out to be uniform for restoring images of data obtained on the basis of different physical principles. In other words, the mathematical basis of the radiotomography and the algorithms for its implementation turn out to be the same for both cases under consideration. Indeed, in the case of propagation of an electromagnetic wave from the satellite to a ground station along the axis z through ionosphere, the electric field amplitude can be expressed as:

$$E(L, t) = E_0 \cos \left(\omega t - \frac{\omega}{c} \int_0^{L(t)} n(z) dz \right), \quad (1)$$

where $L(t)$ is a distance between the satellite station and ground station, $n(z)$ is an electron concentration in the ionosphere plasma, ω is a frequency of the radio wave, c is the speed of the light.

In the case of absorption and scattering of photon beam by dusty plasma layer the Buger law take place:

$$I(\bar{x}_1) = I_0(\bar{x}_1) \exp \left(- \int_{-\infty}^{\infty} \rho(x_1, x_2) d\bar{x}_2 \right), \quad (2)$$

where $I(x_1)$ is an intensity of beam, $\rho(x_1, x_2)$ is an unknown mass density function (\bar{x}_1 and \bar{x}_2 are coordinates in a coordinate system rotated relative to the original (x_1, x_2)). It is obviously, the formulas (1) and (2) contain the common relation like a total electron content (TEC):

$$\text{TEC} = \int_{L_0}^L n(z) dz. \quad (3)$$

Therefore, a single tool for digital image processing and restoration as well as mathematical modeling can be used in the study of various physical phenomena.

DEVELOPMENT OF RADIOTOMOGRAPHY ALGORITHMS:

The processes of scattering, dispersion and absorption accompanying the propagation of an electromagnetic wave lead to the fact that the radio signal slows down and weakens when passing through electron clusters in the ionosphere [1, 3]. The TEC obtained from the signal phase delay data can subsequently be used for computational tomography algorithms and then for estimation of structures for the electron density images obtained [4].

The classification of tomographic methods usually divides iterative, statistical and deterministic ones (the last is based on precise mathematical models). Deterministic methods include methods based on the slice theorem and the Radon transform [5]. In this case, projection is similar to the operation of obtaining data in electromagnetic rays using a parallel beam of radiation. The essence of the process is obtaining a shadow, i.e. for a volumetric object, this is the reduction of a three-dimensional structure to a two-dimensional one, and in the case of a flat object, this is a one-dimensional projection of a two-dimensional structure. In this work, one-dimensional projections of two-dimensional objects are used. The geometric meaning of the Radon transform is to integrate a function along a straight line perpendicular to a vector forming an angle with the axis of the polar coordinate system and passing at a distance measured along the vector (with the corresponding sign) from the origin [5]. In back projection, the orientation of the coordinate system corresponds to each of the projection angles. The method based on the slice theorem connects the projection and the reconstructed image through the one-dimensional Fourier transform of the projection which is a section of the two-dimensional Fourier transform of the two-dimensional reconstructed image [5]. This 1D-spectrum is estimated along a line passing through the origin of the 2D-spectrum and making a certain angle with the axis of abscissa in the frequency space domain. This cutting function is called the slice under a definite angle.

Computational experiments were carried out to restore 2D-images based on deterministic tomography methods. Improving the efficiency of the radiotomography procedures has been obtained by means of the real-valued split-radix fast Fourier transform algorithm developed in our previous papers [6–8].

REFERENCES:

- [1] *Davies K.* Ionospheric Radio Waves. Waltham, Massachusetts ect.: Blaisdell Publ. Co., 1969. 502 p.
- [2] *Popel S. I., Zelenyi L. M., Zakharov A. V.* Dusty Plasma in the Solar System: Celestial Bodies without Atmosphere // *Plasma Phys. Rep.* 2023. V. 49. P. 1006–1013.
- [3] *Tucker A. J.* Computerized ionospheric tomography / The Johns Hopkins Univ. Applied Physics Laboratory. 1998. P. 2–7.
- [4] *Vierinen J., Norberg M., Lehtinen S. et al.* Beacon satellite receiver for ionospheric tomography // *Radio Science.* 2014. V. 49. No. 12, P. 1141–1152.
- [5] *Dudgeon D. E., Mersereau R. M.* Multidimensional Digital Signal Processing. Englewood Cliffs: Prentice Hall, Inc., 1984. 274 p.
- [6] *Krot A. M., Minervina H. B.* Synthesis of fast Fourier transform (FFT) split-radix algorithms for real-valued and Hermite-symmetrical series // *Radioelectronics and Communication Systems.* 1989. V. 32. No. 12. P. 10–15.
- [7] *Krot A. M., Minervina H. B.* Comment: Conjugate pair fast Fourier transform // *Electronics Letters.* 1992. V. 28. No. 10. P. 1143–1144.
- [8] *Krot A. M., Minervina E. B.* Fast algorithms and programs for digital spectral processing of signals and images. Minsk: Navuka and Tekhnika, 1995. 407 p. (in Russian).

SUBLIMATION-DRIVEN DUST ACTIVITY OF PRIMITIVE ASTEROIDS SUGGESTS THAT THEY CONTAIN WATER ICE

V. V. Busarev^{1,2}, E. V. Petrova³, M. P. Shcherbina^{2,1}

¹ Lomonosov Moscow State University, Sternberg Astronomical Institute
Moscow, Russia, busarev@sai.msu.ru

² Institute of Astronomy RAS, Moscow, Russia

³ Space Research Institute RAS, Moscow, Russia

KEYWORDS:

asteroids, *UBVRI* photometry, reflectance spectra, chemical and mineral composition of matter, H₂O ice, sublimation-driven dust activity of asteroids

INTRODUCTION:

Asteroids of taxonomic (spectral) types C, B, F, and G of the Tholen classification [1] and/or those in C-complex of the SMASSII classification [2] with low-temperature mineralogy [3] are considered as bodies of primitive composition. These asteroids are the most numerous in the Main Belt and could form near or beyond the H₂O ice line in early Solar system (e.g., [4–6]). Hence, the probability of finding water ice on them may be rather high.

Since September 2012, we have carried out spectrophotometric and *UBVRI* observations of 112 primitive-type asteroids (including the last survey) and found unusual features, not typical for solid surfaces, in the reflectance spectra of 16 of them (e.g., [7, 8] and references therein). Light-scattering model calculations showed that these features may be induced by the scattering on submicron particles or their aggregates in an optically thin exosphere around the asteroid (e.g., [8, 9]). We supposed that this exosphere may appear due to sublimation of volatiles (mainly H₂O ice) and induced ejection of dust particles from the surface of these bodies, which are called active asteroids (AAs).

Consequently, the observed spectral signs of sublimation-driven dust activity (SDA) and a temporal dust exosphere (DE) generated by it on primitive asteroids indicate that these bodies contain water ice. The more so, as it was shown by numerical simulations, due to a very low thermal conductivity of the surface matter (regolith) of primitive asteroids, water ice could survive in their interiors up to several billion years [10]. However, we may expect that many of the considered asteroids partially (or completely) lose their ice deposits because of strong collisions and fragmentation.

Here we present a new series of spectral observations of the Main-Belt asteroids and the results of searching for SDA in them.

OBSERVATIONS AND MODELING:

In a period of December 2022 to February 2023, we performed next *UBVRI* observations of the Main-Belt asteroids of predominately primitive types located near perihelion [9]. The survey (in a range of 0.366–0.797 μm) covered 65 bodies, and their approximate reflectance spectra were calculated. The analysis of these spectra was aimed at searching for the SDA signs in them, which turned out to be rather weak.

According to the light-scattering simulations for a conventional C-type AA with a tenuous DE, the spectral signs of SDA are as follows (see [7–9] and references therein):

- (1) The short-wavelength part of the spectrum enhances due to the scattering on weakly-absorbing submicron particles; and the larger the optical thickness τ of a DE (to some saturation value), the stronger the effect.
- (2) Maxima and minima, which are unusual for the surface spectrum, appear in the spectrum of the asteroid due to the scattering on aggregates composed of submicron grains; their position in the spectrum depends on the grain sizes and composition, and their intensity grows with increasing τ (to some saturation value).

To solve the problem of detecting very weak SDA, we calculated the reflectance spectra of a conventional C-type AA surrounded by an optically thin DE containing particles of five most widespread compounds — H₂O ice (Ice), astronomical silicates (Sil), olivine (Oli), refractory organics (OrR), and amorphous carbon (AmC). Examples of the models in comparison to that of the surface are shown in Figure 1.

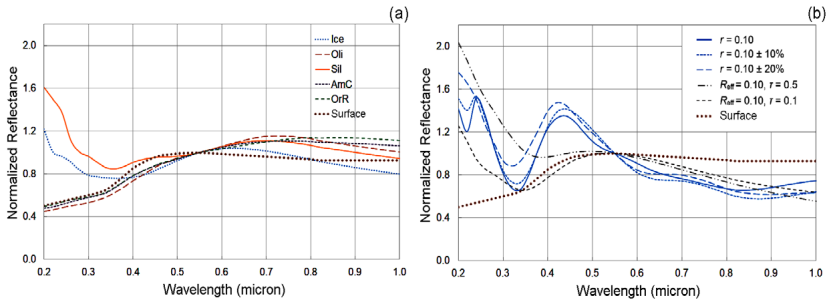


Fig. 1. Normalized reflectance spectra calculated for an AA with a DE: (a) the DE ($\tau = 0.1$) contains homogeneous particles of different composition (the effective radius $R_{eff} = 0.12 \mu\text{m}$); (b) the DE ($\tau = 0.5$ except for one case indicated) contains ice particles, both homogeneous ($R_{eff} = 0.1 \mu\text{m}$) and aggregate (the number of constituents $N = 50$, and the radius $r = 0.1 \mu\text{m}$ or varies within $\pm 10\%$ and $\pm 20\%$ of the average)

As can be seen from Figure 1, the reflectance for an AA with a DE composed of particles of astronomical silicates and water ice substantially grows in the short-wavelength range (corresponding to the *U*-band), which may facilitate their detection. On the other hand, there is one more possibility to reveal the presence of a DE of different composition. It appears due to high-frequency fluctuations of density in the solar wind, which effectively affects electrostatically charged particles in a DE. Although the true nature of these fluctuations has not been established yet, it is likely that they are related to variations in the granular structure of the solar photosphere (e. g., [11, 12]). As for their influence on SDA, the more difference in spectral characteristics of dust particles ejected from the surface of an AA is, the larger fluctuations in the intensity of the light flux from an AA are observed. Obviously, the standard error of the light flux intensity in the *U* band is a measure of these fluctuations.

Thus, from a joint analysis of the modeled and measured spectra of primitive AAs, we come to two criteria for detecting its SDA from their normalized reflectance spectra [9]:

- (1) The normalized reflectance spectrum of a primitive-type asteroid suspected of being active coincides in shape with that calculated for a conventional AA of the corresponding taxonomic type possessing a DE.
- (2) Short-term variations in the intensity of the light flux from an active asteroid should be $\sim 10\%$ and more in the *U* band (with accounting for typical errors in this band not exceeding $\sim 5\text{--}7\%$ under standard photometric conditions) in comparison to the similar quantity for a reference star observed simultaneously with the asteroid in the same frame. To numerically evaluate these variations for the asteroid and the reference star in the *U* band, the standard errors δI of the light flux intensity I should be calculated for the both objects (by at least three serial observations); and the difference $\Delta = (\delta I_{ast} - \delta I_{star})$ as well as the signal-to-noise ratios (SNR_{ast} and SNR_{star}) and $1/\text{SNR}_{ast}$ being a measure of an approximate relative error in the I_{ast} value, should be found. Then, a positive sign of the quantity Δ combined with a condition of $\Delta > 1/\text{SNR}_{ast}$ may be considered as a confirmation of activity in the asteroid.

With the use of these two criteria, we analyzed the approximated reflectance spectra of asteroids observed in the last survey and found that, from 50 primitive-type asteroids (distinguished from the mentioned 65 ones

by the geometric albedo value less than 0.10), three asteroids — 164 Eva, 360 Karlova and 750 Oskar — demonstrate spectral signs of probable SDA, which may be considered as an indication of considerable subsurface deposits of H_2O ice [9] (Figure 2). Similar spectral changes, indicating sublimation-driven dust activity, were detected in asteroid 629 Bernardine during one of the observational nights. Its geometric albedo is somewhat enhanced (0.14 or 0.19 from different sources), which may be a result of heterogeneity in the surface composition of the asteroid.

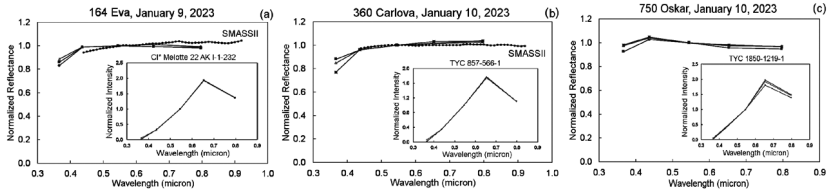


Fig. 2. Normalized reflectance spectra of primitive-type AAs 164 Eva (a), 360 Carlova (b), and 750 Oskar (c). Normalized spectra of the corresponding invariable reference stars are given in the inserts. The reflectance spectra from the SMASII database available for two of these asteroids are shown for comparison

CONCLUSIONS:

- Due to formation of primitive asteroids near or beyond the H_2O ice line in the early Solar System, the probability of detecting ice in them is very high.
- The short-wavelength range corresponding to the photometric band U is the most promising for detecting SDA, as a sign of the presence of water ice, in asteroids of primitive types.
- The SDA of primitive-type asteroids should be considered as a complex process of interaction of sublimation-driven dust activity with the near-surface photoemission electrostatic field, radiation pressure, and the solar wind.

ACKNOWLEDGMENTS:

This work was supported by the Russian Scientific Foundation (grant RNF 22-12-00115, <https://rscf.ru/project/22-12-00115/>).

REFERENCES:

- [1] *Tholen D.J.* // Asteroids II / eds: Binzel R.P. et al. Tucson: Univ. Arizona Press, 1989. P. 1139–1150.
- [2] *Bus S.J., Binzel R.P.* // *Icarus*. 2002. V. 158. P. 146–177.
- [3] *Gaffey M.J. et al.* // Asteroids III / eds: Bottke W. et al. Tucson: Univ. Arizona Press, 2002. P. 183–204.
- [4] *Safronov V.S.* Evolution of the Protoplanetary Cloud and the Formation of the Earth and Planets: transl. Russian. Washington, D.C.: NASA, 1972.
- [5] *Safronov V.S., Ziglina I.N.* // *Sol. Syst. Res.* 1991. V. 25. P. 139–146.
- [6] *Busarev V.V.* A hypothesis on the origin of C-type asteroids and carbonaceous chondrites // Proc. Conf. "Asteroids, Comets, Meteors 2012". 2012. Article 6017. <https://arxiv.org/ftp/arxiv/papers/1211/1211.3042.pdf>.
- [7] *Busarev V.V., Petrova E.V., Irsmbabetova T.R. et al.* // *Icarus*. 2021. V. 369. Article 114634. 18 p.
- [8] *Busarev V.V., Petrova E.V., Puzin V.B. et al.* // *Sol. Syst. Res.* 2024. V. 58. No. 3. P. 315–325.
- [9] *Busarev V.V., Petrova E.V., Shcherbina M.P. et al.* // *Sol. Syst. Res.* 2024. V. 58. No. 6, in press.
- [10] *Schorghofer N.* // *Astroph. J.* 2008. V. 682. P. 697–705.
- [11] *Malaspina D.M., Kellogg P.J., Bale S.D., Ergun R.E.* // *Astrophys. J.* 2010. V. 711. P. 322–327.
- [12] *Domínguez S.V., Utz D.* // *Rev. Modern Plasma Phys.* 2022. V. 6. No. 1. P. 1–33.

LONG-TERM EVOLUTION OF THE DIMORPHOS TAIL

J.-Y. Li, The DART Investigation Team

Sun Yat-sen University, Zhuhai, China, lijianyang@mail.sysu.edu.cn

KEYWORDS:

DART, Didymos, Dimorphos, planetary defense, dust modeling, active asteroids, Hubble Space Telescope

ABSTRACT:

The successful impact of the DART (Double Asteroid Redirection Test) spacecraft into Dimorphos [1] excavated an ejecta composed of dust particles from μm to cm in size [2] with embedded boulders up to ~ 2 m observed [3]. A tail formed from the low-speed ejecta dust due to solar radiation pressure (SRP) [2, 4]. Dust of different particle sizes are sorted out along the tail because smaller particles are accelerated by SRP more than larger particles. Also, depending on the particle size, slow ejecta dust could be trapped in orbit around Didymos before they are slowly pushed out of the binary system by SRP and feed into the tail [5]. Small particles could also be lifted and released from the binary system due to re-impact of the ejecta onto Didymos and Dimorphos, especially with the fast rotation of Didymos [6]. Long-term monitoring of the tail characterizes the large dust particles of a few to tens of cm in size, and probe the dynamic process and re-impact released dust in the binary system. Additionally, it will provide us with a unique context to interpret active asteroids through the Dimorphos tail that has been produced by a controlled impact experiment [2, 7].

We analyzed the Hubble Space Telescope images collected from November 30, 2022, through June 2023 with the WFC3/UVIS to understand the long-term evolution of the tail of Dimorphos. The tail morphology evolution was consistent with dust released within two weeks after the DART impact. The brightness of the tail faded following a broken exponential model. The evolution of the brightness profile along the tail suggested increasing power law slopes of up to -4.7 for the particle size distribution up to 3 cm -radius particles, compared to -3.7 for a few mm to cm particles and -2.7 for smaller particles as measured from the images collected shortly after impact [2]. The increasing slope probably indicated a depletion of cm and larger particles in the tail. A diffuse dust cloud was visible to the south of the main tail, consistent with sub- mm to a few mm particles released up to 8 weeks after impact. Preliminary analysis suggested that the diffuse cloud probably contains the dust lifted by re-impact of the ejecta onto Didymos and Dimorphos. We will discuss the results from these observations and the implications for active asteroids.

REFERENCES:

- [1] *Daly R. T. et al.* Successful kinetic impact into an asteroid for planetary defense // *Nature*. 2023. V. 616. P. 443–447.
- [2] *Li J.-Y. et al.* Ejecta from the DART-produced active asteroid Dimorphos // *Nature*. 2023. V. 616. P. 452–456.
- [3] *Farnham T.L. et al.* Spatial Distribution of the Boulders in the DART Impact Ejecta: A 3-D Analysis // *Lunar and Planetary Science Conf.* 2023. Article 426.
- [4] *Opitom C. et al.* Morphology and spectral properties of the DART impact ejecta with VLT/MUSE // *Astron. Astrophys.* 2023. V. 671. Iss. 11. 7 p.
- [5] *Rossi A. et al.* Dynamical Evolution of Ejecta from the DART Impact on Dimorphos // *Planet. Sci. J.* 2022. V. 3. Iss. 118. 12 p)
- [6] *Trógolo N., Campo Bagatin A., Moreno F., Benavidez P.G.* Lifted particles from the fast spinning primary of the Near-Earth Asteroid (65803) Didymos // *Icarus*. 2023. V. 397. Article 115521.
- [7] *Jewitt D., Hsieh H.H.* The asteroid-comet continuum. 2022. DOI: 10.48550/arXiv.2203.01397.

MIGRATION OF BODIES EJECTED FROM MARS

S.I. Ipatov

*Vernadsky Institute of Geochemistry and Analytical Chemistry RAS
Moscow, Russia, siipatov@hotmail.com*

KEYWORDS:

motion of bodies, ejection of bodies from Mars, probabilities of collisions, terrestrial planets, Earth

INTRODUCTION:

Martian meteorites were found on the Earth. Cosmic ray exposure time of such meteorites presented in [1] were between 0.6 and 15 Myr. Wetherill [2] considered the evolution of the orbits of bodies ejected from Mars in random directions. The velocity of ejection of bodies from the surface of Mars varied from 5 to 7 km/s. The probabilities of collisions of bodies with the Earth were calculated using Opik's formulas. Using the symplectic integration method [3], Gladman [1] simulated the evolution of the orbits of bodies ejected from random positions on the surface of a sphere 200 martian radii in diameter moving radially outward with an ejection velocity v_{ej} from 5.13 to 6.02 km/s. He studied characteristic times before the collisions of these bodies with the Earth and the fraction of bodies that fell onto the Earth. 2100 ejected bodies were considered for ejection from Mars. The planets from Venus to Neptune were included in the simulations. Bodies were excluded from integration when they collided with planets or reached 6 AU from the Sun. In some calculations the launch of bodies occurred at the aphelion of Mars's orbit and in other calculations — at the perihelion of the orbit. Considered time intervals mainly were equal to 15 Myr, but in a few calculations they reached 100 Myr. Gladman [1] noted that for the first 0.1 Myr the ejected bodies stay near the region where they were launched. It was obtained that for different ejection velocities the probability p_e of collisions of bodies with the Earth during 15 Myr were between 0.033 (at $v_{ej} = 5.13$ km/s) and 0.077 (at $v_{ej} = 5.53$ km/s). At $v_{ej} = 5.13$ km/s and $T = 100$ Myr, it was obtained that $p_e = 0.075$.

CONSIDERED MODEL:

In [4] I studied the evolution of the orbits of bodies ejected from the Earth. Below I discuss the evolution of orbits ejected from Mars. Such ejection could often took place during the accumulation of the terrestrial planets and at the late heavy bombardment. In each calculation variant, the motion of $N_o = 250$ bodies ejected from Mars was studied for the fixed values of an ejection angle i_{ej} (measured from the surface plane), a velocity v_{ej} of ejection, and a time step t_s of integration. The gravitational influence of the Sun and all eight planets was taken into account. Bodies that collided with planets or the Sun or reached 2000 AU from the Sun were excluded from integration. The symplectic code from the SWIFT integration package [3] was used for integration of the motion equations. The initial positions of planets in their orbits were the same as those from this package. The results of calculations with different t_s were compared and gave similar results. Most of calculations were made at $t_s = 5^d$. For comparison, a few calculations were made at $t_s = 1^d$ and showed similar results. The motion of bodies ejected from Mars under the gravitational influence of all planets was studied during the dynamic lifetime T_{end} of all bodies, which was often about 200–700 million years in the calculation variants. In some calculations T_{end} exceeded 1 Gyr.

The ejection of bodies from six opposite points of the Mars's surface was studied for a number of values of velocities and angles of ejection of bodies. In the v_f and v_c series of calculations (for points F and C), the motion of the bodies started at most and least distant points of the Earth's surface from the Sun (located on the line from the Sun to the Earth), respectively. In the v_u and v_d series (for points U and D), the bodies started from points

on the Earth's surface with the maximum and minimum values of z (with the z axis perpendicular to the plane of the Moon's orbit), respectively. In the v_w and v_b series (for points W and B), the bodies started from the forward point on the Earth's surface in the direction of the Earth's motion and from the back point on the opposite side of the Earth, respectively. Evolution of orbits of bodies launched from points B and W can differ from that launched from the above four points. In different variants, the values of the ejection angle i_{ej} were 15, 30, 45, 60, 89, or 90°. The ejection velocity v_{ej} was mainly equal to 5.05, 5.1, 5.3, 6, 8, 10, 15, or 20 km/s, but other values of v_{ej} in the range from 5.02 to 5.5 km/s were also considered.

MIGRATION OF BODIES EJECTED FROM MARS:

The probability p_{ma} of a collision of a body ejected from Mars with Mars was considerable only at an ejection velocity v_{ej} close to the parabolic velocity. Below the results for $v_{ej} \geq 5.05$ km/s are presented. For such v_{ej} the values of p_{ma} were relatively small. For ejection of bodies from points C , D , F , and U , the values of p_{ma} were mainly about 0.04–0.25, 0.01–0.04, and 0–0.02 at $5.05 \leq v_{ej} \leq 5.3$, $5.5 \leq v_{ej} \leq 10$, $15 \leq v_{ej} \leq 20$ km/s, respectively. For point B , the value of p_{ma} was typically smaller than for the above points. For point W , $p_{ma} = 0$ at $15 \leq v_{ej} \leq 20$ km/s, and it could exceed 0.3 at $v_{ej} = 5.05$ km/s.

Probabilities p_e of collisions of bodies ejected from Mars with the Earth for points C , D , F , and U were mainly about 0.08–0.16 and 0–0.16 at $5.05 \leq v_{ej} \leq 10$ and $15 \leq v_{ej} \leq 20$ km/s, respectively. For point B , p_e could exceed 0.24. For point W , the values of p_e were in the range between 0 and 0.15.

Probabilities p_v of collisions of bodies ejected from Mars with Venus for points C , D , F , and U were mainly about 0.08–0.2 and 0.02–0.2 at $5.05 \leq v_{ej} \leq 10$ and $15 \leq v_{ej} \leq 20$ km/s, respectively. For point B , the value of p_e could exceed 0.3. For point W , p_e were in the range between 0 and 0.18.

For ejection from points C , D , F , and U , the values of the fraction p_{me} of bodies collided with Mercury were mainly about 0.02–0.08 at $5.05 \leq v_{ej} \leq 20$ km/s. For point B , the value of p_{me} was in a wider range (0.016–0.2) than for the above four points. For point W , $p_{me} = 0$ at $15 \leq v_{ej} \leq 20$ km/s, and it could exceed 0.06 at $v_{ej} = 5.1$ km/s.

The values of the fraction of bodies collided with the Sun were typically between 0.2 and 0.9 for points C , D , F , U , and B . For point W and $15 \leq v_{ej} \leq 20$ km/s, this fraction was 0 as almost all bodies were ejected into hyperbolic orbits in this case. For point B less than 10 % of bodies were ejected into hyperbolic orbits. For other four points, the probability of such ejection varied from 0.02 to 0.9 depending on an ejection velocity and an ejection angle.

Bodies ejected from Mars could collide with the Earth after 0.1 Myr, and some of the bodies could collide with the Earth after hundreds of million years. For example, for point F at $v_{ej} = 6$ km/s, $i_{ej} = 45^\circ$, $t = 5^d$, $N = 250$, there were 32 collisions with the Earth between 0.22 and 270.9 Myr. Among these collisions there were 4, 7, 6, 7, 2, 4, and 2 collisions at time $t < 1$, $1 < t < 5$, $5 < t < 20$, $20 < t < 50$, $50 < t < 200$, $t > 200$ Myr, respectively. In this case about a half of bodies collided with the Earth after 20 Myr, and some Martian meteorites could travel for tens of million years in space before their collisions with the Earth.

CONCLUSIONS:

The probabilities of collisions of bodies ejected from Mars with planets depended on ejection velocities, ejection angles and points of ejection. The probability p_{ma} of a collision of a body ejected from Mars with Mars was considerable only at an ejection velocity v_{ej} close to the parabolic velocity. This probability usually did not exceed 0.04 at $v_{ej} \geq 5.3$ km/s. The fraction p_{me} of bodies collided with Mercury was typically less than 0.08. Probabilities p_e and p_v of collisions of bodies ejected from Mars with the Earth and Venus were about 0.1–0.2 (each) at $5.05 \leq v_{ej} \leq 10$ km/s, with p_v typically a little greater than p_e at $v_{ej} \geq 5.2$ km/s. The probability of ejection of a body into a hyperbolic orbit was less than 0.1 at $v_{ej} \leq 5.3$ km/s, but it could exceed 1 at $v_{ej} = 20$ km/s. For different ejection velocities, angles and points,

the probability of a collision of a body with the Sun could be between 0 and 0.9.

ACKNOWLEDGMENTS:

The studies were carried out under government-financed research project for the Vernadsky Institute.

REFERENCES:

- [1] *Gladman B.* Destination: Earth. Martian meteorite delivery // *Icarus*. 1997. V. 130. P. 228–246.
- [2] *Wetherill G. W.* Orbital Evolution of Impact Ejecta from Mars // *Meteoritics*. 1984. V. 19. P. 1–13.
- [3] *Levison H.F., Duncan M.J.* The long-term dynamical behavior of short-period comets // *Icarus*. 1994. V. 108. P. 18–36.
- [4] *Ipatov S.I.* Growth of the Moon due to bodies ejected from the Earth // *Solar System Research*. 2024. V. 58. P. 94–111. <https://doi.org/10.1134/S0038094624010040>.

EXPERIMENTAL TRANSFORMATION OF THE CHELYABINSK LL5 METEORITE MATTER OF LIGHT-COLORED LITHOLOGY INTO DARK-COLORED LITHOLOGY

E. V. Petrova, V. I. Grokhovsky

Ural Federal University, Ekaterinburg, Russia, evgeniya.petrova@urfu.ru

KEYWORDS:

Chelyabinsk LL5, chondrite, dark-colored lithology, experimental heating, impact, irradiation

INTRODUCTION:

REVIEW. Over the 10 years since the Chelyabinsk planetary event on February 15, 2013, the international meteorite community has published more than 400 works on a comprehensive analysis of this phenomenon. Basic knowledge about the substance is summarized in several publications [1–7]. In addition, data from a detailed study of the substance of both large and small fragments with different lithologies allows interpretation of the history of the formation of the substance of this chondrite before it entered the Earth's atmosphere [8–12]. From the first days, the study of the substance of the ordinary chondrite Chelyabinsk LL5 was carried out in the EXTRA TERRA CONSORTIUM laboratory of the UrFU Institute of Physics and Technology. It was established that the substance of light and dark-colored lithology of the Chelyabinsk LL5 ordinary chondrite turned out to be similar in chemical and mineral composition. In [9], it was assumed that dark-colored lithology was formed as a result of heating of the material of light-colored lithology. This assumption was verified by experimental studies of the meteorite substance after thermal, shock and radiation effects in laboratory conditions.

Experiments on thermal effects:

Heating a series of light lithology samples in an SNVE-9/18 electric vacuum furnace to temperatures of 700–1500 °C made it possible to obtain a wide range of temperature effects on the Chelyabinsk chondrite matter. Analysis of the microstructure and comparison with natural dark-colored lithology and impact melt showed that when heated to 700–900 °C, the main changes occur in metal crystals and troilite. Whereas at 1300–1500 °C partial remelting of minerals and secondary crystallization from the melt are observed. These changes are reflected in the spectral characteristics of the substance, which was recorded experimentally [13, 14]. In addition, a phase transition in troilite was detected by the thermal analysis. The effects of heating the substance were also noted in the gradient of the chemical composition of chromite and the shifts of its Raman peaks [15, 16].

Experiments on impact action on Chelyabinsk chondrite matter:

An experiment on loading a ball of Chelyabinsk chondrite matter with spherically converging shock waves was carried out at the RFNC-VNIITF (Snezhinsk). As a result of exposure within the light-colored lithology, areas with dark lithology (melting of troilite and metal, formation of impact veins, darkening), mixed lithology (melting of silicates without melting of metal and troilite) and impact melt (complete remelting, recrystallization) were formed. The experiment demonstrated that the impact transformation of the Chelyabinsk meteorite rock as a result of one event that could take place during asteroid collisions [17–19].

Irradiation with ions:

Ion implantation experiments were performed using the Pulsar-M ion source at the Institute of Experimental Physics, Ural Branch of the Russian Academy of Sciences. As a result of a set fluence of $5 \cdot 10^{17}$, a surface darkening of the light-colored lithology material occurred, which was noted both visually and recorded in the reflection spectra [20]. The effect of the solar wind on chondrite matter was simulated by this experiment. It explained

the darkening in the optical spectra of the surface of parent asteroids of ordinary chondrites related to the spectra of the internal matter.

Thus, in this work, analogues of dark-colored lithology were experimentally obtained under terrestrial conditions from light-colored lithology material. Analysis of the structure/texture showed that exposure to temperature, shock and ion bombardment lead to darkening of the light-colored lithology, and cause various structural effects.

ACKNOWLEDGMENTS:

The work was supported by the Ministry of Education and Science of the Russian Federation, Project FEUZ-2023-0014. Authors gratefully acknowledge the Ural Federal University Program of Development within the Priority-2030 Program (research funding from the Ministry of Science and Higher Education of the Russian Federation).

REFERENCES:

- [1] *Popova O.P., Jenniskens P., Emel'yanenko V. et al.* Chelyabinsk airburst, damage assessment, meteorite recovery, and characterization // *Science*. 2013. V. 342(6162). P. 1069–1073. DOI: 10.1126/science.1242642.
- [2] *Galimov E.M., Kolotov V.P., Nazarov M.A. et al.* Analytical results for the material of the Chelyabinsk meteorite // *Geochem. Int.* 2013. V. 51. P. 522–539.
- [3] *Kohout T., Gritsevich M., Grokhovsky V. et al.* Mineralogy, reflectance spectra, and physical properties of the Chelyabinsk LL5 chondrite — Insight into shock-induced changes in asteroid regoliths // *Icarus*. 2014. V. 228. P. 78–85.
- [4] *Badyukov D.D., Raitala J., Kostama P., Ignatiev A.V.* Chelyabinsk meteorite: shock metamorphism, black veins and impact melt dikes, and the hugoniot // *Petrology*. 2015. V. 23. P. 103–115.
- [5] *Morlok A., Bischoff A., Padzek M. et al.* Chelyabinsk — a rock with many different (stony) faces: An infrared study // *Icarus*. 2017. V. 284. P. 431–442.
- [6] *Oshttrakh M.I., Maksimova A.A., Klenchar Z. et al.* Study of Chelyabinsk LL5 meteorite fragments with different lithology using Mössbauer spectroscopy with a high velocity resolution // *J. Radioanalytical and Nuclear Chemistry*. 2016. V. 308. P. 1003–1111.
- [7] *Oshttrakh M.I., Maksimova A.A., Chukin A.V. et al.* Variability of Chelyabinsk meteorite stones studied by Mössbauer spectroscopy and X-ray diffraction // *Spectrochimica Acta. Pt. A: Molecular and Biomolecular Spectroscopy*. 2019. V. 219. P. 206–244.
- [8] *Sharygin V.V., Karmanov N., Podgornykh N.M. et al.* Na-Fe-Phosphate globules in impact metal-troilite associations of Chelyabinsk meteorite // *Meteoritics and Planetary Science*. 2015. V. 50. Article 5274.
- [9] *Petrova E.V., Grokhovsky V.I., Muftakhedinova R.F.* Heat Treatment of the Different Structure Zones in the Chelyabinsk Meteorite // *Meteoritics and Planetary Science*. 2016. V. 51. No. S1. Article A513.
- [10] *Righter K., Abell P., Agresti D. et al.* Mineralogy, petrology, chronology, and exposure history of the Chelyabinsk meteorite and parent body // *Meteoritics and Planetary Science*. 2018. V. 50. P. 1790–1819.
- [11] *Kaeter D., Ziemann M., Bottger A.U. et al.* The Chelyabinsk meteorite: New insights from a comprehensive electron microscopy and Raman spectroscopy study with evidence for graphite in olivine of ordinary chondrites // *Meteoritics and Planetary Science*. 2018. V. 53. P. 416–432.
- [12] *Trieloff M., Korochantseva E.V., Buikin A.I. et al.* The Chelyabinsk meteorite: Thermal history and variable shock effects recorded by the ⁴⁰Ar-³⁹Ar system // *Meteoritics and Planetary Science* 2018. V. 53. P. 343–358.
- [13] *Danilenko I.A., Petrova E.V., Yakovlev G.A., Grokhovsky V.I.* Experimental modeling of the thermal effect on Chelyabinsk meteorite // *Meteoritics and Planetary Science*. 2019. V. 54. Iss. S2. Article A82.
- [14] *Kruglikov N.A., Danilenko I.A., Muftakhedinova R.F. et al.* Spectral characteristics of the meteoritic material after the modeling of thermal and shock metamorphism // *AIP Conf. Proc.* 2019. V. 2174(1). Article 020227.
- [15] *Petrova E.V., Maksimova A.A., Danilenko I.A., Grokhovsky V.I.* Thermal effect on the Chelyabinsk LL5 meteorite texture // *Meteoritics and Planetary Science*. 2017. V. 52. Iss. S1. Article A269.
- [16] *Danilenko I.A., Petrova E.V., Zamyatin D.A., Grokhovsky V.I.* Chromite crystals in experimentally heated Chelyabinsk LL5 meteorite // *Meteoritics and Planetary Science*. 2018. V. 53. Iss. S1. Article A50.
- [17] *Petrova E.V., Grokhovsky V.I., Kohout T.R.F. et al.* Shock-Wave Experiment with the Chelyabinsk LL5 Meteorite: Experimental Parameters and the Texture of the Shock-Affected Material // *Geochemistry Intern.* 2019. V. 57. Iss. 8. P. 923–930.

- [18] *Grokhovsky V.I., Muftakhetdinova R.F., Yakovlev G.A. et al.* Post-impact metamorphism of the Chelyabinsk meteorite in shock experiment // *Planetary and Space Science*. 2020. V. 192. Article 105050.
- [19] *Kohout T., Petrova E. V., Yakovlev G. A. et al.* Experimental constraints on the ordinary chondrite shock darkening caused by asteroid collisions // *Astronomy and Astrophysics*. 2020. V. 639. Article A146.
- [20] *Pankov S. A., Petrova E. V., Kruglikov N. A. et al.* Changes in the spectral characteristics of Chelyabinsk chondrite after thermal and radiation exposure // 7th Intern. Conf. Young Scientists "Physics. Technologies. Innovations. PTI-2020": Book of abstr. Ekaterinburg, Russia, 2020. P. 281–283.

ANALYSIS OF THE METEOR SHOWERS CHARACTERISTICS

A. Kartashova¹, V. Efremov², O. Popova²

¹ Institute of Astronomy RAS, Moscow, Russia, akartashova@inasan.ru

² Institute of Geosphere Dynamics RAS, Moscow, Russia

KEYWORDS:

meteors, meteoroids, double-stations observations

INTRODUCTION:

Meteor investigations have been carried out for a long time, but most of the problems of meteor astronomy are still relevant. One of the tasks is to determine the parameters (mass, density, orbital parameters, etc.) of meteor particles with the highest possible accuracy for the study of the flux of meteor matter. Various observational methods are used for these purposes. Currently television observations are widely used. Large amount of observational data are now available on-line. The GMN [1] and IMO [2] data are used in our investigations.

MASS INDEX (S):

The mass frequency distribution of meteor matter is often described by power law, which exponent is named mass index (s). The estimations of mass index s for selected showers are discussed for few cases, where the masses of meteor particles were obtained using different methods (photometric mass, empirical relation estimate). The examples of mass index (s) estimations for Perseids and Geminids are shown on the Figures 1, 2.

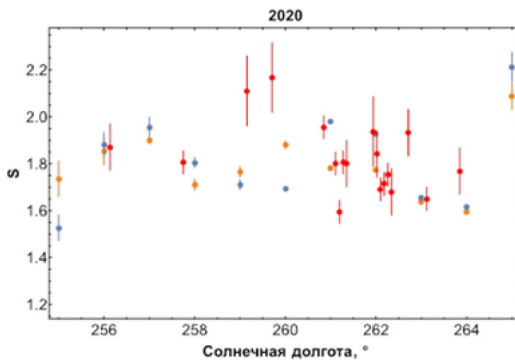


Fig. 1. Distribution of the mass index (s) for Geminids in 2020 (corresponding masses are estimated as follows: blue dots — photometric mass [3], orange dots — empirical relation [4], red dots — the s value calculated by IMO)

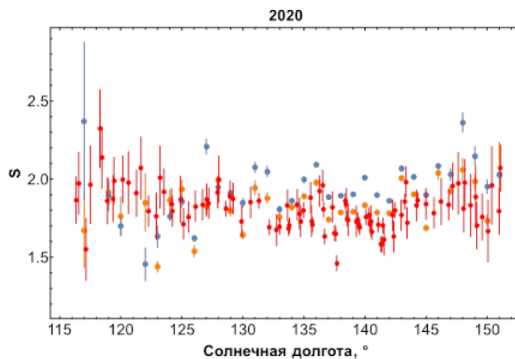


Fig. 2. Distribution of the mass index (s) for Perseids in 2020 (corresponding masses are estimated as follows: blue dots — photometric mass [3], orange dots — empirical relation [4], red dots — the s value calculated by IMO)

Analysis of various properties of selected meteor showers (radiant, orbital parameters, etc.) will be presented.

DISCUSSION:

The analysis has shown that the estimation of the mass index (s) depends on the method of calculating the mass. The spread in estimates can reach 1.7 times. Studies of the properties of meteor showers and sporadic background should be carried out using the same type of data (based on observations on the same type of the equipment) or the relationship between the data used should be known. To study the meteoroid streams structure, it is necessary to obtain observational data from various points spaced by longitude.

ACKNOWLEDGMENTS:

We are grateful to the Global Meteor Network and IMO team for their observations data.

REFERENCES:

- [1] Global Meteor Network (GMN). <https://globalmeteornetwork.org/>.
- [2] International Meteor Network (IMO). imo.net.
- [3] *Bronshthen V.A.* Fizika meteornykh yavlenii (Physics of meteoric phenomena). Moscow: Nauka, 1981. 880 p. (in Russian). 1983.
- [4] *Vida D., Brown P. G., Campbell-Brown M.* Modelling the measurement accuracy of pre-atmosphere velocities of meteoroids // Monthly Notices of the Royal Astronomical Society. 2018. V. 479. No. 4. P. 4307–4319.

ASSOCIATION OF SPORADIC METEORS WITH NEAS OF THE RUBBLE PILE TYPE

S. R. Pavlov, Yu. D. Medvedev, M. Yu. Khovrichev, A. L. Tolstoy

*Institute of Applied Astronomy RAS, Saint Petersburg, Russia
gymax@gmail.com*

KEYWORDS:

sporadic meteors, rubble pile, NEAs, association of the meteors, Global Meteor Network data

INTRODUCTION:

In recent years, numerous studies have actively published findings on the connection between meteoroid streams, comets, and asteroids. It was famous Italian astronomer Schiaparelli who supposed that meteoroids could be produced by comet activity for the first time. He noticed similarities between the orbital elements of Perseids and the third comet detected in 1862. It was long believed that only comets could produce meteoroid swarms and only in the 21st century the first link between meteor showers and asteroids was established. The Geminids meteor shower in December is associated with the Phaeton asteroid [1]. The origin of the Quadrantids is related to the particles ejected from the 2003 EH1, which is a near-Earth asteroid (NEA) [2]. However, these asteroids could conceivably be extinct remnants of comet nuclei.

An analysis of the rotational periods of asteroids, based on the Asteroid lightcurve photometry database [3], reveals that a significant number of asteroids have a rotational period of about 2 hours. This is a specific case of gravitationally bound particles revolving around a spherically distributed mass with a density of about 2 g/cm^3 , and thus it could be a rubble pile. The critical rotational status of these asteroids is maintained due to the YORP effect, where non-gravitational forces are balanced by reactive forces. Angular momentum is lost when dust particles break off and leave the asteroid. The particles lost in this process start to orbit around the Sun though their trajectories remain close to the parent body's orbit for a long time. In such processes, the intensity of particle loss is naturally considerably lower than that of comet nuclei eruptions. However, many rubble pile asteroids within the NEA group could eject enough dust to serve as a source for the observed sporadic meteors.

RESULTS:

A helpful technique for examining the relationship between the orbits of two objects and determining the potential for their common origin is to calculate the D-criterion. This value indicates the degree of similarity between the analyzed orbits.

The Global Meteor Network (GMN) database [4] provides astronomers access to the meteor orbits derived from the baseline observations of the meteor events. It is possible due to the network consisting of a large number of small cameras organized by meteor astronomy enthusiasts.

In this study, we utilized the D-criteria proposed by Southworth and Hawkins (DSH), Drummond (DH), and Kholshchikov (DKH) with accepted threshold values: $DSH = 0.21$, $DH = 0.21$, and $DKH = 0.28$. Additionally, we only considered orbits with relatively good-quality parameter estimations ($\sigma_a < 0.1 \text{ a.u.}$, $\sigma_e < 0.2$, $\sigma_i < 5^\circ$, $\sigma_\Omega < 5^\circ$, $\sigma_\omega < 5^\circ$). We checked the involvement of the following asteroids in sporadic meteor events from the GMN database: 164121 (2003 YT1), 2011 UL21, and 37655 Illapa (1994 PM). We chose asteroids from the NEAs group based on certain criteria: their (MOID) with Earth should be less than 0.05 au, and their diameter should be larger than 140 m, making them potentially hazardous asteroids (PHAs). Additionally, the period of rotation of the asteroid should be less than 3.3 hours.

REFERENCES:

- [1] *Moore P., Rees R.* Patrick Moore's Data Book of Astronomy. 2nd ed. Cambridge University Press, 2011. 275 p.
- [2] *Jenniskens P.* 2003 EH1 is the Quadrantid shower parent comet // The Ephemeris: San Jose Astronomical Association newsletter. 2003. Retrieved 2004-12-17.
- [3] *Warner B. D., Harris A. W., Pravec P.* The asteroid lightcurve database, July 2009 // *Icarus*. 2009. V. 202. Iss. 1. P. 134–146.
- [4] *Vida D. et al.* The Global Meteor Network — Methodology and first results // *Monthly Notices of the Royal Astronomical Society*. 2021. V. 506. P. 5046–5074.

MINERAL CHANGES BY LABORATORY BASED PROTON IRRADIATION ON METEORITES TO UNDERSTAND SPACE WEATHERING AND ASTEROID PROPERTIES

A. Kereszturi^{1,2}, I. Gyollai^{2,3}, S. Biri⁴, Z. Juhász⁴, Cs. Király^{2,5}, R. Rácz⁴, D. Rezes^{1,2}, B. Sulik⁴, M. Szabó^{2,3}, Z. Szalai^{2,5,6}, P. Szávai^{2,5}

¹ HUN-REN Research Centre for Astronomy and Earth Sciences, Konkoly Thege Astronomical Institute, Budapest, Hungary, kereszturiakos@gmail.com

² MTA Centre of Excellence, Budapest, Hungary

³ HUN-REN Research Centre for Astronomy and Earth Sciences, Institute for Geological and Geochemical Research, Budapest, Hungary

⁴ HUN-REN Institute for Nuclear Research, Debrecen, Hungary

⁵ HUN-REN Research Centre for Astronomy and Earth Sciences, Geographical institute, Budapest, Hungary

⁶ ELTE Department of Environmental and Landscape Geography, Eötvös Loránd University, Budapest, Hungary

KEYWORDS:

meteorites, asteroids, space weathering, mineral changes, laboratory analysis

SUMMARY:

Asteroids with impact possibility by hitting the Earth got into the focus of scientific research and applied space technology recently. Such asteroids will be the target of mitigation actions and of space mining activities in the next decades. The understanding of mineral composition of asteroids is difficult as space weathering modifies the composition and structure of their surface, causing feature poor infrared spectra. Laboratory tests of artificial solar wind action on meteorites were realized (Figure 1) and overviewed in this work to simulate space weathering, what caused mineral modification of olivine with the increase of iron content, water loss related mineral changes, and amorphization of the crystalline lattice in general.

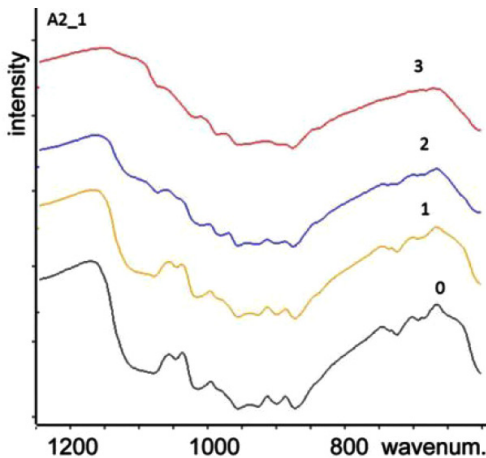


Fig. 1. Example DRIFT detector based infrared reflection spectral curves for the NWA 10580 meteorite sample before irradiation (0), after gradually stronger irradiation actions (1, 2, 3)

Although these changes influence only a thin surface layer of the grains of asteroids with modifying their strength too, as most small (100 m class) asteroids are rubble-pile structured, surface alterations might influence the behavior of these granular aggregates, and thus possible mitigation actions against them. The related possible consequences and future direction of research are summarized at the conference.

ACKNOWLEDGEMENTS:

This project was supported by the K_138594 project of NKFIH. The authors acknowledge the from the Europlanet 2024 RI which has been funded by the European Union's Horizon 2020 Research Innovation Programme under grant agreement No. 871149. Z. J. is grateful for the support of the Hungarian Academy of Sciences through the János Bolyai Research Scholarship.

ATMOSPHERIC DUNES AS POSSIBLE MANIFESTATION OF METEORIC DUSTY PLASMA

Yu. N. Izvekova, S. I. Popel, S. I. Kopnin, T. I. Morozova

Space Research Institute RAS, Moscow, Russia, izvekova@cosmos.ru

KEYWORDS:

dusty plasmas, meteor showers, Earth's dusty ionosphere, nonlinear wave structures, dunes

ABSTRACT:

From 2015 to 2018 periodic luminous wave structures, which were called dunes [1], were observed in the Earth's atmosphere over the Scandinavian countries. The dune wave field extended from Western Sweden to Western Finland. Periodic structures have been observed during auroras and appear as a set of nearly horizontal bands of green emission with an estimated period of 45 km near a certain altitude in the altitude range of 90–110 km. Most dunes we observed in October. Coincidence of the observation time of the dunes and Draconids meteor showers makes it possible to connect periodic structures with the processes occurring in the dusty plasma. We study a dusty plasma system formed in the Earth's ionosphere at altitudes of 90–110 km during meteor showers as a result of meteor ablation and condensation into small grains. Formed solid grains are being charged as a consequence of their interaction with electrons and ions of the ambient plasmas as well as the photoelectric effect in the presence of solar radiation. The development of modulation instability in this system can give rise to linear and nonlinear dust acoustic waves. We have shown that for the parameters of the Earth's dusty ionosphere the conditions for the development of modulation instability are met. If the process of growing of dust acoustic waves is not compensated by other effects, the growth may become large enough to form a nonlinear wave. Nonlinear dust acoustic waves can exist in the form of periodic structures with a large spatial period. We have constructed periodic nonlinear dust acoustic waves and shown that their period can correspond to the period of the observed dunes. The velocity of the structure is small enough so that to an observer on the Earth's surface these structures appear motionless. Thus, we have proposed one more observable manifestation of dusty plasma processes in the Earth's ionosphere.

REFERENCES:

- [1] *Palmroth M., Grandin M., Helin M., Koski P., Oksanen A., Glad M.A., Valonen R., Saari K., Bruus E., Norberg J., Viljanen A., Kauristie K., Verronen P.T.* Citizen scientists discover a new auroral form: Dunes provide insight into the upper atmosphere // AGU Advances. 2020. V.1(1). Article e2019AV000133.

PRELIMINARY RESULTS OF THE POLARIMETRIC OBSERVATION PROGRAM OF NEAS AT THE 2.6-M TELESCOPE OF CRAO AND THE 2-M TELESCOPE OF THE PEAK TERSKOL OBSERVATORY

M. P. Shcherbina¹, N. N. Kiselev^{1,2}, N. V. Karpov¹, E. A. Zhuzhulina²

¹ Institute of Astronomy RAS, Moscow, Russia, mpshcherbina@inasan.ru

² Crimean Astrophysical Observatory, Nauchny, Crimea

KEYWORDS:

NEAs, polarization, observations, phase dependence

INTRODUCTION:

Currently, small bodies of the Solar System, including Main Belt asteroids, near-Earth asteroids (NEAs), asteroids with sublimation-dust activity, active comets in asteroid-like orbits, dormant comet nuclei, and other related objects, are considered as a unified asteroid-comet continuum (ACC). Observations of these bodies using various methods reveal similarities and differences in their physical properties, contributing to a deeper understanding of their nature and the origin and evolution of the Solar System as a whole. It is especially important to observe near-Earth asteroids, as some of them may be potentially hazardous objects (PHOs) for our planet.

Polarimetric studies of NEAs play a crucial role, particularly when conducted over a wide range of phase angles. These studies not only complement spectrophotometric investigations but also provide unique information on the composition, size, shape, and surface structure. These data are critically important for developing strategies to prevent possible collisions with Earth.

RESULTS OF OBSERVATIONS:

Since 2019, the phase angle dependencies of polarization for 19 NEAs have been obtained using the 2.6-m telescope at the Crimean Astrophysical Observatory (CrAO) and the 2-m telescope at the Peak Terskol Observatory (a branch of INASAN). Among these, 17 NEAs were observed for the first time. This constitutes a significant contribution to the total number of observed NEAs, approximately 26 published to date. Data on these objects are presented in Table 1. Detailed descriptions of the equipment used, observation methodologies, and data processing techniques are provided in [1].

Table 1. Observational, physical, and dynamical parameters of NEAs

Name	Date	Phase angle, deg	Dyn. class	PHA	Th/SST*	Albedo	Obs.
162082	2019 10/21– 10/28.	27.1–3.5	Apollo	Y	–	–	Terskol/ CrAO
163373	2020 02/13– 02/16	69.2–109.5	Apollo	Y	–	–	CrAO
52768	2020 03/30– 04/18	70.5–75.9	Apollo	Y	–	–	CrAO
159402	2020 10/06– 11/09	32.1–71.6	Amor	N	–	–	Terskol/ CrAO
(2010 XC15)	2022 12/22– 12/26	58.6–66.7	Aten	Y	–	–	Terskol

Name	Date	Phase angle, deg	Dyn. class	PHA	Th/SST*	Albedo	Obs.
2212 Hephaistos	2022–2023 12/19–01/25	38.3–120.0	Apollo	N	SG/	0.163	Terskol/ CrAO
37638	2023 02/24	47.4	Apollo	Y	–	–	Terskol
4486 Mithra	2023 02/21–03/21	7.9–53.5	Apollo	Y	–	0.297	CrAO
1036 Ganymed	2023–2024 03/21–02/07	5.5–21.4	Amor	N	S/S	0.238	CrAO
1862 Apollo	2023 04/17–04/18	8.3–68.3	Apollo	Y	Q/Q	0.25	CrAO
(2006 HV5)	2023 04/17	73.2	Aten	Y	–	0.246	CrAO
6037	2023 08/16–08/23	38.5–100.3	Apollo	Y	–	–	Terskol
152787	2024 03/11	54.2	Amor	N	–	–	Terskol
417264	2024 03/11	64.9	Amor	N	–	0.062	Terskol
1685 Toro	2023–2024 12/13–03/12	113.6–40.3	Apollo	N	S/S	0.31	Terskol/ CrAO
25330	2024 03/12–05/15	75.7–17.4	Apollo	N	/B	0.052	Terskol/ CrAO
30825	2024 03/12–04/03	49.1–81.5	Amor	N	–	–	Terskol/ CrAO
2063 Bacchus	2024 04/03	47.8	Apollo	N	/Sq	0.203	CrAO
21374	2024 05/12–05/16	23.0–14.9	Amor	N	–	–	Terskol

* Tholen or SMASSII spectral type, from NASA data.

Analysis of data obtained has revealed a significant diversity in the polarimetric properties of the observed objects. We discovered a very rare high-albedo NEA 2010 XC15 with a low maximum degree of polarization, and a low-albedo NEA 25440 with an extremely high degree of polarization. The phase-angle dependencies of the polarization of these asteroids are shown in Figure 1.

A study was conducted to investigate the polarization degree dependencies of asteroids of different taxonomic classes. It was shown that the classification of asteroids based on spectrophotometric data and albedo demonstrates significant scatter when comparing spectral classes with phase angle dependencies of asteroid polarization. This is particularly evident at large phase angles, typical for NEA observations, where polarization reaches high values. Thus, to reliably distinguish taxonomic classes of asteroids, it is necessary to include polarization data.

Red diamonds represent the polarization degree of NEA 2010 XC15, a rare class of high-albedo asteroids. Open circles represent the polarization degree of NEA 25440 with a uniquely high degree of polarization. For compar-

ison, the dashed curve shows the average polarization curve for high-albedo E-type asteroids. Black dots represent data for the low-albedo asteroid (3200) Phaethon.

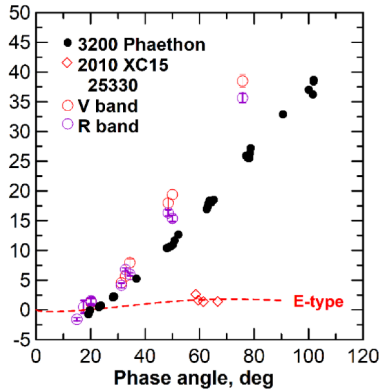


Fig. 1. The phase-angle dependencies of polarization for two types of NEAs

ACKNOWLEDGEMENTS:

The authors express appreciation to the Large-Scale Research Facilities (LSRF) "Zeiss-2000 Telescope" at the Core Shared Research Facilities (CSRF) "Peak Terskol Observatory" of INASAN for the possibility of implementing the program of observations of NEAs.

REFERENCES:

- [1] *Kiselev N. N. et al.* New polarimetric data for the Galilean satellites: Europa observations and modeling // *The Planetary Science J.* 2022. V. 3. No. 6. P. 134.

ULTRAVIOLET IRRADIATION INFLUENCE ON THE LUNAR DUST DYNAMICS

I. Kuznetsov¹, I. Shashkova¹, A. Poroykov², A. Zakharov¹, A. Lyash¹, S. Bednyakov^{1,5}, G. Dolnikov¹, A. Dubov¹, A. Kartasheva¹, M. E. Abdelaal¹, E. Kronrod^{3,4}, O. Voshchan¹

¹ Space Research Institute RAS, Moscow, Russia, kia@cosmos.ru

² National Research University "Moscow Power Engineering Institute" Moscow, Russia

³ Vernadsky Institute of Geochemistry and Analytical Chemistry RAS Moscow, Russia

⁴ Kazan Federal University, Kazan, Russia

⁵ Lomonosov Moscow State University Skobel'syn Institute of Nuclear Physics Moscow, Russia

KEYWORDS:

dust, lunar dust, dusty plasma, dust dynamics

ABSTRACT:

Direct observations of the lunar horizon glow, made over 50 years ago by the Surveyor-7 spacecraft and Apollo-17 astronauts, remain a mysterious phenomenon related to the Moon and are still debated [1, 2]. Various authors have reported significant variations in the electric potential of the lunar surface, reaching as low as minus 4000 V in certain regions [3–5]. The levitation mechanism explanation is rooted in the repulsion between the electrically charged surface and dust grains, a phenomenon observed on many atmosphereless celestial bodies. Solar UV irradiation is suggested as a key driver of particle activity, impacting dust dynamics on asteroids and Martian satellites. [6] estimated the possible electric field on the Moon up to 3000 V/cm.

Experimental simulation approaches, alongside theoretical works, play a crucial role in unraveling the mysteries of dust dynamics. These simulations involve studying the cross-influence of electrostatic fields and UV irradiation, particularly using a 147 nm lightwave, to understand particle activity on airless bodies. In this study, the dynamics of electrostatically lofted Lunar dust were investigated using test particle experimental simulations. The dust environment of airless objects, such as the Moon and Martian moons, was created in specially prepared experimental setup and studied with a machine vision 2-camera registration set-up to understand properties of dust particles injected from these surfaces. The behavior of dust particles under the influence of electrostatic forces near the surface of asteroids and the Moon has been a subject of investigation.

ACKNOWLEDGMENTS:

This work was partially funded by 10th Program of the Experimental Laboratory Astrophysics and Geophysics NCPM.

REFERENCES:

- [1] J.J. Rennilson and D.R. Criswell, *Moon*, 10, 121, 1974.
- [2] H.A. Zook and J.E. McCoy, *Geophysical Research Letters*, 18, 2117, 1991, <https://doi.org/10.1029/91GL02235>.
- [3] T.J. Stubbs, R.R. Vondrak, and W.M. Farrell, *Advances in Space Research*, 37, 59, 2006, <https://www.sciencedirect.com/science/article/pii/S0273117705004989>, the Moon and Near-Earth Objects.
- [4] J.S. Halekas, G.T. Delory, R.P. Lin, T.J. Stubbs, and W.M. Farrell, *Journal of Geophysical Research: Space Physics*, 113, 2008, <https://agupubs.onlinelibrary.wiley.com/doi/abs/10.1029/2008JA013194>.
- [5] W. Farrell, T. Stubbs, R. Vondrak, G. Delory, and J. Halekas, *Geophysical Research Letters*, 34, L14201, 2007.
- [6] B.R. De and D.R. Criswell, *Journal of Geophysical Research (1896–1977)*, 82, 999, 1977, <https://agupubs.onlinelibrary.wiley.com/doi/abs/10.1029/JA082i007p00999>.

ELECTROMAGNETIC PHENOMENA IN DUST PARTICLE DYNAMICS UNDER SIMULATED MARTIAN ATMOSPHERE: AN EXPERIMENTAL STUDY

M. E. Abdelaal^{1,2}, I. V. Dokuchaev², M. A. Zaitsev², Yu. N. Izvekova², E. A. Malinovskaya³, I. A. Kuznetsov², O. N. Voshchan², A. N. Lyash², A. E. Dubov², A. A. Kartasheva², G. G. Dolnikov², A. V. Zakharov²

¹ Moscow Institute of Physics and Technology, Moscow, Russia

² Space Research Institute RAS, Moscow, Russia

³ Institute of Atmospheric Physics RAS, Moscow, Russia

KEYWORDS:

electromagnetic discharges, dust particle dynamics, simulated Martian atmosphere, vacuum environment, dust storms

ABSTRACT:

Understanding the electromagnetic discharges associated with dust particle dynamics in the Martian atmosphere is crucial for predicting the behavior of dust storms on Mars. In this study, we investigate these phenomena using a simulated Martian atmosphere within a controlled vacuum environment, where CO₂ gas was introduced to replicate the atmospheric composition of Mars (Figure 1). The experimental setup, integrated with a highly sensitive antenna system from the ExoMars-2022 project, enabled precise detection of electromagnetic discharges generated during dust particle interactions (Figure 2). Our experimental results demonstrate that dust particles, when subjected to Martian-like atmospheric conditions, generate distinct electromagnetic discharges (Figure 3). These discharges, likely driven by triboelectric charging and particle collisions [1, 2].

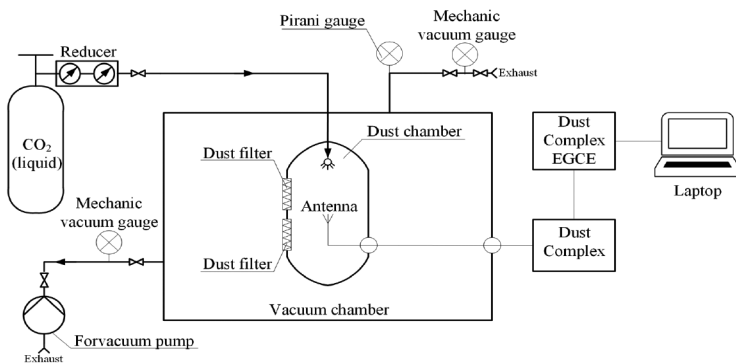


Fig. 1. The scheme of the experimental installation



Fig. 2. Image of the Electromagnetic Analyzer (EMA) on the barbell

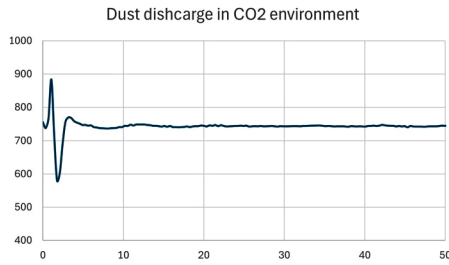


Fig. 3. Dust discharge signal in simulated Martian environment

The findings of this research provide new insights into the dust particle dynamics on Mars and their role in the generation of electromagnetic phenomena. Understanding these processes is essential for future planetary exploration missions, as dust storms on Mars can affect both the operation of spacecraft and the safety of human explorers [3]. The study also highlights the potential impact of Martian dust storms on communication systems and the design of dust-resistant equipment. By advancing our knowledge of dust-related electromagnetic phenomena, this research contributes to the broader understanding of Martian atmospheric behavior and the challenges posed by its dynamic dust environment.

REFERENCES:

- [1] *Delory G. T., Farrell W. M., Atreya S. K. et al.* Oxidant enhancement in Martian dust devils and storms: Storm electric fields and electron dissociative attachment // *Astrobiology*. 2006. V. 6(3). P. 451–462. DOI: 10.1089/ast.2006.6.451.
- [2] *Farrell W. M., Delory G. T., Hillard G. B. et al.* Electric and magnetic signatures of dust devils from the 2000-2001 MATADOR desert tests // *J. Geophysical Research: Planets*. 2004. V. 109. Iss. E3. <https://doi.org/10.1029/2003JE002088>.
- [3] *Merrison J. P., Gunnlaugsson H. P., Nørnberg P. et al.* Determination of the Wind Induced Detachment Threshold for Granular Material on Mars Using Wind Tunnel Simulations // *Icarus*. 2012. V. 217. Iss. 2. P. 456–459. <https://doi.org/10.1016/j.icarus.2007.04.035>

THE EFFECT OF COMETARY OUTBURSTS ON THE ORBITS OF COMETS IN THE OORT CLOUD

A. Y. Merkulova, A. K. Pavlov, D. V. Belousov

loffe Institute, Saint Petersburg, Russia, alinamer0722@gmail.com

KEYWORDS:

comets, Oort cloud, cometary outbursts, cosmic rays, free radicals

INTRODUCTION:

The Oort Cloud is the source of long-period comets. The upper layer of comets in the Oort Cloud is intensively bombarded by galactic cosmic rays (GCR) at temperatures of about 10 K. Radicals and ions are produced in the ice when irradiated by energetic particles at these low temperatures. Experiments at temperatures of 10–100 K show effective accumulation of radicals in ice [1, 2]. The temperature of the surface layer of a comet can increase due to a passing star or a supernova outburst. It can lead to a process of rapid recombination of the radicals [2]. As a result, significant energy is released, resulting in gas and dust flashes [2]. Recombination can also occur spontaneously when the radical concentration exceeds $\sim 1\%$ [3].

Early proposed mechanisms affecting comet orbits and ejection from the Oort Cloud based on gravitational disturbances, which do not depend on comet size [4]. Non-gravitational mechanism for orbital perturbations in the Oort Cloud first proposed in paper [5]. These perturbations result from an additional impulse generated by gas and dust outbursts caused by radical recombination in the comet's surface layers. The effect of a single outburst on the stability of cometary orbits in the Oort Cloud shows that a comet with radii ≤ 1 km on a highly elliptical orbit could be ejected into the inner Solar System [5].

In our study, we develop the mechanism proposed in study [5] for the case of multiple outbursts in the orbits of comets during their existence in the Oort Cloud. Repeated outbursts on a single comet could lead to a relative reduction in the number of small-radius comets, potentially explaining the observed decrease in long-period comets with diameter ≤ 1 km [6].

MODEL:

The process of radical recombination can be spontaneous (critical concentration of radicals $\sim 1\%$) [7]. This concentration accumulates in the comet's surface layer over 10–150 million years [2]. Our model assumes comet outbursts every ~ 100 million years over 4 billion years. We simulate orbital parameter changes for 100,000 Oort Cloud comets with radii from 3 to 0.3 km. The direction of each outburst pulse is set randomly. In our model, calculations stop if the comet's perihelion distance becomes $q_{final} \leq q_{critical}$ (15 AU [4]) or if its final eccentricity is $e \geq 1$ (indicating the comet has left the Solar System).

Figure 1 shows the percentage change in the number of comets over 4 billion years with radii from 3 to 0.8 km (total number of comets 100 thousand for each radius).

Figure 2 shows the number of comets leaving the Oort Cloud with radii from 0.6 to 0.3 km. Unlike comets with radii from 0.8 to 3 km, those of these smaller radii not only enter but also exit the Solar System. Comets entering the inner Solar System are shown in red, while those leaving the Solar System are represented in green.

RESULTS:

Repeated comet outbursts on a single body significantly increase the number of comets leaving the Oort cloud. The percentage of comets with a radius from 3 to 0.6 km that have been injected into the Solar system is 0.02–9.89%. Comets with a radius ≤ 0.5 km can effectively leave the Solar system. The fraction of comets with a radius from 0.5 to 0.3 km that have

escaped from the Solar system is 14.31–93.17 %. Repeated cometary outbursts can lead to the depletion of small bodies in the Oort cloud and are able to explain the observed [6] decrease in the number of long-period comets with diameters ≤ 1 km.

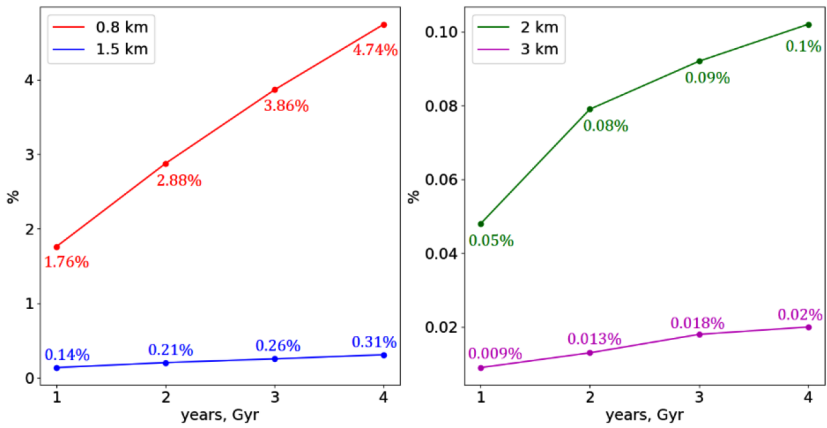


Fig. 1. Percentage of comets entering the inner Solar System due to outbursts over 4 billion years with radii ranging from 0.8 to 3 km

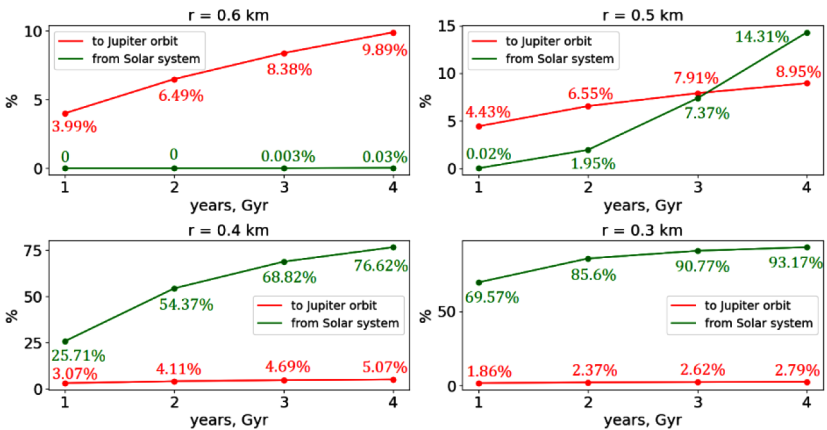


Fig. 2. Percentage of comets leaving the Oort Cloud with radii ranging from 0.6 to 0.3 km

ACKNOWLEDGMENTS:

This work has been supported by the grant of the Russian Science Foundation, RSF 24-22-00257, <https://rscf.ru/project/24-22-00257/>.

REFERENCES:

- [1] Moore M.H., Donn B., Khanna R., A'Hearn M.F. Studies of proton-irradiated cometary-type ice mixtures // *Icarus* 1983. V. 54. P. 388–405. DOI: 10.1016/0019-1035(83)90236-1.
- [2] Pavlov A.K., Belousov D.V., Tsurkov D.A., Lomasov V.N. Cosmic ray irradiation of comet nuclei: a possible source of cometary outbursts at large heliocentric distances // *Monthly Notices of the Royal Astronomical Society*. 2022. V. 511. No. 4. P. 5909–5914. DOI: 10.1093/mnras/stac497.
- [3] Moore M.H., Hudson R.L. Far-infrared spectral studies of phase changes in water ice induced by proton irradiation // *Astrophys. J.* 1992. V. 401. No. 353. DOI: 10.1086/172065.
- [4] Fernandez J.A. Comets: Nature, dynamics, origin and their cosmogonical relevance // *Astrophysics and Space Science Library* / ed. Burton W. Dordrecht: Springer, 2005.
- [5] Belousov D.V., Pavlov A.K. Non-gravitational mechanism of comets' ejection from the Oort cloud due to cometary outbursts // *Solar System Research* 2023. V. 57. No. 6. P. 629–635. DOI: 10.1134/S0038094623060023.

- [6] *Boe B., Jedicke R., Meech K. J. et al.* The orbit and size-frequency distribution of long period comets observed by Pan-STARRS1 // *Icarus* 2019. V. 333. P. 252–272. DOI: 10.1016/j.icarus.2019.05.034.
- [7] *Hudson R. L., Moore M. H.* A far-IR study of amorphous ice: An unreported oscillation between amorphous and crystalline phases // *J. Phys. Chem.* 1992. V. 96. P. 6500–6404. DOI: 10.1021/j100194a072.

INFLUENCE OF SIZE AND SHAPE OF AN ASTEROID ON PERTURBATIONS IN ITS ROTATIONAL DYNAMICS DURING CLOSE APPROACH TO THE EARTH

K. S. Lobanova^{1,2}, A. V. Melnikov¹

¹ Pulkovo Observatory RAS, Saint Petersburg, Russia, melnikov@gaoran.ru

² Saint Petersburg State University, Saint Petersburg, Russia

KEYWORDS:

near-Earth objects, asteroids, close encounters, rotational dynamics, 99942 Apophis, 367943 Duende, 2012 TC4, 2023 BU, Yarkovsky effect

INTRODUCTION:

The vast majority of known asteroids are small bodies (diameter $D < 100$ m). The sizes and shapes of small asteroids are usually unknown, however, there are estimates of D derived from absolute stellar magnitude and albedo under a number of assumptions. The period P of an asteroid's own rotation is related to the size of the asteroid (see, for example, [1]). Small asteroids typically have a fast ($P < 5$ h) rotation. Larger asteroids ($D > 100\text{--}1000$ m) are characterized by rotation with $P = 5\text{--}100$ h. During the secular orbital evolution, a number of asteroids experience close approaches to the Earth (at a distance of several Earth radii — R_E). In terms of asteroid-comet hazard, it is of great interest to study the effect of the approaches on the rotational and orbital dynamics of the asteroid. It is important to estimate the magnitude of perturbations arising in the rotation of the asteroid [2, 3] and their influence on its further orbital dynamics.

RESULTS:

Disturbances in the rotational dynamics of asteroids of different sizes

By means of numerical experiments on modeling close approaches of asteroids to the Earth, the influence of rotational velocity, orientation of the rotational axis, and shape parameters of an asteroid on the magnitude of perturbations in its rotational dynamics is studied. The dynamics of asteroids (99942) Apophis ($D \approx 340$ m, $P \approx 30$ h), (367943) Duende ($D \approx 30$ m, $P \approx 8$ h), 2012 TC4 ($D \sim 10$ m, $P \approx 12$ min) and 2023 BU ($D \sim 10$ m, $P \approx 2$ min) was considered. The methodology presented in [4] was used for this study. The values $\Delta P = P_{final} - P_0$ and $\Delta\gamma = \gamma_{final} - \gamma_0$, where P_{final} and γ_{final} are the values taken after the approach to the Earth, were determined on the set of initial values (set before the approach) of the asteroid's rotational period P_0 and the angle between the rotational axis and the perpendicular to the orbital plane γ_0 . It was found that asteroids with a relatively slow rotation ($P > 5$ h) are characterized by significant perturbations (see also [3, 4]): in the case of Apophis and Duende, the values of ΔP can reach tens of hours and $\Delta\gamma$ — tens of degrees when approaching the Earth. Figure 1 presents the examples of diagrams $\Delta P(P_0, \gamma_0)$ and $\Delta\gamma(P_0, \gamma_0)$ for the case of Duende's approach to the Earth in 2013. According to [5], the position of Duende is marked for two possible post-approach rotational models ($P_0 = 8.7$ h; $\gamma_0 = 27^\circ, 160^\circ$). It follows from Figure 1 that for $P_0 = 8.7$ h and $\gamma_0 = 27^\circ$ we have $\Delta P \approx 4.2$ h and $\Delta\gamma \approx 4^\circ$. The analysis of the diagrams for asteroids with fast rotation ($P < 1$ h) has shown that the perturbations are negligibly small (see also the discussion in [6]): in the case of 2012 TC4 $|\Delta P| < 10^{-5}$ min, $|\Delta\gamma| < 0.01^\circ$; for 2023 BU, the detected amplitude of perturbations is even smaller. The conclusions about the magnitude of perturbations obtained for the considered sample of asteroids can possibly apply to other asteroids with fast and slow rotation.

The influence of asteroid shape on ΔP and $\Delta\gamma$:

The shape of an asteroid is usually approximated by a triaxial ellipsoid with semimajor axes $a > b > c$. The ratios of the moments of inertia ($A/C, B/C; A < B < C$) are related to $(c/b, b/a)$ [7] and, together with other parameters of the problem (P_0, γ_0, e, d), determine the magnitude of perturbations

in the rotational dynamics of an asteroid (in the considered setting [4]) arising during its approach to the Earth. The influence of uncertainties in the knowledge of asteroid figure ($c/b, b/a$) on ΔP and $\Delta \gamma$ is studied. It was found that at fast rotation ($P < 1$ h) even considerable errors in the knowledge of the asteroid shape (c/b and b/a) do not affect the estimation of perturbation values significantly. On the contrary, at relatively slow asteroid rotation ($P > 5$ h), inaccurate specification of asteroid shape parameters in numerical experiments can lead to significant underestimation of perturbation magnitudes. Figure 2 shows examples of $\Delta P(c/b, b/a)$ and $\Delta \gamma(c/b, b/a)$ diagrams for Duende with $\gamma_0 = 27^\circ$. It can be seen that the errors in the estimates of ΔP and $\Delta \gamma$ after close approach of Duende to the Earth in 2013 can amount to several hours and tens of degrees, respectively.

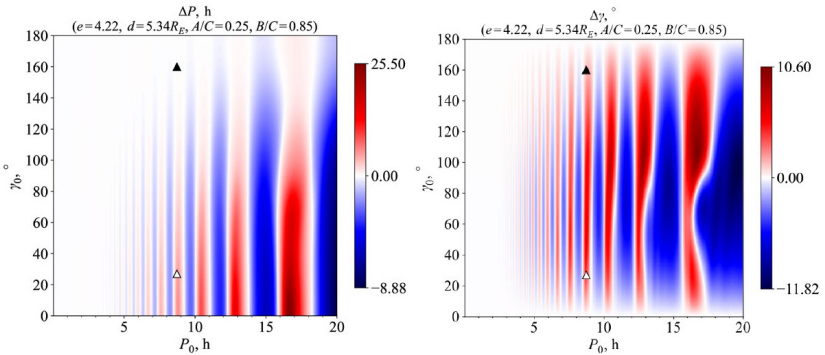


Fig. 1. Dependences of the change of Duende's rotational period ΔP and the inclination of the rotational axis to the orbital plane $\Delta \gamma$ on the initial values P_0 and γ_0 due to close approach to the Earth in 2013. The adopted orbit parameters ($e, d = a(e-1)$) and the ratios of the asteroid's moments of inertia ($A/C, B/C$) are shown in the figures. The triangles indicate two possible positions of the asteroid [5]

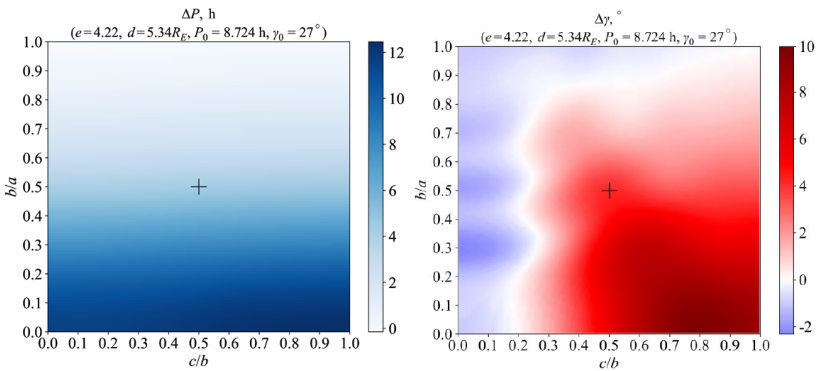


Fig. 2. Dependences of ΔP and $\Delta \gamma$ on asteroid's shape parameters c/b and b/a for Duende. The adopted orbit parameters (e, d) and the initial values of the parameters (P_0, γ_0) of asteroid's rotation are shown in the figures. The mark indicates the position of the asteroid [3]

The influence of ΔP and $\Delta \gamma$ on the value of the Yarkovsky effect:

The influence of perturbations in the rotational dynamics of asteroids on the value of the Yarkovsky effect [8] appearing in their orbital dynamics is considered. It was found that in the case of Apophis, due to its approach to the Earth in 2029, almost a twofold change in the modern value of the parameter A_2 is possible. The main role in the change of A_2 is played by perturbations arising in the orientation of the asteroid's rotational axis ($\Delta \gamma$) during its close approach to the Earth. For asteroids with fast rotation ($P < 1$ h) perturbations in the value of asteroid's period (ΔP) become more important for the change of A_2 . Perturbations that occurred in the rotational dynamics of asteroids Duende, 2012 TC4, and 2023 BU had no noticeable effect on their A_2 values.

ACKNOWLEDGEMENTS:

The study was funded by a grant Russian Science Foundation No. 23-22-00306, <https://rscf.ru/project/23-22-00306/>.

REFERENCES:

- [1] *Fenucci M., Micheli M., Gianotto F. et al.* An automated procedure for the detection of the Yarkovsky effect and results from the ESA NEO Coordination Centre // *Astronomy and Astrophysics*. 2024. V. 682. Article A29.
- [2] *Boldrin L. A. G., Araujo R. A. N., Winter O. C.* On the rotational motion of NEAs during close encounters with the Earth // *European Physical Journal Special Topics*. 2020. V. 229. No. 8. P. 1391–1403.
- [3] *Melnikov A. V.* Rotational dynamics of asteroids approaching planets // *Solar System Research*. 2022. V. 56. No. 4. P. 241–251.
- [4] *Lobanova K. S., Melnikov A. V.* Disturbances in the rotational dynamics of asteroid (99942) Apophis at its approach to the Earth in 2029 // *Solar System Research*. 2024. V. 58. No. 2. P. 208–219.
- [5] *Benson C. J., Scheeres D. J., Moskovitz N. A.* Spin state evolution of asteroid (367943) Duende during its 2013 earth flyby // *Icarus*. 2020. V. 340. Article 113518.
- [6] *Lee H.-J., Āurech J., Vokrouhlický D. et al.* Spin change of asteroid 2012 TC4 probably by radiation torques // *Astronomical J.* 2021. V. 161. No. 3. Article 112.
- [7] *Kouprianov V. V., Shevchenko I. I.* The shapes and rotational dynamics of minor planetary satellites // *Solar System Research*. 2006. V. 40. No. 5. P. 393–399.
- [8] *Vokrouhlický D., Milani A., Chesley S. R.* Yarkovsky effect on small near-Earth asteroids: mathematical formulation and examples // *Icarus*. 2000. V. 148. P. 118–138.

3D SHAPE RECONSTRUCTION OF AN ASTEROID FROM ITS LIGHT CURVES AS A CONVEX POLYHEDRON

A. L. Tolstoy, Yu. D. Medvedev, S. R. Pavlov
Institute of Applied Astronomy RAS, al.tolstoy@iaaras.ru

KEYWORDS:

3D shape of asteroid, asteroid Urania, light curves, shape reconstruction, convex polyhedron

INTRODUCTION:

Reconstruction of an asteroid shape is a topical challenge for the Solar system researchers studying the dynamics of small celestial bodies. The knowledge of the shape of a body allows to calculate more accurate models of motion which take into account the complex translational-rotational motion of an object considered as a rigid body. The usage of light curves is one of the most accessible resources for an asteroid shape reconstruction. So far, we know only one open database (Damit, <https://astro.troja.mff.cuni.cz/projects/damit/>) containing asteroid models based on light curves.

METHOD:

In this paper we present a method to approximate the shape of an asteroid as a convex polyhedron from its light curves, based on global minimization of objective function. The algorithm searches for the minimum of the sum of the squares $O-C$ (residuals between the observed and calculated values of the stellar magnitude). The search is carried out by the following parameters determining the shape of the polyhedron: the number of sides, their areas and directions, the direction of the spin axis and the period of rotation. The proposed method was tested while reconstructing a model polyhedron from the synthetic light curves obtained at multiple phase angles.

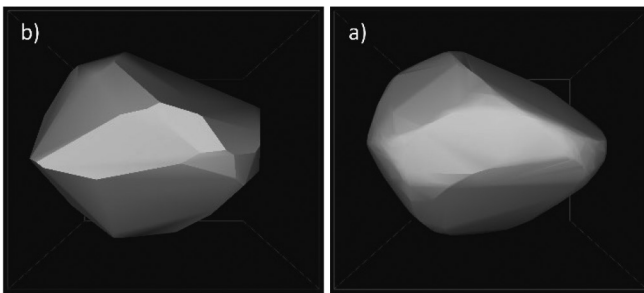


Fig. 1. Model polyhedron (a) and reconstructed polyhedron (b)

Figure 1a shows the shape of the asteroid Urania taken from the DAMIT database [1]. The surface of the asteroid is represented by 1007 triangular sides. Figure 1b shows the result of optimization for the synthetic light curves. Reconstructed shape is presented as a fifty-sided polyhedron defined as a sequence of areas and angles determining the normals to the sides. The calculations performed show that the quality of the shape reconstruction is largely influenced by the number and the accuracy of observations obtained at various phase angles. Therefore observations obtained at different phase angles are needed for the reliable shape reconstruction. In the future, we are planning to test the algorithm on the asteroids which have shape estimates obtained from other types of observations.

ANALYSIS OF SCENARIOS FOR THE FORMATION OF THE YOUNG EMILKOWALSKI ASTEROID FAMILY

E. D. Kuznetsov, V. S. Safronova, A. S. Perminov, M. A. Vasileva
*Ural Federal University, Yekaterinburg, Russia, eduard.kuznetsov@urfu.ru,
v.s.safronova@urfu.ru, alexander.perminov@urfu.ru, vasilyeva.maria@urfu.ru*

KEYWORDS:

Emilkowalski family, family formation scenario, numerical modelling, convergence of nodes and pericentres, Kholshchevnikov metrics, cascade decay, Yarkovsky effect

INTRODUCTION:

The young Emilkowalski asteroid family is located in the central Main Belt: semi-major axis $a = 2.60$ a.u., eccentricity $e = 0.15$, inclination $i = 17.75^\circ$. In 2006 Nesvorný and Vokrouhlický [1] discovered Emilkowalski family as a cluster of three asteroids in close heliocentric orbits: (14627) Emilkowalski, (126761) 2002 DW10, and (224559) 2005 WU179. The first estimate of the age of the family at 220 ± 30 kyr [1] showed that it is a young family. Pravec et al. [2] estimated the taxonomic type of asteroid (14627) Emilkowalski based on photometric observations as type D.

In [2] and [3], new family members were discovered, bringing the number of asteroids in the family to nine. Age estimates of the “main asteroid (14627) Emilkowalski — secondary asteroid” pairs were obtained in papers [2] and [3]. It was shown that at least two decay events of the parent asteroid of this family occurred in the last 5 Myr. This is consistent with the scenario of cascading disintegration of the parent body. Four new members of the Emilkowalski family were discovered in [4]. Thus, 13 asteroids that are members of the Emilkowalski family are currently known.

In this paper, we consider the young Emilkowalski asteroid family from the point of view of studying the formation process and attempt to reconstruct the chronological sequence of the parent body breakup. For this purpose, we: 1) numerically investigate the dynamical evolution of asteroids based on known nominal orbits, considering the influence of the Yarkovsky effect, 2) estimate the ages of all possible pairs among the asteroids of the family and based on these estimates 3) construct a basic scenario of the family formation.

MODELLING THE DYNAMIC EVOLUTION OF ASTEROIDS:

Numerical modelling of the motion of asteroids of the Emilkowalski family was performed using the Orbit9 software included in the OrbFit software package (<http://adams.dm.unipi.it/orbfit/>). When modelling the dynamical evolution, perturbations from eight major planets and the dwarf planet Pluto, the Sun's oblateness, and relativistic effects were considered. The osculating elements of asteroid orbits from the AstDyS catalogue for the epoch MJD 60200 were taken as initial ones. The integration intervals were 5 and 2 Myr.

Different variants of the evolution were considered: without considering the diurnal Yarkovsky effect and with this effect considered. The influence of the diurnal Yarkovsky effect was considered in the form of a constant drift rate da/dt of the semi-major axis of the asteroid's orbit a . The drift rate was estimated either from the known physical and thermophysical parameters of asteroids, or parameters characteristic of the given taxonomic class were used, if all asteroids, as well as the main asteroid of the (14627) Emilkowalski family, are of type D.

Estimation of the drift rate of the semi-major axis da/dt was performed using a modified version of the Orbit9 software included in the OrbFit package [5] (<https://github.com/Fenu24/OrbFit>), which provides the possibility of taking into account the influence of the Yarkovsky effect and the YORP effect on the basis of setting the dynamic (period of axial rotation and in-

clination of the rotation axis), physical (density) and thermophysical (heat capacity, thermal conductivity, radiation and absorption coefficients of surface layers) parameters of the asteroid.

The age of the pairs was estimated using a method based on the search for moments of convergence of the nodes and perihelion orbits (synchronous zeroing of the longitude differences of the ascending nodes $\Delta\Omega = 0$ and perihelion arguments $\Delta\omega = 0$) (see, e.g., [6]). Estimates of the age of pairs T were obtained as the average of $T = (T_\Omega + T_\omega)/2$ moments of zeroing the differences between the longitudes of the ascending nodes T_Ω and the perihelion arguments T_ω . In the following, we used estimates for which the relative moment difference $\delta T = (T_\Omega - T_\omega)/T < 0.1$, which provides the proximity of the zeroing moments of the differences between the longitudes of the ascending nodes and the perihelion arguments necessary for obtaining age estimates. When several evolution variants with different values of the drift rate of the semi-major axis were considered for an asteroid, the interval of possible ages of a pair was estimated.

In addition to estimates of the moments and time intervals corresponding to the convergence of the nodes and perihelion of the orbits at different drift rates of the semi-major axes of the orbits, estimates of the values of the Kholshchevnikov metrics ρ_2 and ρ_5 [7] were obtained when constructing the family formation scenario and their differences $\rho_2 - \rho_5$ were calculated. The ρ_2 metric is defined in the five-dimensional space of Keplerian orbital elements a, e, i, Ω, ω (the position of the body in the orbit is not considered). The metric ρ_5 is defined in the factor space of positional orbit elements a, e, i (at all possible orientations of orbital planes and apsidal lines). A small value of the difference between the metrics $\rho_2 - \rho_5$ is a necessary condition for the youth of the pair [6].

SCENARIO FOR THE FORMATION OF THE EMILKOWALSKI ASTEROID FAMILY:

The Emilkowalski family formation scenario was constructed based on a joint analysis of the moments of convergence of the nodes and perihelion orbits and the values of the Kholshchevnikov metrics. The construction of the scenario was divided into three stages. At the first stage, the moments of simultaneous convergence of nodes and perihelion orbits were analyzed for cases of asteroid orbits convergence with the orbit of the main asteroid of the (14627) Emilkowalski family. As a result, groups of asteroids corresponding to the sequence of parent body destruction events were identified. At this stage, asteroids whose orbits do not converge with the orbit of (14627) Emilkowalski were excluded from consideration. At the second stage, the proximity of the selected pairs of orbits was analyzed based on estimates of the values of the Kholshchevnikov metrics ρ_2 and ρ_5 , as well as their difference $\rho_2 - \rho_5$. It was assumed that the values of metrics and their difference for the subsequent event were smaller than for the previous one. At the third stage, we analyzed the possibility of the formation of family members as a result of cascade fission of fragments of the parental body of the family. Figure 1 shows the scheme of the constructed scenario, where for each parent body the range of fragment ages in kyr (red font) is indicated in the order of their location on the scheme. For each family member, the number or name and size in meters are given.

CONCLUSIONS:

A scenario of the formation of the Emilkowalski family was constructed based on the analysis of the evolution of the nominal orbits of asteroids. We used the method of convergence of the nodes and perihelion orbits together with the Kholshchevnikov metrics to estimate the age of the pairs. The constructed model shows that the family was formed as a result of cascading destruction of the parent body. It is possible that the family is significantly younger than previously thought, with an age of less than 1.5 Myr. We plan to test this conclusion based on the results of a study of the probabilistic evolution.

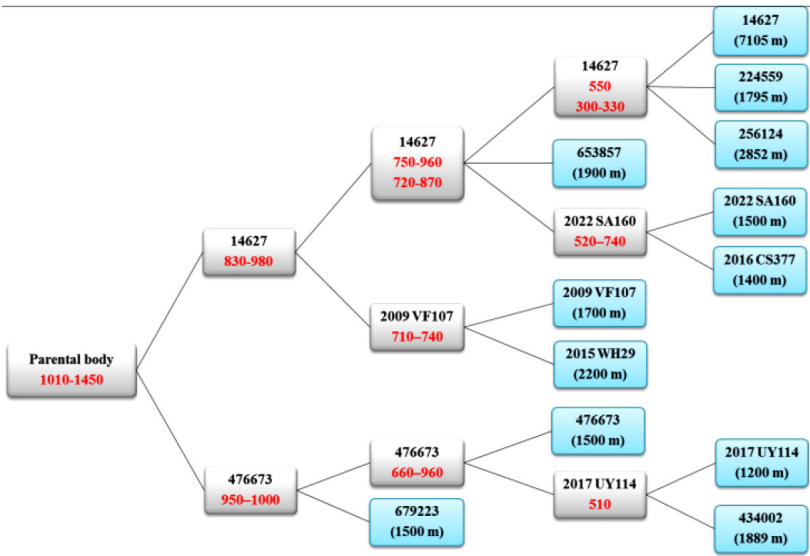


Fig. 1. Emilkowalski family formation scenario

ACKNOWLEDGMENTS:

The study was funded by the Russian Science Foundation grant No. 24-22-00143, <https://rscf.ru/en/project/24-22-00143/>.

REFERENCES:

- [1] Nesvorný D., Vokrouhlický D. New candidates for recent asteroid breakups // *The Astronomical J.* 2006. V. 132. No. 5. P. 1950–1958.
- [2] Pravec P., Fatka P., Vokrouhlický D. et al. Asteroid clusters similar to asteroid pairs // *Icarus.* 2018. V. 304. P. 110–126.
- [3] Fatka P., Pravec P., Vokrouhlický D. Cascade disruptions in asteroid clusters // *Icarus.* 2020. V. 338. Article 113554.
- [4] Kuznetsov E. D., Vasileva M. A., Perminov A. S., Safronova V. S. Search for new members of young asteroid families // *Solar System Research.* 2024 (in Press).
- [5] Fenucci M., Novakovic B. MERCURY and ORBFIT packages for numerical integration of planetary systems: implementation of the Yarkovsky and YORP effects // *Serbian Astronomical J.* 2022. V. 204. P. 51–63.
- [6] Kuznetsov E. D., Rosaev A. E., Plavalova E., Safronova V. S., Vasileva M. A. A Search for young asteroid pairs with close orbits // *Solar System Research.* 2020. V. 54. No 3. P. 236–252.
- [7] Kholshchevnikov K. V., Kokhirova G. I., Babadzhanyan P. B., Khamroev U. H. Metrics in the space of orbits and their application to searching for celestial objects of common origin // *Monthly Notices of the Royal Astronomical Society.* 2016. V. 462. P. 2275–2283.

THE PSP/WISPR DUST TRAIL AND THE GEMINID STREAM

G. O. Ryabova

Tomsk State University, Tomsk, Russia, galina.ryabova@mail.tsu.ru

KEYWORDS:

meteor, meteoroid, mathematical model, video observations, observational bias

ABSTRACT:

Recently Battams et al. [1] reported detection of a dust trail observed near the orbit of the asteroid Phaethon by the instrument WISPR for the Parker Solar Probe satellite. The key finding of this work is a clear separation of the dust trail and the orbit of Phaethon as a function of true anomaly. Inspired by the work I decided to research into this situation using my numerical model of the Geminid meteoroid stream [2]. I would like to share some results obtained in the process and related mostly to the comparison with the orbits of the observed Geminids from the most precise video catalogues Koten et al. [3] and Borovička et al. [4]. It was found that a strong observational bias exists and it is not always possible to judge a meteoroid stream exclusively from ground observations.

ACKNOWLEDGEMENTS:

This work was supported by the state assignment of Ministry of Science and Higher Education of the Russian Federation (theme No. FSWM-2024-0005).

REFERENCES:

- [1] *Battams K., Gutarra-Leon A. J., Gallagher B. M. et al.* Continued PSP/WISPR Observations of a Phaethon-related Dust Trail // *ApJ*. 2022. V. 936, Iss. 1. Article 81. 19 p.
- [2] *Ryabova G. O.* On mean motion resonances in the Geminid meteoroid stream // *Planet. Space Sci.* 2022. V. 210. Article 105378. 11 p.
- [3] *Koten P., Spurný P., Borovička J., Stork R.* Catalogue of video meteor orbits. Pt 1 // *Publ. Astronomical Inst. Czechoslovak Acad. Sciences*. 2003. No. 91. P. 1–32.
- [4] *Borovička J., Spurný P., Šrbený L.* Data on 824 fireballs observed by the digital cameras of the European Fireball Network in 2017–2018. II. Analysis of orbital and physical properties of centimeter-sized meteoroids // *Astronomy and Astrophysics*. 2022. V. 667. Article A158. 24 p.

SOME REMARKS ABOUT THE EARTH'S QUASI-SATELLITES POPULATION

V. V. Sidorenko

Keldysh Institute of Applied Mathematics RAS, Moscow, Russia
vvsidorenko@list.ru

KEYWORDS:

asteroids, quasi-satellites, mean-motion resonance

INTRODUCTION:

A quasi-satellite is an object that moves in the vicinity of a planet at a distance significantly less than the distance from this planet to the host star, and at the same time always remains outside its Hill sphere [1]. The quasi-satellite mode of orbital motion is realized at 1:1 resonance of the mean motions of this object and the planet (Figure 1). Under certain conditions, the quasi-satellite mode (QS-mode) can transform into other modes of resonant motions (typically, into a horseshoe mode).



Fig. 1. The orbital motion of a quasi-satellite and its host planet: *a* — is a Sun-centered reference frame that preserves the orientation in the absolute space. The quasi-satellite and the planet move around the Sun with the same orbital period in elliptic and in circular orbits respectively; *b* — is a Sun-centered frame rotating with the mean orbital motion of the planet

CURRENTLY KNOWN QUASI-SATELLITES OF THE EARTH:

To date, eight asteroids are known to be quasi-satellites of the Earth: (164207) 2004GU9, (277810) 2006FV35, 2013LX28, 2014OL339, (469219) Kamo'oalewa, 2020PP1, 2022YG, 2023FW13. Their sizes range from ~10 m to ~100 m, eccentricities e from 0.07 to 0.46, inclinations i from 2.3 to 50°. No regularities have yet been identified in the distribution of the values of the argument of perihelion ω and the longitudes of the ascending node Ω .

APPLICATION OF PERTURBATION THEORY TO STUDY QUASI-SATELLITE MOTIONS:

In QS-mode the asteroid's motion is weakly perturbed heliocentric. This makes it possible to apply perturbation theory for analytical studies of quasi-satellite motions [2–5].

Below we limit the analysis only to the behavior of the resonant phase $\varphi = \lambda - \lambda'$ (λ and λ' are the mean longitudes of the asteroid and planet, respectively). As a model of the system "Sun + planet + asteroid", the restricted circular three-body problem is used. After averaging over the orbital motions and the proper choice of units, the behavior of the resonant phase can be described by the equation

$$3 \frac{d^2 \varphi}{dt^2} + \mu \frac{\partial W}{\partial \varphi} = 0, \quad (1)$$

where time t is introduced so that the mean motion of the planet $n' = 1$, $\mu \ll 1$ is the part of the planet's mass in the total mass of the system, $W(\varphi, \omega, e, i)$ is the averaged disturbing function.

The expression for the disturbing function averaged taking into account 1:1 resonance of mean motions can be written as

$$W(\phi, \omega, e, i) = \frac{1}{2\pi} \int_0^{2\pi} \left[\frac{1}{|\mathbf{r}(\lambda) - \mathbf{r}'(\lambda'(\lambda))|} - (\mathbf{r}(\lambda), \mathbf{r}'(\lambda'(\lambda))) \right] d\lambda.$$

Here the vectors $\mathbf{r}(\lambda)$ and $\mathbf{r}'(\lambda')$ in the integrand define the position of the asteroid and the planet for the corresponding values of their mean longitudes. In the resonant motion under consideration these longitudes are connected by the relation $\lambda'(\lambda) = \lambda - \phi$.

In the quasi-satellite mode of motion, the resonant phase ϕ oscillates in the vicinity of zero (Figure 2).

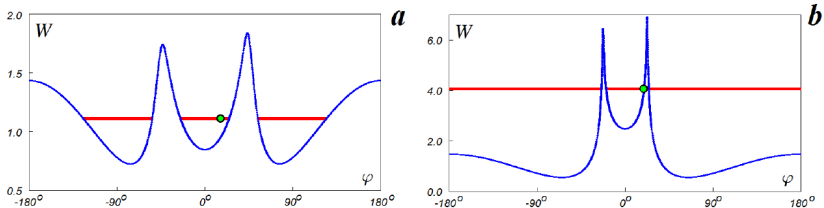


Fig. 2. Averaged disturbing function $W(\phi, \omega, e, i)$ for asteroids (277810) 2006FV35 (a) and 2022YG (b). The red line indicates the value of the energy integral along the solution of equation (1), corresponding to the observed motion of the asteroid. The dot marks the current value of the resonant phase.

Figure 2 demonstrates a remarkable tendency: for most Earth's quasi-satellites, the value of the resonant phase at the moment of their discovery is located near the border of the interval of its variation. It can be used to estimate the number of such objects in near-Earth space.

REFERENCES:

- [1] Kogan A. Yu. Quasi-satellite orbits and their applications // Proc. 41st Congr. Intern. Astronautical Federation / ed. R. Jehn. 1990. P. 90–97.
- [2] Mikkola S., Innanen K. Orbital stability of planetary quasi-satellites // The Dynamical Behavior of Our Planetary System / ed. R. Dvorak, J. Henrard. 1997. P. 90–97.
- [3] Namouni F. Secular interactions of coorbiting objects // Icarus. 1999. V. 137. P. 293–314.
- [4] Namouni F., Christou A. A., Murray C. D. Coorbital dynamics at large eccentricity and inclination // Phys. Rev. Lett. 1999. V. 83. P. 2506–2509.
- [5] Sidorenko V. V., Neishtadt A. I., Artemyev A. V., Zelenyi L. M. Quasi-satellite orbits in the general context of dynamics in the 1:1 mean motion resonance: perturbative treatment // Celestial Mechanics and Dynamical Astronomy. 2014. V. 120. P. 131–162.

ACCUMULATION AND RECOMBINATION OF RADICALS AS AN ENERGY SOURCE FOR ACTIVE PROCESSES IN ICY BODIES OF THE SOLAR SYSTEM

A. K. Pavlov¹, G. A. Kucherov², A. Y. Merkulova¹, D. V. Belousov¹

¹ Ioffe Institute, Saint Petersburg, Russia, anatoli.pavlov@mail.ioffe.ru

² Peter the Great Saint Petersburg Polytechnic University
Saint Petersburg, Russia, glebkucherov2002@gmail.com

KEYWORDS:

free radicals, Kuiper belt, Oort cloud, icy bodies, liquid water

INTRODUCTION:

Observations indicate that processes of active energy release occur inside many icy bodies of the Solar System at long distances from the Sun. Such processes can occur inside the satellites of giant planets. For example, plumes of water vapour have been detected from the surface of Saturn's moon Enceladus, and it is now believed that there must be an ocean of liquid water beneath its icy surface. In the case of Enceladus and other icy satellites, the observed energy release can be explained by tidal friction, but data obtained using the James Webb Telescope indicate that the icy bodies of the Kuiper belt, such as the dwarf planets Eris and Makemake, can also be active [1]. The activity of these bodies cannot be explained using tidal friction, so we need to look for other sources of energy. In the work [2], a mechanism was proposed to explain the cometary outbursts at large distances from the Sun. The work [2] proposed the accumulation of H and OH radicals in the surface layers of the comet under the influence of cosmic rays at low temperatures as an energy source. This work considers a model for large icy bodies with a similar approach, but the accumulation of radicals occurs not due to cosmic rays, but due to the decay of radionuclides throughout the entire volume of the body.

MODEL:

A number of studies have shown that when a critical concentration of radicals accumulates ($\geq 1\%$), the process of their spontaneous recombination can begin with the rapid release of a large amount of energy [2, 3]. Our model assumes that a sufficiently large concentration of radicals has accumulated throughout the entire volume of the body and their spontaneous recombination has occurred in a small-sized region in the center of the body, leading to a sharp increase in temperature in this area. The rate of recombination depends exponentially on temperature: $K(T) = K_0 \cdot \exp(-U_a/k_b T)$, where K_0 is the recombination constant, U_a is the activation energy and k_b is the Boltzmann constant. Therefore, due to the increase in temperature, the recombination process propagates further throughout the entire volume of the body.

We considered a homogeneous porous body with a radius of 20 km, consisting of water ice, frozen CO and CO₂ gases, and dust. Water ice was considered in two forms: amorphous and crystalline. At temperatures above 120 K, an exothermic irreversible transition from the amorphous form of ice to the crystalline form occurs, accompanied by the sublimation of CO and CO₂ gases that were captured in the amorphous ice.

The temperature increase was simulated depending on the composition of the body, its porosity, thermal conductivity and initial temperature. The initial temperatures were set in the range from 5 to 50 K, which correspond to surface temperatures in the Oort cloud and the Kuiper belt.

RESULTS:

It was shown that at certain values of the concentration of radicals (from 1.5 to 3.9%), which can be accumulated during the life of the Solar System, the temperature inside the body can reach 273 K. Such a temperature can be maintained inside the body for times of the order of a million years, as

can be seen from Figure 1. It was also shown that the process under consideration weakly depends on the initial temperature of the body and can occur even in the Oort cloud.

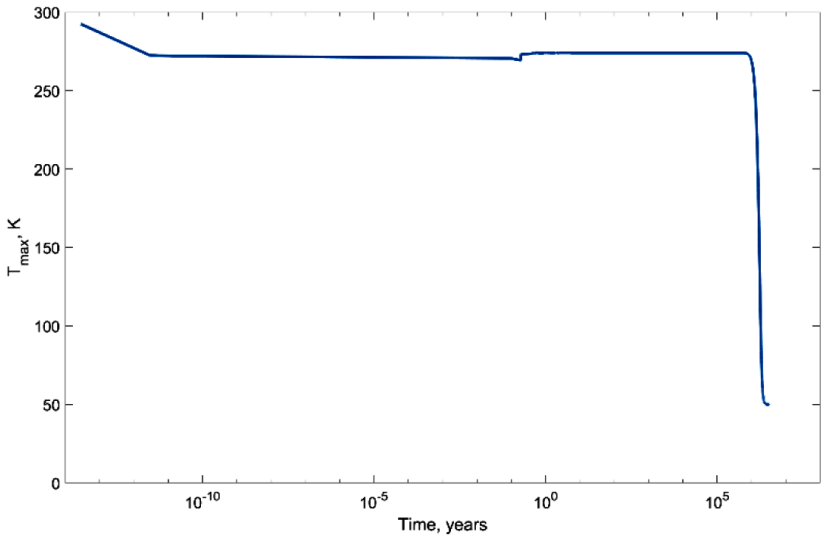


Fig. 1. Dependence of the maximum temperature on time inside the body with a radius of 20 km consisting of the mixture of amorphous ice with trapped gases and dust for a radical concentration of 3.1 %

REFERENCES:

- [1] Grundy W. M., Wong I., Glein C. R. et al. Measurement of D/H and $^{13}\text{C}/^{12}\text{C}$ ratios in methane ice on Eris and Makemake: evidence for Internal activity // *Icarus*. 2024. V. 411. Article 115923. <https://doi.org/10.1016/j.icarus.2023.115923>.
- [2] Belousov D. V., Pavlov A. K. Cometary outbursts in the Oort cloud // *Icarus*. 2024. V. 415. Article 116066. <https://doi.org/10.1016/j.icarus.2024.116066>.
- [3] Shabalin E., Kulagin E., Kulikov S., Melikhov V. Experimental study of spontaneous release of accumulated energy in irradiated ices // *Radiation Physics and Chemistry*. 2003. V. 67. P. 315–319. [https://doi.org/10.1016/S0969-806X\(03\)00059-8](https://doi.org/10.1016/S0969-806X(03)00059-8).

A SYSTEM TO DETECT DAY-TIME ASTEROIDS (SODA) OF THE “MILKY WAY” PROJECT

A. Shugarov, B. Shustov

Institute of Astronomy RAS, Moscow, Russia, shugarov@inasan.ru

KEYWORDS:

wide field telescope; asteroid hazard problem; space telescope; unmanned spacecraft; decameter asteroids

ABSTRACT:

The asteroid hazard problem poses a threat not only from large (>100 m) but also from relatively small decameter bodies. As was demonstrated by the Chelyabinsk event on February 15, 2013 collisions of small (decameter class) Near-Earth objects (NEOs) with the Earth can pose a danger to the inhabitants of our planet. Such bodies are faint and can be systematically detected only in near-Earth space. Moreover, half of them approach the Earth from the side of the day-time sky and they can only be detected with special space-born facilities.

A civil space safety program “Milky Way” has been under development in Russia since 2022. The NEO problem (asteroid/comet hazard) is a part of this program. We propose to build two segments regarding the NEO problem:

- ground-based network: a network of small/moderate aperture wide-field optical telescopes to search for asteroids in the night-time hemisphere;
- space-based segment: a spacecraft at the L1 point of the Sun-Earth system to search for asteroids in the day-time hemisphere which are unobservable with ground-based telescopes.

A part of the “Milky Way” program implies a launch of a spacecraft aimed to detect 10 m asteroids coming from the sunward hemisphere and to predict space weather and monitor Sun activity from the Sun-Earth L1 point.

The payload SODA (System of Observation Day-time Asteroids) consists of a set of wide field of view telescopes with an aperture of 30 cm, it is under development at INASAN. Detection will be carried out using a barrier technique, afterwards dangerous objects will be tracked until they approach the Earth.

The efficiency of asteroid monitoring from L1 can be significantly improved using a triangulation tracking mode if two spacecraft are operated simultaneously. Cooperation within BRICS is welcome to build the second spacecraft to operate at L1.

A combination of space-based (SODA) and ground-based projects, e.g. BITDN (BRICS Intelligent Telescope and Data Network) proposed by BRICS Astronomy Working Group, is a proper way to provide a realistic real-time warning system against decameter-sized impactors.

A general outline of the SODA payload is presented and some new features are given in more detail.

REFERENCES:

- [1] *Shugarov A., Shmagin V., Boqian X. et al. // 7th IAA Planetary Defense Conf. 2021. 100.*
- [2] *Shugarov A., Shustov B., Naroenkov S. // Open Astronomy. 2018. 27. 132.*
- [3] *Shugarov A. S., Shustov B. M. // INASAN Science Reports. 2022. 7. 85.*
- [4] *Shustov B.M., Shugarov A.S., Naroenkov S.A., Prokhorov M.E. // Astronomy Reports. 2015.*

SECULAR EVOLUTION AND STABILITY OF RINGS AROUND ROTATIONALLY ASYMMETRICAL BODIES. REVISITING THE PROBLEM

B. P. Kondratyev^{1,2,3}, V. S. Kornoukhov^{1,2}

¹ *Moscow State University, Faculty of Physics, Moscow, Russia*
work@boris-kondratyev.ru

² *Sternberg Astronomical Institute, Moscow State University, Moscow, Russia*

³ *Pulkovo Observatory RAS, Saint Petersburg, Russia*

KEYWORDS:

rings around small celestial bodies and the problem of their confinement, self-gravity of Gaussian rings, azimuthally averaged potential of the central body, equations of secular evolution of rings, dwarf planet Haumea

ABSTRACT:

A method has been developed for studying the secular evolution and stabilization of the shape of rings in small celestial bodies that do not have shepherd satellites. A model of a compound ring consisting of two close, generally non-coplanar elliptical Gaussian rings has been constructed. The self-gravitation of the ring is taken into account through the mutual gravitational energy of the boundary rings W_{mut} . The function W_{mut} is presented as a series with an accuracy of up to the 4th power of small eccentricities and mutual inclination of the rings. The secular evolution of a compound ring is described by differential equations in special (collective) variables. For rings without a central body (this is the problem 1), a closed system of 8 differential equations is obtained using the mutual energy function. The evolution of rings in the azimuthally averaged potential of a rotating triaxial body is also studied (this is the problem 2); in this problem, another system of eight differential equations was obtained. In both problems, in addition to the general case, two particular ones are considered: i) the case of coplanar elliptical rings, and ii) the case of circular rings with a tilt. The theory is applied to study the recently discovered ring of the dwarf planet Haumea. It is shown that without taking into account self-gravity, the nodal precession time of the Haumea ring is equal to $T_{\Omega} = 12.9 \pm 0.7d$ but taking into account the self-gravity of the ring can reduce this period. It is established that self-gravity does indeed contribute to the preservation of the ring shape without invoking the hypothesis of shepherd satellites. Criteria for the preservation of the shape of the rings were obtained, which made it possible to estimate the interval for the ratio of the ring mass to the mass of Haumea $10^{-4} < m/M < 10^{-3}$. Taking into account the optical thickness of the ring $\tau \approx 0.5$, it was shown that the Haumea ring with a mass of $m/M \approx (1-2) \cdot 10^{-4}$ can consist of ice particles of size $d_0 \approx 0.7-1$ m.

THE NEW FORMULA FOR THE ANGULAR VELOCITY OF ROTATING EQUILIBRIUM FIGURES

B. P. Kondratyev

¹ *Lomonosov State University, Sternberg Astronomical Institute, Faculty of Physics, Moscow, Russia, work@boris-kondratyev.ru*

² *Central Astronomical Observatory at Pulkovo, Saint Petersburg, Russia*

KEYWORDS:

equilibrium figures, homogeneous and inhomogeneous, polytropic equation of state, angular velocity of rotation, outer and inner components of gravitational energy, constant of integration, level surfaces

ABSTRACT:

The purpose of the report is to derive a new formula for the angular velocity of rotation of equilibrium figures of a gravitating fluid. An important feature of this formula is that the angular velocity is represented through the components of the internal and external parts of the gravitational energy of the body. Two variants of deriving the new formula are considered: i) for homogeneous equilibrium figures, and ii) for a wide class of inhomogeneous figures with a polytropic equation of state. The adequacy of the new formula is established and it is proven that for homogeneous bodies this formula gives the known expressions for the angular velocity for classical Maclaurin spheroids and Jacobi ellipsoids. For the first time, it became necessary to express the constant integration of the equations of motion through the polytropic index and three global characteristics: mass, total gravitational energy, and rotational energy of the body. The advantage of this formula is that it can describe not only ellipsoidal equilibrium figures, but also equilibrium figures of any other geometric shape, including toroidal. This expands the scope of application of the theory of equilibrium figures. The developed method is applied to a two-component model of the dwarf planet Haumea.

CONSTRUCTION OF TRANSFER TRAJECTORIES OF THE SPACECRAFT TO ASTEROIDS PASSING NEAR SUN-EARTH LIBRATION POINTS

M. V. Pupkov¹, N. A. Eismont¹, O. L. Starinova², K. S. Fedyaev¹

¹ Space Research Institute RAS, Moscow, Russia, m.pupkov@iki.rssi.ru

² Samara University, Samara, Russia

KEYWORDS:

libration points, spectrum-roentgen-gamma, near-earth asteroids, Apophis asteroid, unstable manifolds

INTRODUCTION:

This work is devoted to the study of possible options for transferring a spacecraft operating in the vicinity of the Sun-Earth libration point to a trajectory of approach to a near-Earth asteroid. A bounded orbit in the vicinity of the L_2 libration point of the Sun-Earth system of the Spectrum-Roentgen-Gamma (SRG) space observatory [1] was chosen as the initial orbit. Asteroid Apophis [2] was chosen as the target celestial body, which will pass near the L_2 Sun-Earth libration point on April 11, 2029, and two days later it will approach the Earth at a distance of about 30 000 km from its surface.

METHODS FOR CONSTRUCTING TRAJECTORIES:

The main requirements for the transfer trajectories of the SRG observatory to the Apophis asteroid are: the total value of the characteristic velocity should not exceed 200 m/s (according to the current fuel reserves), and after the asteroid flyby, the spacecraft should return to the vicinity of the L_2 libration point of the Sun-Earth system. In accordance with these conditions, two methods of constructing transfer trajectories are proposed.

The first method is to change the orbit near the libration point to one that will allow a close encounter with the celestial body. This method is the simplest in terms of implementation, but requires more fuel consumption.

The second method is to transfer the SRG observatory to a trajectory from the set of unstable manifold. It requires a large number of impulses to approach the Apophis asteroid and more time to return to the libration point L_2 compared to the first method. However, the advantage is significant fuel economy.

NUMERICAL SIMULATION RESULTS:

Figure 1 shows the transfer trajectory according to the first method. The date of the impulse implementation — March 3, 2029 — is marked with the number (1). The number (2) indicates the point of closest approach to the asteroid. The cost of the characteristic velocity is 175 m/s.

Figure 2 shows the scheme of the multi-impulse transfer of the SRG observatory to the Apophis asteroid. In this case, 4 impulses are needed: to transfer the spacecraft to the trajectory of an unstable manifold, to change the inclination of the geocentric orbit for a close flyby of Apophis, to transfer the SRG observatory to an orbit near the L_1 libration point of the Sun-Earth system and to return to the vicinity of the L_2 libration point.

CONCLUSION:

Two ways of constructing transfer trajectories of the SRG space observatory to the near-Earth asteroid Apophis are given. In all these cases, there are enough fuel reserves on board to carry out this kind of mission. It is shown that after the passage of a celestial body, it is possible to return the spacecraft to the vicinity of the initial orbit to continue performing the main tasks.

REFERENCES:

- [1] Eismont N. A., Kovalenko I. D., Nazarov V. N. Orbital motion and attitude control of the Spectrum – Röntgen – Gamma space observatory // Astronomy Letters. 2020. V. 46. No. 4. P. 263–274.

- [2] *Shuvalov V.V., Svetstov V.V., Artem'eva N.A.* Asteroid Apophis: evaluating the impact hazards of such bodies // *Solar System Research*. 2017. V. 51. No. 1. P. 44–58.

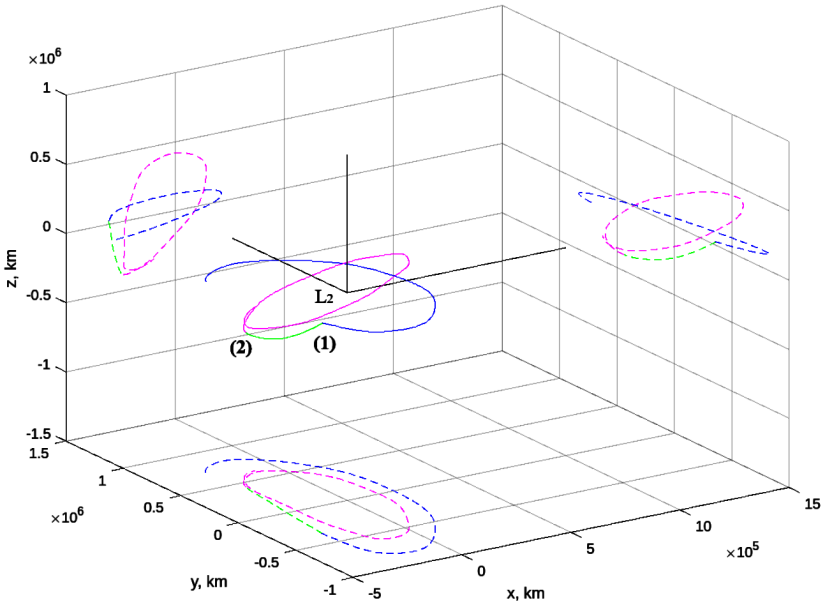


Fig. 1. The transfer trajectory of the SRG spacecraft to the Apophis asteroid, as designed according to the first method

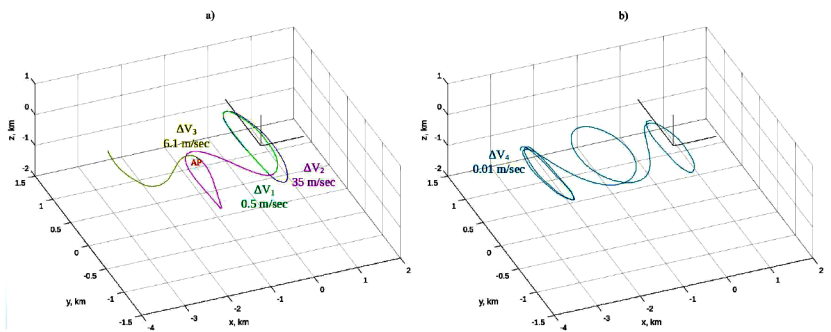


Fig. 2. The transfer trajectory of the SRG spacecraft to the Apophis asteroid, as designed according to the second method: a) the flight section to Apophis and the L_1 Sun-Earth libration point, b) the section of return to the L_2 libration point

ON THE OUTBURSTS OF THE CENTAUR 174P/ECHECCLUS

Yu. D. Medvedev, Yu. A. Chernetenko, S. R. Pavlov

Institute of Applied Astronomy RAS, Moscow, Russia, medvedev@iaaras.ru

KEYWORDS:

comet 174P/Echeclus, outbursts of brightness, positional observations, comet's gas-dust jets

INTRODUCTION:

We have investigated the possible causes of outbursts of (60558) Echeclus, which also has a cometary designation 174P. The orbit of the comet lies between Jupiter and Neptune thus 174P belongs to the group of centaurs. An important feature of the comet is that non-periodic outbursts of brightness, up to 6 stellar magnitudes, were observed. We focused our research on exploring the possibility of using positional observations to determine the parameters of an assumed gas-dust jet formed during outbursts.

CALCULATION:

Positional observations of the comet Echeclus were taken from the catalogue of Minor Planer Center. We calculated the orbit taking into account gravitational perturbations from 8 planets, Pluto, Ceres, Pallas, Vesta and relativity effects. The residuals of the orbit fit (O-C) showed systematic deviations in positional observations, which correlated with the outbursts of the apparent magnitude on the lightcurves. We determined the initial speed and the direction of matter ejection from deviations in O-C. We also tried to determine the diameter of the particles, but it turned out to be insensitive to deviations in O-C due to the comet's large distance from the Earth and the Sun and the low density of the gas jet hence small non-gravitational accelerations of the dust.

We calculated initial values motion of an average particle using the method described in the paper [1]. The system of differential equations describing the motion of a dust grain has been integrated numerically on the intervals of outbursts which were defined from the comet's lightcurves. Assuming that the center-of-light coincides with the position of the dust grain during the outbursts we calculated the new values of O-C. These values formed the right part of the conditional equations. The differential coefficients of the initial values of the particle motion were calculated using the finite difference method. Then the system was solved using the least squares method (LSM). This procedure allowed us to determine the gas-dust jet parameters during the outbursts in 2005 and 2017. The results obtained indicate that it is likely that in December 2005, the comet's fragments were ejected, some of which fell on the comet's nucleus between 2007 and 2017. Collisions of these fragments with the comet's surface could probably lead to a multiple increase in the comet's brightness.

REFERENCES:

- [1] *Chernetenko Yu., Medvedev Yu. Parameters of Dust Jets in Comet Encke's Coma // Monthly Notices of the Royal Astronomical Society. 2020. V. 493. Iss. 4. P. 5499–5505.*

ANALYSIS OF THE SURFACES OF CELESTIAL BODIES APPLYING EQUAL-AREA PROJECTIONS OF THE TRIAXIAL ELLIPSOID

M. V. Nyrtsov¹, A. I. Sokolov¹, A. E. Zubarev², M. E. Fleis³, N. A. Kozlova²

¹ *Lomonosov Moscow State University, Moscow, Russia*

nyrtsovmaxim@gmail.com

² *Moscow State University of Geodesy and Cartography, Moscow, Russia*

n_kozlova@miigaik.ru

³ *Institute of Geography RAS, Moscow, Russia, fleis.maria@yandex.ru*

KEYWORDS:

triaxial ellipsoid, equal-area projections, hypsogram, approximating surface, hypsometric map

ABSTRACT:

For mapping non-spherical celestial bodies, it is advisable to use a triaxial ellipsoid as a mathematical surface. Popular GIS software does not provide the ability to perform calculations on this surface, and developing projections for it is quite complicated. The equal-area cylindrical projection of the triaxial ellipsoid that we previously obtained [1] allows us to calculate the areas of any objects using the created map and compare them with each other.

If a shape model of a celestial body is available, it is possible to calculate geodetic heights relative to a triaxial ellipsoid and display them on a hypsometric map. The technique for calculating heights is presented in [2] and is based on the joint use of the equation of the normal to the surface of a triaxial ellipsoid passing through a given point in space and the equation of the surface itself and solving the resulting sixth degree equation by the Sturm method. A hypsometric map of a celestial body in an equal-area projection allows to calculate the areas of elevation steps and construct a hypsogram that shows the distribution of areas across elevation ranges.

Applying of the equal-area cylindrical projection of the triaxial ellipsoid and the described method for calculating geodetic heights, we constructed hypsograms for Saturn's moon Hyperion, asteroid 433 Eros and Mars' moon Phobos. The parameters of the ellipsoids approximating Phobos and Eros were taken from the report of the International Astronomical Union [3], and shape models from the Planetary Data System [4]. For Phobos, a shape model based on the results of processing by the SRC camera [5] was also used. For Hyperion, due to the chaotic nature of its rotation, there is an ambiguity in the definition of the coordinate system [2, 6]. Therefore, when constructing the hypsogram, we applied the parameters of the approximating ellipsoid and a shape model that we determined [7].

The constructed hypsograms can be used as a tool to assess the correspondence of the approximating ellipsoid to the physical surface of a celestial body. For Hyperion, the best-fit ellipsoid was determined, derived under the condition of minimum deviation from the physical surface, without taking into account the physical parameters of rotation and center of mass, therefore the hypsogram has the form of a normal distribution of heights, with a peak in the center. In the case when the center of mass of the body does not coincide with its geometric center or when there are differences in the direction of the axes of the body and the axes of the reference frame, the histogram will have significant deviations.

Also, the constructed hypsograms can be used to select a scale when creating a hypsometric map of a celestial body. For larger area elevation ranges, a more frequent scale may be recommended.

ACKNOWLEDGMENTS:

The research was carried out according to the State assignments No. 121051400061-9 (M.V. Nyrtsov, A.I. Sokolov), No. 124071100067-9

(A. E. Zubarev, N. A. Kozlova) and FMWS-2024-0009 No. 1023032700199-9 (M. E. Fleis).

REFERENCES:

- [1] *Fleis M. E., Nyrtsov M. V., Sokolov A. I.* Cylindrical projection of triaxial ellipsoid: precise formulae and elliptical integrals // *Geodezia i Kartografia*. 2022. V. 83. No. 4. P. 26–38 (in Russian). DOI: 10.22389/0016-7126-2022-982-4-26-38.
- [2] *Sokolov A. I., Nadezhdina I. E., Nyrtsov M. V., Zubarev A. E., Fleis M. E., Kozlova N. A.* Mapping Hyperion in Projections of the Triaxial Ellipsoid Based on a New Reference Network and a Digital Terrain Model // *Solar System Research*. 2024. V. 58. No. 1. P. 112–121.
- [3] *Archinal B. A., Anton C. H., A'Hearn M. F. et al.* Report of the IAU Working Group on Cartographic Coordinates and Rotational Elements: 2015 // *Celestial Mechanics and Dynamical Astronomy*. 2018. V. 130.
- [4] PDS Asteroid/Dust Archive / Planetary Data System. Small Bodies Node. <https://sbn.psi.edu/pds/archive/asteroids.html>.
- [5] *Nadezhdina I. E., Zubarev A. E.* Formation of a reference coordinate network as a basis for studying the physical parameters of Phobos // *Solar System Research*. 2014. V. 48. No. 1. P. 269–278.
- [6] *Harbison R. A., Thomas P. C., Nicholson P. C.* Rotational modeling of Hyperion // *Celestial Mechanics and Dynamical Astronomy*. 2011. V. 110. No. 1. P. 1–16.
- [7] *Slodarz N. A., Zubarev A. E., Nadezhdina I. E., Kozlova N. A.* Hyperion (C7): control point network and shape model. Difficulties and solutions // 13th Moscow Solar System Symp.: Abstr. Book. 2022. P. 201.

LONG-TERM PRESENCE OF COSMIC MASSES NEAR LIBRATION POINTS

T. V. Salnikova, E. I. Kugushev

Lomonosov Moscow State University, Moscow, Russia
tatiana.salnikova@gmail.com, kugushevi@yandex.ru

KEYWORDS:

unstable equilibrium, Lyapunov systems, localized movement

INTRODUCTION:

We consider a dynamic system whose equilibrium position is non-degenerate and unstable according to Lyapunov. It is shown that for any sufficiently small positive value of the total energy of the system, there is a motion of the system with a given energy value that begins at the boundary of the region where motion is possible and does not leave a small neighborhood of the equilibrium position. We call such movements localized. Application of this new approach to study the behavior of cosmic masses near the libration points of the restricted circular three-body problem allows one to obtain interesting possible types of trajectories.

PROBLEM SETTING:

We discuss a new type of motion—movements localized in the vicinity of an unstable equilibrium position [1]. An essential condition for the presence of such movements is the limitation of system movements along “unstable directions.” For natural systems with gyroscopic and dissipative forces, this is ensured by the conservation or non-increase of the total mechanical energy.

The use of topological methods in the analysis of such motions makes it possible to abandon the conditions of analyticity and non-resonance, which are mandatory for the presence of periodic solutions in Lyapunov systems.

Let us consider the planar restricted circular three-body problem. Two massive bodies (material points) M_1, M_2 , due to mutual gravitational attraction, move in the same plane in circular orbits around their center of mass. The third body of a sufficiently small mass m , which does not influence the movement of massive bodies, moves in their orbital plane. In a non-inertial coordinate system, with the origin at the center of mass of the first two bodies, one of the axes in the orbital plane passes through M_1, M_2 , the second is perpendicular to it in the orbital plane, the third axis is directed along the vector of constant angular velocity. On a rotating orbital plane, mass m , under the influence of attractive forces to M_1 and M_2 and inertial forces, has 5 positions of relative equilibrium-libration points L_1, \dots, L_5 . Two of them — at the vertices of equilateral triangles with bases M_1, M_2 — triangular Lagrange libration points, are points of local maximum for the reduced potential, their degree of instability is equal to two, and according to Kelvin’s theorem, gyroscopic stabilization is possible in the linear approximation.

The collinear libration points L_1, L_2, L_3 belonging to the straight line M_1-M_2 (one point between M_1, M_2 , the other two on opposite sides of the ends of this segment) have a degree of instability of 1, so according to the Kelvin – Chetaev theorem they cannot be stabilized by adding dissipative and gyroscopic forces.

Due to the theoretical results, we have localized trajectories for the planar problem under consideration, as well as for the spatial motion of the third mass. Numerical simulations for specific parameters of the Earth-Moon system illustrate the theoretical conclusions. The presence of many trajectories that are located near libration points for a long time is justified by the following *Lemma*:

“Let us fix the energy level $h > 0$. Then for any arbitrarily large time $T > 0$, near localized motion there is a set of non-zero measure trajectories that do not leave the vicinity of the unstable equilibrium position during time T ”.

CONCLUSION:

The presence of particles remaining for a long time near collinear libration points has been proven under various perturbations, for example, with the addition of non-autonomous gyroscopic forces, dissipative forces, etc. In this case, the conditions of Lyapunov’s theorem on the existence of periodic solutions near a non-degenerate unstable singular point are not satisfied. But localized solutions exist; the corresponding trajectories remain close to them for quite a long time.

The evolution of the system near triangular libration points, the degree of instability of which is even, is studied separately.

The necessary condition on the parameters (masses of the main bodies) for the possibility of gyroscopic stabilization (stability in the linear approximation) is not essential in our proof of the existence of a new type of trajectories — localized in the vicinity of an unstable equilibrium position.

REFERENCES:

- [1] *Kugushev E.I., Salnikova T.V.* Existence of localized motions in the vicinity of an unstable equilibrium position // Proc. Steklov Mathematical Institute. 2024, V. 4.

ON THE PARAMETERS OF NEOS ENCOUNTERS WITH THE EARTH

R. V. Zolotarev, B. M. Shustov

Institute of Astronomy RAS, Moscow, Russia, rv_zolotarev@mail.ru

KEYWORDS:

asteroids, near-Earth objects, asteroid encounters with the Earth

INTRODUCTION:

To build more efficient systems for detecting and monitoring dangerous celestial bodies of natural origin, it is necessary to know the properties of the distribution of such bodies in near-Earth space. In this work, near-Earth space (NES) is defined as the space inside a sphere with a radius of 0.01 au. (which approximately equal to the radius of the Hill sphere) around the Earth. Various objects of natural origin constantly enter the NES. By definition, a near-Earth object (NEO) is an asteroid (NEA) or comet (NEC) with a perihelion distance of less than 1.3 au. The modern understanding of a dangerous body includes objects up to 10 m in size [1]). The purpose of this work is to study the distribution of NEOs with a size of 10 m or larger entering NES, according to the directions of entry and the velocity of approach to the Earth. A similar study was carried out previously in works [2–4] based on the data available at that time. Over the past time, new data has appeared and new requests have appeared.

METHODIC:

To solve the problem, it is necessary to trace the dynamic evolution of the NEOs population over a sufficiently large time interval (~ several dozen characteristic periods of the NEOs), noting all the entries of asteroids into the NES sphere. When using this technique, the task can be divided into two parts: 1) building a model of the population of NEOs with object sizes of 10 m or more; 2) integration of the movement of asteroids with recording of approaches to the Earth.

To build the NEO model, the open source NEOMOD software package [5] was used. The package takes into account the sources of NEOs and generates distributions of NEOs in absolute magnitude H and orbital elements of the asteroids. A population with 1 million objects with $H < 28$ was generated. Taking this into account, subsequent distributions will be given in normalized form (i.e. the expected number of real objects). At the second stage, the movement of a given population of asteroids was integrated, in which approaches to the Earth were monitored. The open code REBOUND [6] was used. The integration technique included MERCURIUS [7] and IAS15 [8] numerical integrators (which are included in the REBOUND standard library). Since the integration step cannot be arbitrarily small, the asteroid was not detected exactly on a sphere with a radius of 0.01 au, but with some delay, i.e. at a smaller distance from the Earth (but not more than 0.0008 a. u. from the border).

RESULTS:

According to the simulation, the number of model asteroids entering the NES over the estimated time interval (110 years) was 9950. From this, an estimate can be made for the average expected frequency of asteroids entering the NES. Since the calculation was carried out for 1 million model NEOs, which is approximately 1/11.5 of the total population of NEOMOD-generated NEO population, the expected number of occurrences in the NES is $(9950/110) 11.5 \approx 1040$ asteroids per year. Naturally, most of these entries are made by small-sized asteroids.

Figure 1 shows the rate of entry of asteroids into the sphere of NES w.r.t. to angle Sun-Earth-asteroid, normalized per unit of solid angle and unit of time. The figure highlights the increased concentration of objects in the direction of the Sun (0° in the figure) and in the opposite direction (180°). If we conditionally highlight the region of angles smaller than 90° (corresponds to the “simple” definition of the daytime sky), then it is easy to see that about

half of the entries into the NES occur from the daytime hemisphere. Note that the obtained distribution is close in shape to that obtained earlier in [3], obtained using the NEOPOP model with a smaller number of asteroids.

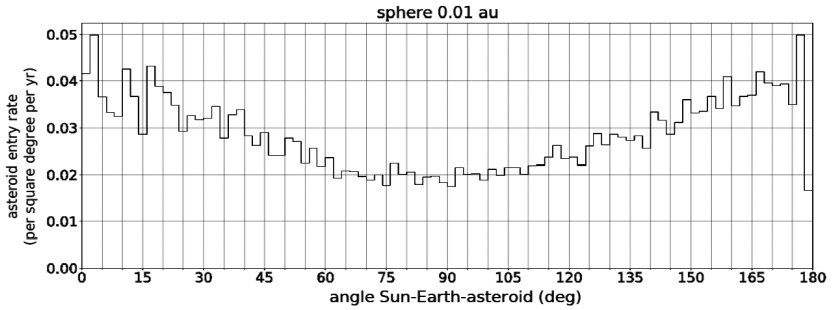


Fig. 1. Distribution of the flux density of asteroids entering the NES, by the angle between the direction to the Sun and the direction to the asteroid. 0° corresponds to the direction to the Sun

If we consider the distribution of the flux of incoming asteroids in all directions a particularly striking feature is the decreased density in the directions corresponding to approximately the Earth's apex. Such a decrease in density is not observed in the opposite direction. In simpler terms, there are significantly more asteroids "catching up" with the Earth than there are asteroids that the Earth "catches up" with. This is due to the structure of the NEA distribution by orbital elements.

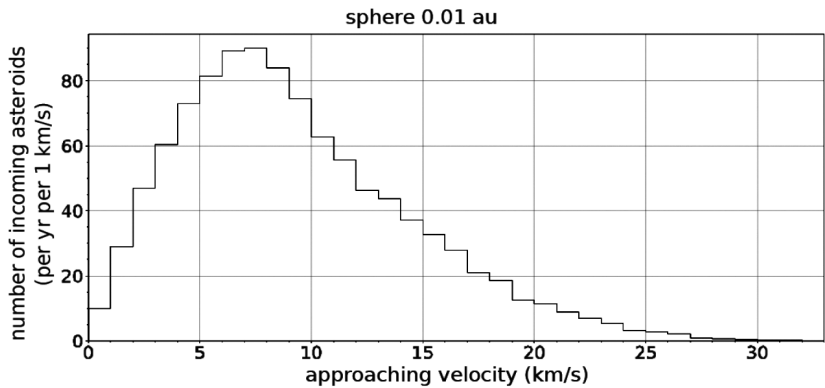


Fig. 2. Distribution of asteroids entering in the NES by the velocity of approach to the Earth

Figure 2 shows the distribution of the velocity of approach, i.e. the rate of change of distance from an asteroid entering the NES to the Earth. The maximum of the distribution is at approximately 7.5 km/s. (the value of the total spatial velocity is obviously higher). Of course, with further approach to the Earth the velocity of approach will increase. A very small proportion of asteroids entering the NES approach the Earth at a velocity of more than 30 km/s. The shape of the distribution and the position of the maximum are in qualitative agreement with the distribution constructed in [9] based on the data available at that time.

SUMMARY:

As a result of the calculations, an estimate was obtained for the frequency of decameter class asteroids entering the NES, which is approximately 1000 entries per year. At the same time, there are on average about four NEOs in the NES at any given time. These are mainly relatively smaller NEAs. It should be noted that the estimate for the number of decameter and larger asteroids in the full NEO population in the NEOMOD program is approximately 11.5 million, which differs significantly from the estimate in

the NEOPOP package, which predicts a population of about 65 million objects. According to NASA data [10], the same estimate gives about 45 million asteroids. Therefore, in order to use quantitative estimates, it is necessary to determine the expected population size and scale the expected number of approaches in accordance with the selected model.

In connection with the issues of asteroid-comet hazard, it is important to note that up to half of the asteroids enter the near-Earth space from the daytime hemisphere and cannot be detected by ground-based and near-Earth optical means.

ACKNOWLEDGEMENTS:

This work is supported by Russian Science Foundation (project 22-12-00115, <https://www.rscf.ru/project/22-12-00115/>).

REFERENCES:

- [1] *Shustov B.M., Shugarov A.S., Naroenkov S.A., Prokhorov M.E.* Astronomical aspects of cosmic threats: new problems and approaches to asteroid-comet hazard following the chelyabinsk event of February 15, 2013 // *Astronomy Reports*. 2015. V. 59. No. 10. P. 983–996.
- [2] *Shustov B.M., Naroenkov S.A., Emel'yanenko V.V., Shugarov A.S.* Astronomical aspects of building a system for detecting and monitoring hazardous space objects // *Solar System Research*. 2013. V. 47. No. 4. P. 288–295.
- [3] *Shustov B.M., Naroenkov S.A., Efremova E.V.* On population of hazardous celestial bodies in the near-Earth space // *Solar System Research*. 2017. V. 51. No. 1. P. 38–43.
- [4] *Vereš P., Jedicke R., Wainscoat R. et al.* Detection of Earth-impacting asteroids with the next generation all-sky surveys // *Icarus*. 2009. V. 203. No. 2. P. 472–485.
- [5] *Nesvorný D., Vokrouhlický D., Shelly F. et al.* NEOMOD 2: An updated model of Near-Earth Objects from a decade of Catalina Sky Survey observations // *Icarus*. 2024. V. 411. Article 115922.
- [6] *Rein H., Liu S.-F.* REBOUND: an open-source multi-purpose N-body code for collisional dynamics // *Astronomy and Astrophysics*. 2012. V. 537. Article A128
- [7] *Rein H., Hernandez D.M., Tamayo, D. et al.* Hybrid symplectic integrators for planetary dynamics // *Monthly Notices of the Royal Astronomical Society*. 2019. V. 485. No. 4. P. 5490–5497.
- [8] *Rein H., Spiegel D.S.* IAS15: a fast, adaptive, high-order integrator for gravitational dynamics, accurate to machine precision over a billion orbits // *Monthly Notices of the Royal Astronomical Society*. 2015. V. 446. No. 2. P. 1424–1437.
- [9] *Naroenkov S.A., Shustov B.M.* Distribution of velocities of potentially hazardous objects // *Cosmic Research*. 2012. V. 50. No. 3. P. 221–225.
- [10] NASA. National preparedness strategy for near-earth object hazards and planetary defense. 2021. <https://www.whitehouse.gov/wp-content/uploads/2023/04/2023-NSTC-National-Preparedness-Strategy-and-Action-Plan-for-Near-Earth-Object-Hazards-and-Planetary-Defense.pdf>.

UNSOLVED PROBLEMS OF GRAVITATIONAL MODELS OF THE ORIGIN OF SATURN'S VISIBLE DENSE RINGS AND HOW J. K. MAXWELL'S DISCOVERY IN 1856 THAT DENSE RINGS ARE NOT SOLID, BUT CONSIST OF SEPARATE CHUNKS OF MATTER, CAN HELP IN THIS

V. V. Tchernyi, S. V. Kapranov

¹ *Modern Science Institute, Science and International Business Research
Moscow, Russia, chernyv@mail.ru*

² *A. O. Kovalevsky Institute of Biology of the Southern Seas RAS
Sevastopoi, Russia, arcanzas@rambler.ru*

KEYWORDS:

origin of Saturn's rings, separation of ice pieces in rings, diamagnetism of ice in space

ABSTRACT:

Scientists of Cassini mission have concluded that there is no gravitational model that convincingly explains the origin of Saturn's visible dense rings. Based on Maxwell's discovery in 1856 that these rings are not continuous, but consist of individual chunks of matter, and Cassini's data on the diamagnetism of ice in these rings, we show that Saturn's magnetism can contribute to the origin and stability of visible dense rings at the planet's equator, composed of separate ice chunks. It confirmed by the data and images of Cassini probe.

How J. C. Maxwell's discovery that the visible dense rings are not continuous may help explain their origin and the fact that they are composed of separate individual ice chunks:

Space of the solar system is not empty; there is gravity and magnetism. They are the main forces of nature in planetary space acting on objects. The origin of Saturn's visible dense rings, consisting of ice chunks, is still in question. Their origin and behavior differ significantly from the well-studied diffuse rings of microparticles.

In fact, gravitational models only explain how ice could have penetrated a protoplanetary cloud of Roche radius in the early Saturn nebula or later, and added icy debris to fill it and further form rings as a result of the tidal disruption of a Titan-sized body passing by Saturn, or from various collisions between two icy bodies [1–6]. Unfortunately, we cannot conclude that all presented gravitational models are completely correct in their title, since they do have only intention, which noted in it. Moreover, in the text of all these articles they do not have description of the physical process itself of the origin of a disk of rings at the Saturn's equator, the formation of a thin structure of rings in their groups and explanation of the equilibrium separation of ice chunks in rings observed by Cassini probe in 2004–2017.

It is necessary to note that without consideration of these processes in the theory of the origin of dense rings, there is no point in discussing their age. This means there is no gravitational model that convincingly explains the origin and observed features of visible dense rings of Saturn [7–10].

In our study, we found that Saturn's magnetism might contribute to the origin and stability of visible dense rings at Saturn's equator and help improve explanation of the observed features such as their thin structure and equilibrium separation of ice chunks in rings.

Cassini found that ice chunks in dense rings consist of 90–95 % water ice [11], and the ratio of deuterium and hydrogen isotopes turned out to be the same as for Earth's ice. Of the 20 types of ice on Earth, ice XI is more

suitable for the dense rings of Saturn [12]. It has stable parameters below 73K and exhibits diamagnetic behavior.

The magnetic field provides the force of diamagnetic expulsion. Then all the ice chunks within Roche limit-size cloud began to have additional force to shift their orbits into the plane of the magnetic equator where their energy have a minimal value. It is process of magnetic anisotropic accretion, associated with influence of Saturn's magnetic field in the protoplanetary cloud on the ice chunks [13]. At the end of the movement, the orbits of all the chunks of ice form a stable disk of visible dense rings at Saturn's equator. Eventually all ice chunks are trapped in a tree-dimensional magnetic well at Saturn's equator.

Cassini discovered that Saturn's magnetic equator almost coincides with the geographical one [14]. In the inner region of the total magnetospheric field of Saturn, where there is a location of visible dense rings predominates the own magnetic field of planet, which looks very stable and in it dominates the dipolar component B_0 [15]. With data of Cassini probe, we have found solution to the problem of the mutual interaction of the gravitational and magnetic fields with diamagnetic ice chunks moving around Saturn in a protoplanetary cloud [16].

The ice chunks of dense rings remain separate; otherwise, they can stick together and form another satellite [17]. The fact that rings along the orbit are not continuous, but consist of separate chunks of matter, was studied and proven by J.C. Maxwell [18]. At that time, there was no evidence that chunks of the rings' matter consist of ice and that ice has diamagnetic behavior. These data obtained by Cassini probe only in 2004–2017 [19].

The Newtonian dynamics of a single chunk of ice are different from the dynamics of chunks of ice collected in rings on Saturn's equator. Ice chunks in the rings repel each other under influence of magnetic force and are attracted each other under the influence of gravity. From the balance of gravitational attraction and magnetic repulsion, we have derived the expression for equilibrium and stable distance between ice chunks in the rings [20, 21]. These results confirmed by the data and images of Cassini probe in 2004–2017.

REFERENCES:

- [1] Safronov V. S. Evolution of the protoplanetary cloud and formation of the Earth and the planets. Jerusalem: Israel Program for Scientific Translation, 1972. 206 p.
- [2] Fridman A. M., Gor'kavyi N. N. Physics of Planetary Rings: Celestial Mechanics of Continuous Media. N.Y.: Springer, 1999. 437 p.
- [3] Charnoz S., Morbidelli A., Dones L. et al. Did Saturn's rings form during the late heavy bombardment? // *Icarus*. 2009. V. 199. Iss. 2. P. 413–4128. DOI: 10.1016/j.icarus.2008.10.019.
- [4] Canup R. M. Origin of Saturn's rings and inner moons by mass removal from a lost Titan-sized satellite // *Nature*. 2010. V. 468. P. 943–946.
- [5] Wisdom J., Dbouk R., Militzer B. et al. Loss of a satellite could explain Saturn's obliquity and young rings // *Science*. 2022. V. 377. No. 6612. P. 1285–1289. DOI: 10.1126/science.abn1.
- [6] Teodoro L. F. A., Kegerreis J. A., Estrada P. R. et al. A recent impact origin of Saturn's rings and mid-sized moons // *Astrophysical J.* 2023. V. 955. No. 2. Article 137.
- [7] Crida A., Charnoz S. Solar System: Recipe for Making Saturn's Rings // *Nature*. 2010. V. 468. P. 903–905. DOI: 10.1038/nature09738.
- [8] Cuzzi J. N., Burns J. A., Charnoz S. et al. An Evolving view of Saturn's dynamic rings // *Science*. 2010. V. 327. No. 5972. P. 1470–1475. DOI: 10.1126/science.1179118.
- [9] Esposito L. W. Composition, structure, dynamics, and evolution of Saturn's rings // *Annual Review of Earth and Planetary Science*. 2010. V. 38(1). P. 383–410. DOI: 10.1146/annurev-earth-040809-152339.
- [10] Crida A., Charnoz S., Hsu H.-W., Dones L. Are Saturn's Rings Actually Young? // *Nature Astronomy*. 2019. V. 3. P. 967–970.
- [11] Poulet F., Cuzzi J. N. The composition of Saturn's rings // *Icarus*. 2002. V. 160. Iss. 2. P. 352–358. DOI: 10.1006/icar.2002.6967.
- [12] Hemley R. J. Effects of high pressure on molecules // *Annual Review of Physical Chemistry*. 2000. V. 51(1). P. 763–800. DOI: 10.1146/annurev.physchem.51.1.763.

- [13] *Tchernyi V. V., Kapranov S. V.* How Saturn could create rings by itself: The third force of diamagnetic expulsion and the mechanism of the magnetic anisotropic accretion of the origin of Saturn's rings // *arXiv.org/abs/2104.03967*. 2021.
- [14] *Dougherty M., Cao H., Khurana K. K. et al.* Saturn's magnetic field revealed by the Cassini grand finale // *Science*. 2018. V. 362. No. 6410. DOI: 10.1126/science.aat5434.
- [15] *Andre N., Blanc M., Maurice S. et al.* Identification of Saturn's magnetospheric regions and associated plasma processes: synopsis of Cassini observations during orbit insertion // *Reviews of Geophysics*. 2008. V. 46. Iss. 4. <https://doi.org/10.1029/2007RG000238>.
- [16] *Tchernyi V. V., Kapranov S. V.* Contribution of Magnetism to the Origin of Saturn's Rings // *The Astrophysical J.* 2020. V. 894. No. 1. Article 62. DOI: 10.3847/1538-4357/ab8475.
- [17] *Tchernyi V. V., Kapranov S. V.* The Role of diamagnetism in the separation of particles and sharp edges of the Saturn's rings // *arXiv.org/abs/2204.03414*. 2022.
- [18] *Maxwell J. C.* On the stability of the motion of Saturn's rings // *Monthly Notices of the Royal Astronomical Society*. 1859. V. 19. P. 297–304.
- [19] *Tchernyi V. V., Kapranov S. V.* To the problem of the properties of Saturn's rings' ice // *Research Notes of AAS*. 2021. V. 5. No. 10. Article 255. DOI:10.3847/2515-5172/ac348c.
- [20] *Tchernyi V. V., Kapranov S. V.* J.C. Maxwell had almost solved the rings origin problem, but in his time, there was no data on particles // *Space Research Today*. Letter to the Editor. April 2024. No. 219. P. 80–85.
- [21] *Tchernyi V. V., Kapranov S. V., Belodedov M. V.* The Repulsion Force Between Ice Bodies in Dense Rings of Saturn, J.C. Maxwell Proposed in 1856 // *Advances in Theoretical and Computational Physics*. 2024. V. 7. No. 3. P. 1–3.

**SESSION 5. SMALL BODIES (SB -PS)
POSTER SESSION**

CONNECTION OF THE APRIL CHI-LIBRIDIS METEOR SHOWER WITH NEAR-EARTH ASTEROIDS

M. V. Sergienko¹, Y. A. Nefedyev¹, A. O. Andreev²

¹ Kazan Federal University, Kazan, Russia, maria_sergienko@mail.ru

² Kazan State Energy University, Kazan, Russia, andreev.alexey93@gmail.com

KEYWORDS:

meteoroids, meteoroid streams, asteroids, small bodies of the Solar system, the orbits evolution

ABSTRACT:

The search for genetic connections between small celestial bodies is important in terms of developing an evolutionary theory and for establishing the distribution of near-Earth meteoroid matter. In near-Earth space there are a large number of meteoroid complexes for which there are no established connections with their parent bodies [1]. Therefore, the question of the origin and the degree of danger to the Earth among the members of this association remains open. A significant proportion of the discovered meteoroid showers are small with low zenith hourly number (ZHR). According to the IAU Meteor Data Center, the April chi-Librids meteor shower is listed as number 140 in the *List of all showers* and there is no information on its parent body. The April chi-Librids meteor shower is a minor one with an unidentified parent body. We have searched for its genetic connections with near-Earth asteroid groups using our own modernized synthetic method [2]. The author's modernized synthetic method is a modification of the one described in [3] by expanding it to a number of criteria. Using the modernized synthetic method for the April chi-Librids meteor shower, an algorithm was created to assign threshold values to each of the criteria proposed in the method. And for the selection of parent bodies associated with the April chi-Librids meteor shower, we applied the author's approach based on the *P* factor which is calculated individually [4]. We used meteoroid orbits from the EDMOND and CAMS television catalogues. As a result of establishing genetic connections between the April chi-Librids meteor shower and the near-Earth asteroids of the Apollo group, the following parent bodies were selected: 2013 YC, 2015 DU180, 2011 BT59, 2013 WM. For the identified parental bodies, the obtained genetic relationships were analyzed using various methods.

ACKNOWLEDGEMENTS:

This work was supported by Russian Science Foundation, grant No. 24-72-10083.

REFERENCES:

- [1] Kokhirova G. I., Babadzhanov P. B. Current Knowledge of Objects Approaching the Earth // *Solar System Research*. 2023. V. 57. Iss. 5. P. 467–485.
- [2] Sergienko M. V., Andreev A. O., Nefedyev Y. A. The modernized synthetic method for searching connections between Near-Earth objects // *LPI Contributions*. 2024. No. 3036. P. 6137.
- [3] Sergienko M. V., Sokolova M. G., Kholshchevnikov K. V. Multifactorial method of search for small bodies in close orbits // *Astronomy Reports*. 2020. V. 64. Iss. 12. P. 1087–1092.
- [4] Sergienko M. V., Sokolova M. G., Andreev A. O., Nefedyev Y. A. Search for possible connections of the h-Virginids meteor shower with near-Earth asteroids // *J. Physics: Conference Series*. 2021. V. 2103. Article 012037.

LOW-FREQUENCY NONLINEAR DUST-ACOUSTIC PERTURBATIONS IN THE DUSTY MAGNETOSPHERE OF SATURN: ZAKHAROV – KUZNETSOV EQUATION DESCRIPTION

D. V. Shokhrin¹, S. I. Kopnin², S. I. Popel²

¹ *National Research University, Higher School of Economics, Moscow, Russia*
shokhrin3@mail.ru

² *Space Research Institute RAS, Moscow, Russia*

KEYWORDS:

dusty plasma, Zakharov – Kuznetsov equation, dust-acoustic solitons, kappa distribution, Saturn's magnetosphere

ABSTRACT:

We present a description of low-frequency nonlinear dust-acoustic waves in the dusty magnetosphere of Saturn, which contains two types of electrons (hot and cold) following the kappa distribution, magnetospheric ions, and charged dust particles [1]. The Zakharov – Kuznetsov equation [2] for the corresponding conditions is derived, describing the nonlinear dynamics of dust-acoustic waves in the case of low frequencies and a pancake-shaped wave packet along the external magnetic field. It is shown that, under the conditions of Saturn's magnetosphere, solutions of the Zakharov – Kuznetsov equation exist in the form of one-dimensional and three-dimensional solitons. Possible observations of such solitons in future space missions are discussed.

REFERENCES:

- [1] *Kopnin S.I., Shokhrin D.V., Popel S.I. // Plasma Phys. Rep., 2024. V. 50. No. 1. P. 55.*
- [2] *Petviashvili V.I., Pokhotelov O.A. Gordon and Breach, Reading. 1992.*

DUST INJECTION INTO THE PLASMA SHEATH NEAR THE SURFACE OF ACTIVE ASTEROIDS

S. Y. Kuznetsov^{1,2}, V. V. Busarev^{2,3}

¹ Lomonosov Moscow State University, Faculty of Space Research
Moscow, Russia, imarpus@gmail.com

² Lomonosov Moscow State University, Sternberg Astronomical Institute
Moscow, Russia, busarev@sai.msu.ru

³ Institute of Astronomy RAS, Moscow, Russia

KEYWORDS:

active asteroids, dust, dynamics, exosphere, surfaces, regolith

INTRODUCTION:

When asteroids pass near perihelion, in the depths of which water ice may be preserved, a thin dust exosphere is formed, consisting of submicron-sized particles. The mechanism for the formation of such a dust exosphere is the sublimation of subsurface deposits of water ice or the consequences of impact events that cause gas flows that lead to the formation of a temporary dust exosphere.

DYNAMICS OF DUST PARTICLES:

The forces acting on dust particles are divided into two types: gravitational [1–3] and non-gravitational. Non-gravitational forces include:

- Vapor pressure on dust particles during sublimation. It sets the initial conditions under which the particle begins to move until the influence of other forces becomes dominant.
- Solar radiation pressure, which is one of the main mechanisms for the removal of particles from the dusty exosphere of asteroids.
- Electrostatic forces [4–6] can pull particles from the surface of the asteroid to a height of up to several meters and allow them to “levitate”.

All of the above forces have a significant effect on the dynamics of dust particles of 0.01–1 μm in size. Thus, under steady-state conditions, the pressure of sunlight quickly removes small dust particles from the vicinity of the asteroid. Thus, the dynamics of the motion can be described by the following DE:

$$\ddot{\vec{r}} = -\frac{GM\vec{r}}{r^3} + \frac{Q_d(t)}{m_p} [E(\vec{r}) + \vec{r} \times B(\vec{r})] + \frac{1}{m_p} F_{\text{SRP}}(\vec{r}),$$

where $Q_d(t)$ is the charge, m_p is the mass of the dust particle, $F_{\text{SRP}}(\vec{r})$ is the solar radiation pressure, and $E(\vec{r})$ and $B(\vec{r})$ are the electric and magnetic fields, respectively.

Although at high altitudes gravity and solar radiation pressure are the main forces influencing the dynamics of dust particles, at the same time near the surface electrostatic forces make a greater contribution. When the asteroid surface interacts with the solar wind, the day side of the asteroid is charged positively due to the predominance of photoelectrons. At the same time, a plasma-dust shell with a thickness of up to several meters [6, 2] is formed above the surface of the asteroid, near the subsolar point. Under such conditions, charged dust tends to migrate to the day side. As follows from 2D modeling [1–3], the greatest potential difference is located near the terminators, where the plasma-dust layer reaches its maximum thickness, as a result of which the electrostatic field can accelerate the movement of small charged particles so much that they leave the gravitational field of the asteroid [5], [6].

CONCLUSION:

The electrostatic field and solar radiation pressure on the illuminated side of an active asteroid can lead to the formation of a thin and relatively stable dust exosphere (with a thickness in the range of 10–10³ m and an optical thickness $t < 0.5$ consisting of particles of a minimum size (0.01–1.0 μm)

in the form of a plasma-dust layer close to the surface provided that the rate of ejection of dust particles into this layer during the sublimation of H_2O ice exceeds the rate of their ejection by the electrostatic field near the terminator.

ACKNOWLEDGMENTS:

This work was supported by the Russian Foundation for Basic Research (grant No. 22-12-00115, <https://www.rscf.ru/project/22-12-00115/>).

REFERENCES:

- [1] *Poppe A. R.* An improved model for interplanetary dust fluxes in the outer Solar System // *Icarus*. 2016. V. 264. P. 369–386.
- [2] *Hartzell C. M.* Dynamics of 2D electrostatic dust levitation at asteroids // *Icarus*. 2019. V. 333. P. 234–242.
- [3] *Yu W., Han D., Wang J. J.* Numerical modeling of dust dynamics around small asteroids // *AIAA SPACE 2016*. <https://arc.aiaa.org/doi/pdf/10.2514/6.2016-5447>.
- [4] *Collier M., Farrell W., Stubbs T.* The lunar dust pendulum // *Advances in Space Research*. 2013. VI. 52. P. 251–261.
- [5] *Nitter T., Havnes O.* Dynamics of dust in a plasma sheath and injection of dust into the plasma sheath above moon and asteroidal surfaces // *Earth Moon and Planets*. 1992. V. 56. No. 1. P. 7–34.
- [6] *Lee P.* Dust levitation on asteroids // *Icarus*. 1996. V. 124. P. 181–194.

THE INFLUENCE OF THE MAGNETIC FIELD ON THE PROCESSES OCCURRING IN THE DUSTY PLASMA OF METEOROID TAILS

T. I. Morozova, S. I. Popel

Space Research Institute RAS, Moscow, Russia, timoroz@yandex.ru

KEYWORDS:

meteoroids, dusty plasmas, meteoroid tail, modulational interaction, electrophonic noises, low-frequency perturbations, magnetic field fluctuations, lower-hybrid waves, Langmuir waves, ion acoustic waves

INTRODUCTION:

Electrophonic noises from meteoroid flight simultaneously with the passage of meteor body as well as arising of magnetic field fluctuations during meteoroid flight are very interesting and mysterious phenomena which still do not have definite explanation. In this work it is explained by the development of modulational interaction of different wave modes.

DISCUSSION:

Modulational instability of different wave modes in meteoroid tails are described. Influence of magnetic field on the processes in meteoroid tail is considered. Passages of meteoroids can lead to a number of observational effects in meteoroid tails, such as electrophonic noises and arising of fluctuations of magnetic fields [1–6]. In particular, this can be the modulation instability of different wave modes.

It is shown that ion acoustic, Langmuir and lower-hybrid waves can propagate in plasma of meteoroid tails [2–4].

Modulation instability of lower hybrid waves with frequencies range in several kHz that can explain the whole range of observed low-frequency noises together with modulational instability of electromagnetic waves associated with the dust acoustic mode, ion acoustic mode and Langmuir waves. The last one can explain arising of electrophonic noises in the wide range of frequencies.

In cases of magneto-modulational instability, magnetic fields can arise, the magnitudes of which are comparable with the observed magnetic fields during experiments with magnetometers, and transverse electromagnetic oscillations can also propagate, which, reaching the Earth's surface, can be perceived as electrophonic noises heard simultaneously with passage of meteoroids. The influence of meteor flares on the parameters of the dusty plasma of meteoroid tails is considered depending on the height of the passage of meteoroids. The characteristic concentrations of dust particles in meteoroid tails during flares with height are estimated. It is shown how the concentration of dust particles increased during flares will affect the magnitude of the instability increments and the conditions for its development.

ACKNOWLEDGMENTS:

The work was supported by Grant of Russian Science Foundation No. 23-72-01066, <https://rscf.ru/project/23-72-01066/>.

REFERENCES:

- [1] *Morozova T.I., Kopnin S.I., Popel S.I.* Modulation interaction in the dusty plasma of meteoroid tails // *Geomagnetism and Aeronomy*. 2021. V. 61. No. 6. P. 794–802.
- [2] *Morozova T.I., Popel S.I.* Ion-Sound Waves during the Interaction of Meteoroid Tails with the Earth's Ionosphere // *Plasma physics reports*. 2024. V. 50. No. 7. P. 829–833.
- [3] *Morozova T.I., Popel S.I.* Lower hybrid waves during the interaction of meteor tails with the Earth's ionosphere // *Plasma Physics Reports*. 2022. V. 48. No. 7. P. 635–638.
- [4] *Morozova T.I., Popel S.I.* Modulation interaction of Langmuir waves and the occurrence of magnetic fields in meteoroid tails // *Plasma Physics Reports*. 2022. V. 48. No. 10. C. 924–928.

- [5] *Zgrablić G., Vinković D., Gradečak S.* Recording of electrophonic sounds from Leonid fireballs // *J. Geophysical Research*. 2002 V. 107. Iss. A7. P. SIA11-1–SIA11-9. <https://doi.org/10.1029/2001JA000310>.
- [6] *Trautner R., Koschny D., Witasse O. et al.* ULF-VLF electric field measurements during the 2001 Leonid storm // *Proc. Asteroids, Comets, Meteors (ACM 2002) Intern. Conf. 2002.* / ed. B. Warmbein. ESA SP-500. 2002. Article 161.

MERCURIAN DUSTY EXOSPHERE: EFFECTS OF ANOMALOUS DISSIPATION

Yu. N. Izvekova, S. I. Popel, A. P. Golub'

Space Research Institute RAS, Moscow, Russia, izvekova@cosmos.ru

KEYWORDS:

dusty plasma, Mercury, exosphere, anomalous dissociation, levitating dust particles

INTRODUCTION:

The anomalous dissipation related to the effect of charging of dust particles that gives rise to new physical phenomena, effects, and mechanisms represents one of the main specific features of dusty plasma that makes it different from conventional plasma containing no charged dust particles. We analyze the process of anomalous dissipation in the context of description of the dynamics of dust particles in dusty plasma of the Mercury's exosphere. An analytical description of oscillations of a dust particle above the surface of Mercury is presented. The frequency of charging of dust particles that characterizes the anomalous dissipation determines the damping of such oscillations. It is demonstrated that the anomalous dissipation is important for substantiation of the model of levitating dust particles that is used for description of dusty plasma above Mercury. The results of numerical simulations that justify the use of the discussed model are presented.

DUST DYNAMICS ABOVE THE SURFACE OF MERCURY:

We use the model that represents the generalization of the self-consistent electrostatic model of dusty plasma near the Moon that was presented in [1] and developed further [2–3] for description of charged-dust behavior above the Mercury's surface. However, an important specificity of Mercury relative to the Moon that has an impact on the properties of the plasma-dust system has to be taken into account, namely, the fact that Mercury has a magnetosphere. Parameters of the solar wind near Mercury are different at the aphelion and perihelion of its orbit. Characteristic magnitude of the magnetic field in the Mercury's magnetosphere is equal to 10^{-3} G [38]. These data allow making an estimate of the Larmor radii of electrons and ions of the solar wind in the Mercury's magnetosphere. We find that for electrons 0.1 and 10 km for ions. This means that the solar-wind particles do not reach the surface of Mercury when dusty plasma is analyzed at the point located not too close to the Mercury's magnetic poles. In this case, the solar wind does not have to be taken into account when calculating parameters of dusty plasma at low altitudes above Mercury.

The anomalous dissipation in dusty plasma is characterized by ν_c — the so-called charging frequency of the dust particles. Equations describing the damped oscillations of a dust particle can be obtained for the situation when the dusty plasma is located above the areas of the Mercury surface illuminated by the Sun that are not too close to its magnetic poles and for the situation when the dusty plasma is located above the surface areas near the magnetic poles. In the process, it should be taken into consideration that the expressions governing frequency are different in these two cases. Damping of the dust-particle oscillations is related to processes of charging of dust particles in both situations. Consequently, the anomalous dissipation in dusty plasma related to processes of charging of dust particles in the case of Mercury can lead to damping of oscillations upon dust-particle motion above the surface of the planet, similar to the case of the Moon.

The numerical calculations have shown that, for the largest ($a > 100$ nm) dust particles that can be lifted above the Mercury's surface due to the electrostatic processes, characteristic damping time of the dust-particle oscillations is much shorter than time $T_M \approx 3 \cdot 10^6$ s that characterizes the duration of the daytime on Mercury. Figure 1 demonstrates that oscillations of a dust particle damping within a time interval much shorter than time $T_{M'}$, i.e., dust particles can be considered levitating during nearly entire time

of their presence above the surface of Mercury. The approximation of levitating particles can thus be used for description of dusty plasma at angle between the local surface normal and the direction to the Sun $\theta = 87^\circ$.

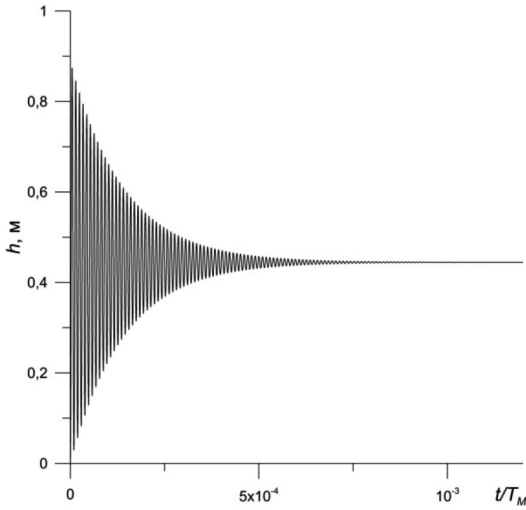


Fig. 1. The time dependence of altitude h of a dust particle with a radius of $a = 0.30 \mu\text{m}$, for the conditions of the perihelion and the area of the Mercury's surface not too close to its magnetic poles at $\theta = 87^\circ$

CONCLUSIONS:

In this study, we analyzed the anomalous dissipation in dusty plasma related to the effect of charging of dust particles in the context of description of their dynamics in the Mercury's exosphere. The equation that describes oscillations of a dust particle above the Mercury's surface the damping of which is determined by the frequency of charging of the dust particles that characterizes the anomalous dissipation was obtained. It is demonstrated that the anomalous dissipation plays an important role for substantiating the applicability of the approximation of levitating particles for description of dusty Mercury's exosphere above the areas of its surface illuminated by the solar radiation. The importance of processes of anomalous dissipation for the case of dusty plasma in the Mercury's exosphere is thus proved. The method presented in this work is useful for analysis of dusty plasma systems near atmosphereless bodies of the Solar system such as the Martian moons comets, etc.

REFERENCES:

- [1] Popel S. I., Kopnin S. I., Golub' A. P., Dol'nikov G. G., Zakharov A. V., Zelenyi L. M., Izvekova Yu. N. Dusty plasma at the surface of the moon // *Sol. Syst. Res.* 2013. V. 47. P. 419–429.
- [2] Popel S. I., Izvekova Yu. N., Golub' A. P. On anomalous dissipation in plasma of dusty Mercury's exosphere // *Plasma Phys. Rep.* 2023. V. 50. No. 2. P. 237–246.
- [3] Izvekova Yu. N., Popel S. I., Golub' A. P. Nonlinear Dust Acoustic Waves in Exosphere of Mercury // *Plasma Phys. Rep.* 2023. V. 49. P. 1214–1219.

WATER FORMATION ON ASTEROIDS AND DUSTY PLASMA SYSTEM ABOVE THE ASTEROID'S SURFACE

A. Yu. Dubinsky, S. I. Popel, Yu. S. Reznichenko

Space Research Institute RAS, Moscow, Russia, dubinsky@cosmos.ru

KEYWORDS:

asteroids, regolith, water, silicon dioxide, silver sulfide, dusty plasmas above the asteroid's surface

ABSTRACT:

The formation of water molecules in asteroid regolith is considered. A possibility of releasing oxygen atoms as parts of silver hydroxide molecules from the crystal lattice of silicon dioxide in regolith has been demonstrated. Silver hydroxide, in turn, can react with hydrogen relatively easily, resulting in the formation of water and silver. This demonstrates the possibility of the formation of water molecules included in the near-surface soil of an asteroid. The proposed mechanism for the formation of water molecules does not require such an unlikely event as two solar wind protons hitting the same point. In the situation under consideration, it is only required that the end of the proton track falls in the region where the elements of the quartz lattice, for example, metal sulfide, are in contact with each other. The presence of water molecules in the soil of an asteroid can affect the photoelectric properties of its regolith and the parameters of the dusty plasma system above the asteroid's surface. A way to identify the nature of the formation of water on an asteroid can be a combination of the method of finding water on asteroids, based on the detection of dust near the surfaces of these space objects, as well as a method using the detection of neutron fluxes passing through areas of the surface of the space body.

ACKNOWLEDGEMENTS:

The study was supported by the Russian Science Foundation grant No. 24-12-00064, <https://rscf.ru/project/24-12-00064/>.

REFERENCES:

- [1] *Busarev V. V., Petrova E. V., Puzin V. B., Barabanov S. I., Shcherbina M. P., Kuznetsov S. Yu.* An Optically Thin and Thick Dust Exosphere of Active Asteroids: Spectral Signs and Possible Formation Mechanisms // *Sol. Syst. Res.* 2024. V. 58. P. 315–325.
- [2] *Mitrofanov I. G., Sanin A. B., Boynton W. V. et al.* Hydrogen Mapping of the Lunar South Pole Using the LRO Neutron Detector Experiment LEND // *Science.* 2010. V. 330, P. 483–486. DOI: 10.1126/science.118569.

SPECTRAL ANALYSIS AND CLASSIFICATION OF NEAR-EARTH AND MARS-CROSSING ASTEROIDS USING GAIA DR3 DATA

M. P. Shcherbina^{1,2}, D. A. Kovaleva¹

¹ *Institute of Astronomy RAS, Moscow, Russia, mpshcherbina@inasan.ru*

² *Lomonosov Moscow State University, Sternberg Astronomical Institute Moscow, Russia*

KEYWORDS:

Gaia Data Release 3, near-Earth asteroids, Mars-crossers, spectral classes, reflectance spectra

THE GAIA SPACE MISSION:

Gaia is a mission of the European Space Agency launched on December 19, 2013. The primary goal is to create a three-dimensional map of the stars in the Milky Way and obtain new data about objects in the Solar System. The spacecraft is equipped with two telescopes and two spectrophotometers — the Blue Photometer (BP) and the Red Photometer (RP), operating in the wavelength ranges of 330–680 nm and 640–1050 nm, respectively. The Data Release 3 (DR3) focuses on Solar System objects, including the reflectance spectra of planetary satellites, Main belt asteroids, near-Earth objects, Mars-crossers, and other groups. The reflectance spectra are calculated by dividing the flux by a solar analog spectrum and normalizing it at a wavelength of 550 nm. The published spectra have been verified for internal consistency and have a signal-to-noise ratio $S/N > 13$. Gaia's reflectance spectra have been compared with data from ground-based telescopes and other space missions, showing good agreement for bright objects. For each Solar System object, a reflectance spectrum is calculated at 16 points representing integral reflectance values [1].

NEAR-EARTH ASTEROIDS AND MARS-CROSSERS:

This study analyzes Gaia data for near-Earth asteroids and Mars-crossers. Near-Earth asteroids (NEAs) are divided into the Atens, Apollos, and Amors groups based on their orbital parameters. These asteroids are of interest due to their proximity to Earth and potential collision threats. Mars-crossers are asteroids whose orbits intersect Mars's orbit, allowing the study of dynamic processes and the migration of small bodies in the Solar System.

EVALUATION OF ASTEROID SPECTRAL GROUPS:

This work logically continues the study by [2], which focused solely on near-Earth asteroids, and includes observations of these objects obtained using instruments from the Terskol Observatory (a branch of INASAN). An assessment of the spectral class membership was conducted for 731 Mars-crossers in addition to the 109 asteroids mentioned in the previous study.

To briefly recall the methodology described in detail in the work of [2]:

1. Data on asteroids were collected, including spectral class assessment according to any classification (Tholen or SMASS II), geometric albedo, rotation period, diameter, and orbital data necessary for further analysis. The data were taken from the NASA database (<https://ssd.jpl.nasa.gov/horizons/>).
2. Each spectrum was passed through a constructed "spectrophotometric corridor," the construction of which is described in the work of [2] and references therein.
3. After this, class membership was assessed. In cases of ambiguity, asteroids could be assigned multiple classes, especially when characteristic absorption bands were not clearly defined.
4. Narrow spectral classes and subclasses were combined into broader spectral groups to avoid assigning asteroids to multiple similar classes. The C-group includes classes B, C, Cb, Cg, Ch, Cgh, and correlates with classes B and F in the Tholen taxonomy. The S-group consists of classes

S, A, Q, R, K, L, and intermediate classes Sa, Sq, Sr, Sk, Sl. The X-group includes classes X, M, E, P according to the Tholen classification, and intermediate classes Xe, Xc, Xk. Minor groups are rare classes Ld, T, D, V, O. Some asteroids may show signs of both high-temperature and low-temperature classes (S and C); such objects were classified as mixed groups.

Among the 731 reflectance spectra of Mars-crossers, 92 asteroids could not be definitively assigned to any class, and thus were excluded from further consideration. For 556, a spectral class assessment was made for the first time (based on the absence of class data in the NASA database). The number of Mars-crossers assigned to each of the listed spectral groups, as well as the distribution of near-Earth asteroids from the work of [2], is shown in Table 1.

Table 1. Distribution of Spectral Groups of Near-Earth Asteroids and Mars-Crossers Based on GDR3 Data with Supplementary Spectrophotometric Observations from the Terskol Observatory [2]

Asteroids	Total Number	C-group	S-group	X-group	Minor group	Mixed
Mars-crossers	639	154	359	25	27	74
Atens	7	3	1	1	1	1
Apollos	57	12	36	1	3	5
Amors	43	8	28	0	6	1
Total number	746	177	424	27	37	81

DISTRIBUTION OF ASTEROIDS BY SPECTRAL GROUPS:

The determination of the spectral group membership of near-Earth asteroids (NEA) and Mars-crossers is presented in Figure 1. The percentage of major spectral groups is quite similar: about 60% of the objects belong to the S-group, and 20–25% to the C-group. However, among Mars-crossers, a higher number of objects exhibit signs of mixed mineralogy, possibly due to more active collisional evolution.

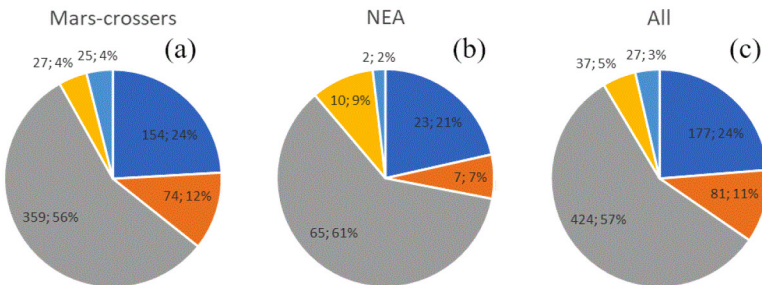


Fig. 1. Distribution by spectral groups: (a) Mars-crossers; (b) near-Earth asteroids; (c) complete sample from Gaia DR3 + observations of some near-Earth asteroids at the Terskol Observatory

Approximately the same distribution is maintained for asteroids of different sizes. Of course, the diameter values of Mars-crossers and NEAs are determined only for a small number (311 asteroids, including 234 Mars-crossers and 77 NEAs). It should also be noted that diameter data may be inaccurate due to difficulties in determining this parameter.

The results coincide with those of a similar study by [3], which also examined reflectance spectra of NEAs and Mars-crossers in a sample of about 1,000 objects obtained using ground-based observation tools: about 60% of the population are S-type asteroids, 20% are C-type, and the remaining classes make up 20%. Note that the overlap of the object samples of our study and the study from [3] is less than 20%.

Analysis of the distribution of asteroids of various spectral groups according to the values of semi-major axis and perihelion distance of orbits shows that C-type asteroids cover almost the entire range of semi-major axis val-

ues. At the same time, S-type asteroids are predominantly concentrated closer to the inner edge of the Main Belt, which is related to their high-temperature mineralogy.

It is noteworthy that despite the numerical predominance of the S-group, primitive-type asteroids (C-group) are also found at small perihelion distances. The presence of such asteroids in this zone may explain the observed sublimation activity of primitive asteroids. This phenomenon is confirmed by the correlation of their activity with the passage of the perihelion zone, as noted in several studies, such as the work of [4].

ACKNOWLEDGMENTS:

M. P. Shcherbina acknowledges a support from the grant Russian Science Foundation No. 22-12-00115, <https://www.rscf.ru/project/22-12-00115/>.

REFERENCES:

- [1] Gaia Collaboration. Gaia Data Release 3-Summary of the content and survey properties // *Astron. and Astrophys.* 2023. V. 674. Article A1. 22 p.
- [2] *Shcherbina M. P., Kovaleva D. A., Shustov B. M.* Gaia Data Release 3: Distribution of Spectral Groups of Near-Earth Asteroids // *Solar System Research.* 2024. V. 58. P. 359–366.
- [3] *Binzel R. P. et al.* Compositional distributions and evolutionary processes for the near-Earth object population: Results from the MIT-Hawaii near Earth object spectroscopic survey (MITHNEOS) // *Icarus.* 2019. V. 324. P. 41–76.
- [4] *Busarev V. V. et al.* Search for signs of sublimation-driven dust activity of primitive-type asteroids near perihelion // *Sol. Syst. Res.* 2023. V. 57. No. 5. P. 449–466.

NEW MAP OF EUROPA: UPDATE FROM JUNO MISSION DATA

**V. P. Khlestunova, N. A. Kozlova, N. A. Slodarch, A. A. Kokhanov,
V. A. Nerusin, I. E. Nadezhdina**

*Moscow State University of Geodesy and Cartography, MIIGAiK
Extraterrestrial Laboratory, Moscow, Russia*

KEYWORDS:

Europa, Juno, planetary cartography, geology, Jupiter satellites, Galilean satellite

INTRODUCTION:

In September 2022, the Juno spacecraft, while exploring the Jupiter system, performed a flyby PJ45 (Perijove 45) and transmitted to the Earth 4 images of the surface of Europa, each of 43 fragments. These data formed the basis of a new small-scale geological mapping of Europa by Erin et al. [1] and allowed us to improve the photomosaic of Europa. In this study, we have combined these two latest cartographic products and created a thematic map of the second Galilean satellite. The map summarizes the latest data on Europa, is intended for a wide range of users, and continues the series of planetary maps created at MExLab MIIGAiK Laboratory based on the results of the Juno mission [2].

DATA AND METHODS:

Our new Europa mosaic consists of 345 images: 301 Galileo images (with a resolution from 8 m/pixel to 2 km/pixel), 28 Voyager images (2–20 km/pixel), and 4 Juno images.

Image orthorectification was performed in SpaceMosaic software on the basis of the DEM obtained from the points of the new control points network [3].

The mapping was performed in ArcGIS software. The geological structures are shown according to the geological map [1]. The names of relief features are given in accordance with the Gazetteer of Planetary Nomenclature [4] and translated into Russian. The cartographic grid and coordinates of the objects are presented in the planetographic coordinate system with the longitude positive count to the West, as accepted by IAU.

The map is designed to summarize archive and new data on Europe and to make it available to a wide range of users. The map is compiled in the Lambert equal-area transverse azimuthal projection at a scale of 1:12 000 000. The polar regions up to 60° latitude are given in the Lambert equal-area normal azimuthal projection and at a scale of 1:24 000 000. The new created orthomosaic of Europe became the cartographic base for the map, on which geological structures were overlaid from the geologic map (when displaying them on our map, the corresponding colors were used with a slight correction to improve readability and the possibility of joint analysis with previous cartographic works). Feature names of surface objects are given in accordance with the Gazetteer of Planetary Nomenclature and in Russian. As supplementary materials, the map presents several large-scale insets of Europe regions with their digital elevation models (DEMs) [5] and a brief description text.

RESULTS:

As a result, we present a new mosaic of Europa together with a new map of the hemispheres. These products and their analysis are of great importance for understanding the satellite structures and processes that form Jupiter's satellites. The use of images obtained by Juno allows us not only to complement previous studies but also to compare their results.

ACKNOWLEDGMENTS:

The research was carried out according to the State assignment No. 124071100067-9 (FSFS-2024-0001).

REFERENCES:

- [1] *Erin J. Leonard D. Patthoff A., Senske D. A.* Global Geologic Map of Europa. U.S. Geological Survey. 2024.
- [2] *Melnikova M. A., Nerusin V. A., Zubarev A. E. et al.* New Global Mosaic of Ganymede. Detailed DEMs and Maps. 2022.
- [3] *Zubarev A. E., Nadezhdina I. E., Brusnikin E. S. et al.* A technique for processing of planetary images with heterogeneous characteristics for estimating geodetic parameters of celestial bodies with the example of Ganymede // *Solar System Research*. 2016. V. 50. No. 5. P. 352–360.
- [4] *Gazetteer of Planetary Nomenclature*. <https://planetarynames.wr.usgs.gov/Page/EUROPA/target>.
- [5] *Becker H. N., Lunine J. I., Schenk P. M. et al.* A complex region of Europa's surface with hints of recent activity revealed by Juno's Stellar Reference Unit. // *J. Geophysical Research: Planets*. 2023. V. 128. Article e2023JE008105. <https://doi.org/10.1029/2023JE008105>.

ASTROMETRIC REMEASUREMENT OF PULKOVO PHOTOGRAPHIC OBSERVATIONS OF THE 433 EROS TAKEN FROM 1900 TO 1940

M. Yu. Khovrichev, D. A. Bikulova, N. V. Narizhnaya, T. A. Vasilyeva
Pulkovo Observatory RAS, Saint Petersburg, Russia, gmymax@gmail.com

KEYWORDS:

near-Earth asteroids, 433 Eros, Yarkovsky effect

INTRODUCTION:

The (433) Eros is one of the most well-explored asteroids. A significant sample of high-quality data is available for this object from old photographic measurements of the end of the XIX century to modern space-based and radar data. One of the interesting aspects of the investigation of the (433) Eros is the attempts to determine A_2 acceleration which is usually explained by the Yarkovsky effect. Various authors provide different A_2 estimates (see [1, 2]) and discuss the nature of A_2 of this asteroid due to the high obliquity of its rotational axis (about 89°). The (433) Eros is a relatively big asteroid ($34.4 \times 11.2 \times 11.2$ km). Hence, this body couldn't reach a significant Yarkovsky drift value even with suitable rotational axis orientation. Therefore, the use of old astrometric measurements should lead to a certain clarity in this discussion. However, investigators ([1],[2]) note the poor quality of old photographic measurements (the astrometric error is about several arcsec). This enhances the importance of digitizing the corresponding photographic plates and re-measuring the positions in the Gaia system. We performed this work for the old astronegatives captured at the Pulkovo Observatory and present the results in this paper.

OBSERVATIONS, SCANNING, AND DATA REDUCTION:

Brief description of the photographic plates used

Photographic observations of the (433) Eros were performed at Pulkovo Observatory with the Normal astrograph (hereafter PNA; $D = 0.33$ m, $F = 3.463$ m). Photographic plates of 16×16 cm in size were used. Hence, the effective field of view (FOV) $2 \times 2^\circ$. The corresponding angular scale is 59.56 arcsec/mm.

Digitization details:

All measurements were performed with the Mobile Digitizing Device (MDD, [3]). This system allows us to scan a 12×12 cm area of each photographic plate. An opportunity to analyze all target images in one FOV of the camera is an advantage of the MDD. Relatively low resolution (MDD scale for the PNA plates is 1.07 arcsec/pix⁻¹) limits the astrometric quality. The field distortion pattern parameters of the MDD lens was determined by comparing scans of the same plate taken with the MDD and NAROO machine (Paris Observatory, [4]). The typical positional error of the MDD calibration is about $1 \mu\text{m}$ (about 0.04 arcsec).

Fitting the (433) Eros images:

The parameters of the stellar image point spread function (PSF) were established for each scan by utilizing well-saturated Gaia stars. Only background level, flux, and x, y position of the photocenter are calculated for stellar-like sources by the Levenberg-Marquardt procedure. All shape parameters were the same for all stellar images. This approach was suitable for the (433) Eros images taken using short exposures (1–4 min). In certain instances, particularly during early observations, an hour-long exposure was captured.

Hence, the trail-like asteroid images were on the scans. The natural way to fit such an image is the convolution of the stellar PSF by linear segment. Figure 1 demonstrates source image from the scan and the fitting quality.

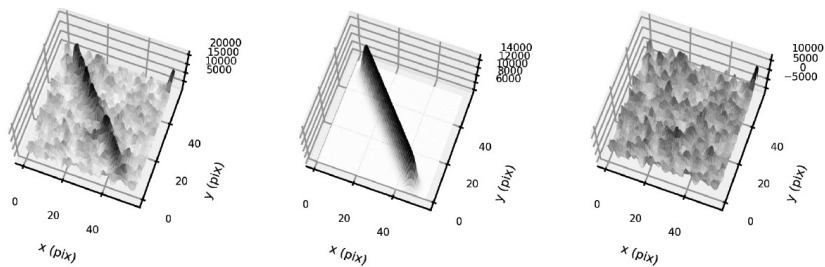


Fig. 1. The illustration of the asteroid trail fitting. The left plot is a source image from the scan (plate B031, 1900, Aug, 22). The model trail constructed using PSF convolution is in the center. The right graph is the result of 'source-model' subtraction

RESULTS:

Astrometric calibration includes two stages. The first of them was NAROO-based distortion correction. The second stage is an astrometric reduction by linear model to calculate the (433) Eros positions in the Gaia DR3 system. Comparison with the NASA Horizons ephemerides was performed. Typical O–C values are within the 0.2–0.4 arcsec range in both coordinates. The asteroid's positional errors from the fitting and astrometric calibration procedures are about 0.1–0.2 arcsec. Figure 2 demonstrates a significant advantage of our measurements compared to the same epoch MPC data.

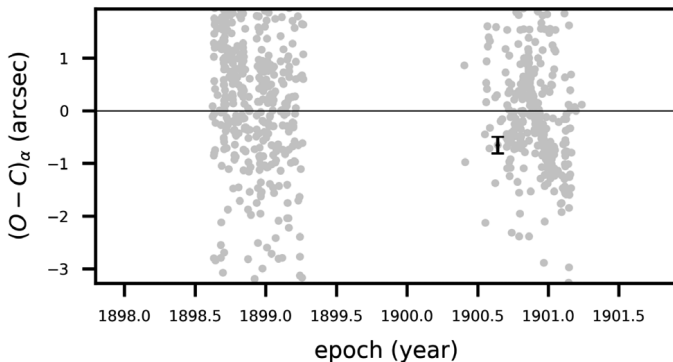


Fig. 2. The values of (O–C) in RA for (433) Eros for the 1898–1901 epoch range are based on NASA Horizons ephemerides and MPC-data (in gray). The black dot with the error bar is the result extracted from one of the Pulkovo plates

CONCLUSIONS:

We present a remeasurement of old photographic plates, providing important raw data for dynamical studies of the Amor group asteroid (433) Eros. We reprocessed 17 astronegatives (1–3 exposures per plate) taken with the Normal astrograph of the Pulkovo Observatory between 1900 and 1940 to obtain the positions of the (433) Eros in the Gaia DR3 system. Photographic plates were digitized with the Pulkovo Mobile Digitizing Device. The convolution of the linear segment was performed with the stellar PSF to construct the model of the asteroid trail. In total, 28 positions have been determined with an accuracy of 0.1 to 0.2 arcsec.

ACKNOWLEDGMENTS:

The study was funded by a grant Russian Science Foundation 23-22-00306 'The synergy of perturbances between the rotational and orbital motions of the asteroids approaching planets', <https://rscf.ru/en/project/23-22-00306/>.

REFERENCES:

- [1] *Del Vigna A., Faggioli L., Milani A. et al.* Detecting the Yarkovsky effect among near-Earth asteroids from astrometric data // *Astronomy and Astrophysics*. 2018. V. 617. Article A61.
- [2] *Dziadura K., Oszkiewicz D., Spoto F. et al.* The Yarkovsky effect and bulk density of near-Earth asteroids from Gaia DR3 // *Astronomy and Astrophysics*. 2023. V. 680. Article A77.

- [3] *Khovritchev M. Y., Robert V., Narizhnaya N. V. et al.* Astrometric measurement and reduction of Pulkovo photographic observations of the main Saturnian satellites from 1972 to 2007 in the Gaia reference frame // *Astronomy and Astrophysics*. 2021. V. 645. Article A76.
- [4] *Robert V. et al.* The NAROO digitization center. Overview and scientific program // *Astronomy and Astrophysics*. 2021. V. 652. Article A3.

VERIFICATION OF THE ASSOCIATION BETWEEN THE 2002 GJ8, 2016 NO16 ASTEROIDS AND THE AUGUST DRACONIDS (AUD)

M. Yu. Khovrichev, S. R. Pavlov, A. L. Tolstoy, D. A. Bikulova

Institute of Applied Astronomy RAS, Saint Petersburg, gmymax@gmail.com

KEYWORDS:

Near-Earth asteroids, meteor shower parent body, discrimination criteria of orbit similarity, August Draconids, 2002 GJ8 and 2016 NO16

INTRODUCTION:

Currently, there is clear evidence linking near-Earth asteroids (NEAs) to certain meteor showers. For example, one of the well-known meteor showers, Quadrantids, is caused by the meteoroid particles ejected from the NEA 2003 EH1. Another case is the Taurid Complex asteroids associated with several meteor showers [1].

Confirmation of the meteor shower parent-body status for known NEA adds new details to the Solar system dust complex formation scenario and understanding of the NEA population properties. It inspires astronomers to conduct investigations to compare the orbits of Near-Earth Asteroids (NEAs) with the orbits of meteor streams. Commonly, investigators refer to the nominal orbits of meteor streams in the IAU database. It allows researchers to find possible links based on analysis of all available asteroid orbits. The paper [2] follows the mentioned way and states that 2002 GJ8 and 2016 NO16 are likely parent bodies for the August Draconids meteor shower. Our investigation aimed to check this conclusion using the Global Meteor Network database [3] which represents the present-day quality of the worldwide meteor observation network.

DATA ANALYSIS AND ITS RESULTS:

The best way to confirm the connection between an asteroid and a meteor shower is by comparing their orbits using a suitable similarity criterion. The required meteor data is available from the GMN database [3]. This network (<https://globalmeteornetwork.org/>) provides worldwide monitoring of meteor events using small cameras. The survey is limited by the brightness (up to 2 mag) but gives the values of the meteoroid orbital parameters thanks to thousands of baseline meteor detections. These orbital elements of the meteoroids and their mass estimates can be accessed through the Python code by request to the GMN database.

The combination of the orbit similarity criteria:

Various criteria can be used to compare the orbits of the Solar system bodies and draw conclusions about their similarity. Using a combination of these parameters is a good approach for our purpose. The performed analysis allowed us to find meteoroid orbits that satisfy criteria introduced by Southworth and Hawkins (D_{SH}), Drummond (D_H), and Kholshchevnikov (D_{KH}). The threshold values are $D_{SH} = 0.21$, $D_H = 0.21$, and $D_{KH} = 0.28$. Additionally, we only considered orbits with relatively good-quality parameter estimations ($\sigma_a < 0.1$ a.u., $\sigma_e < 0.2$, $\sigma_i < 5^\circ$, $\sigma_\Omega < 5^\circ$, $\sigma_\omega < 5^\circ$).

The results:

We have analyzed the current GMN database, which contains about 1.4 million records covering approximately 6 years of observations. In this analysis, we identified 1107 AUD meteors associated with 2016 NO16 and 679 AUD meteors associated with 2002 GJ8. The August Draconids (AUD) is a weak meteor shower with a ZHR of about 3 at maximum. As a result, the number of detections is quite expected. However, it is important to note that this result cannot be considered as final confirmation that both asteroids are the parent bodies of this meteor shower.

Additional information for more precise conclusions can be obtained by analyzing the asteroid's physical parameters. Indeed, significant meteoroid ejection from the asteroid surface is expected for the rubble pile asteroids that typically have low albedo values. The 2002 GJ8 has a diameter of about 1 km with an albedo value of 0.018 ± 0.01 [4]. Such an uncertainty remains a possibility for the wide interpretation range. Another possible reason for the meteoroid trail formation by the 2002 GJ8 is that its orbit is similar to the Jupiter family comet. Physical data for the 2016 NO16 is unavailable yet.

CONCLUSIONS:

The GMN database was analyzed to examine the association between two near-Earth asteroids, 2002 GJ8 and 2016 NO16, and the August Draconids (AUD) meteor shower. A total of 1786 records of the GMN database were classified as meteoroid orbits, possibly linked with the mentioned asteroids using the combination of two discrimination criteria and Kholshchevnikov's metric (679 and 1107 records correspondingly). This supports these asteroids' AUD parent body status, but final confirmation is still required. The AUD radiant likely has a complex structure due to being a blend of two closely located meteoroid streams.

ACKNOWLEDGMENTS:

The study was funded by a grant Russian Science Foundation 24-22-20044 "Investigation of a low-mass fraction of meteoroid streams associated with the near-Earth asteroids", <https://rscf.ru/en/project/24-22-20044/>.

REFERENCES:

- [1] Babadzhanov P.B. Search for meteor showers associated with Near-Earth Asteroids. I. Taurid Complex // *Astronomy and Astrophysics*. 2001. V. 373. P. 329–335.
- [2] Dumitru B.A., Birlan M., Popescu M., Nedelcu D.A. Association between meteor showers and asteroids using multivariate criteria // *Astronomy and Astrophysics*. 2017. V. 607. Article A5.
- [3] Vida D. et al. The Global Meteor Network — Methodology and first results // *Monthly Notices of the Royal Astronomical Society*. 2021. V. 506. P. 5046–5074.
- [4] Trilling D.E. et al. NEOSurvey 1: Initial Results from the Warm Spitzer Exploration Science Survey of Near-Earth Object Properties // *The Astronomical Journal*. 2016. V. 152. Iss. 6. Article 172.

DETERMINATION OF THE SMALL METEOR PARTICLES PROPERTIES FROM OBSERVATIONAL DATA

V. Efremov¹, O. Popova¹, D. Glazachev¹, A. Kartashova²

¹ *Sadovsky Institute of Geosphere Dynamics RAS, Moscow, Russia*
efremov.vv@phystech.edu

² *Institute of Astronomy RAS, Moscow, Russia*

KEYWORDS:

meteors, meteoroids, ablation, Perseid shower

INTRODUCTION:

Meteoroids hold the information about the structure and composition of matter in the initial stages of the development of the Solar system. Large part of meteor particles do not reach the Earth's surface, and their properties should be determined indirectly based on observational data. The energy deposition due to interaction of the meteor particle with the Earth's atmosphere determines the light and ionization, which are observed by different techniques. The energy deposition depends on ablation rate and deceleration of the meteor particle. The ablation and deceleration are determined by the particle size and density, as well as the angle and speed of entry into the atmosphere. To determine the properties of the meteor particles different models should be applied to observational data.

DESCRIPTION OF THE MODEL:

Light curves are usually reproduced with the help of two most common ablation models. The first model assumes that the entire incoming energy flux is consumed for ablation. The second model suggests that the incoming energy is expended on heating, radiation and ablation of the meteor. The mass loss itself is determined by the saturated vapor pressure. Parameters that determine the rate of mass losses include ablation heat and dependence for saturated vapor pressure. Both models include a number of coefficients, which also affect the obtained results.

DISCUSSION:

The work used double-station observations of the 2016 Perseid shower. One of the used ablation models is applicable to small meteoroids, so meteors weaker than -2m were selected. Light of a number of meteor events were reproduced using two ablation models. Corresponding meteor particles parameters were determined. The presentation will discuss used models, their results and uncertainty, and factors, which affect obtained results.

ACKNOWLEDGMENTS:

V. Efremov, O. Popova, D. Glazachev were funded by the program "Development of an complex model of the entering cosmic objects action on the internal and external geospheres and assessment of the consequences of these impacts" (No. 1021052706222-8-1.5.4). We thank J. Oberst, A. Margolis for their SPOSH observations.

STREAMS AND ASSOCIATIONS OF METEORIODS ACCORDING TO THE RESULTS OF RADAR OBSERVATIONS IN HISAO FOR JANUARY 1970

M. Narziev, F. H. Khujanazarov

*Institute of Astrophysics of National Academy of Science of Tajikistan
Dushanbe, Tajikistan, mirhusseyn_narzi@mail.ru*

KEYWORDS:

meteor shower, meteor association, orbital similarity criterion, meteoroid, radiant, orbital elements, mass, density

ABSTRACT:

Based on the measured data of radiant's, velocities and orbital elements of 2743 meteors, using the direction-finding-time radio method in HisAO from January 1 to January 16, 1970 and from January 18 to January 31, 1970, meteoroids were identified as meteor streams and associations. The identification of meteor streams and associations was carried out in three stages: a) graphically; b) by speed and c) application of the Southward-Hawkins and Jopek criteria. As a result, out of 279 clusters of radiant's identified by the graphical method, 154 groups were actually obtained, which were identified with meteor streams and associations. For all streams and associations of meteoroids, are provided the data (of) on the coordinates of radiant's, velocities, orbital elements, as well as the average mass and density of meteoroids. The average masses of meteoroids of streams and associations are in the range $4.4 \cdot 10^{-4}$ – $1.7 \cdot 10^{-1}$ g, and densities in the range 0.3 – 6.4 g/cm³.

ASTEROID (4) VESTA: SPECTROPHOTOMETRIC PRESUPPOSITIONS OF THE PRESENCE OF A LARGE CRATER 20 YEARS BEFORE ITS DISCOVERY BY THE DAWN SPACECRAFT

V. D. Vdovichenko, V. G. Tejfel, G. A. Kharitonova

Fesenkov Astrophysical Institute, Almaty, Kazakhstan, vdv1942@mail.ru

KEYWORDS:

asteroid, Vesta, photometry, spectrophotometry, pyroxene

INTRODUCTION:

The main motivation for the preparation of this retrospective report was an interesting and extensive article published recently [1]. It examines in detail on 30 pages the possibility of the composition of the soil on the surface of asteroid (4) Vesta, consisting of carbonaceous chondrites. Moreover, the authors of the article come to a well-founded negative result. It is not entirely clear why such a task arose, since at least 40 years ago and later the presence of pyroxene on Vesta was established, and throughout the entire surface of the asteroid. The latter was confirmed by our spectral observations in 1988–1989. The most interesting thing is that these observations gave rise to the assumption of the presence of a large impact crater on Vesta, which formed a deeper layer with an increased pyroxene content. At the time, these results went unnoticed. But 20 years later, in 2011, the Dawn spacecraft actually discovered a huge crater on Vesta. Therefore, we considered it advisable to return to the past and describe in a more generalized form the ongoing research of the asteroid Vesta in Kazakhstan within the framework of the all-Union solar system research programs.

The first attempts at spectral observations of Vesta were made in 1956 with the help of the Bredikhinsky astrograph with a 13-degree objective prism, brought to Alma-Ata from the Pulkovo Observatory by G. A. Tikhov in 1941. A number of Vesta spectrograms were obtained with this instrument [2]. Moreover, signs of changes in the reflection spectrum during the rotation of the asteroid were noted. But these studies were not continued. But in 1986, at the observatory of the Astrophysical Institute, a cycle of electrophotometric observations of Vesta was performed on the 0.6-meter Zeiss-600 telescope [3], which clarified the question of the magnitude of the asteroid's rotation period. Even more valuable were the carefully thought-out spectrophotometric observations with a three-channel spectrometer on the 0.7-m AZT-8 telescope in 1986–1988 with the special task of studying variations in the pyroxene absorption band in the near infrared with a center of 920 nm during the rotation of the asteroid [4–7].

However, at the time, the results published by us, despite their originality and relevance, did not attract due attention and went practically unnoticed.

The boldest assumption at that time was made (by V. D. Vdovichenko and F. P. Velichko [4–7]) about the mineralogical composition of the asteroid's surface and the existence of a large impact crater on one of the asteroid's poles on Vesta. The observed increased pyroxene concentration in some part of the asteroid could be a result of the exposure of deeper soil as a result of such an impact.

More than twenty years later, the validity of such an assumption was actually confirmed by the discovery of a large crater formation on Vesta, found on asteroid images obtained from the Dawn spacecraft that reached Vesta in 2011.

PHOTOMETRY OF THE ASTEROID VESTA — 1986:

With only sporadic observations, some uncertainty remained: is the actual rotation period 5 h and 20 min, or can it be twice as long, for example, due to the almost symmetrical shape of the asteroid. Therefore, during the Ves-

ta-86 All-Union program, we organized electrophotometric observations of the asteroid with the longest possible duration of consecutive measurements from September 2 to September 8, 1986. All seven consecutive nights were favorable for observations using an electrophotometer with recording on a recorder. In parallel with the measurements of the asteroid's brightness, the brightness of two stars was measured, and it was not necessary to change the signal amplification ranges. At the same time, one measurement cycle of all three objects took no more than 5–6 minutes, and the full observation interval per night ranged from 4.5 to 5.3 hours.

During the observation period, the asteroid's phase angle and geocentric distance to it varied from 14.9 to 12.5° and from 1.530 to 1.495 astronomical units, respectively. The observed light curves of Vesta were corrected for these changes, found by the time variation of the maxima and minima of its brightness obtained in each observation cycle.

The reduced values of the relative brightness of Vesta were distributed according to their belonging to either an even or an odd 5-hour cycle of brightness fluctuations. Figure 1 shows the averaged brightness curves of Vesta for even and odd cycles.

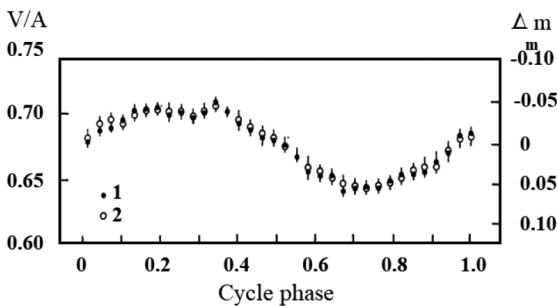


Fig. 1. The curve of the change in the brightness of the asteroid Vesta during its rotation: 1 — even period, 2 — odd period [3]

It can be seen that both curves practically coincide both in amplitude and in general appearance and, importantly, in some characteristic details (small depressions at rotation phases 0.28 and 0.90).

To further confirm the complete similarity of both curves, calculations were performed with an estimate of the quantiles of the Student's distribution, which confirmed the convergence even with the parameter 0.95.

Thus, it can be assumed that the true rotation period of Vesta is actually 5.342 hours, and not twice as long.

VESTA SPECTROPHOTOMETRY:

The Vesta spectrum has a pronounced first absorption band of pyroxene centered at 920 nm. However, the observations carried out to investigate changes in the intensity and profile of this band during the rotation of the asteroid were practically absent. Such observations make it possible to trace the distribution of a substance containing pyroxene over the surface of Vesta. In addition, they can serve as an independent method for determining the rotation period of this asteroid.

To this end, we conducted observations of the asteroid Vesta on the 70 cm AZT-8 reflector of the Astrophysical Institute using a spectrometer that allows for one-time registration of the object's brightness in two widely spaced sections of the spectrum. During 7 nights in September – October 1986, detailed photometric studies of changes in the brightness of the asteroid Vesta in the continuous spectrum ($\lambda = 550$ nm) and in the absorption band of pyroxene centered at $\lambda 920$ nm were carried out. [4]

For the first time, we reliably recorded intensity variations in the core of the first pyroxene absorption band on the Vesta surface. However, these results have not yet explained the reasons for the observed changes. In general, there may be several such reasons.

The detected variations in the center of the first pyroxene band, the amplitude of which is $0^m.06 \pm 0^m.01$, may be due to the following factors:

- change in the depth of the pyroxene absorption band ($\lambda_{\text{eff}} = 920 \text{ nm}$);
- changing the slope of the continuous spectrum in the wavelength range of 550–1250 nm;
- variations in the absorption band profile due to the superposition of bands of other absorbing components (for example, olivine with $\lambda_{\text{eff}} = 1010 \text{ nm}$);
- a shift in the position of the band due to a change in the composition of the bands that define it.

If the variations in the depth of the absorption band during the rotation of Vesta are mainly related to the pyroxene content on the surface of the asteroid, then, as our data show, in the region corresponding to the maximum of the light curve, the content of this mineral is greater than in the minimum region at the light curve. The influence of the degree of maturity or fragmentation of the pyroxene-containing substance on the surface of the asteroid is also possible.

The correlated composite light curves we have identified in the continuous spectrum and in the core of the pyroxene band for all observation dates within the measurement accuracy are consistent with each other and with the previously indicated period of Vesta 5 h.342.

INVESTIGATION OF THE PROFILE OF THE FIRST PYROXENE BAND AT VESTA:

In the course of searching for an answer to the question of the causes of the intensity variations we observed in the core of the first pyroxene absorption band on the surface of Vesta, we conducted additional observations of the asteroid, but now in terms of studying the profile of the first pyroxene band itself.

The observations covered the core of the band, its wings, as well as the adjacent area of the continuous spectrum. Figure 2 shows variations in the profile of the first pyroxene absorption band in the Vesta spectrum and brightness variations in the center of the pyroxene absorption band for three dates.

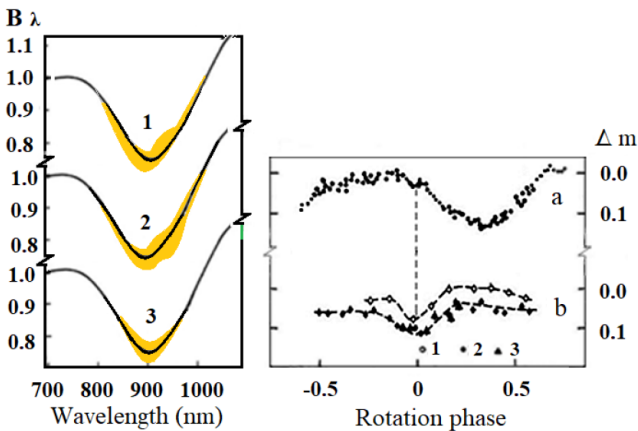


Fig. 2. On the left — Variations of the profile of the first pyroxene absorption band in the Vesta spectrum. In stellar magnitudes, the light curve of the asteroid Vesta at $\lambda 650 \text{ nm}$, obtained on February 8, 1988, is shown on the upper right. In the lower right, variations of the center of the pyroxene absorption band for three dates

Attention is drawn to the discrepancy between the moment of the minimum in the pyroxene absorption band and the moments of the extremes of the light curve in the visual region of the spectrum. Measurements over three dates show that the band reaches its maximum depth approximately 1 h (≈ 0.2 rotation phases) after the maximum of the asteroid's light curve, remaining fairly symmetrical relative to its extremum. This indicates that

some spectrometrically recorded detail on the surface of the asteroid has at least large-scale geometric symmetry. In this case, the band turns out to be the least deep in the area of the minimum of the light curve. In this aspect, the position on the observed part of the surface of Vesta is such that it manifests itself no more than during 0.4 full rotation of the asteroid around its axis. The absence of a noticeable “plateau” in the minima of the curve in Fig. 2b allows us to determine the lower limit of the part of the Vesta surface occupied by the “spot”.

According to our estimates, it turns out that the marked area (“pyroxene albedo spot”) is localized in the southern hemisphere of an asteroid having an almost spherical or slightly elongated shape, and covers at least 20–30° in longitude and latitude. The upper limit of the size of the “spot” can reach up to 40° in diameter [5].

Based on the results obtained, Vdovichenko and Velichko it was suggested that on one “hemisphere” it is quite possible that there is a large, relatively young impact formation in the form of a large crater, providing the maximum brightness of the asteroid in the visual area and the corresponding maximum depth of the pyroxene absorption band [4–7].

The analysis of the individual spectra obtained by us at different phases of Vesta rotation reveals a tendency to shift the center of the first band to the long-wavelength region of the spectrum with an increase in the depth of the absorption band. If we take as a basis laboratory data on the composition of pyroxenes [8], according to which the wavelength of the absorption band center depends on the relative calcium content in the mineral, then the effect we have identified can be considered as evidence that the supposed “pyroxene spot” on the surface of the asteroid may have a higher calcium content. This may, most likely, mean that the rocks in this area are more represented by eucrite, which are more rich in iron and calcium than diogenite — silicate rocks with a higher magnesium content.

These were the results of our studies [2–7] of the asteroid Vesta in 1986–1988, which were appropriately confirmed in the subsequent space mission to explore Vesta using the Dawn spacecraft in 2011–2012 [9, 10].

INFORMATION ABOUT VESTA BASED ON THE RESULTS OF THE DAWN SPACE MISSION:

NASA’s Dawn space probe, the first space mission to Vesta, was launched on September 27, 2007.

The probe approached the asteroid in August 2011 and was in orbit around the asteroid for one year.

He transmitted a complete image of the asteroid Vesta, which is a cold, rocky, cratered world.

The most noticeable detail is a huge crater about 500 km across, occupying the entire South Pole and named after Rheasilvia, who was the mother of Romulus and Remus.

Spectrometric analysis shows that the crater exposed several layers of Vesta’s crust and partially its mantle.

The visible and infrared mapping spectrometer has detected a type of mineral known as diogenite, characteristic of the lower region of the Vesta crust. The upper part of the crust, however, has more eucritic material. Diogenites are silicate rocks with a higher magnesium content than eucrites, which are more rich in iron and calcium. The differences in minerals between the north and south indicate that in the deep layers of the crust of the southern Rheasilvia region, diogenite material rich in pyroxene prevails, while the equatorial region seems to preserve the most ancient mineralogy rich in calcite [9,10].

CONCLUSION:

Thus, the results of our scientific research turned out to be in the wake of rapidly unfolding space programs to explore the bodies of the Solar system. Many of the predictions, results and conclusions of our research have been appropriately confirmed in subsequent space missions.

ACKNOWLEDGMENT:

The work is carried out within the framework of the Project No. BR20280974 “Program of fundamental astrophysical research in Kazakhstan: observations and theory”, financed by the Ministry of Education and Science of the Republic of Kazakhstan.

REFERENCES:

- [1] *Massa G., Palomba E., Longobardo A. et al.* Ciarniello Search for carbonaceous chondrites evidence on Vesta through the detection of carbonates // *Icarus*. 2024. V. 409. Article 115870.
- [2] *Teifel V.G.* Spectrophotometry of minor planets (4) Vesta and (15) Eunomia // *Proc. Astrotechnics Sector of the Academy of Sciences of the Kazakh SSR*. 1960. V. 8. P. 171–175.
- [3] *Aksenov A. N., Egorov Yu. A., Teifel' V. G., Kharitonova G. A.* The rotation period of the asteroid 4 Vesta // *Pis'ma Astron. Zh.* 1987. V. 13(7). P. 616–620.
- [4] *Vdovichenko V.D., Velichko F.P. et al.* Asteroid 4 Vesta. Photometry in the visual range of the spectrum and the absorption band // *Astronomicheskiy Vestnik (Moscow, USSR)*. 1988. V. 22. No. 2. P. 147–152.
- [5] *Vdovichenko V.D., Velichko F.P. et al.* Variations of the profile of the first absorption band of piroxene in the Vesta spectrum: Circular of the Shamakhi Astrophysical Observatory. Baku: ELM, 1989. No. 87. P. 28–29.
- [6] *Vdovichenko V.D., Velichko F.P. et al.* Asteroid 4 Vesta. Absorption variations in the Piroxene band are 0.92 microns // *Kinematics and Physics of celestial bodies*. 1990. V. 6. No. 2. P. 70–76.
- [7] *Vdovichenko V.D., Velichko F.P. et al.* Asteroid 4 Vesta: the relationship between variations in brightness V and absorption in the 0.92 μm pyroxene band. AC No. 1543. P. 29–30.
- [8] *Adams J.B.* Visible and near-infrared diffuse reflectance spectra of pyroxenes // *J. Geophys. Res.* 1974. V. 79(32). P. 4829–4836.
- [9] *De Sanctis M. C., Ammannito E., Capria M. T. et al.* Vesta's mineralogical composition as revealed by the visible and infrared spectrometer on Dawn // *Meteoritics and Planetary Science*. 2013. V. 48. Iss. 11. P. 2166–2184. <https://onlinelibrary.wiley.com/doi/10.1111/maps.12138>.
- [10] *Yingst R. A., Mest S. C., Garry B. W. et al.* A Geologic Map of Vesta Produced Using a Hybrid Method for Incorporating Spectroscopic and Morphologic Data // *The Planetary Science J.* 2023. V. 4. No. 9. <https://iopscience.iop.org/article/10.3847/PSJ/acebe9/pdf>.

A MODEL OF GIANT PLANETS SATELLITES MASS DISTRIBUTIONS OVER THE SEMI-MAJOR AXES OF THE ORBITS

N. I. Perov^{1,2}, A. I. Smirnov²

¹ Cultural and Education Organization named after Valentina V. Tereshkova
Yaroslavl, Russia, perov@yarplaneta.ru

² Yaroslavl State Pedagogical University named after K. D. Ushinsky
Yaroslavl, Russia

KEYWORDS:

Solar system, planets, satellites, mass, orbits, distributions, statistical criterion, example of the Neptunian system

INTRODUCTION:

There are about 300 satellites near the planets of the Solar system (<https://nssdc.gsfc.nasa.gov/planetary/factsheet/neptuniansatfact.htm>). Their origin is one of the cosmogonic problems of the system [1]. Below we draw attention to some patterns in the satellite systems of the giant planets, using the example of the Neptune system (Table 1), (Figure 1).

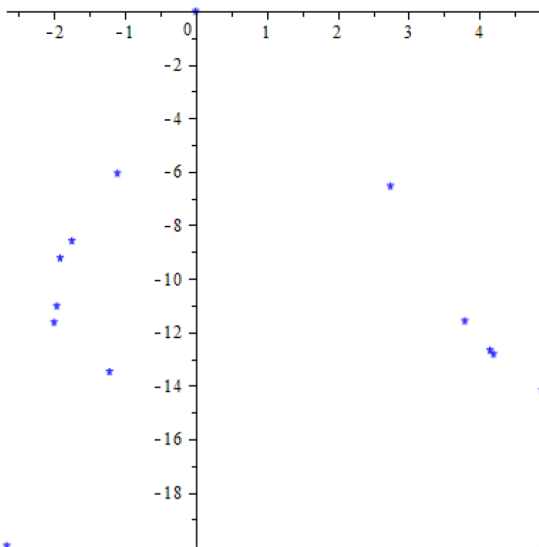


Fig. 1. Mass of the Neptunian satellites depended upon the semi-major axes of the orbits. Observations. Natural logarithms of the ratios of the satellites' mass and Triton and the ratios of the semi-major axes of the orbits of the satellites and Triton are used. The lower extreme points correspond to the mass of hypothetical kilometer-size satellites near Neptune and near the sphere of action of Neptune in respect of the Sun

Table 1. Neptunian system

Satellite	Mass, kg	Semi-major axis, km
Naiad	$1.9 \cdot 10^{17}$	48 227
Thalassa	$3.5 \cdot 10^{17}$	50 074
Despina	$2.1 \cdot 10^{18}$	52 526
Galatea	$4 \cdot 10^{18}$	61 953
Larissa	$4.9 \cdot 10^{18}$	73 548
Hippocamp	$3 \cdot 10^{16}$	105 300
Proteus	$5 \cdot 10^{19}$	117 646
Triton	$2.14 \cdot 10^{22}$	354 800

Satellite	Mass, kg	Semi-major axis, km
Nereid	$3.1 \cdot 10^{19}$	5 513 400
Halimede	$2 \cdot 10^{17}$	15 728 000
Sao	$6.7 \cdot 10^{16}$	22 422 000
S/2002 N5	–	23 400 000
Laomedeia	$5.8 \cdot 10^{16}$	23 571 000
Psamathe	$1.5 \cdot 10^{16}$	46 695 000
Neso	$1.7 \cdot 10^{17}$	48 387 000
S/2021	–	50 760 000

MODEL “MASS – SEMI-MAJOR AXIS OF THE SATELLITE ORBIT”:

Let’s consider the following model of mass (M) of the Neptunian satellites depended upon the semi-major axes (a) of their orbits. (Mass M measured in mass of Triton, the semi-major axes a of the orbits measured in semi-major axis of Triton).

$$M = A(a - a_{\min})^{B_1} (a_{\max} - a)^{B_2} \left(\exp\left(C(a - a_{\min})^{D_1} (a_{\max} - a)^{D_2}\right) - 1 \right)^E \quad (1)$$

Here, $A = 2.85747197 \cdot 10^{15}$; $B_1 = 4.96535946$; $B_2 = 6.03057457$;
 $C = 1000.29176078$; $D_1 = -1.95660769$; $D_2 = -0.25435013$;
 $E = 0.00999998247$; $a_{\min} = 0.069785794$; $a_{\max} = 242.710518668$;
 $M_{\min \text{ hyp}} = 2.08246564 \cdot 10^{-9}$.

Extrema meanings of parameters in the formula (1) are equal to

$$M_{\max} = M(1.05977406595646608058240) = 1.01967090098113200860501.$$

$$M_{\min 1} = M(0.06978579478739334788414) = 0.$$

$$M_{\min 2} = M(109.422396021551962184034) = 3.41963496441844086945 \cdot 10^{-8}.$$

The points of flexures are equal to

$$M_{f_1} = M(0.764874053595360224149165) = 0.472005392976947560455984.$$

$$M_{f_5} = M(1.35265947908686252667394) = 0.774434654362412856771645 \text{ (Figure 2).}$$

FISHER CRITERION (F) FOR THE STATISTICS (1):

$$f_1 = 7; f_2 = 13. F = 1.214888 \cdot 10^5. F_{0.01;7;13} = 4.44. F > F_{0.01;7;13} = 4.44 \text{ [3].}$$

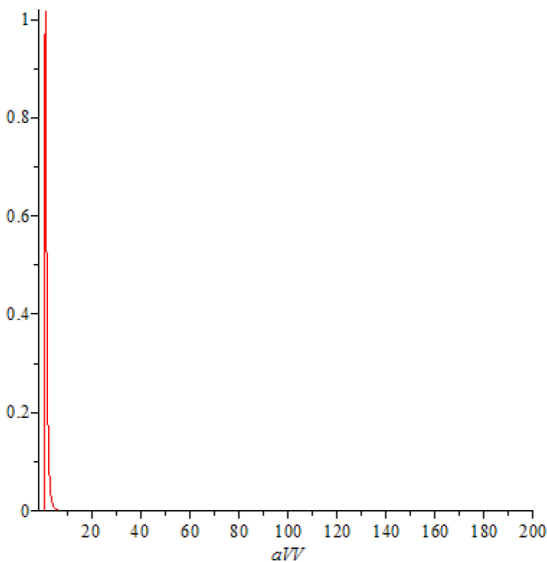


Fig. 2. Mass (measured in mass of Triton) of the Neptunian satellites depended upon the semi-major axes of the Neptunian satellites orbits (measured in semi-major axis of Triton)

CONCLUSION:

According to the Fisher criterion [2], statistics (1) are significant at the level of 0.01. In the future, it is supposed to find the dependencies "the mass of the satellite and the semi-major axis of its orbit" for other giant planets and use these dependencies to localize the satellites of exoplanets.

REFERENCES:

- [1] *Murray C. D., Dermott S. F.* Solar System Dynamics. Cambridge University Press, 2009. 558 p.
- [2] *Abramovitz M., Stegun I. A.* Handbook of Mathematical Functions with Formulas, Graphs and Mathematical Tables. NBSAM. Series-55.1964.

ON THE EVOLUTION OF INITIAL CIRCULAR ORBITS OF COMETS WITH VARIABLE MASS

N. I. Perov^{1,2}, A. S. Nikolaeva²

¹ Cultural and Educational Center named after Valentina V. Tereshkova
Yaroslavl, Russia, perov@yarplaneta.ru

² Yaroslavl State Pedagogical University named after K. D. Ushinsky
Yaroslavl, Russia

KEYWORDS:

Sun, comet, variable mass, gravitation, solutions of differential equations in closed forms

INTRODUCTION:

As it is known, comets are the most interesting objects from the point of view of constructing analytical theories of their motion and the most difficult for celestial mechanics [1–5]. Below an analytical method for studying the evolution of the orbit of a celestial body (comet) with a variable mass is presented.

FUNDAMENTAL EQUATION:

Let us consider the Meshchersky–Levi–Civita equation for isotropic radiation or absorption with zero velocity of matter by a comet moving in a certain medium. In accordance with works [2] and [3] we have the vector differential equation (1) of the particle m .

$$\frac{d(m\mathbf{v})}{dt} = -\frac{GMm\mathbf{r}}{r^3}. \quad (1)$$

Here, $m(t)$ is the mass of the comet depending on time t , M is the mass of the Sun, G is the gravitational constant, \mathbf{r} is the heliocentric radius-vector of the comet, \mathbf{v} is the velocity of the comet relative to the Sun. Equation (1) has an integral of motion (angular momentum L is conserved) (2)

$$[\mathbf{r}, m\mathbf{v}] = \mathbf{L}. \quad (2)$$

Let's assume that the mass of the comet (m) changes according to the law

$$\frac{dm}{dt} = Dr^n. \quad (3)$$

With a small decrease ($D < 0$) or increase ($D > 0$) in the mass of the comet in one revolution around the Sun, we represent the increment of the orbital period T of the comet as

$$\Delta t = \frac{3\pi}{(GM)^{1/2}} a^{1/2} \Delta a. \quad (4)$$

For the dependence of the mass m of the comet on the major semi-axis of the circular orbit of the comet, taking into account the relations (3) and (4), we obtain the expression.

$$m = m_0 + \frac{3\pi D}{(GM)^{1/2}(n+3/2)} (a^{n+3/2} - a_0^{n+3/2}), \quad (5)$$

where m_0 is the initial mass of the comet. From the condition

$$\dot{\mathbf{r}} \cdot \dot{\mathbf{r}} = GM \left(\frac{2}{r} - \frac{1}{a(t)} \right), \quad (6)$$

taking into account equations (1) and (6), we make an equation for determining $da(t)/dt$

$$v^2 \frac{1}{m} \frac{dm}{dt} = -\frac{da/dt}{2a^2} GM. \quad (7)$$

When moving to the polar angle φ , using the relation (2) for weakly perturbed circular orbits, we find

$$\frac{da}{dt} = \frac{da}{d\varphi} \cdot \frac{d\varphi}{dt} = \frac{da}{d\varphi} \cdot \frac{L}{ma^2} = \frac{da}{d\varphi} \cdot \frac{m_0(GMa_0)^{1/2}}{ma^2}. \quad (8)$$

Substituting relations (3) and (8) into equation (7), after separating the variables φ and a with subsequent integration, we come to an expression for a , in which expression (5) for the mass m of the comet is not explicitly used.

$$a = \frac{a_0}{\left[(n+2) \frac{2D}{m_0} \sqrt{\frac{1}{GM}} \cdot a_0^{n+3/2} \phi + 1 \right]^{1/(n+2)}} \tag{9}$$

If in the expression (9) $n = -2$, then to determine a we use the ratio limit $(1/(bx + 1))^{1/x} = e^{-b}$ for $x = 0$.

EXAMPLES:

As an example, consider the evolution of the initially circular orbit of a comet with the following known data: $m_0 = 2.2 \cdot 10^{14}$ kg, $r_0 = 100$ AU, $v_0 = 2983.663303$ m/c, $D = \pm 18600$ kg/c (for the comet of Galley for the heliocentric distance of 1 AU), $n = -2.1$ — to eliminate the division by "0" in the formula (9), $G = 6.674 \cdot 10^{-11}$ m³/(kg·s²), $M = 2 \cdot 10^{30}$ kg. The following units of length — L_u , time — T_u and mass — M_u were used in the calculations: $L_u = 150 \cdot 10^9$ m, $T_u = 5.028388096 \cdot 10^6$ s, $M_u = 2 \cdot 10^{30}$ kg. When we using these units of measurement of astronomical quantities, the gravitational constant $G = 1$. The results of numerical experiments at $300 \leq \varphi \leq 3000$ rad are presented in the Figures 1–4.

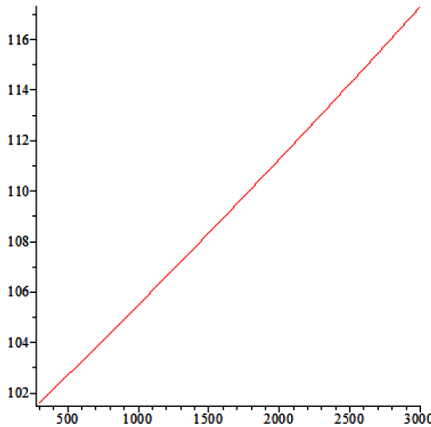


Fig. 1. $D < 0$. The removal of the comet from the Sun. The major semi-axis a (AU) of the circular orbit of the comet is increasing with increasing of the polar angle φ (rad)

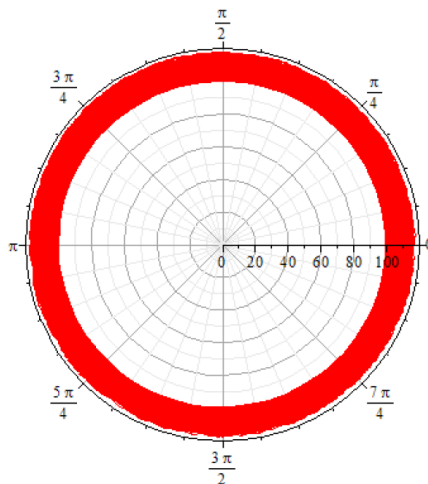


Fig. 2. $D < 0$. The removal of a comet from the Sun. The major semi-axis a (AU) of the circular orbit of the comet is increasing with increasing of the polar angle φ (rad)

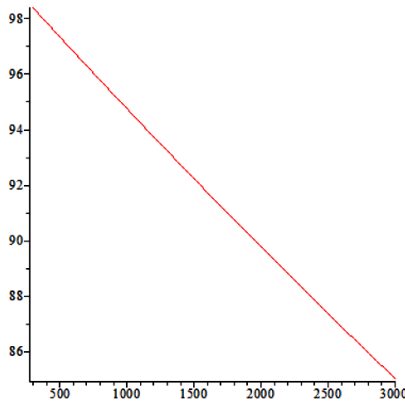


Fig. 3. $D > 0$. The approach of the comet and the Sun. The major semi-axis a (AU) of the circular orbit of the comet is decreasing with increasing of the polar angle φ (rad)

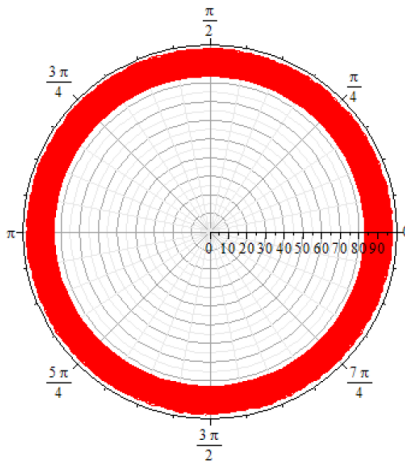


Fig. 4. $D > 0$. The approach of the comet and the Sun. The major semi-axis a (AU) of the circular orbit of the comet is decreasing with increasing of the polar angle φ (rad)

REFERENCES:

- [1] *Jeans J. H.* Astronomy and cosmogony. Cambridge: Univ. Press, 1929.
- [2] *Meschersky I. V.* Work on the Mechanics of Bodies of Variable Mass. Moscow; Leningrad; Gos. Isd. Techn. Teor. Lit., 1949 (in Russian).
- [3] *Omarov T. B.* Dynamics of gravitating systems of metagalaxies. Alma-Ata: Nauka, 1973.
- [4] *Kuryshv V. I., Perov N. I.* Equations of motion of binary systems with variable masses // Astron. Zhurnal. 1981. T. 58. P. 886–887 (in Russian).
- [5] *Luk'yanov L. G.* Conservative two-body problem with variable masses // Astronomical Letters. 2005. V. 31(8). P. 563–568.

SESSION 6. EXTRASOLAR PLANETS (EP) ORAL SESSION

MIGRATION OF PLANETESIMALS IN THE TRAPPIST-1 AND GLISSE 581 EXOPLANETARY SYSTEMS

S.I. Ipatov

*Vernadsky Institute of Geochemistry and Analytical Chemistry RAS
Moscow, Russia, siipatov@hotmail.com*

KEYWORDS:

motion of planetesimals, probabilities of collisions, exoplanets, TRAPPIST-1, Glisse 581

INTRODUCTION AND CONSIDERED MODEL:

Earlier I studied migration of planetesimals in our solar system [1–3] and in the Proxima Centauri exoplanetary system [4–6]. The aim of the calculations presented below was to study the mixing of planetesimals at the late stages of accumulation of planets in the TRAPPIST-1 and Glisse 581 system. For all planets, I made the estimates of the fraction of planetesimals that were initially located close to the orbit of one of the planets and then collided with each planet. The TRAPPIST-1 system consists of a star with a mass equal to 0.0898 solar masses and seven planets located relatively close to each other (see Table 1). Initially it was considered that the extrasolar system Glisse 581 contains the star with a mass equal to 0.307 of the solar mass and five planets (*b*, *c*, *d*, *e*, and *g*). Now it is supposed that there are only three planets (*b*, *c*, *e*) located closer to the star. The existence of planet *g* remained controversial. Masses and semi-major axes and eccentricities of orbits of the exoplanets are presented in Table 2. These values were different for calculations with 3 and 5 planets. In my calculations with 5 planets, eccentricities and inclinations of orbits of planets were considered to be equal to 0. The number N_0 of initial planetesimals in each calculation variant equaled to 250 or 1000. The semi-major axes of their orbits were near the semi-major axis of one of the planets and were between a_{\min} and a_{\max} . The values of a_{\min} and a_{\max} are presented in Tables 1 and 2. Initial eccentricities of orbits of planetesimals were equal to 0.02 or 0.15. Their initial inclinations equaled to $e_0/2$ rad. Greater eccentricities could be caused by the previous mutual gravitational influence of planetesimals. I studied the evolution of the orbits of planetesimals under the gravitational influence of the star and the planets. Planetesimals that collided with planets or the star or reached 50 AU from the star were excluded from integration. The symplectic code from the SWIFT integration package [7] was used for integration of the motion equations. The considered time integration step t_s equaled to 0.01, 0.02, 0.04, or 0.1 days. The results of calculations with different t_s were compared and mainly gave similar results. In each variant, the calculations were made for the same disk and for fixed values of e_0 and t_s .

Table 1. Orbital elements, masses m (in Earth masses m_E) of exoplanets in the TRAPPIST-1 system, and the values of a_{\min} and a_{\max} for the considered disks near planets *b*, *c*, *d*, *e*, *f*, *g*, *h*

	m/m_E	a , AU	e	a_{\min} , AU	a_{\max} , AU
<i>b</i>	1.37	0.0115	0.0062	0.0094	0.0137
<i>c</i>	1.31	0.0158	0.0065	0.0137	0.0190
<i>d</i>	0.39	0.0223	0.0084	0.0190	0.0258
<i>e</i>	0.69	0.0292	0.0051	0.0258	0.0339
<i>f</i>	1.04	0.0385	0.0101	0.0339	0.0427
<i>g</i>	1.32	0.0468	0.0021	0.0427	0.0544
<i>h</i>	0.33	0.0619	0.0057	0.0544	0.0694

Table 2. Semi-major axes a and eccentricities e of orbits and masses m (in Earth masses m_E) of exoplanets in Gliese 581 and values a_{\min} and a_{\max} for considered disks of planetesimals near planets b, c, d, e , and g

disk	m/m_E	a, AU	e	$a_{\min}' \text{AU}$	$a_{\max}' \text{AU}$
e	1.7; 1.657	0.02815; 0.029	0.0; 0.125	0.022	0.0344
b	15.8; 15.2	0.0406; 0.041	0.0; 0.022	0.0344	0.0563
c	5.5; 5.65	0.0721; 0.074	0.0; 0.087	0.0563	0.1
g	2.2	0.13	0.0	0.1	0.174
d	6.98	0.218	0.0	0.174	0.25

PROBABILITIES OF COLLISIONS OF PLANETESIMALS WITH PLANETS IN THE TRAPPIST-1 EXOPLANETARY SYSTEM:

The results of calculations showed that, as the Earth and Venus, several planets in the TRAPPIST-1 exoplanetary system accumulated planetesimals initially located at the same distance. Some calculations with $N_0 = 250$ were discussed in [8]. Below I present the results for $N_0 = 1000$ and $t_s = 0.01$ or $t_s = 0.02$. Most of collisions of planetesimals with planets took place in less than 10 Kyr. For disks b-g more than a half of collisions were during the first 1 Kyr. However, last collisions of planetesimals with planets could be after a few million years. There were no collisions of planetesimals with the host star. Not more than 3% of planetesimals were ejected into hyperbolic orbits. The fraction of planetesimals collided with the 'host' planet (compared to collisions with all planets) typically decreased with the considered time interval. For disks c-h, the fraction f_1 of planetesimals that collided with the host planet was between 0.37 and 0.63 at $e_0 = 0.02$ and between 0.27 and 0.53 at $e_0 = 0.15$. The second and third values (f_2 and f_3) of the fraction of planetesimals that collided with a neighbouring planet were in the ranges 0.17–0.28 and 0.11–0.17 at $e_0 = 0.02$ and were 0.2–0.32 and 0.08–0.19 at $e_0 = 0.15$. For disk b and $e_0 = 0.02$, f_1 was 0.78–0.8, f_2 was 0.18–0.2, and f_3 was 0.01–0.012 (the range is for calculations with a step t_s equaled to 0.01 and 0.02). For disk b and $e_0 = 0.15$, f_1 was 0.74, f_2 was 0.22–0.23, and f_3 was 0.015–0.021. The fraction of collisions of planetesimals with the 'host' planet was usually smaller for disks located farther from the star. In each variant, including the migration from outside of the disk h, collisions were with all planets. Therefore, the outer layers of neighboring planets in the TRAPPIST-1 system can include similar material if there were many planetesimals near their orbits at the late stages of planetary formation.

PROBABILITIES OF COLLISIONS OF PLANETESIMALS WITH PLANETS IN THE GLISSE 581 EXOPLANETARY SYSTEM:

Some calculations for the Gliese 581 system with $N_0 = 250$ for 5 planets and 10 Myr were discussed in [9]. Later such calculations were made for greater time intervals. First below I discuss the results of calculations which are similar for calculations with 3 and 5 planets. In such calculations there were no collisions with a star. The fraction p_{ej} of ejected planetesimals was greater for disks located more far from the star. For disks corresponded to planets, p_{ej} mainly did not exceed 0.05. For disks close to the star, most of collisions of planetesimals with planets took place during the first 1 Kyr. However, a few planetesimals could stay in elliptical orbits for millions and tens of million years. Some planetesimals initially located near one of the planets could fall also onto most other planets.

For calculations with 5 planets, about 20–60 % and less than 10 % of planetesimals still moved in elliptic orbits after a few hundred Myr at $e_0 = 0.02$ and $e_0 = 0.15$, respectively. At $T = 10$ Myr and $e_0 = 0.02$, the fraction of initial planetesimals that collided with a host planet was about 0.4–0.46 for disks e, b, and d, about 0.3 for disk c, 0.18 for disk g. At $T = 10$ Myr and $e_0 = 0.15$, such fraction was 0.5, 0.8, 0.4, 0.2, and 0.5 for disks e, b, c, g, and d, respectively. The fraction of planetesimals collided with one of the neighbouring planets (close to the host planet) for disks e, b, c, g, and d equaled to 0.26, 0.06, 0.04, 0.09, and 0.04 at $e_0 = 0.02$. It equaled to 0.5, 0.12, 0.4, 0.35, and 0.15 at $e_0 = 0.15$. Note that for disk g at $e_0 = 0.15$, the fractions of bodies

collided with planets c and d (each) were greater than the fraction of planetesimals collided with the host planet g.

For calculations with 3 planets at $N_0 = 1000$, the number of bodies left in elliptical orbits after 1 Myr was much smaller than for calculations with 5 planets mainly due to eccentric orbits of planets for 3 planets. For 3 planets, evolution of all three disks finished in less than 1.3 Myr at $e_0 = 0.15$, and in not more than 1.1 Myr for disks e and b at $e_0 = 0.02$. At the end of evolution and $e_0 = 0.02$, the fraction of initial planetesimals that collided with a host planet was about 0.44, 0.74, and 0.56 for disks e, b, and c, respectively. At $e_0 = 0.15$ it was 0.4, 0.79, 0.52, respectively. The fraction of planetesimals collided with one of the neighbouring planets (close to the host planet) for disks e, b, and c equaled to 0.50, 0.20, and 0.36 at $e_0 = 0.02$, respectively. At $e_0 = 0.15$ it was 0.52, 0.15, 0.40, respectively. For migration of planetesimals from outside of disk c, the ratio of collisions of planetesimals with planets c and b equaled 2 and 2.7 for at $e_0 = 0.02$ and $e_0 = 0.15$, respectively. These results show that outer layers of neighbouring exoplanets in the Glisse 581 exoplanetary system can include similar material.

CONCLUSIONS:

Outer layers of neighbouring exoplanets in the TRAPPIST-1 and Glisse 581 systems can include similar material, if there were a lot of planetesimals near their orbits at the late stages of the accumulation of the exoplanets. Most of collisions of planetesimals with planets in these exoplanetary systems took place in less than 10 Kyr, but some bodies can still move in elliptical orbits after millions or tens of million years.

ACKNOWLEDGMENTS:

The studies were carried out under government-financed research project for the Vernadsky Institute.

REFERENCES:

- [1] *Ipatov S.I.* Migration of bodies in the accretion of planets // *Solar System Research*. 1993. V. 27. No. 1. P. 65–79. <https://www.academia.edu/44448077/>.
- [2] *Ipatov S.I.* Probabilities of collisions of planetesimals from different regions of the feeding zone of the terrestrial planets with forming planets and the Moon // *Solar System Research*. 2019. V. 53. No. 5. P. 332–361. DOI: 10.1134/S0038094619050046.
- [3] *Marov M.Ya., Ipatov S.I.* Migration processes in the Solar System and their role in the evolution of the Earth and planets // *Physics – Uspekhi*. 2023. V. 66. No. 1. P. 2–31. <https://doi.org/10.3367/UFNe.2021.08.039044>.
- [4] *Ipatov S.I.* Delivery of icy planetesimals to inner planets in the Proxima Centauri planetary system // *Meteoritics and Planetary Science*. 2023. V. 58. No. 6. P. 752–774. <https://doi.org/10.1111/maps>.
- [5] *Ipatov S.I.* Stable orbits in the feeding zone of the planet Proxima Centauri c // *Solar System Research*, 2023. V. 57. No. 3. P. 236–248. <https://doi.org/10.1134/S0038094623030036>.
- [6] *Ipatov S.I.* Motion of planetesimals in the Hill sphere of the star Proxima Centauri // *Solar System Research*. 2023. V. 57. No. 6. P. 612–628. DOI: 10.1134/S0038094623060047.
- [7] *Levison H.F., Duncan M.J.* The long-term dynamical behavior of short-period comets // *Icarus*. 1994. V. 108, p. 18–36.
- [8] *Ipatov S.I.* Mixing of planetesimals in the TRAPPIST-1 exoplanetary system // 13th Moscow Solar System Symp. 2022. P. 378–380.
- [9] *Ipatov S.I.* Mixing of planetesimals in the Glisse 581 planetary system // 14th Moscow Solar System Symp. 2023. P. 333–335. DOI: 10.21046/14MS3-2023.

DEVELOPMENT OF THE ANALYTICAL MODELS OF PROTOPLANETARY FORMATION IN EXTRASOLAR SYSTEMS WITHIN THE FRAMEWORK OF THE STATISTICAL THEORY

A. M. Krot

*United Institute of Informatics Problems of the National Academy of Sciences of Belarus, Laboratory of Self-Organization System Modeling, Minsk, Belarus
alxkrot@newman.bas-net.by*

KEYWORDS:

formation of protoplanets, statistical theory, slow-flowing gravitational condensation, general equation of distribution of the specific angular momentum, initial protoplanetary cloud model, thermal emission of particles model

INTRODUCTION:

In previous works, a statistical theory of the formation of cosmogonical bodies (the so-called spheroidal body) was proposed [1–4]. Within the framework of this theory, evolutionary equations of statistical mechanics were derived, and on the basis of the proposed statistical model of spheroidal bodies, a well-known problem of gravitational condensation of infinitely distributed cosmic media was solved [2], as well as a new universal stellar law was derived [3], and a non-stationary wave Schrödinger-like equation (with a logarithmic nonlinearity) was obtained [4] describing the processes of formation of a cosmogonical body.

Within the framework of theoretical researches, analytical models (the conglomerate model of “cold fusion” and the thermal emission model of “hot fusion”) of the formation of protoplanets have been developed [5].

THE MODEL OF “COLD FUSION” — A UNIFORMLY ROTATING SPHEROIDAL BODY MODEL FOR THE PROTOPLANETARY CLOUD FORMATION:

Indeed, the statistical theory of gravitating spheroidal bodies is considered for the development of analytical models of the formation of protoplanets in our Solar and the extrasolar systems. According to the statistical theory developed in [1–3], the probability density distribution function $f(\lambda)$ of the specific angular momentum λ is described by the formula:

$$f(\lambda) = \frac{\alpha(1 - \varepsilon_0^2)}{2\Omega} \exp\left\{-\frac{\alpha(1 - \varepsilon_0^2)}{2\Omega}\lambda\right\}, \quad (1)$$

where $\alpha = \alpha(t)$ is the gravitational condensation parameter [1–3], ε_0^2 is the square of the eccentricity, Ω is the uniform angular velocity of rotation of the gravitating flattened gas-dust protoplanetary cloud ($\Omega = \text{const}$). The paper [5] also derives a general difference equation for the distribution of the specific angular momentum of forming protoplanets:

$$\lambda_n = 2\bar{\lambda} + \lambda_{n+1} + \frac{\lambda_{n+1} - \lambda_{n-1}}{\exp(-(\lambda_{n+1} - \lambda_{n-1})/2\bar{\lambda}) - 1}, \quad (2)$$

since the specific angular momentum (for particles or planetesimals) is averaged in the process of conglomeration (during the formation of a planetary embryo). As a result, a new law of planetary distances (generalizing the Schmidt law) was theoretically derived in [2].

THE MODEL OF “HOT FUSION” — THERMAL EMISSION OF PARTICLES MODEL OF PROTOPLANETARY CLOUD FORMATION:

An alternative thermal emission model of the formation of protoplanets in the Solar and extrasolar systems is also developed in [1, 5]. Within the framework of this model, a formula for the thermal distribution function $f_r(\lambda)$ of

the specific angular momentum λ for particles moving in elliptical orbits in a gravitational field (as a result of their thermal emission) is obtained:

$$f_T(\lambda) = \frac{m_0 \Omega_1}{2k_B T} \cdot \exp\left(-\frac{m_0 \Omega_1}{2k_B T} \lambda\right), \quad (3)$$

where k_B is the Boltzmann constant; T is a temperature; m_0 is a mass of the particle; Ω_1 is the angular velocity during its orbital motion.

According to the developed thermal emission model (of thermal runaway of particles), only 0.8 % of the total number of particles in our Solar System that make up the protoplanetary cloud have an angular momentum 15.6 times greater than the angular momentum of the remaining 99 % of particles [5]. This conclusion is fully consistent with the well-known fact (noted by Ter Haar back in 1948) of the nonuniform distribution of angular momentum in our Solar system. As noted in [5], exponential laws of planetary distances operate in many extrasolar systems, so that the analytical models (1) and (3) reliably describe the processes of formation of protoplanets.

REFERENCES:

- [1] *Krot A. M.* A Statistical Theory of Gravitating Body Formation in Extrasolar Systems. Cambridge Scholars Publ., 2021. 817 p. <https://www.cambridgescholars.com/product/978-1-5275-6222-6>.
- [2] *Krot A. M.* A statistical approach to investigate the formation of the solar system // *Chaos, Solitons and Fractals*. 2009. V. 41. No. 3. P. 1481–1500. <https://doi.org/10.1016/j.chaos.2008.06.014>.
- [3] *Krot A. M.* On the universal stellar law for extrasolar systems // *Planet. Space Sci.* 2014. V. 101C. P. 12–26. <http://dx.doi.org/10.1016/j.pss.2014.05.002>.
- [4] *Krot A. M.* The generalized nonlinear Schrödinger-like equation of cosmogonical body forming: Justification and determination of its particular solutions // *Partial Differential Equations in Applied Mathematics*. 2022. V. 5. Article e100376. <https://doi.org/10.1016/j.padiff.2022.100376>.
- [5] *Krot A. M.* On the analytical models of protoplanetary formation in extrasolar systems // *Space: Science and Technology*. 2022. V. 2022. Article 9862389. 19 p. <https://doi.org/10.34133/2022/9862389>.

STUDY OF STABILITY OF THE COMPACT PLANETARY SYSTEM K2-72

E. D. Kuznetsov, A. S. Perminov

Ural Federal University, Yekaterinburg, Russia

eduard.kuznetsov@urfu.ru, alexander.perminov@urfu.ru

KEYWORDS:

compact planetary system, mean-motion resonances, tides, dynamic evolution, stability

INTRODUCTION:

At present, several dozen compact planetary systems containing more than two planets with masses of the order of the Earth's mass are known. It is shown that the stable evolution of compact planetary systems requires the presence of resonances that prevent close encounters of planets moving in neighboring orbits (see, for example, the five-planet systems Kepler-80 [1], K2-138 [2] and the seven-planet system TRAPPIST-1 [3]). In this case, resonances between pairs of planets can form chains. The longest resonance chain known to date is realized in the TRAPPIST-1 system: 8:5 – 5:3 – 3:2 – 3:2 – 4:3 – 3:2 [4]. In the K2-138 system, five planets form the longest chain consisting of identical 3:2 resonances [2]. On the other hand, simulation results show that in wide systems with massive planets, chains of high-order resonances can lead to the destruction of planetary systems [4].

We consider the dynamic evolution of the compact four-planetary system K2-72. Star K2-72 is an M-type dwarf. The system contains three Earth-like planets and one super-Earth. We searched for low-order resonances within the uncertainty of determining the periods of the planets. We considered a few scenarios for the evolution of the K2-72 system over 100 Myr using the Posidonius software [5], which considers tidal interactions.

RESONANT ARGUMENTS:

When analyzing the resonance properties of planetary systems, it is necessary to study the behavior of the resonance arguments. For two planets i and $i+1$, which are in resonance of mean motions $k_i/(k_i - l_i)$, the resonance argument can be given as follows [6]:

$$\Phi_{i,i+1,i+s} = (k_i - l_i)\lambda_i - k_i\lambda_{i+1} + l_i\omega_{i+s}, \quad (1)$$

where l_i is the order of resonance, λ_i, λ_{i+1} are the mean longitudes of planets i and $i+1$, respectively, ω_{i+s} is the longitude of the pericenter of the orbit of planet i ($s=0$) or $i+1$ ($s=1$). For the next pair of planets $i+1$ and $i+2$, which are in resonance $k_{i+1}/(k_{i+1} - l_{i+1})$, the resonance argument is defined as follows:

$$\Phi_{i+1,i+2,i+1+s} = (k_{i+1} - l_{i+1})\lambda_{i+1} - k_{i+1}\lambda_{i+2} + l_{i+1}\omega_{i+1+s}. \quad (2)$$

Instead of two resonances between two adjacent pairs of planets, one can consider three-body resonances. In this case the three-body resonance is a chain of two two-body resonances $k_i/(k_i - l_i)$ and $k_{i+1}/(k_{i+1} - l_{i+1})$ with the resonance argument which does not depend on the pericenter longitude [6],

$$\Phi_{i,i+1,i+2}^{p,p+q,q} = p\lambda_i - (p+q)\lambda_{i+1} + q\lambda_{i+2}, \quad (3)$$

where $p = l_{i+1}(k_i - l_i)$, $q = l_i k_{i+1}$. For three-body resonances we will use the following notation: $(p, -(p+q), q)$.

COMPACT PLANETARY SYSTEM K2-72:

Host star K2-72 is an M2 dwarf with a mass of $0.27_{-0.09}^{+0.08}$ solar masses M_\odot and a radius of $0.33_{-0.03}^{+0.03}$ radii of the Sun. Table 1 gives the parameters of the K2-72 planetary system. The radii R of the planets are expressed in Earth radii R_E . Planetary masses m are expressed in Earth masses M_E and calculated from the radii of the planets R , assuming that the density of a planet ρ depends on its radius R as [9].

$$\rho = 2.43 + 3.39 \left(\frac{R}{R_E} \right) g \text{ cm}^{-3} \quad (4)$$

for $R < 1.5R_E$. The orbital elements P , e , i , g are the period, eccentricity, inclination, periaapsis argument, respectively. The moment T_{conj} corresponds to the conjunction of the planet with the star.

Table 1. Parameters of the planetary system K2-72 [7, 8]

Parameter	K2-72 b	K2-72 c	K2-72 d	K2-72 e
R, R_E	1.08 ± 0.11	1.16 ± 0.13	1.01 ± 0.12	$1.29^{+0.14}_{-0.13}$
m, M_E	$1.39^{+0.58}_{-0.44}$	$1.80^{+0.85}_{-0.63}$	$1.09^{+0.55}_{-0.39}$	$2.65^{+1.18}_{-0.85}$
P , day	5.577212 ± 0.00042	15.189034 ± 0.0031	$7.760178^{+0.001496}_{-0.001496}$	$24.158868^{+0.003726}_{-0.003850}$
e	$0.11^{+0.02}_{-0.09}$	$0.11^{+0.02}_{-0.09}$	$0.11^{+0.02}_{-0.09}$	$0.11^{+0.02}_{-0.09}$
i , deg	$89.15^{+0.59}_{-0.86}$	$89.54^{+0.32}_{-0.44}$	$89.26^{+0.5}_{-0.7}$	$89.68^{+0.22}_{-0.32}$
g , deg	7.49^{+120}_{-134}	16.83^{+113}_{-138}	14.28^{+114}_{-137}	11.39^{+117}_{-136}
T_{conj} , JD – 2450000	7010.376 ± 0.002	6989.465 ± 0.005	$6984.788^{+0.008}_{-0.007}$	6987.054 ± 0.005

NUMERICAL SIMULATIONS:

For compact systems, an important factor affecting evolution is tidal interaction; therefore, we considered a few scenarios for the evolution of the K2-72 system over 100 Myr using the Posidonius software [5], which takes into account tidal interactions. At nominal values of the periods and eccentricities, the simulation ended with the decay of the system 3 Myr after the start of integration. This is because at eccentricities of 0.11, the distance at the apocenter of the orbit of the planet K2-72 b becomes greater than the distance at the pericenter of the orbit of the planet K2-72 d. If the initial values of eccentricities of orbits of all planets are set equal to the minimum value of 0.02, the system remains stable over the entire considered interval of 100 Myr for all values of star masses from 0.18 to 0.35 M_\odot .

The results of simulations including tidal interactions show that the compact four-planet system K2-72 can have a stable dynamical evolution in the absence of low-order resonances. Based on the results of numerical simulations with the Posidonius software, we obtained limits on the maximum values of eccentricities of the orbits of the planets, at which the system remains stable over 100 Myr (see Table 2). If the initial eccentricity values are greater than those given in Table 2, the system decays. If the orbital eccentricities do not exceed 0.03, the evolution of the compact planetary system K2-72 over 100 Myr remains stable even in the presence of tidal perturbations. In case the initial eccentricities of the orbits of the three planets are equal to 0.04, the eccentricities of the orbits of one of the planets K2-72 d or K2-72 e should not exceed 0.03 to ensure the stability of the system.

Table 2. Initial values of orbital eccentricities, at which the planetary system does not disintegrate

K2-72 b	K2-72 c	K2-72 d	K2-72 e
0.04	0.04	0.04	0.03
0.04	0.04	0.03	0.04
≤ 0.03	≤ 0.03	≤ 0.03	≤ 0.03

We showed that the compact planetary system K2-72 likely evolves beyond low-order resonances. A significant change in the semi-major axes of the orbits of the K2-72 b and K2-72 d planets leads to the moving of the adjacent planets b–d and d–c out of the 7/5 and 8/5 resonance regions, respectively. The adjacent planets K2-72 d and K2-72 c are located far from the 2/1 resonance, which excludes the possibility of forming chains of mean motion resonances and, hence, three-planet mean motion resonances.

CONCLUSIONS:

The study shows that the compact planetary system K2-72 is not resonant. Under initial conditions corresponding to the masses and orbital elements of the planets determined from observations with their errors taken into account, the evolution of the K2-72 system is stable and regular over of 100 Myr for initial orbital eccentricities not exceeding 0.3.

ACKNOWLEDGMENT:

The study was supported by the Russian Ministry of Science and Higher Education via the State Assignment Project FEUZ-2020-0038.

REFERENCES:

- [1] *MacDonald M.G., Ragozzine D., Fabrycky D.C. et al.* Dynamical Analysis of the Kepler-80 System of Five Transiting Planets // *The Astronomical J.* 2016. V. 152. Article 105. 18 p.
- [2] *MacDonald M.G., Feil L., Quinn T., Rice D.* Confirming the 3:2 Resonance Chain of K2-138 // *The Astronomical J.* 2022. V. 163. Article 162. 12 p.
- [3] *Luger R., Sestovic M., Kruse E. et al.* A seven-planet resonant chain in TRAPPIST-1 // *Nature Astronomy.* 2017. V. 1. Article 0129. 8 p.
- [4] *Murphy M.M., Armitage P.J.* Instability from high-order resonant chains in wide-separation massive planet systems // *Monthly Notices of the Royal Astronomical Society.* 2022. V. 512. P. 2750–2757.
- [5] *Blanco-Cuaresma S., Bolmont E.* Studying tidal effects in planetary systems with Posidonius. A N-body simulator written in rust // *EWASS Spec. Session 4: Star-planet interactions (EWASS-SS4-2017).* 2017. DOI: 10.5281/zenodo.1095095.
- [6] *Huang S., Ormel C.W.* The dynamics of the TRAPPIST-1 system in the context of its formation // *Monthly Notices of the Royal Astronomical Society.* 2022. V. 511. P. 3814–3831.
- [7] *The Extrasolar Planets Encyclopaedia.* <http://exoplanet.eu/catalog/>
- [8] *Dressing C.D., Vanderburg A., Schlieder J.E. et al.* Characterizing K2 Candidate Planetary Systems Orbiting Low-mass Stars. II. Planetary Systems Observed During Campaigns 1-7 // *The Astronomical J.* 2017. V. 154. Article 207.
- [9] *Weiss L.M., Marcy G.W.* The Mass-Radius Relation for 65 Exoplanets Smaller than 4 Earth Radii // *The Astrophysical J.* 2014. V. 783. Article L6.

THE MASS-PERIOD DISTRIBUTION OF LOW-MASS EXOPLANETS DISCOVERED BY THE RADIAL VELOCITY METHOD. IMPROVEMENT OF THE OBSERVATIONAL SELECTION CORRECTION METHOD

A. E. Ivanova, V. I. Ananyeva, A. V. Tavrov

Space Research Institute RAS, Moscow, Russia, anastasia.ivanova@cosmos.ru

KEYWORDS:

exoplanets, statistics, radial velocity

ABSTRACT:

The distribution of low-mass planets is strongly distorted by observational selection, since planets of this type are the most difficult to detect. Correct determination of the distribution of low-mass exoplanets is necessary for refining planet formation models and correct estimates of the abundance of Earth-like planets.

A method for correcting the observed distributions of exoplanets has been developed, taking into account the signal-to-noise ratio and the number of radial velocity measurements. The correction result shows that in the region of 0.0061–0.02 Jupiter masses the distribution of exoplanets follows a power law $dN/dm \propto m^{-1}$ and in the region of ~ 0.03 Jupiter masses a break is observed.

REFERENCES:

- [1] *Ananyeva V. et al.* Distribution of Exoplanets at FGK Stars by Mass and Orbital Period Accounting for the Observational Selection in the Radial Velocity Method // *Atmosphere*. 2023, 14, 353.
- [2] *Ananyeva V.I. et al.* Correction of observational selection when analyzing statistics of exoplanets discovered by the radial velocity technique // *Izvestiya Krymskoi astrofizicheskoi observatorii*. 2023. V. 119. No. 4. P. 70–75.

WEBSITE ON EXOPLANETS PLANETARY SYSTEMS (ALLPLANETS.RU)

V. I. Ananyeva, A. V. Tavrov

Space Research Institute RAS, Moscow, Russia, a-lada@yandex.ru

KEYWORDS:

exoplanets, catalog, database, website

ABSTRACT:

Since 2005, on the domain allplanets.ru a website has been operating — a domestic catalog of exoplanets based on a database of exoplanets and their host stars (allplanets.ru). The site publishes almost daily the latest news on exoplanet research. There are historical reviews and an art gallery. The site allows you to conduct statistical studies of exoplanets, and also contains a selection of popular scientific materials in the field of research of the Solar system planets and exoplanets. It will be useful to both researchers and science popularizers, astronomy teachers and a wide range of readers.

The screenshot shows the website's interface. At the top, there's a navigation bar with the title 'ПЛАНЕТНЫЕ СИСТЕМЫ' and a search bar. Below that, there's a 'Сводная таблица экзопланет' (Summary table of exoplanets) section. This section is divided into two columns: 'по алфавиту' (by alphabet) and 'по дате обновления' (by update date). The table lists various exoplanets with their names and discovery dates. On the right, there's a 'Новости планетной астрономии' (News of planetary astronomy) section with several news items and a 'Таблицы' (Tables) section with links to various data tables.

Figure 1. Home page of the site allplanets.ru

KINETIC MODELLING OF THE SUPER-HOT JUPITER KELT9B

I. F. Shaikhislamov^{1,2}, I. B. Miroshnichenko¹, A. V. Shepelin¹,
S. S. Sharipov¹, M. P. Golubovsky¹, M. S. Rumenskikh^{1,2},
A. G. Berezutsky¹

¹ *Institute of Laser Physics SB RAS, Novosibirsk, Russia,*

ShaikhislamovIldar@yandex.ru

² *Institute of Astronomy RAS, Moscow, Russia*

KEYWORDS:

hot exoplanets, transit absorption

INTRODUCTION:

Hot exoplanets with close orbits have a unique feature of hydrodynamic outflow of their upper atmospheres. The planetary wind is caused by such an important factor of space weather as the intensity of ionizing radiation. The outflow of the upper atmospheres of hot exoplanets is a complex phenomenon, and quantitative interpretation of observational data requires complex numerical modeling. Kelt9b appears to be a unique planet. Absorption in the lines of excited hydrogen H α (656.3 nm), H δ (1282 nm) and excited oxygen (777.4 nm) was observed. The host star of spectral class A has extreme intensity in the NUV and optical range and very weak XUV emission. This leads to a completely different mechanism of atmospheric heating due to photoionization of excited states, rather than photoionization of atoms from the ground state [1].

RESULTS OBTAINED:

We applied a three-dimensional multi-fluid code [2], upgrading it to calculate non-LTE populations of excited levels of elements — H I, C I, C II, O I, Mg I, Mg II. To calculate the level populations, all processes associated with photoexcitation, photoionization and electron impact were taken into account. For the hydrogen atom, transitions between different excited states were also taken into account. It was found that the excitation of the H I(n2) state and subsequent photoionization by photons with $\lambda < 365$ nm heats the atmosphere by orders of magnitude more efficiently than direct photoionization by photons with $\lambda < 91.2$ nm. An important factor is the capture of Ly α photons in the dense atmosphere, which significantly increases the population of the H I(n2) state. However, the overall heating rate is significantly reduced, since the average energy of photoelectrons created by the spectrum of the parent star does not exceed 1 eV.

We compared the calculated absorption in the H α , H δ , and O I lines with observations and found good agreement. This allowed us to constrain the main parameters of Kelt9b and clarify the details of the heating of its upper atmosphere.

REFERENCES:

[1] *García Muñoz A., Schneider P. C. // ApJ. 2019. V. 884. Iss. L43.*

[2] *Shaikhislamov I. F., Khodachenko M. L., Lammer H. et al. // MNRAS. 2018. V. 481. P. 5315–5323.*

MAGNETOSPHERE OF OSIRIS IN THE STELLAR WIND STREAM

Krotov A. S.^{1,2}, Belenkaya E. S.¹, Alexeev I. I.¹, Lavrukhin A. S.¹

¹ *Lomonosov Moscow State University, Skobeltsyn Institute of Nuclear Physics, Moscow, Russia, a-krotov.2014@mail.ru*

² *Lomonosov Moscow State University, Faculty of Physics, Moscow, Russia*

KEYWORDS:

exoplanets, stars, magnetic field, Alfvén Mach number, Alfvénic wings

ABSTRACT:

We investigate the Osiris (HD 209458 b) environment dependent on the stellar wind conditions. It is shown that depending on the stellar wind mode of flowing around the exoplanet, the structure of its magnetosphere changes dramatically. The central star HD 209458 is a solar-type yellow dwarf. Magnetic field of HD 209458 b was indirectly estimated by studying the escape of hydrogen from the exoplanet's environment [1]. We use a paraboloid model of the magnetospheric magnetic field, developed for exoplanets and show how the structure of the Osiris's magnetosphere depends on the Alfvén Mach number, M_A , of the stellar wind. With an increase in the magnitude of the magnetic field of the stellar wind and, accordingly, with a decrease in the Alfvén Mach number to values less than 1, Alfvén wings arise instead of a comet-like magnetosphere with a bow shock ahead of it. Alfvén wings create a direct connection between the exoplanet and the parent star, carried out by a magnetic field.

REFERENCES:

- [1] *Kislyakova et al.* Magnetic moment and plasma environment of HD209458b as determined from Ly- α observations // *Science*. 2014. V. 346. Article 981.

CHEMICAL DIVERSITY OF EXOPLANETARY ATMOSPHERES AND ITS OBSERVATIONAL EVIDENCE

M. Rumenskikh^{1,2,3}, I. F. Shaikhislamov^{1,2}, M. P. Golubovskiy¹

¹ *Institute of Laser physics SB RAS, Novosibirsk, Russia,
marina_rumenskikh@mail.ru*

² *Institute of Astronomy RAS, Moscow, Russia*

³ *Pushkov Institute of Terrestrial Magnetism, Ionosphere and Radiowave Propagation RAS, Moscow, Russia*

KEYWORDS:

hot exoplanets, transit spectroscopy, trace elements, high-resolution observations, MHD modelling

ABSTRACT:

Modern telescopes are unveiling an ever-growing wealth of information about exoplanetary atmospheres. Over the past decades, discoveries have been made in exoplanetary systems that have no counterparts in our Solar System. A prime example is hot exoplanets that orbit their parent stars at distances much closer than Mercury to the Sun, yet possess masses up to several times that of Jupiter. These exoplanets often boast extensive atmospheres rich in diverse chemical elements.

The detailed study of elemental composition in exoplanetary atmospheres allows us to delve deeper into their structural complexities. Absorption lines from heavier elements form much closer to the photometric radius of hot exoplanets compared to hydrogen lines, providing a unique opportunity to probe multiple atmospheric layers through different spectral lines. Moreover, multi-wavelength spectroscopy offers a refined method for determining the physical and chemical properties of these systems, enabling a better understanding of the chemical kinetics within exoplanetary atmospheres. By analyzing absorption spectra, we gain insights into how these atmospheres evolve under the influence of stellar radiation and winds, offering new perspectives that broaden our understanding of the Solar System.

This work presents the findings obtained using a three-dimensional, multi-component magneto-hydrodynamic (MHD) model that incorporates radiation transfer and kinetic simulations of excited states. The study focuses on several hot exoplanets, leveraging transit observations with varying spectral resolutions. The three-dimensional model was used to interpret these observations, shedding light on the complex interactions within the atmospheres of hot exoplanets.

ACKNOWLEDGMENT:

The work was supported by Russian Science Foundation grant No. 23-12-00134, <https://rscf.ru/project/23-12-00134/>.

A SELF-CONSISTENT MODEL OF THE INFLUENCE OF THE HOST STAR ON THE ATMOSPHERE OF SUB-NEPTUNE GJ3470B

A. A. Avtaeva, V. I. Shematovich, A. G. Zhilkin
Institute of Astronomy RAS, nastyaavt@gmail.com

KEYWORDS:

exoplanet, planetary atmospheres, kinetic models, aeronomic model, stellar wind, self-consistent atmospheric model

ABSTRACT:

The exoplanet atmospheres are being actively studied, especially in connection with the launch of new instruments such as the James Webb Space Telescope and the high-resolution CRRES+ spectrometer installed at VLT in Chile, capable of obtaining spectra of the atmospheres of exoplanets. The evolution of planetary atmospheres is one of the most interesting questions in modern astronomical research. In 2012, the hot neptune GJ 3470b [1] was discovered orbiting the red M dwarf GJ 3470 at a distance of 0.0348 AU from its host star. The parameters of the planet GJ 3470b ($R_p = 3.88 \pm 0.32 R_E$, $M_p = 12.58 \pm 1.3 M_E$) show that it is located on the upper border of sub-neptunes. The proximity to the host star of this hot sub-neptune makes it possible to explore how low-mass exoplanets in low orbits evolve under the influence of host stars. In most of the developed models, only thermal processes of atmospheric loss such as the hydrodynamic outflow and atmospheric evaporation are taken into account [2, 3], but non-thermal kinetic processes are not taken into account, although, as our recent studies have shown [4, 5], non-thermal processes are comparable to thermal ones in terms of their contribution to the rate of atmospheric loss. Studying and evaluating the contribution of suprathermal particles to modern aeronomic models of planetary atmospheres, as well as the effect of charge exchange of stellar wind proton with neutral exospheric atoms, is a complex computational task that requires solving the kinetic Boltzmann equation for supra-thermal particles [6]. During an stellar flare and/or coronal mass ejection, the influence of the host star on atmospheric escape increases significantly. The report presents the results of studying atmospheric changes due to thermal and non-thermal processes of atmospheric loss. Using as an example the exoplanet GJ 3470b, a self-consistent atmospheric model is presented, including an aeronomic model of the atmosphere [7] and kinetic models for calculating the contribution of suprathermal particles to atmospheric losses due to the effects of XUV radiation and stellar wind plasma of the host star [4, 8].

ACKNOWLEDGMENT:

This work was supported by the Russian Science Foundation, project No. 22-12-00384.

REFERENCES:

- [1] *Bonfils X., Gillon M., Udry S. et al.* A hot Uranus transiting the nearby M dwarf GJ 3470. Detected with HARPS velocimetry. Captured in transit with TRAPPIST photometry // *Astronomy and Astrophysics*. 2012. V. 546. Article A27. 8 p.
- [2] *Owen J.E.* Atmospheric Escape and the Evolution of Close-In Exoplanets // *Annual Review of Earth and Planetary Sciences*. 2019. V. 47. P. 67–90.
- [3] *Shaikhislamov I. F., Khodachenko M. L., Lammer H. et al.* Global 3D hydrodynamic modelling of absorption in Ly α and He 10830 Å lines at transits of GJ3470b // *Monthly Notices of the Royal Astronomical Society*. 2021. V. 500. Iss. 1. P. 140421413.
- [4] *Avtaeva A. A., Shematovich V. I.* Nonthermal Atmospheric Loss of the Exoplanet GJ 436b due to H₂ Dissociation Processes // *Solar System Research*. 2021. V. 55. Iss. 2. P. 150–158.
- [5] *Avtaeva A. A., Shematovich V. I.* Nonthermal Atmospheric Losses for the Exoplanet GJ 3470b // *Astronomy Reports*. 2022. V. 66. Iss. 12. P. 1254–1261.

- [6] *Shematovich V.I., Marov M.Ya.* Escape of planetary atmospheres: physical processes and numerical models // *Physics-Usppekhi*. 2018. V. 61. Iss. 3. Article 217.
- [7] *Zhilkin A. G., Gladysheva Yu. G., Shematovich V.I., Bisikalo D.V.* Aeronomic Model of Hydrogen-Helium Upper Atmospheres of Hot Giant Exoplanets // *Astronomy Reports*. 2023. V. 67. Iss. 12. P. 1329–1347.
- [8] *Avtayeva A. A., Shematovich V.I.* Kinetic Model of the Effect of the Stellar Wind on the Extended Hydrogen Atmosphere of the Exoplanet π Men c // *Astronomy Reports*. 2023. V. 67. Iss. 10. P. 979–990.

COMPARATIVE ANALYSIS OF THE PHOTOEVAPORATION AND CORE- POWERED MASS-LOSS EFFICIENCY FOR THE ATMOSPHERE OF THE YOUNG MINI- NEPTUNE HD207496B

R. A. Evdokimov¹, V. I. Shematovich²

¹ *Korolev Rocket and Space Corporation "Energia", Korolev, Moscow Region, Russia, evdokimovrom@yandex.ru*

² *Institute of Astronomy RAS, Moscow, Russia, shematov@inasan.ru*

KEYWORDS:

exoplanets, mini-neptunes, super-earths, Fulton gap, atmospheric dissipation, thermal atmospheric escape, photoevaporation, core-powered mass-loss

INTRODUCTION:

Mini-neptunes are one of the most common types of exoplanets, with a radius of 2 to $4R_{\oplus}$ and a mass of up to $10M_{\oplus}$. They are distinguished from super-earths by their relatively low average density, indicating an abundance of volatiles in their composition. Exoplanets of this type may have extensive hydrogen-helium envelopes of primordial composition and/or thick water mantles. On the mass-radius diagram, the regions corresponding to super-earths and mini-neptunes are separated by the so-called Fulton gap — a range of radius values ($1.6-1.8R_{\oplus}$), in which transiting planets are observed much less frequently [1]. This gap is likely a natural boundary between two populations of exoplanets. The origin of this gap may be associated with the presence or absence of extended hydrogen-helium atmospheres. In some cases, exoplanets with a mass of up to several Earth masses and formed in short-period orbits may initially have no atmospheres of primordial composition. However, a scenario is quite possible, in which an exoplanet, starting its evolutionary path as a mini-neptune, subsequently loses its gaseous envelope. As a result, a bare core remains, which is either a super-earth or an ocean planet (depending on the water content) [2]. There are various mechanisms of atmospheric loss, both thermal and non-thermal [3]. Much attention was paid studying the loss of the atmosphere under the influence of XUV radiation from the host star (photoevaporation) [4]. It was shown that this phenomenon can explain the existence of the Fulton gap [4]. Noticeably less attention has been paid to an alternative mechanism — the loss of the hydrogen-helium envelope under the influence of the heat flow from the hot core of the young planet [5]. Under certain conditions (equilibrium temperature, initial mass of the exoplanet), this mechanism can be very effective and suitable for a qualitative explanation of the formation of the Fulton gap without taking into account photoevaporation [5]. It was shown that both of these mechanisms must take place, and at different evolutionary stage, they can dominate alternately [6]. In this case, photoevaporation makes a more significant contribution to the formation of the Fulton gap, but the core-powered mass-loss significant effects on the "relief" of the gap. To study the process of dissipation of the mini-neptunes atmospheres, the observation of young exoplanets in the Fulton gap or near it is of great importance, since they must be in the process of losing their envelopes. Such exoplanets include mini-neptune HD207496b [2]. According to observational data, HD207496b has a mass of about $6.1 M_{\oplus}$ and a radius of about $2.25R_{\oplus}$. The estimated equilibrium temperature is 743 K. The parent star is a young orange dwarf of spectral class K2.5V. The estimated age of the star (and, accordingly, the exoplanet) is about 520 million years. The semi-major axis of the exoplanet's orbit is 0.0629 ± 0.0011 AU, eccentricity is 0.231. In [2], for the observed values of the planet's radius and mass, two extreme variants of its structure were proposed — a dry rocky core of iron-silicate composition, surrounded

by a hydrogen-helium envelope, as well as a rocky core with a water mantle, practically devoid of a primordial atmosphere (ocean world). For these two options, a calculation was made of the loss of the hydrogen-helium envelope in the past and future using the photoevaporation mechanism. For the variant of a rocky core with an envelope, it was found that at the moment, with a core radius of $1.74R_{\oplus}$, the height of the atmosphere is $0.51R_{\oplus}$. The mass fraction of the atmosphere in the exoplanet's mass is about 0.005 (0.5%). It was established that immediately after the formation of the exoplanet, its envelope should have been about 2.2% of the total mass, and the radius of the exoplanet should have been slightly more than $3R_{\oplus}$. It is estimated that photoevaporation will lead to complete loss of the primary atmosphere within the next 500 million years. In addition to the results of [2], we considered the loss of the atmosphere under the influence of heat flow from the core. Numerical simulations were performed using the mathematical model presented in [5]. In this case, photoevaporation was not taken into account. We considered both the loss of the atmosphere of HD207496b in the future (observed values of the planets mass and radius, as well as model parameters of the core and envelope from [2] were used as initial parameters), and dissipation of the atmosphere in the past (the initial state was the specified simulation result from [2]). It was found that for the considered version of the internal structure of HD207496b, the escape of the atmosphere under the influence of the heat flow from the core is negligible. The exoplanet has a sufficiently large mass, a relatively low equilibrium temperature so that after formation the atmosphere relatively quickly contracts, and cools, avoiding dissipation. Thus, for the considered HD207496b model, the process of photoevaporation of the primary atmosphere should be dominant. However, we have shown that this result depends quite strongly on the mass and temperature of the exoplanet. In further studies the additional factors such as the possible presence of a water mantle around the rocky core (the heat capacity of the core increases and the gravity at its boundary decreases), the radiogenic and tidal heat release in the core should be taken into account.

References:

- [1] *Fulton B. J. et al.* The California-Kepler Survey. III. A Gap in the Radius Distribution of Small Planets // *AJ*. 2017. V. 154. Iss. 109. Article 1703.10375.
- [2] *Barros S. C. C. et al.* The young mini-Neptune HD 207496b that is either a naked core or on the verge of becoming one // *A and A*. 2023. V. 673. Iss. A4.
- [3] *Shematovich V. I., Marov M. Y.* Escape of planetary atmospheres: physical processes and numerical models // *Physics Uspekhi*. 2018. V. 61(3). Article 217.
- [4] *Owen J. E., Jackson A. P.* Planetary evaporation by UV & X-ray radiation: basic hydrodynamics // *MNRAS*. 2012. V. 425. Iss. 4. P. 2931–2947.
- [5] *Ginzburg S., Schlichting H. E., Sari R.* // *ApJ*. 2016. V. 825. Iss. 29.
- [6] *Owen J. E., Schlichting H. E.* Mapping out the parameter space for photoevaporation and core-powered mass-loss // *MNRAS*. 2024. V. 528. P. 1615–1629.

MEASUREMENT OF REACTION RATES OF METASTABLE HELIUM ATOM FOR ASTROPHYSICAL APPLICATIONS

M. P. Golubovsky¹, I. F. Shaikhislamov¹, M. S. Rumenskikh^{1,2}

¹ Institute of Laser Physics SB RAS, Novosibirsk, Russia
maxym9121@gmail.com

² Institute of Astronomy RAS, Moscow, Russia

KEYWORDS:

laboratory modeling, metastable helium, plasma, absorption, numerical simulation

INTRODUCTION:

In this paper we present the proposal of measurement of atomic processes relevant for astrophysics in laboratory experiments. Many rates, very important for interpretation of astronomical observations, are known only from theoretical calculations. The line 1083 nm of metastable triplet helium is widely used to probe atmospheres and plasmaspheres of transiting exoplanets. Reliable interpretation of measurements by telescopes requires verification of rates of population and depopulation of metastable helium used to derive plasma parameters from observational data. Plasma Facility KI-1 is suitable to simulate conditions relevant for hot gas-plasma atmospheres of close-orbit exoplanets. As a preliminary step we performed the numerical modeling and developed the set-up, which will allow to derive relevant rates by measuring absorption in the 1083 nm line in helium plasma.

ANALYTICAL CALCULATION OF LINE ABSORPTION:

To calculate absorption in 1083 nm line in helium plasma the kinetic model of population of levels of helium atom is needed. It was developed earlier and we use our previous work [1]. The model includes such processes as recombination, radiative decay and transitions via collisions with electrons, hydrogen atoms and molecules. We assume the following parameters that are typical for theta-pinch plasma at KI-1: $n(\text{He}^+) = 10^{13} \text{ cm}^{-3}$, $n(\text{He}) = 10^{10} \text{ cm}^{-3}$, $n(\text{He}) = 10^{10} \text{ cm}^{-3}$, $n_e = 10^{13} \text{ cm}^{-3}$. The temperature was changed from 0.1 to 10 eV. At $T = 1 \text{ eV}$ the kinetic model gives the population of metastable helium atoms $n(\text{He}[2^3\text{S}]) = 10^{7.8} \text{ cm}^{-3}$.

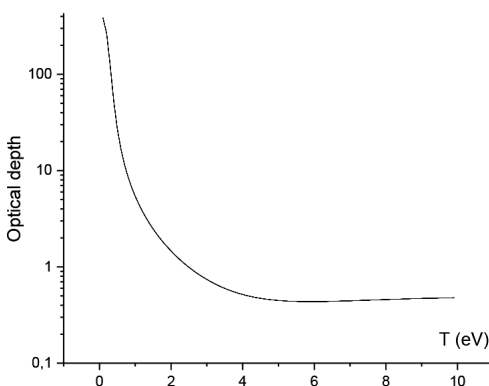


Fig. 1. Optical depth as a function of a temperature

The optical depth is calculated for a 1 km length using the density of metastable atoms and the cross-section given by Voigt profile and taken at the line center, $\tau = n(\text{He}[2^3\text{S}])\sigma_{\text{max}}L$. Figure 1 shows the optical depth as a function of temperature. Thus, for parameters expected in experiment at KI-1 the optical depth equals 1 at $T \approx 2.5 \text{ eV}$. As the characteristic size of plasma is of the order 1 m, the multi-pass scheme is needed to measure the absorption.

EXPERIMENTAL SET-UP:

Verification of rates will be made by comparing absorption calculated based on theoretical values with the measured in experiment. The proposed set-up consists of light source of wide spectral range which covers 1083 nm. The light from the source is divided into two parts via fiber splitter. One part is delivered into concave high quality resonator placed in plasma. The resonator by multiple reflections increases the effective path by several hundred times. Second part moves outside plasma and serves for calibration and comparison. The absorption is measured by monochromator with resolution <0.1 nm.

ACKNOWLEDGMENTS:

This work is done in the frame of ELAG section of National Center for Physics and Mathematics.

REFERENCES:

- [1] *Shaikhislamov I. F. et al.* Global 3D hydrodynamic modelling of absorption in Ly α and He 10830 A lines at transits of GJ3470b // Mon. Not. R. Astron. Soc. OUP. 2021. V. 500. P. 1404–1413.

**SESSION 6. EXTRASOLAR PLANETS (EP-PS)
POSTER SESSION**

SUPERFAST EXOPLANETS AND MOTION OF THE SUN AND EARTH

V. A. Kotov

Crimean Astrophysical Observatory, Nauchny, Russia, vkotov@craocrimea.ru

KEYWORDS:

Sun, pulsations, Solar system, Earth, exoplanets, dark matter

ABSTRACT:

It is shown that superfast exoplanets tend to revolve around “parent” stars with the orbital periods commensurable with timescales P_0 and/or $2P_0/\pi$, where $P_0 \approx 3^{-2}$ days, a pulsation period of the Sun [1]. We note also: (a) close connection of the P_0 timescale with the rotation period of the Sun, $P_S \approx 3^2 P_0$ (synodic) [2], and the primary periods of Earth (daily, $P_D \approx 3^2 P_0$, and orbital, $P_Y \approx 3^8 P_0/2$), (b) the principal role of the spatial scale $cP_0 \approx 19.24$ AU for the Solar system’s structure (with c , speed of light, and the factor π for inner orbits), and (c) the timescale P_0 appears to be the best commensurate one for rotation periods of the most massive and fast-spinning objects of our planetary system, including Earth, Mars, Jupiter and Saturn. A hypothesis is advanced that (I) P_0 , P_S , P_Y and P_D present fundamental timescales of the World, tied to the tendency of periodic motion of cosmic objects to recur in time and space (in accordance with the Schrödinger’s [3] “tendency for order, regularization and reproduction”, triumphant in biology), (II) this tendency presents physical basis for emerging of life on Earth, and (III) the phenomenon of special, “privileged” timescales (including perhaps the Universe’s “age” 13.75G-years too) gives simple resolution of the dark matter problem. But true physical nature of the timescale P_0 , which seems to be at the borders of “a cosmic miracle”, is hidden yet under seven seals.

REFERENCES:

- [1] Kotov V., Haneychuk V. Sixfold enhancement of solar pulsations: 1974–2018 // *Acta Astrophys. Taurica*. 2023. V. 4. No. 2. P. 1–5.
- [2] Kotov V.A. Is the Earth’s motion linked to the spin rotation of the Sun? // *Adv. Space Res.* 2019. V. 63. P. 3385–3389.
- [3] Schrödinger E. What is life? The Physical Aspect of the Living Cell. Dublin: Dublin Institute for Advanced Studies, 1955. 88 p.

MAGNETIC EXOPLANETS IN THE SUB-ALFVENIC STELLAR WIND MAY ACT AS A KIND OF INTERPLANETARY MAGNETIC FIELD COLLIMATOR

E. S. Belenkaya

*Skobeltsyn Institute of Nuclear Physics Lomonosov Moscow State University
Moscow, Russia, elena.belenkaya.msu@gmail.com*

KEYWORDS:

exoplanets, stars, Alfven radius, stellar wind, Alfven wings

DIGITAL FORMATS FOR FIGURES:

A lot of exoplanets are close to their parent stars. The regime of stellar wind passing by them depends on the distance between the star and the exoplanet and the properties of the host star. This can be a sub-Alfvenic or super-Alfvenic mode. If a magnetic exoplanet is located outside the Alfven radius, a teardrop-shaped magnetosphere develops with a bow shock ahead of it. If exoplanet is placed within the Alfven radius, their magnetosphere will turn into Alfven wings. The Alfven radius is the distance from the star at which the kinetic and magnetic energy densities are equal. It is shown how the transition from a teardrop-shaped magnetosphere to Alfven wings can be achieved by increasing the magnitude of the stellar wind magnetic field with the direction preferred for reconnection and how the bundle of open field lines is transformed during this process.

**SESSION 7. ASTROBIOLOGY (AB)
ORAL SESSION**

THERMODYNAMIC TRANSFORMATION OF ORGANIC MICROSYSTEMS AS AN IMPETUS FOR THE EMERGENCE OF LIFE FORMS ON EARTH AND OTHER PLANETS

V. N. Kompanichenko

*Institute for Complex Analysis of Regional Problems RAS, Birobidzhan, Russia
kompanv@yandex.ru*

KEYWORDS:

origin of life, astrobiology, planet, thermodynamics of systems, hydrothermal fluid, bacterial cell, metabolism, anabiosis

ABSTRACT:

The concept of thermodynamic inversion (TI) considers the transition of prebiotic organic microsystems into initial life forms through revolutionary change of the balances "total contribution of entropy to total contribution of free energy" and "total contribution of informational entropy to total contribution of information" in the system with positive to negative values [1]. The negentropic barrier that separates chemical and biological systems as consequence of the second law of thermodynamics, is overcome due to powerful impulse of free energy entering in a prebiotic system at the expense of high-frequency oscillations of physico-chemical parameters in the environment. According to this approach, stages of the origin of life are not disappeared during the biosphere evolution, but conserved in the anabiotic process and repeats, when a bacterial cell exists from anabiosis. The following stages of the origin of life in fluctuating conditions of hydrothermal on early Earth were reconstructed on this basis [2, 3].

- The first stage: self-assembly of prebiotic microsystems. Initial organic (prebiotic) microsystems involved in the process of formation of primary life forms were multicomponent. They had a lipid membrane, probably with incorporated amino acids. According to the TI concept, self-assembly of microsystems proceeded in an oscillatory mode. ATP and sugars were probably absent at this because of a high temperature in the medium (>100 °C).
- The second stage: formation of protocells. Appearance of a weak energy-giving process of respiration in the microsystems, which facilitate concentrating free energy in them. Acceleration of the movement of lipids in membrane structures, associated with an increase in their fluidity. Appearance of supra-entropic information (the contribution of information became prevalent over the contribution of informational entropy), related with the ability of the forming protocells for active (intensified) response to oscillating conditions in the environment. Establishment of a tendency towards concentration of (structural) information in clusters of microsystems.
- The third stage: formation of living subcells. The synthesis of unsaturated fatty acids began. The permeability barrier began to form, as well as the transport and energy-giving functions of the membrane. Simultaneously with the increase in the energy function of the membrane, the level of reactive oxygen species increased, for the neutralization of which a non-enzymatic antioxidant system of the subcell formed. At the same time, the foundation of the primary structure of the protein-synthesizing apparatus of the subcell took place, but the matrix synthesis of protein macromolecules was still absent. Energy equivalents (ATP) in the absence of biosynthesis have not yet been in demand.
- The fourth stage (growth): emergence of primary living cells (progenotes). During this stage, the formation of the growth cell cycle took place, which led to the appearance of the first living vegetative cells, as

constituent elements of the primary populations. The acid-base reactions of phosphates associated with the transfer of protons began to dominate in energy conversion processes and led to the widespread use of ADP and ATP. At this time, the genetic apparatus of the cell began to form as its informational basis. The targeted synthesis of enzymatic proteins that followed ensured active cell metabolism.

- The fifth stage: Early biological evolution of the initial prokaryotes to the oldest species of archaea and bacteria.

So, the scheme of the microorganisms origin on Earth are briefly summarized as follows: Stage 1 — unlife; Stages 2 and 3 — protolife; Stages 4 and 5 — life (as we know it).

The following consequences for astrobiology follow from the TI concept: simple life should be rather wide-spread phenomenon in the Universe; within the solar system at least Mars, Europa and Enceladus possess the four required conditions for the origin of life (availability of water, organic matter, energy source, fluctuations in the medium); one cannot expect existence of living systems on a basis on another (different from Earth's) combination of organic molecules if this combination allows to maintain surplus of free energy and information in respect to entropy; evolution of primary life forms (protolife) on other space bodies could stop at the more primitive level than even simplest prokaryotic microorganisms on Earth.

REFERENCES:

- [1] *Kompanichenko V.N.* Thermodynamic Inversion: Origin of Living Systems. Cham, Switzerland: Springer Intern. Publ, 2017. 275 p.
- [2] *Kompanichenko V., El-Registan G.* Advancement of the TI concept: defining the origin-of-life stages based on the succession of a bacterial cell exit from anabiosis // AIMS Geoscience. 2022. V. 8. No. 3. P. 398–437.
- [3] *Kompanichenko V.* Abiotic-to-biotic transition of organic systems starting with thermodynamic inversion // Guidebook for Systems Applications in Astrobiology / eds. V. Kolb, B. Clark. CRC Press, 2023. Ch. 8. P. 164–176.

THERMOPHILES: THE EXTRAORDINARY EXTRATERRESTRIALS NEXT DOOR

S. A. Bulat^{1,2}, J. M. F. Martins³, J. R. Petit³

¹ Petersburg Nuclear Physics Institute named by B. P. Konstantinov of National Research Centre "Kurchatov Institute", Gatchina, Leningrad region, Russia
bulat_sa@pnpi.nrcki.ru

² Institute of Physics and Technology, Ural Federal University
Ekaterinburg, Russia

³ University Grenoble Alpes, CNRS, IRD, Grenoble INP, IGE, Grenoble, France

KEYWORDS:

thermophiles, Antarctica, Lake Vostok, Oxford Nanopore sequencing, Ence-ladus, Europa

INTRODUCTION:

The objective was to search for microbial life in Lake Vostok, a subglacial lake in Antarctica [1]. This involved analyzing natural ice samples obtained through deep ice coring during a Russian expedition to access the lake. The ice samples studied were type I and contained mineral inclusions. The main goal of the research was to re-assess previous microbial findings, which were originally obtained using Sanger sequencing, using the high-throughput Oxford Nanopore sequencing technology.

SANGER SEQUENCING:

The Sanger sequencing technique was used to analyze bacterial 16S rRNA genes in subglacial Lake Vostok and it led to the discovery of thermophiles. Ice samples from a depth of 3561 and 3607 m, containing sediment inclusions, were studied. The analysis revealed the presence of *Hydrogenophilus thermoluteolus*, a beta-Proteobacteria from hot springs, in both samples [2, 3]. This suggests a geothermal system may be beneath Lake Vostok's cold-water body.

OXFORD NANOPORE SEQUENCING:

To confirm the presence of thermophiles in Lake Vostok, we conducted additional testing on accretion ice samples from different depths using high-throughput nanopore sequencing. The segments from 3607, 3608, 3607 m (2 segments), and 3709 m were included in the testing. We utilized the same genomic DNA and broader-in-coverage degenerate primers for the v3-v4 region of 16S rRNA genes. For the first time, we also included nanopore controls (sham DNA isolation/negative PCR, nanopore reagents) to ensure the accuracy of our results.

Several million reads were obtained for all five amplicons. However, only sample 3608 showed the presence of thermophiles in the records. Out of 1,643,669 reads analyzed for this sample, 88% were classified. Among these, 279 (0.02 %) reads were assigned to the moderate thermophile *Meiothermus hypogaeus* NBRC 106114, which belongs to the *Deinococcus-Thermus* phylum and was isolated from a hot spring in Japan. No reads for this find were recorded in other ice samples and controls. This discovery could imply the presence of a new thermophile in the native accretion ice of Lake Vostok. The absence of detectable reads for *Hydrogenophilus thermoluteolus* may be due to the use of different primers or the variable microbiota content of the pressurized ice (1 m corresponds to 100 years).

MORE HOT DISCOVERIES:

During the study of "thermophiles-in-ice," four more ice cores from Lake Vostok water were analyzed using nanopore sequencing to detect thermophiles. They came from depths of 3698, 3709, 3715, and 3721 m. No signs of *Meiothermus* sp. or *Hydrogenophilus* sp. were found in any of the ice cores. However, the study unexpectedly revealed the presence of three other moderate thermophiles belonging to the *Bacillota* phylum in the 3709 m core (and one in the 3715 m core). Additionally, two newly discovered thermophiles, *Thermaerobacter litoralis*, and *Thermoanaerobacter thermocopriae*, were detected in several reads in the natural accretion ice sample at

3608 m. This provides strong evidence for the presence of thermophiles in the ice.

PROSPECTS:

Oxford Nanopore sequencing technology has proven to be an efficient tool in recording and proving the microbial content present in subglacial Antarctic water reservoirs. The discovery of mesophilic thermophiles suggests that unique cell populations might reside in faults offshore of the subglacial Lake Vostok. These organisms could provide valuable insights into searching for extraterrestrial thermophiles on the icy moons of Jupiter and Saturn.

REFERENCES:

- [1] *Bulat S., Petit J.-R.* Vostok, Subglacial Lake // Encyclopedia of Astrobiology / eds. Gargaud M. Berlin; Heidelberg: Springer, 2023. P. 3206–3212.
- [2] *Bulat S. A. et al.* DNA signature of thermophilic bacteria from the aged accretion ice of Lake Vostok, Antarctica: implications for searching for life in extreme icy environments // Intern. J. Astrobiology. 2004. V. 3. P. 1–12.
- [3] *Lavire C. et al.* Presence of *Hydrogenophilus thermoluteolus* DNA in accretion ice in the subglacial Lake Vostok, Antarctica, assessed using *rrs*, *cbb* and *hox* // Environmental Microbiology. 2006. V. 8. P. 2106–2114.

SYSTEMS APPROACH TO ASTROBIOLOGY

O. R. Kotsyurbenko

Yugra State University, Khanty-Mansiysk, Russia kotsor@mail.ru

*Network of Researchers on the Chemical Evolution of Life
Leeds, United Kingdom*

KEYWORDS:

system approach, astrobiology, biosignatures, microbial communities

ABSTRACT:

System organization is the inherent property of the universe and is observed at different scales. Biological systems are one of the most complex systems with regard to their organization. A complex system consists of a large number of independent interacting elements, that leads to an increase in its emergent properties.

The biosphere is the highest-level biosystem on any habitable planet elsewhere in space. The only known biosystem on a planetary scale is the Earth's biosphere that can be considered as a model in the search for extraterrestrial life. Microbial systems as basic biosystems are a key object of search in the concept of extraterrestrial life. Microorganisms especially bacteria and archaea (prokaryotes), represent the first stable system within the biosphere in which all other living organisms are acting. The stability of such a system depends on the key role of prokaryotes in the cycles of biologically important elements. Microbial systems are formed on the basis of trophic interactions, and their role is determined by the requirement of a higher-level system.

One of the most interesting systems in this regard is the methanogenic microbial community, which plays a crucial role as a source of the greenhouse gas methane into the Earth's atmosphere.

In extraterrestrial ecosystems, methanogens can potentially function as part of a simple biosystem. They are able to grow exclusively on inorganic compounds, synthesizing all the substances necessary for living using carbon dioxide as the only source of carbon.

The dominant concept of habitability includes the necessary presence of four key factors: the main biogenic elements CHNOPS, energy sources, favourable physicochemical conditions, and universal solvent (water). The modern concept of the habitable zone of various planets considers not only conditions for the surface life forms, but also endohydrospheres of some Jovian and Saturnian satellites and isolated atmospheric life hypothetically inhabiting the cloud layer of Venus. The main criterion for the stability of the global biosystem is the involvement of living organisms in biogeochemical cycles.

Since at the moment there is no evidence for the existence of extraterrestrial life, practical astrobiology is aimed at developing a methodology for its search in which the main aspect is relevant biosignatures. In this regard, the analysis of biological systems on Earth can make an important contribution to defining the type of such biosignatures and their connection to hypothetical life activity in extraterrestrial ecosystems.

Due to the limited technical capabilities of a single space mission, researchers develop a methodology for detecting only a certain number of possible biosignatures. Obviously, the type of detected biosignatures can give direct (biomacromolecules or cells) or only indirect (gas composition, geological processes) indication of the presence of extraterrestrial life. Besides, when searching for direct evidence, it should be taken into account that extraterrestrial living forms may differ significantly from the terrestrial life and, therefore, will not necessarily be detected by methods developed for terrestrial organisms.

In this respect, it is important to search for the most general principles and features of living organisms that could be applied to different life forms.

SURFACE BACTERIAL DYNAMICS AND BIOSAFETY ASSESSMENT DURING THE LUNAR PALACE 365 BIOREGENERATIVE EXPERIMENT

Y. Fu, Y. Lu, J. Yang, H. Liu

Institute of Environmental Biology and Life Support Technology, School of Biological Science and Medical Engineering, Beihang University Beijing, China, fuyuming@buaa.edu.cn

KEYWORDS:

bacterial community dynamics, bioregenerative life support system (BLSS), biosafety, antibiotic resistance genes (ARGs), biodegradation

ABSTRACT:

Our study investigates the dynamic variation of bacterial populations within the bioregenerative life support system (BLSS), a critical component for sustainable habitats in extraterrestrial environments supporting human survival. We utilized the ground-based BLSS test platform, referred to "Lunar Palace 1" (LP1), to examine bacterial dynamics in an ecosystem integrating plant production, human cultivation, and equipment maintenance. Our findings reveal distinct bacterial compositions among crew members and functional areas within the LP1 system, yet overall stability throughout the 370-day experiment. Importantly, we observed low abundance of potential pathogens, minimal antibiotic resistance, and negligible impact on equipment materials, suggesting favorable biosafety attributed to plant integration. Our work enhances understanding of microbial communities in BLSS and underscores the importance of incorporating green plants to bolster environmental biosafety and sustainability in long-term space exploration missions.

ASTROBIOLOGICAL ISSUES OF THE AURORAL NITRIC OXIDE FORMATION IN THE N_2 - O_2 ATMOSPHERES OF THE TERRESTRIAL-TYPE PLANETS

V. I. Shematovich¹, D. V. Bisikalo^{1,2}, G. N. Tsurikov¹, A. G. Zhilkin¹

¹ Institute of Astronomy RAS, Moscow, Russia, shematov@inasan.ru

² National Center of Physics and Mathematics, Sarov, Russia

KEYWORDS:

terrestrial planet, auroral event, kinetic modeling, nitric oxide as an atmospheric biomarker

INTRODUCTION:

The detection of an N_2 - O_2 atmosphere on a terrestrial-type exoplanet located in the habitable zone (HZ) around its host star may be an important sign of the presence of biological activity on it [1]. The search for N_2 - O_2 dominant atmospheres of exoplanets, in turn, is a difficult observational task. The separate detection of N_2 and O_2 molecules may be a false positive sign of biological activity on the planet, since an abiotic pathway [1] can effectively form these molecules. Only a few molecules formed in the N_2 - O_2 atmosphere are potential biomarkers that can be detected using instruments on existing and future space missions. These include the molecules N_2O , NO_2 , NO and N_2 - O_2 dimers. Nitric oxide is a potential biomarker in the N_2 - O_2 atmospheres of terrestrial exoplanets, which can be detected [2] by space missions, including the planned launch of the Russian Spektr-UV observatory. From observations in the polar regions of the Earth's thermosphere, it is known that important sources of this molecule formation are the precipitation of high-energy auroral electrons into the planet's atmosphere, as well as non-thermal processes accompanying them.

It is known that the processes associated with the interaction of the stellar wind with the atmosphere of a terrestrial-type planet, accompanied by the precipitation of electrons, can contribute to an increase in the concentration of NO in the upper atmosphere. It leads to an increase in the probability of detecting this molecule, especially on exoplanets in the HZs of stars more active than the Sun. To test this hypothesis, initially, we modified the kinetic Monte Carlo model (kMCM) of the precipitation of high-energy auroral electrons into the polar atmosphere of the Earth [3], which was used to study the dissociation of atmospheric N_2 when they collide with high-energy electrons, leading to the formation of superheated nitrogen atoms. Using the results of this model, the kinetic energy distribution function of the formed superheated nitrogen atoms, a kMCM model was developed to describe the kinetics and transfer of these superheated N atoms in the polar regions of the Earth's atmosphere [4].

The main purpose of this work is to estimate the effect of energetic electron precipitation and non-thermal processes induced by this precipitation on the formation of nitrogen oxide in the atmosphere of the terrestrial-type planets orbiting the active host stars. For this purpose, the mentioned kMC models of the interaction of high-energy electrons [3] and superthermal $N(^4S)$ atoms [4] with the ambient atmospheric gas are used. A model of odd nitrogen chemistry with molecular and turbulent diffusion has also been developed, which makes it possible to model the high-altitude profiles of NO in the upper atmospheres of terrestrial planets.

RESULTS:

1. The validation of the developed models for the upper atmosphere of the Earth has shown that the precipitation of high-energy electrons in the polar atmosphere is the dominant source of nitrogen oxide formation. The results of calculations of volumetric NO concentrations using the developed models for various cases of auroral electron eruptions are consistent with other models and observations (see, e.g., [3, 4]).

2. Studies of the influence of the activity of host stars on the N_2 - O_2 atmospheres of terrestrial-type planets have shown that an increase in the energy fluxes of precipitating electrons, which is a consequence of disturbances in the stellar wind, can significantly increase the efficiency of the thermal channel for the formation of nitrogen oxide in the atmospheres under consideration. Thus, the peak values of the volume concentration of NO can reach $3 \cdot 10^9 \text{ cm}^{-3}$ and $1 \cdot 10^{10} \text{ cm}^{-3}$ with a continuous flow of energy of precipitating electrons $Q_0 = 100 \text{ erg} \cdot \text{cm}^{-2} \cdot \text{s}^{-1}$ and the characteristic energy of precipitating electrons $E_0 = 1$ and 4 keV, respectively. For comparison, the concentrations of this molecule in the Earth's atmosphere for electron energy fluxes in $1 \text{ erg} \cdot \text{cm}^{-2} \cdot \text{s}^{-1}$ reach values of $2.4 \cdot 10^8$ and $2.8 \cdot 10^8 \text{ cm}^{-3}$ for the same characteristic energies.
3. Based on the results of calculations in this report, the conclusions of [4] were confirmed that the dissociation of molecular nitrogen by an electron impact during the precipitation of auroral electrons with high energies is the main source of suprathreshold nitrogen atoms $N(^4S)$ in the polar regions of the atmospheres of terrestrial planets. Despite the low content of suprathreshold atoms in the atmosphere, their contribution to the stiff system of chemical reactions describing the odd nitrogen chemistry, as well as their contribution to the non-thermal formation of NO (through interaction with O_2), is significant. In the case of permanent precipitation of electrons in the atmosphere of a model terrestrial-type planet, even with the small values of energy flux $Q_0 = 1 \text{ erg} \cdot \text{cm}^{-2} \cdot \text{s}^{-1}$, the concentration of nitrogen oxide formed in the non-thermal channel can be 20 and 70 times higher than the concentration of this molecule formed in the thermal channel at characteristic electron energies $E_0 = 1$ and 4 keV, respectively. Moreover, due to the effective formation of superthermal nitrogen atoms at high energy fluxes of precipitating electrons, non-thermal NO formation is also effective. As a result, the increase in the concentration of this molecule with an increase in Q_0 can be almost linear. At $Q_0 = 100 \text{ erg} \cdot \text{cm}^{-2} \cdot \text{s}^{-1}$, according to the calculations the maximum of this concentration can reach values of $5 \cdot 10^{11}$ and $2 \cdot 10^{12} \text{ cm}^{-3}$ at characteristic electron energies of 1 and 4 keV, respectively, i.e., two orders of magnitude higher than the peak NO value formed in the thermal channel. The conclusions obtained are also valid for column concentrations of NO.
4. These results are extremely important for determining the strategy for searching for the atmospheric biomarker NO using the planned Spektr-UV observatory in the atmospheres of terrestrial-type exoplanets located within the range of active stars. Estimates show that exoplanets orbiting the active host stars are best suited for searching for this molecule, since the atmospheres of these planets are sufficiently heated and, therefore, expanded, which increases the chances of detecting a light transmission signal in the spectral bands of NO (γ -bands) in the near ultraviolet range (205–248 nm) [2]. The significant formation of nitrogen oxide obtained in calculations during disturbances in the stellar wind and subsequent precipitation of high-energy electrons in the atmospheres of exoplanets, in turn, can improve the conditions for detecting this molecule using the Spektr-UV space observatory. In any case, taking into account this factor will allow us to expand the number of exoplanets — potential objects of observation by space telescopes.

ACKNOWLEDGMENT:

We acknowledge the financial support of the Russian Science Foundation, grant No. 22-12-003644 <https://rscf.ru/project/22-12-00364/>.

REFERENCES:

- [1] *Sproß L., Scherf M., Shematovich V.I. et al.* Life is the Only Reason for the Existence of N_2 - O_2 -Dominated Atmospheres // *Astronomy Reports*. 2021. V. 65. P. 275–296.
- [2] *Tsurikov G.N., Bisikalo D.V.* On the Possibility of Observing Nitric Oxide on Terrestrial Exoplanets Using the WSO-UV Observatory // *Astronomy Reports*. 2023. V. 67. P. 125–143.

- [3] *Bisikalo D., Shematovich V., Hubert B.* The Kinetic Monte Carlo Model of the Auroral Electron Precipitation into N₂-O₂ Planetary Atmospheres // *Universe*. 2022. V. 8. P. 437–446.
- [4] *Shematovich V., Bisikalo D., Tsurikov G.* Non-Thermal Nitric Oxide Formation in the Earth's Polar Atmosphere // *Atmosphere*. 2023. V. 14. P. 1092–1104.

REACTIVE OXYGEN SPECIES: POSSIBLE IMPLICATIONS FOR THE EMERGENCE OF LIFE

S. Jheeta

*Network of Researchers on the Chemical Emergence of Life,
sohan@sohanjheeta.com*

KEYWORDS:

emergence of life, reactive oxygen species, evolution, extinction, ROS

ABSTRACT:

How did life begin on the Earth? Although there are more than twenty hypotheses in literature which claim the way forward for the emergence of life, in this vein, the reactive species of oxygen may have played an equally pivotal role. Whilst it is true that the chemistry of Reactive Oxygen Species (ROS) has been known about since the 1950's (and has often been referred to as free radicals in the commercial sector), its part in the emergence of life was, perhaps, first put forward by Prof Nick Lane (UCL) in his aptly named book entitled: "OXYGEN: The Molecule that Made the World (2003)". However, according to the molecular orbital theory it is now considered that dioxygen (also referred to as a singlet, $1O_2$) is a highly unstable molecule compared to triplet oxygen $3[O_2]$ — the latter is more stable as its two π^* electrons have parallel spins. As a result of its instability, singlet dioxygen can form numerous reactive species, as exemplified as follows: superoxide (\bullet , peroxide (\bullet) anions; hydrogen peroxide (H_2O_2), hydroxyl radicals ($\bullet OH$), hydroxyl ion (OH^-), Nitric oxide (NO), nitrogen dioxide (NO_2) and peroxytrite ($ONOO^-$).

Reactive species of oxygen can react with numerous other elements to form innumerable varieties of ions, free radicals and molecules; in essence, ROS can either donate unpaired electrons, or alternatively by accept electrons from other species. The fact that these newly formed exotic species are generated by ROS, warrants further investigation into the possible role it played in the emergence of life on Earth.

NO PROBLEM WITH THE WATER PROBLEM: USING UBIQUITOUS NANOGEOCHEMICAL CONDITIONS TO ACHIEVE ABIOTIC RNA SYNTHESIS IN WATER

F. Trixler

Ludwig-Maximilians-Universität München, Munich, Germany, f.trixler@lmu.de

KEYWORDS:

origin of life, RNA, water problem, water paradox, prebiotic chemistry, chemical evolution, nanogeochemistry, nanogeoscience, nanofluid

ABSTRACT:

Water has a paradoxical effect on life: the synthesis of nucleic acids (RNA, DNA) and proteins is thermodynamically prohibited by water and existing biopolymers are degraded by it via hydrolysis. Despite these effects water is the basis for all life as we know it. Models on prebiotic chemical evolution have to deal with this paradox which is called "the water problem" in theories on the origins of life. Existing approaches on prebiotic RNA synthesis need special conditions such as dry-wet cycles to temporarily remove water via evaporation, setting high temperatures, adding condensing agents or using other solvents than water. But these approaches have a disadvantage when considering a key principle in evolution: evolutionary conservatism. This principle is derived from observations that evolution always builds on existing pathways. By taking this principle into consideration prebiotic plausible hypotheses on chemical evolution and abiotic biopolymerisation should be based on conditions which are compatible or very close to the known physicochemical conditions in living cells.

In this talk a way to induce abiotic, spontaneous syntheses of RNA is presented that runs entirely in water [1, 2]. Results based on fluorometry, PCR, capillary gel electrophoresis and next generation sequencing reveal the formation of RNA strands with sequence complexity and lengths of up to 4000 nucleotides and more. This is achieved by exploiting non-classical properties of water. Such properties arise when a nanofluid behaviour of water emerges between micro- and nanoparticles in a dense aqueous suspension. In a geological context aqueous particle suspensions are ubiquitous settings and represent nanogeochemical environments for vicinal and nanoscale confined water. Dense aqueous particle suspensions with such non-classical, temporal nanoconfined water between particles can be regarded as being analogous to the highly crowded intracellular environment of living cells. Our abiotic RNA synthesis approach within an analogous nanogeochemical model setting can thus be regarded as being consistent with the conservative nature of evolution and is discussed in this talk as a plausible prebiotic solution to the water paradox.

REFERENCES:

- [1] Greiner de Herrera A., Markert T., Trixler F. Temporal nanofluid environments induce prebiotic condensation in water // *Communications Chemistry*. 2023. V. 6. No. 69. <https://doi.org/10.1038/s42004-023-00872-y>.
- [2] Trixler F. Origin of Nucleic Acids // *Prebiotic Chemistry and the Origin of Life* / eds. A. Neubeck, S. McMahon. Springer Nature. 2021. P. 117–137. https://doi.org/10.1007/978-3-030-81039-9_5.

NEARBY SUPERNOVAS AND GAMMA RAY BURSTS AS POSSIBLE SOURCES OF THE SHARPLY INCREASE OF MUTATIONS RATE AND LETHAL EFFECTS FOR EARTH'S BIOSPHERE

A. K. Pavlov

loffe Institute, Saint Petersburg, Russia, anatoli.pavlov@mail.ioffe.ru

KEYWORDS:

cosmic rays, Supernova, mutations, mass extinction

INTRODUCTION:

The work considers the modelling of nearby supernova (SN) effects on Earth's biosphere via cosmic rays (CRs) accelerated by shockwaves. The rise of the radiation background on Earth resulted from the external irradiation by CR high-energy particles and internal radiation in organisms by the decay of cosmogenic ^{14}C is evaluated. We have taken into account that the CR flux near Earth goes up steeply when the shockwave crosses the Solar System, while in previous works the CR transport was considered as purely diffusive. Our simulations demonstrate a high rise of the external ionization of the environments at Earth's surface by atmospheric cascade particles that penetrate the first 70–100 m of water depth. Also, the cosmogenic ^{14}C decay is able to significantly increase the internal irradiation of the surface biosphere and deep ocean organisms. We analyzed the probable increase in mutation rate and estimated the distance between Earth and an SN, where the lethal effects of irradiation are possible. Our simulations demonstrate that for SN energy of around 10^{51} erg the lethal distance could be ~ 18 pc. We also analyzed Galactic Gamma Ray Bursts and solar superflares as possible sources similar effects.

According to long-lived radionuclide ^{60}Fe concentration measurements in the deep-sea manganese crust, at least two supernova (SN) explosions have occurred at a distance of less 100 pc from Solar system during the last 10 million years [1]. Modern models of cosmic ray (CR) acceleration demonstrate that there is a sharp rise in the cosmic ray (CR) intensity at the shockwave and beyond. So the local CR flux is increased when the SN shock has crossed the Solar System. Then it remains almost constant during the period from hundreds to hundreds of thousands of years depending on the SN kinetic energy E_{SN} and on the distance L between Earth and an SN.

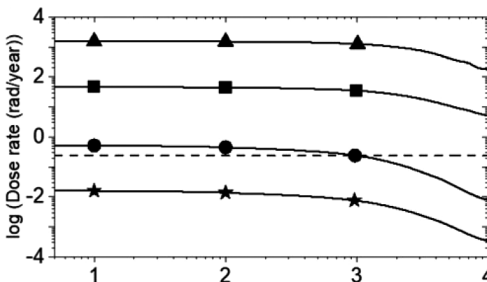


Fig. 1. The average absorbed dose rates of external irradiation as functions of the water depth (Triangles — $L = 6.5$ pc, Squares — $L = 17$ pc, Circles — $L = 42$ pc, Stars—modern local interstellar spectrum). Horizontal dashed lines represent the modern radiation background from all terrestrial sources (UNSCEAR, 2008)

We used the CR fluxes $J(E,t)$ at the forward shock taken from the results of numerical simulations of the particle shock acceleration performed by [2]. Using Geant4 code, we carried out simulation of the nuclear cascade in the atmosphere that is produced by CR particles. Then we calculated the accumulation of external ionizing radiation in water at the Earth surface

for different depth of water layer. Ionization losses in water are very close to the losses in any organisms and they were used for estimating absorbed doses. Dose accumulation rate is presented on Figure 1.

Besides the external ionization by CRs, there is also an internal irradiation increase of organisms because of additional production of cosmogenic radionuclides in the atmosphere and their subsequent absorption. From the point of biological impact, the most effective isotope is ^{14}C , because all organic molecules consist of carbon. Therefore, radiocarbon decay makes significant contribution to the internal irradiation and, thus, potential DNA damage in cells. That raises the rate of mutations and the probability of extinctions if the $^{14}\text{C}/^{12}\text{C}$ isotopic ratio is high enough. The results of internal radiation doses increases are presented on Figure 2

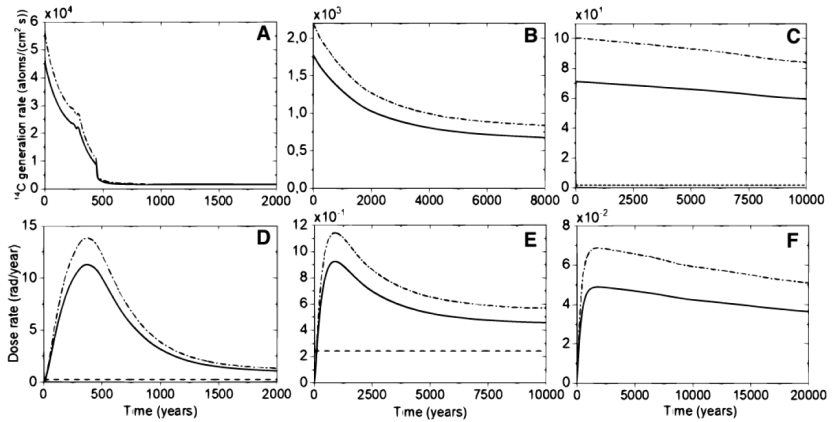


Fig. 2. The ^{14}C production rates in the atmosphere (A, B, C) and absorbed dose rates in the biosphere (D, E, F) resulted from ^{14}C decay and calculated using the CR spectra from the work of Zirakashvili and Ptuskin (2012) as functions of time for $L = 6.5$ pc (A, D), $L = 17$ pc (B, E), $L = 42$ pc (C, F). The moment $t = 0$ corresponds to the moment of the maximum of the CR intensity, when the SN shock crosses the Solar System. Dotted horizontal line in panel C and dashed horizontal lines in panels D and E represent the current ^{14}C production rate in the atmosphere ~ 1.7 atoms/cm 2 -s and the current radiation background from all terrestrial sources (0.24 rad/year), respectively. The low geomagnetic field case with $\mu = 0.1$ is illustrated by the dash-dotted curves, and the case $\mu = 1$ is shown by the solid curves.

CONCLUSION:

The CRs from nearby SNe are able to trigger mutations and mass extinctions of terrestrial organisms.

REFERENCES:

1. Wallner A., Froehlich M. B., Hotchkis M. A. C. et al. 60Fe and 244Pu deposited on Earth constrain the r-process yields of recent nearby supernovae // *Science* 2021. V. 372(6543). P. 742–745. DOI: 10.1126/science.aax3972.
2. Zirakashvili V. N., Ptuskin V. S. Numerical simulations of diffusive shock acceleration in SNRs // *Astropart Phys.* 2012. V. 39–40. P. 12–21. DOI: 10.1016/j.astropartphys.2011.09.003.

BIOLOGICAL RESEARCHES IN THE DEEP UNDERGROUND FACILITIES OF BAKSAN NEUTRINO OBSERVATORY AND IT'S RELEVANCE TO ASTROBIOLOGY ANALOGUE STUDIES

M. P. Zarubin¹, E. V. Kravchenko¹, K. A. Tarasov¹, A. M. Gangapshev², A. S. Yakhnenko¹

¹ Dzhelepov Laboratory of Nuclear Problem, Joint Institute for Nuclear Research, Dubna, Russia, mzarubin@jinr.ru

² Institute for Nuclear Research, Moscow, Russia

KEYWORDS:

deep subsurface life, Baksan Neutrino Observatory, astrobiology analogue, extremophiles, cosmic radiation

ABSTRACT:

The deep underground laboratories of the physical research centers are highly perspective for conducting biological experiments in the fields of biophysics, radiobiology, astrobiology, microbiology and medicine. Molecular Genetics Group of Dzhelepov Laboratory of Nuclear Problems of the Joint Institute for Nuclear Research (Dubna) initiated collaborative biological research in the tunnel of Baksan Neutrino Observatory (INR RAS, Neutrino village) and in the deep underground low radiation background laboratory (DULB-4900), located 2 km underground, beneath Andyrchy mountain (3937 m. a. s. l.), which is 21.9 km from dormant volcano Elbrus (North Caucasus, Russia).

The biological experiments have been started in December of 2019 [1, 2] and aimed to record for the first time the response to nearly complete absence of natural background radiation at the transcriptomic level in the complex model organism – fruit fly *Drosophila melanogaster*. Fruit flies were exposed in low background radiation conditions of DULB-4900 (~ 16 nGy·h⁻¹) and natural background radiation conditions in the surface building (~ 190 nGy·h⁻¹), that resulted in more than 10-time reduction of background radiation, and the transcriptomic analysis was performed. The results were analyzed through comparative transcriptomic analysis with assumption of effects of various types of stresses. The list of 77 differentially expressed genes was obtained for *D. melanogaster* exposed to low background radiation in DULB-4900 relatively to organisms in the natural background radiation [1]. For fruit flies in DULB-4900, genes, associated with immune response and response to stimuli, were up-regulated, and genes, involved in primary metabolic processes, were down-regulated. Changes in gene expression reflected an adaptive response to conditions of DULB-4900, which are stressful and not typical for terrestrial organisms, possibly due to the chronic lack of external natural stimuli [1]. Further biological experiments are focused on the impact of the cosmic component of natural background radiation and mainly on high-energy or relativistic muons (>1 GeV/c), which are close to atmospheric muons and in this way effects in organism can be simulated. On that goal, experiments are carried out in DULB-4900 of Baksan Neutrino Observatory, which provides almost complete shielding of atmospheric muons, and at muon beam of U-70 accelerator facility of NRC IHEP (Protvino). Notably, the impact of secondary cosmic radiation is an important issue for astrobiology and the study is relevant to many locations in the Universe [3].

Studies of Molecular Genetics Group of Dzhelepov Laboratory of Nuclear Problems is focused on natural mechanisms of extreme stress-resistance [4], due to this another branch of biological researches in Baksan Neutrino Observatory is dedicated to studies of deep underground microorganisms surviving in 2-km-deep granitic rocks. Studies of Deep Life (>1 km) reveal one of the less investigated ecosystems on Earth, which has an outstand-

ing potential for astrobiology analogue researches [5, 6]. Baksan Neutrino Observatory is one of the deepest easily-accessible locations in North Caucasus and Russia and, notably, it is in proximity to Elbrus Volcanic Center. Our group performs metagenomic analysis of the biofilm community of deep underground mineral spring. The study was accomplished by the cultivation of some microorganisms and have already lead to the discovery of several novel genera and species of bacteria [7]. The exploration of unique microbial communities in Baksan Neutrino Observatory is an opportunity to discover one of the deepest microbiomes ever studied in North Caucasus and Russia, which can contribute to studies of the global distribution of life in deep underground environments. In conclusion, this study outlines that deep underground locations of Baksan Neutrino Observatory are perspective as the astrobiology relevant-site.

REFERENCES:

- [1] *Zarubin M., Gangapshev A., Gavriljuk Y. et al.* First transcriptome profiling of *D. melanogaster* after development in a deep underground low radiation background laboratory // PLoS One. 2021. V. 16. No. 8. DOI: 10.1371/journal.pone.0255066.
- [2] *Zarubin M. P., Kuldoshina O. A., Kravchenko E. V.* Biological Effects of Low Background Radiation: Prospects for Future Research in the Low-Background Laboratory DULB-4900 of Baksan Neutrino Observatory INR RAS // Phys. Part. Nucl. 2021. V. 52. No. 1. P. 19–30. DOI: 10.1134/S1063779621010056.
- [3] *Ferrari F., Szuszkiewicz E.* Cosmic rays: A review for astrobiologists // Astrobiology. 2009. V. 9. No. 4. P. 413–436. DOI: 10.1089/ast.2007.0205.
- [4] *Zarubin M., Azorskaya T., Kuldoshina O., S. Alekseev et al.* The tardigrade Dsup protein enhances radioresistance in *Drosophila melanogaster* and acts as an unspecific repressor of transcription // iScience. 2023. V. 26. No. 7. Article 106998. DOI: 10.1016/j.isci.2023.106998.
- [5] *Onstott T. C. et al.* Paleo-Rock-Hosted Life on Earth and the Search on Mars: A Review and Strategy for Exploration // Astrobiology. 2019. V. 19. No. 10. P. 1230–1262. DOI: 10.1089/ast.2018.1960.
- [6] *Bashir A. K. et al.* Taxonomic and functional analyses of intact microbial communities thriving in extreme, astrobiology-relevant, anoxic sites // Microbiome. 2021. V. 9. No. 1. DOI: 10.1186/s40168-020-00989-5.
- [7] *Tarasov K. et al.* *Cytobacillus pseudoceanisediminis* sp. nov., A Novel Facultative Methylophilic Bacterium with High Heavy Metal Resistance Isolated from the Deep Underground Saline Spring // Curr. Microbiol. 2023. V. 80. No. 1. P. 31. DOI: 10.1007/s00284-022-03141-8.

THE EXO-UV PROGRAM: LATEST ADVANCES OF EXPERIMENTAL STUDIES TO INVESTIGATE THE BIOLOGICAL IMPACT OF UV RADIATION ON EXOPLANETS

X. C. Abrevaya^{1,2,3}, P. Odert³, M. Leitzinger³, O. Opezzo⁴,

G. J. M. Luna⁵, M. R. Patel⁶, A. Hanslmeier³

¹ Instituto de Astronomía y Física del Espacio, UBA-CONICET, Buenos Aires, Argentina, *ximena.abrevaya@gmail.com*

² Facultad de Ciencias Exactas y Naturales, UBA, Buenos Aires, Argentina

³ Department of Astrophysics and Geophysics, Institute of Physics, University of Graz, Austria

⁴ Departamento de Radiobiología, Comisión Nacional de Energía Atómica, Argentina

⁵ 5CONICET — Universidad Nacional de Hurlingham, Hurlingham, Argentina

⁶ School of Physical Sciences, Open University, Milton Keynes, U.K

KEYWORDS:

astrobiology, flares, stellar activity, habitability, microorganisms, interdisciplinary

ABSTRACT:

The EXO-UV program is an international interdisciplinary collaboration between astrophysicists and biologists aimed to seeking and expanding the characterization of UV radiation (UVR) environments of exoplanets through an approach that involves a combination of astrophysical studies with biological experiments. UVR is of relevance because reaches the surface of the planet and can constrain the surface habitability of a planet. The particular wavelengths within the UVR range will depend on the atmospheric composition of the planet and the spectral energy distribution of the star. Moreover, high UVR fluxes that are emitted during flares and superflares are of high interest to be studied in this context because of the so far limited information about their biological impact. This EXO-UV program successfully gave origin to the first experimental study about the biological effects of high UVR fluences on life, such as those emitted during flares or superflares. This study involved the planet Proxima b, the closest potentially habitable exoplanet to the solar system, which orbits a dM star, Proxima Centauri [1]. As next step in our program, we focused in the TRAPPIST-1 planetary system as it has been of high interest for the scientific community since its discovery in 2017. The TRAPPIST-1 system, which orbits the ultra-cool dwarf star TRAPPIST-1, consists of seven planets, three of them supposed to be in the habitable zone (e, f, and g). Among the research intended to evaluate the chances of these planets to host life, several studies aimed to investigate the impact of stellar UVR on the planetary surfaces both from quiescent and flare fluxes. The approach involved in studies carried out by other authors, implied the use of calculations derived from data existing in the literature from experiments with microorganisms irradiated at low fluence rates and fluences. In contrast to this approaches, we performed specific laboratory experiments to re-evaluate the results obtained previously by other authors. Our results show that previous studies underestimated the chances of “life as we know it” to tolerate these fluences, both in the case of UVR-tolerant or susceptible microorganisms. Other experimental studies made by our group now intend to study the biological effect of repetitive flares. In this talk, I am going to present the latest results that are part of our EXO-UV program.

REFERENCES:

- [1] Abrevaya X. C., Leitzinger M., Opezzo O. J. et al. The UV surface habitability of Proxima b: first experiments revealing probable life survival to stellar flares // MNRAS. 2020. V. 494. P. L69–L74.

**SESSION 7. ASTROBIOLOGY (AB-PS)
POSTER SESSION**

VARIATIONS OF F10,7 ON NEW DATES OF METEOR SHOWER MAXIMA

A. B. Tertyshnikov

Institute of Applied Geophysics, Moscow, Russia, atert@mail.ru

KEYWORDS:

cosmic dust, meteor showers, solar radiation, K-index, ar-index, variations, generalized portraits

ABSTRACT:

Applied results of astrophysical research are most often associated with cosmic dust and meteor showers. The collection of meteor observations from around the world provides a comprehensive study of meteor showers and their relationship to comets and interplanetary dust. The International Meteor Organization has been operating since 1988. In 2006, the International Astronomical Union officially approved the names of meteor showers, the number and the three-letter code, and determined their characteristics. At the same time, there were small discrepancies in the dates of the maxima of the “new” and “old” meteor showers before 2006, which led to the study of their manifestation in the intensity of variations in solar activity. To form a “generalized portrait” of variations in solar activity in the maxima of meteor showers, data on the solar radiation flux at a wavelength of 10.7 cm (F10,7) were used. To increase the uniformity and comparability of the analyzed data, a sliding 5-day window and normalization of current average daily values were used to increase the comparability and uniformity of the data. In the analysis of the new dates, 135 strong and medium-intensity meteor showers 2019–2023 and 30 weak meteor showers were used. The variations of the normalized F10.7 value amounted to tenths of a percent and differed for flows of different intensity. The coefficient of variation of the normalized value F10.7 is maximum per day for the maximum of strong and medium meteor showers and minimum for weak ones. The coefficient of asymmetry and the coefficient of kurtosis were maximal on the next day after the date of the maximum meteor shower, and for weak ones — on the date of the meteor shower, but with a lower amplitude. Thus, a weak effect of variations of the normalized value of F10.7 in the maxima of strong and medium flows was revealed. Perhaps because of the turbidity of the atmosphere. For comparison, estimates obtained for the “old” 175 dates of maximum meteor showers 2019–2023 were used. At the same time, variations of F10.7 turned out to be more pronounced than for the “new” dates. According to the “old” dates, there are features of changes in the K-index and the ar-index on the eve of the maximum meteor showers. According to the “new” dates, these effects are absent. What unites the “new” and “old” dates of meteor shower maxima is the presence of small variations of F10.7, which can initiate the onset of thermodynamic variations in the middle and lower atmosphere. Perhaps this is the effect of a slight turbidity of the atmosphere. The technical means of recording meteor and cosmic dust, as well as the effect of the “dust pause” in the upper atmosphere, are considered.

BACTERIA OF THE COOLANT FLUID TRIOL FROM THE ACTIVE THERMAL CONTROL SYSTEM OF THE INTERNATIONAL SPACE STATION

A. A. Guridov¹, S. N. Zaitsev², S. V. Poddubko¹

¹ Institute for Biomedical Problems RAS, Moscow, Russia, gaa1707@mail

² Khrunichev State Research and Production Space Center, Moscow, Russia

KEYWORDS:

spore-forming bacteria, Bacillus, ISS, planetary protection, radiation, coolant fluid, ATCS

ABSTRACT:

The International Space Station is a permanent home not only for astronauts, but also a habitat for bacteria, which are constant companions of humans in anthropogenic habitats. The most studied ecological niches on the ISS are the internal surfaces of the station, since they are in constant contact with humans and are of interest for medical monitoring of the contamination of microorganisms in a hermetically sealed object in Earth orbit. However, one of the unexplored niches on the ISS turned out to be the coolant of the Active Thermal Control System (ATCS) of the ISS Russian Segment modules. A liquid called "Triol" circulates in the internal hydraulic loop, collects heat from instruments and equipment, transfers it to the external hydraulic circuit and then to the radiators-emitters of the thermal control system of the ISS RS module.

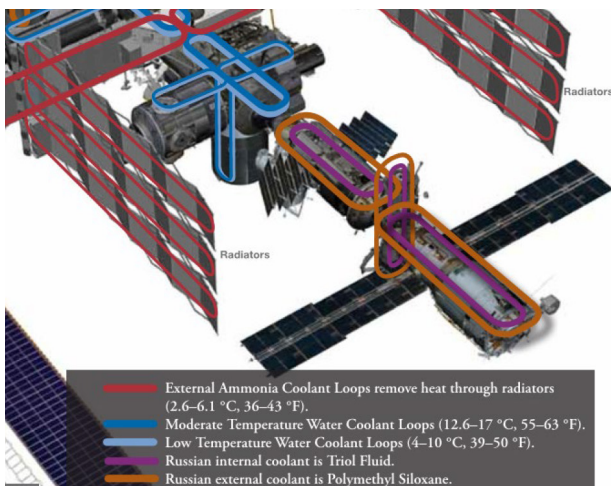


Fig. 1. Thermal Control System of ISS [1]

In order to study the possible habitats of bacteria on the ISS, a sample of the coolant fluid was analyzed. A sample of Triol fluid was delivered to Earth from the ISS in October 2023 inside a replacement pump panel for the internal hydraulic circuit. The replacement pump panel was opened under aseptic conditions in the microbiology laboratory and the Triol fluid contained therein was collected in sterile vials. Next, the liquid was studied for the content of viable bacterial cells by plating on various nutrient media. In different portions of Triol, different numbers of viable cells were found from $3 \cdot 10^1$ to $2.2 \cdot 10^4$ colony-forming units, which may be due to the formation of aggregates by bacteria since a small sediment was observed at the bottom of the vial with liquid. As a result of inoculation on solid TSA medium, viable strains of bacteria of the following species were detected: *Paenibacillus glucanolyticus*, *Bacillus mycoides*, *Bacillus subtilis*, *Bacillus licheniformis*, *Bacillus mojavensis*, *Bacillus halotolerans*. The isolated bacterial

strains were identified using a Biotyper Sirius MALDI-TOF MS mass spectrometer from Bruker using the method of automatic identification by mass spectrometry of proteins. The discovered bacterial species are spore-forming. Endospores are resting, extremely stable forms formed by bacteria of the phylum Bacillota, to which the bacterium can be reduced under unfavorable conditions. Endospores allow bacteria to remain dormant for long periods of time, even centuries. The Active Thermal Control System on the ISS RS has been in operation since the station's inception, so it is assumed that the discovered strains of bacteria were in Earth's orbit for up to 25 years "in a preserved form" inside the thermal control system. Perhaps the ability to form spores allowed the bacteria to survive in the Triol fluid under extreme operating conditions on the ISS.

An important factor limiting the ability of bacteria to survive in space is a higher background radiation. Therefore, in order to study the resistance to radiation of isolated cultures, suspensions of strains from the Triol sample obtained from the ISS were irradiated with gamma radiation with a dose of 15 kGy. Then the surviving spores were counted by plating on TSA nutrient medium. This dose was chosen as a lethal for many spore-forming *Bacillus* strains [2], and therefore sterilizing dose, used in various industries. Bacterial strains isolated from a Triol fluid sample stored on Earth at the manufacturer's plant were selected as a reference group of strains. As in the case of "space" strains, different spore-forming species of the phylum Bacillota (*P. glucanolyticus*, *B. mycoides*, *Cytobacillus firmus*, *Bacillus horikoshii*, *Bacillus circulans*) were found in the control "terrestrial" sample. An experiment with irradiation showed a decrease in the number of viable spores by 6-7 orders of magnitude for "space" strains, while almost no viable spores were found among "terrestrial" strains (a decrease in the number of viable spores by 8-10 orders of magnitude). This phenomenon can be explained by selection under the pressure of the factor of increased background radiation, through which the "space" strains passed during the twenty-five years of forced "exposure" on the ISS. Therefore, the most resistant spores were discovered during microbiological analysis of the sample from the ISS. If the bacteria have undergone a mechanism of adaptation to a set of conditions inside the ISS RS thermal control system, then additional research is needed on the ability of these bacteria to multiply inside the Triol fluid and, thus, acquire new properties.

New data on the ability of bacteria to survive or even multiply within liquid thermal control systems of spacecraft should be taken into account for space missions controlled by planetary protection requirements. The possibility of bacteria to contaminate the environment from spacecraft thermal control systems as a result of emergency situations should also be considered when planning the microbial load in such spacecraft.

REFERENCES:

- [1] Reference guide to the International Space Station. National Aeronautics and Space Administration, 2010. 140 p.
- [2] Kharin S. A., Deshevaya E. A., Fialkina S. V. et al. Studies of the resistance of "terrestrial" and "space" *Bacillus licheniformis* strains to the extreme spaceflight factors // *Aviakosmicheskaya i Ekologicheskaya Meditsina*. 2022. V. 56. No. 1. P. 76–85 (in Russian).

INFORMATION

address:

Space Research Institute (IKI)

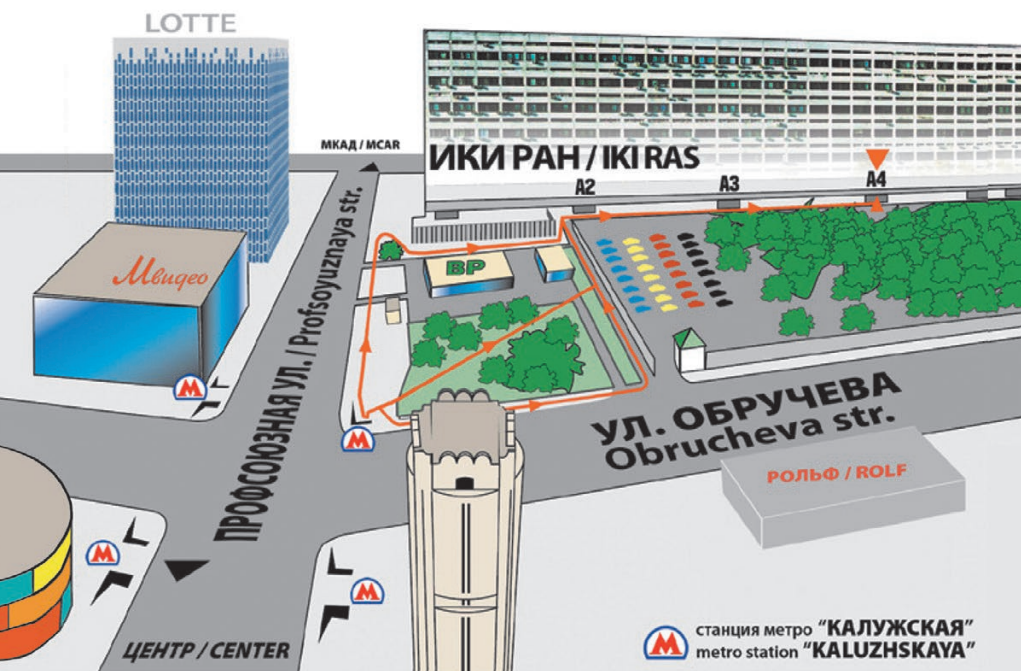
Profsoyuznaya street 84/32

post code 117997

metro station: Kaluzhskaya

Moscow, Russia





ИКИ РАН

площадь академика Келдыша
метро «Калужская», первый вагон из центра, по тоннелю – прямо,
по второму поперечному тоннелю – направо, выход на площадь,
далее по стрелкам на схеме

IKI RAS

You should get off at "Kalyzhskaya" metro station using the southern exit.
After leaving a station lobby through glass doors you should go straight
to the end of the tunnel, then take right and use the stairs to get to the surface.
From this point you may follow either arrow on this map

REGISTRATION AND INFORMATION DESK

location: IKI, entrance A-4

time:

21 october, 9:00–18:00

22–25 october, 10:00-18.00

ORAL SESSIONS

location:

IKI conference hall, second floor

Sessions: Mars, Venus, Giant Planets, Moon and Mercury, Small Bodies, Extrasolar Planets Astrobiology

21–25 october

POSTER SESSIONS

online discussion

COFFEE BREAKS, WELCOME PARTY, RECEPTION

location:

- IKI Winter Garden, second floor – Coffee Breaks
- IKI conference hall, second floor – Welcome Party
- IKI exhibition hall, ground floor – Reception

INTERNET ACCESS AND WIFI

there is Internet access in and near the conference hall

SOCIAL PROGRAM

	BOLSHOI	OPERETTA	MUSICAL THEATER	NOVAYA OPERA	HELIKON	KREMLIN	MMDM
20.10	12.00 New Stage, opera LE NOZZE DI FIGARO 19.00 New Stage, opera LE NOZZE DI FIGARO	14.00 musical ANNA KARENINA 19.00 musical ANNA KARENINA	19.00 opera, première NOT LOVE ALONE				
21.10			19.00 opera EVGENIY ONEGIN				
22.10	19.00 Historic Stage, organ music concert AUTUMN FANTASY	19.00 musical performance GRAF ORLOV		19.00 theatre performance PETR 1			
23.10	19.00 New Stage, opera TOSCA	19.00 musical performance GRAF ORLOV	19.00 opera AIDA	19.00 theatre performance PETR 1	19.00 Shakhovskaya Hall KAFFEEKANTATE 20.30 Shakhovskaya Hall KAFFEEKANTATE		
24.10	19.00 Historic Stage, ballet LA FILLE DU PHARAON 19.00 New Stage, opera TOSCA	19.00 musical performance GRAF ORLOV	19.00 opera AIDA			19.00 ballet RAYMONDA	
25.10	19.00 Historic Stage, ballet LA FILLE DU PHARAON 19.00 New Stage, opera TOSCA	19.00 musical performance GRAF ORLOV		19.00 theatre performance BELIY. PETERSBURG			19.00 Svetlanovsky Hall, concert CONCERTO GRANDIOSO. CLASSICO
26.10	12.00 Historic Stage, ballet LA FILLE DU PHARAON 19.00 Historic Stage, ballet LA FILLE DU PHARAON 19.00 New Stage, opera TOSCA	14.00 musical performance GRAF ORLOV 19.00 musical performance GRAF ORLOV					19.00 Svetlanovsky Hall, concert SERGEY GILIN AND OKESTRA SYMFO-JASS
27.10	12.00 Historic Stage, ballet LA FILLE DU PHARAON 19.00 Historic Stage, ballet LA FILLE DU PHARAON 19.00 New Stage, opera TOSCA	14.00 musical performance GRAF ORLOV 19.00 musical performance GRAF ORLOV					

BOLSHOI

<https://bolshoi.ru/>

BOLSHOI THEATRE

OPERETTA

<https://mosoperetta.ru/>

OPERETTA THEATRE

MUSICAL THEATER

<https://stanmus.ru/>

STANISLAVSKY AND NEMIROVICH-DANCHENKO MUSIC THEATRE

NOVAYA OPERA

<https://novayaopera.ru/>

NOVAYA OPERA

HELIKON

<https://www.helikon.ru/>

HELIKON OPERA

KREMLIN

<https://kremlinpalace.org/>

STATE KREMLIN PALACE

MMDM

<https://www.mmdm.ru/>

MOSCOW INTERNATIONAL PERFORMING ARTS CENTER

LUNCH POINTS NEAREST TO IKI



- ИНСТИТУТ КОСМИЧЕСКИХ ИССЛЕДОВАНИЙ РАН,**
столовая, 1 этаж, секция А3
SPACE RESEARCH INSTITUTE,
Food center, Ground Floor, Section A3
- ТЦ “КАЛУЖСКИЙ”,**
ул. Профсоюзная, 61А, зона ресторанов, 2 этаж
“KALUZHSKIY” Market Center,
Profsoyuznaya Street, 61A, 2 Floor
- КАФЕ “АНДЕРСОН”,**
ул. Обручева, 30/1
CAFÉ “ANDERSON”,
Obrucheva street, 30/1
- ИНСТИТУТ ПРИКЛАДНОЙ МАТЕМАТИКИ РАН,**
столовая, 1 этаж
INSTITUTE OF APPLIED MATHEMATICS,
Food center, Ground Floor

